4th International Conference

ELMECO-4

ELECTROMAGNETIC DEVICES AND PROCESSES IN ENVIRONMENT PROTECTION

Nałęczów, Poland
September 2003

Conference Proceedings

Centre of Excellence for the Application
of Superconducting and Plasma Technologies
in Power Engineering

Institute of Electrical Engineering
& Electrotechnologies

Lublin University of Technology, Poland

38A Nadbystrzycka St.
20-618 Lublin
Poland
www: http://volt.pol.lublin.pl, http://www.asppect.pl
e-mail: elmeco@eltecol.pol.lublin.pl
tel/fax (+48-81) 5381289, 5253694

The conference has been supported by the European Commission within the 5th Framework Programme - ASPPECT No ENK6-CT-2002-80668

4th International Conference

ELECTROMAGNETIC DEVICES AND PROCESSES IN ENVIRONMENT PROTECTION ELMECO - 4

September 2003

Nałęczów – Poland

Organised by:

Centre of Excellence for the Application of Superconducting and Plasma Technologies in Power Engineering
Institute of Electrical Engineering and Electrotechnologies
Lublin University of Technology, Poland

ISBN

Wydawnictwo Drukarnia Liber
ul. Szczerbowskiego 6, Lublin
tel./fax (81) 442 54 44

CONTENTS

Preface

The Conference „Electromagnetic Devices and Processes in Environment Protection" ELMECO was held in 2003 for the fourth time. Previous Conferences were held in 1994, 1997 and 2000. The Chair of Electrical Engineering always conducted pro-ecological activities in the field of electrical engineering. These activities were intensified in 1989 after recovering the independence and the commencement of educational projects TEMPUS within a framework of PHARE Programme. In the period of 1990 – 1993 the project JEP 0112/90 was realized, the main objective of which was the introduction to educational curricula for electrical engineers the speciality "Electromagnetic devices and technologies in environment protection". One of the activities realized within the project was the organization of international conference "Electromagnetic Devices and Processes in Environment Protection "ELMECO". The Conference ELMECO-1 was held in 1994 in Kazimierz on the premises of Journalists Guest House. 75 participants attended the conference. It was financially supported by the US Army. The following conferences ELMECO-2, ELMECO-3 and ELMECO-4 were held at the Training Centre "Energetyk" in Nałęczów and they were supported by TEMPUS Programme – JEP 0112/90 and JEP 11088/96.

The organizing institution of ELMECO Conference – the Institute of Electrical Engineering and Electrotechnologies in 2002 acquired within 6 Framework Programme the status of the Centre of Excellence for the Application of Superconducting and Plasma Technologies in Power Engineering (ASPPECT) and the financial support for the period 2003 – 2005. ELMECO-4 Conference followed by the workshops was organised as one of the activities of ASPPECT project. It gathered 70 participants who presented 53 scientific papers. Invited papers were presented by the following scientists: Prof. J.S. Chang (McMaster University, Canada), Prof. A.J. Moses (Wolfson Centre for Magnetics Technology, Cardiff University, UK), Prof. H.E. Wagner (Ernst-Moritz-Arndt-University, Greifswald, Germany), Prof. J. Janca (Technical University of Brno, Czech Republik), Prof. B. Mazurek (Electrotechnical Institute, Wrocław, Poland), Prof. I. Pollo (The Private University for the Protection of Environment, Radom, Poland), Prof. J. Mizeraczyk (Institute of Fluid Flow Machinery, Polish Academy of Sciences, Gdańsk, Poland), Prof. Z. Kołaciński (Technical University of Łódź, Poland), Prof. K. Cedzyńska (Technical University of Łódź, Poland), Prof. A. Cieśla (AGH-University of Science and Technology, Poland), Prof. K. Szmidt-Szałowski (Warsaw University of Technology, Poland), Prof. B. Susła (Poznań University of Technology, Poland).

Selected papers on plasma issues were published in the Journal of Advanced Oxidation Technologies and all papers presented during the Conference ELMECO-4 after discussion and reviewer's remarks have been included in this Proceedings.

I would like to thank all involved in the organization of the conference and in preparation for printing. I also want to thank all participants of the conference and invite to attend next ELMECO-5 in September 2005.

Tadeusz Janowski

PLASMA FOR ENVIRONMENT

4th International Conference **ELMECO**
Nałęczów, Poland
September 2003

PULSED ARC ELECTROHYDRAULIC DISCHARGE WATER TREATMENTS; NEXT GENERATION DIRECT PLASMA DRINKING AND WASTE WATER TREATMENT PROCESSES

Jen-Shih CHANG

Department of Engineering Physics
McMaster University
Hamilton, Ontario, Canada L8S 4M1

Abstract

Plasma treatment of drinking and waste water is not new. In the past, water was treated by ozone generated by non-thermal plasmas and this type of water treatment is called "the remote plasma method", where active species was generated by plasma and then injected to water. More recently, UV treatments for the water becomes essential for disinfections and this type of water treatments is called "indirect plasma method" since plasma generated UV lights was indirectly contact with water with thin glass. Direct plasma water treatment is the next generation technique which generates plasma inside water and simultaneously oxidize inorganics, urenna compounds and the VOCs in water as well as disinfections. In this paper, recent developments on the direct water treatment Pulsed Arc Electrohydraulic Discharge (PAED) will be critically reviewed and compared with Pulsed Corona ED, Pulse Power ED and Glow Discharge water treatment, etc.

INTRODUCTION

Electrohydraulic discharge plasma techniques have been used in various industrial water treatments such as removal of foreign objects (rust, Zebra mussels, etc.) deposited onto a wall [1,2,3], killing bacteria [7,9], controlling water qualities [4,5,6,8], decontamination of sludges [12], etc. Three different types of electrohydraulic discharge systems were used. The first system is based on the pulsed corona, the second system used pulsed arc discharges and the third system was pulsed power. The characteristics of these three different electrohydraulic discharge systems are compared in Table 1.

The pulsed corona system is operated at 10^2 to 10^3 Hz and the peak current is below 100 A with nsec order voltage rise. A streamer corona is generated in water and only weak shock waves and a small amount of bubbles are observed [10,11], however, this system generates strong UV radiation [13] and formation of radicals such as O_3, OH, etc., in

narrow region near corona discharge electrodes. The pulsed arc system is operated at 10^{-2} to 10^{2} Hz and the peak current is above 1 kA with μsec order voltage rise [14]. An arc channel generates strong shock wave with cavitation zone [15] and inside the bubbles is ionized (plasma bubbles) [16] as well as to form transient supercritical water conditions [18]. The strong ultraviolet emission and high radical density are observed to be only short-lived in cavitation zone [17]. Based on above principle, the pulsed arc system is mainly applied to sludge treatments or removal of foreign deposits from pipe walls and the pulsed corona system is limited to water quality control or killing bacteria. In this work, the pulsed arc electrohydraulic discharge plasma water treatment will be reviewed.

Table 1. Characteristics of different electrohydraulic discharge.

	Pulsed Corona (PCED)	**Pulsed Arc (PAED)**	**Pulsed Power (PPED)**
Operating Frequency [Hz]	10^{2}-10^{3}	10^{-2}□-$10^{□2}$	10^{-3}□-10
Current [A]	10-10^{2}	10^{3}□-10^{4}	10^{2}□-10^{5}
Voltage [V]	10^{4}□-10^{6}	10^{3}□-10^{4}	10^{5}□-10^{7}
Voltage Rise [sec]	$10^{□-7}$□-$10^{□-9}$	$10^{□-5}$□-$10^{□-6}$	10^{-7}□-10^{-9}
Pressure Wave Generation	weak	strong	strong
UV Generation	weak	strong	?

EXPERIMENTAL APPARATUS

Schematics of the pulsed arc power supply is shown in Figure 1. The system consists of three components: the constant current charger, the high voltage switch/power storage unit, and the arc electrodes (acoustic transmitter). Basic discharge control units with power supply are shown in Figure 1. The discharge system is driven by 120~130V input with constant current charging circuits. Once the current is charging 50 μf main capacitance, high voltage will be imposed between two air gap electrodes in a mechanical switch and the gap will be closed by pulsed discharges. The current stored in capacitances will flow into the electrode gap in the reactor with contaminated water and generate the arc channel. Control of charging voltage, V_{ch}, hence current or power, will be done by the air gap distances as shown in Figure 2, where it is only slightly influenced by primary side voltage and matching impedance before the air gap.

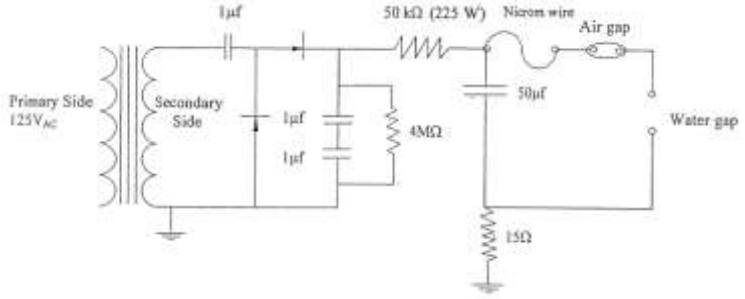

Fig. 1. Schematic of the pulsed arc power supply.

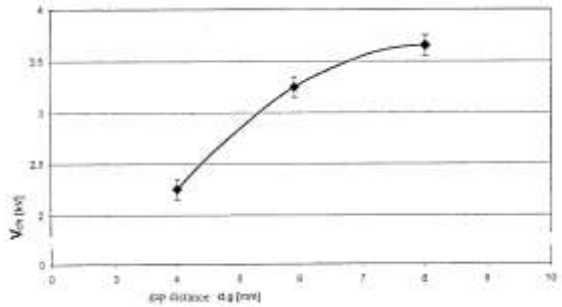

Fig. 2. Air gap breakdown voltage as a function of electrode gap distance [23].

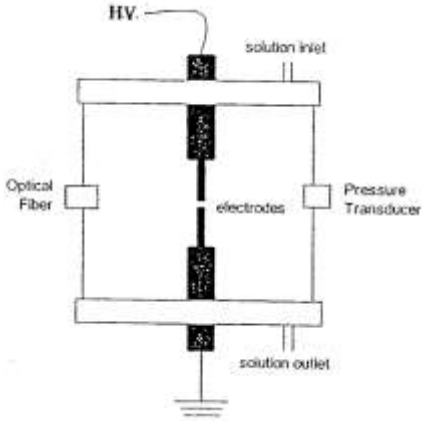

Fig. 3. Schematic of the pulsed arc electrodes and test reactor [23].

The pulsed arc and generated acoustic wave characteristics were tested in 30.48 cm diameter test chamber and are also shown in Figure 3. The transmitter is placed in the centre of chamber vertically and the wave propagation is measured at the wall as shown in Figure 3. Pressure waveforms are measured by the Piezo pressure transducer (Columbia Research Laboratories Inc., Model 4108) with electrostatic amplifier (Columbia Research Laboratories Inc., Model 4103). Tektronics 468 digital scope (400 MHZ) are used for record pressure, discharge current and voltage waveforms, and then analyzed by personal computers. Optical emission was observed by fibre optic spectrometer (PC1000 Ocean Optics Inc.). The pH was measured by pH metre (HANNA Inst. Co.) and ammonia ions in water were measured by ammonia sensor and water quality meter (5012 and U21EX, Horiba, Ltd.).

EXPERIMENTAL RESULTS

Typical current, voltage and power waveforms for a single-phase fresh water test are shown in Figure 4 for applied voltage at 2.3 kV. Figure 4 shows that the arc current and

voltage waveforms are dumping waves and wave approximately dumping to zero after 5.5×10^{-5} sec (55 μsec). Voltage waveform was immediately reduced from initial 2.3 kV after discharge current started to rise, then saturated at 750V for 20-30 μsec, and started to decrease again when the current became maximum around 1.2×10^{-5} sec. Hence, the power waveform exhibits behaviour similar to current waveforms as shown in Figure 5. The magnitude of the maximum current and power are around 4~5 [kA] and 3~4 [MW] respectively. The current rise (10 to 90% maximum) is around 4×10^{-5} [s] and the maximum dI/dt is 10^9 to 10^{10} [A/s], therefore a similar level EMP (electromagnetic pulse) protection design is required for circuits as lightning discharges. Then both maximum current, I_{max}, and maximum power, W_{max}, increase with increasing charging voltage V_{ch} as shown in Figure 5.

A typical pressure waveform observed at 15.8 cm from the pulsed arc is shown in Figure 5 for V_o = 2.3 kV. Figure 6 shows that a positive pressure wave P_s (shock wave) initially generated by an arc passing through this point followed by negative pressure waves P_E (Expansion Waves). During the discharge, an electromagnetic interference as well as the pressure induced by electromagnetic fields, i.e. $p = \underline{E} \bullet \underline{D} + \underline{H} \bullet \underline{B}$, is observed by a piezo-type pressure sensor. A shock wave with a 500~600 [kPa] maximum was observed after the pressure wave reached sensors at $6\sim7\times10^{-5}$ [sec] (Mach Number, M = 2 to 3) then the expansion wave will follow after $8\sim9\times10^{-5}$ [sec] with ~100 [kPa]. Wall reflections keep generating oscillating pressure waveforms as shown in Figure 6. The rise of the pressure wave is around $5\sim10\times10^{11}$ [Pa/s]. Both P_{Smax} and P_{Emax} increase with increasing V_{ch} as shown in Figure 7 except higher V_{ch} region for expansion waves. The magnitude of acoustic emission impulse is below 1 Pa μsec which is safe for small fish with body mass below 10^{-2} g but enough to kill bacteria [19] (see Appendix). The magnitude of pressure is the order of 0.1 MPa hence near the supercritical conditions can be generated inside the reactor.

A typical optical emission characteristics from the arc zone observed at the wall of the reactor via pyrex glass window is shown in Figure 8, where the cut off optical emission wavelength of the present optical system is below 295 and above 700 nm. Figure 8 shows that the strong 400 nm to 650 nm emissions as well as 320 and 380 nm (UV-A) emissions. The UV-A and UV-B are also evident in the reactor but UV-C cannot be confirmed with the present system because of the limitations of the optical system and light attenuation from 15.8 cm water. Figure 9a shows the optical emission intensity of (380 nm), the maximum emission as a function of V_{ch} for various times after discharge onset, where Figure 9b shows the reconstruction of the maximum optical intensity waveforms based on Figure 9a. The emission of light is similar to current and power waveforms but on a slightly different time scale as expected. The existence of OH, H and UV lights as shown in Figures 8 and 9 are expected to enhance chemical reactions as well as impacts to the microorganisms.

AN EXAMPLE FOR TREATMENT OF CHEMICAL CONTAMINANTS

PAED treatments with trace ammonia compounds and phenol were shown in Fig. 10. The pH value moved to neutral value (pH = 7) with increasing treatment time for NH_4OH as shown in Fig. 10, while the pH value slightly increases with increasing treatment time for Phenol. Based on spectroscopic observations of the present pulsed-arc system PAED generates strong UV radiation and formation of radicals such as O_3, OH, etc.; therefore,

these results evidenced that the effect of radical generation for pH alterations. This result also indicated that alkaline pH value is moving to neutral, and pulsed-arc has strong OH radical generation. Figure 10b also shows that a few kWh/m^3 cumulative energy inputs were required to remove 1 [mol/m^3] of NH_4OH by PAED.

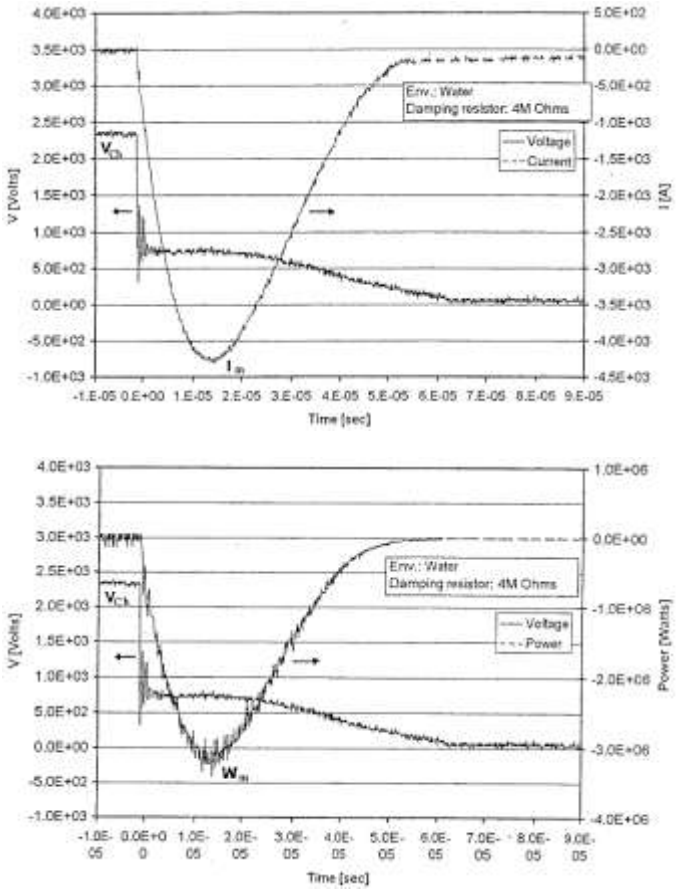

Fig. 4. Typical current (a), voltage (a) and power (b) waveforms for V_{ch}=2,3 kV [23].

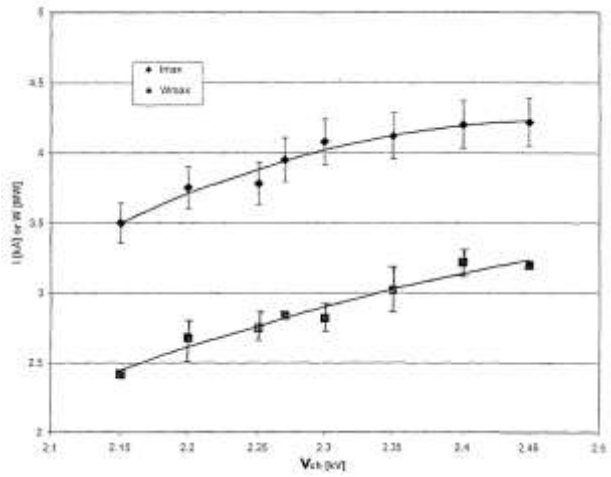

Fig. 5. Maximum current and power as a function of charging voltage [23].

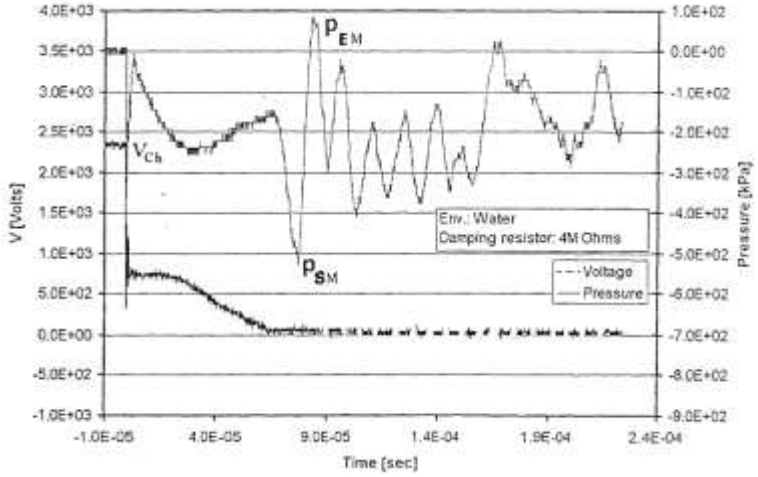

Fig. 6. Typical pressure waveforms corresponding to Fig. 4 [23].

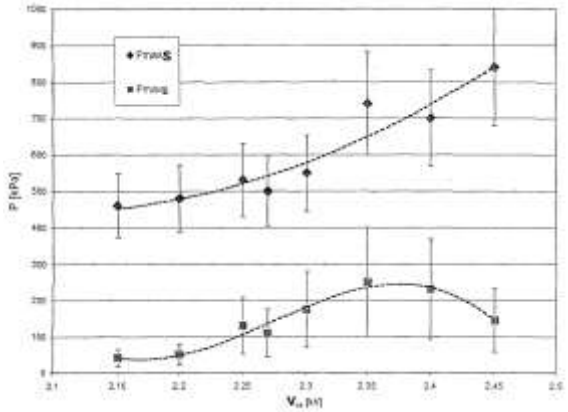

Fig. 7. Maximum and minimum pressures as a function of charging voltages [23].

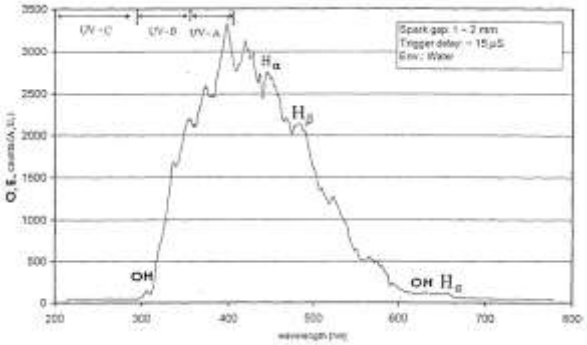

Fig. 8. Typical optical emission spectrum corresponding to Fig. 4 [23].

AN EXAMPLE FOR DISINFECTION OF WATER

The drinking water industry is faced with microbial contaminants that are challenging to remove or inactivate with conventional treatment technologies. Specialized and often costly technologies are required to treat particularly challenging target compounds such as protozoan pathogens (e.g., *Cryptosporidium parvum*) and viruses (e.g., adenovirus). Plasma technologies have the capability to treat water by several mechanisms including: shock waves, UV irradiation, radical reactions, electron processes, ionic reactions and thermal dissociation. Depending on the method of plasma generation, these technologies can take advantage of some or all of the aforementioned mechanisms. The three categories of plasma technologies are remote, indirect, and direct. Remote plasma technologies involve plasma generation in a location other than the medium to be treated (e.g., ozone). Indirect plasma technologies generate plasma near to, but not directly within, the medium to be treated (e.g., UV, electron beam). Direct plasma technologies (e.g., PAED and pulsed power electrohydraulic discharge (PPED)) have been developed that generate plasma

directly within the medium to be treated thereby increasing treatment efficiency by 1) direct application and 2) provision of all possible treatment mechanisms [22, 24].

PAED is a direct plasma technology in which the rapid discharge of stored electrical charge across a pair of submerged electrodes generates electrohydraulic discharges and forms a local plasma region. PAED effectively treats a range of contaminants broader than that of other conventional and emerging technologies [22]. Preliminary research has indicated that PAED offers advantages over indirect plasma methods in that it can provide comparable or superior treatment of microorganisms, algae, volatile organics, nitrogenous municipal waste compounds, and some inorganics [20-26]; these findings are qualitatively summarized in Table 2 [22]. Moreover, these benefits are available concurrently from one technology. As well, preliminary investigations conducted with a limited number of target compounds have indicated that effective water treatment with PAED utilizes less than 50% of the kilowatt-hours required by other plasma technologies (e.g., UV) for equivalent levels of treatment [28].

Table 2. Comparison of Plasma and Conventional Water Treatment Processes [22].

Target Compounds	Cl/ClO_2	Ozone	Electron Beam	PCED	PAED	UV-C
microorganisms	adequate	good	adequate	good	good	good
oxidation power	good	good	good	good	good	none
algae	none	partial	none	partial	good	adequate
urine components	adequate	good	good	good	good	none
VOCs	none	adequate	good	good	adequate	none
inorganics	none	partial	partial	adequate	adequate	none

Depending on the technology, the disinfection mechanisms of plasma technologies include 1) high electric fields; 2) reactions with radicals such as ozone, hydrogen peroxide etc; 3) UV irradiation; 4) thermal reactions; 5) pressure waves; and 6) electromagnetic pulses (EMP). The disinfection mechanisms and there relative strength in PAED systems are summarized in Table 3.

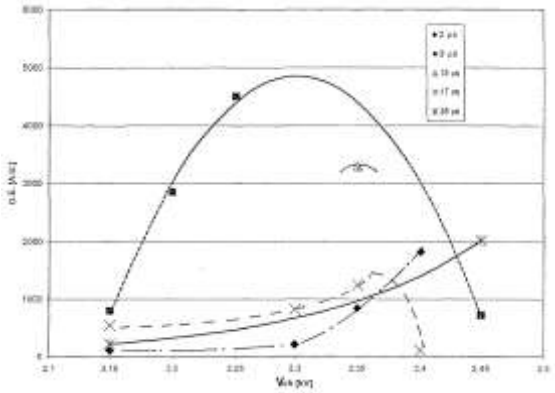

Fig. 9. Optical emission intensity as a function of charging voltage for various delay times from onset [23].

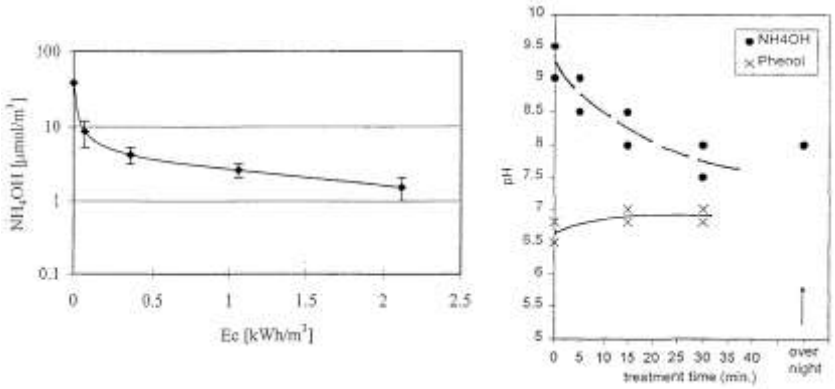

Fig. 10. The pH transient as a function of treatment time for NH_4OH and Phenol (a) and NH_4OH concentration in water as a function of cumulative energy input (b) [23].

Table 3. Summary of Electrohydraulic Discharge Disinfection Mechanisms.

Mechanism	PCED	PAED	PPED
High Electric Field	small	none	strong
Pressure Wave	none	strong	strong
UV Irradiation	small	strong	none?
Radical Reactions	small	strong	strong
Thermal	none	strong	none
EMP	none	none	strong

PAED systems are operated with low current rise at voltages of only a few kV and will generate strong UV, pressure waves, and high-density radicals in a cavitation zone. This low frequency (1 to 10 Hz) range also generates high temperature in a narrow arc channel. The strength of the pressure wave results in propagation from 10 to 100 m in flow channels, contributing to disinfection over a significantly wide range of detention times if the reactor design is optimized.

The relative ease of disinfection of *E. coli*, as compared to protozoan pathogens such as *Cryptosporidium parvum*, is commonly recognized. *E. coli* disinfection has been achieved with several treatment technologies, including UV irradiation [27]. Many strains of *E. coli* have demonstrated an ability to repair after irradiation with low- and medium-pressure UV.

E. coli inactivation with electrohydraulic discharges was first reported by Ching et al. [24]. From this work, the disinfection of 3 L of a 4.0 x 10^7 cfu/mL *E. coli* suspension in 0.01 M PBS at pH 7.4 by 50 consecutive electrohydraulic discharges with 4MJ/pulse.

Figure 1 shows the $\log_{10}$ inactivation of *E. coli* cells in PBS after a number of electrohydraulic discharges at an aqueous electrode gap distance of 1 mm. This figure clearly indicates average *E. coli* inactivation of 2.6-, 3.3-, and 3.6-log after the respective application of 6, 18, and 30 electrohydraulic discharges (corresponding to detention times of approximately 0.8, 1.5, and 5.8 minutes respectively). A logit plot of these data was not

constructed because of the relatively small number of data points and the high level of disinfection achieved within the first data point (6 electrohydraulic discharges).

It is noteworthy that the pattern of *E. coli* inactivation observed in the present experiments is similar to that observed by Ching et al. [24], in that the rate of inactivation is initially high, and decreases as the number of electrohydraulic discharges increases. The present observations differ from those of Ching et al. [23], however, as the present experiments achieved a slightly higher level of *E. coli* inactivation for the same number of discharges. This difference may be due to the fact that the present experiments employed a PAED system, while Ching et al. [24] used a PPED system. While both systems fall under the category of direct plasma technologies, they operate slightly differently, and as a result the UV radiation generated by PPED is much weaker than that generated by PAED [22].

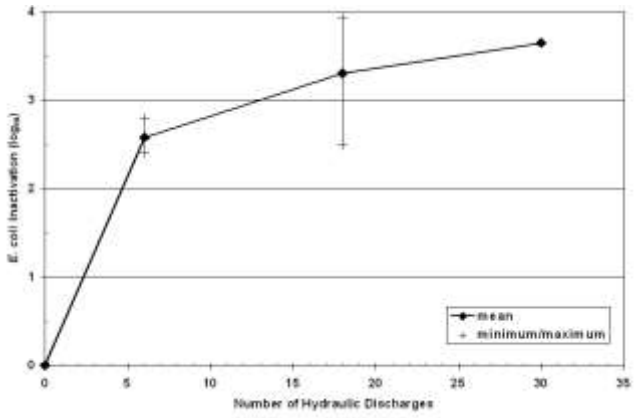

Fig. 11. PAED inactivation of *E. coli* suspended in 0.01M PBS at pH 7.4, 0.3 kJ/pulse [21].

CONCLUDING REMARKS

Preliminary experimental investigations have been conducted to study electrohydraulic discharge characteristics based on the pulsed arc. The results show that:

(1) the current rise in the present system is a few 10 μsec and a few MW peak power can be injected to the water every 18 sec;
(2) the discharge currents increases with increasing applied charging voltage;
(3) the pulse arc discharge generates strong shock and expansion waves near the arc electrodes to create cavitation zone;
(4) the shock and expansion wave strength are the order of magnitude of a few 0.1 MPa which may generate the supercritical conditions;
(5) the strong UV-A and UV-B emissions were observed from the pulsed arc zone;
(6) a significant water conductivity effect on PAED onset was observed;
(7) based on the present experimental observations, the mechanism of the pulsed arc electrohydraulic discharge water treatments may be due to UV generation, strong cavitations, and H_xO_y radicals for chemical contaminants removal and disinfections.

Based on the present experimental observations the mechanism of the pulsed arc electrohydraulic discharge water treatments can be summarized in Figure 12. The results support the strong advanced oxidation capacity as well as disinfection of water through pressure waves, radicals and UV radiations.

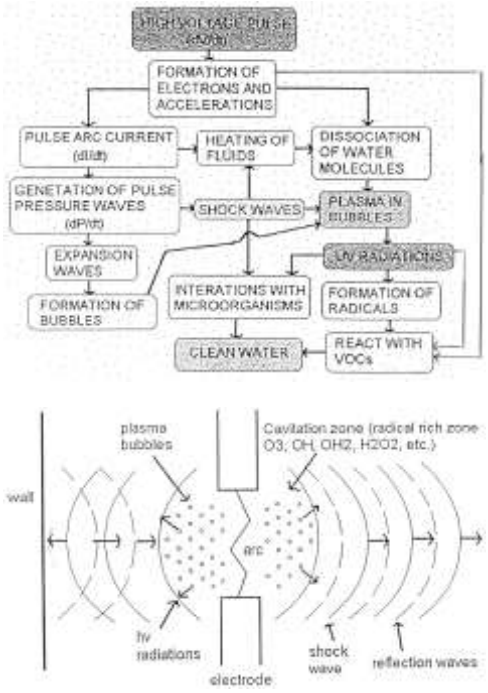

Fig. 12. Proposed mechanism of PAED water treatment.

ACKNOWLEDGEMENTS

The authors wish to thank N. Karpel Vel Leitman, A. Bryden, P.C. Looy, G. Touchard, S. Dickson, M.B. Emelko, T. Kaneda, Y. Uchida, B. Legube, K. Urashima, J. Mizeraczyk, B. Locke, H. Ramat, and K. Yoshimura for valuable discussions and comments. This work is supported partly by Natural Sciences and Engineering Research Council of Canada.

REFERENCES

[1] A.D. Bryden (1995), U.S. Patent No. 5,432,756.
[2] R.A. Lewis Enterprises Inc. (1996), Zebra Mussel Control Alternative Plasma Sparker Technology for the Pilot Plant Project Report to City of St. Albans and the Wergemnes-Panton Water District Inc.

[3] A. Kawabe (1996), Karyoku Genshiryoku Hatsuden, 47, 16-28.
[4] Wasser Barth GmbH (1996), Commercial catalogues.
[5] V.L. Goriachev, A.N. Bratsev, V.N. Feduikovich, P.G. Rutberg, H.W. Greene, P.E. Chism Jr. (1995), U.S. Patent 5,454, 513.
[6] A.K. Sharma, B.R. Locke, P. Arce and W.C. Finney (1993), J. Hazardous Waste and Hazardous Materials, 10, 209-219.
[7] M. Sato, T. Ohgiyama and J.S. Clements (1996), IEEE Trans. Indust. Appl., 32, 106-112.
[8] A.A. Joshi, B.R. Locke, P. Arce and W.C. Finney (1995), J. Hazardous Materials, 41, 3-30.
[9] B.-L. Qin, G.V. Barbosa-Canovas, B.G. Swanson, P.D. Pedrew and R.G. Olson (1998), IEEE Trans. Indust. Appl., 34, 43-50.
[10] F. Jomni, A. Denat and F. Aitken (1996), Conf. Record of ICDL'96, pp. 247-250.
[11] V.S. Teslenko, A.J. Zhukov, V.V. Mitrofanov (1995), Lett. ZhTF, 21, 20-26.
[12] D. Warren, J. Russel and T. Siddon (1996), AOT-3, Cincinnati, Oct. 27-29, 1996.
[13] M.R. Hoffman (1997), Proc. 2nd Int. Environ. Appl. Adv. Oxid. Tech., EPRI Report CR-107581, pp. 3-28 3-45.
[14] J.W. Robinson (1973), J. Appl. Phys., 44, 76; and (1967), J. Appl. Phys., 38, 210.
[15] E.A. Martin (1958), J. Appl. Phys., 31, 255.
[16] J.W. Robinson, M. Ham and A.N. Balaster (1973), J. Appl. Phys., 44, 72-75.
[17] L. Jakob, T.M. Hashem, S. Burki, N.M. Guidny and A.M. Braun (1993), Photochem. Photobiol. A: Chem., 7, 97.
[18] V.G. Ben'Kovskii, P.I. Golubnichii and S.I. Maslennikov (1974), Phys. Acoust., 20, 14-15.
[19] J.T. Yelverton (1981), Presentation for 102th Acoustic Soc. of America.
[20] J.S. Chang, P.C. Looy, K. Urashima, A.D. Bryden and K. Yoshimura (1998), Proc. 1998, Asia-Pacific AOT Workshop, pp. 148-153.
[21] M.B. Emelko, S.E. Dickson and J.S. Chang, (2003), Proceeding AWWR 2003 meeting – in press.
[22] J.S. Chang, 2001. Recent Development of Plasma Pollution Control Technology: A Critical Review. Sci. Technol. Adv. Mat. 2:571-576.
[23] J.S. Chang, K. Urashima, Y. Uchida, Y., and T. Kaneda, 2002. Characteristics of Pulsed Arc Electrohydraulic Discharges and Their Application to Water Treatments. Tokyo Denki Daigaku Kogaku Kenku Journal. 50:December, pp. 1-12.
[24] W.K. Ching, A.J. Colussi, H.J. Sun, H. Nealson and M.R. Hoffmann, 2001. Escherichia coli Disinfection by Electrohydraulic Discharges. Environ. Sci. Technol. 35:20:4139-4144.
[25] N. Karpel Vel Leitner, K. Urashima, A. Bryden, H. Ramot, G. Touchard and J.-S. Chang, 2001. Mechanism of VOC Removal by Pulsed Arc Electrohydraulic Discharge Systems. In: Proceedings from the Third International Symposium on Non-Thermal Plasmas, April 23 – 27, J.-S. Chang, J. Kim (eds.), Kimm Press, Tajun, Korea, pp. 39-44.
[26] P.S. Lang, W.K. Ching, D.M. Willberg and M.R. Hoffmann, 1998. Oxidative Degradation of 2,4,6-Trinitrotoluene by Ozone in an Electrohydraulic Discharge Reactor. Environ. Sci. Technol. 32:20:3142-3148.
[27] D.M. Willberg, P.S. Lang, R.H. Hochemer, A. Kratel and M.R. Hoffmann, 1996. Degradation of 4-Chlorophenol, 3,4-Dichloroaniline, and 2,4,6-Trinitrotoluene in an Electrohydraulic Discharge Reactor. Environ. Sci. Technol. 32:20:3142-3148.

[28] D.G. Harris, V.D. Adams, D.L. Sorenson and M.S. Curtis, 1987. Ultraviolet Inactivation of Selected Bacteria and Viruses with Photoreactivation of Bacteria. Wat. Res. 21:6:687-692.
[29] Y. Uchida, K. Urashima, J.-S. Chang, T. Kaneda, Y. Uchida, K. Shimazaki, Y. Tomita and S. Watanabe, 2002. Optical Characteristics of Capillary U-Tube Ar-Hg High Frequency Glow Discharge Plasmas and its Application for Ammonia Compound Contaminated Water Treatments. J. Adv. Oxid. Technol. 5:2:186-192.
[30] J.L. Zimmer and R.M. Slawson, 2002. Potential Repair of Escherichia coli DNA Following Exposure to UV Radiation from Both Medium- and Low-Pressure UV Sources Used in Drinking Water Treatment. Appl. Environ. Microbiol. 68:7:3293.

4th International Conference **ELMECO**
Nałęczów, Poland
September 2003

APPLICATION OF DIRECT AND NON DIRECT DE-NO_X PLASMA TECHNOLOGIES

Iwo POLLO

The Private University of the Protection of Environment
ul. Zubrzyckiego 6, 26-600 Radom,

Abstract

There are two most important components of exhaust gases having acid properties and being dangerous for the environment. There are sulfur oxides and nitrogen ones. In past years the chemical technology of SO_2 limitation is well developed. The ground idea was using of chip basic substances like calcium oxide or calcium hydroxide. Its interaction with sulfur oxide with oxidation of intermediate products gives calcium sulfate VI being solid substance versus neutral the environment. Possibilities of the reduction of NO_x emission are much more complicated. No insoluble nitrates exist and so no solid product of the interaction of nitrogen oxides, also after secondary oxidation is to obtain. The proposed chemical methods of deNO_x technologies are based mainly on the conception of the catalytic or not-catalytic decomposition, also in the presence of selected reducing agents like ammonia, hydrogen, some hydrocarbons. On other way the oxidation of NO and NO_2 in the presence of water vapour and some alkaline substances could be taken onto consideration. The product – alkaline nitrate V – can be treated as a commercial product. Especially ammonium nitrate is a commonly applied fertilizer.

In course of the last tens of years several plasma chemical methods have been proposed. Only few of them have been developed to the pilot plant level but they are very attractive from the technical point of view. The technology is relatively simple and there exist no problems like catalyst poisoning. The using of electrical discharge can effect by the decomposition of NO_x to the elements. This aim was realized using various electrical systems for to generate of active plasmas. The first proofs were executed in the barrier discharges, in the d.c. and a.c. asymmetric (corona) discharges with various electrodes configuration: wire – tube, wire – plane, point – plane, point – hemisphere. In the same geometry of facilities the using of pulse discharges gave very good results. The decomposition of NO (as well as of higher nitrogen oxides) is a simple and quick process but it conceals some unexpected problems. Although NO represents a non-stable chemical individuals, its decomposition run with high activation energy. In the presence of oxygen oxidation of nitrogen monooxide can introduce new individuals also enhancing the energy consumption. The addition of reducing agents makes the process more stable. Most interesting way is using calculated amounts of ammonia in presence of elevated concentration of oxygen. In this case the decomposition of NO_x goes on only

partially. A significant amount of nitrogen oxides can be oxidized and in the presence of water vapour transformed into ammonia nitrate. This substance can be partially separated as a commercial product, partially by acting of the discharges can be decomposed to elements. An other, non direct plasma chemical method is connected to the process of ozone synthesis. Ozone as a very strong oxidizing agent causes quickly the oxidation of nitrogen oxides, There is possible to obtain nitric acid or, after addition of basic substances, nitrates with a good yield.

1. INTRODUCTION

In the years 1870 - 1880 the first reports concerning low pH of the rains in some countries have been published [1]. The phenomenon dead not seam alarming, its dependence on the human activity was not suspected. The more accurate analytic data have been obtained much later. They indicated, that acidity of the water of water or snow is connected to the contain of sulfuric acid ac well as of the nitric one. Both these acids appear as the result of oxidation and hydratation of sulfur dioxide and nitric oxides. Both groups of oxides can be treated as natural components of the atmospheric air. Sulfur compounds are emitted during the volcanic eruptions, nitrogen oxides are forming from oxygen and nitrogen during the thunder discharges. Especially nitrogen oxides synthesis should be treated as positive and desired process completing nitrogen losses in soil.

As the result of development of the world economy quantity of emitted acid oxides increased. The source was not in the nature more. A lot of industrial processes, especially burning of fuels for to produce energy or for to move the transport objects become to be large emitters of many pollutants, including compounds causing acidification of the environment. Especially the lakes and forests on the northern hemisphere were affected, but also many historical monuments as well as c new constructions have been damaged.

Between two groups of oxides giving strong acids sulfur compounds were taken as more dangerous and probably their emission control should be less difficult. Really, in course of few years several chemical technologies for "deSOx" process were developed with a commercial success [2]. Their idea is similar. Sulfur dioxide will be chemisorbed in the suspension of calcium carbonate or of calcium hydroxide:

$$SO_2 + CaCO_3 = CaSO_3 + CO_2 \quad (1)$$

$$SO_2 + Ca(OH)_2 = CaSO_3 + H_2O \quad (2)$$

In the presence of small quantities of oxygen there is possible to oxidize $CaSO_3$ to $CaSO_4$. Depending on the process condition calcium sulfate can be obtained in form having various quantity of bonded water. The expected product is mainly gypsum $CasO_4.2H_2O$.

This facilities for to exploit this method are contemporaneously used as rule in power stations.

An other way to prevent the emission of SO_2 is diminishing of sulfur quantity in the natural flue. In case of solid flue (coal) this conception can be realized by flotation. The natural gas contains commonly sulfur in form of hydrogen sulfide. A part of them will be oxidized to sulfur dioxide. Both these substances react giving pure elementary sulfur:

$$2H_2S + SO_2 = S + 2H_2O \quad (3)$$

For "deNOx" process several processes have been developed [3-5].

The most important emitters of NO_x are power plants and motor vehicles. In both cases the high temperature burning process is the main cause of nitrogen oxides formation. Nitrogen oxides being present in the exhaust gases derive mainly from two sources. One of them is the large group of nitrogen organic derivates being present in the raw flue, especially in coal. The other is relatively high burning temperature in presence of air. The components of air, nitrogen and oxygen, react together giving nitrogen oxides. The chemistry of nitrogen oxides is much more complicated than of sulfur oxides one. In case of sulfur only two oxides should be taken into account: sulfur dioxide and sulfur trioxide (SO_2 and SO_3). Nitrogen forms with oxygen a large group pf compounds, a part of them exists in dimeric or even polymeric forms. The first of them, dinitrogen oxide N_2O (named also nitrogen suboxide or laugh gas) is relatively stable and of low toxicity. It does not react with oxygen, is slightly soluble in water. The next is nitrogen monooxide NO, in water almost non soluble. It reacts slowly, but in irreversible process, to nitrogen dioxide (forming "prompt" dinitrogentatraoxide N_2O_4). This oxide reacts with water giving mixture of nitric acid III and nitric acid V. Nitric acid III is not stable. In the result a part of nitrogen dioxide in course of there action with water will be reduced to nitrogen monoxide and in the solution no nitric acid III can be determined. NO and NO_2 can form N_2O_3 giving with alkaline solutions salts of HNO_2. These group of oxides can be oxidized (p. ex. by ozone) to dintrogenpentoxide N_2O_5.

Tab. 1. Simple nitrogen – hydrogen & nitrogen – oxygen compounds

Compound	H/N(-)	H/N, O/N	O/N	ox.deg.
NH_3	-3			-3
$NH_2NH_2 = N_2H_4$	-2			-2
NH	-1			-1
N_2		0		0
N_2O			0,5	1
NO, $(NO)_2$			1	2
N_2O_3			1,5	3
NO_2, N_2O_4			2	4
N_2O_5			2,5	5
NO_3			3	6
HN_3	-1/3			-1/3
$NH_3HN_3 = N_4H_4$	-1			(-1/3\\3}
NH_2OH	-3		1	-1
$H_2N_2O_2$ ~ {HNO}	-1		1	1
HNO_2	-1		2	3
HNO_3	-1		3	5
NH_4NO_2	-2		2	-3\\3
NH_4NO_3	-2		3	-3\\5

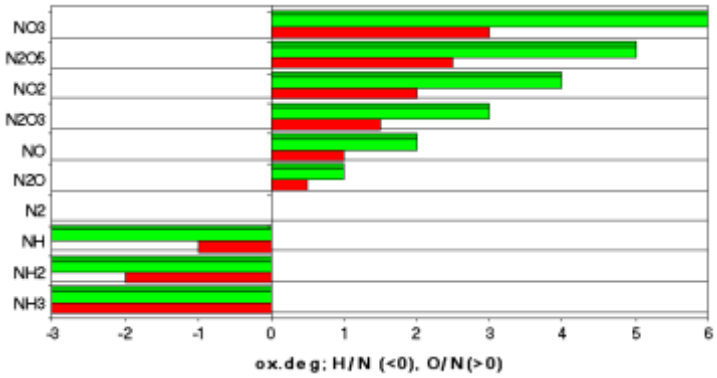

Fig. 1. Oxydation degree of selected simple nitrogen compounds

As the result in the table 1 and figure 1 the variety of derivates in the system H-N-O has been presented. As the consequence chemical species of this system represents many various properties. The compounds with H/N value <0 are reducing agents, the oxides are mainly oxidants. Ammonia is an alkaline, nitric acid V (HNO_3) is one of strongest acids being also strong oxidant. Nitrogen oxides have acid properties excluding neutral: suboxide N_2O and monooxide NO. But nitrogen dioxide forms with traces of water molecules nitric acids III and V. And ammonia forms with both salts, named commonly nitrite and nitrate. They are very interesting, because each of them contains two nitrogen atoms of various oxidation level. They are relatively unstable, especially NH_4NO_2. It decomposes easy to free nitrogen and water. The decomposition can occur explosively. This property is used in some methods of NO_x destruction.

The combustion processes and most part of chemical reactions causing emission of nitrogen oxides produce nitrogen monooxide NO. This compound reacts slowly to nitrogen dioxide. The limiting of this phenomenon can be realized either on the way of prevention of NO forming and emission in the source or by its decomposition still inside of the emitter. The sorption systems are not preferable because only small amount of reactants being good sorbing agents for nitrogen monoxide. Additionally this pollutant is mainly very diluted in large volumes of exhaust gases. The absorption could be realized, when the obtaining of a commercial product was assured. Normally this is not the case and absorption seems to be much to expensive.

Several methods for the prevention of NOx emission were elaborated. Thermal and catalytic reduction processes are here important. Between them two groups are to distinguish: non-selective reduction and selective one.

In the first of them hydrogen, methane, carbon monooxide, hydrocarbons as reducing agents were used. The second one is utilizes ammonia. In both cases the end product is free nitrogen The differences of commercial methods are connected to catalysts, to the details of facilities and to the process temperature.

2. PLASMA ACTION ON THE SYSTEM $N_2 – O_2 – NO_X$

The first essays to apply plasma environment in the system $N_2 – O_2$ was synthesis of nitrogen oxides as a step in the process of the production of nitric acid in the electrical arc.

During the investigations also the decomposition of nitrogen oxides has been taken into consideration. Arc plasma has relatively high temperature (~6000 K). Then the results gave rather the influence of temperature. Much later the non-equilibrium plasmas were used for to investigate the process of NO decomposition [6]. There were executed works concerning the decomposition of NO in the silent discharge and than in the corona one. The corona discharges were for this aim generated by the direct current, than also by the alternating one. In the last works the pulse corona discharges have been developed.

The chemistry of the nitrogen monoxide decomposition by plasma action is complicated enough. In the table 2 the most important reactions have been presented.

The direct action of non-equilibrium plasmas on nitrogen monooxide costs much energy. However the summarized reaction is exothermic:

$$2\ NO = N_2 + O_2; \qquad \Delta H << 0 \qquad (4)$$

the real process path is:

$$NO + e = N + O \qquad \Delta H >> 0 \qquad (5)$$

$$N+N = N_2 \qquad \Delta H << 0 \qquad (6)$$

$$O+O = O_2 \qquad \Delta H << 0 \qquad (7)$$

Exothermic reactions [6] and [7] causes the rising of the temperature, they cannot cause the start of reaction [5].

Tab. 2. Processes accompanying NO decomposition in the corona discharge plasmas

Lp	Proces	$\Delta H^{\#}$ [kJ/mol]	K	Remarks
1	$NO + e = N + O + e$			$O(^3P)$ or $O(^1D)$,
1'	$NO \rightarrow ½\ N_2 + ½\ O_2$	92.42		summarized 0,96 eV/molecule
1"	$N + O = NO$	-267,24		$\Delta H^{\#}$: kJ/mol NO
1a	$NO + h\nu = N + O$			$N(^4S)$, λ = 182.8; 191 nm ~ 175 – 190 nm
1b	$NO + h\nu = NO^+ + e$			λ = 121.6 nm
2	$O + O + M = O_2 + M$	-247.64		kJ/(1 mol O)
3	$N + N + M = N_2 + M$	-471.29		kJ/(1 mol N)
4	$O_2 + e = 2\ O + e$			*e > 5.2 eV* but through excited state O_2^*, e > 8.3 eV
5	$N_2 + e = 2\ N(^4S) + e$			*E > 9, 82 eV* $N(^4S)$ ground state nitrogen atom
5a	$N_2 + e = 2\ N(^2D) + e$			$N(^2D)$ – metastable nitrogen atom
6	$N + NO = N_2 + O$	-313.8	$2.2*10^{-11}$ [$[cm^3/s]$	
7	$N + O_2 = NO + O$	-133.5	$1.4*10^{-11}* \exp(3570)/T$ $[cm^3/s]$	

8	$NO^+ + e = N(^2D) + O$		$1*10^{-7}*(0{,}001T)^{-1.5}$ [cm^3/s]	Depending on the energy of electron
8a	$NO^+ + e = N(^4S) +$			
9	$N(^2D) + O_2 = NO + O_2$			
10	$O + NO + M = NO_2 + M$	-306		
10a	$O + NO = NO_2 + h\nu$			
11	$O_2 + 2\,NO = 2\,NO_2$		$9*10^{-39}*\exp(413/T)$	
12	$NO_2 + e = NO + O$			
13	$NO_2 + O = NO + O_2$	-192		
14	$NO_2 + h\nu = NO + O$			$\lambda < 399$ nm
15	$O + O_2 + M = O_3 + M$			
16	$O_3 + NO = NO_2 + O_2$	- 200	$0.95*10^{-12}*\exp(-1240/T)$ [cm^3/s]	
17	$O_3 + NO_2 = NO_3 = O_2$	-105		
18	$NO_3 + e$ (or $h\nu$) $= NO + O_2$			$\lambda = 500 - 700$ nm
19	$O^* + N_2 + M = N_2O + M$			
20	$N_2O + O^* = NO + O_2$		$9*10^{-11}$	

The experiments on the NO decomposition in the corona discharges confirm the high energy consumption and additionally show, that this process is very slow. This phenomenon is caused by the slow energy transfer in the corona discharge condition.

The experiments on the nitrogen monoxide decomposition in negative corona discharge have been executed. There was applied six corona – reactors with various inner diameter. Their diameters on the Fig. 2 are shown.

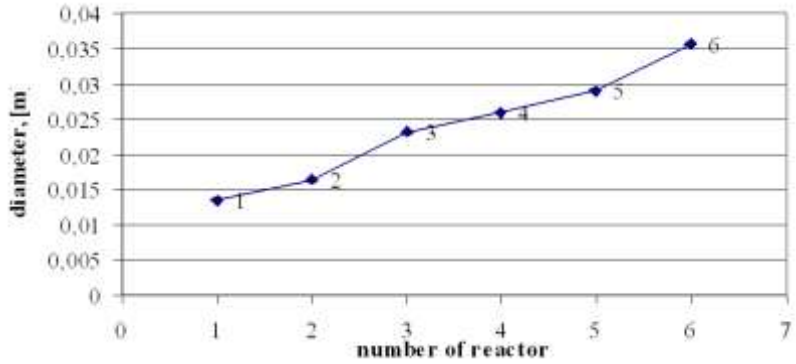

Fig. 2. Inner diameter of dorona discharge reactors.

During the experiments various tension values have been used. The lowest one was connected to the break potential, over the highest the sparks appeared. The relative high NO concentration (>10 000 ppm) has been applied.

In the Fig. 3 the decomposition degree for the highest tension is presented.

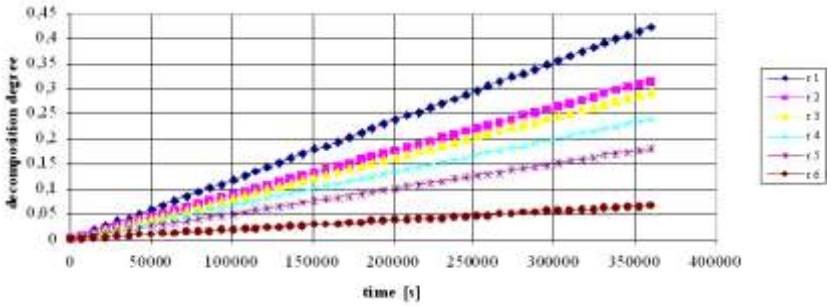

Fig. 3. Conversion of NO versus time, 34,5 kV
No. of in reactor in caption

The obtained dependences in the indicated range of time are represented by straight lines. A long time is needed for to decompose a significant value of the decomposition degree. No reducing agents were added, the inlet gas was dried on the phosphorous pentoxide. When the gas saturated by water vapor was used, the rate of reaction was approx. ten times faster. In case of wet gas the decomposition can be almost completely, when for the dry gas some amount of NO rests. This phenomenon can be explained by the inverse reaction. Electrical discharge decomposes noitrogen oxide, but it causes also its synthesis from oxygen and nitrogen. Then the reaction of NO decomposition must be considered as reversible:

$$2NO \xrightarrow{\text{plasma}} 2N + 2O \rightarrow N_2 + O_2 \qquad (8)$$

As well as in the presence of water molecules the nitric acids will be formed,, NO can be completely removed from gas phase.

The consideration of the energy impact on the reacting plasma systems resulted with the conclusion that the enhancement of the corona discharge power should improve the process. Pulse corona discharge enables to realize this demand. A large number of investigations using pulse tension was executed. The presence of water vapor and limited quantity of some reducing agents like ammonia was taken into consideration to. Now a day the using of pulse corona environment is the best direct plasma process for to remove nitrogen oxides from exhaust gases. Excellent works concerning this process have been executed by many research groups of professors like Chang in Canada, Masuda, Mizuno, Yamabe in Japan, Morvova in Slovakia, Penetrante in USA, Rea in Italy, Mizeraczyk in Poland. Prof. Chmielewski uses successfully electron beam [7-27]. Also in our laboratoty series of investigations were executed [28-38].

The experiments with the pulse corona discharges have been executed also in our laboratory. Some results are presented on the Fig. 4, 5 and 6. The start concentration of nitrogen oxide was: 500, 150 and 50 ppm. The average power value was 5, 40 and 75 W. For the lowest power the experimental data are situated on the straight line like in case of

unipolar corona. For higher values of discharge power the lines are changing their shape and the NO removing is deeper.

There are many advantages of using pulse corona discharge in presence of ammonia. One of them is possibility to obtain as product ammonium nitrate, being a good fertilizer. This process can be also adapted to the common removing of nitrogen oxide with sulfur dioxide.

As the non – direct plasma technology for NO removing is using of strong oxidants. Acting by ozone on nitrogen monooxide in the presence of water there is possible to obtain nitric acid. Ozone is produced in silent (barrier) discharge facilities. Then the plasma – step is ozone synthesis and oxidation of NO can occur in the other but neighbor set up.

The chemistry of this process is complicated and not yet fully investigated. The first reaction is oxidizing of NO:

$$NO + O_3 = NO_2 + O_2 \quad (9)$$

This reaction goes on very fast but for economy of process more important is reaction:

$$2NO_2 + O_3 = N_2O_5 + O_2 \quad (10)$$

Oxidation of NO_2 to dinitrogen pentoxide is necessary for to obtain stable nitric acid. But summarizing both reactions one obtains:

$$2\ NO + 3O_3 = N_2O_5 + 3\ O_2 \quad (11)$$

For full oxidation of one molecule NO is necessary one and half molecule ozone. The desired process should be:

$$2\ NO + O_3 = N_2O_5 \quad (12)$$

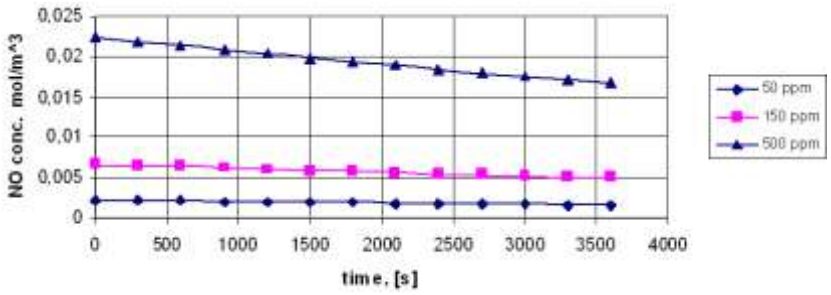

Fig. 4. NO concentration versus time discharge power 5 W

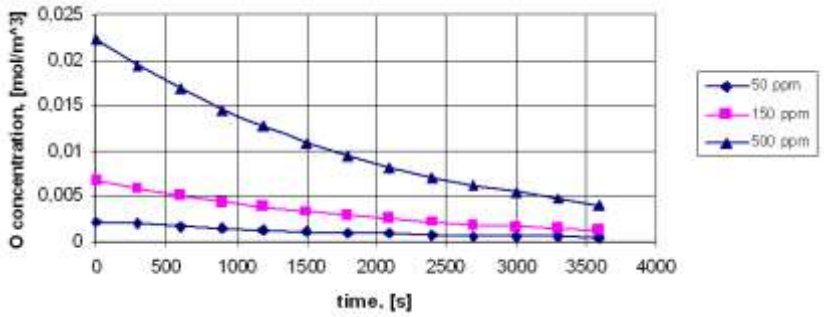

Fig. 5. NO concentration versus time, power 40 W

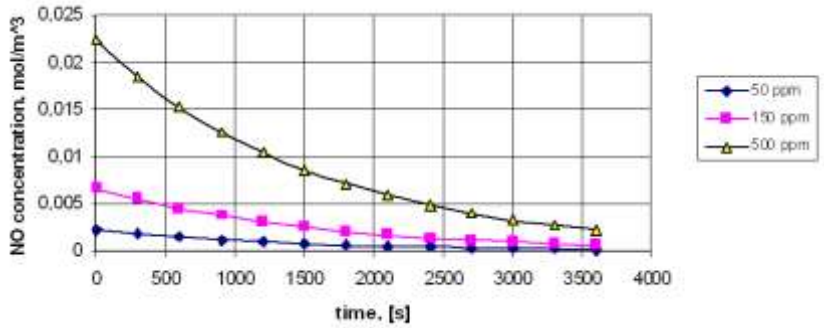

Fig. 6. NO concentration versus time, power 70 W

As well all these reactions are exoenergetic, no theoretical obstacle to realize reaction (12). In this case all oxygen atoms of ozone can take part in oxidation. Practically this reaction does not run and experiments of various catalysts gave no expected result. However elimination of nitrogen oxides using ozone is a very effective technology and it found support in last time.

Never the more the addition of even substoichiometric amounts of ozone causes the enhancement of the absorption of NO in the water sprinkled packed column. In the Fig. 7 this phenomenon is shown.

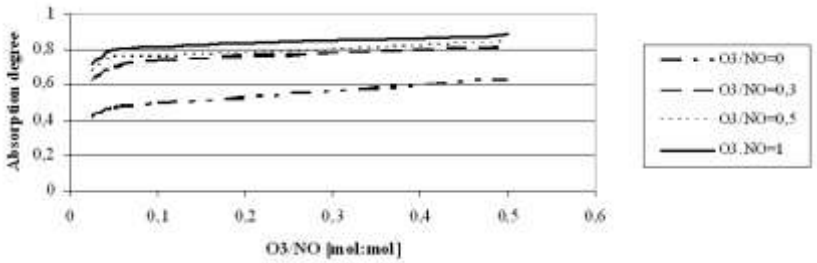

Fig. 7. Dependence of NO absorption degree versus ozone to nitrogen oxcide fraction.

In outlet water nitric acid is present. Its concentration is relatively small, but this solution can be used as absorption liquid in nitric acid factories.

3. CONCLUSIONS

There are many possibilities to use the plasma generated by electrical discharge for to decompose or to oxide nitrogen oxides. A part of them causes decomposition of NO to oxygen and nitrogen molecules. An other group of technologies enables to obtain commercial products like ammonium nitrate or diluted nitric acid. The development of plasma methods needs collaboration of chemists with experts on electric discharge supply. The corona discharge system can be supplied by D.C. or A.C. sources but as best seems to be a pulse supply. It is possible that other advanced solutions like "superimposed discharge" or other hybrids can make the plasma methods fully competitive on the world market.

REFERENCES

[1] Lean G., Hinrichsen D.: Atlas of the Environment, second edition. Helicon Publishing Ltd, London 1992
[2] Warych J.: Oczyszczanie przemysłowych gazów odlotowych, WNT Warszawa 1988
[3] Kuropka J.: Oczyszczanie gazów odlotowych z tlenków azotu. Wydawn. Politechniki Wrocławskiej, Wrocław 1988
[4] Bistroń S.: Metody przeciwdziałania emisji tlenków azotu ze źródeł przemysłowych do powietrza atmosferycznego. PAN, 1978, Wrocław
[5] Straszko J., Parus W., Kalisiak B.: Proc. Symp. 'POLEMIS II', 1884, Szklarska Poręba p.87
[6] Schmidt-Szałowski K.: Acta Agrophysica 2002, 80, 303
[7] Masuda S. : Report on Novel dry deNOx/deSOx Technology, in: NATO ASI Series, G34(B), Springer Verlag Berlin – Heidelberg 1993, p. 131
[8] Okumura T., Masuda S., Satoh S., Sakai T., Tagashira H: J.Phys. D, Appl, Phys. 1994, 27, p. 801
[9] Kubo M., Takahashi K. Inomata T. Moriwaki T. Okazaki S.: Proc. 8th Intern. Symp. on Plasma Chemistry 1987, vol. 2, p. 828
[10] Masuda S.: Pure & Appl. Chemistry 1988, 60, No 5, p. 727
[11] Masuda S., Hosikawa S., Tu. K., Wang Z.: Journ Electrostatics 1995, 34, p. 415

[12] Yamabe Ch., Okamoto K. Huang S.F.: proc. 5th Intern. Symp. ‘HAKONE V’ 1996, Milovy, p. 62
[13] Kanazawa S., Chang J.S, Round G., Sheng G. Okhubo T. Nomoto Y., Adachi T.: Journ Electrostatics 1997, 36, p. 651
[14] Yamabe Ch., Okamoto K., Huang S.: Proc. 5th Intern. Symp. ‘HAKONE V’ 1996, Milovy p 62
[15] Gasparik R., Yamabe C., Ihara S., Satoh S.: Proc. 11th Symp. on Elementary Processes and Chemical Reactions in Low Temp. Plasma 1998, Low Tatra, vol. 1, p.59
[16] Mizuno A., Shimizu K., Yanagihara K., Kinoshita K., Tsunoida K., Kim H., Katsura S.: Proc. IEE Ind. Appl. SOc. Annual Meeting 1996, San Diego, p. 1808
[17] Guan P., Hayashi N., Satoh S., Yamabe Ch., Vacuum 2002, 65, p. 469
[18] Chang J.S.: IEE Trans. On Plasma Sciences 1991, 19, No 6, p. 1152
[19] Park J., Tomicic L., Round G., Chang J.: J.Phys. D, Appl, Phys. 1999, 32, 1006
[20] Mizeraczyk J., Chang J.S., Jogan K., Nagai K, Yoshioka T.: Proc. Intern Symp. ‘HAKONE IV”, 1993 Bratislava, p. 81
[21] Vogtlin G.E., Penetrante B.M.: in NATO ASI Series, G34(B) 1993, Springer Verlag Berlin – Heidelberg, p. 186
[22] Morvova M., Gasparik R., Hensel K. Svehla B.: Proc. 5th Intern. Symp. ‘HAKONE V’ 1996, Milovy p. 92
[23] Mizeraczyk J., Dors M., Nichipor G.: Polish Journ of Appl. Chemistry 1998, 42, 129
[24] Dors M.: Eliminacja tlenków azotu z symulatorów gazów odlotowych za pomocą wyładowania koronowego, Thesis 1999, Instytut Maszyn Przepływowych PAN, Gdańsk
[25] Jasiński M.: Zastosowanie wyładowania mikrofalowego typu ‘torch’ do dekompozycji gazów ekologicznie szkodliwych. Thesis 2003, Instytut Maszyn Przepływowych PAN, Gdańsk
[26] Jasiński M., Mizeraczyk J., Zakrzewski Z.: Acta Agrophysica 2002, 80, 393
[27] Chmielewski A,G., Iller E., Zimek Z., Licki J.: Rad. Phys. Chem. 1992, 40, Bo 4, p. 321
[28] Pollo I., Rea M., Wroński M.: Zeszyty Naukowe Wyższej Szkoly Pedagogicznej w Opolu1993, Chemia XVI, p. 44
[29] Pollo I., Rea M., Wroński M.: Proc. Intern. Conference "Elmeco 94", Lublin 1994, p. 23
[30] Wroński M., Rea M., Pollo I.: Proc. 5th Intern. Symp. ‘HAKONE V’ 1996, Milovy p. 57
[31] Pollo I.: Nitrogen Oxides as an Environmental Problem, in: "Risk Assesment of Chemicals in the Environment" (M.L. Richardson ed.), published by Royal Soc. of Chemistry, London 1995 (GB), p. 312
[32] Jaroszyńska-Wolińska J.: Studium procesu sorpcji tlenku azotu z gazów rozcieńczonych z zastosowaniem ozonu. Thesis 1983, Instytut Podstaw Inżynierii Środowiska, Zabrze
[33] Pollo I., Jaroszyńska-Wolińska J.: in: "Chemistry for Protection of the Environment" (edited by L. Pawłowski, A.J. Verdier, W.J. Lacy): Elsevier 1984, Amsterdam - Oxford - N.York - Toronto, p. 445
[34] Wolińska J., Pollo I.: Proc. 12th Intern. Symp. on Plasma Chemistry 1995, Minneapolis p. 1131
[35] Pollo I., Jaroszyńska-Wolińska J.: Zaszczita Atmosfery 1986, Dresden, No 1/86, p. 41

[36] Wroński M., Pollo I.:1997: Plazmochemiczna technologia DENOx, Proc. Symp.. 'II Kongres Technologii Chem.' 1997 Wrocław, t.1. s. 251
[37] Jaroszyńska-Wolińska J., Pollo I. 1995: Proc. 12th Intern. Symp. on Plasma Chemistry, Minneapolis (USA) 1995, p. 1131
[38] Jaroszyńska-Wolińska J., Pollo I. 1997: Nitrogen Monooxide Oxidation with Ozone as a Method of its Emission Control, in: "Chemical Processes in Low Temperature Plasma", Wydawnictwa Uczelniane Polit. Lubelskiej, 1997,Lublin, p. 51

TECHNOLOGIES FOR WATER AND AIR IMPROVEMENT

4th International Conference **ELMECO**
Nałęczów, Poland
September 2003

NUMERICAL SIMULATION OF OZONE CONCENTRATION IN NON-THERMAL PLASMA REACTOR

Jarosław DEKOWSKI, Jerzy MIZERACZYK

Centre for Plasma and Laser Engineering, Institute of Fluid Flow Machinery, Polish Academy of Sciences, Fiszera 14, 80-231 Gdańsk, Poland
e-mail: jmiz@imp.gda.pl

Abstract

In this paper results of one-dimensional numerical simulation of ozone molecule transport along a corona radical shower (CRS) non-thermal plasma reactor are presented. This simulation was performed to explain the experimental results on the ozone concentration in the CRS reactor presented by Mizeraczyk et al. in [6]. They found that the ozone molecules produced in the discharge zone were transported from their origin to both regions of the CRS reactor, the downstream and the upstream, i.e. also against the main gas flow. In the simulation it was assumed that the ozone was transported by molecular diffusion, main flow convection and upstream convection caused by the electrohydrodynamic(EHD) secondary flow. The obtained results are in agreement with the experimental results presented in [6]. The EHD secondary flow is concluded to be responsible for the ozone transport upstream, i.e. against the main gas flow.

Keywords: corona radical shower, NO, streamer corona discharge, non-thermal plasma, EHD, ozone.

1. INTRODUCTION

Non-thermal plasma techniques [1] have become an important tool for controlling the emission of various gaseous pollutants, such as acid gases (SO_x, NO_x, HCl, etc.), greenhouse gases (CO_x, N_xO_y, para-fluorocarbons, etc.), ozone depletion gases (freons, halons, etc.), volatile organic compounds (VOCs, e.g. toluene, xylene, etc.) and toxic gases (Hg, dioxins, etc.). The main advantages of the non-thermal plasma techniques are small space volume, low cost, high pollutant removal and energy efficiencies.

Recently, Ohkubo et al. [2] and Kanazawa et al. [3] measured the two-dimensional distribution of ground-state NO density by the Laser Induced Fluorescence (LIF) in

needle-to-plate and corona discharge radical shower (CDRS) non-thermal plasma reactors, respectively, showing that the concentration of NO molecules decreased not only in the streamer corona discharge and downstream regions of the reactor but also upstream of the discharge region. The reason of the NO removal in the upstream region of the discharge was not clear. However, the results of numerical and experimental investigations [4] on the electrohydrodynamic (EHD) secondary flow (ionic wind) in electrostatic precipitators allow a supposition [5] to be made that the EHD flow may be capable of transporting the long-live active species (e.g. ozone) from the discharge region to the upstream reactor region. If so, the long-live active ozone (or other species) produced in the discharge region could be transported by the EHD flow into the upstream region to oxidize or reduce NO molecules and efficiently decrease their concentration there, as was observed in [2, 3]. Mizeraczyk et al. [6] conducted an experiment to elucidate the effect of the EHD flow on ozone transport in the CDRS reactors. Their measurement of the ozone distribution along the CDRS reactor showed the presence of ozone in the upstream region of the reactor, and the visualization of the flow in the CDRS reactor confirmed the supposed existence of a strong EHD flow in the CDRS reactor. Thus, the EHD flows could easily distribute the ozone inside the reactor, even far into the upstream direction of the reactor.

CDRS reactors have been recently proved to be one of the most efficient non-thermal plasma reactor systems used for NO_x removal [7]. The performance of the CDRS reactors can be improved by the transport of the long-life species, caused by he EHD secondary flow, as it was suggested in [6]. However, this suggestion was not sufficiently supported by evidences.

In this paper new arguments for the ozone molecule transport by the EHD flow along a CDRS non-thermal plasma reactor are presented. Basing on the velocity field measurements of the EHD flow in the CDRS reactor by Particle Image Velocimetry (PIV) [8], a simple phenomenological model of the ozone transport in the CDRS reactor was proposed. The results of the computer simulation based on this model explained the main features of the ozone distribution in the CDRS reactor, measured by Mizeraczyk et al. [6], establishing the EHD flow as the main cause of the ozone transport from the discharge region upstream.

2. EXPERIMENT

Since the phenomenological model is based on the experimental results presented in [6,8], those experiments are briefly described bellow.

A schematic of the experimental apparatus used in [6] and [8] is shown in Fig. 1. The reactor was an acrylic box (100 mm x 200 mm x 1000 mm). A stainless-steel pipe (4 mm in diameter) with 18 stainless-steel nozzle electrodes (1.5 mm outer diameter, 1 mm inner diameter, 5 mm length), soldered into the pipe, was used as CDRS electrode. It was mounted in the middle of the reactor, in halfway between two grounded parallel plate electrodes (200 mm x 600 mm). Positive polarity DC high voltage was supplied through a 10 MΩ resistor to the pipe with nozzle electrodes. The operating voltage was varied from 0 to 31 kV to develop a stable streamer corona discharge from each nozzle to the plate electrodes. The discharge was run at room temperature under atmospheric pressure.

Two gas flows, the main and the additional, were established in the CDRS reactor. The main gas (ambient air) flowed along the reactor, driven by an induced fan. The average velocity of the main gas flow was varied from 0.18 to 0.8 m/s. The additional gas

(N_2:O_2:CO_2=80%:5%:15%) was injected through the nozzles into the main gas flow with a flow rate varied from 0.25 to 1.5 l/min (exit gas velocity 0.3-1.8 m/s).

The concentration of ozone, produced by the streamer corona discharge, was measured along the reactor, on the x axis placed 1 cm below the pipe electrode. The working gas was sampled along the x axis using a cylindrical plastic sampling probe (1 mm in diameter), through which the working gas was sucked into a calibrated FTIR spectrophotometer having a long-path measuring cell, where ozone concentration was measured. Results of ozone concentration measurements are shown in Fig. 2 [6]. Ozone molecules are present in both the downstream and upstream regions of the CDRS reactor. For the main gas flow velocities higher than 0.18 m/s, the ozone concentration exhibits a maximum around the discharge zone due to the ozone production and decreases when moving upstream and downstream. At the lowest main gas flow velocity tested (0.18 m/s), the ozone concentration distribution does not exhibit any maximum around the discharge zone and it does not decrease when moving downstream.

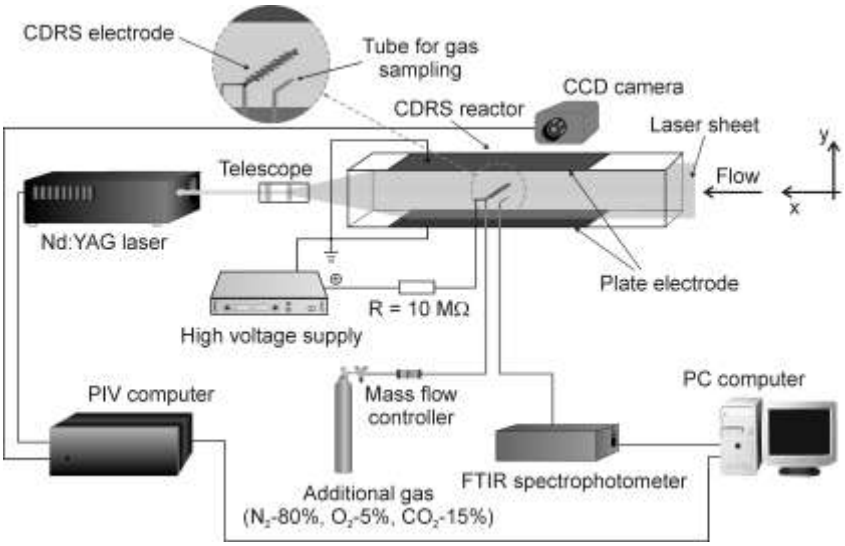

Fig. 1. Experimental set-up.

The flow structures in the CDRS reactor were measured using PIV method [8]. The flow velocity field was measured in the plane perpendicular to the plate electrode (x-y plane in Fig. 1) passing through the central discharge nozzle. A result selected from [8] is presented in Fig. 3. It is seen that pairs of strong vortices are formed by EHD forces at both sides of the discharge electrode. The gas in the upstream vortices moves against the main flow from the CDRS electrode upstream. Then it separates into two streams. Each of the streams turns towards the corresponding plate electrode, and after passing along the plate electrode each stream returns back to the CDRS electrode. The gas in the downstream vortices behaves similarly with a difference, that it circulates in opposite direction.

3. MODEL OF OZONE TRANSPORT

Bellow a simple model of the ozone transport in the CDRS reactor is presented. In this model the transport of O3 molecules by the EHD secondary flow is introduced in a phenomenological way.

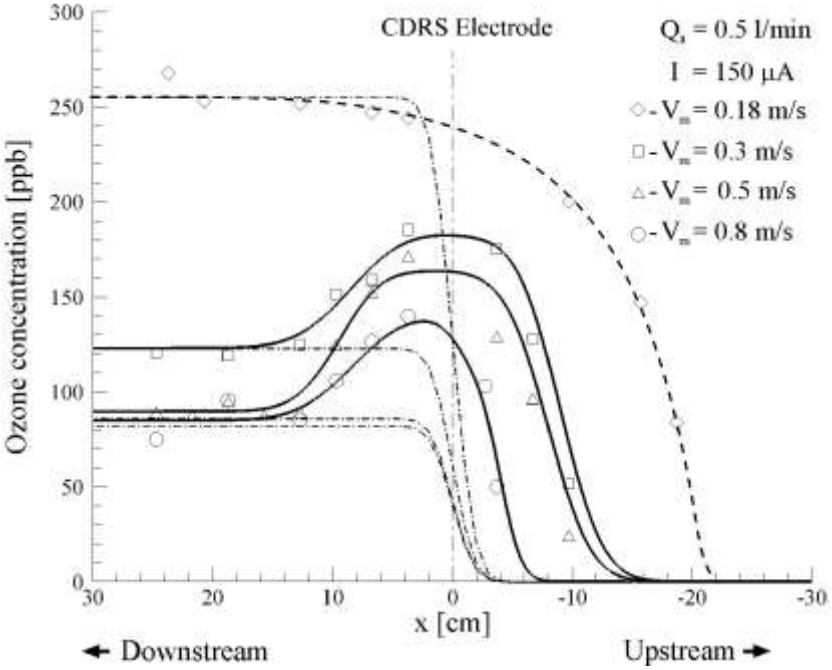

Fig. 2. Ozone concentration distributions along the CDRS reactor during the positive DC streamer corona discharge for various main gas (air) flow velocities V_m.
The points – experimental data [6]. The solid lines – calculation results based on the simple model of one-dimensional ozone transport, which involves the EHD flow. The dash-dotted lines – calculation results based on the simple model without the EHD flows. The dashed line fits the experimental points for V_m= 0.18 m/s.

It is a one-dimensional model, i.e. all quantities are uniform in the yz plane and any changes occur in x direction only (Fig. 1). It is assumed that the generation of O_3 molecules occurs in the centre of the reactor around x = 0, i.e. around the CDRS electrode. The main gas uniformly flows into the reactor with a constant average velocity V_m. In this model it is assumed that O_3 molecules are transported in the main flow direction only by convection, as illustrated by the light–grey paths in Fig. 3. The possible influence of the EHD secondary flow on the O_3 molecules transport in the main flow direction is neglected in this approximation. However, it is assumed that EHD secondary flow, seen as twin-vortices in the upstream and downstream regions, transport O_3 molecules against the main flow. It is illustrated by the dark-grey paths, which follow the upstream and downstream vortex

streamlines in Fig. 3. The upstream EHD transport causes fast removal of O_3 molecules from the CDRS electrode region, operating as an ozone sink (marked as "-" in Fig. 3) in this region. The EHD upstream vortices delivers O_3 molecules to the main flow on the rim of the upstream vortices (marked as "+" in Fig. 3). The EHD downstream vortices deliver a part of O_3 molecules from the rim of the downstream vortices (the fields marked "-") back to the CDRS electrode region, becoming additional sources of O_3 molecules in the vicinity of the CDRS electrode (marked with "+" in Fig. 3).

In this model, it is assumed that O_3 molecules diffuse from the place of their origin upstream and downstream due to their density gradient. It is assumed that there is no loss of O_3 molecules in the reactor (on the walls or in the chemical reactions with species of the operating gas). The turbulence mixing, transport due to temperature gradient etc., apparently existing in the CRS reactor are neglected in this model. Also the transport of O_3 molecules by the additional flow from the CDRS electrode nozzles is neglected.

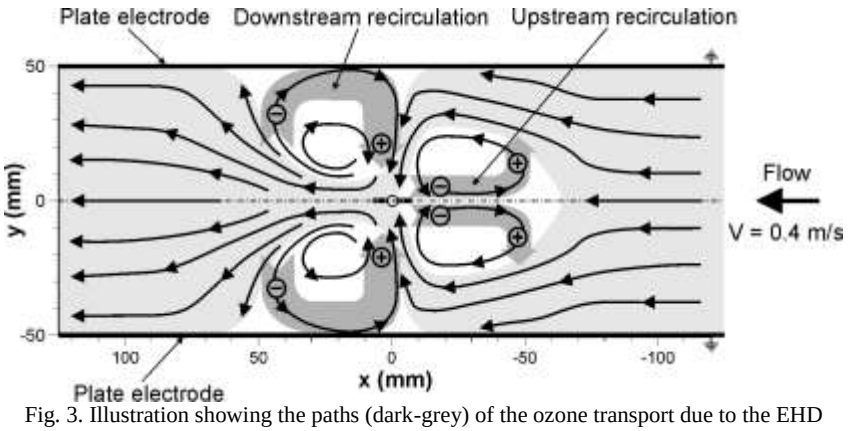

Fig. 3. Illustration showing the paths (dark-grey) of the ozone transport due to the EHD flow [8].

In each point along the reactor the time-dependence of O_3 number density is described by the continuity equation

$$\frac{\partial n}{\partial t} = S - \nabla \cdot \mathbf{J}, \tag{1}$$

where: S – is O_3 source and sink term, vector **J** - is the current density (flux) of O_3 molecules.

When a gradient of O_3 molecules number density exists along x direction, the current density **J** of O_3 molecules crossing a unit area at right angle to it in a unit time is:

$$\mathbf{J} = n \cdot \mathbf{V_m} - D \cdot \nabla n, \tag{2}$$

where: n is the number density of O_3 molecules, vector $\mathbf{V_m}$ is the constant convection drift velocity (the average velocity of the operating gas), D is the diffusion coefficient of O_3 molecules in the operating gas.

In general, the source and sink term S in equation (1) is a complex function of x. We simplify it by assuming a discrete distribution of the sources and sinks of O_3 molecules along x axis (Fig. 3). We assume that

$$S(x) = S_p^+(x) + S_{up}^+(x) + S_{down}^+(x) - S_{up}^-(x) - S_{down}^-(x), \quad (3)$$

where: $S_p^+(x)$ is the production rate of O_3 molecules in the vicinity of the CDRS electrode (at x = 0), $S_{up}^+(x)$ is O_3 source on the rim of the upstream vortex, $S_{down}^+(x)$ is O_3 source at around x = 0 mm, $S_{up}^-(x)$ is O_3 sink at around x = 0 mm, $S_{down}^-(x)$ is O_3 sink on the rim of the downstream vortex. As said, the origin of these sourses and sinks is the EHD transport of ozone.

It is assumed that the number density of O_3 molecules produced by the discharge in a unit length in a unit time is described by a Gaussian function

$$S_p^+(x) = \frac{S_{po}^+}{w_p\sqrt{\pi}} \exp\left(\frac{x}{w_p}\right)^2, \quad [S] = cm^{-4}s^{-1}, \quad (4)$$

which exhibits its maximum $[S_p^+(x)]_{max} = \frac{S_{po}^+}{w_p\sqrt{\pi}}$ at x = 0. The parameter w_p defines the distance (in [cm]) at which O_3 production rate falls to $[S_p(x)]_{max}/e$. By varying the parameter w_p the characteristic of the O_3 source can be changed. For small w_p the O_3 source is "sharp" and the O_3 production is practically limited to a zone around x = 0, i.e. close to the CDRS electrode. For large w_p the O_3 production spreads more uniformly along the x axis, still with its maximum at x = 0. Parameter S_{po}^+, independent of x, is the total O_3 production in a unit time, according to the normalization:

$$\int_{-\infty}^{+\infty} S_p^+(x)dx = S_{po}^+, \quad [S_{po}^+] = cm^{-3}s^{-1}. \quad (5)$$

Also it is assumed that the source and sink terms $S_{up}^+(x)$, $S_{down}^+(x)$, $S_{up}^-(x)$ and $S_{down}^-(x)$ are described by Gaussian functions. This means that the sources and sinks are discretely but smoothly distributed along x axis. The widths of the sources and sinks on x axis are, in principle, different.

It is assumed that O_3 molecules are transported by the EHD flow from the CDRS electrode region (the sink marked "-" at around x = 0 in Fig. 3) upstream and dispersed into the main flow on the upstream vortex rim (the source marked "+" in Fig. 3). The number density of O_3 molecules $S_{up}^-(x)$ removed in a unit length in a unit time from the O_3 production region and transported upstream is assumed to be proportional to O_3 number density n(x) at around x = 0

$$S_{up}^-(x) = R_{up}n(x). \quad (6)$$

The proportionality factor R_{up} (in [s^{-1}]) in (6) is the removal rate coefficient described by a Gaussian function

$$R_{up} = \frac{R_{up}^{0}}{w_{up}^{-}\sqrt{\pi}} \exp\left(\frac{x}{w_{up}^{-}}\right)^{2} \tag{7}$$

where R_{up}^{0} [s^{-1}] is the relative removal rate of O_3 molecules around x = 0. Parameter w_{up}^{-} defines the width of the Gaussian function.

Then it is assumed that all the O_3 molecules drawn from the CDRS region by the EHD flow upstream are dispersed into the main flow on the upstream vortex rim, which becomes an additional source of O_3 molecules. The O_3 molecule number density (in a unit length and in a unit time) delivered to the main flow on the upstream vortex rim by the EHD flow is

$$S_{up}^{+}(x) = \frac{S_{up}^{+0}}{w_{up}^{+}\sqrt{\pi}} \exp\left(\frac{x - x_{up}}{w_{up}^{+}}\right)^{2} \tag{8}$$

where

$$S_{up}^{+0} = \int_{-\infty}^{+\infty} S_{up}^{-}(x)dx \tag{9}$$

is the total number density of O_3 molecules in a unit time dispersed by the EHD flow on the upstream vortex rim, w_{up}^{+} describes the width of the Gaussian function in (8).

It is assumed that the number densities of O_3 molecules drawn at around x = 0 and dispersed on the upstream vortex rim in a unit time are equal, i.e.,

$$S_{up}^{+0} = \int_{-\infty}^{+\infty} S_{up}^{+}(x)dx = \int_{-\infty}^{+\infty} S_{up}^{-}(x)dx. \tag{10}$$

Similarly we define the sink and source of O_3 molecules in the EHD-driven downstream vortex $S_{down}^{+}(x)$ and $S_{down}^{-}(x)$.

After inserting (2) and (3) into (1), equation (1) was solved numerically for the steady-state condition ($\frac{\partial n}{\partial t} = 0$). The solution fulfils the boundary condition: $\frac{\partial n}{\partial x} = 0$ for L=50 cm, where L is the distance from the CDRS electrode in the upstream and downstream directions.

In the calculations we assumed that the diffusion coefficient of O_3 is equal to that of O_2 in air (D = 0.2 cm^2s^{-1} [9]). The O_3 production parameter w_p was varied in a reasonable range (1 cm < w_p < 5 cm). It did not essentially change the results. The results presented in Fig. 3 correspond to w_p = 2 cm. The total O_3 production in a unit time, i.e. parameter S_{po} was estimated for each operating gas velocity V_m from the corresponding ozone concentration (constant) at the reactor exit, i.e. from that found experimentally at x > 30 cm

downstream (Fig. 3). The parameters of source and sink terms for the upstream and downstream recirculation of O_3 molecules were chosen to fit the experimental results.

We also calculated the ozone concentration distribution along the CRDS reactor, neglecting the EHD transport of ozone.

4. RESULTS AND CONCLUSIONS

Both results of the calculation of the ozone distribution, i.e. with and without EHD transport are presented in Fig. 2. The calculation results which take into account the EHD transport of ozone (solid curves) fit reasonably the experimental points for main flow vleocities of 0.3, 0.5 and 0.8 m/s. The solid curves in Fig. 2 reflects the main features of the experimentally found ozone distribution along the CDRS reactor, i.e. the presence of ozone in the upstream region, O_3 distribution maxima around the CDRS electrode and constant O_3 distribution at the reactor exit. On the contrary, those peculiarities of the ozone distribution could not be revealed by the calculations when the EHD transport was neglected, leaving the diffusion and convection transport. The phenomenological model presented in this paper fails to describe the ozone distribution at V_m= 0.18 m/s. This is likely due to a different flow pattern of the flow at a main flow velocity V_m= 0.18 m/s, which is 3-dimensional rather than 2-dimensional.

Concluding, the EHD transport of ozone against the main flow in the CDRS reactor, phenomenologically introduced into the ozone transport equation, enabled the ozone distribution along the CDRS reactor to be explained, in particular the presence of ozone molecules far in the downstream direction.

REFERENCES

[1] J.S. Chang, P. Lawless, T Yamamoto, IEEE Plasma Sci., 19, 1152-1166, 1991.

[2] T. Ohkubo, S. Kanazawa, Y. Nomoto, J. Mizeraczyk, 35th Annual Meeting – IEEE Industry Applications Society, Roma, Italy, Ed.: IEEE Industry Applications Society, 1&2, 864-867, 2000.

[3] S. Kanazawa, Y. Shuto, N. Sato, T. Ohkubo, Y. Nomoto, J. Mizeraczyk, J.S. Chang, IEEE Trans. Ind. Appl., 39, 2, 333-339, 2003.

[4] L.B. Loeb, Ed. Berkeley C.A., University of California Press, 1965, pp. 402-407.

[5] J. Mizeraczyk, J. Dekowski, J. Podliński, M. Dors, M. Kocik, J. Mikielewicz, T. Ohkubo, S. Kanazawa, IEEE Trans. on Plasma Sci., 30, 1, 164-165, 2002.

[6] J. Mizeraczyk, J. Podliński, M. Dors, M. Kocik, T. Ohkubo, S. Kanazawa, J.S. Chang, Czech. J. Phys, Suppl. D, 52, D413-D420, 2002

[7] K Urashima, S.J. Kim, J.S. Chang, J. Adv. Oxid. Tech., 6, 123-131, 2003.

[8] M. Kocik, J. Dekowski, J. Mizeraczyk, S. Kanazawa, T. Ohkubo, J. S. Chang, Proceedings of 2003 Annual Meeting of the Institute of Electrostatics Japan, Noda, Japan, 2003, pp. 189-194.

[9] E.A. Filimonova, R.H. Amirov, H.T. Kim, I.H. Park, J. Phys. D: Appl. Phys., 33, 1716–1727, 2000.

4th International Conference **ELMECO**
Nałęczów, Poland
September 2003

CORONA DISCHARGE-MOLECULAR SIEVE HYBRID SYSTEM FOR NO_X ABATEMENT

Mirosław DORS, Jerzy MIZERACZYK

Centre for Plasma and Laser Engineering, Institute of Fluid Flow Machinery, Polish Academy of Sciences, Fiszera 14, 80-231 Gdańsk, Poland
e-mail: mdors@imp.gda.pl

Abstract

The objective of this work was to investigate NO_x removal with a hybrid system consisting of a DC corona discharge and a molecular sieve at a room temperature (22ºC). In the hybrid reactor a positive DC corona discharge was generated between a hollow needle and a flat mesh. A gas mixture of N_2(80%):O_2(5%): CO_2(15%):NO(200ppm), simulating a flue gas, flowed through the tube with a flow rate of 1 l/min. The obtained results showed that due to absorption of NO_2, resulted from NO oxidation, by molecular sieve placed in the corona discharge region, NO_x removal increased significantly. It was also found that the number of NO molecules oxidised into NO_2 does not depend on initial NO concentration. Thus, in the presence of the molecular sieve in the discharge region, the removal of NO is not controlled by gas phase chemical kinetics but by surface processes.

Keywords: corona discharge, catalysts, molecular sieve, nitrogen oxides.

1. INTRODUCTION

Investigations carried out in laboratories and pilot plants showed that removal of NO_x from flue gases by corona discharges may be efficient [1, 2]. However, the energy consumption in this new technology is still not acceptable for commercial use and is to be improved.

A technology competitive to the corona discharge processing is the selective catalytic reduction (SCR) which has proved its efficiency in NO_x removal [3]. In the SCR process, ammonia (NH_3) and a catalyst operating at a relatively high temperature range of 280-430ºC are used to reduce NO_x to N_2 and H_2O which are harmless products. The efficiency of NO_x removal using the SCR method is up to 90 %.

In the corona discharge processing, the dominant mechanism of NO_x removal is its oxidation to gaseous HNO_3 which then is converted to NH_4NO_3 solid particles by adding NH_3 [4-9]. Among many corona discharge types, the most efficient in NO_x removal is a

corona radical injection (CRI) [6, 7]. In the CRI reactor, NH_3 is introduced through a hollow needle electrode into the corona discharge zone where NH_3 molecules dissociate to NH_2 and NH radicals. These radicals react with NO_x molecules converting them into NH_4NO_3 solids. The record NO_x removal energy yield of the CRI method is 40-250 g/kWh at NO_x removal efficiency of 95-100 % [7].

In recent years hybrid plasma-catalyst systems have been proposed because of their capability to reduce NO_x into N_2 and other harmless molecular gases [10-18]. A typical hybrid system consisted of a corona discharge and a catalyst operating at temperature over 120°C. In some hybrid systems, first the corona discharges were used for oxidizing NO into NO_2, and then the SCR processing with NH_3 was used to convert NO_2 into N_2 and H_2O [10-12]. The efficiency of NO_x removal using hybrid plasma-catalyst systems was up to 98 % at an energy yield up to 55 g/kWh [12]. In other hybrid systems, hydrocarbons were added to the flue gas polluted with NO_x to improve its removal [14-16].

When temperature of the flue gas is lower than 120°C, the main product of NO_x removal in the presence of NH_3 is NH_4NO_3, which deposits on the surface of the catalyst causing deactivation of catalytic reduction of NO_x [19]. This work was aimed at studying NO_x removal in a hybrid system consisting of a DC streamer corona discharge with a molecular sieve operating under low temperature (22ºC) without addition of NH_3. In this new method, NO_2 produced in the corona discharge by oxidation of NO was adsorbed in the molecular sieve what inhibited reverse reaction of reduction of NO into NO_2. The performance of our hybrid corona discharge–molecular sieve reactor is described below.

2. EXPERIMENTAL SET-UP

The hybrid corona discharge-molecular sieve reactor used in this experiment is the similar to that presented in [19]. The positive DC corona discharge was generated between a stainless steel hollow needle electrode and grounded flat mesh electrode (1 mm x 1 mm) made of brass. The outer and inner diameter of the hollow needle was 2 mm and 1.6 mm, respectively. The hollow needle-mesh spacing was 40 mm. The molecular sieve 5 A was placed on the mesh so that the hollow needle-molecular sieve spacing was about 30 mm.

The positive polarity DC high voltage (15-38 kV) was applied through a 10 MΩ resistor to the hollow needle electrode. The time-averaged discharge current varied in the range of 50-200 μA.

A gas mixture of N_2(80%):O_2(5%):CO_2(15%):NO, simulating a flue gas, was supplied through the hollow needle and then flowed through the reactor with a flow rate of 1 l/min. Initial concentration of NO in the gas mixture was either 200 ppm or 100 ppm.

Concentrations of NO and NO_2 in the working gas at the reactor inlet and outlet were measured by absorption spectroscopy method using a Perkin-Elmer 16 PC FTIR spectrophotometer.

3. RESULTS

The removal efficiency of NO from the working gas by processing it with the corona discharge without the molecular sieve was no higher than 20 % (at 7 W, Fig. 2a). As it is seen in Fig. 2b, concentrations of NO_2 corresponds to the amount of removed NO, what means that all removed NO molecules were oxidized into NO_2.

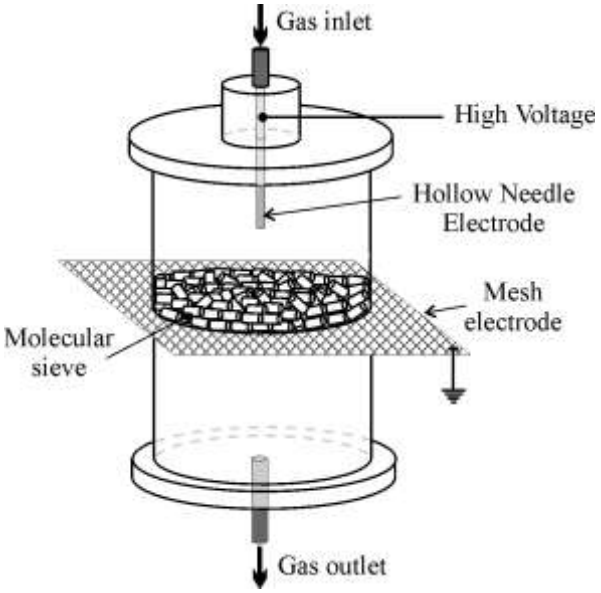

Fig. 1. Experimental set-up.

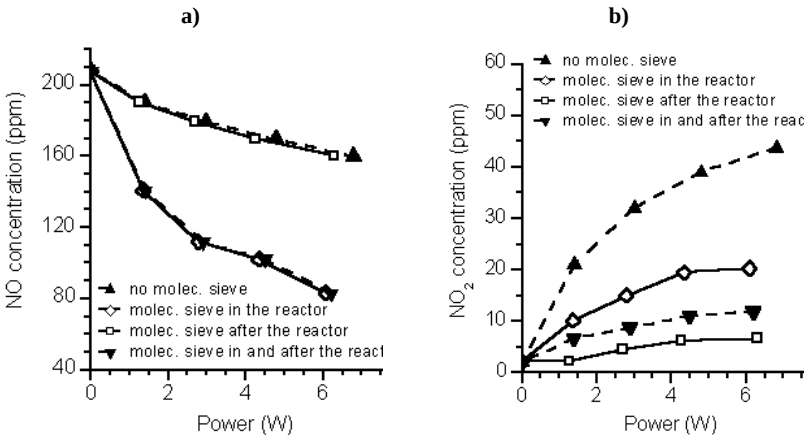

Fig. 2. Concentrations of NO and NO_2 in the working gas at the reactor outlet as a function of corona discharge power. Initial NO concentration 200 ppm.

When the gas exiting the corona discharge reactor flowed through the molecular sieve, then almost all NO_2 molecules were absorbed. Since the molecular sieve used in the experiment does not absorb NO, the removal efficiency of NO was the same as that obtained without using the molecular sieve.

It must be noticed, that concentrations of NO and NO_2 presented in Fig. 2 for the case without the molecular sieve are not adequate to the total number of NO molecules oxidized into NO_2. This number was much higher but a significant part of produced NO_2 was reduced back into NO due to reaction:

$$NO_2 + O \rightarrow NO + O_2 \qquad (1)$$

what resulted in higher concentration of NO and lower concentration of NO_2 at the reactor outlet.

The total number of NO molecules oxidized into NO_2 is close to that measured when the molecular sieve was placed in the corona discharge region. Then, NO removal increased up to 60 % at 6.1 W (Fig. 2a) and the number of NO_2 molecules, resulted from NO oxidation, was so high that a part of them could not be absorbed by the molecular sieve. Thus, NO_2 concentrations (Fig. 2b, line marked with ◇) were higher than those measured when the gas exiting the "empty" corona discharge reactor flowed through the molecular sieve (Fig. 2b, line marked with □). Even additional portion of the molecular sieve, placed after the hybrid corona discharge-molecular sieve reactor, could not absorb all NO_2 molecules (Fig. 2b, line marked with ▼).

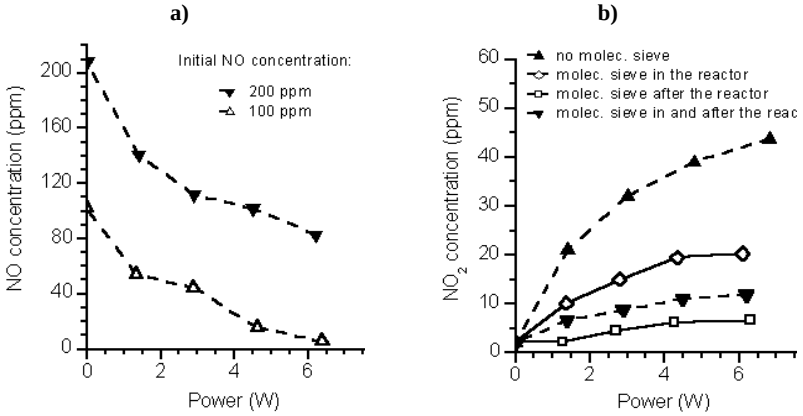

Fig. 3. Concentrations of NO and NO_2 in the working gas at the reactor outlet as a function of corona discharge power. Initial NO concentration 200 ppm and 100 ppm. The molecular sieve was placed in and after the corona discharge reactor.

When NO_2 molecules were removed from the corona discharge region by absorption in the molecular sieve, then removal of NO and concentration of NO_2 in the gas exiting the hybrid system did not depend on the initial NO concentration (Fig. 3). The number of NO oxidized into NO_2 was constant for specified corona discharge power. This suggests, that in the hybrid system consisting of the corona discharge and the molecular sieve NO removal

is not controlled by the gas phase chemical kinetics but by processes on the surface of the molecular sieve.

From the results presented in the Fig. 3 one can conclude that using two-stage system consisting of two corona discharge-molecular sieve hybrid reactors may result in NO_x removal efficiency of over 90 % what is comparable to other hybrid plasma-catalyst systems in which gaseous additives are used.

4. SUMMARY AND CONCLUSIONS

In this paper results of investigation of the performance of a hybrid corona discharge-molecular sieve reactor to be used for NO_x removal from the flue gases are presented. The gas mixture, which simulated a flue gas, was N_2(80%):O_2(5%):CO_2(15%):NO(200ppm). The corona discharge processing of the gas mixture was carried out: without the molecular sieve, with the molecular sieve in the corona discharge region and with the molecular sieve in and after the corona discharge region.

The investigation showed that:

- Due to absorption of NO_2, resulted from NO oxidation, by molecular sieve placed in the corona discharge region, NO_x removal increased significantly (from 20 % to 50 % at a corona discharge power of 6.1 W);
- The number of NO molecules oxidised into NO_2 does not depend on the initial NO concentration. Thus, in the presence of the molecular sieve in the discharge region, the removal of NO is not controlled by gas phase chemical kinetics but by surface processes.

The obtained results showed that non-thermal plasma methods of NO_x removal from flue gas should be directed into the removal of NO_2 *in statu nascendi*, i.e. from the non-thermal plasma region, where NO_2 is produced from NO as a result of plasma chemical reactions. This strategy was followed by using proposed hybrid reactor consisting of the corona discharge and molecular sieve.

REFERENCES

[1] J.S. Chang, in: Non-thermal Plasma Techniques for Pollution Control, Eds. B.M. Penetrante and S.E. Schultheis, Springer-Verlag Berlin Heidelberg, NATO ASI Series, 1993, vol. G 34 (A), pp. 1-32.

[2] E. M. Van Veldhuizen, Electrical Discharges for Environmental Purposes, Nova Science Publishers, New York, 2000.

[3] A.K. Hjalmarsson, Int. J. of Ener. Res. 14 (1990) 813-820.

[4] A. Mizuno, K. Shimizu, T. Matsuoka, S. Furuta, IEEE Trans. Ind. Appl. 31 (1995) 1463-1467.

[5] G. Dinelli, L. Civitano, M. Rea, IEEE Trans. Ind. Appl. 26 (1990) 535-541.

[6] K. Urashima, J.S. Chang, J.Y. Park, D.C. Lee, A. Chakrabarti, T. Ito, IEEE Trans. Ind. Appl., 34 (1998) 934-939.

[7] J.S. Chang, K. Urashima, M. Arquilla, T. Ito, Combust. Sci. and Tech., 133 (1998) 31-47.

[8] J.Y. Park, I. Tomicic, G.F. Round, J.S. Chang, J. Phys. D: Appl. Phys. 32 (1999) 1006-1011.

[9] K. Onda, K. Kato, Y. Kasuga, JSME International Journal, Series B, 39 (1996) 202-210.

[10] H.H. Kim, K. Takashima, S. Katsura, A. Mizuno, J. Phys. D: Appl. Phys. 34 (2001) 604-613.
[11] T. Hammer, S. Broer, Plasma Enhanced Selective Catalytic Reduction of NO_x for Diesel Cars (1998), Society of Automotive Engineers Technical Paper Series, No. 982428.
[12] T. Hammer, S. Broer, Plasma Enhanced Selective Catalytic Reduction of NO_x in Diesel Exhaust: Test Bench Measurements, Society of Automotive Engineers Technical Paper Series, No. 1999-01-3633.
[13] H. Suhr, G. Weddigen, Combust. Sci. Technol. 72 (1990) 101-115.
[14] K. Shimizu, T. Oda, IEEE Trans. Ind. Appl. 35 (1999) 1311-1318.
[15] T. Oda, T. Kato, T. Takahashi, K. Shimizu, J. Electrostatics 42 (1997) 151-157.
[16] T. Yamamoto, C.-L. Yang, M. R. Beltran, Z. Kravets, (1997) IEEE Ind. Appl. Society Annual Meeting, New Orleans, USA, pp. 1956-1960.
[17] B.S. Rajanikanth, S. Rout, Fuel Processing Technology, 74 (2001) 177-195.
[18] T. Kawasaki, S. Kanazawa, T. Ohkubo, J. Mizeraczyk, Y. Nomoto, Thin Solid Films 386 (2001) 177-182.
[19] M. Dors, J. Mizeraczyk, Czech. J. Phys., 52 (2002) D406-D412.

4th International Conference **ELMECO**
Nałęczów, Poland
September 2003

ELECTROHYDRODYNAMIC TRANSPORT OF NH_4NO_3 IN A NON-THERMAL PLASMA REACTOR

Mirosław DORS[1], Marek KOCIK[1], Janusz PODLIŃSKI[1], Jerzy MIZERACZYK[1], Seiji KANAZAWA[2], Toshikazu OHKUBO[2], Jen-Shih CHANG[3]

[1] *Centre for Plasma and Laser Engineering, Institute of Fluid Flow Machinery, Polish Academy of Sciences, Fiszera 14, 80-231 Gdańsk, Poland*
e-mail: mdors@imp.gda.pl
[2] *Department of Electrical and Electronic Engineering, Oita University, 700 Dannoharu, Oita 870-1192, Japan*
[3] *Department of Engineering Physics, McMaster University Hamilton, Ontario, L8S 4M1 Canada*

Abstract

In this paper results of the Particle Image Velocimetry (PIV) investigation of the transport of NH_4NO_3 aerosols produced in a corona radical injection (CRI) reactor during NO_x removal process are presented. The PIV investigation, in which NH_4NO_3 aerosols were employed as tracers, showed that NH_4NO_3 aerosols are transported and distributed in the CRI reactor by the EHD secondary flow (ionic wind). The flow structures generated in the CRI reactor are similar to those found in other corona discharge reactors. The deposition of NH_4NO_3 aerosols in the CRI reactor was not homogeneous. The highest density of the deposited NH_4NO_3 aerosols was on the plate electrode surface where the corona discharge streamers terminated. This was caused by a high velocity of NH_4NO_3 aerosols on their way from the nozzle electrode to the plate electrode.

Keywords: corona discharge, EHD flow, nitrogen oxides, ammonium nitrate.

1. INTRODUCTION

Among many corona discharge types, the most efficient in NO_x removal is a corona radical injection (CRI) [1-3]. In the CRI reactor, a radical precursor gas is introduced into the main flow of the NO_x polluted gas. The radicals produced by the corona enhance NO_x removal. Mostly ammonia is employed as a radical precursor. NH_3 is introduced through a hollow needle electrode into the corona discharge zone where NH_3 molecules dissociate

to NH_2 and NH radicals. These radicals react with NO_x molecules converting them into N_2 and H_2O by reductions and generates ammonium NH_4NO_3 aerosols. The record NO_x removal energy yield of the CRI method is 40-250 g/kWh at NO_x removal of 95-100 % [2]. Also hydrocarbons were used as a radical precursor [2].

This work was aimed at studying the production and movement of NH_4NO_3 aerosols produced in a corona radical shower reactor. The study was carried out using the Particle Image Velocimetry (PIV) technique. NH_4NO_3 aerosols were expected to be tracers sufficiently good for the PIV measurements. In addition to the fundamental interest in the NH_4NO_3 solid behaviour in the corona radical shower reactors, this investigation is related to the topical question - where NH_4NO_3 aerosols are produced, in the discharge region or outside it.

2. EXPERIMENTAL SET-UP

A schematic of the experimental apparatus is shown in Fig. 1. The CRI reactor was an acrylic rectangular reactor (100 mm x 125 mm x 700 mm). A brass hollow needle (2 mm outer diameter, 1.6 mm inner diameter) was used as a CRI electrode. The grounded electrode was a stainless-steel plate. The distance between the electrodes was either 30 mm or 50 mm. DC high voltage with positive polarity was applied through a 10 MΩ resistor to the CRI electrode.

Two gas flows, the main and the additional, were established in the reactor similarly like in the experiment of Kanazawa et al. [4]. The main gas (dry air with NO) flowed along the reactor with a flow rate of 3 L/min. The additional gas [dry air with NH_3 and Ar (1.0 %)] was injected through the hollow needle into the main gas flow with a flow rate of 0.5 L/min. The concentration of NO as well as NH_3 in the experiment of Kanazawa et al. [4] was 200 ppm. However, at these concentrations of NO and NH_3 the density of NH_4NO_3 aerosols produced in our experiment was too low to employ them as tracers in the PIV measurements. Thus, we increased NO and NH_3 concentrations to 0.5 %.

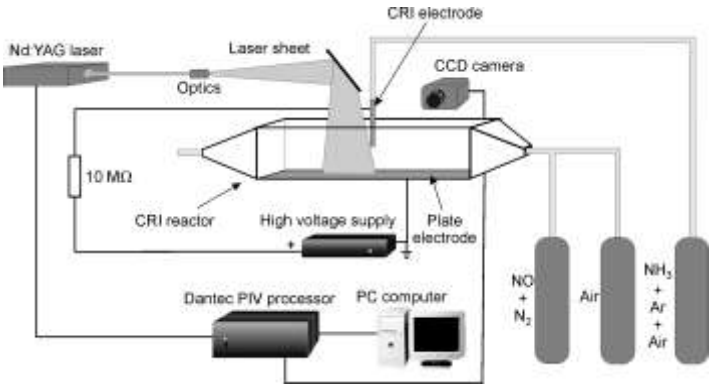

Fig. 1. Experimental set-up.

The PIV equipment consisted of a twin second harmonic Nd-YAG laser system (λ=532 nm, pulse energy 50 mJ), imaging optics (a cylindrical telescope), CCD camera,

image processor (Dantec PIV 1100), and PC computer. The laser sheet of a thickness of 1 mm, formed from the Nd-YAG laser beam by a cylindrical telescope was introduced into the CRI reactor, perpendicularly to the plate electrode. The NH_4NO_3 particle images were recorded by the Kodak Mega Plus ES 1.0 CCD camera, which could capture two images with a minimum time separation of 2 μs. The CCD camera active element size was 1008×1018 pixels. The captured images were transmitted by the Dantec PIV 1100 image processor to the PC computer for digital analysis. The final result of this analysis were maps of the velocity field of NH_4NO_3 aerosols.

When the interelectrode distance was 30 mm, the velocity field maps presented in this paper are composed of several adjacent velocity fields (from 2 to 4), each of an area of 25 x 25 mm. At the interelectrode distance of 50 mm, each velocity field map is a single field of an area 50 x 50 mm. All the presented velocity field maps resulted from the averaging of 15-25 measurements, i.e. the velocity maps are time-averaged.

3. RESULTS

The corona discharge generated in the CRI reactor was not uniformly distributed around the hollow needle edge. The corona discharge is seen in Fig. 2 as a narrow conical streamer starting from one point at the hollow-needle edge the position of which changed irregularly.

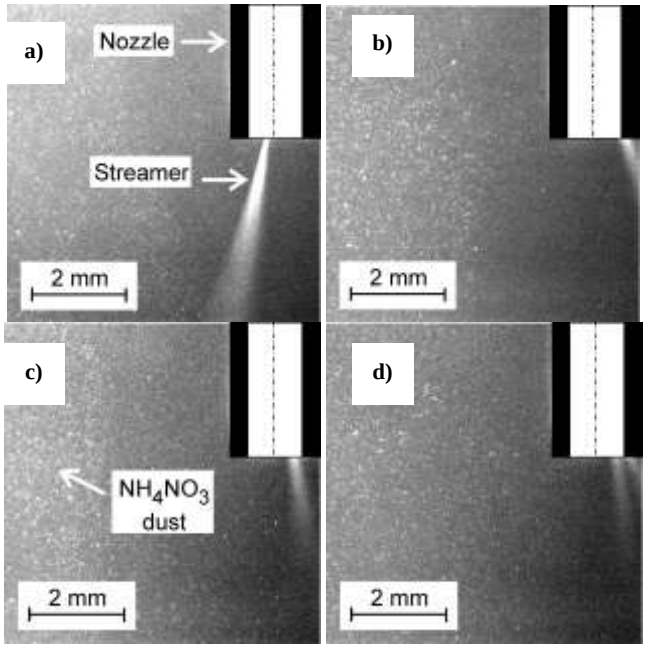

Fig. 2. Temporal images of the downstream area around the hollow-needle during corona discharge. Exposure time of each image was 133 ns. Interelectrode distance 30 mm. The main flow comes from the right side. NH_4NO_3 solid dust is shown.

The main consequence of such nature of the corona discharge is that velocity field patterns of NH_4NO_3 aerosols measured by PIV are not symmetric in relation to the hollow needle. The asymmetry increases with increasing distance between the hollow needle and plate electrode.

We observed that without the high voltage applied to the hollow needle electrode, NH_4NO_3 aerosols were not produced in the reactor. Their production started when the glow corona discharge mode was established. However, the efficient production of NH_4NO_3 aerosols started in the streamer corona discharge mode, when an optimum voltage was set as in [4]. This optimum voltage was 24 kV and 33 kV at an interelectrode distance of 30 mm and 50 mm, respectively. In both cases the corona discharge current was about 300 μA. All the PIV measurements were carried out at the optimum voltage.

When interelectrode distance was 30 mm, the bulk NH_4NO_3 aerosols move in the entire measurement area more or less perpendicularly to the plane electrode with the highest velocities in the discharge region just below the hollow needle (up to 4 m/s, Re=550, EHD=7×10^6, Fig. 3). As the flow field pattern shown in Fig. 3 resulted from averaging of 20 individual measurements, lasting 6 s in total, the position of the streamer on the nozzle could randomly vary.

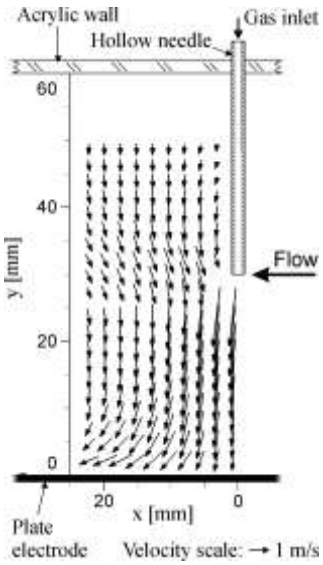

Fig. 3. Flow velocity field downstream of the hollow needle in the CRI reactor. Main gas [air:NO(0.5%)] flow rate - 3 l/min, additional gas [air:Ar(1.0%):NH_3(0.5 %)] flow rate - 0.5 l/min. The distance from the hollow-needle to the plate electrode - 30 mm. Applied voltage and corona discharge current - 24 kV and 300 μA, respectively. x - distance from the hollow-needle electrode.

As it is seen in Fig. 3, NH_4NO_3 aerosols flow first along the corona discharge and then along the plate electrode outwards. The relatively fast flow along the corona discharge disturbs electrohydrodynamically the main flow [5] in the reactor (Re=8, EHD=5.9×10^6), causing formation of large vortices, both downstream and upstream of the hollow needle, as seen in Figs. 4a and 4b. The vortices are formed about 75 mm from the hollow needle. The similar vortices were found in a needle-to-plate corona discharge reactor through which dry air (without NO and NH_3) flowed [5].

The bulk NH_4NO_3 aerosols circulates in the whole measurement area towards the corona discharge region, following the electrohydrodynamically disturbed flow pattern. It gives impression of sucking NH_4NO_3 aerosols present in the reactor by the fast flow directed towards the corona discharge region. After the experiment, it was found that NH_4NO_3 aerosols deposited the whole inner surface of the CRI reactor and also outer reactor ducts.

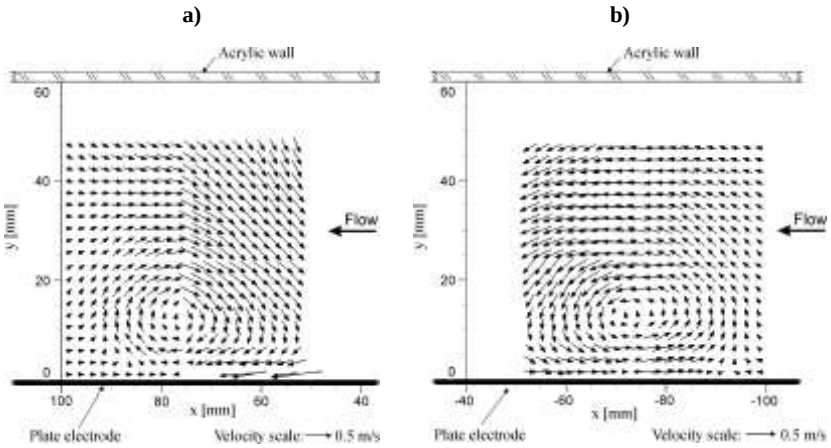

Fig. 4. Flow velocity fields in a distance of 50-100 mm from the hollow needle in the CRI reactor: a) downstream, and b) upstream. Main gas [air:NO(0.5%)] flow rate - 3 l/min, additional gas [air:Ar(1.0%):NH_3(0.5 %)] flow rate - 0.5 l/min. The distance from the hollow-needle to plate electrode - 30 mm. Applied voltage and corona discharge current - 24 kV and 300 μA, respectively. x - distance from the hollow-needle electrode.

4. CONCLUSIONS

In this paper results of the PIV measurements of the transport of NH_4NO_3 aerosols produced in the CRI reactor during NO_x removal process are presented for the first time.

The results showed that:

- NH_4NO_3 aerosols can be employed as tracers for PIV measurements;
- NH_4NO_3 aerosols are transported and distributed in the CRI reactor by the EHD secondary flow (ionic wind);
- Flow structures generated in the CRI reactor are similar to those found in other corona discharge reactors;
- Deposition of NH_4NO_3 aerosols in the CRI reactor was not homogeneous. The highest density of deposited NH_4NO_3 aerosols was on the plate electrode surface below the nozzle electrode. This was caused by a high velocity of NH_4NO_3 aerosols in the corona discharge region, directed more or less perpendicularly to the plate electrode.

From the obtained results it is difficult to answer where NH_4NO_3 aerosols were produced: in the corona discharge region or outside it. NH_4NO_3 aerosols were present in the entire measurement area, also very close to the hollow needle outlet. This means that they might be either produced in the corona discharge region or transported to the vicinity of the nozzle by the electrohydrodynamically generated vortices. Thus, the question on the place of NH_4NO_3 aerosols origin is still open.

It must be noticed that the PIV measurements of the velocity field were carried out only in one plane, passing through the hollow needle, parallel to the reactor side walls. To know the comprehensive flow velocity field pattern in the reactor, three dimensional map of the velocity field has to be measured.

REFERENCES

[1] J. S. Chang, P.C. Looy, K. Nagai, T. Yoshioka, S. Aoki, A. Maezawa, IEEE Trans. Ind. Appl., 32, 131-136, 1998.

[2] J. S. Chang, K. Urashima, M. Arquilla, T. Ito, Combust. Sci. and Tech., 133, 31-47, 1998.

[3] K. Urashima, J.S. Chang, J.Y. Park, D.C. Lee, A. Chakrabarti, T. Ito, IEEE Trans. Ind. Appl., 34, 934-939, 1998.

[4] S. Kanazawa, J. S. Chang, G.F. Round, G. Sheng, T. Ohkubo, Y. Nomoto, T. Adachi, Combust. Sci. and Tech., 133, 93-105, 1998.

[5] J. Mizeraczyk, J. Dekowski, J. Podliński, M. Dors, M. Kocik, J. Mikielewicz, T. Ohkubo, S. Kanazawa, IEEE Trans. Plasma Sci., 30, 164-165, 2002.

4th International Conference **ELMECO**
Nałęczów, Poland
September 2003

MEASUREMENT OF THE FLOW VELOCITY FIELDS IN MULTI-FIELD POSITIVELY POLARIZED WIRE-PLATE ELECTROSTATIC PRECIPITATOR

Janusz PODLIŃSKI[1], Jerzy MIZERACZYK[1], Jarosław DEKOWSKI[1], Marek KOCIK[1], Jen-Shih CHANG[2]

[1] *Centre for Plasma and Laser Engineering, Institute of Fluid Flow Machinery, Polish Academy of Sciences, Fiszera 14, 80-231 Gdańsk, Poland, e-mail:* janusz@imp.gda.pl

[2] *Department of Engineering Physics, McMaster University, Hamilton, Ontario, L8S 4M1 Canada*

Abstract

In this paper results of the Particle Image Velocimetry measurements of the flow velocity fields in a wire–to–plate type electrostatic precipitator with seven positively polarized wire electrodes and one or two grounded plate electrodes are presented.

Keywords: electrostatic precipitator, corona discharge, EHD flow, PIV, flow measurement, velocity field.

1. INTRODUCTION

Electrostatic Precipitators (ESPs) operating with high overall collection efficiency, are not effective in the removal of fine particles [1] which can contain toxic trace elements. Therefore, there has long been an interest in improving the ESP collection of fine particles.

The motion and precipitation of particles in the duct of an ESPs depends on the particle properties, electric field, space charge and gas flow field. It was shown that a significant interaction between these factors exists, resulting in considerable turbulent flow structures in the volume between the stressed and collecting electrodes [2]. However, there is not yet clear whether these turbulent flow structures enhance or reduce fine particle precipitation process.

To elucidate the influence of the electrically generated flow disturbances on the gas cleaning process, the flow patterns in the ESPs were studied using various visualization and laser techniques [3, 4, 5]. Recently, the Particle Image Velocimetry (PIV) was used in investigations of the flow fields in ESPs, in particular in investigations of the electrohydrodynamically induced secondary flow patterns [6, 7, 8].

In this paper results of the PIV measurements of the flow velocity fields in a wire-to-plate type ESP with seven positively polarized wire electrodes and one or two grounded plate electrodes are presented.

2. EXPERIMENT

In general, the flow pattern in the ESP has 3-dimensional character [3]. At present, imaging of the 3-dimensional velocity field in the ESP is technically unattainable. However, measurements of the velocity fields in several planes, which are perpendicular and parallel cross sections in the ESP are feasible. Such measurements could be quite informative on the spatial characteristics of the flow in the ESP, although being far from the full picture which can be only obtained from 3-dimensional measurements.

In this experiment we aimed at measuring the velocity field in one plane perpendicular to the wire and plate electrodes (a perpendicular section, the first experiment) and in several planes parallel to both electrodes (parallel sections, the second experiment). However, the latter measurement was not feasible when both plate electrodes were present in the ESP because the opaque plate electrode protrudes observation of the flow pattern in the planes parallel to the electrodes. Therefore could measured the velocity field in the planes parallel to the electrodes only when one of the plate electrode was removed.

The apparatus used in this experiment consisted of an ESP, high voltage supply and standard PIV equipment for the measurement of velocity field (Fig. 1).

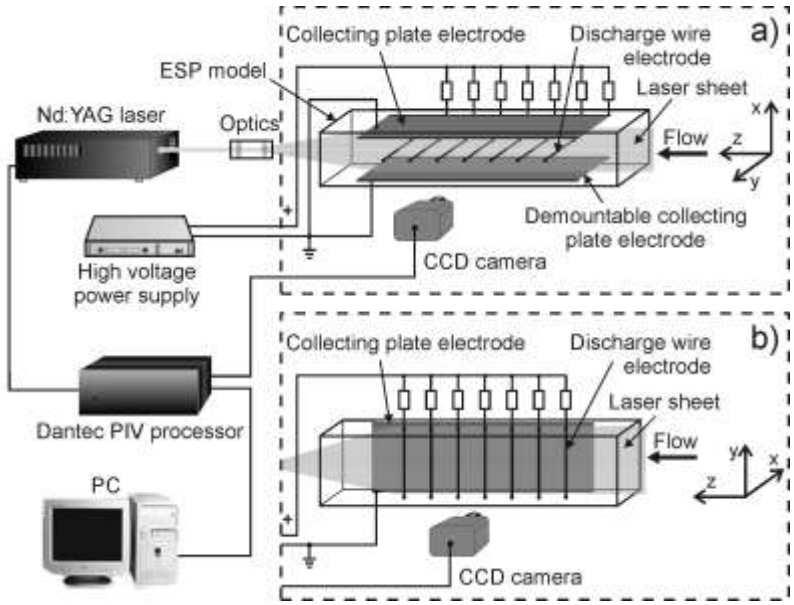

Fig. 1. Experimental set-up for measurements of the velocity field in the ESP:
a) perpendicular section (two plate electrodes present);
b) parallel section (single plate electrode present).

In the first experiment, when the velocity field was measured in the perpendicular section, the ESP was a plane-parallel acrylic duct, 200 mm wide, 160 mm high and 1600 mm long (Fig. 1a). In the centre of the duct, at the top and bottom acrylic walls two collecting stainless-steel plate electrodes (200 mm x 1000 mm) were mounted. The distance between plate electrodes was 100 mm. In the middle between the plate electrodes seven stainless-steel wire electrodes (diameter of 1 mm, length of 200 mm) were placed, parallel to the plate electrodes (Fig. 1a). They were fixed in the acrylic side-walls. The distance between wire electrodes was 100 mm and the distance from each wire to the plate electrodes was 50 mm.

In the second experiment, when the velocity field was measured in the parallel sections, the same plane-parallel acrylic duct was used. However, one of the plate electrodes was removed to make the observation of the flow in the parallel sections possible (Fig. 1b). After removing one of the plate electrodes, the distance between the wire electrodes and the acrylic wall was 80 mm.

The absence of the second plate electrode influenced apparently the velocity field patterns in the ESP, which are supposed to be different to those in a two-plate electrode ESP, in particular in the space between the wires and the acrylic wall. On the other hand, we expected that main features of the velocity field patterns of the typical ESP with two plate electrodes should be preserved to same extend in the space between the wires and the plate electrode in the single-plate ESP.

The positive voltage applied to the wire electrodes was 24 kV (for the ESP with two plate electrodes) or 26 kV (for the ESP with single plate electrode). The discharge current was 650 μA and 540 μA for two plate electrode and single plate electrode arrangement, respectively. The voltage was supplied to each wire through a 10 MΩ resistor. Air seeded with cigarette smoke (size of less than 1 μm in dry air) was blown through the reactor duct with an average velocity of 0.14 m/s and 0.6 m/s (for the ESP with two plate electrodes) and with an average velocity of 0.14 m/s (for the ESP with single plate electrode). In this paper results for an average velocity of 0.14 m/s only are presented. It is assumed that the cigarette smoke particles follow the gas flow, showing its structure.

The PIV equipment consisted of a twin second harmonic Nd-YAG laser system (λ=532 nm, pulse energy 50 mJ), imaging optics (cylindrical telescope), CCD camera, image processor (Dantec PIV 1100) and PC computer. The laser sheet of thickness of 1 mm, formed from the Nd–YAG laser beam by the cylindrical telescope was introduced into the ESP to form observation planes. The particle images were recorded by the Kodak Mega Plus ES 1.0 CCD camera. The captured images were transmitted by the Dantec PIV 1100 image processor to the PC computer for digital analysis.

The laser sheet, which defines the observation plane, was placed either perpendicularly to the wire electrodes at their half-length (measurement in the perpendicular section when the ESP had two plate electrodes, Fig. 1a) or parallel to the wire electrodes (measurement in the parallel sections when the ESP had only single plate electrode, Fig. 1b). The parallel planes of observation were set at four distances from the wires, forming the plane I – between the acrylic wall and the wires at x = - 25 mm, and planes II, III and IV – between the wires and the plate electrode at x = 5 mm, x = 25 mm and x = 45 mm, respectively (x – distance from the wire electrodes, Fig. 3).

The velocity field maps presented in this paper are composed of several adjacent velocity fields (in Fig. 3 they are marked as rectangular A - G). All the velocity fields resulted from the averaging of 100 measurements, which means that each presented result is time-averaged.

3. RESULTS

When the PIV method is used for the velocity field monitoring of the gas flow in which electric forces do not exist, the obtained velocity field structure corresponds to the motion of the undisturbed primary gas flow. However, when electric forces exist in the flow, the velocity field shows the flow structure changed by the electrohydrodynamic (EHD) forces.

Flow patterns in the section perpendicular to the wires

The flow velocity field measured by the PIV and the corresponding streamlines in the section perpendicular to the wires in the ESP with seven wire electrodes and two plate electrodes are shown in Fig. 2. At relatively low primary flow velocity the seed particles were removed very fast from the gas by electrostatic precipitation. The particle removal was higher with increasing distance from the first wire electrode upstream. Beyond the third wire electrode the gas was almost free from the seed particles, which caused the PIV measurement impossible to carry out in this areas. Therefore, the flow velocity field and streamlines in Fig. 2 are limited only the area with 3 first electrodes.

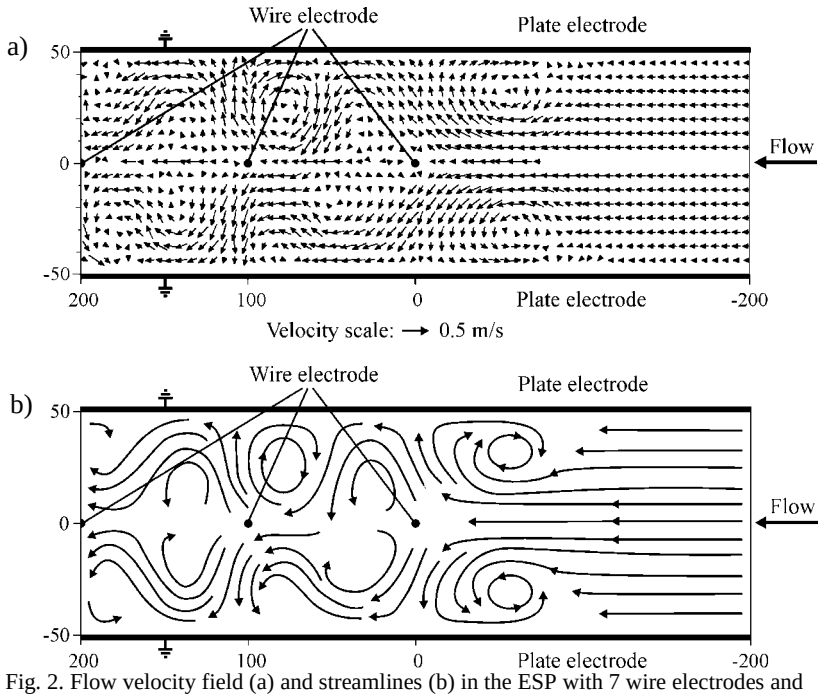

Fig. 2. Flow velocity field (a) and streamlines (b) in the ESP with 7 wire electrodes and 2 plate electrodes (only the area with 3 first electrodes). Primary flow average velocity of 0.14 m/s, applied positive voltage of 24 kV, discharge current 650 μA. The observation plane was placed perpendicularly to the wire electrodes at their half-length. Positions of the wires are marked by dots. Dimensions in mm.

At a primary flow average velocity of 0.14 m/s, the Reynolds number was Re = 466; the EHD number – $E_{hd} = 3.7*10^6$, and the ratio of the EHD number to the Reynolds number squared - $E_{hd}/Re^2 = 17$ [9]. The parameters used to calculate Re and E_{hd} were: primary flow velocity V = 0.14 m/s, air dynamic viscosity $\nu = 15 \times 10^{-6}$ m^2/s, air density $\rho = 1.205$ kg/m^3, ion mobility (N_2^+ in air) $\mu_i = 2.93 \times 10^{-4}$ m^2/Vs, characteristic length (wire-plate distance) L = 0.05 m, discharge area (covered by 7 wire electrodes on two plate electrodes) A =2 x 700 mm x 200 mm = 0.28 m^2, total discharge current I = 650 μA. Since the $E_{hd}/Re^2 >> 1$, the electric force was dominating over the inertial one, disturbing heavily the primary flow. Strong vortexes (with local velocities up to 0.4 m/s) were formed in both the upstream and the downstream regions of the ESP (Figs. 2a and b). The upstream region vortexes, with their centres placed around 60 mm from the wire electrode, were stable and regular.

Flow patterns in the sections parallel to the wires

In this case, at a primary flow average velocity of 0.14 m/s, discharge area (covered by 7 wire electrodes on the single plate electrode) A = 700 mm x 200 mm = 0.14 m^2, total discharge current I = 540 μA, and the other parameters as for the ESP with two plate electrodes, the Reynolds number - Re = 466, the EHD number - $E_{hd} = 6.1*10^6$, and the ratio of the EHD number to the Reynolds number squared - $E_{hd}/Re^2 = 28$. As in the case of two plate electrodes, the $E_{hd}/Re^2 >> 1$. Therefore the flow between the wires and the plate was expected to be disturbed by the EHD forces.

The streamlines in four parallel planes, described above, in the ESP with seven wire electrodes and single plate electrode are shown in Fig. 3. The streamlines were drawn basing on the corresponding PIV velocity fields.

The influence of the EHD forces on the flow structure is clearly seen in Fig. 3. The lowest influence of the EHD forces on the flow is seen in the plane I (x = -25 mm), situated in the space between the wire electrodes and the acrylic side-wall, thus outside of the discharge area. As seen, in this plane the EHD forces caused the gas to move opposite to the direction of the primary flow in the area D. This probably resulted in small vortexes seen in the areas B and C.

In the plane II (x = 5 mm) the influence of the EHD forces is greater than in the plane I. A pair of large vortexes near the wire electrode No 1 (the area B) and large areas without flow in the plane II near the wire electrodes No 3-7 are seen. In the area A (upstream from the wire electrode No 1), the gas is forced to flow against the primary gas flow direction.

In the plane III (x = 25 mm) a pair of vortexes in the transit area between A and B (similarly as in the plane II) and pairs of vortexes in the areas E, F, G (corresponding to the wire electrodes No 4-7) are present. In the area A, the gas flows opposite to the flow direction of the primary gas.

In the plane IV (x = 45 mm, situated 5 mm before the plate electrode) strong flow along the plate electrode directed either in accordance to or against the direction of the primary flow are present. This is understandable, assuming that there is a strong flow from each wire electrode perpendicularly to the plate electrode. Such a flow has to break up before the plate electrode into streams flowing along the plate electrode. This is seen as the flow moving upstream and downstream. In the area A a strong flow moves oppositely to the direction of the primary gas flow, resulting in the vortexes around z = -200 mm.

In each measured plane, the flow patterns in areas E, F and G (corresponding to the wire electrodes No 5-7) are similar. It seems that in these areas regular and reproducible

flow patterns are form, while the transit areas A-D, corresponding to the wire electrodes No 1- 4 exhibit irregular flow patterns. We may anticipate that the regular flow patterns seen in the areas E-G would be reproduced if the wire electrode number is larger than 7.

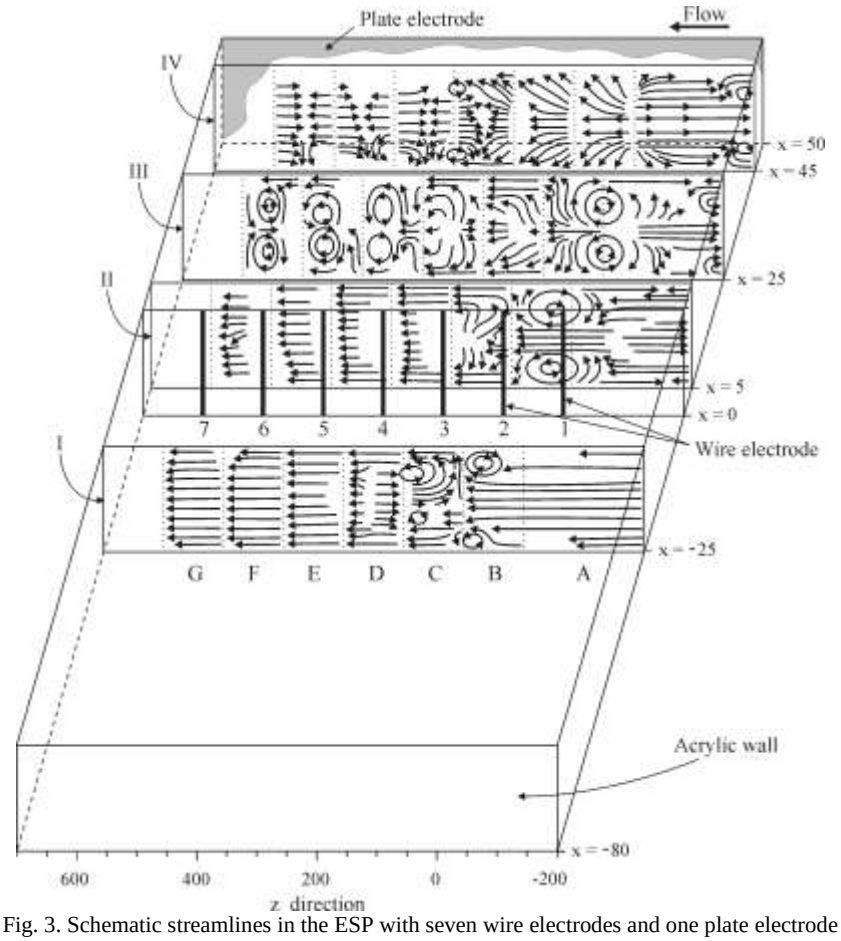

Fig. 3. Schematic streamlines in the ESP with seven wire electrodes and one plate electrode at a primary flow average velocity of 0.14 m/s, applied positive voltage of 26 kV, discharge current 540 μA. The observation planes were placed parallel to the wire electrodes. Dimensions in mm, x – distance from the wire plane. A-G – measurement subareas, 1-7 – wire electrode numbering.

Outline of the flow velocity field in an ESP

The following three-dimensional outline of the vortexes in the ESP with seven wire electrodes and single plate electrode as in Fig. 4 (only region around wires No 4 -7

is shown) can be deduced from the measurements presented above. The vortexes in plane A (situated perpendicularly to the wire electrodes at their half-length) are drawn on the basis of the results presented in Fig. 2 and Fig. 3. The vortexes drawn in the plane B (situated parallel to the wire electrodes, 25 mm before the plate electrode) correspond to the results presented in Fig. 3 (plane III).

The 3-D flow pattern outline based on the experimental results presented in this paper shows that the flow in the ESP is complex, with vortexes in the planes parallel and perpendicular to the wire electrodes. This is in agreement with the results presented in [3].

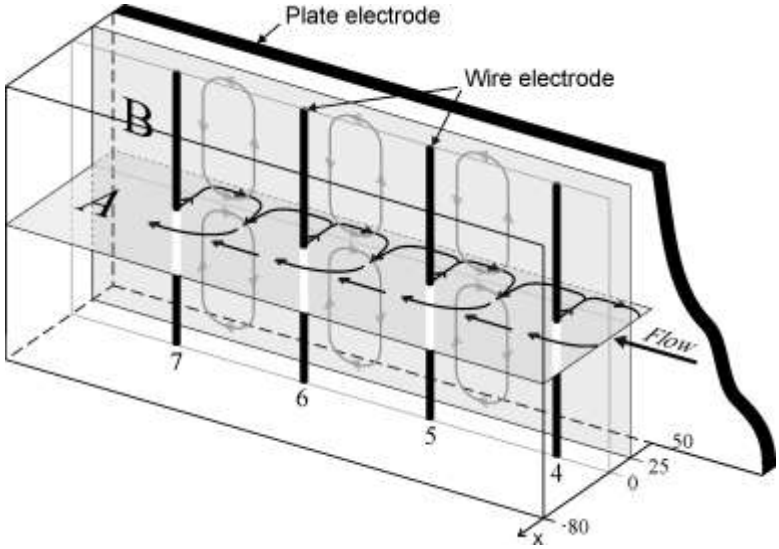

Fig. 4. 3D outline of the vortexes in planes A and B (shaded)around the wires No 4 -7 in the ESP.

4. SUMMARY AND CONCLUSIONS

In this paper the flow velocity fields and streamlines measured by the PIV in a wire-to-plate type ESP are presented. The ESP had seven wire electrodes positively polarized and one or two plate electrodes. The measurement planes were placed either perpendicularly to the wire electrodes at their half-length or in four planes parallel to the wire electrodes.

The presented results confirmed that the presence of the electric field causes significant changes in the flow patterns in the ESP. In the ESP with a primary flow average velocity of 0.14 m/s, the EHD induced secondary flow (having velocity of several tens of cm/s) with strong vortexes in the downstream and upstream regions is formed.

This investigations confirmed that the flow patterns in the ESP at positive voltage polarity are 3-dimensional as shown in previous publications [3].

The presented flow velocity patterns illustrate complex nature of the EHD induced secondary flow in the ESPs, which can be revealed by 3–dimensional measurements of the velocity fields.

ACKNOWLEDGEMENTS

This work was supported by the Foundation for Polish Science (FNP, subsidy 8/2001) and the State Committee for Scientific Research (grant KBN PB 1756/T10/01/21).

REFERENCES

[1] A. Mizuno, IEEE Trans. Dielectrics and Electrical Insulation, 7-5, 615-624, 2000.
[2] P. Atten, F.M.J. McCluskey, A.C. Lahjomri, IEEE Trans. Ind. Appl., 23-4, 705-711, 1987.
[3] G.A. Kallio, D.E. Stock, IEEE Trans. Ind. Appl., 26-3, 503-514, 1990.
[4] J.H. Davidson, P.J. McKinney, IEEE Trans. Ind. Appl., 27-1, 154-160, 1991.
[5] S.J. Park, S.S. Kim, Aerosol Science and Technology, 33 (3), 205-221, 2000.
[6] J. Mizeraczyk, M. Kocik, J. Dekowski, M. Dors, J. Podliński, T. Ohkubo, S. Kanazawa, T. Kawasaki, J. Electrostatics, 51-52, 272, 2001.
[7] J. Mizeraczyk, J. Dekowski, J. Podliński, M. Kocik, T. Ohkubo, S. Kanazawa, J. Visualization, 6, 2, 125-133, 2003.
[8] M. Kocik, J. Podliński, J. Dekowski, M. Dors, J. Mizeraczyk, Proc. SPIE, 5229, 301-304, 2003.
[9] IEEE-DEIS-EHD Technical Committee, IEEE Trans. Dielectrics and Electrical Insulation, 10-1, 3-6, 2003.

4th International Conference **ELMECO**
Nałęczów, Poland
September 2003

HYDROPHILISATION OF NON-WOVEN TEXTILES BY MEANS OF SURFACE BARRIER DISCHARGE AT ATMOSPHERIC PRESSURE

Jan JANCA, Pavel STAHEL, Vilma BURSIKOVA, Zdenek NAVRATIL

Department of Physical Electronics, Faculty of Sciences,
Masaryk University, Kotlářská 2, 611 37 Brno, Czech Republic,
pstahel@physics.muni.cz

Abstract

The aim of the present work was to investigate the surface modification of non-woven polypropylene textiles by means of plasma treatment at atmospheric pressure in order to improve their hydrophilic properties. The polypropylene non-woven spun-bond textiles with surface weight of 20 g/m^2 were used as the samples. The surface activation was provided by surface barrier discharge at atmospheric pressure where the operation frequency was 6 kHz. The surface energy of treated and untreated textile was investigated by means of contact angle measurement with four different liquids using the Surface Energy Evaluation System (SEE System). The surface energy was calculated according to acid-base theory, which enables besides the polar and dispersion part of the surface energy also to determine the acid (electron-donor) and base (electron-acceptor) components. The surface energy was correlated to the wetting properties of the materials studied by industrial permeability tests.

In the present paper the hydrophilic properties and aging of plasma treated polypropylene samples with the plasma conditions and plasma exposition time are discussed.

Keywords: plasma; atmospheric pressure; surface energy; surface modification.

1. INTRODUCTION

Recently the plasma treatment becomes as a very attractive tool for control of the polymer surface properties while keeping the desirable bulk properties. In many industrial applications there is a need to modify the surface of polymers with keeping theirs desired bulk properties. The chemical activation of the surfaces is the most often used method for their activation, however the ecological requirements force the industry to search

alternative methods protecting the environment. As one of the most prospective and cheap solutions become the surface modification of polymers in low-temperature plasma.

The polypropylene (PP) materials have many advantages such as high strength to weight ratio, ability to recycle, low price and so one. However, their low surface energy (approximately 20 - 25 mJ/m^2) requires finding methods for surface activation. In [1] the increase of the wettability of the non-woven PP textiles by means of surface discharge at atmospheric pressure was described.

The main objective of the recent paper is to study of the activated surface of these materials by means of contact angle (CA) measurement.

2. EXPERIMENTAL

In the recent study the plasma activation of polypropylene textiles was carried out by surface discharges (SD) [1] operating at atmospheric pressure. The AC driving voltage had frequency of 6 kHz. The surface discharge was carried out on the surface of the insulating plate (glass, ceramics or polycarbonate). The insulating layer was fully covered with metal electrode from bottom side. On the other side of the insulating plate the metal electrode consisted of 18 strips (10 cm long and 1 mm wide) with a 9 mm distance between them. The electrodes were connected together. The whole arrangement was maintained in deposition chamber. The PP non-woven textile was drawn with controlled speed through the chamber between the metal electrodes and the glass insulator plate. The discharge appears along the PP non-woven textile surface in the decreasing initial electric field from the side of the thin metal strips. The active area of the surface discharge was 200 cm^2. In our experiments dry air and nitrogen was used as the buffer gas. The studied textiles were produced by Pegas a.s. Bučovice and surface density of PP textiles was 20 g/m^2.

The contact angle was measured directly from the observation of the solid-liquid meniscus. This method is often used for smooth surfaces, however its application for wettable materials is more complicated. In this case the determination of the contact angle immediately after the liquid was dropped on the PP surface is of crucial importance. After dropping a series of sessile drop images were taken by CCD camera in order to determine not only the initial contact angle, but also the change of the sessile drop in time due to wetting of the PP material.

For the calculation of the surface free energy of the non-woven PP textiles the acid-base theory was used [2]. This theory enables to determine besides the dispersion part of the surface energy also its acid-base components. As it was shown in the literature [3], these components may play important role in the case of the surface activation of PP materials as well as in the case of their aging.

The so-called “acid –base” theory enables to determine also the electron-acceptor and electron-donor parameter of the surface tension.

The total surface tension is a sum of its apolar and polar components:

$$\gamma = \gamma^{LW} + \gamma^{AB} \qquad (1)$$

where LW indicates the total apolar (dispersive), Lifshitz-van der Walls interaction, and AB refers to the acid-base or electron-acceptor/ electron-donor interaction according to Lewis.

The surface energy can be calculated according to Young-Dupré equation expressed by terms as electron-donor γ^+ and electron acceptor γ^- parameters:

$$(1+\cos\theta)\gamma_i = 2(\sqrt{\gamma_i^{LW}\gamma_j^{LW}} + \sqrt{\gamma_i^{+}\gamma_j^{-}} + \sqrt{\gamma_i^{-}\gamma_j^{+}}) \quad (2)$$

where i refers to liquid and j refers to solid material. The values can be determined from contact angle measurement with three liquids of which two must have polar component. The polar component is given by:

$$\gamma_j^{AB} = 2\sqrt{\gamma_j^{-}\gamma_j^{+}} \quad (3)$$

The liquids and their characteristic parameters used for contact angle measurement are listed in the following table:

Table 1 List of testing liquids used. The total surface energy and their components are given in mJ/m^2.

Testing liquid	γ_{tot}	γ^{LW}	γ^{AB}	γ^{+}	γ^{-}
Distilled water	72,8	21,8	51.0	25,5	21,8
Glycerol	64,0	34,0	30.0	3.9	57.4
Ethylene glycol	48,0	29.0	19.0	3.0	30.1
Dijodinmethane	50,8	50.8	~ 0	0	0

Water permeability of samples before and after plasma treatment was determined measuring the time necessary for the penetration of 5 ml of the testing liquid across the sample.

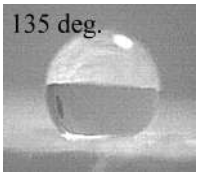

Fig. 1. Water drop on the un-treated PP surface.

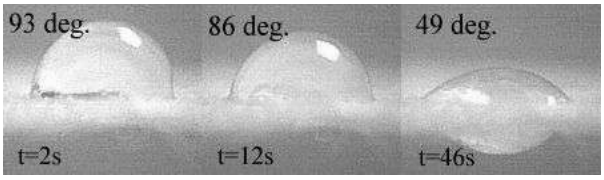

Fig. 2. The dependence of the water contact angle on time due to wetting of the spun-bond PP textile.

The contact angle was measured by means of the SEE (Surface Energy Evaluation) system developed by the authors of the present work. The observation of the solid-liquid meniscus is often used method for smooth surfaces, however its application for wettable materials is problematic. In this case the determination of the contact angle immediately after the liquid was dropped on the PP surface is of crucial importance [4].

After dropping a series of sessile drop images were recorded by CCD camera in order to determine not only the initial contact angle, but also the change of the sessile drop in time due to wetting of the PP material. In Fig. 1 the water drop on the untreated PP surface is shown. In Fig. 2 the dynamic evolution of the water contact angle and water drop size in time is illustrated. On the basis of the study of the drop behaviour on the PP surface is possible to distinguish the dynamic wetting from dynamic spreading of the liquid [4].

3. RESULTS AND DISCUSSION

Plasma treatment of PP proceeds by a free-radical mechanism that introduces a wide variety of oxidized functional groups and basic nitrogen containing groups onto the surface of the treated polymer. In Fig. 3 the calculated values of the total surface free energy of PP textile and in Fig. 5 the components o the total free energy depending on the treatment time are depicted. Liquids listed in Table 1 made the contact angle measurements and the surface energy calculations were made according to Eq. (2). The polar part γ^{AB} of the surface energy of the untreated material was almost negligible. The significant increase in surface energy after 1-minute treatment was caused mainly by the significant increase of the surface energy component indicating the base character of the studied surface. Approximately after 3s the saturation of all components of the surface free energy was reached.

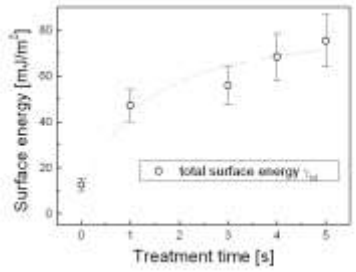

Fig. 3. The dependence of the total surface energy of PP textile on the treatment time.

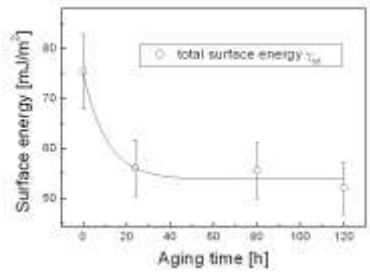

Fig. 4. The dependence of the total surface energy on the storage time for PP material treated 5s by surface barrier discharge.

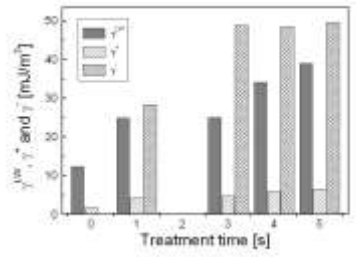

Fig. 5. Dependence of the PP non-woven total surface energy γ^{tot} and its apolar γ^{LW}, polar γ^{AB}, acid γ^{+} and base γ^{-} components on the treatment time.

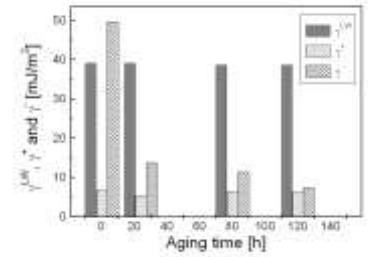

Fig. 6. Dependence of the PP non-woven total surface energy γ^{tot} and its apolar γ^{LW}, polar γ^{AB}, acid γ^{+} and base γ^{-} components on the storage time.

The time dependence ("aging") of the wettability of plasma treated samples was studied by measuring the contact angle and permeability up to several days after treatment. After the plasma activation by means of air and nitrogen surface discharge with supplied

power 60 and 100 W, the samples were stored in air atmosphere at 23 ^{o}C. The permeability and contact angle of sample were measured after the subsequent time steps. Fig. 4 gives the dependence of the surface energy of PP-textile treated 5s on the storage time. The decrease of the surface energy of the plasma treated material due to aging (Fig. 6) was caused mainly by rapid decrease of the base (electron-donor) component of the surface energy. Fig. 7 shows the dependence of the water contact angle and the water permeability on the treatment time in air surface discharge. In our case the plasma was supplied with 5 kHz sinus signal with amplitude 7 kV and the supplied power was 60 W. Fast increase in permeability was observed during the first 3 s, followed by a slow increase with increasing plasma exposure time. The water contact angle linearly decreases with increasing exposure time.

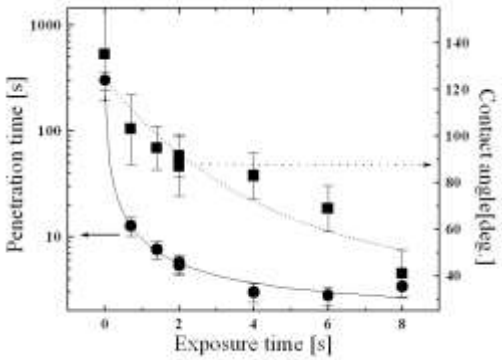

Fig. 7. Dependence of contact angle and water permeability as a function of surface discharge exposure time.

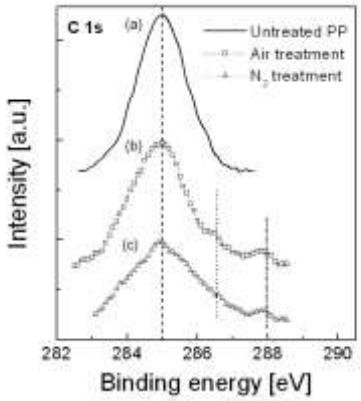

Fig. 8. XPS C 1s core level spectra of the studied surface: (a) untreated PP non-woven textile; (b) plasma treat ed PP non-woven textile at air; (c) plasma treated PP non-woven textile at nitrogen atmosphere.

The results obtained on the contact angle and permeability measurements were completed by XPS analysis of the studied materials. In Fig. 8 the C 1s core level spectra for the air and nitrogen treated and non-woven PP textiles are shown. The untreated PP surface exhibits a narrow peak 285.0 eV, which belongs to C-C and C-H_x bonds. In the case of the plasma treated surfaces the C 1s signals show a multi-peak structure, however the peaks are rather broad and an accurate determination of the particular contributions is difficult. The main contribution belongs to the C-C and C-H_x bonds at 285 eV. The asymmetry on the high binding energy side is probably due to bonding states -CH_2-C=N (286.4 eV), C–O (286.5 eV), C=O (288.0) and O=C-NH at 288.2 eV.

4. CONCLUSION

The hydrophilisation of non-woven PP textiles in barrier surface discharge was investigated. The dependence of the surface energy on the treatment time and on the storage time was studied by contact angle measurements. The obtained results were compared with the results on permeability tests and XPS analysis. The main contribution to the increase of the surface energy from the increase of the apolar and partially of the base part of the surface energy. On the other side, the aging is caused mainly by the rapid decrease of the base part of the surface energy, which could be related to the non-stable nitrogen containing surface contamination. The total surface energy of the PP non-wovens after 140 hours of storage was still ~ 48 mJ/m^2 .

ACKNOWLEDGEMENTS

The present work was supported by GAČR contract No.202/02/0880, 202/02/D097 and by MSM:143100003, COST 527.20.

REFERENCES

[1] P. Sťahel, J. Janča, D. P. Subedi: Czech. J. of Phys. (Suppl. D) 52:(2002)750.
[2] R.J. Good: Contact Angle, Wettability and Adhesion ed. K.L. Mittal 1993, 3.
[3] M.M. Chehimi, Adhesion promotion techniques Ed. by K.L. Mittal, (1999) 27.
[4] K. Grundke, M. Boerner and H.J. Jacobasch: Colloids and Surfaces 58: (1991) 4.

4th International Conference ELMECO
Nałęczów, Poland
September 2003

INVESTIGATIONS OF NOx REDUCTION WITH THE APPLICATION OF PLASMA GENERATED IN BARRIER DISCHARGES

Justyna JAROSZYŃSKA-WOLIŃSKA

Department of Chemical Technology, Lublin University of Technology,
Nadbystrzycka 40, 20-618 Lublin, Poland,
e-mail: jwtchem@akropolis.pol.lublin.pl

Abstract

A problem of NOx removal from industrial flue gases is very actual and technologically important because of high costs related to the application of hitherto used removal methods and a variety of emission sources. Over the recent decade a substantial development of processes with the use of non-thermal plasma has been noted.

The presented research work represents a certain part a greater research project. It aimed at finding the possibility to increase the oxidation degree of nitrogen monoxide at simultaneous absorption in water by preliminary mixing of purified gas with oxygen and performing the absorption in a two-stage way (oxygen - ozone). Such procedures if it proved to be successful could show the way to increase the degree of gas purification at the same amount of ozone used and reduce the demand for this very useful oxidiser.

Keywords: ozone, non-thermal plasma, ozone oxidation, NOx, reduction.

1. INTRODUCTION

The idea of obtaining a homogenous discharge in a reactor resembling a silent discharge setup was developed by (S. Okazaki et all) ten years ago. Since then conditions for the realization of that concept have been investigated as well as other application possibilities for that environment as, for example, to a PCVD (Plasma Chemical Vapor Deposition) process. Studies on various plasma sources are important also from the point of view of their analytical applications such as the atmosphere protection, waste gases emission control and solid wastes neutralization. Ozone synthesis development can be also understood as a research into the field of environmental technology.

There is a couple of chemical methods for a NOx removal from industrial flue gases such as catalytic reduction or oxidation that leads to obtaining of easily removable higher

oxides.. Over the recent decade a substantial development of processes with the use of non - thermal plasma has been noted. Presently used technologies of a selective catalytic reduction (SCR) and a selective non-catalytic reduction (SNCR) require an application of additional substances such as ammonia or urea. Catalytic reduction methods also require an application of high temperatures, which in industrial conditions with big quantities of gas can be costly. Oxidation methods, and especially the ones that apply ozone, are characterized by high efficiency and lack of wastes and therefore they are subject of extensive laboratory research.. Actual significance of the problem can be proved by the latest reports (Ozone News, vol. 28, No 5/2000, p.9) by an American environment protection agency (U.S.EPA) about an attempted commercialization of the NOx removal process with the use of ozone within a program of evaluation of technologies in the environment protection (Environmental Technology Verification Program ETV). The process is so actual and attractive that American researchers (BOC Group, Inc., Murray Hill, N.J) obtained for their version of that method, recently implemented in Midland (USA), the prestigious 2001 Kirkpatrick Award for Chemical Engineering Achievements, (Ozone News, vol.29, No6/2000, p15.).

Simultaneous considerable development of ozone production technologies (reduced energy costs) contributed to the increased interest in that strong and ecological oxidizer. Some application tests have been even performed (Ozone News,vol 29.No 6/2000). The Author has been researching within the mentioned field for many years now and among other achievements co-authored 3 Polish patents related to the process. An application of a non-thermal plasma to oxidize nitrogen oxides with ozone requires a determination of optimal parameters that decide over the process efficiency. To this end it is necessary to fathom and explain the mechanism of chemical and physical changes (chemical reactions and a process of mass exchange) occurring in the process. The process of nitrogen oxide oxidation with ozone runs towards the formation of N_2O_5. It is a quick process but it is composed of many-stages.

The key question there is to recognize mechanisms of individual reactions and to determine their competitiveness. which will make a basis for elaborating a global description of the process and finding optimal conditions for its running.

2. OBJECTIVE AND SCOPE

The application of ozone as an oxidizing agent makes a potentially effective although not fully tried yet utilization method for the NOx removal from flue gases. It is a wasteless method and with technological possibilities of obtaining a high rate of gas purification. Although a NOx removal by means of ozone economically seems to be a very promising process from the technological point of view its mechanism is quite complex and also not fully recognized. Assuming a quite simple mechanism of the NOx oxidation process at the first approximation it can be described by the following reactions: (1-5)

NO	+	O_3	---------	NO_2	+ O_2	(1)
NO_2	+	O_3	--------	NO_3	+ O_2	(2)
NO_2	+	NO_3	--------	N_2O_5		(3)
2 NO_2	+	O_3	---------	N_2O_5	+ O_2	(4)
N_2O_5	+	H_2O	--------	2 HNO_3		(5)

The above given reactions make the first step that is necessary to describe the process so that its first approximation could show its basic character which in reality is much more complex. The reactions run much quicker than it is in the case of CO to CO_2 or SO_2 to SO_3 oxidation by means of ozone. The performed tests prove that the NO oxidation process runs in a much complex way. In the first reaction nitrogen monoxide gets oxidised to NO_2 with only one oxygen atom from ozone. Next, NO_2 gets oxidised to NO_3 and then a reaction between those two oxides takes place towards the formation of N_2O_5 which in turn by the action of water can be changed into nitric acid (N_2O_5 immediately reacts even with moisture contained in flue gases forming HNO_3). Based on experimental results a simplified criterion equation has been elaborated and it has confirmed practical applicability of the method for the NOx removal by means of ozone. To develop the process to a larger scale it is necessary to fathom mechanisms of the component processes and to find main parameters that determine efficiency of the whole process.

3. EXPERIMENTAL METHODS

The presented research work deals mainly with classical silent discharges that form in a homogenous electric field when at least one electrode is separated from the gaseous zone by a dielectric layer. Experiments were performed cyclically for three electrodes within the range of voltage values of 4.0 – 7.5 kV, discharge gaps have been 1, 1.5, 2 mm at the frequency of 50 Hz (Fig. 1). For all the electrodes measurements have been performed within the range of the inlet gas flow rate of 30 - 100 dcm3/h. And prior to them dynamic measurements (Lissajous figures) have been performed taken. The experimental results are presented in the form of the ozone concentrations versus specific energy Becker's parameter and in the form of energy efficiency versus ozone concentration function for individual electrodes. First attempts of ozone application appeared to be quite efficient but the subsequent experiments on semi-technological scale revealed some of its disadvantages such as a tendency to produce hardly removable aerosols. However recently new economic calculations concerning ozone applicability have been reported. Moreover, it offers also chance to obtain products (nitrates and nitrites) in a much purer form and better meeting market requirements than the products obtained with the application of other methods including utilisation ones [2]. It aimed at finding a possibility to increase the oxidation degree of nitrogen monoxide at simultaneous absorption in water by preliminary mixing of purified gas with oxygen and performing the absorption in a two-stage way (oxygen-ozone). Such procedures if it proved to be successfully could show the way to increase the degree of gas purification at the same amount of ozone used and reduce the demand for this expensive oxidiser (Fig. 2).

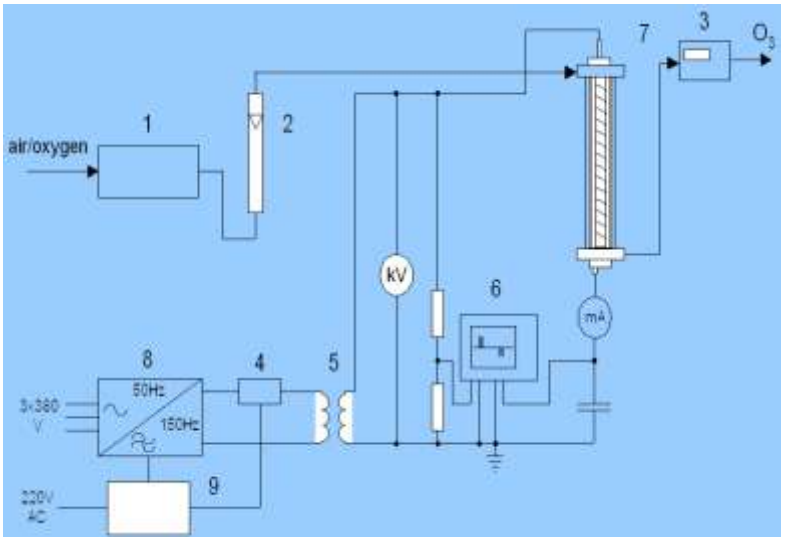

Fig. 1. Electrical circuits and measurement systems for plasma generation
1- air cleaning and drying system, 2 – rotameter, 3- ozone concentration measurement, 4- excess current protection, 5- autotransformer, 5- transformer HV, 6- oscilloscope, 7- ozonizer, 8- frequency converter , 9- panel control.

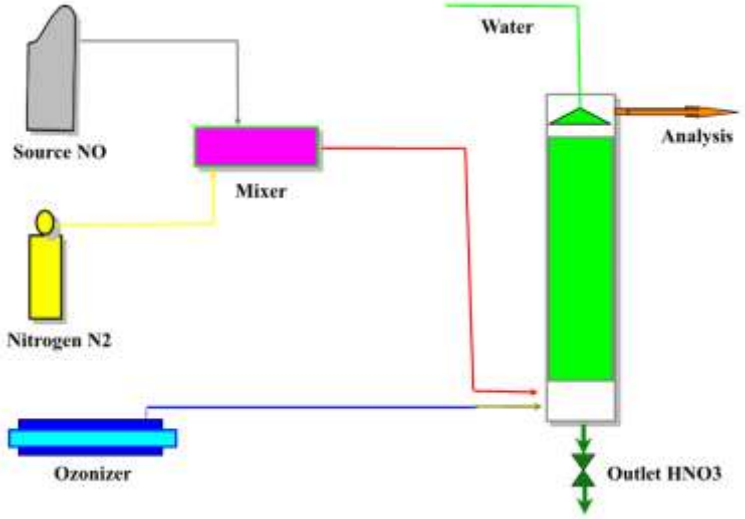

Fig. 2. NOx reduction of with the application of plasma generated in barrier discharges

4. CONCLUSIONS

The presented research work deals with the NOx removal from industrial flue gases by means of non-thermal plasma products and its main objective is to determine optimal parameters that decide over the process efficiency. To determine such parameters it is necessary to recognize mechanisms of the reactions that occur during the process.

The main research efforts have been focused on selecting optimal composition of an oxidizing mixture (O_2, O_3) with regard to NO, which limits efficiency of the method as well as on analysing kinetics and energy consumption of the process. To reach that objective it is necessary to recognize kinetics of reactions that lead to the formation of higher nitrogen oxides. The application of such a good oxidizer as ozone and testing its reactiveness with the above mentioned molecules aims at oxidizing the gases up to N_2O_5 so that subsequently applied simple sorption in water could cause a total elimination of NO and a formation of nitric acid that is a useful product. On the other hand, thermodynamic calculations show that it is possible to oxidize nitrogen monoxide directly to the pentooxide from which would significantly accelerate the very oxidation stage and would prevent disproportioning of the dioxide as a result of the reaction with water.

It is particularly important to explain how a selection of initial conditions influences final conditions of the process. The next objective is to determine competitiveness of reactions described by the equations (1-4). An important question is whether the process produces more of NO_2 or of N_2O_5. Another one is whether an excessive amount of ozone can be a factor outbalancing the process towards the formation of only N_2O_5.

The first stage of the project has been concluded by an experimental elaboration of a criterion equation for the initial parameters of the process. In the next stage a detailed description of energy phenomena involved in the four basic reactions will be elaborated and preliminary investigations into factors that limit the process will be performed.

Contemporary quantum chemistry makes it possible to thoroughly analyze basic reactions, their energy aspects as well as the nature of transient states. That full set of calculation methods can be applied to explain the way nitrogen oxides react with ozone, kinetics of those processes, and what is the fundamental nature of the chemical reactions. This task will be an objective of the next stage of the Author's research.

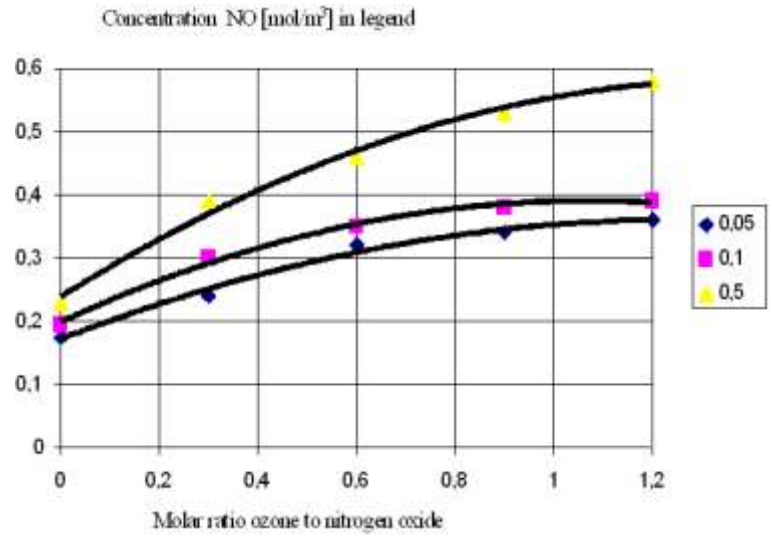

Fig. 3. NO removal rate vs. O_3-to-NO molar ratio
(without preliminary oxidation by oxygen)

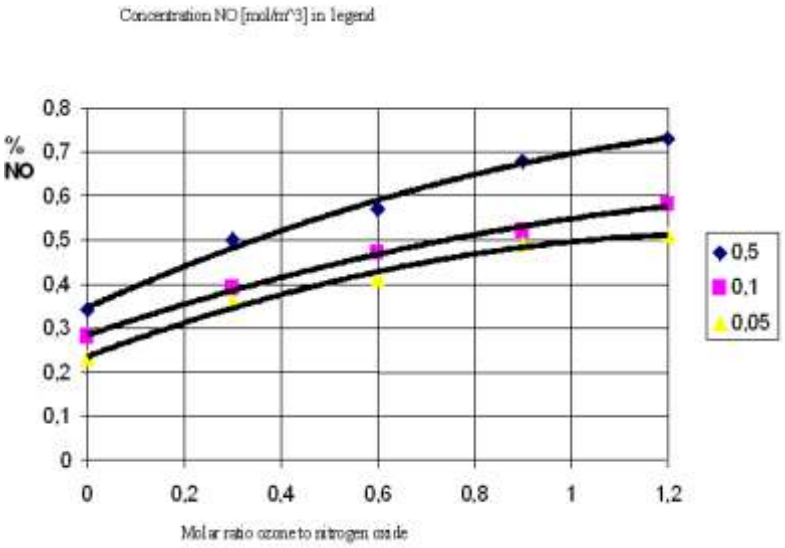

Fig. 4. NO removal rate vs. O_3-to- NO molar ratio
(with preliminary oxidation by oxygen)

RERERENCES

[1] Pollo Iwo, Jaroszyńska-Wolińska Justyna,, Informacja zaszczita atmosfery, 1978, 4, pp. 73-76.

[2] Hoigne J., Bader H.: Rate constants of reactions of ozone with organic compounds in water, Wat. Res, 1983, pp. 173-182.

[3] Pollo I., Wroński M., Ozonek J.Jaroszyńska-Wolińska J., Dielectric thickness and rate of ozone production, Polish Journal of Applied Chemistry, 1995, 39, pp.503-510.

[4] Jaroszyńska- Wolińska J., Wroński M., Zając A.,Pollo I.: Kinetics of ozone decomposition in water solution containing phosphoric buffers. Proc. Reg. Conf. on Ozone Generation and Application to Water and Waste Water Treatment, Moscow, 1998, pp. 695-710.

[5] Peyrous R.., Pignolet P. and Held B., J. Phys. D; Appl. Phys., 1989 , 22, 1658-1667.

[6] Manning T.J., Ozone Sci. Eng, 2000, 22, pp. 53-64.

[7] Vitrac H., Guespin J., Brisset J.L., Interaction between a non thermal oxygenated plasma and aqueous solutions. Proc. 7th Int. Symp. High Pressure Low Temp. Plasma Chem. (Greisfswald, Germany 2000, pp. 393-397.

[8] Vitrac H., Guespin J., Brisset J.L., Proc. Water Air & Soil Treatment by Advanced Oxidation Technologies; Innovative and Commercial Applications (Poitiers, France) 2001, p. 59.

[9] Appleton A. T., Lukes P., Finney W. C. and Locke B. R., Study of the effectiveness of diffrent hybrid pulsed corona reactors in degrading aqueous pollutants. Proc. Proc.8 th Int. Symp. on High Pressure Low Temperature Plasma Chemistry, Hakone–8 , (Puhajave , Estonia) , 2002, 2, pp. 313-317.

[10] Jaroszyńska-Wolińska J., Wroński M.: The influences of high voltage electrode design on electrical parameters of the ozone generator, Polish Journal of Chemical Technology, 2002, 4 No 2, pp.8-11.

[11] Jaroszyńska-Wolińska J., Wroński., Ozonek., Pollo I.: Efficiency of an ozone synthesis process realized in ozonizers of various high –voltage inner electrode designs, Proc.8 th Int. Symp. on High Pressure Low Temperature Plasma Chemistry, Hakone–8, (Puhajave, Estonia), 2002, 2, pp. 210-214.

[12] Jaroszyńska-Wolińska J., Mieszawska A., Pomorska K., Decomposition of BTX with the application of products of plasma generated in barrier discharges. Acta Agrophysica 2002, 80, pp. 375-382.

[13] Ozone News, 2000, vol. 28, No 5, p. 9.

[14] Ozone News, 2000, vol. 29, No 6, p 15.

ACKNOWLEDGEMENTS

The research has been supported by The Ministry of Scientific Research and Information Technology within the frame of the research project 4T 09B03425 in the years 2003-2006.

4th International Conference **ELMECO**
Nałęczów, Poland
September 2003

MICROWAVE PLASMA SOURCE FOR GAS PROCESSING

Dariusz CZYLKOWSKI, Mariusz JASIŃSKI, Zenon ZAKRZEWSKI

Centre for Plasma and Laser Engineering, Institute of Fluid Flow Machinery
Polish Academy of Sciences, Fiszera 14, 80-231 Gdańsk, Poland
e-mail: mj@imp.gda.pl

Abstract

Microwave sustained plasma has found practical applications in various fields, like gas purification, environmental protection, elemental analysis, surface modification etc. In this presentation we report results of an experimental study of the continuous and pulsed operation of a single-nozzle TIAGO system at a frequency of 2.45 GHz.

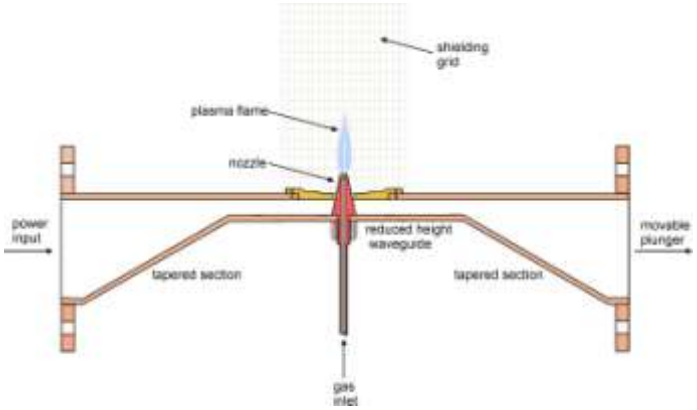

Fig. 1. Schematic of the microwave torch plasma generator.

All reported results were obtained for argon discharges with gas flow rates of single l/min and microwave power up to 1 kW. We conclude that the single nozzle microwave plasma torch TIAGO can be operated with a good power efficiency and stability, both in continuous and pulsed regimes.

Keywords: atmospheric pressure plasma, microwave discharge, microwave plasma torch, pulsed discharge.

1. INTRODUCTION

Recently, microwave gas discharges at atmospheric pressure have attracted interest in gas processing. Especially for gas purification applications [1], such discharges have been most often sustained within quartz tubes. Another solution, for example used in decomposition of gaseous pollutants [2, 3], is to use a microwave plasma torch configuration, where the discharge is excited at the tip of a gas nozzle within a stream of gas flowing directly into the ambient atmosphere. Recently pulsed discharges are worth studying. Pulsed microwave excitation could allow to determine the influence of the microwave pulse power and length, and the pulse-to-pause ratio on the efficiency of gas processing. Also a pulsed operation of such discharges becomes of interest because of the expected higher effectiveness in decomposition of hazardous gas components. They may prove more efficacious and energetically effective than continuous discharges.

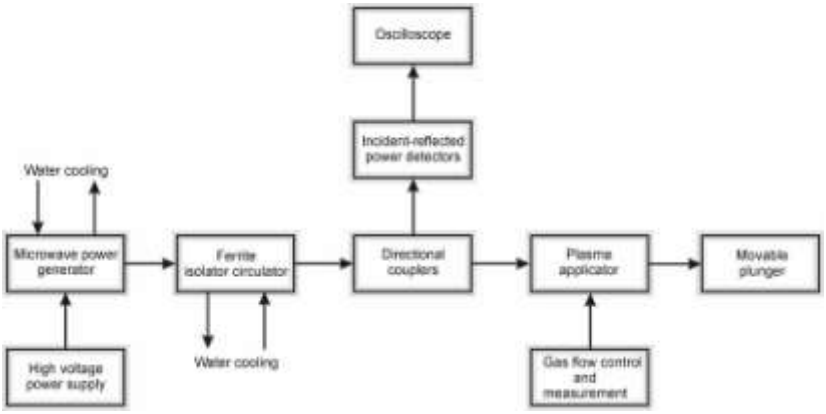

Fig. 2. Schematic diagram of the experimental apparatus.

2. EXPERIMENTAL SETUP

Various designs of plasma sources, based either on the coaxial line or the waveguide technique, have been developed. We used in our experiments the applicator designated TIAGO, first introduced in 2001 [4]. The overall view of the microwave torch plasma generator is shown in figure 1. It is a waveguide based device (internal dimensions: width 109 mm, height 54 mm) with a section of reduced height (10 mm). The microwave power is fed from the waveguide directly into the torch structure; therefore such a plasma generator can be operated at high power levels. The end of the structure, opposite to the power input, is terminated with an impedance tuning element in a form of a movable plunger. Plasma is sustained at the extremity of the metallic nozzle in the gas flowing out directly into the surrounding atmosphere. We used a copper nozzle with a single outlet channel located along the nozzle axis. The main advantages of this plasma torch are simplicity and compactness, so it is easy to produce at low cost. When this microwave torch plasma generator was applied for decomposition of gaseous pollutants the nozzle was enclosed within a quartz reactor [3]. Then the composition of the gas before and after the

plasma processing was determined using the FTIR spectrophotometer. For example, in that system the efficiency of chlorofluorocarbon (CCl_3F) destruction reached 100%.

Figure 2 presents the schematic diagram of the experimental apparatus. The power is supplied to the torch system from a 2.45 GHz magnetron generator with the possibility of pulsed modulation. Calibrated directional couplers are used either with thermistor power meters (in the case of continuous mode of operation) to measure incident and reflected powers at the applicator input or, in the case of the pulsed operation, with crystal detectors to make oscilloscope recordings of these power values.

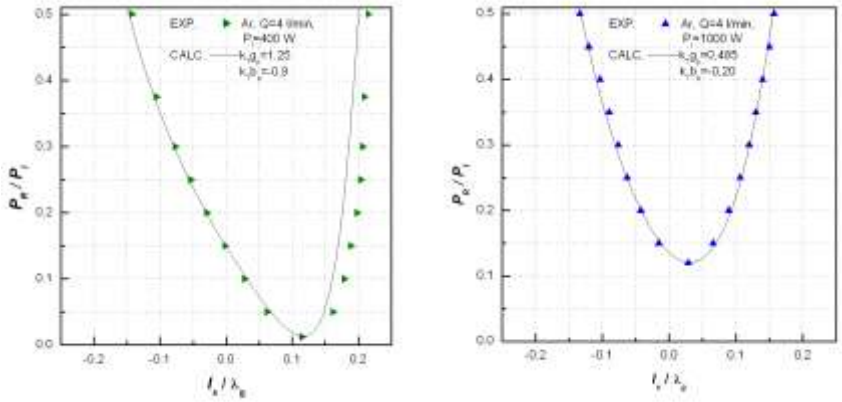

Fig. 3. Measured and calculated tuning characteristics for different incident power level (400 W, 1000 W).

3. RESULTS AND CONCLUSIONS

All measurements were made with discharges in argon at flow rate of single l/min and microwave power up to 1 kW. Under continuous work conditions, plasma parameters are constant with time and the movable plunger position can be readily set for the highest efficiency of power transfer. During pulsed regime the microwave power is fed to the torch system in a form of pulses, while the position of the plunger remains fixed. The proper choice of this position requires the knowledge of the electrodynamic characteristics of the plasma source taken during continuous work mode. Thus, these characteristics have to be beforehand determined experimentally over the whole range of microwave power delivered to the discharge. In Fig. 3, the measured and calculated tuning characteristics of the plasma applicator are presented at two values microwave power (400 W, 1000 W). Figure 4 shows the influence of argon flow rate on the fraction of the incident power reflected at the applicator input for a fixed plunger position, while figure 5 presents microwave reflected power for chosen movable plunger position ($\frac{l_s}{\lambda_g} = 0.089$). Figures 6-7 shows oscilloscope recordings of the incident and reflected microwave power for fixed plunger positions and for different pulse duration (25 and 40 μs, respectively). The period of the pulse cycle is 1 ms. To assure reignition the pulses are superimposed on a constant microwave background

power of 200 W. As it can be seen, the chosen movable plunger position ($\frac{l_s}{\lambda_g} = 0.089$) assures relatively low level of reflected microwave power at the applicator input.

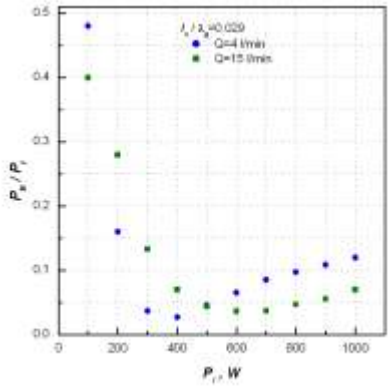

Fig. 4. The influence of argon flow rate on the fraction of the incident power reflected at applicator input for fixed plunger position.

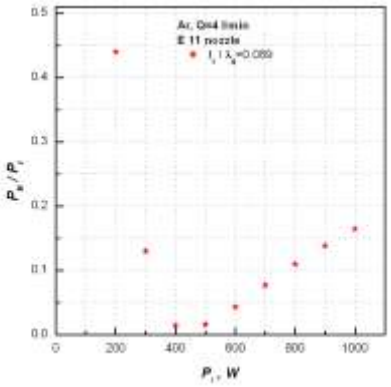

Fig. 5. The fraction of the incident power reflected at applicator input for chosen plunger position ($\frac{l_s}{\lambda_g} = 0.089$).

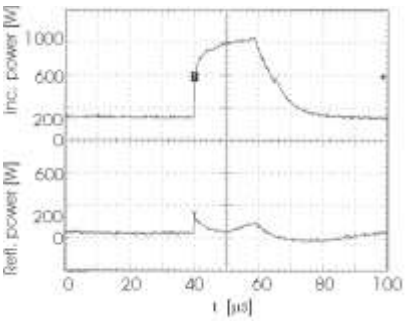

Fig. 6. Oscilloscope recordings of the incident and reflected power for l_s/λ_g=0.089 (pulse duration 25 μs).

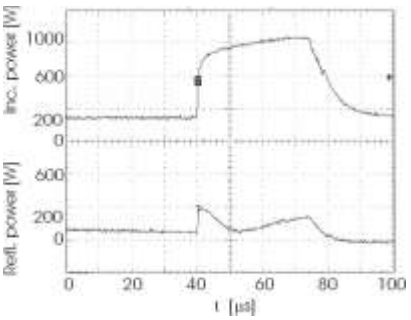

Fig. 7. Oscilloscope recordings of the incident and reflected power for l_s/λ_g=0.089 (pulse duration 40 μs).

We conclude, that the chosen conditions of operation of the torch assure a satisfactory microwave power balance over the whole period of the pulse cycle and, in particular, within the pulse duration. According to this we conclude that the single nozzle microwave plasma torch TIAGO can be operated with a good power efficiency and stability, both in continuous and pulsed regimes.

ACKNOWLEDGEMENTS

This research was supported by the State Committee for Scientific Research (KBN) under the program PB 1124/T09/2003/24 and by the Institute of Fluid Flow Machinery, Polish Academy of Sciences under the program IMP PAN O3/Z1/T1.

REFERENCES

[1] J.C. Rostaing, F. Bryselbout, M. Moisan, J.C. Parent, C. R. Acad. Sci. Paris, t.1, Serie IV, (2000) p. 99-105.
[2] Y. Kobouzi, M. Moisan, J.C. Rostaing, C. Trassy, D. Guerin, D. Keroack, Z. Zakrzewski, Journal of Applied Physics, 93 (2003), pp. 9483-9496.
[3] M. Jasiński, J. Mizeraczyk, Z. Zakrzewski, T. Ohkubo, J.S Chang, J. Phys. D: Applied Physics, 35 (2002), pp. 2274-2280.
[4] M. Moisan, Z. Zakrzewski, J.C. Rostaing, Plasma Sources Sci. Technol., 10 (2001), pp. 1-8.

4th International Conference **ELMECO**
Nałęczów, Poland
September 2003

NUMERICAL MODEL OF TEMPERATURE DISTRIBUTION FOR A PLASMA ARC

Jarosław DIATCZYK, Henryka Danuta STRYCZEWSKA

Institute of Electrical Engineering & Electrotechnologies, Lublin University of Technology
Nadbystrzycka 38A, 20-618 Lublin, Poland
e-mail: jard@eltecol.pol.lublin.pl dankas@eltecol.pol.lublin.pl

Abstract

For pollution control the non-thermal plasma seems to be the most convenient source of energetic electrons [1]. In the electric arc the non-thermal condition can be obtained with fast gas flow through the discharge volume at atmospheric pressure, like DC glow discharge or AC gliding arc discharge. To obtain the non-equilibrium low temperature plasma conditions in large volume of treated gases, the temperature of electrons and its distribution in the discharge chamber is one of the fundamental parametersy. This paper presents results of two-dimensional temperature simulation for the atmospheric pressure plasma arc.

Keywords: plasma temperature, numerical temperature simulation.

1. MATHEMATICAL MODEL

The governing equations describing the plasma flow are the Navier-Stokes relations of mass, momentum and energy conservation in the radial and axial directions:

$$\frac{\partial}{\partial z}(\rho u)+\frac{1}{r}\frac{\partial}{\partial r}(r\rho v)=0 \tag{1}$$

$$\frac{\partial}{\partial z}(\rho u^2)+\frac{1}{r}\frac{\partial}{\partial r}(r\rho u v)=2\frac{\partial}{\partial z}\left(\mu\frac{\partial u}{\partial z}\right)+\frac{1}{r}\frac{\partial}{\partial r}\left(r\mu\frac{\partial u}{\partial r}\right)+\frac{1}{r}\frac{\partial}{\partial r}\left(r\mu\frac{\partial v}{\partial z}\right)-\frac{\partial \rho}{\partial z} \tag{2}$$

$$\frac{\partial}{\partial z}(\rho u v)+\frac{1}{r}\frac{\partial}{\partial r}(r\rho v^2)=\frac{\partial}{\partial z}\left(\mu\frac{\partial v}{\partial z}\right)+\frac{2}{r}\frac{\partial}{\partial r}\left(r\mu\frac{\partial v}{\partial r}\right)+\frac{\partial}{\partial z}\left(\mu\frac{\partial u}{\partial r}\right)-\frac{2\mu v}{r^2}-\frac{\partial p}{\partial r} \tag{3}$$

$$\frac{1}{r}\frac{\partial}{\partial r}\left(r\lambda\frac{\partial T}{\partial r}\right)-\rho u c_p\frac{\partial T}{\partial z}-\rho v c_p\frac{\partial T}{\partial r}+\sigma E^2=0 \tag{4}$$

$$E=\frac{I}{2\pi\int_0^R \sigma\cdot r\cdot dr} \tag{5}$$

where:

r	– radial coordinate;	v	– radial gas velocity;
z	– axial coordinate;	u	– axial gas velocity;
μ	– gas viscosity;	ρ	– gas density;
σ	– electrical conductivity;	λ	– thermal conductivity;
c_p	– specific heat;	T	– temperature;
P	– gas pressure;	E	– voltage;
I	– current.		

The reactor geometry (Fig. 1), boundary conditions and start-up parameters usee in numerical simulation are given below:

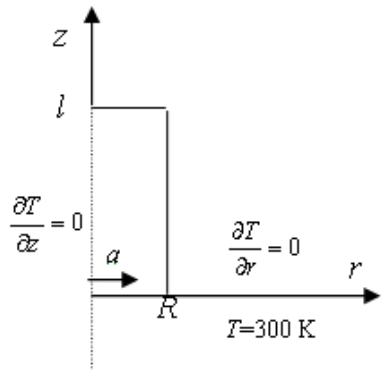

Fig. 1. Reactor geometry.

- Boundary conditions:
- symmetric axis (z): $\frac{\partial T}{\partial r}=0$
- chamber wall ($r = R$): T = 300 K
- chamber exit ($z = l$): $\frac{\partial T}{\partial z}=0$
- source temperature (cathode): different in each point
- Start-up parameters:
- axial gas velocity: u = 10 m/s;
- operation pressure: p = 1 atm;
- current: I = 1 A;
- cathode radius: a = 3 mm;
- canal length: l = 20 mm;
- canal width: R =9 mm.

Cathode temperature is different in each point and can be calculated from equation (6):

$$T=\frac{T_{\max}}{a^2}\left(a^2-r^2\right)+T_0 \tag{6}$$

where:

T_{max} – maximum cathode temperature; T_0 – temperature outside cathode;
a – distance from midpoint of cathode; r – radial coordinate

Figure 2 presents the assumed cathode temperature as a function of distance from midpoint of the cathode.

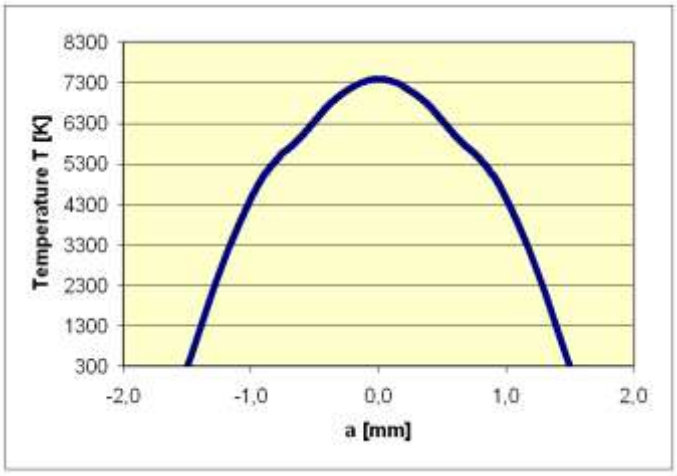

Fig. 2. Cathode temperature.

2. MAIN ASSUMPTIONS AND NUMERICAL METHOD

Due to reactor geometry the calculations are carried out in cylindrical coordinates. The fluid is characterized by a laminar flow of Argon as the carried gas; conduction, radiation losses and energy exchange through elastic collisions between electrons and heavy particles are taken into account; axial convection and diffusion of particles are neglected. We assume that following transport coefficients are the function of temperature:

- electrical conductivity (σ),
- thermal conductivity (λ),
- specific heat (c_p),
- viscosity (μ);

The linearized block implicit (LBI) method developed by Briley & McDonald [10, 11] is used to solve equations numerically. This method was originally developed for the solution of the compressible Navier-Stokes equations for non-reactive flows.

These equations are discretized in space to first-order accuracy by central differencing (upwind differencing caused numerical instability).

$$T_{i,j} = \frac{1}{4}\left[T_{i,j-1}\left(1-\frac{k}{2R}\right) + T_{i,j+1}\left(1+\frac{k}{2R}\right) + T_{i-1,j} + T_{i+1,j} + \frac{\sigma E^2}{\lambda} k^2 \right] \tag{7}$$

where:

$T_{i,j}$ – electron temperature for a grid point (i,j);
k – mesh step.

Numerical algorithm starts from input start-up parameters and boundary conditions. In next step the T-matrix calculation starts. The algorithm stops if difference between values of temperature calculated in previous and current step (for each cell of T-matrix) is less then 10 K or if number of iteration exceeds 100. In this point for better resolution we can increase the T-matrix dimension. Simulation results are presented in Figure 4.

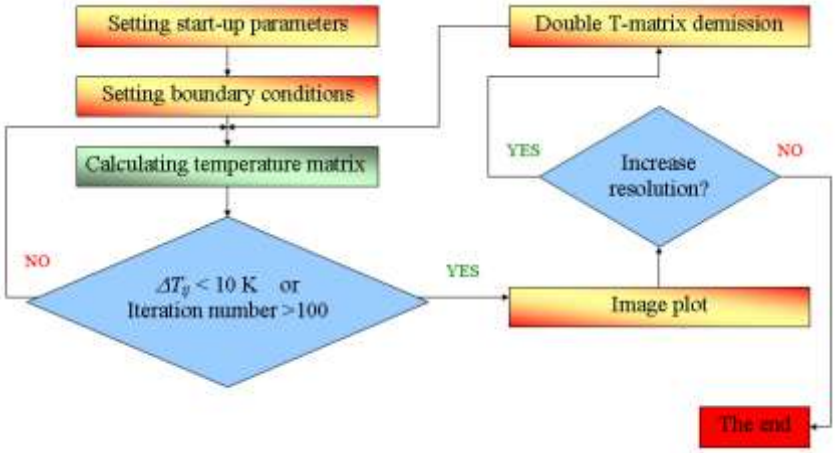

Fig. 3. Algorithm diagram.

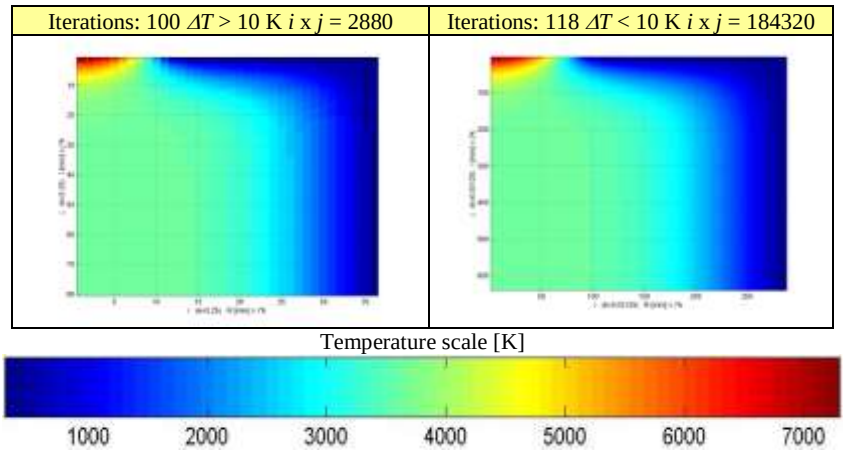

Fig. 4. Simulation results.

3. VERIFICATION METHOD

In the next step of our research we intend to construct the stand for diagnostic the temperature distribution with the aid of optical spectrographic method. The electron temperature T_e can be determined by means of plasma gas excitation temperature T_{exc} ($T_e \approx T_{exc}$) based on the relative intensities of the atomic lines of plasma carrier gas, which for argon are: wavelength λ = 451.07, 452.23, 516.23 and 518.78 nm. The basic expression for the intensity I_{nm} of atomic emission lines used for determination temperature T_e has the form [9]:

$$I_{nm} = A_{nm} h \nu_{nm} N \frac{g_n \exp\left(-\frac{E_n}{kT_e}\right)}{Z(T)} \tag{8}$$

where:

A_{mn}	- Einstein coefficient of the transition;	h	- Planck's constant;
ν_{nm}	- frequency of the atomic line;	k	- Boltzmann constant;
N	- concentration of atoms in the ground state;	$Z(T)$	- sum of the states;
g_n	- statistical weight of the upper state;	E_n	- excitation energy.

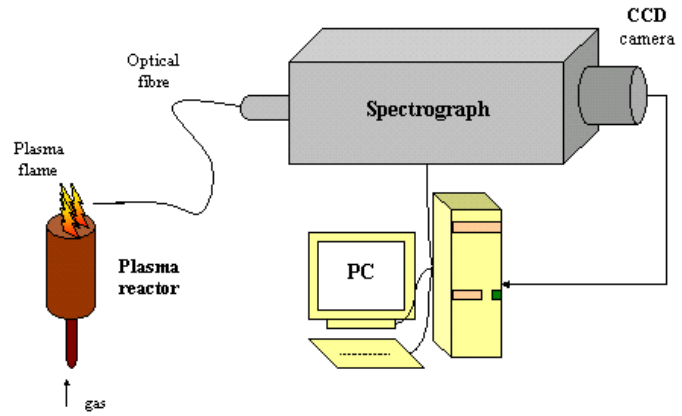

Fig. 5. Optical verification method.

4. CONCLUSION

The aim of the paper was to define the theoretical bases of temperature distribution in the plasma reactor with gliding arc. Mathematical model was implemented in MATLAB workspace. The simulations were performed with parameters taken from the experimental results drawn from other authors investigations (papers) [2], [4].

The simulation results show, that in the analyzed geometry the temperature is distributed uniformly in the majority of the discharge chamber and obtained results are consistent with experiments. The presented model employs some adjustable parameters, and therefore enables the simulation of different arc jet plasma reactors with laminar gas flow. The numerical model for turbulence gas flow and laboratory stand for optical verification of the simulation results are to be the next step of our research.

REFERENCES

[1] K. Schmidt-Szałowski "Plasma processes for the environment protection", Acta Agrophysica, 2002, 80, pp.303-308

[2] R. Nawrowski, A. Tomczewski "Pole temperatury w reaktorze plazmy", II Konferencja naukowo – Techniczna „Zastosowanie komputerów w elektrotechnice" Kiekrz, 1997, pp.163-165

[3] H.D. Stryczewska „New supply system of the non-thermal plasma reactor with gliding arc" Archives of Electrical Engineering , vol. XLVI, No 4, (1997), pp.379-399
[4] R. Girard. J.B. Belhaouari, J.J. Gonzalez, A.Gleizes "Two-temperature study of a decaying SF_6 arc plasma" Centre de Physique des Plasmas et de leurs Applications de Toulouse, 2001.
[5] A.Kamińska, R.Nawrowski, A.Tomczewski "The coupling between the electric field and the thermal field in plasma generator", Abstracts 7th Internatinal IGTE Symposium, Austria, Graz, September 22-26, 1996, pp.2-19.
[6] J. Janca, A. Talsky "Unipolar high frequency discharges I", Fac. Sci. Nat. Univ. Purkynianae Brunensis, 1965, pp.51-62.
[7] J. Janca, C. Tesar, Int. Symp. On High Pressure, Low Temperature Plasma Chemistry, HAKONE V, Milovy, Czech Republic, 1996, pp.161-164.
[8] M. Jasinski, A.Brablec, V.Kudrle, J.Mizeraczek, Z.Zakrzewski "Spectroscopic Investignation of Electron and Neutral Gas Temperatures in Microwave Torch Plasmas at Atmospheric Pressure", Centre of Plasma and Laser Engineering, Institute of Flow Machinery, Poland; Department of Physical Electronics, Masaryk University, Czech Repablic, 1999.
[9] Л.А.Луизова "Оптические методы диагностики нискотемпературной плазмы", 2001.
[10] V. Babu, S. M. Aithal, and V. V. Subramaniam, J. Propul. Power 12, 1114 (1996).
[11] S. M. Aithal, V. V. Subramaniam, and V. Babu, Paper AIAA-96-3295 presented at the 32nd AIAA/ASME/SAE/ASEE Joint Propulsion Conference, Lake Buena Vista, Florida, July 1–3, 1996.

4th International Conference **ELMECO**
Nałęczów, Poland
September 2003

TRANSFORMER SUPPLY SYSTEM OF PLASMA REACTOR

Grzegorz KOMARZYNIEC, Henryka Danuta STRYCZEWSKA

Institute of Electrical Engineering and Electrotechnologies,
Lublin University of Technology,
38A Nadbystrzycka St., 20-618 Lublin
e-mail: komag@eltecol.pol.lublin.pl
e-mail: dankas@eltecol.pol.lublin.pl

Abstract

Supply system of plasma reactors should assure proper plasma parameters for plasma-chemical processes. Transformer has been the basic element of all supply systems of GlidArc plasma reactors. For the supply of GlidArc plasma reactors, both single-phase and triple-phase transformers are used depending on the construction of the supply system and the construction of the plasmatron. Operating plasma reactor is higly non-linear receiver that introduces significant unbalance load to the supply system.

Kewords: plasma reactors, supply system, transformer.

1. INTRODUCTION

Transformer has been the basic element of all supply systems of GlidArc plasma reactors. It allows for mutual operation of arc device with power network. Supply system of plasma reactors should assure proper plasma parameters for plasma-chemical processes. Therefore, apart from the transformers the following elements have often been used in supply systems: chokes, resistors, condensers, diodes, and transistors. Transformers used for this purpose have special construction. Reliability and low exploitation and investment costs are crucial elements that should be taken into consideration at the stage of transformers design and construction for industrial scale. The supply system is the factor that often decides on industrial application of plasma reactor. In case of GlidArc plasma reactors, the supply system based on the transformer of special construction consists of the integrated system that uses non-linearity of magnetic circuit and the integration of fundamental functions of the system are obtained: initial ionisation of inter electrode space, continuous discharge during reactor's operation cycle and fault current limitation in a single device.

2. PLASMA REACTOR

For the supply of GlidArc plasma reactors, both single-phase and triple-phase transformers are used depending on the construction of the supply system and the construction of the plasmatron. Plasmatrons can be made as two-electrode or multi-electrode systems and they may have additional ignition electrode. (Fig. 1). Supply parameters essentially influence the properties of generated plasma. Proper operation of plasma reactor is carried out at the voltage of 1-2kV. Such voltage does not assure discharge ignition in the reactor. Ignition voltage at the electrode gaps applied in practice reach the value of about 10kV. The application of the ignition electrode enables to separate the discharge ignition in plasma reactor from proper operation cycle. Such solution requires supply systems of special design, that would allow for both functions.

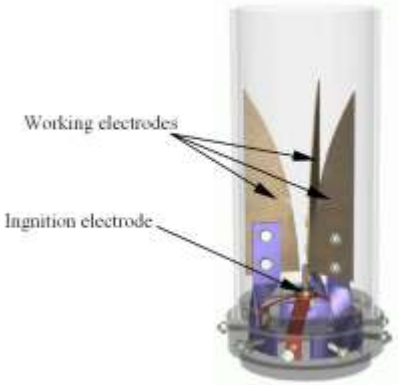

Fig. 1. Triple electrode plasma reactor with the ignition electrode.

3. SUPPLY SYSTEM

The solution of triple-electrode supply system of plasma reactor with the ignition electrode is presented in Fig. 2. Magnetic circuit of the transformer use four wound and cut cores. Spatial location of cores create 3-phase 5-limb transformer. Primary and secondary windings are placed on three inner limbs. Primary windings are in Star:Star configuration, secondary winding in Star:Star (neutral connected) configuration. They supply the working electrodes of the plasmatron with the voltage of about 1-2kV.The windings of outer limbs are in series connection with neutral. Such windings are necessary for the ignition and they supply the working electrode with the voltage of 10kV.

Supply system based on the above construction is under investigation presently. Transformer's operation both on it's linear part of magnetising characteristics and in the state of saturation is being analysed. The research comprise mainly the value of harmonics in outer limbs as well as the shape of voltage induced in windings of the limbs. The shape of the voltage supplying the ignition electrode of the plasma reactor has an impact on the efficiency of the ignition.

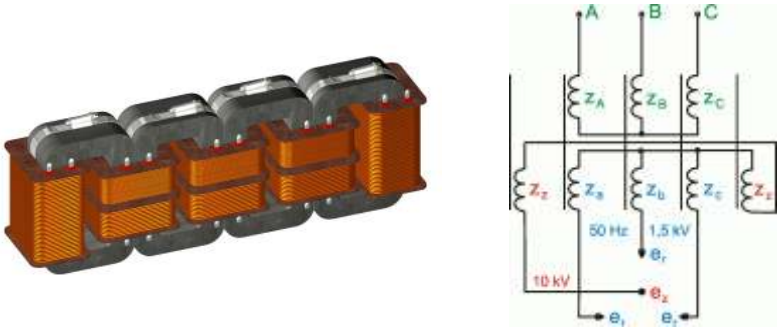

Fig. 2. 3-phase 5-limb transformer for the supply of triple-electrode GlidArc plasma reactor with the ignition electrode. Z_A, Z_B, Z_C – primary windings; Z_a, Z_b, Z_c – secondary windings; E_r – working electrodes; E_z – ignition electrode.

The voltage initiating the ignition of electric discharge in plasmatron is the voltage sum of the ignition electrode and working electrode. The most favourable conditions for the ignition emerge when both voltages reach maximal values at the same time. The frequency of the voltage supplying the ignition electrode significantly influence the efficiency of discharge ignition. At voltage of 50 Hz frequency the most suitable conditions for discharge ignition emerge every 3,3ms. In this case the ignition voltage of 150Hz frequency seems to be the most favourable (Fig. 3).

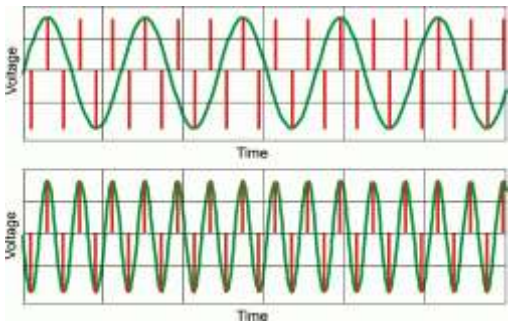

Fig. 3. Voltage of 50Hz and 150Hz on the background of ignition spectrum.

4. LOAD

Operating triple-electrode plasmatron with the ignition electrode is higly non-linear receiver that introduces significant unbalance load to the supply system. It influences the circulation and the shape of streams in the core of 5-limb transformer. Four operation states of the supply system could be specified (Fig. 4). No-load state is connected with the ionisation of inter-electrode gaps. Ionization zones emerge between each couple of working electrodes and between the ignition electrode and each operating electrode, thus there are six ionization zones. Voltage sufficient for air ionisation that would enable to break inter-electrode gap and run the discharge, may be present only between the ignition electrode and

one operating electrode. The next state of supply system's operation is related to the process of breaking the above mentioned gap. The system has been loaded with non-linear arc resistance between the ignition electrode and one of working electrodes (Fig. 5). Processes related to the discharge in triple-electrode system with the ignition electrode have not been investigated in detail so far however, it is possible to predict the operation state in which electric discharge is burning between two working electrodes. The last operating state is connected with the real operating cycle in which the discharge is burning among all operating electrodes (ignition electrode is not involved there). The distributions of the resistance and inter-electrode voltage for this state are presented in Fig. 5.

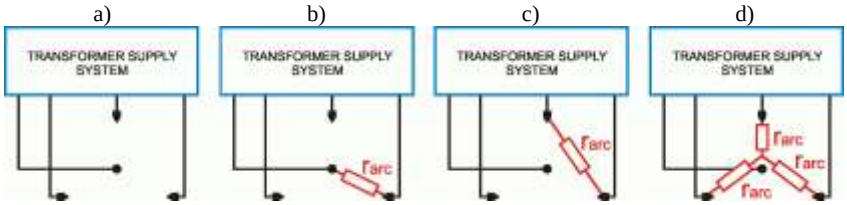

Fig. 4. Operation states of the supply system of triple-electrode GlidArc plasma reactor with the ignition electrode. a) no-load state, b) discharge ignition, c) discharge between the pair of working electrodes, d) discharge among three working electrodes – proper cycle of plasmatron's operation.

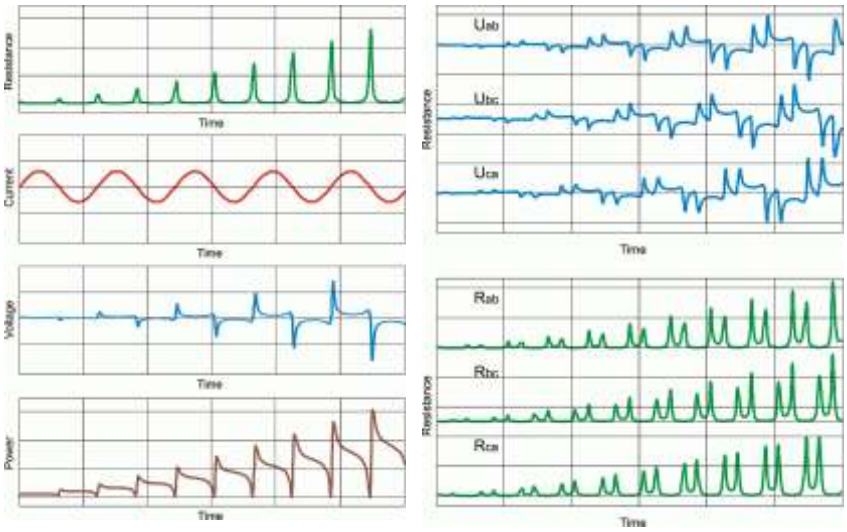

Fig. 5. Distributions of the resistance, current, voltage and power of gliding arc discharge in double and triple-electrode system.

5. SUMMARY

During the elaboration of the supply system for GlidArc plasma reactor the important issue is to obtain such shape of the ignition voltage that would keep the discharge between the electrodes and short non-current breaks between subsequent operation cycles. Additional difficulties are deeply connected with high non-linear arc resistance and significant asymmetry of transformer's load, which essentially influence the circulation and the shape of the streams in 5-limb core. Further investigations are focused on analysing the phenomena connected with the ignition and arc burning in triple-electrode system, testing non-linear and asymmetrical influence of GlidArc plasma reactor on the operation of 5-limb core as well as the selection of such conditions that would assure proper ignition and continuous discharge burning in triple-electrode system. The results of the analysis will be then verified by the measurements taken on the 5-limb transformer model.

REFERENCES

[1] H. D. Stryczewska, G. Komarzyniec, Gliding arc discharge in the triple-electrode system, W-wa 2002.

[2] G. Komarzyniec, An analysis of phenomena in the gliding arc discharge, Master Thesis, Technical University of Lublin, Poland, 2001 (in Polish).

4th International Conference **ELMECO**
Nałęczów, Poland
September 2003

DETERMINATION OF PARAMETERS OF THE ELECTRIC DISCHARGE MODEL

Leszek JAROSZYŃSKI

Institute of Electrical Engineering and Electrotechnologies,
Lublin University of Technology, Nadbystrzycka 38A, 20-618 Lublin, Poland
e-mail: leszekj@weber.pol.lublin.pl

Abstract

In this paper, the Mayr's electric arc model modified by the author has been described. Modification allows computer simulation of the supply circuit of the GlidArc non-thermal plasma reactor. The method of the determination of numerical model parameters based on experimental data has been presented. The comparison of the numerical simulation with laboratory results has also been shown.

Keywords: gliding arc numerical model, analogue behavioural modelling, PSpice.

1. INTRODUCTION

Numerical analysis of the plasma reactor supply system performed with the aid of an electric circuit simulator is a valuable method for evaluating operation of a supply and a non-linear load. However, computer simulation of the gliding arc plasma reactor (GlidArc) requires a specific model of the electric discharge.

Many conceptions of electric arc mathematical modelling have already been elaborated. They can be divided into two major categories: physical/mathematical models (arc channel models) and adaptive models (so-called "black-box" models). Solving simulation problem with the help of a computer application such as PSpice imposes the use of a "black-box" electric discharge model. Supply circuit electric waveforms may be calculated with proper accuracy, though detailed analysis of plasma channel parameters is unachievable.

The following models are among well-known concepts of adaptive modelling: Cassie's model, Mayr's model, Schwartz's model, Urbanek's model. However, none of them directly satisfies the needs of the numerical simulation of the gliding arc plasma reactor [1]. It takes place because GlidArc reactor is a non-linear load which is characterized by cyclic discharge expansion: starting from high voltage ignition, through rapid elongation, until its fading due to cooling caused by the working gas stream.

2. GLIDING ARC DISCHARGE

The gliding electric discharge has already been successfully utilised for the gas purification in many environment protection technologies [1]. The chemical reactions are conducted with the help of free radicals generated by the non-thermal plasma. These processes take place in the plasma generator, which general idea has been shown in figure 1 (so called "GlidArc I" plasma reactor).

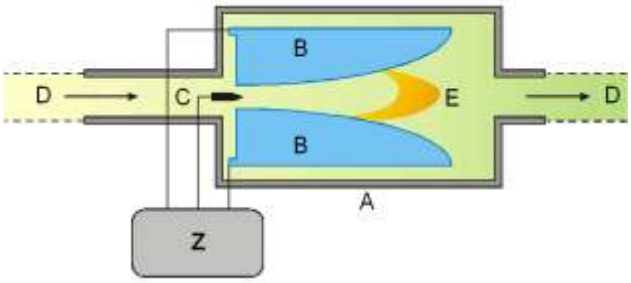

Fig. 1. Idea of the GlidArc I plasma reactor: A – processing chamber, B – working electrodes, C – striking electrode, D – gas flow, E – gliding arc discharge, Z – supply circuit [2].

In this apparatus, the electric discharge is initiated in the region where the distance between two (or more) knife-shaped working electrodes is the smallest. Central striking electrode provides high voltage for discharge ignition. After the ignition, the discharge is forced to glide along working electrodes by the fast moving flow of the treated gas. The discharge is extinguished when its power consumption exceeds possibilities of the supply circuit. Then the whole process is starting anew. The period of the single cycle of the reactor operation depends mainly on electrode shape and dimensions, thermal parameters of a treated gas, gas velocity and can be equal up to several periods of 50 Hz supply network voltage.

3. GLIDING ARC MODEL

The use of the well-known black-box electric arc models for the computer simulation of gliding electric discharge produces some problems. It gives improper static u-i characteristic of the electric arc in the low current range. The dynamic behaviour of the discharge described by so-called arc time-constant is unsuitable. The simulation of cyclic operation of the GlidArc plasma reactor is impossible. It doesn't permit the simulation of electric ignition (high voltage breakdown).

That is why, the modification of Mayr's electric arc model (1) has been made.

$$\frac{1}{G}\frac{\mathrm{d}G}{\mathrm{d}t} = \frac{1}{\tau_{\mathrm{M}}}\left(\frac{Ei}{P_0} - 1\right) \tag{1}$$

where: G - unitary arc conductance, E - arc electric field strength, i - arc current, P_0 - unitary power dissipated from discharge, τ_{M} - Mayr's arc time-constant.

The modification consists in the introduction of the linear function $p_0=f(g)$ (2), which describes power dissipated from the discharge.

$$p_0(g) = a \cdot g + c \tag{2}$$

where: a, c – constants.

This approach allows simple and effective control over static discharge u-i characteristic. Additionally, it permits to take into account an expansion of gliding discharge by the introduction of functions $a(l)$ and $c(l)$, where l is a discharge length [3].

The values of constants a and c have been calculated using dynamic u-i characteristic of the discharge (Fig. 2) taken during laboratory tests of the GlidArc plasma reactor.

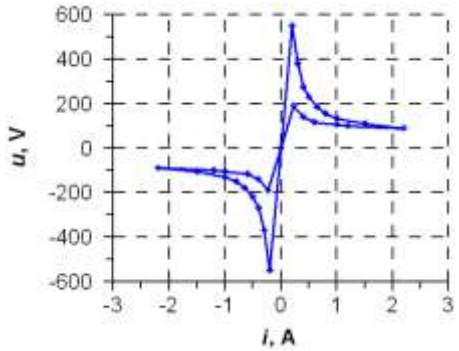

Fig. 2. Dynamic u-i characteristic of the electric discharge during one period of supply voltage.

Slopes of the u-i characteristic have been approximated using function derived from equation (2). Approximating curves 1 and 2 (Fig. 3) have enabled the calculation of static u-i characteristic 3 [4].

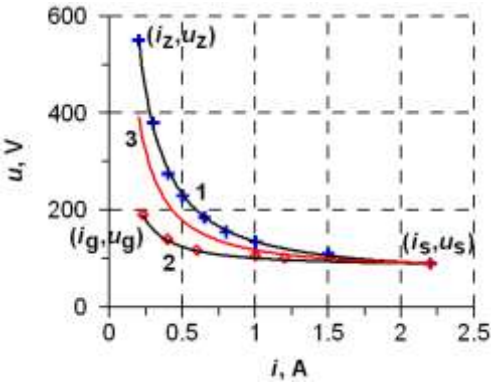

Fig. 3. Approximation of dynamic and static u-i discharge characteristics.

The static u-i characteristic has allowed to determine values of the constants a and c (a=5000 V^2, c=75.8 W or unitary values: a_0=81E6 V^2/m^2, c_0=9650 W/m).

The usage of Mayr's definition (3) has been the first attempt to calculate the value of discharge time-constant.

$$\tau_{\mathrm{M}} = \frac{Q_0}{P_0} \tag{3}$$

where: Q_0 - energy needed for e-times alteration of the arc conductance.

Constant value of τ_{M}=0.13 ms has been evaluated near maximum of the discharge conductance g.

Assuming sinusoidal variation of the discharge current, the second attempt to find function $\tau(g)$ has been made. Knowing relation (2), it is possible to transform Mayr's equation (1) to the formula (4).

$$\tau(g) = \frac{\dfrac{i^2}{ag + c} - g}{\dfrac{\mathrm{d}}{\mathrm{d}t} g} \tag{4}$$

Figure 4 shows results of the second attempt. Both relations between discharge "constant" τ and discharge conductance obtained for dg/dt>0 and dg/dt<0 have been approximated using polynomial (5).

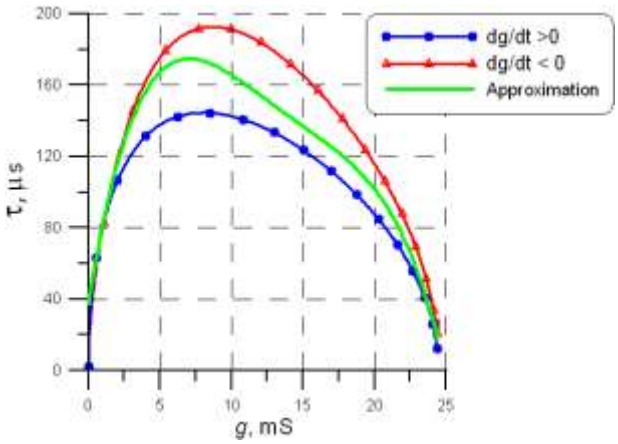

Fig. 4. Time-constant vs. discharge conductance.

$$\tau(g) = 37{,}1 \cdot 10^{-6} + 50{,}2 \cdot 10^{-3}\mathrm{g} - 6{,}23\mathrm{g}^2 + 304\mathrm{g}^3 - 5{,}53 \cdot 10^{3}\mathrm{g}^4 \tag{5}$$

4. COMPUTER SIMULATION

Electric discharge model described above has been used for simulation with the help of analogue behavioural blocks of the PSpice. Non-linear arc conductance described on the basis of the modified Mayr's equation can be expressed in formula (6).

$$i = u_{\mathrm{ER}} \cdot \int \left[\frac{g}{\tau_{\mathrm{p}}} \left(\frac{u_{\mathrm{ER}}^2 g}{ag + c} - 1 \right) \right] \mathrm{d}t \tag{6}$$

Equation (6) leads to the simulation scheme presented in figure 5 (version with constant value of τ_{M}).

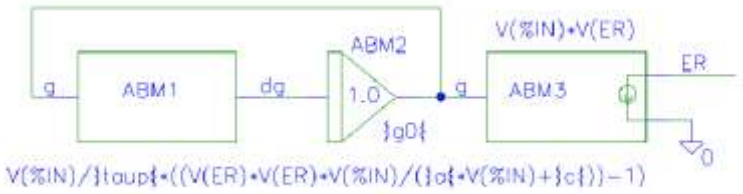

Fig. 5. Analogue behavioural model of the electric discharge (PSpice): ABM1 – voltage controlled voltage source, ABM2 – integrator (with given initial condition), ABM3 – voltage controlled current source.

The transient analysis of the circuit presented above and the similar circuit taking into consideration function (5) has been made. The comparison between dynamic discharge u-i characteristics is shown in figure 6.

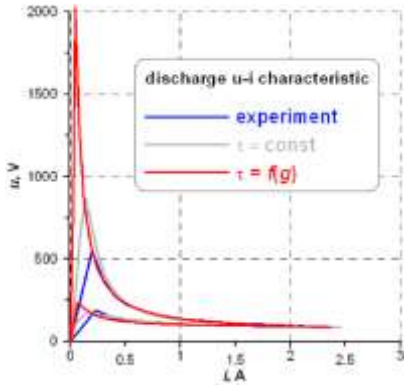

Fig. 6. Comparison of dynamic discharge u-i characteristics.

5. CONCLUSION

The extension of Mayr's switching arc model proposed by the author is possible, therefore this modified equation can be applied in analysis of operation of the GlidArc I plasma reactor and the integrated supply system. Unfortunately, the introduction of time-constant – conductance relation to modified Mayr's model seriously lowers stability of the computer simulation (PSpice). However, the introduction of relation $\tau=f(g)$ doesn't improve correspondence between experimental results and computer simulation in the low current range. Proper determination of τ=const has almost the same effect and it doesn't degrade the simulation performance. Discrepancy between measurement and simulation might be elucidated in two ways: mathematical discharge model based on heat balance doesn't take into consideration high voltage phenomena, which appear to have significant effect on u-i characteristic in low current range.

REFERENCES

[1] T. Janowski, L. Jaroszyński, H. D. Stryczewska, Modification of the Mayr's electric arc model for gliding arc analysis, XXV ICPIG: International Conference on Phenomena in Ionized Gases: Proceedings, Nagoya, Japan, 2001.

[2] H. Lesueur, A. Czernichowski, J. Chapelle, Apparatus for the generation of low temperature plasmas by the formation of gliding electrical discharges, Patent application, France, National registration no 8814932; May 20th, 1990.

[3] L. Jaroszyński; H. D. Stryczewska, Computer simulation of the electric discharge in GlidArc plasma reactor, Electromagnetic devices and processes in environment protection - The Third International Conference ELMECO 2000: Conference Proceedings, Lublin-Nałęczów, Poland, 2000.

[4] L. Jaroszyński, Parameters of the numerical model of electric discharge (in Polish), Międzynarodowa Konferencja z Podstaw Elektrotechniki i Teorii Obwodów IC-SPETO 2002: Proceedings, Gliwice-Ustroń, Poland, 2002.

4th International Conference **ELMECO**
Nałęczów, Poland
September 2003

COMPUTER SIMULATION OF THE SUPPLY SYSTEMS OF THE GLIDING ARC PLASMA REACTORS

Leszek JAROSZYŃSKI

Institute of Electrical Engineering and Electrotechnologies,
Lublin University of Technology, Nadbystrzycka 38A, 20-618 Lublin, Poland
e-mail: leszekj@weber.pol.lublin.pl

Abstract

The attempt to test the possibility of using electromagnetic supply circuit for the GlidArc II plasma reactor has been described in this paper. The results of the computer simulation of the integrated supply loaded with the moving electrode reactor have been presented. The numerical analysis has been performed with the help of PSpice.

Keywords: gliding arc plasma reactor, integrated electromagnetic supply system, PSpice.

1. INTRODUCTION

Non-thermal plasma reactors have been lately utilized in various areas of science and industry. The gliding arc plasma reactor (GlidArc) is an interesting type of these devices. This apparatus uses electrical energy for the production of specific electrical discharges. Appropriate concentrations of free radicals can be obtained under nearly atmospheric pressure conditions. Non-thermal plasma generated in the reactor has the ability to initialize chemical reactions, which are rather difficult to carry out under different conditions. Requisite parameters of the plasma generated by the electric discharge may be achieved in two ways [1].

Gliding arc reactors are non-linear electric loads, which make specific demands on power supply circuits. The electric discharge must be ignited by the high voltage, then it has to be sustained in the wide range of its length variation. The supply circuit must limit the current to the value of a few amperes. The power supply must be able to operate periodically (ignition, elongation, fading, and the whole process starting anew).

2. GLIDING ARC PLASMA REACTORS

In the first type of the mentioned device (GlidArc I) the electric discharge burning between stationary working electrodes is destabilized by the stream of gas processed with the help of non–thermal plasma (Fig 1).

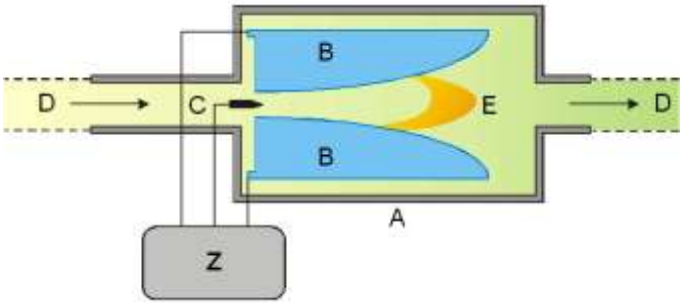

Fig. 1. Idea of the GlidArc I plasma reactor: A – processing chamber, B – working electrodes, C – striking electrode, D – gas flow, E – gliding arc discharge, Z – supply circuit [1].

In the second type of gliding arc plasma reactor (GlidArc II) electrical discharge is rapidly stretched between moving working electrodes (Fig. 2). The advantage of the second construction is that the proper apparatus operation is independent of the velocity and pressure of the working gas. It gives possibility of flexible control over the time of the plasma processing [1].

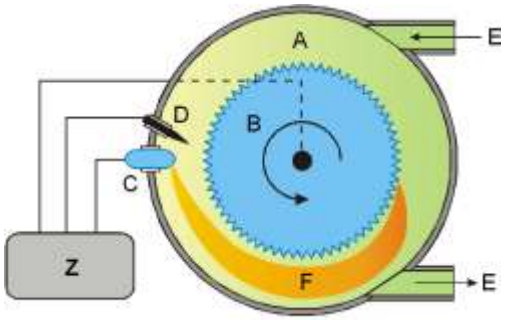

Fig. 2. Idea of the GlidArc II plasma reactor: A – processing chamber, B – rotating electrode, C – stationary electrode, D – optional striking electrode, E – gas flow, F – "gliding" quasi-arc discharge, Z – supply circuit.

3. ELECTROMAGNETIC SUPPLY SYSTEM

Electromagnetic supply system (so-called "integrated power supply") [2] constructed in the Institute of Fundamental Electrical Engineering and Electrotechnologies completely fulfils requirements mentioned in the introduction. This construction has repeatedly proven its practical advantages as the supply circuit of the type I gliding arc plasma reactor (Fig. 3) [3]. That is why the attempt to test the possibility of using integrated supply circuit for the GlidArc II plasma reactor has been made (Fig. 4).

The electromagnetic supply system consists of three single-phase working transformers Tr1, Tr2, Tr3 and an ignition transformer Tr4 (Fig. 3). Working transformers supply electric energy to the discharge. They provide voltage of a few kV and frequency of 50 Hz (power system frequency). The third harmonic, which is generated by non-linear magnetic cores of working transformers has the biggest contribution in the current of the primary winding of the ignition transformer. That is why, the striking voltage frequency equals 150 Hz (the amplitude is approximately 10 kV in most cases).

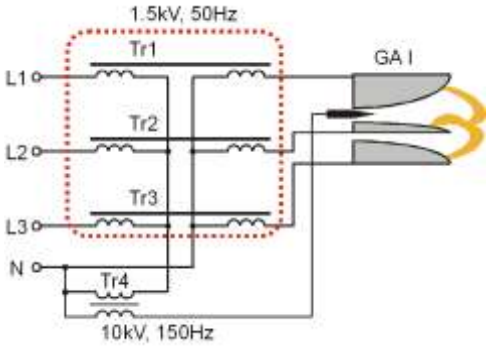

Fig. 3. Schematic diagram of the integrated supply circuit of GlidArc I plasma reactor.

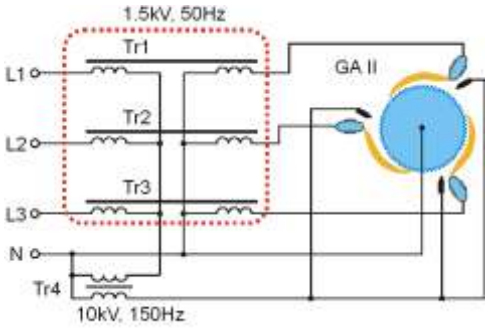

Fig. 4. Schematic diagram of the integrated supply circuit of GlidArc II plasma reactor.

4. COMPUTER SIMULATION OF THE SUPPLY SYSTEM

Computer simulation of the electromagnetic supply system has been made using PSpice. Simplified simulation scheme has been shown in figure 5. It consists of four transformers with non-linear magnetic cores described by the Jiles-Atherton magnetic hysteresis model. There is also the artificial neutral point subcircuit, which is made of capacitors configured in a star. It is necessary for the operation of ignition transformer. Additional capacitor connected in parallel to the primary winding of ignition transformer helps to adjust amplitude of the striking voltage.

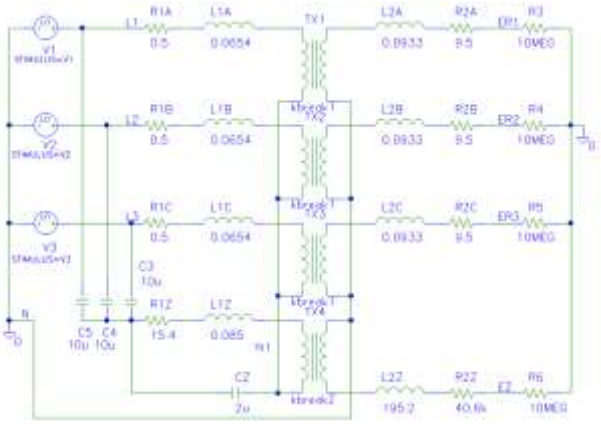

Fig. 5. Simulation diagram of the supply system (no-load state).

Numerical values of circuit components have been determined during laboratory tests of the supply system model. Same basic electric waveforms in no-load state have been presented in figure 6. The waveforms have been evaluated for both configurations of the gliding arc plasma reactor.

a) b)

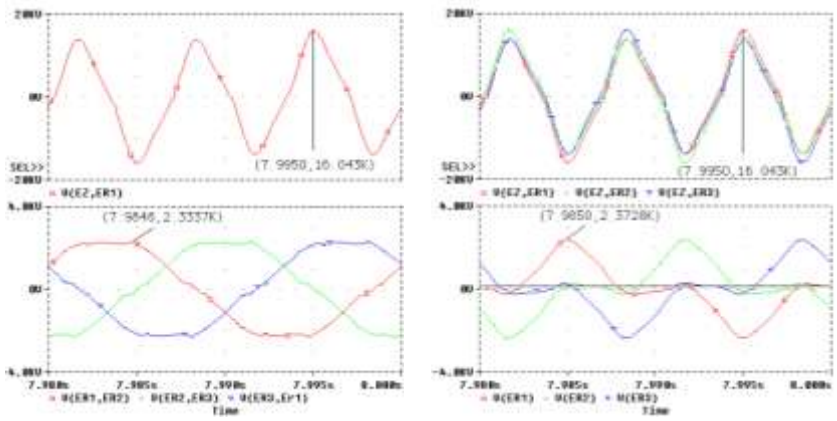

Fig. 6. Striking voltage (upper) and interelectrode voltage (lower):
a) GlidArc I plasma reactor, b) GlidArc II plasma reactor.

In figure 7, the comparison of the load characteristics has been shown. The graphs have been determined for resistive linear loads.

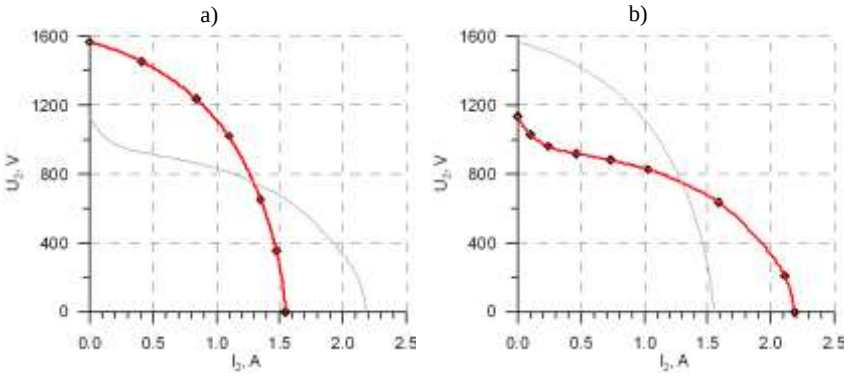

Fig. 7. Load characteristic of the supply system (U_1=400V):
a) GlidArc I plasma reactor, b) GlidArc II plasma reactor.

The computer simulation of the supply circuit loaded with the gliding electric discharge has also been made. Selected electric waveforms obtained for GlidArc I and GlidArc II reactors have been presented in figures 8 and 9. One cycle of the reactor operation has been compared in both figures.

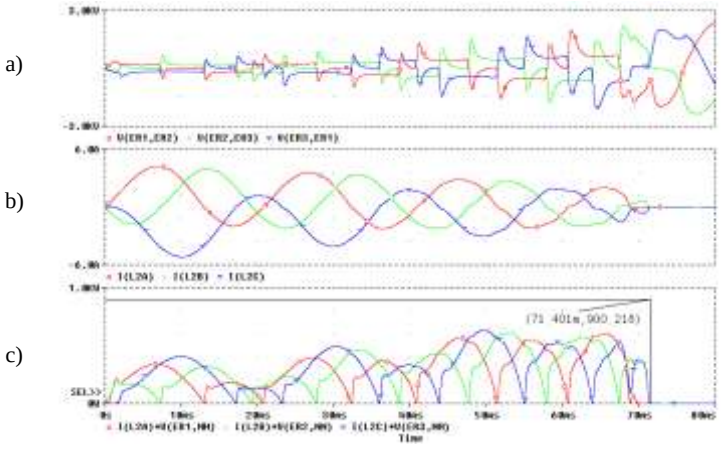

Fig. 8. GlidArc I reactor waveforms: a) output voltages,
b) discharge currents, c) discharge instantaneus power.

a)

b)

c)

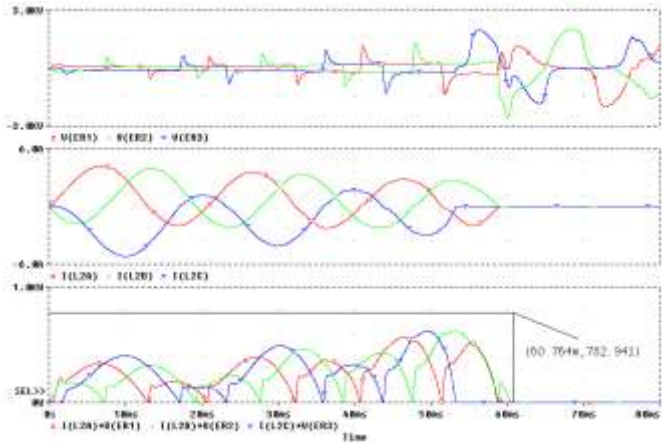

Fig. 9. GlidArc II reactor waveforms: a) output voltages, b) discharge currents, c) discharge instantaneous power.

5. CONCLUSION

The integrated supply system is capable of supplying both types of triphase gliding arc plasma reactors. It is possible to configure the GlidArc II reactor in two ways: rotating electrode + three stationary electrodes or three pairs of rotating + stationary electrodes.

Supply system generates the striking voltage of the same parameters in every tested configuration of the gliding arc plasma reactor. Interelectrode voltages have similar amplitudes in no-load state. Considerable distortion of output phase voltage caused by third harmonic, results in the ratio of GlidArc I to GlidArc II rms output voltages equal 1:0.68. This shouldn't impact on ignition because of the concurrence of peak values of output voltage and striking voltage.

Considering the same model of the discharge expansion, computer simulation shows the operation cycle of GlidArc II reactor, which lasts approx. 61 ms (85 % of GlidArc I cycle). Despite the ratio of short-circuit currents equals 1:1.42, the simulated discharge currents have similar waveforms and amplitudes in both GlidArc reactors. Active power given off during one operation cycle of the GlidArc II reactor equals 783 W (87 % of GlidArc I active power).

REFERENCES

[1] A. Czernichowski, Plasmas for destruction of H2S and mercaptans, Oil & Gas Science And Technology, vol. 54, no. 3, May-June 1999.

[2] T. Janowski, H. D. Stryczewska, Zasilacz plazmotronu do prowadzenia reakcji chemicznych, Polish patent PL 172152, 1997.

[3] H. D. Stryczewska, T. Janowski, Integrated supply system of the plasma reactor energised from three phase supply network, International Symposium on High Pressure Low Temperature Plasma Chemistry HAKONE VII: Contributed Paper, Greifswald, Germany, 2000.

4th International Conference **ELMECO**
Nałęczów, Poland
September 2003

THE EFFECT OF MAGNETIC FIELD ON SCALE PREVENTION IN THE INDUSTRIAL BOILERS

Mostafa GHOLIZADEH[1], M. R. BENAM[2]

[1] *Chemistry Department, Teacher Training University, Sabzevar, Iran*
Telfax: + 98 (571)4411161, e-mail: m_gholizadeh@sttu. ac.ir
[2] *Physics Department, Payame Noor University, Fariman, Iran*

Abstract

We have investigated the effect of magnetic field on the scale formation in the industrial boilers. It was found that passing water through a static magnetic field about 6000 G reduces the scale formation and protects the boiler from internal corrosion. It seems that the presence of the magnetic field modifies the local ionic concentrations via Lorentz Force and therefore changes the morphology of the mineral crystals. This effect causes the shape of the crystals change from a dendristic form to a disk-shape form that is less likely to form a scale.

Keywords: magnetic water treatment, scaling, corrosion, Lorentz force.

1. INTRODUCTION

The magnetic technology has been cited in the literature and investigated since the turn of the 19th century, when Lodestones and naturally occuring magnetic mineral formations were used to decrease the formation of scale in cooking and laundry applications. Today, advances in magnetic and electrostatic scale control technologies have led to their becoming reliable energy savers in certain applications [1-4].

One of the serious short comings of desalination of saline and brakish waters by desalination and membrane methods is the deposition of scale on the surface of heat exchange equipments and reverse - osmosic membranes [5].

Donaldson emphasises that in order to understand the effect, you first need to know what the scale is? Salt being heated and cooled and mixed with chemicals in all sorts of heating and processing plants are not necessarily well behaved [6].

For example, in desalination, an increase in temperature causes the following sequence:

$$
\begin{aligned}
&2HCO_3^- \rightarrow CO_3^{2-} + CO_2 + H_2O \\
&Ca^{2+} + CO_3^{2-} \rightarrow CaCO_3(calcite) \\
&Ca^{2+} + CO_3^{2-} \rightarrow CaCO_3(aragonite)
\end{aligned} \qquad (1)
$$

The lime scale problem in hard water arises because the solubility of $caco_3$ decreases with increasing temperature [7].

Despite its ubiquity, there is relatively little scientific literature on magnetic water treatment. It is not clear now, or even if, it works. Unlike chemical water softening, magnetic treatment should have no direct effect on water chemistry (unless the magnets are in contact with the water) yet, it is claimed to alter the morphology and adhesion of calcium carbonate scale [8]. Published data are often contradictory. For example, there is some dispute as to whether the deposits of calcium carbonate from magnetically treated water are predominantly calcite or aragonite.

These are the two common natural forms of $CaCO_3$, with rhombohedral and orthorhombic crystal structures, respectively.

The efficacity of magnetic treatment is reported to last from tens of minutes to hundred of hours, there is a review of the literature by Baker and Judd [9]. The authors claim the important factors which promote magnetic forces (responsible for the changes in crystallization) are the conductivity of the solution, the linear flow velocity of the fluid, and the flux density of the field.

Upon reviewing the Literature, we arrived at the conclusion that most reported successful applications of "AQUA CORRECT" have occurred in continuously recirculating systems enabling repeated treatment of the process water (especially in the industrial boilers) [10].

2. EXPERIMENT

To have a permanent magnet in a compact form a unit called "AQUA CORRECT" (H.P.S CO. DN= 25, 1 inch, flow 4 m^3/h) was used .

The coaxial magnetic system of this instrument can produce a static magnetic field about 6000 G and a stainless steel strainer was used before this instrument (Fig. 1).

Fig. 1. The magnetic instrument and stainless steel strainer

The equipment was connected to a pipeline system and also to the boilers. Water Pump was installed before the magnetic instrument in order to pumpaging tap water through the "AQUA CORRECT" in the boilers (Fig. 2).

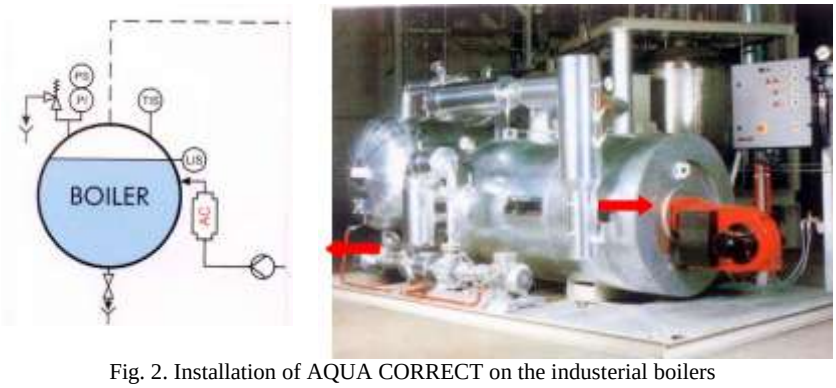

Fig. 2. Installation of AQUA CORRECT on the industerial boilers

In our experiment water had to flow through a coaxial magnetic gap, with a magnetic field area about 1.25 cm^2. The flow rate of water was checked before the installation. The direction of flow of water was adjusted to be prependicular to the field. A stainless steel strainer was placed inside the equipment to capture the suspended impurities present in the water.

About 24 hours after installation the boiler's Jacket was considered. The flow rate and condition of the pipelines and chemical properties of water were also checked. Every three months thereafter the pipelines were opened and studied. After one year final observations were made with respect to the internal conditions of the pipeline and also conditions of the boilers and so the chemical properties of water.

On the basis of over one year of research in this field, we have reached the following conclusions:

1. The magnetic water treatment will require a sufficiently fast, continuous flow of fluid. If magnetohydrodynamic forces are responsible for the action of the device, continuous fluid flow is required to generate these forces.
2. The magnetic field must be of sufficient strength and oriented 90^oC relative to the direction of fluid flow (Fig. 3).

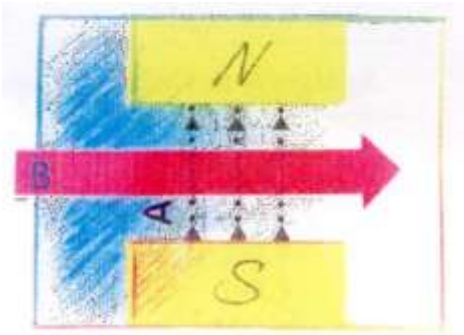

A: lines of magnetic field.
B: direction of fluid.

Fig. 3. Effective factors in the magnetic field

3. The new pipeline fitted with the AQUA CORRECT was found to be well protected from scale formation and internal corrosion, whereas the pipe without the equipment was badly damaged by scale formation and internal corrosion occurred inside the pipe (Fig. 4).

a)

b)

Fig. 4. a) before installation the magnetic apparatus,
b) after installation the magnetic apparatus

4. After installation of the magnetic instrument on the boilers the boiler's Jackets and pipelines system were automatically cleared and the solid material became loose and fell off. Thus, the life span of the boilers could be increased.

3. RESULTS AND DISCUSSION

The chemical properties of scaling water before and after the magnetic instrument was studied . In this order the lime scale was produced by heating the water to 80-85^{o}C after waiting for few times and the scale was examined by powder X-ray diffraction (Table 1).

Table 1. The change of mass percentages of crystal forms of calcium carbonate due to magnetic water treatment

Crystal forms of $CaCO_3$	Calcite %	Aragonite %
Tap water	65	35
Magnetic water treatment	27	73

The results has been shown, the ratio of aragonite/calcite is remarkably increased, in the magnetic water treatment (Fig. 5).

a)

b)

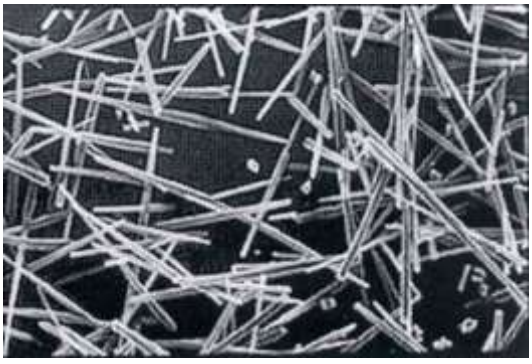

Fig. 5. a) The lime scale deposits (mainly aragonite form) obtained from water with magnetic treatment,
b) The lime scale deposits (mainly calcite form) obtained from tap water

Therefore, the presence of the magnetic field changes, the direction of the crystal growth to the aragonite which is a softer type of scale and less likely to form an adhesive scale, consequently can be easily removed.

Comparing the scale formed in the surface of the boilers before and after magnetic treatment, shows a significant decreasely of the scale. One explanation for this process due to the presence of the Lorentz Force.

This force causes the opposite ionic charges move in opposite directions and therefore decreases the adhesion scale formation, on the jacket of boilers, and also corrosion considerably (Fig. 6).

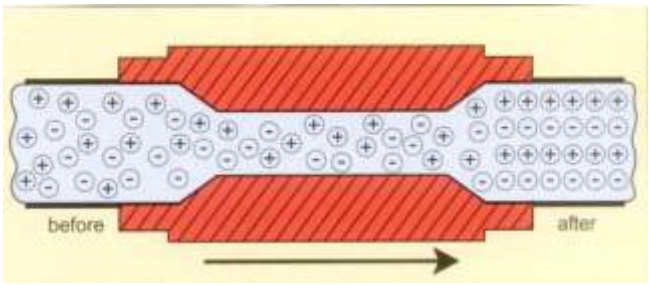

Fig. 6. Configuration of ionic particles in magnetic field

ACKNOWLEDGEMENTS

The authors are grateful for partial support of this work by Sabzevar Teacher Training University and Fariman Payam-e-Noor University Research Councils.

REFERENCES

[1] a) A.M. Pritchard, "Deposition of hardness Salt", Foul. Sci. and Technol. Proc. NATO Adv. Study Ins. Adv. Foul. Sci. and Technol. 1988, 261-273. b) I.J. Lin, J. Yotvat, J. Magn. Mater., 83 (1-3) 1990, 525.
[2] V.A. Laptev and A.V. Tioutine, Rail Engineering International Edition No. 2, 1996, 6-7.
[3] T. Het, H_2O, vol. 21, No. 18, 1988, 517.
[4] B. Welder, E.P. Partridge, Industrial and Engineering Chemistry vol. 46, 1954, 954.
[5] A.T. Pilipenko et al., "Methods of scale prevention in desalination of saline waters" Khimiya i Technologiya Vody, vol. 13, No. 11 1991, 996-1013.
[6] Donaldson, "Scaling down the water problem", Chemistry in Britain, March 1990, 209.
[7] W. Strum, J.P. Morgan, "Aquatic chemistry", Wiley, New York, 1940.
[8] J.M.D. Coey et al., "Magnetic water treatment", J. Magn. Mater., 209, 2000, 71-74.
[9] J.S. Baker, S. J. Judd, Water Res. 30, 1996, 247.
[10] J.S. Baker, S.A. Parsons, Industrial Process Water Treatment, 1996, 36.

4th International Conference **ELMECO**
Nałęczów, Poland
September 2003

CONCEPTION OF THE WATER QUALITY IMPROVEMENT IN PIPING SYSTEMS, BY ELECTROMAGNETIC FILTER USAGE

Dariusz KOWALSKI[1], Mykola GIROL[2], Małgorzata IWANEK[1]

[1] *Lublin University of Technology, 20-618 Lublin ul. Nadbystrzycka 40, Poland*
e-mail: Kowalski.D.@fenix.pol.lublin.pl
[2] *Water Management University, 33000 Riwne, Soborna 11, Ukraine*
e-mail: M.M.Girol@RSTU.RV.UA

Abstract

The article presents new conception of water quality improvement in water supply systems, by intermediary water stations equipped with electromagnetic filters. Traditional methods of counteraction to the problem of secondary water pollution in distribution nets are still not satisfied, so the research of new method is very necessary.

Proposed conception of water quality improvement contains the intermediary water treatment stations usage, localised directly on distribution nets. Usage of electromagnetic filters as the main part of water treatment technology eliminates problems that occur with traditional filters.

Keywords: water quality, distribution net, water electromagnetic filter, intermediary water stations.

1. INTRODUCTION

The primary aim of water piping systems is water supplying, in satisfactory quantity, pressure and quality, to final users. Polish and European Union directives describe the quality of the water in such systems [1, 2]. Ideal situation for water supply systems is when input and output water has the same, high parameters. Unfortunately, in practice, the secondary water pollution (**SWP**) can be observed in existing water distribution systems.

The secondary pollution can be observed as a significant deterioration of physical, chemical and microbiological water properties and system hydraulic parameters. That deposition can be entrained by water, in condition of hydraulic strikes and dynamic changes of water demands. In this moments the final user observes the essential growth of water pollution. Prescribed situation occurs, in most cases, at the final part of water distribution systems, during the period of high water demand (the morning one mainly) [3, 4].

At the recent time the development of SWP phenomena can be observed, even in systems supplied by ground water with good quality. Probably it is the effect of overdimension of existing pipes in relation to actual users demands [5,7,8]. The existing pipe nets work as a wide biochemical reactor with long time of storage [9]. It provides to essential deterioration of water quality in distribution system area. These phenomena concern great majority of water supply systems in Poland, so it is necessary to look for counteraction and prevention methods.

The aim of paper is presentation of conception of the water quality improvement in water supply systems, by usage of, localised directly on distribution net, intermediary water treatment station, equipped with electromagnetic filters.

2. COUNTERACTIONS AND PREVENTION METHODS OF SWP

One of the most popular methods of secondary water pollution prevention is system geometry shaping and pipe dimension design, to receive the water flow with higher then sedimentation velocity. Of course this method can be used in new created systems mainly.

In cases, when obtaining of optimal velocity is impossible, above all in existing systems, it is necessary to realise the counteraction activity of SWP results. The most popular method of counteraction is rinsing of selected conduits and greater parts of chosen water supply systems. Unfortunately this solution can be not enough effective, especially when rinsing process is provided without directed forced flow condition [8,10].

One of the faults of this method is essential loss of water, which is drained from the system during rinsing process. The other problem is rinsing frequency. Specific of the rinsing process demands the activity of exploitation service every time. It can be provided periodically, after users' signals or basing on elaborated instructions – everything is independent of real necessity.

3. CONCEPTION OF INTERMEDIARY WATER TREATMENT STATIONS (WTS) LOCALISED DIRECTLY ON DISTRIBUTION NET

One of the water quality improvement methods in SWP condition can be usage of intermediary WTS localised directly on distribution net [10]. The main task of those stations, continuously realised, is to remove pollutants out of water, during their flow through the system. This solution has series advantages over traditional rinsing method. There are continuity of pollutant removing process, elimination of water loss and possibility of secondary disinfection, which can limit the biological processes.

The fault of presented solution is the additional pressure losses in WTS area. As the effect, the pump power must be higher, which provides to greater cost of water transport through the system. Of course there is good moment to remember that water loss and labour consumption of traditional rinsing process also rise that cost. In cost aspect it is necessary to elaborate the WTS construction, which eliminate the essential pressure loss. Very interesting solution of that problem can be usage of electromagnetic filters.

4. WATER ELECTROMAGNETIC FILTERS

The water electromagnetic filter uses the strong magnetic field to intercept ferromagnetic pollutants included in flowing through water [6,11]. The electromagnetic

field, which fills whole space of the filter, takes the role of porous filtration media (Fig. 1 right).

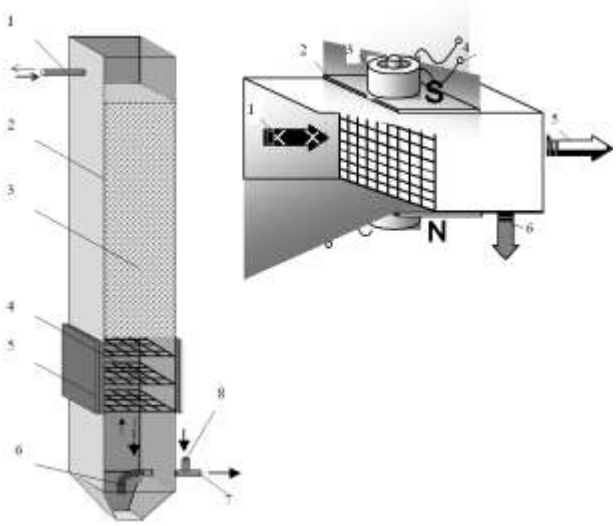

Fig. 1. Right - The idea scheme of water electromagnetic filter with wire net structure: 1 - water input, 2 - magnetic conduit, 3 - electromagnet, 4 - supply conduits, 5 - water output, 6 - output of rinsing water. Left - The idea scheme of electromagnetic filter combined with granular floating fill: 1 - clear water output and input of rinsing water, 2 - package, 3 - granular floating fill, 4 - electromagnetic separator, 5 - electromagnet, 6, 7 - rinsing water output, 8 - water input.

At the outer side there is the magnet core, connected to flat magnet conduit covering all width of filter package. Described solution allows to equalise the magnetic field in the filter. The usage of wire net as the magnetic attachment provides to creation the strong magnetic force in nodes. Magnetic force factor reaches 10^{10} A^2 m^{-3} [6,11]. During the filter's work, at water purification mode, contaminated water flows through the wire net's holes. Ferromagnetic pollutants are intercepted at net nodes.

Efficiency of contaminant by ferromagnetic pollutants water treatment at the plant of described construction reaches 97-99,8 % [4,5], although the higher described value needs the plant modification. It is necessary to attach the granular floating fill to described electromagnetic filters, to intercept the para and diaferromagnetics after their pass through the magnetic nets (Fig. 1 left).

The laboratory and industrial tests indicate that the loss of water pressure head in described filters is essentially lower then in traditional filters, reaching about 0,1 mH_2O. All operation cycles of such filters can be easily automated. It is also important, that the regeneration process, basing on simple rinsing, doesn't need the pump usage. Rinsing process is very short - about 30 second - and provides to minimisation of water losses.

Additional aspect in usage of water electromagnetic filters, basing on strong magnetic field, is bactericidal effect, which can reach almost 99% [6].

5. COMPARISON OF TRADITIONAL AND ELECTROMAGNETIC FILTERS USAGE

Comparison of traditional an electromagnetic filters, as the main objects of WTS will be done using example of the city with 15 thousand inhabitants, localised in Lublin region.

OBJECT

The idea scheme of selected water supply system is presented in Fig. 2. Deterioration of quality parameters of water in distribution system occurred especially in housing estate area, where about 1300 persons live [4]. All conduits in selected area and the rest of the city were made of zinc coated steel pipes. Exploitation period of the water system amounts near 10 years in the housing estate area and 25 in the rest of the city.

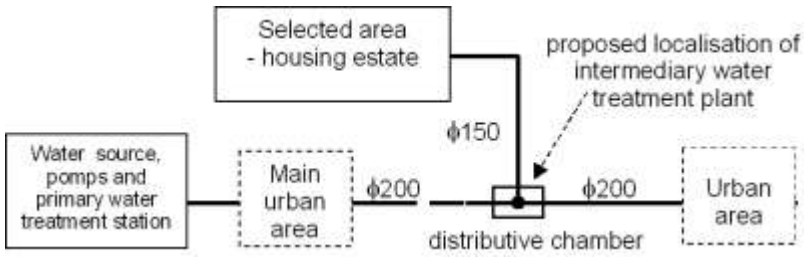

Fig. 2. Idea scheme of selected communal water supply system.

The low quality of the water at the houses inner installations provided to numerous tenants' complains to local municipal government and water supply entertainment. Complains was confirmed by local sanitary-epidemiological station. Realised tests discovered the following average pollutant concentration: pH – 7,4, water hardness 3,93 mval/dm^3, Fe – 1,62 mg/dm^3 (acceptable limit 0.3 mg/dm^3), Mn – 0,24 mg/dm^3 (acceptable limit 0,1 mg/dm^3). Maximum values occasionally received even Fe – 21,2 mg/dm^3, Mn – 0,32 mg/dm^3. The essential water deterioration occurs mainly at the top morning water demands [4].

Realised expertise [4] discovered that the main source of the pollutants in water is the distribution net itself. The influence of the pipes localised at the housing estate area has mainly corrosion origin and was estimated on 0,1 mgFe/dm^3. In this situation only the previous part of the water distribution system can be the source of pollutants, which exceed limits.

Proposed by authors of the paper solution of the presented problem can be installation of intermediary water treatment plant at the localisation presented in Fig. 2. The aim of that station must be iron and manganese removing from supplied by municipal distribution system water. The alternative situation, when each house or each user has individual filters, was refused.

TRADITIONAL STATION OF WATER TREATMENT

The traditional water treatment station, for presented above conditions, has a rapid filter with quartz packing with following parameters: filter diameter - 1.4 m, working period to regeneration - 1 week, predicted pressure fall 0.05 MPa. The idea scheme of the WTS with traditional filter is presented in Fig. 3.

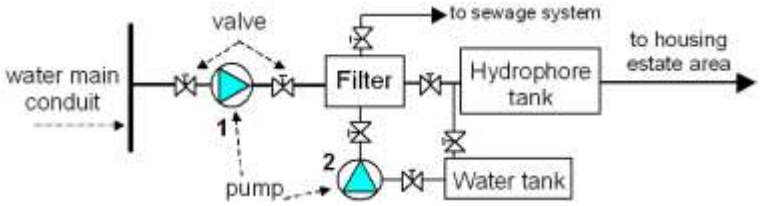

Fig. 3. Idea scheme of intermediary water treatment station with traditional rapid filter.

Installation of traditional rapid filter, as the main element of intermediary WTS causes some problems:

- whole water provided to housing estate area must be filtrated, in independence of their quality; the period of water quality limit exceeding amounts only few hours a day,
- the predicted pressure fall must be compensated by pump (1) usage,
- collaboration of filter and pump, in conditions of variable water flow (depended on water demands) indicates the element of flow equalisation, e.g. a hydrophore tank,
- filter must be regenerate periodically, so the pomp (2) and the water tank is necessary,
- regeneration period brakes the water supply to final users,
- whole station needs the essential space for installing, which can be difficult in urban area.

STATION WITH ELECTROMAGNETIC FILTER

The usage of water electromagnetic filter with floating granular fill as the main element of intermediary WTS provides to essential simplification in comparison with traditional porous filter (Fig. 4). Additionally the full automation can provide minimisation of man factor during the normal work of the described station.

The advantages of presented solution over traditional stations are clearly visible. Simplification of water treatment technological scheme and minimisation of necessary space, make possible the installation of such solution almost in all places in water distribution net.

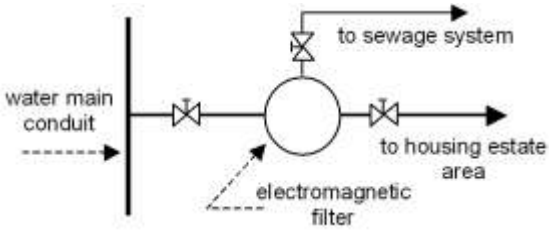

Fig. 4. Idea scheme of intermediary water treatment station with electromagnetic filter.

Of course presented solution needs the electrical energy supply but experiments indicate that energy demands are lower then for water pumping connected with traditional porous filter stations. It is still necessary to realise the economic analysis of both described solutions.

6. CONCLUSIONS

- The **SWP** problem, as the effect of economic and political changes, concerns the great majority of existing water supply systems in Poland and Western Europe.
- The common reason of **SWP** is pipe corrosion products.
- Proposed conception of water quality improvement, contains usage of the intermediary WTS, localised directly on distribution nets, mainly at the beginning of the housing estate areas.
- The traditional filter usage in the proposed intermediary **WTS**, provides to numerous complications, connected with water treatment technology, necessity of compensation of essential additional hydraulic resistance and big space demanded for installation. All of these reduce the possibility of application of intermediary stations.
- Usage of electromagnetic filters as the main part of intermediary **WTS** can be the solution of mentioned problem. It is possible to localise stations almost in each part of water distribution net, without essential hydraulic flow problems.
- It is still necessary to make the economic analysis of water electromagnetic filter usage in intermediary WTS, in industrial scale conditions.

Paper realised in 4 T09D 04624 research program of State Committee for Scientific Research.

REFERENCES

[1] Rozporządzenie Ministra Zdrowia z dnia 04.09.2000 r. (Dz.U. nr 82, poz. 937, z dnia 04.10.2000), w sprawie warunków jakim powinna odpowiadać woda do picia i na potrzeby gospodarcze.

[2] Instruction of European Union Council no 98/83/EEC, from 3rd November 1998, about quality of water assigned to people demands. Official Journal of the European Communities No L. 330. 5.12.98.p. 32-54.

[3] Bobruk P., Bonetyński K., Kowalski D.: Badanie możliwości ochrony jakości wody w układzie osiedlowej sieci wodociągowej. I kongres Inżynierii Środowiska - Lublin. Materiały, Monografie Komitetu Inżynierii Środowiska PAN, 2002, vol.11.

[4] Bonetyński K., Kowalski D., Stelmach K.: (1999) Skutki stosowania normy 0.5 mgFe/dm^3 w wodzie uzdatnionej na przykładzie wybranego wodociągu komunalnego. Ochrona Środowiska 4/1999.
[5] Girol M.M., Semczuk G.M.: К рационализации технико-экономических параметров систем водопроводно-канализационного хозяйства. Гидромелиорация и гидротехническое строительство. Сборник научных трудов. Выпуск 27, 2002. 199-207 с.
[6] Girol M.M., Zhurba M.G., Semczuk G.M., Yakimchuk B.N.: Доочистка сточных вод на зернистых фильтрах. Под общ.ред. Н.Н.Гироля. СП ООО «Типография» Левобережная», К. 1998.
[7] Kulbik M.: Ochrona jakości wody w sieci wodociągowej przez wymuszenie ukierunkowanego przepływu. Gaz Woda i Technika Sanitarna nr 10/1998.
[8] Kropla – Informator Miejskiego Przedsiębiorstwa Wodociągów i Kanalizacji w Lublinie. 1/99.
[9] Neyman-Olańczuk K., Mikołajski S., Wargin A.: Jakość wody w sieci wodociągowej Gdańska. Seminarium nt. „Historia i rozwój wodociągów i kanalizacji miasta Gdańska". Gdańsk, listopad 1997.
[10] Patent application (Poland) P 355520.
[11] Patent application (Ukraine) Б.И.№39, 23.10.89, №1516583, Б.И.№ 18, 15.05.92, №1733046, Б.И.№26, 15.07.91, №1662691

4th International Conference **ELMECO**
Nałęczów, Poland
September 2003

EVALUATION OF THE INFLUENCE OF STATIC ELECTRICITY ON INDOOR AIR QUALITY

Zygmunt J. GRABARCZYK

Central Institute for Labour Protection – National Research Institute
00-701 Warszawa, ul. Czerniakowska 16, POLAND
e-mail: zygra@ciop.pl; zygmunt.grabarczyk@acn.waw.pl

Abstract

The precipitation and charging of particulates in indoor air is a dynamic process, which is influenced by a number of factors. The electrostatic field (ESF) caused by static charges accumulated on dielectric boundary surfaces of the room can enhance the precipitation. It is shown that at moderate ESF intensity, the precipitation rate is an exponential function of the ratio of surface charge accumulated in the room and volume of the room. It was shown experimentally that the precipitation rate is a non-monotonic function of ESF intensity. At sufficiently high values field intensities (depending on the volume of the room) air ions are removed by the field and the charging of aerosol particulates is considerably slowed down, so the aerosol less sensitive to the electric field than at low field intensity.

Keywords: air ions, air quality, aerosol, electrostatic field.

1. INTRODUCTION

In the industrialized countries people spend an increasing amount of time in buildings. In the USA it is nearly 90% of the total time in a year which people spend indoors. This results in increased significance of the indoor environment as the basic human life environment. Inside buildings people are exposed to numerous environment factors of moderate and low intensity or concentration for a long part of the life, so evaluation of the health effects is difficult. One of such complex problems is the well-known "sick building syndrome". Static electricity (ES) is a significant factor in many kinds of rooms (office, living, industrial) equipped with materials and devices made from synthetic materials, especially in seasons of low air relative humidity (RH). ES is burdensome when RH is lower than about 40%. According to this author's observations the positive electrostatic potential of TV or old computer monitor screens and the negative potential of the floor and furniture coverings sometimes increase up to several kilovolts and can remain at that level for hours. In some cases the electrostatic field (ESF) is a permanent factor of the indoor

environment. The knowledge about the relations between ESF and indoor air quality is not satisfactory. The enhanced deposition of dust onto charged surfaces is well known and the correlation between the intensity of the ESF and the level of aerosol pollution seems probable. On the other hand preliminary measurements made by author in five office buildings showed this correlation to be weak and strongly disturbed even by slow air exchange due to gravitational ventilation. For this reason experiments in small tightly closed space were carried out, to find the potential influence of ESF on dust density and indoor air quality.

2. METHODES

An air capacitor with parallel plates was placed inside the chamber shown in Fig. 1.

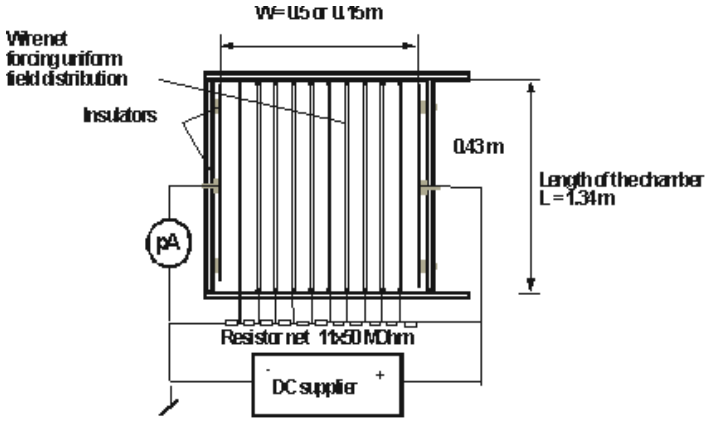

Fig. 1. A cross-section of the experimental chamber with a plate capacitor inside

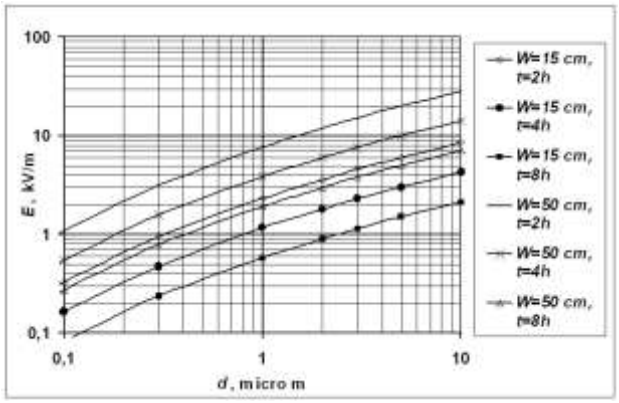

Fig. 2. Minimum *E* able to force particulate carrying charge mean for the population of size *d*, to pass the distance *W* during time *t*

The volume of the chamber was 0.29 m^3 or 0.09 m^3. Dust particulate concentration inside was measured with a HIAC-ROYCO Micro-Air 5230 laser counter. Samples were taken from the centre of the smaller chamber every hour and only after 2 or 4 or 8 hours from the centre of the larger one. Each sample was 0.47 % or 1.5% of the total volume of the capacitor respectively. The intensity of the ESF was changed from 0 up to 20 kV/m. A sample of natural indoor aerosol was introduced into a chamber before every measurement. There was no corona discharge and natural ionizing radiation was the only source of small air-ions. The duration of observation was chosen to be of order of the expected time of flight across the whole distance W by the particulate carrying the charge value mean for the population of the diameter d (see Fig. 2, calculated on the basis of data given by Friedlander, 2000, after Fuchs and Sutugin).

The climatic conditions were as follows: RH=34% SD 11.7%; t = 23.2 0C SD 1.7 ^{0}C.

3. RESULTS

The measurements were carried for two particle size ranges: 300 – 400 nm and 1000 – 2500 nm. In two different particle sizes, there dominate two different particle charging mechanisms. For particles 300 – 400 nm dominates the diffusion mechanism of charging, dependent only on time and concentration of small air ions. In the range 1000 – 2500 nm the dominant effect is field charging, dependent on time of exposure, small air ion concentration and ESF intensity.

Particle concentrations as a function of ESF intensity and time of exposure $n(E,t)$ are related to concentration at t=0 and E=0 (gravitational and diffusion precipitation only). The ESF intensity increased the rate of dust particle precipitation 3- to 6-fold compared to precipitation by sedimentation and thermal diffusion only. The final concentration of the particles in the vicinity of the field was about 1.5- 4-fold smaller than that without the field.

The results of the measurements for two ranges of particle size and two sizes of the chamber are shown in Fig. 3, 4, 5 and 6.

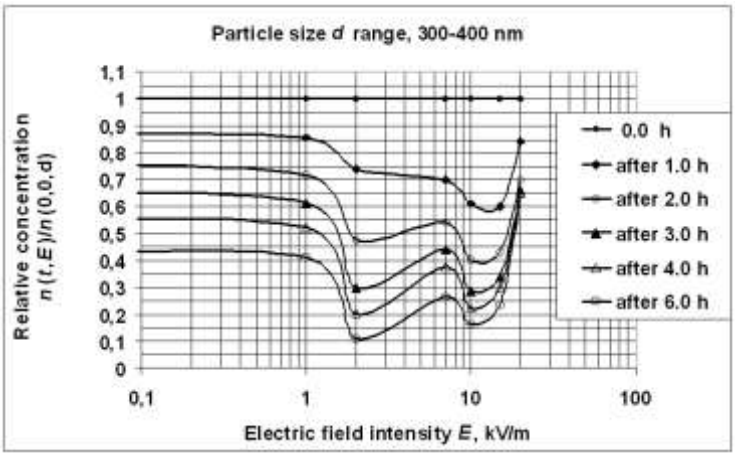

Fig. 3. Dependence of particle concentration with field intensity E and time of exposure t, for diffusion charging, in larger chamber – W = 0.5 m.

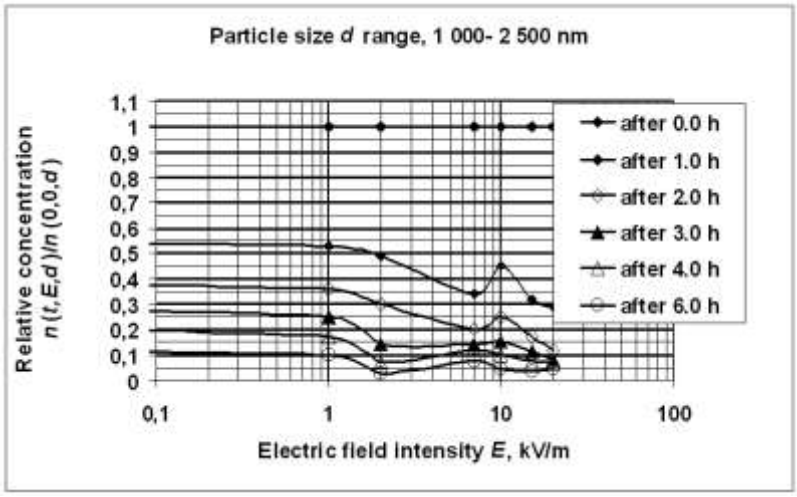

Fig. 4. Dependence of particle concentration with field intensity *E* and time of exposure *t*, for field charging, in larger chamber – *W* = 0.5 m.

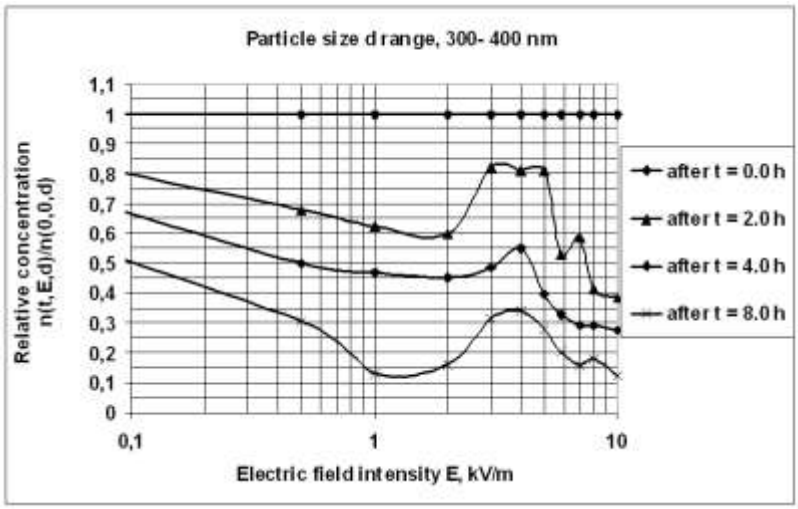

Fig. 5. Dependence of particle concentration with field intensity *E* and time of exposure *t*, for diffusion charging in smaller chamber – *W* = 0.15 m.

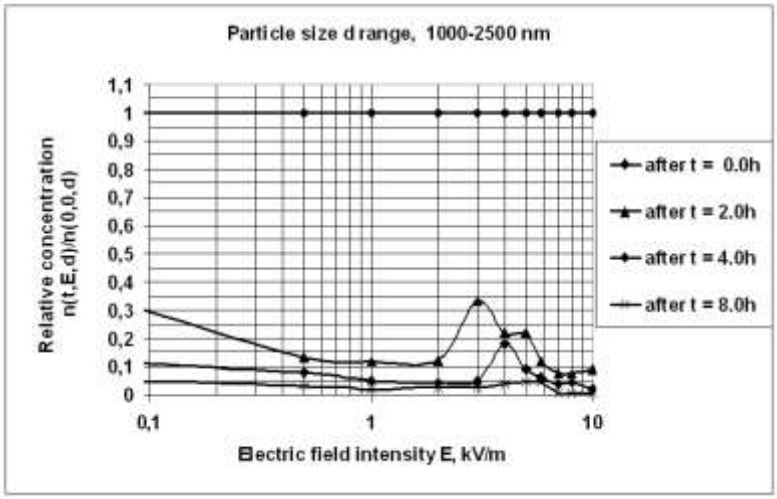

Fig. 6. Dependence of particle concentration with field intensity E and time of exposure t, for field charging, in smaller chamber – W = 0.15 m.

4. DISCUSSION AND CONCLUSIONS

The functions $n(E,d,t)$ were not monotonic in the E domain. In both chambers the local maximum of $n(E,d,t)$ was found. Its value and the value of the respective E were significantly different for both chambers. It seems that the major factor deciding on the location of the local maximum is the distance between the electrodes W. This is the evidence of two simultaneous and opposite processes caused by the electric field. In thermodynamic equilibrium for the small values of E it can be shown that the function $n(E,d,t)$ is monotonic in the first approximation (when the sedimentation and diffusion is neglected). Particle concentration is proportional to the following function:

$$\frac{n(t)}{n(t=0,E=0)} \approx \exp\left(-\frac{k_m(d)}{W}Et\right) = \exp\left(-\frac{k_m(d)}{\varepsilon_0 V}Qt\right) \tag{1}$$

where k_m is the mean value of the mobility of particles with the diameter d, W is distance between parallel electrodes and Q is the equivalent total charge accumulated in the chamber capacity of volume V.

That tendency is in accordance with the results of up to about 2 kV/m. For higher values of E the air ion density changes along the chamber in direction x (-W/2, +W/2) according to the approximate formula (Grabarczyk, [1]):

$$n_{i\mp}(q,n,E,W,x) = \frac{q}{\beta n}\left\{1-\exp\left[\frac{\beta n}{k_{i\mp}E}\left(x \pm \frac{W}{2}\right)\right]\right\} \tag{2}$$

where $n_{i\pm}$ is small ion (positive/negative) concentration, k_i is a small ion mobility, q is the rate of ion generation by ionizing radiation, β is a coefficient of attachment small ions by particles.

Total ion concentration decreases with an increase E, so the effectiveness of charging of particulates decreases for diffusion mechanism and probably decreases for field mechanism. As a number of collecting particles is increasing function of $|E|$ and ion concentration and the decreasing function of E/W, so the there must be the local maximum of precipitation efficiency for some value of E, and for higher values of E, efficiency should decrease with rising E up to the moment of corona or spark discharge. It is not the case, probably because of too simple model. It must be taken under consideration in future investigation that ESF force the charge separation, and at the boundaries of the chamber room the ion atmosphere is locally unipolar. So in that case the local charging efficiency at the electrode surfaces is probably much higher again and the efficiency of precipitation rises with E again.

Presented measurements results must be take with care because the testing aerosol was atmospheric one and not reproducible from test to test. Also some changes of air humidity and the rate of ion generation could influence the results. The time of the experiment was about four months, so the aerosol properties couldn't be the same all the time.

ACKNOWLEDGEMENTS

This study is part of the National Strategic Program "Occupational Safety and Health in the Working Environment" supported in 1998-2001 by the State Committee for Scientific Research of Poland and the National Programme "Adaptation of Working Conditions in Poland to European Union Standards" supported in 2002–2004 by the State Committee for Scientific Research of Poland. The Central Institute for Labour Protection – National Research Institute is the Programmes main co-ordinator.

REFERENCES

[1] Grabarczyk, Z. J. Influence of the static electricity on the indoor small air ion concentration, in Conference Proceedings of the Third International Conference ELMECO 2000, Electromagnetic Devices and Processes in Environment Protection. 2000, Lublin Technical University.

[2] Grabarczyk, Z.J. Influence of Indoor Electrostatic Fields on Particle Concentration. J. Aerosol Science, 2003, EAC 2003, Madrid, Spain. pp. S 1285-1286

[3] Friedlander, S.K. Smoke, dust and haze. Fundamentals of aerosol dynamics. Oxford University Press, New York. 2000.

4th International Conference **ELMECO**
Nałęczów, Poland
September 2003

EFFICIENCY OF ELECTROSTATIC FILTER WITH MESH COLLECTOR PERPENDICULAR TO THE AIR-FLOW

Zygmunt J. GRABARCZYK

Central Institute for Labour Protection – National Research Institute
00-701 Warszawa, ul. Czerniakowska 16, POLAND
e-mail: zygra@ciop.pl; zygmunt.grabarczyk@acn.waw.pl

Abstract

A model of an electrostatic air cleaner in which porous material perpendicular to the air-flow was degenerated to a single sheet of wire grid was tested. The test stand consisted of a non-conducting pipe in which, two single metallic grids were placed perpendicularly to the long axis of the pipe and to electric field and ion stream. Discharging electrodes placed on the surface of inlet, HV DC supplied grid, and facing the collecting grid were distant about 0.035 m from collecting grid. The linear air-flow speed was 0.5 m/s. Particulate density in the 0.3-2.5 μm range, was measured in front of and behind the filter with a HIAC-ROYCO 5230 laser counter. The function of filter efficiency against ionic current and the voltage of discharge electrodes were measured. Efficiency was higher than 95% for the least sensitive particles in the 0.3-0.5 μm range.

Keywords: electrostatic filter, electrostatic precipitator, corona discharge.

1. INTRODUCTION

There are two main kinds of electrostatic air cleaners – industrial precipitators with the electric field and ion current perpendicular to the air stream and filters with the porous material perpendicular to the air stream. Usually the electric field and air ion stream is parallel to the air stream in the filters. This is believed that charged particles are collected inside the porous material with higher efficiency than those electrically neutral. The major advantage of these filters is that it is possible to make them very short. The greatest disadvantage of the filters is the resistance to the air-flow. To decrease resistance, the filter material should be very porous, but the bigger the size of the pores, the lower the filter efficiency. Analysis of electrostatic filters by Pnueli [1] and Mermelstein [2] showed that particles are caught mainly on the surface of the conducting filter material. So it seems that very thin filters could have nearly the same efficiency as thick ones, but much lower air-

flow resistance. The simplest kind of degenerated porous filter material is a single layer grid. To prevent particles from passing through the mesh the electric field and preliminary electric charging can be used. The present work was undertaken to verify that hypothesis.

2. METHODES

The effectiveness of a model filter was investigated experimentally. A model of a filter in which perpendicular porous material was replaced by a filter degenerated to a single sheet of wire mesh was tested.

The test stand (Fig. 1) consisted of a non-conducting pipe in which, two single grids were placed perpendicularly to the long axis of the pipe [3]. Both grids were made of 1 mm steel wire with square holes with 1-mm sides. Discharging electrodes were placed on the surface of one grid, on the side facing the other mesh. The 10 mm long electrodes were made of 0.1-mm steel wire and they were fixed every 4 mm. The distance between the electrodes and the filter mesh was about 0.035 m and the linear air-flow speed was 0.5 m/s. The diameter of the filter channel was 70 mm.

The electrodes were supplied with high DC voltage from a regulated supplier. Particulate density in the 0.3-2.5 μm range, was measured alternately in front of and behind the filter. A HIAC-ROYCO laser counter 5230 was used. The function of filter efficiency *versus* ionic current and the voltage supplying the discharge electrodes were measured.

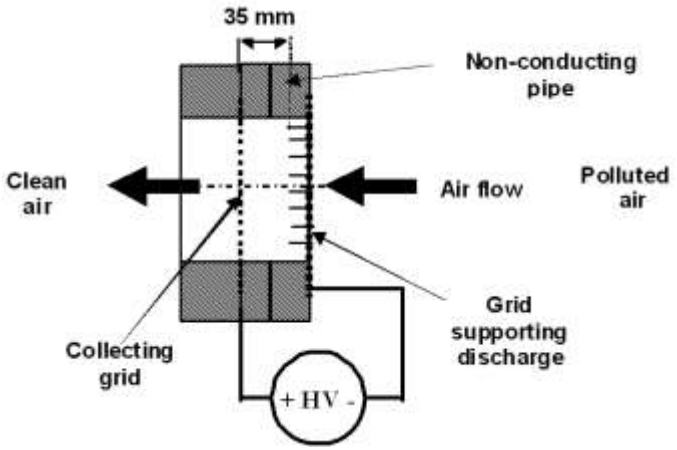

Fig. 1. Cross section of the air filter with single metallic grid particle collector

For comparison aim, there were made measurements of filtration efficiency with polypropylene fibrous electret filter. Two mm thick layer of polypropylene was put on the collecting grid.

3. RESULTS

Results of measurements for filter with single grid as a particle collector are shown in Fig. 2. Results for filter with added electret layer are shown in Fig. 3.

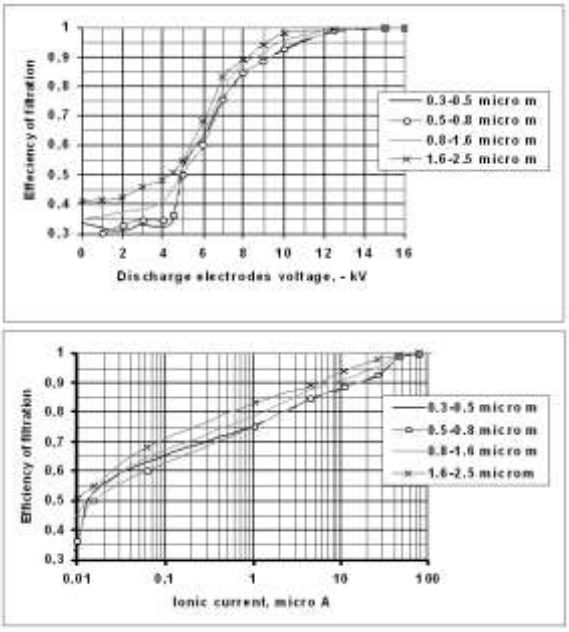

Fig. 2. Dependence of filtration efficiency of a single grid filter on the voltage supplying discharge electrodes (upper) and ionic current (lower)

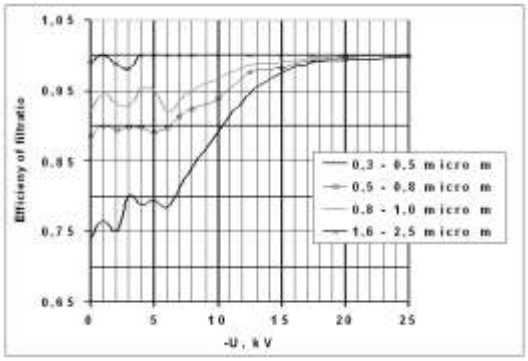

Fig. 3. Dependence of filtration efficiency on the voltage supplying discharge electrodes of a filter with 2 mm electret filter on the collecting grid

4. DISCUSSION AND CONCLUSIONS

The results presented in section 3, show that the most fraction of particles is precipitated onto the inlet surface of the filter material. That means that filter degenerated to the semi-transparent surface is highly effective, like the electret filter. The single metallic

grid was enough to achieve a very high effectiveness, higher then 95% with the low air-flow resistance. The filter is in fact a kind of electrostatic precipitator, as the phenomenon of precipitation is the main mechanism of particle removing.

The presented solution has two disadvantages which are generation of the ozone and calculation of the precipitated pollutants on the grid wires. The ozone concentration was not measured but its concentration was higher then the human level of perception (about 0,01 mg/m^3). The further work should be carried out for ozone generation limiting. For the second disadvantage that kind of cleaner is appropriate for moderate polluted indoor air cleaning, where low noise of air flow is desirable.

The important advantage of the grid filter is very small length. It is worth of further investigating also, the possibility of the use of such a filter as an aerosol diluter with current or voltage control of the dilution factor.

The presented precipitator could be also effective for nanometer size, as showed Alonso *et al.* [4], by adding a few additional collecting metallic grids. This introduced the diffusion mechanism of precipitation of nanoparticles.

ACKNOWLEDGEMENTS

This study is part of the National Strategic Program "Occupational Safety and Health in the Working Environment" supported in 1998-2001 by the State Committee for Scientific Research of Poland and the National Programme “Adaptation of Working Conditions in Poland to European Union Standards” supported in 2002–2004 by the State Committee for Scientific Research of Poland. The Central Institute for Labour Protection – National Research Institute is the Programmes main co-ordinator.

REFERENCES

[1] Pnueli, D. et al. Electrostatic porous filter with a blocking electrode. J. Aerosol Science, vol.31, No. 11, 2000, pp. 1371-1379.

[2] Mermelstein, J. et al., Electrostatically enhanced stainless steel filters: Effect of filter structure and pore size on particle removal. Aerosol Science and Technology. vol. 36, No. 1, 2002, pp. 62-75.

[3] Grabarczyk, Z.J. Electrostatically enhanced efficiency of a single metallic mesh filter. In Chiu-Sen Wang (ed.), Sixth International Aerosol cConference. Abstracts. Taipei, 2002, pp. 963-964.

[4] Alonso, M. et al. A diffusion-electrostatic precipitator for collection of nanometer particles. In Chiu-Sen Wang (ed.), Sixth international aerosol conference. Abstracts. Taipei, 2002, pp. 983-984.

4th International Conference **ELMECO**
Nałęczów, Poland
September 2003

ELECTRICALLY ASSISTED DEVICES FOR DUST CONTROL
Part 1. Dry electrostatic methods

Anatol JAWOREK , Marcin LACKOWSKI, Tadeusz CZECH, Andrzej KRUPA

Institute of Fluid Flow Machinery, Polish Academy of Sciences
80-952 Gdańsk, ul. Fiszera 14, POLAND, jaworek@imp.gda.pl

Abstract

Three types of pollutants in exhaust gases can be recognized: noxious gases, liquid mists and dusts. They require different methods for removal them, and frequently, electrical processes are the most effective in removal such contaminants. Conventional methods of gas cleaning, including electrostatic precipitators are modernized since a couple of decades but the problem of low-efficiency window in dust particle size remains still unsolved. Many new electrically assisted designs have been proposed for the purpose of increasing the cleaning efficiency. Among them are conventional equipments with electrical assistance, which augment the removal of dust particles in submicrometer size range. Recent developments in electrically assisted gas cleaning devices are reviewed and critically discussed in the paper.

Keywords: gas cleaning, gas filtration, electrostatic precipitators, electrocyclons.

1. INTRODUCTION

The first part of the paper reviews newly developed methods aimed at improvement of conventional electrostatic precipitators and filters by applying electrical forces. The collection efficiency of the electrostatic precipitators was improved by adding electrostatic agglomerators or by construction of multistage precipitators. Two classes of electrically assisted filters can be met in publications: fabric filters, and granular-bed filters. Electret filters are a special class of fabric filters, which are built from permanently electrically charged fibers. Electret filters generate strong electrostatic field close to the fiber surface, and are able to remove very fine particles with higher efficiency than conventional filters. Granular bed filters are made of small granules such as sand, glass beads, or plastic balls placed in a dielectric container between two electrodes to which alternating electric voltage

is applied. The granules are polarized by the electric field and become the collection sites for small dust particles.

2. ELECTRICALLY ASSISTED BAG FILTERS

Filters are made of media with small pores or openings, usually smaller than the size of the particles to be removed. A gas flows through the filter, but the particles are too large to pass the openings, and are captured on the upstream side of the filter or within the pores, building up a dust cake. Aside from electrostatic precipitators, fabric bag filters are the most frequently used in the industrial conditions. Fabric filters use textile fabric as the filter media shaped usually into bag or envelope. The electrical forces were employed to these filters in order to more efficient removal of fine particles, and extending their lifetime [1-8]. An example of a design of such filter is shown in Fig. 1. In this type of filter, the particles can be either precharged by a corona discharge in a separate stage prior to the filtration stage with corona-free electric field, or simultaneously charged and precipitated in one device.

The fabric filters can also be improved by applying a set of wires close to the upstream or downstream surface of a fabric filter [9-11]. The electric field is produced by maintaining the wires at high potential. The electric field reduces the pressure drop and penetration by almost an order of magnitude as compared to standard fabric filters. The collection efficiency can be as high as 99.9% for PTFE or 99.4% for glass fibers, while the power consumption can be lower than a few W/m^2 [9]. The collection efficiency of bag filters can be also increased by charging the particles electrically using a corona discharge [11,12].

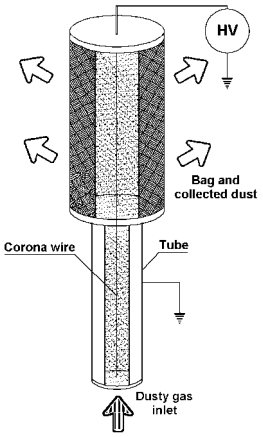

Fig. 1. Electrically assisted bag filter.

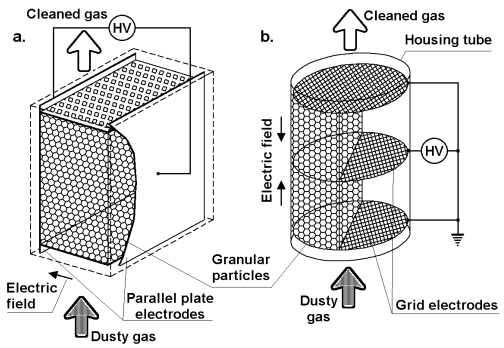

Fig. 2. Electrically energized granular-bed filter.

It was discovered by Bhutra and Payatakes [13], and at the same time by Oak and Saville [14] that charged particles are captured in the form of long and thin dendrites on the from side of the fiber with week penetration to within the bag. This structure remains free

gaps within dust cake causing lower pressure drop. Particles larger than 1 μm are collected mainly by impacting while those smaller than 0.1 μm are collected due to Brownian diffusion. The dust under an action of the electric field is mostly deposited in the regions were the distance between fibers was larger leaving shorter gaps free for the air to pass [9]. Frederick [3] noticed that the electric force causes the dust to form tight "bridges" between the fibers that results in that the cake is more porous. The operating period of the filter can therefore be longer .

Electrical energization of fibrous filters causes enhanced collection efficiency, particularly in far submicrometer size range. The penetration for such particles can be decreased from typically 90% down to about 10% or lower. The pressure drop can be reduced because of voids formed within the cake under an action of the electric field. Regeneration of electrostatically enhanced bag filters is much easier and efficient because the particles form a cake mainly on the front surface of the filter. Biodegradable fibrous filters were also considered to be involved to production [15].

3. ELECTRICALLY ENERGIZED GRANULAR-BED FILTERS

The granular-bed filters are made of small granules, which can be of sand, ceramics, plastic balls, glass beads, or metal globules placed in a container (a tube) through which contaminated gas flows. In non-electrified granular-bed filters, the diffusion deposition is dominant for small dust particles (<0.2 μm in diameter), while larger particles (>4 μm) are captured due to interception or inertia. Within these limits the collection efficiency decreases down to about 20% [16]. The collection efficiency of granular bed filters can be increased by applying external electric field. In the electrically energized bed filters the granules are polarized by this field, and are used as collection sites for smaller dust particles. The particles can be precharged prior to entering the bed that further increases the collection efficiency.

Four types of electrostatically augmented granular-bed filters can be distinguished: fixed bed, fluidized bed, moving bed, and dry particle scrubbers. The fluidized bed differs from fixed bed in that it is less dense packed, and the bed can be 'bubbled' by flowing gas. The moving bed is characteristic in that the granules are permanently transported through the duct through which the dusty gas flows. In dry particle scrubbers the granules falling down through the chamber and collect the dust particles. Two principal configurations of electrostatic granular bed filters are possible: with cross-flow and co-flow of the gas to the electric field (Fig. 2) [17]. The advantage of using electrostatically augmented granular beds is that the electrostatic forces cause attraction of the particles to the collectors.

The electrostatically augmented bed filters are more efficient in cleaning the gas by reduced residence time because the collection surface area per unit volume of the bed is larger than in conventional bed filters. The cleaning of the bed from collected particles is also easier. In comparison to conventional electrostatic precipitator the distance which a particle has to trace to the collector is much shorter. This make it possible to reduce the gas residence time needed for its cleaning that allows reduction of the volume of the device. The disadvantage of this type of filter is relatively high pressure drop.

4. ELECTRET FILTERS

Electret is a dielectric material, which produces permanent electric field without externally applied voltage. Electrets are produced by either polarization in an electric field

or by charge implantation to a dielectric material. Electret filters can be charged by triboelectric charging, corona charging or by electrospinning process. Ions produced during the process of charging are implanted and frozen in the host material. The charge embodied to the fiber can be up to 50 $\mu C/m^2$. Electret filters produced from polypropylene, polycarbonate, or polyurethane generate strong electrostatic field close to the dielectric surface, and are able to remove very fine particles. Such filters can be less dense that results in lower pressure drop. Typical pressure drop is 1-200 Pa for the air face velocity of 0.05 m/s. Modern electret filters are not affected by higher temperatures and humidity, and their operation life is sufficiently long for industrial applications. Fibers produced by electrospinning can by of nanometer size, and exhibit extremely high filtration efficiency of 99.97%, due to a great charge density [18].

The shortcoming of traditional electret filter is that the electric field can be neutralized by gas ions deposited on the fiber surface reducing thus the collection efficiency. A pseudo-electret fiber was therefore developed by Inculet et al. [19-21]. The pseudo-electret filter consists of an assembly of two closely located and mutually isolated thin wires to which a dc potential of up to 500 V is applied. High non-uniform electric field generated near the dielectric surface attracts and captures fine particles due to the dielectrophoretic force. The polarity of dc voltage applied to the wires is periodically reversed every few minutes, and the electric field reduced due to the effect of depolarisation can be restored in the pseudo-electret filter.

5. ELECTRICALLY ENERGIZED CYCLONES (ELECTROCYCLONES)

Cyclones utilize centrifugal acceleration of dust particles to precipitate them on the chamber walls. The acceleration can range from 5g for large installations to 2500g for small cyclones. Conventional cyclones are suited to remove large particles, usually larger than a few micrometers. Finer particles can only be removed if additional forces are imposed to them.

The collection efficiency of a cyclone can be augmented by electrical means by placing an electrode in its axis. High voltage applied to the electrode causes ion generation due to corona discharge, similar to a conventional electrostatic precipitator. The particles are charged by these ions and transported to the walls due to electrostatic forces in conjunction with the centrifugal force. Luckner et al. [22] noticed that the particles can be also deposited on the central electrode due to electric attraction. Primary particles of the size of 10 - 30 nm can form large aggregates of a few micrometers in diameter, and dendrites on the walls [23]. The diameter of electrocyclones is usually limited to 1.8 m and the dust loading to about 4.5 g/m^3 because of corona quenching for larger dimensions and loading [11].

Electrically energized cyclones are, however, of low collection efficiency in removal of fine particles, smaller than 1 μm, because the drag force, which bears the dust particles, is usually larger than the electrostatic force. Decreasing gas velocity within the cyclone improves electrostatic effects but also decreases inertial forces preventing thus centrifugal precipitation of larger particles. The electrocyclones are also ineffective for particles of high resistivity. For these reasons the electrocyclones are therefore of low practical value.

6. MULTISTAGE ELECTROSTATIC PRECIPITATORS.

Multistage electrostatic precipitator is a gas-cleaning device in which the charging and precipitation processes are separated. This type of devices was designed to avoid back-corona discharge, when dust of high resistivity has to be removed from an exhaust gas.

Two-stage electrostatic precipitator was considered first by Masuda and Hosokawa [24] to control the emission of high resistivity dust. The collection section was made of 4 electrodes spaced at 150 mm. Different types of the precharger were developed and tested in multistage electrostatic precipitators since that times: the Masuda boxer charger [25, 26]; a nozzle charger equipped with corona electrodes, through which the particles flowed with high velocity [27], corona-triode charger [27], a quadrupole precharger with four passive rods placed at a square corners and a discharge electrode at the centre of this arrangement [28, 29], and the alternating electric field charger [30-32].

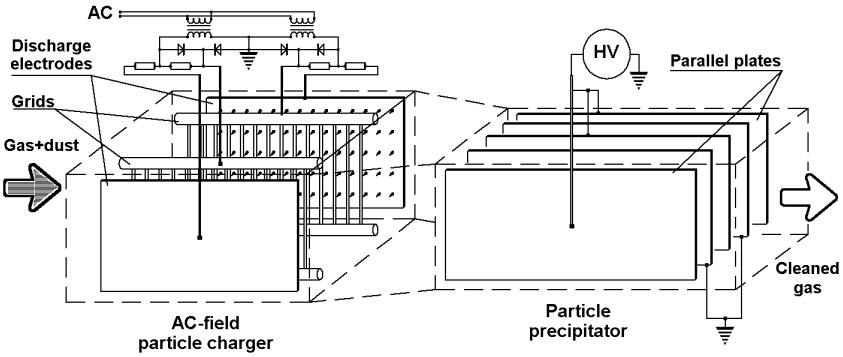

Fig. 3. Two-stage electrostatic precipitator with alternating electric field charger.

An example of a two-stage electrostatic precipitator is shown in Fig. 3 [32]. The charging stage is accomplished using the alternating electric field charger, a device that allows charging the particles to higher levels than conventional DC-corona chargers. The precipitation stage was created by a set of five parallel plates, two of which were maintained at high potential and the remainder grounded. The collection efficiency of multistage electrostatic precipitators was not higher than 90% in the submicrometer range. The disadvantage of multistage electrostatic precipitators is higher re-entrainment of low-cohesive particles from the collection electrodes and higher energy consumption.

7. CONCLUSIONS

The collection efficiency of conventional gas cleaning devices can be increased by employing electrical forces to particle removal. Electrically energized fibrous filters have enhanced collection efficiency, particularly in submicrometer size range, and their penetration is sometimes lower than 1%. The pressure drop can also be reduced in this type of filter. Electret filters can be even better, but their permanent electric field can be neutralized by gaseous ions, reducing thus the collection efficiency. A pseudo-electret fiber with periodically reversed polarity of the electrodes was therefore proposed. Such filters perform high collection efficiency over a long time period with negligible energy

consumption. Similarly, the collection efficiency of granular bed filters was also enhanced due to polarization of the granules after applying an external electric field to them. Electrical augmentation of the collection efficiency of conventional cyclones however failed at present. Multistage electrostatic precipitators allow avoiding the back-corona discharge, but higher re-entrainment of the particles can be observed for low cohesive dust. Moisturizing of the dust layer may be one of possible remedies to this drawback.

REFERENCES

[1] Havlicek V., The improvement of efficiency of fibrous dielectric filters by application of an external electric field. Int. J. Air Water Pollut. 4, No.314, (1961) 225-236.

[2] Iinoya K., Makino K., Application of electric field effects to dust collection filters. J. Aerosol Sci. 5, (1974) 357-372.

[3] Frederick E.R., Fibres, electrostatics, and filtration: A review of new technology. J. Air Poll. Contr. Assoc. 30, No.4, (1980) 426-431.

[4] Plaks N., Fabric filtration with integral particle charging and collection in combined electric and flow field. Part I: Background, experimental work, analysis of data, and approach to the development of a mathematical engineering design model. J. Electrostatics 20, (1988) 247-266.

[5] Plaks N., Fabric filtration with integral particle charging and collection in combined electric and flow field. Part II: Development and verification of the mathematical engineering design model. J. Electrostatics 20, (1988) 267-290.

[6] Wang Ch.S., Electrostatic forces in fibrous filters - a review. Powder Technol. 118, No.1-2, (2001) 166-170.

[7] Luckner H.J., Gradoń L., Podgórski A., Wertejuk Z., Aerosol particle filtration in the fibrous filters at the presence of external electric field. I. Experimental investigations. Inz. Chem. Proc. 19, No. 4, (1998) 891-903.

[8] Podgórski A., Luckner H.J., Gradoń L., Wertejuk Z., Aerosol particle filtration in the fibrous filters at the presence of external electric field. I. Theoretical model. Inz. Chem. Proc. 19, No. 4, (1998) 865-889.

[9] Lamb G.E., Constanza P.A., A low energy electrified filter system. Filtr. Separ. 17, (1980) 319-322.

[10] Lamb G.E.R., Constanza P.A., O'Meara D.J., Electrical stimulation of fabric filtration. Part II. Mechanism of particle capture and trials with a laboratory baghouse. Text. Res. J. 10, No.10, (1978) 566-573.

[11] Henry R.F., Podolski W.F., Saxena S.C., A review of electrostatically augmented gas cleaning devices for particulate removal. IEEE Trans. Ind. Appl. 21, No.4, (1985) 939-949.

[12] Lee J.-K., Kim S.-Ch., Shin J.-H., Lee J.-E., Ku J.-H., Shin H.-S., Performance evaluation of electrostatically augmented air filters coupled with a corona precharger. Aerosol Sci. Technol. 35, No.4, (2001) 785-791.

[13] Bhutra S., Payatakes A.C., Experimental investigation of dendritic deposition of aerosol particles. J. Aerosol Sci. 10, (1979) 445-446.

[14] Oak M.J., Saville D.A., The buildup dendrite structures on fibers in the presence of strong electrostatic fields. J. Coll. Interface Sci. 76, No.1, (1980) 259-262.

[15] Ciach T., Biodegradable filters for aerosol separation. J. Aerosol Sci. 30, Suppl.1, (1999) 747-748.

[16] Gutfinger Ch., Tardos G.I., Theoretical and experimental investigation on granular bed dust filters. Atmosph. Envir. 13, No.6, (1979) 853-867.
[17] Chang J.S., Mielke S., Ogata S., Scott R.C., Electromechanics and fluidization characteristics of co-flow type electrofluidized beds. J. Electrostatics 25, No.2, (1990) 135-144.
[18] Tsai P.P., Schreuder-Gibson H., Gibson P., Different electrostatic methods for making electret filters. J. Electrostatics 54, No.3-4, (2002) 333-341.
[19] Inculet I.I., Lackner J.R., Micron-sized particle filtration with dual wire artificial electret fibres. IEEE Trans. Ind. Appl. 31, No.5, (1995) 942-946.
[20] Inculet I.I., Castle G.S.P., Slanina M., Duca M., Pseudo-electret filter for micron sized particles in 300^{o}C exhaust gases. IEEE Ind. Appl. Soc. Annual Meeting, Rome, 8-12 Oct. 2000, (2000) 802-806.
[21] Inculet I.I., Castle G.S.P., Slanina M., Duca M., Pseudoelectret filter for micrometer-sized particles in exhaust gases at 210^{o}C. IEEE Trans. Ind. Appl. 38, No.1, (2002) 64-68.
[22] Luckner H.J., Wertejuk Z., Gradoń L., Podgórski A., Rolecka A., Odpylanie powietrza w cyklonach wspomaganych zewnętrznym polem elektrycznym. (Air cleaning by cyclons with external electric field assistance.) Inz. Aparat. Chem. 37, No.3, (1998) 9-14.
[23] Peukert W., Wadenpohl C., Industrial separation of fine particles with difficult dust properties. Powder Technol. 118, No.1-2, (2001) 136-148.
[24] Masuda S., Hosokawa Sh., Performance of two-stage type electrostatic precipitators. IEEE Ind. Appl. Soc. Cof. Rec., (1982) 1094-1101.
[25] Masuda S., State of art of precharging. 2nd Int. Conf. Electrostatic Precipitators, Kyoto, Nov.1984, (1984) 177-185.
[26] Masuda S., Washizu M., Mizuno A., Akutsu K., Boxer-Charger. A Novel Charging Device for High Resistivity Powders. Conf. Electrostatic Precipitation, Leura, Australia, 21-24 Aug. 1978.
[27] McLean K.J., Electrostatic precipitators. IEE Rev. 135, Pt.A, No.6, (1988) 347-61.
[28] Jayaram S., Castle G.S.P., Chang J.S., Berezin A.A., Looy P.C., Mangal R., Mozes M.S., Semipilot plant pulse energized cold-precharger electrostatic precipitator tests for collection of moderately high resistivity flyash particles. IEEE Trans Ind. Appl. 32, No.4, (1996) 851-857.
[29] Chang J.S., Looy P.C., Webster C., Berezin A.A., Zukeran A., Ito T., The collection of fine particles by an electrostatic precipitator with quadrupole prechargers. 7th Int. Conf. Electrostatic Precipitation. 20-25 Sept 1998, Kyongju, Korea, (1998) 620-627.
[30] Jaworek A., Krupa A., Airborne Particle Charging by Unipolar Ions in AC Electric Field. J. Electrostatics 23, (1989) 361-370.
[31] Lackowski M., Unipolar charging of aerosol particles in alternating electric field. J. Electrostatics 51-52, (2001) 225-231.
[32] Jaworek A., Krupa A., Adamiak K., Dust particles removal in novel type two-stage electrostatic precipitator. Electrostatics 2003, Inst. Phys. Conf. Series (in print).

4th International Conference **ELMECO**
Nałęczów, Poland
September 2003

THE REAL EMISSION OF FUMES FROM CARS

Stanisław WALUSIAK, Marcin BUCZAJ, Wiktor PIETRZYK

Lublin University of Technology, Department of General Electrotechnology
ul. Nadbystrzycka 38a, 20-618 Lublin, Poland
e-mail: swal@elektron.pol.lublin.pl

Abstract

The 20th century technical progress and the need of transport brought to the revolution in the range of motorization. In spite of undoubted benefits, the technical progress caused same negative changes in our natural environment. In order to avoid further degradation in our natural environment people have introduced recently new standards for range emissions of fumes from cars.

The realized research is aimed at the real emission of fumes from cars and the comparison of received results to obligatory standards. The vehicles produced by various manufactures in different years and different mileage were examined. The intention is to represent all vehicles. The research consisted on the five-element analysator of fumes, TecnoTest model 488. The results of research on CO content in fumes for the examined vehicles are represented in Fig. 1.

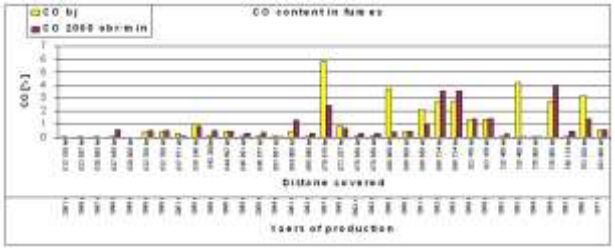

Fig. 1. CO content in fumes for the examined cars

It is visible in the results of research, that 40% of all cars do not comply with standard requirements, relating to the emission of fumes from cars. This is counted to the recent restriction of standards for the emission of fumes from cars, where CO limit in fumes decreased from 4,5% to 0,5% for new cars. Under the rules in European Union, the quantity of vehicles where CO emissions exceed actual standard there are 14 cars in 60 examined ones. This makes 23,3% of all tested vehicles.

Keywords: fuel injection systems, cars, dusts, engine.

1. INTRODUCTION

Technological revolution all over the word allows constructing still more and more perfect and reliable systems. The progress concerns also motorization, which is aimed to improve users' standards simultaneously decreasing harmful effects on natural environment. The use of non-regenerating energy sources (petroleum-derived compounds), the necessity of recycling of used parts and inefficient cars, and which is the most important exhaust gases emission are the main disadvantages of motorization.

The emission of fumes results from chemical reactions occurring in fuel engines during combustion processes in the air. In the result of ideal combustion of fuel that is, usually, hydrocarbon (HC), in oxygen in the air, carbon dioxide (CO_2) and water (H_2O) are produced. In real fuel engines, however, incomplete combustion occurs and thus toxic and undesirable chemical compounds are produced. These include carbon oxide (CO) and fuel residues such as: hydrocarbons (HC) and nitric oxide (NO_X). The chemical content is also influenced by proportions of fuel–air mixture.

To prevent over emission of exhaust gases maximum concentration of these compounds in the fumes is specified in each country. Both the car producers and users are obliged to adhere to these standards. According to the law, the car in which the standards are excessed can not be allowed into traffic. The analysis of the exhaust gases is usually performed during periodical technical examination of the car.

The purpose for this research is to find how tested cars meet Polish standards in relation to the emission of fumes.

2. THE RANGE OF RESEARCH

According to the regulations valid currently in Poland, allowable concentrations of particular chemical compounds in fumes from automobiles equipped with an ignition engine, depends on the date of its first registration. Currently, cars are divided into three groups. The first group consists of cars registered by 1st Oct.'86. The second group contains cars that were registered between 1st Oct.'86 and 1st Jul.'95. The third group includes cars registered since 1st Jul.'95.

The standards for the first and the second group of cars includes only CO concentration. For the first group the maximum concentration of CO is 4.5% and in the second group 3.5%.

Requirements for the cars from the third group are totally different and much more restrictive. In this case the limiting concentration of CO are 0.5% for idle run and 0.3% for rotational speed from 2000 to 3000 prm, of hydrocarbons HC – 100 ppm. Moreover, for the cars with λ probe the values of excess air coefficient at increased rotational speed should be ranged from 0.97 to 1.03.

As we can see the evaluation of nitrogen oxides NO_X is not required at present. However, as these compounds are the main component of exhaust gases, the introducing proper standards is now postulated.

To obtain reliable results, tests were carried out in an authorised service station on 60 cars.

They were different makes, mileage and year of production. Particular quantities in each group were the following:

- 2 cars registered by 1st Oct. '86.
- 18 cars registered between 1st Oct.'86 and 1st Jul.'95.
- 40 cars registered since 1st Jul.'95.

Toxicity test were carried always when engines were heated over 80°C at properly active injection systems. The measurements were taken with a five-component exhaust-gas analyzer TecnoTest model 488.

The range of this research consisted mainly on two aspects:

- comparison between real emission to the limits indicated in standards;
- the influence of mileage on the content of harmful compounds in fumes.

The first aspect of this analysis enables us to identify the proportion of cars at our motorways fulfilling the established standards concerning the content of toxic compounds in the exhaust gases.

The second aspect of our research will reveal the influence of the car's mileage, so also the degree of car wear, on exhaust gases emission.

3. TEST RESULTS

To make the presentation of the results more clear, the number of presented results has been limited to 30. Table 1 presents the specification of cars subject to subsequent tests.

Table 1. The specification of cars chosen for the results presentation

No	Type	Year of production	Mileage [km]	No.	Make of a car	Year of production	Mileage [km]
1.	Renault Megane	2001	012 100	16.	Fiat 125p	1987	070 619
2.	Opel Astra	1999	023 887	17.	Ford Fiesta	1995	073 287
3.	Polonez Atu	1997	026 800	18.	Opel Vectra	1992	078 650
4.	Fiat Uno	1999	027 655	19.	Fiat Uno	1996	098 600
5.	Skoda Felicia	1999	029 800	20.	Fiat Uno (gaz)	1996	098 600
6.	Skoda Felicia	1999	032 700	21.	Fiat Uno	1991	098 650
7.	Daewoo Matiz	2001	037 671	22.	Daewoo Nexia	1992	098 734
8.	Fiat Brava	1998	038 248	23.	Ford Escort	1989	103 476
9.	Fiat Seicento	1999	042 300	24.	Opel Astra (gaz)	1993	128 458
10.	Daewoo Nexia	1996	044 697	25.	Opel Astra	1993	128 460
11.	Fiat Siena	1996	045 891	26.	Polonez Caro	1994	136 000
12.	Daewoo Matiz	2000	046 877	27.	Polonez Caro (gaz)	1994	136 000
13.	Polonez Caro	1994	053 667	28.	Opel Astra	1993	140 134
14.	Daewoo Matiz	2001	054 000	29.	BMW	1990	183 200
15.	VW Golf	1992	068 090	30.	Fiat 125p	1977	293 000

Following measurements have been performed in all cars:

- CO concentration in the exhaust gases at idle running of the engine;
- CO concentration in the exhaust gases at the rotational speed of the engine of 2000 prm;
- CO_2 concentration in the exhaust gases at idle running of the engine;
- CO_2 concentration in the exhaust gases at the rotational speed of the engine of 2000 prm;
- HC concentration in the exhaust gases at idle running of the engine;
- HC concentration in the exhaust gases at the rotational speed of the engine of 2000 prm;
- excess air coefficient λ at idle running;
- excess air coefficient λ at the rotational speed of the engine of 2000 prm.

Test results of particular exhaust gas concentration and excess air coefficient λ are presented in Figs. 1÷4. The graphs indicate: car type, year of production and mileage at the time of tests.

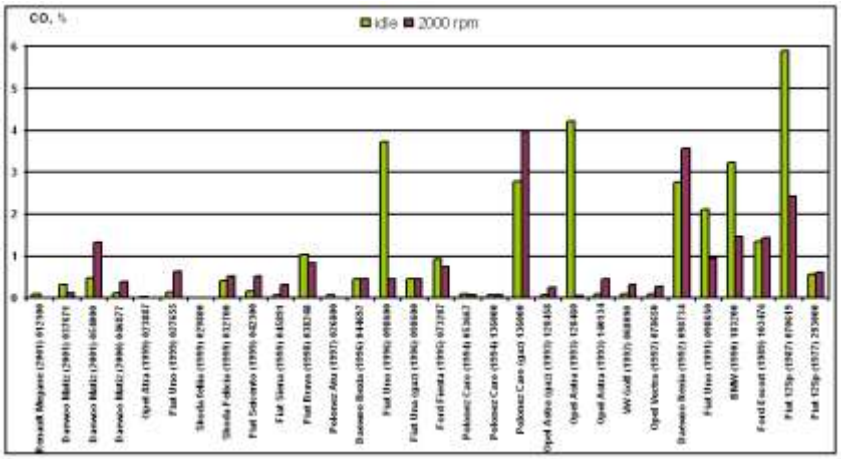

Fig. 1. Carbon oxide concentration CO in exhaust gas from cars

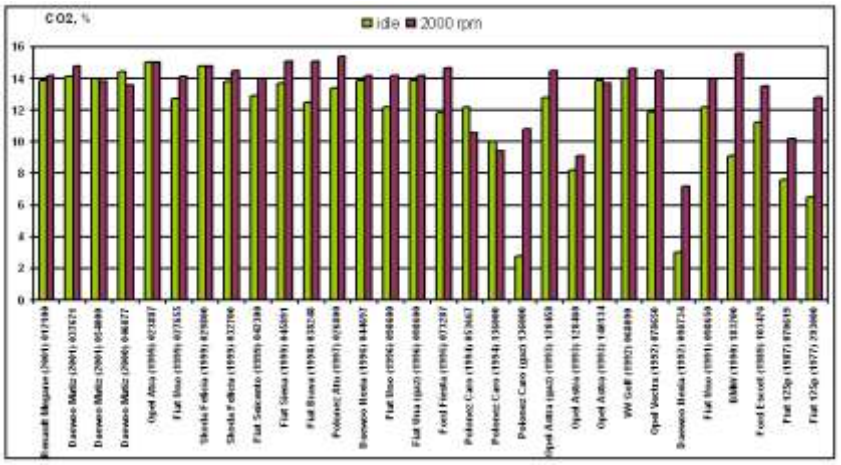

Fig. 2. Carbon dioxide concentration CO_2 in exhaust gas from cars

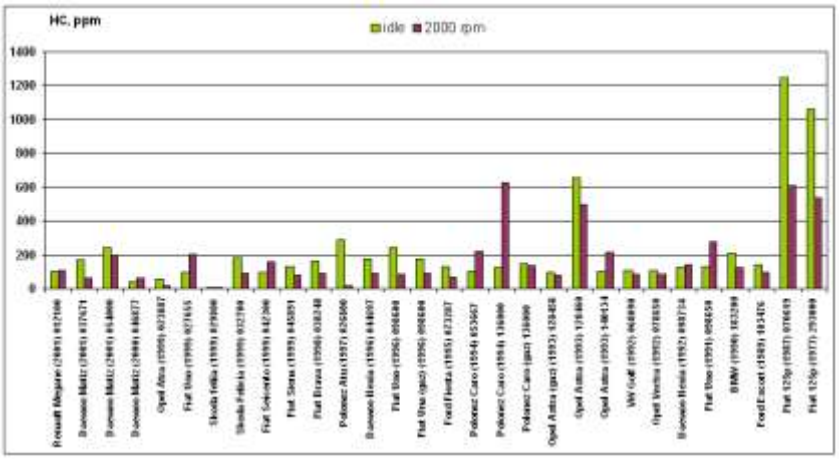

Fig. 3. Hydrocarbon contents HC in exhaust gas from cars

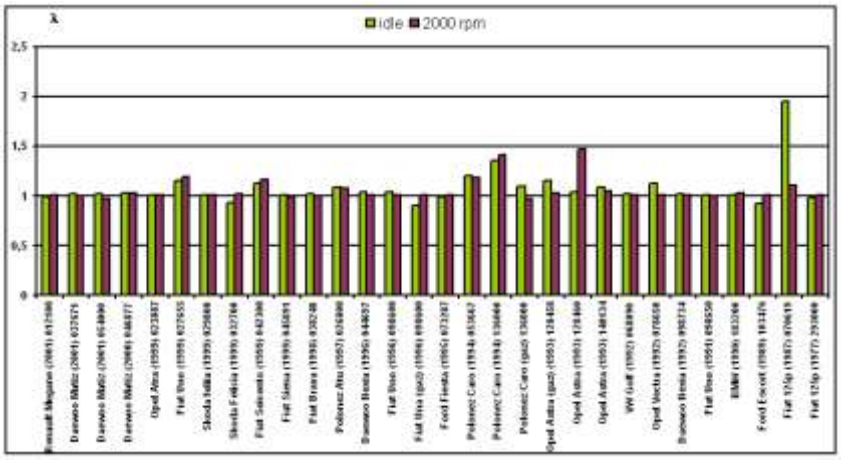

Fig. 4. Excess air coefficient λ in exhaust gas from cars

Conclusions from results are presented in Fig. 5, i.e.: total number of cars that do not meet pollution criteria is 24 which is 40% including: 0% of the ones produced by 1st Oct.'86, 6.7% of those from between 1st Oct.'86 and 1st Jul.'95 which makes 4 items and 20 items which is 33.3% of the ones produced since 1st Jul.'95.

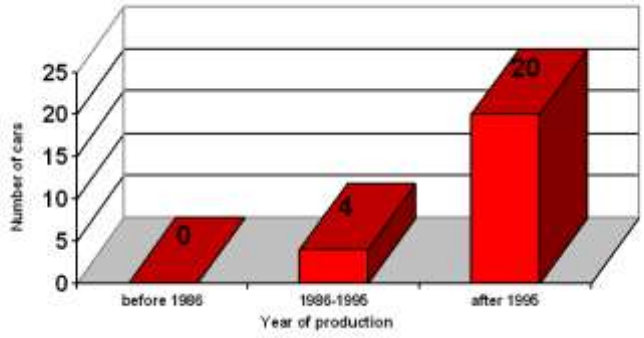

Fig. 5. Number of cars exceeding allowable limits
of emissions of harmful exhaust gas components

Under the rules in European Union, the quantity of vehicles where CO emissions exceed actual standard there are 14 cars in 60 examined ones. This makes 23,3% of all tested vehicles.

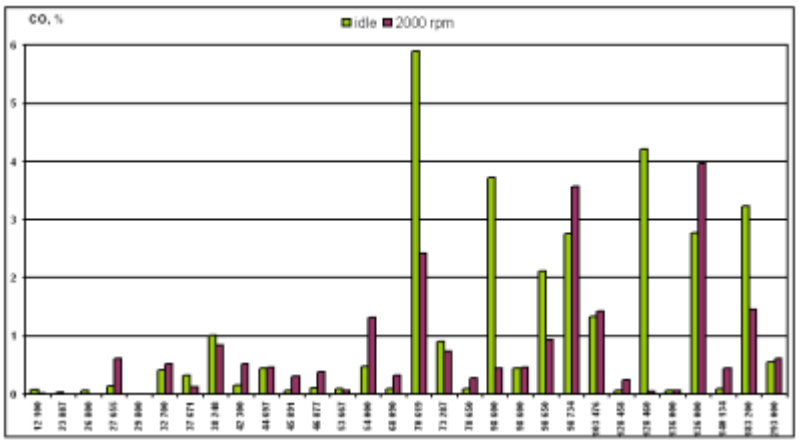

Fig. 6. Carbon oxide concentration CO in exhaust gases from tested cars vs milleage

Fig. 6 presents the results of the evaluation of CO concentration in exhaust gas. The results indicate that the car's mileage, which reflects the engine wear, influences the CO concentration in exhaust gas. In the group of cars with the mileage above 70000 km, more than 50% of the cars had the emission of CO above 1%. A closer look at these cars shows that they had been produced before 1995. So we can say that modern construction solutions, which must fulfill sharpened standards, also after a long exploitation do not lose quality parameters. That may be the result of application of electronical systems operating the work of the engine and standard providing the cars with catalysts.

4. CONCLUSION

1. On the basis of the analysis of electronic fuel injection systems, one can find that in the most modern systems the content of harmful compounds has been minimized.
2. Additional use of a catalyst reduces toxicity of fumes, too.
3. It is visible on the basis of service tests that the content of CO and HC compound in exhaust gases varies along with the level of maladjustment and wear.
4. Low content of toxic compounds in fumes from recently produced cars results from the application of a closed loop control system employing lambda probe co-operating with a three-way catalyst.
5. Restrictions on exhaust emissions have forced car manufacturers to use the most modern technology design. Definitely, CO emissions from recently produced cars have decreased, however, the number of them still exceeds maximal concentrations stated in restricted standards.

REFERENCES

[1] Merkisz J.: Ekologiczne aspekty stosowania silników spalinowych. WPP, Poznań, 1994.
[2] Kasedorf J.: Zasilanie wtryskowe benzyną. WKiŁ, Warszawa, 2000.
[3] Trzeciak K.: Diagnostyka samochodów osobowych. Wydawnictwo Komunikacji i Łączności, Warszawa 2000.

PLASMA PROCESSING

4th International Conference **ELMECO**
Nałęczów, Poland
September 2003

Progress in the Diagnostics of Filamentary Gas Discharges Applied to Environmental Protection

Hans-Erich WAGNER[1], Ronny BRANDENBURG[1], Kirill KOZLOV[2]

[1] *Institute of Physics, University of Greifswald, 17489 Greifswald, Germany, wagner@physik.uni-greifswald.de*

[2] *Department of Chemistry, Moscow State University, 119992 GSP Moscow, Russia*

Abstract

Filamentary gas discharges at atmospheric pressure, namely barrier discharges and coronas, produce highly non-equilibrium plasmas in a controllable way at moderate gas temperature. They provide the effective generation of atoms, radicals and excited species by energetic electrons. Consequently, they have found a large field of applications, among others in environment protection. The controlled application of these discharges requires a good understanding of their physical properties and the knowledge of the basic plasma parameters. Historical milestones on this way and the progress in the plasma diagnostics are listed of. Recently, the technique of spatially resolved cross-correlation spectroscopy (CCS) (with a resolution in the sub-ns and sub-mm range) has been used to contribute to a better understanding of these discharge types. The application of this method to dielectric-barrier discharges is discussed in more detail.

1. INTRODUCTION

Dielectric-barrier discharges (DBDs) and coronas (CDs) are plasmas far from the equilibrium. Besides the ozone synthesis, the scope of their applications covers incoherent ultraviolet (UV) or vacuum ultraviolet (VUV), excimer radiation in excimer lamps, the generation of highly intensive coherent radiation in CO_2 lasers, flat plasma displays of large dimensions, surface treatment (modification, cleaning, etching) and layer deposition as well as various applications in the field of environmental protection (pollution control, destruction of hazardous compounds) [1-6, 20].

Decisive advantage of the DBDs and CDs for the wide field of applications is the non-thermal plasma conditions at low gas temperatures and at elevated (typically atmospheric) pressure. They provide high-energy electrons which are able to generate reactive particles (atoms, radicals, excited species, ions) and – under selected conditions - of short wavelength radiation. This generation is controlled by the plasma parameters, mainly by the

reduced local electric field strength and by the electron density. Therefore their knowledge is of essential importance for the desired control of the plasma processes.

Experimental and theoretical studies of DBDs and CDs have a long history [1-16]. However, despite of the considerable progress in the understanding of the properties of these discharges, the knowledge of this subject nowadays appears to be insufficient to provide an adequate quantitative theoretical description for the discharge behaviour. Main reasons for this situation are the difficulties to investigate experimentally the dynamics of the filamentary plasmas, requiring an up to sub-ns temporally and, in the case of DBDs, a sub-mm spatially resolution.

2. BASIC PROPERTIES OF THE BARRIER DISCHARGE AND CORONA

DBDs and CDs belong to the group of cold non-equilibrium plasmas, characterized by a kinetic electron temperature of about 1 ... 10 eV and a near room gas temperature. Typical electrode arrangements of planar and cylindrical DBDs and of CDs are shown in Fig. 1, together with important operation parameters. Usually the DBD operates in the so-called filamentary mode. If the local electric field strength in the gas gap arrives the ignition level, the breakdown starts at many points followed by the development microdischarges. The microdischarges are of some nanosecond duration. There are many excellent monographs and papers on the physics of these discharges, e.g. [1-6, 13-18, 21].

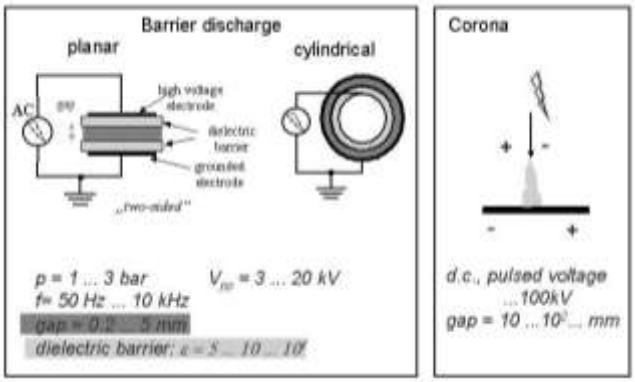

Fig. 1. Typical electrode arrangements of barrier and corona discharges.

3. MILESTONES OF THE DIAGNOSTICS

The diagnostics of DBDs and CDs has a long tradition. Important milestones are summarized in **table 1**, together with relevant references. These milestones are correlated to the available experimental technique. Therefore, the progress in the discharge diagnostics for both kinds of discharges proceeded relatively parallel. The diagnostics started with electric and oscillographic investigations of the discharge properties [22-24]. Nowadays, modern experimental techniques allow spatially, temporally and spectrally resolved

measurements. Under selected conditions the densities of relevant reactive species as well as the local basic plasma parameters have been determined, respectively [17, 32-39].

Table 1. Milestones of the discharge diagnostics.

Technique	plasma	contribution	references
Electric Measurements	DBD	discovery of BD filaments	Buss, 1932 [22]
		detailed current pulse and charge measurements	Hirth, Kogelschatz et al. 1983 [23]
	CD	detection of Trichel pulses	Trichel, 1938 [24]
Streak Photos	DBD	streamer mechanism	Heuser, Pietsch, 1985 [25]
	CD	streamer characterization	Marode, 1975-81 [19]
Emission / Absorption Spectroscopy	DBD	emission of He, N_2/O_2;	Vinogradov, Wiesemann, 1997 [26]
		rotational temperature,	
		nitrogen metastables;	Bibinov, Fateev, et al., 2001 [27]
		radius of microdischarge	
	CD	spectra	Teich, 1993 [29]
Cross-correlation Spectroscopy	DBD	spatio-temporally and spectrally resolved diagnostics of filaments;	Kozlov et.al., 1993-95 [30]
		determination of the local electric field strength and relative electron density;	Kozlov, Wagner et al., 2001 [17]
		2D diagnostics of microdischarges in N_2/O_2	Brandenburg, Morozov et al., 2003 [32]
	CD	corona wave propagation	Ikuta, Kondo, 1980 [28]
			Teich, 1993 [29]
Stark Broadening /	DBD	determination of relative electron density in Xe;	Müller et.al., 1997 [33]
Splitting		determination of electric field strength in H_2 ;	Wujec et.al., 2003 [34]
		concept of 2D electric field measurement in Xe	Jiang, Bowden et al., 2003 [35]
LIF, TALIF, ICCD	DBD	Spatio-temporally resolved detection of N atoms	Schulz-von der Gathen, Döbele et.al., 2001 [36]
	CD	streamer propagation,	Veldhuizen, Rutgers et al., 2000 [37]
		detection of NO_x	Kanazawa, Okhubo, Mizeraczyk et al., 2002 [38, 39]

4. DETERMINATION OF BASIC PLASMA PARAMETERS OF BARRIER DISCHARGES BY CROSS-CORRELATION SPECTROSCOPY

The determination of the spectrally and spatio-temporal resolved luminosity from statistically distributed filamentary discharges succeeded by the technique of CCS. In the eighties this method has been applied for the first time to the investigation of the “point-to plane” coronas of both polarities [28], in the nineties to CDs [29] and DBDs [17, 18, 30]. The CCS has been demonstrated to be a powerful tool to analyse the spatio-temporal structure of these plasmas in air (and different N_2/O_2 mixtures) at atmospheric pressure. In case of DBDs, the measurements have been sufficient for the quantitative estimation of the electric field and relative electron density in single microdischarges [17]. The knowledge of

these basic plasma parameters allowed a more deep understanding of the process of the electrical breakdown, including the discharge physics and chemistry. Recently, the 2D diagnostics of microdischarges by CCS has been started [32]. The main idea of the technique of CCS is to replace a direct measurement of the single pulse luminosity of a repetitive light pulse emitter by a statistically averaged determination of the correlation function between two optical signals, both originating from the same source. The first one of these signals (so-called "synchronizing signal") is used to define a relative time scale, the second one ("main signal") has to be detected with a probability at least one order of magnitude lower, than that one of the synchronizing signal. The measured quantity is actually a time delay between these two signals, and the recorded quantity is a probability density function for the light pulse intensity evolution. A general scheme of the experimental set-up and measurement procedure is presented in Fig. 2.

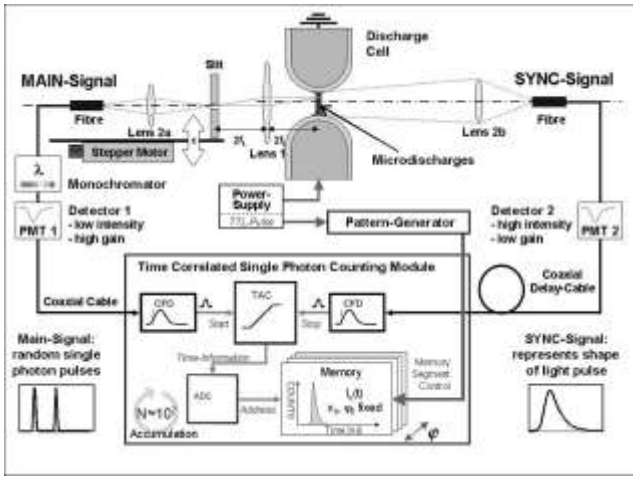

Fig. 2. A general diagram of the apparatus and measurement procedure [17, 18]. Abbreviations: SYNC – Synchronizing; MC – Monochromator; PMT – Photo-multiplier; TTL – Transistor-Transistor Logic; CFD – Constant Fraction Discriminator; TAC – Time-to-Amplitude Converter; ADC – Analogue-to-Digital Converter; φ is the phase of the feeding sinusoidal voltage.

A single microdischarge DBD, periodically generated at a defined position has been used as an emitter of repetitive light pulses. The localization could be realized by a spherical electrode arrangement (by means of test-tubes). One more advantage of such a geometry of the discharge cell is the possibility to observe not only the volume part of the DBD, but the surface discharges as well, provided that the range of axial scanning exceeds the gap width. Spatial resolution and scanning over the microdischarge axis was provided by the optical system shown in the left upper part of the figure. Monochromatic light of the main signal was detected by highly sensitive photo-multipliers, operating in single photon counting mode.

The main characteristics of our CCS measurements are summarized in the **table 2**. More details on this technique are given in [17, 18].

Table 2. Resolution parameters of the CCS measurements [17].

Quantity	Resolution
Time (50 ns scale)	< 0.15 ns
Space (axial direction)	0.1 mm
Wavelength	0.3 nm
Phase of feeding voltage	$\varphi = 2\Pi / 16$

In Fig. 3, an example of the temporally and spatially resolved development of microdischarges in synthetic air for the N_2 $(C^3\Pi_u)_{v'=0} \rightarrow N_2$ $(B^3\Pi_g)_{v''=0}$ transition of the second positive system and the N_2^+ $(B^2\Sigma_u^+)_{v'=0} \rightarrow N_2$ $(X^2\Sigma_u^+)_{v''=0}$ transition of the first negative system of nitrogen is shown, also covering the pre-breakdown phase as well as the afterglow phase. These selected transitions correspond to extremely different excitation energies of the nitrogen molecule (ΔE = 11 eV) and N_2^+ ion (ΔE = 19 eV), respectively. These measurements are the basis for the derivation of the electric field strength in air at atmospheric pressure. The used kinetic model and details of the calculation are given in [17, 18]. The spatially and temporally resolved values of reduced electric field strength as well as the relative density of electrons for the conditions of Fig. 3 are summarized in Fig. 4.

The results of figs. 3 and 4 can be summarized as follows: The discharge breakdown starts by an ionisation wave, which propagates within 1,…2 nanoseconds from the surface of the anode to the cathode (= range of maximum local electric field strength), followed by a dark phase (= low electric field strength / low energy of electrons, respectively). After that a further intensive "glow" of the second positive system appears near the anode, indicating excitation processes by electrons of large density but low energy. The highest intensity of the first negative system has been observed at the cathode. It corresponds to the region of the highest electric field strength (and electron energy, respectively).

5. SUMMARY AND CONCLUSIONS

Barrier discharges and coronas produce highly non-equilibrium plasmas in a controllable way at moderate gas temperature. They provide the effective generation of atoms, radicals and excited species by energetic electrons. Consequently, they have found a large field of applications, among others in environment protection. The controlled application of these discharges requires a good understanding of their physical properties and the knowledge of the basic plasma parameters. Milestones on this way and the progress in the plasma diagnostics are listed of. Nowadays, the modern experimental technique allows spatially, temporally and spectrally resolved measurements. Under selected conditions the densities of relevant reactive species as well as the local basic plasma parameters have been determined, respectively. Nevertheless this progress, hard efforts must be done to realize an adequate diagnostics of the really complex situation in filamentary plasmas applied to the environment protection (pollution control, destruction of hazardous compounds, …).

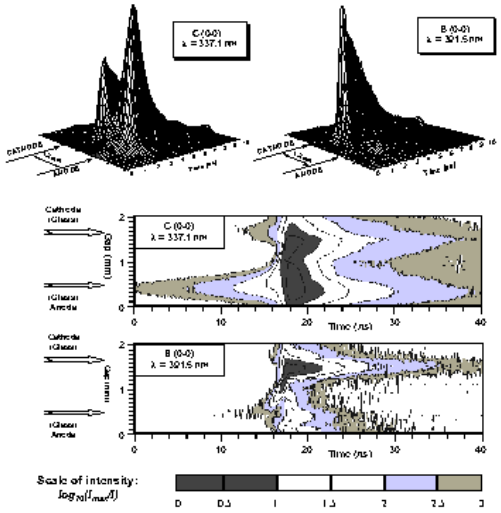

Fig. 3. Spatially and temporally resolved spectral intensities of the N_2 $(C^3\Pi_u)_{v'=0} \rightarrow N_2$ $(B^3\Pi_g)_{v''=0}$ transition of the second positive system and the $N_2^+(B^2\Sigma_u^+)_{v'=0} \rightarrow N_2$ $(X^2\Sigma_u^+)_{v''=0}$ transition of the first negative system of nitrogen (conditions: synthetic air, p=1bar, flow rate=700sccm , V_{pp}=13kV, f= .5kHz, d=1.2mm, glass dielectrics) [17].

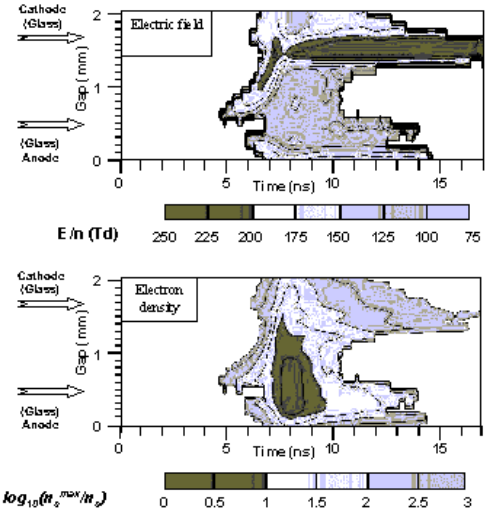

Fig. 4. Spatially and temporally resolved local reduced field strength and relative electron density of the single microdischarge in synthetic air [17] (conditions as in Fig. 3).

ACKNOWLEDGEMENTS

The DFG-Sonderforschungsbereich 198 'Kinetics of partially ionised gases' supported this work.

REFERENCES

[1] Eliasson B, Kogelschatz U. IEEE Transactions on Plasma Science 1991; 19(2): 309.
[2] Kogelschatz U, Eliasson B, Egli W. J. Physique IV (France) 1997; C4:47.
[3] Samoilovich V, Gibalov V, Kozlov K. Physical chemistry of the barrier discharge, Düsseldorf 1997: DVS-Verlag GmbH.
[4] Kogelschatz U. Dielectric-barrier Discharges: Their History, Discharge Physics, and Industrial Applications, Plasma Chemistry and Plasma Processing 2003; 23(1):1-45.
[5] Manheimer W, Sugiyama L E, Stix Th H (Eds.). Plasma Science and the Environment, AIP Press 1997.
[6] van Veldhuizen E M. Electrical Discharges for Environmental Purposes, Nova Scieme Publishers,. 2001.
[7] Suzuki M, Naito Y. Proc. Jap. Acad. 1952; 84 : 83.
[8] Eliasson B, Hirth M, Kogelschatz U. J. Phys.D: Appl. Phys. 1987; 20: 1421.
[9] Braun D, Küchler U, Pietsch G J. J. Phys.D: Appl. Phys.1991; 24: 564.
[10] Braun D, Gibalov V, Pietsch G. Plasma Sources Sci. Technol. 1992; 1: 166.
[11] Gibalov V I, Samoilovich V G, Filippov Yu V. Russ. J. Phys. Chem.1981; 55: 471.
[12] Yoshida K, Tagashira H. Memoirs Kitami Inst. Technol. 1986; 18: 11.
[13] Gibalov V I, Pietsch G J. J. Phys. D: Appl. Phys. 2000; 33: 2618.
[14] Pietsch G J. Contrib. Plasma Phys. 2001; 41(6): 620.
[15] Raether H. Electron Avalanches and Breakdown in Gases, Butterworths London 1964.
[16] Nasser E. Fundamentals of Gaseous Ionization and Plasma Electronics, Wiley-Inter-Science 1971.
[17] Kozlov K V, Wagner H-E, Brandenburg R, Michel P. J. Phys.D: Appl. Phys. 2001; 34: 3164.
[18] Kozlov K V, Dobryakov V V, Monyakin A P, Samoilovich V G, Shepeliuk O S, and Wagner H-E, Brandenburg R, Michel P. In: Selected Research Papers on Spectroscopy of Nonequilibrium Plasma at elevated Pressures, Vladimir N. Ochkin, Editor, Proceedings of SPIE Washington (USA) 2002; volume 4460: p.165.
[19] Marode E. In: NATO Series ASI 1981; Serie B volume 89: p.119.
[20] Roth R J. Industrial Plasma Engineering, Vol.1: Principles, Vol. 2: Applications to non- thermal plasma processing, IoP Publishing, printed in the UK 2000 / 2002.
[21] Wagner H-E, Brandenburg R, Kozlov KV, Sonnenfeld A, Michel P, Behnke JF. Vacuum 2003; 71: 417-436.
[22] Buss K. Arch. Elektrotech 1932; 26: 261-265 (in German).
[23] Hirth M, Kogelschatz U, Eliasson B. Int. Symp. on Plasma Chemistry, Montreal (Canada) 1983; 3: 663.
[24] Trichel G W. Phys. Rev. 1938; 54: 1078.
[25] Heuser C. Thesis RWTH Aachen (Germany) 1985 (in German).
[26] Vinogradov I P, Wiesemann K. Plasma Sourcs Sci. Technol. 1997; 6: 307.
[27] Bibinov N K, Fateev A A, Wiesemann K. J. Phys. D: Applied Phys. 2001; 34: 1819; Plasma Sourcs Sci. Technol. 2001; 10: 579.
[28] Kondo K, Ikuta N. J. Phys.D: Appl. Phys 1980; 13: L33-38.

[29] Teich T H. Emission spectroscopy of corona discharges, In: NATO ASI Series, Non-Thermal Plasma Techniques for Pollution Control, ed. by Penetrante B.M. and Schultheis S.E., Vol. G34, Part A, Springer-Verlag, Berlin, 1993, p.230-247.
[30] Kozlov K V, Shepeliuk O, Samoilovich V. Int. Conf. on Gas Discharges and their Applications, Tokyo (Japan)1995; 2:142.
[31] Kozlov KV. In: Proc. 7th Int. Symp. on High Pressure Low Temperature Plasma Chemistry, ed. by Wagner H.-E., Behnke J. F. and Babucke G., Greifswald, Germany, pp. 292-8.
[32] Brandenburg R, Kozlov K V, Wagner H-E, Michel P, Yurgelenas Yu V. In: Proc. XXVIth ICPIG (Germany, Greifswald) 2003: IV-39.
[33] Gerova E, Müller S. In: Proc. XXIIIth ICPIG (France, Touluse) 1997: IV-120.
[34] Wujec T, Janus H W, Jelenski W. J. Phys.D: Appl. Phys. 2003; 36: 868.
[35] Jiang T, Bowden M D, Visser B, Kroesen G M W. In: Proc. XXVIth ICPIG (Germany: Greifswald) 2003; Vol. 1, p. 197.
[36] Lukas C, Spaan M, Schulz-von der Gathen V, Thomson M, Wegst R, Döbele H F, Neiger M. Plasma Sources Sci. Technol. 2001; 10: 445.
[37] van Veldhuizen E M, Rutgers W R. J. Phys. D: Appl. Phys. 2002; 35: p. 2169.
[38] Kanazawa S, Ito T, Shuto Y, Ohkubo T, Nomoto Y, J. Mizeraczyk J., J. of Electrostatics 2002; 55: p. 343.
[39] Ohkubo T, Kanazawa S, Nomoto Y, Mizeraczyk J, Proceedings of SPIE, Vol. 4460(2002)318.

4th International Conference **ELMECO**
Nałęczów, Poland
September 2003

LOW TEMPERATURE PLASMA METALLURGY REDUCTION OF TUNGSTEN IN PLASMA REACTORS

Jan JANCA[1], Vlastimil BROZEK[2], Marek ELIAS[1], Zdeněk FRGALA[1], Vít KUDRLE[1]

[1] *Department of Physical Electronics, Faculty of Science, Masaryk University, Kotlářská 2, CZ-61137 Brno, Czech Republic, e-mail: Jan92@physics.muni.cz*
[2] *Institute of Chemical Technology, Technická 5, CZ-16628 Prague, Czech Republic, e-mail: vlastimil.brozek@vscht.cz*

Abstract

The new plasma chemical reduction techniques of tungsten precursors were investigated with the aim of producing tungsten powder with high sintering activity, permitting to increase the density of tungsten compact products above the hitherto technological limit. The application of non-isothermic hydrogen plasma allows the initiation of reduction processes at low temperature of neutral gas.

Keywords: plasma chemical reduction, inductive coupled RF plasma, tungsten metal powder, spectral monitoring, plasma parameters, porosity, tungsten sintering, tungsten carbide.

1. INTRODUCTION

The influence of tungsten reduction parameters on the nucleation and crystal growth has been described from different points of view [1-4]. The tungsten metal powder production by hydrogen reduction usually proceeds in several temperature steps in the furnace between 600 - 1100°C. The input reactants are WO_2 – WO_3, resp. WO_{3-x} oxides obtained by thermal breakdown of precursors based on tungstate salts. The reduction process does not represent the simple conversion of oxides to the metals according to often cited reaction

$$WO_3 + 3\ H_2 = W + 3\ H_2O \qquad (1)$$

but there occur the simultaneous reduction and chemical transport reaction, which influence in a decisive manner the morphology, the physical and chemical properties of the final product. Creation of volatile tungsten oxide-hydroxide $WO_2(OH)_2$ and/or $WO_3.H_2O$ in

the W-O-H system plays an important role. The complicated transport reaction connected with its condensation influences the morphology and grain size of final product - tungsten metal powder. In addition, the thermal cycle represents a refinement process, too. Impurities in reactants affect not only the thermodynamics but also the kinetic conditions of mass transfer.

The industrial and laboratory reduction process of tungsten metal powder production are carried out in two different types of devices, static (push furnace) or rotating tube furnaces. The modern furnaces with rotation tube reflect the new findings about diffusion controlled process with lowered aerodynamic resistance of powdered reactants and about generated water vapour motion through the layers of the reactant and product mixture.

In the macroscale of reduction furnace the reduction time or retention time of reactants in zones with changeable temperature is pursued. The motion of powdered mass throughput compared with the flow of gaseous reactants is given by the mentioned conditions. From the stoichiometric standpoint the input H_2/H_2O ratio is decisive for the reaction course, which results from initial moisture and changes of this ratio during proper reduction. The part of initially present or by reduction created water vapour is consumed for the $WO_2(OH)_2$ formation. Powdered reactant can in the course of reduction include all known forms of tungsten oxides. Their relations depend on previous processing of various forms of ammonium tungstates. Thus the density, porosity and grain size of reactant layer is influenced.

From the gaseous reactants only a small quantity passes through the moving powdered layer under non-isothermal conditions. In the layer, with the thickness of few centimetres, the laminar flow of gaseous reactant can change into a turbulent one. The flow change is caused also by the increase of the quantity of water vapour. The controlling diffusion process takes place not only by hydrogen diffusion through the surface, but also into the reactant pores. The water vapour diffuses out of the pores and its desorption plays an important role.

This complicated system was in our study complemented by another dominating factor, i.e. atomisation and ionisation of molecular hydrogen by means of capacitively/inductively coupled RF discharge. It is impossible to predict the success of this affect of such technical arrangement because the number of moles of atomic hydrogen increases and changes the diffusion conditions. At the same time the reactivity grows and influences the formation of volatile products. Another important matter is that through this modification the hydrogen from cracked ammonia in situ can be utilized.

The diffusion of necessary amount of atomic hydrogen into individual grain pores of solid phase becomes more complicated, however the surface reactions are simplified due to recombination effects [5].

The most important process of powder metallurgy of tungsten is it's sintering. The relative density of the product and its contraction after sintering depends above all on its sinterability. The technical definition of the limit of sinterability was suggested by Agte [3] for the conditions that press of the sample of 5 mm thickness made of metal powder by pressing by the surface pressure 300 MPa, should have the density of 75 % after the sintering of 1 hour in protective gas or in vacuum. A great effect on the sinterability is that of the size of the grain of tungsten powder, it morphology and the measuring surface. Of course, the high degree of purity of the powder and/or the content of sintering additives is important.

2. EXPERIMENTAL

PLASMA CHEMICAL REACTOR

For the reduction of dihydrogen-decaammonium-dodecatungstate tetrahydrate (ammonium para-tungstate, APT) we used two barrel shaped quartz reactors, in which the reduction was carried out under reduced pressure (0.1 - 1.2 kPa). First was used the capacitively coupled (CC) barrel reactor [6, 7]. The central part of the discharge tube made of quartz (inner diam. of 4.2 cm, length of 90 cm) was inserted into an electrically heated tubular oven. Vacuum tightness of the tube was accomplished by means of two stainless steel flanges. The inner quartz cylinder (outer diam. 3.9 cm, length 30 cm) may be rotated. Both edges of the inner cylinder were bent inside by 2 mm to prevent possible escape of pulverised APT during the rotation. We used hydrogen as the working gas with possible admixture of argon. The discharge was maintained by means of two cylindrical electrodes, placed in the exterior of discharge tube near the ends of the oven. The rf power (max. 500 W) was fed from generator (13.56 MHz) through an impedance matching network. Due to a capacitive character of the discharge, the plasma was strongly non-isothermal.

A complete description of a plasma discharge requires a choice of heating mechanisms and the geometric configurations that sustain these mechanisms. In the capacitively coupled RF plasma reactor the currents in the main body of the plasma lead to ohmic heating, while the voltage across the sheath leads to stochastic sheath heating. With the external coupling the power is transmitted to the plasma through the capacitance of the dielectric wall of a tubular reactor.

The second barrel shaped quartz reactor in which the reduction of APT was investigated was inductively coupled (IC) and consists of outer quartz tube (inner diam. 8.6 cm, length 50 cm) and inner quartz cylinder (outer diam. 8 cm, length 30 cm) - Fig. 1. Vacuum tightness of the reactor was accomplished by means of two brass flanges. Output flange besides being connected to a pumping system contained also a removable cover with feedthrough for turnable rod. Using this rod the inner quartz cylinder may be rotated. Feeds of the working gases as pressure gauges were placed in input brass flange. The working pressure and flow rate of gases were controlled by mass flow meters and by system of needle valves. The throttle valve reduced the pumping speed during the reduction process. High frequency power from generator (27 MHz, max. power 4 kW) was fed through the matching network to the coil with the inner water cooling. Light irradiated from the rf discharge was continuously recorded by monochromator Jobin-Yvon HR 320 with CCD. Recorded atomic and molecular spectra were used for the monitoring of the plasma reduction APT process [8].

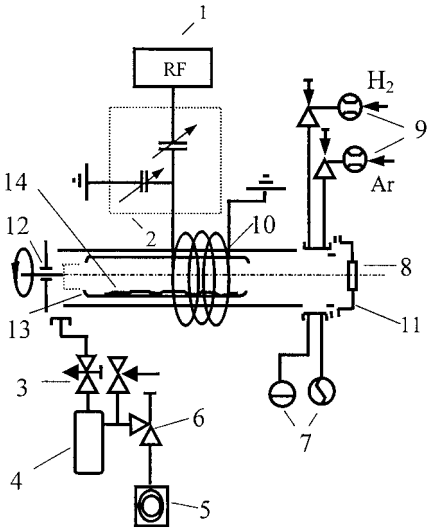

Fig. 1. RF barrel reactor with inductive coupling. 1- RF generator (27 MHz), 2 – matching network, 3 – throttle valve, 4 – cold trap, 5 - pumping system, 6 – valve, 7 – vacuum gauges (membrane, Pirani), 8 – quartz observing window, 9 – mass flow meters, 10 – outer quartz reactor tube with coil , 11 – inlet flange, 2 – outlet flange, 13 – inner quartz rotating cylindrical tube, 14 – pulverized APT sample.

TUNGSTEN SINTERING

The mixture of tungsten and nickel in the mass ratio 99:1 was pressed on the hydraulic press PITE 30. The value of the pressing pressure was 100 MPa and the time of load was 4-5 s. The sintering took place in a vacuum furnace PVG – 80 with a horizontally positioned chamber and a double mantle cooled with water. The heating of the furnace is graphite. Thermal insulation is made of graphite insulation Sigrafil. A two-step pumping vacuum system consists of the Roots and rotating oil vacuum pump. Hydrogen was employed as the process gas, argon as carrier and cooling gas.

REACTANTS

Experimental investigation of plasma chemical reduction was performed with ammonium para-tungstate from OSRAM Bruntal Ltd, produced by used cemented carbides recyclation. The hydrogen purity was 99,8 % with 0,2 % oxygen, the purity of argon was 99,996 %.

ANALYTICAL METHODS

Diffractograms of reactants and products were made on Diffractometer System XRD 3000 (Seifert, Germany) (CoKα) device. Powder diffraction data were compared with database PDF 2. The density, porosity and pore surface were determined on mercury porosimeter Autopore 9200 Micromeritics and helium densitometer Accupyc 1330 Micromeritics. The images of microstructure were made with electron scanning microscope CamScan 4DV, Cambridge UK. For the thermal analysis Derivatograph Q-1500 D, MOM Budapest was used.

3. RESULTS AND DISCUSSION

According to differential thermal analysis, $(NH_4)10[H_2W_{12}O_{42}].4H_2O$ dehydrates in the range 20 - 100°C to anhydrous salt. In the interval 180 - 225°C transformation

$$(NH_4)_{10}[H_2W_{12}O_{42}] \rightarrow (NH_4)_6[H_2W_{12}O_{40}].\ 2H_2O + 4\ NH_3 \qquad (2)$$

leads to dihydrogen-hexaammonium-dodecatungstate dihydrate (by another name ammonium meta-tungstate AMT). In relatively wide temperature interval 230°C to 325°C, ammonia and water vapour are released and ammonium meta-tungstate transforms into anhydrous diammonium dodecatungstate

$$(NH_4)_6[H_2W_{12}O_{40}].\ 2H_2O \rightarrow (NH_4)_2[W_{12}O_{37}] + 4\ NH_3 + 5\ H_2O \qquad (3)$$

The tungsten oxide is formed at temperatures over 400°C with further release of ammonia and water vapour (eq.4).

$$(NH_4)_2[W_{12}O_{37}] = 12\ WO_3 + 2\ NH_3 + H_2O. \qquad (4)$$

In Fig. 2 the APT thermal decomposition at two different rates of heating gradients (5 and 30 K/min) is presented. The case at 30 K/min is similar to experimental conditions in our IC plasma reactor. The temperature difference in the first and second step of thermal decomposition is shifted rather at 50° C.

Under certain conditions non stoichiometric tungsten bronze $(NH_4)_xWO_3$ can arise. In most cases however ammonia dissociates and hydrogen partially reduces the tungsten trioxide to lower oxides. Most known is the blue oxide (TBO)) $WO_{2,9}$ resp. $W_{20}O_{58}$ with a density 7,15 g cm^{-3}. Another oxide $WO_{2,72}$ ($W_{18}O_{49}$) which has a violet colour and a density 7,78 g cm^{-3} is formed.

The crystallographic features and extraordinary stoichiometry are caused through partial replacement of common octahedral edges that form by interlayer shift (so-called Crystal Shear Structures - CSS). The partial reduction of intermediate products by cracked ammonia in our apparatus was supported by capacitive/inductive RF discharge, eventually by flow of generated hydrogen plasma.

The experimental conditions are summarized in Table I. The external reactor temperature (capacitive coupling only) was maintained by adjusting the electric current passage through the oven heating. If 400 W input was transferred into capacitive RF-discharge, the initiation of which leads to the temperature increase of about 30°C.

Tab. I. Conditions of reduction experiments.

Capacitive (CC) or inductive (IC) coupling	temperature (^oC)	P_{total} (Pa)	H_2 flow (sccm)	P (W)
CC	500-700	1000	270-540	100
IC	700-800	150-300	200-500	2200
IC	700-800	400-500	650-700	2200

For the reasons of plasma discharge maintaining in rotational apparatus it is necessary to standardise the flow of plasma creating gases. Therefore we investigated the influence of changes in hydrogen amount. This was achieved by means of argon dilution. The goal of this experimental series was the examination of relations between working temperature in reactor, stoichiometry of hydrogen and maintaining the RF-discharge in the diluted mixture H_2-Ar with respect to maximum yield of tungsten powder.

The kinetics of the reduction process was monitored by NH, OH, H_2, H_β atomic and molecular spectra. The results are summarised in Fig. 2.

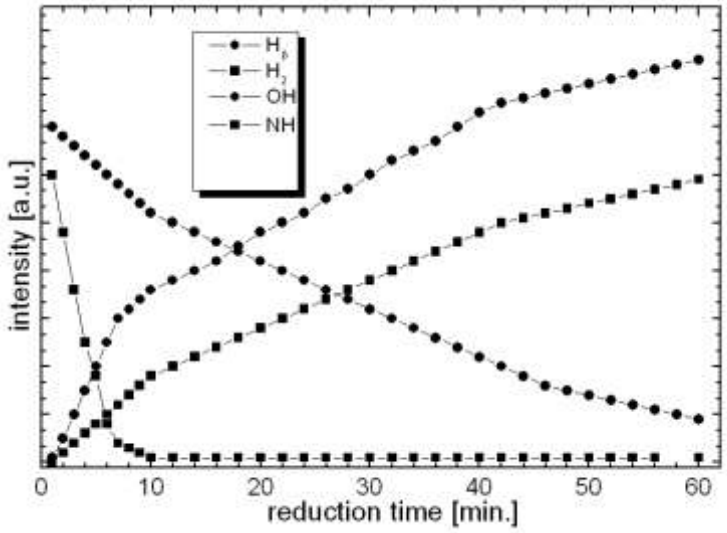

Fig .2. Time dependence of selected atomic lines and molecular bands intensities used for the monitoring during the plasma reduction process.

The moisture influence on nucleation conditions of powdered metal is primary interest. Besides the reduction temperature the dynamic moisture in the reactant layer attributes to nucleation and tungsten grain growth. In the presence of hydrogen above 420°C the reactant is only WO_2. The presence of WO_2 as main intermediate product was determined on the diffractogram of APT sample reduced at 600°C. The low moisture during further reduction of $WO_2 \Rightarrow W$ at low layer thickness results in high degree of nucleation and fore to finer grain size. These products are expected to prove increased reactivity (sinterability). On the contrary high moisture suppresses the nucleation rate and leads to a coarser grain size.

Our results confirmed the known technological experience about reduction temperature influence on tungsten grain size connected with loss of reactivity and sinterability by higher temperatures. In Fig. 3a is shown the distribution of grain sizes of tungsten powder reduced at 600° C in hydrogen plasma.

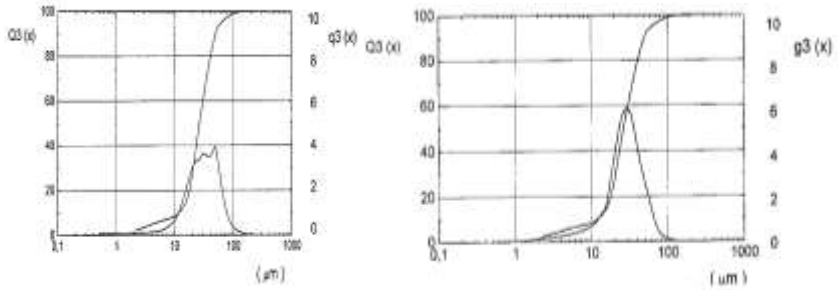

Fig. 3a and 3b. Granulometric distribution curve of tungsten powder reduced from APT (90 – 100)mm. Tungsten powder reduced in H_2 plasma (a) and by molecular H_2 (b).

The input amount of APT determines the water vapour quantity released during the reduction process. The water vapour retention (local moisture of powder) influences the nucleation and the conditions of metallic particle growth. Therefore a direct proportion exists between layer thickness and final grain size of product.

The overall porosity of powdered layer and its permeability is given by superposition of macroporosity (the space between grains) and microporosity of individual oxide grains. For this measurement the +80 –100 μm APT fraction was selected. The specific surface was 0,527 m^2g^{-1}, average pore size was 244 nm.

From the loose volume and density it follows that the porosity of free poured layer of APT is about 20 %, the porosity value of tungsten oxides prepared by APT thermal decomposition increased to 75 %. To this value it is necessary to add the internal porosity of individual grains, which is characterised not only by the increase of average pore size to 447 nm but also a remarkable growth of specific surface to 2,76 $m^2 g^{-1}$.

High porosity of powdered layer, in which better flow of gas mixture H_2-H_2O during reaction, leads to creation of tungsten with finer grain size. The mixing then lowers the value of hydrodynamic and aerodynamic resistance to a minimum. For the diffusion flow the porosity of proper reduced precursor is decisive. Increased hydrogen flow lowers the value of H_2O/H_2 ratio and shifts the equilibrium in the direction of finer products. The dew point, which is connected with temperature and H_2O/H_2 ratio, is a parameter pursued in the production as a qualitative indicator of reduction direction. The hydrogen that has high moisture leads to coarse tungsten grains.

For sintering tests products were chosen prepared by the reduction of the starting coarse-grained APT (80 – 100 μm) in hydrogen plasma at partial pressure of hydrogen 200 Pa and the time of reduction 3 hours – see Fig. 4a. For comparison, under the same conditions tungsten was sintered by the reduction of APT with molecular hydrogen at temperature 800 °C, which is the lowest temperature applicable in industrial production. The granulometric composition of this powder material is presented in Fig. 4b.

Diffractograms of powders exhibit a typical broadening of diffraction lines with the decreasing reduction temperature, because the originating small crystals have not sufficient resolution power for the diffraction of the employed X-ray radiation of CoK_{α}. Part of the evaluated diffractogram is represented in Fig. 5.

For an approximate definition of the thickness of particles in the direction perpendicular to the reflecting plane (hkl) the Scherrer formula was used

$$L_{hkl} = 0.89\,\lambda / B_{ps} \cos\theta$$

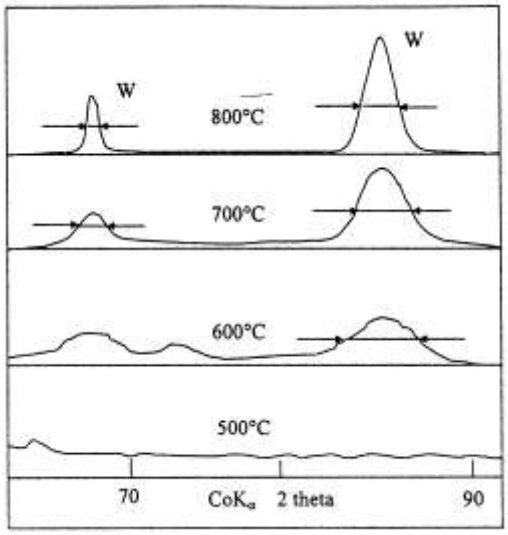

Fig. 4. Broadening of W diffraction lines of samples reduced in H_2 – plasma at different temperatures.

where $B^2_{ps} = B^2_m - B^2_s$ are half-widths of the diffraction lines of the sample and the calibration material (in rad). The widths of the diffraction lines and the thickness of the particles in the direction perpendicular to the reflecting planes (200) and (211) are given in Table II. The individual reduced samples of powdered tungsten were mixed with the additive 1 weight % of nickel powder. The mixture was ground for the purpose of further pulverisation in the laboratory ball mill for the period of 8 hours. The pressure 100 MPa compressed the homogenised mixture for the period of 4-5 s to form cylinders of 10 mm diameter and 10 mm height. The furnace was computer controlled.

Tab. II. Broadening of W diffraction lines and diameter of particles in the perpendicular direction with respect to (200) and (211) planes.

Sample	B_{ps} (200) [rad]	L_{200} [Å]	B_{ps}(211) [rad]	L_{211} [Å]
W from APT reduced at 600°C, 60 min., 10000 Pa H_2	0.0088	220	0.0106	209
700°C, 60 min.	0.0141	137	0.0176	125
800°C, 60 min.	0.0159	121	0.0141	114
W from APT reduced at 800oC,120 min., 250 Pa H_2	0.0077	251	0.0091	241
W from APT reduced at 800oC,120 min., 300 Pa H_2	0.0082	236	0.0096	230

From the records of sintering process it is evident that the maximum temperature achieved (sintering temperature) was 1450 °C. The sintering process lasted altogether 32 hours. At the temperature 800 °C hydrogen was fed in the amount of 800 l/hour. Before feeding the hydrogen the furnace was evacuated to the value of 10^{-3} Pa. As the fingerprint of the sintering activity of tungsten powder is the final density after sintering.

The density of the samples was measured in the helium densitometer and in the Hg-pycnometer – Fig. 5a, b. The two methods yielded numerical different results, nevertheless in relative values significant for judging the effect of sintering, see Table III.

Tab. III. Analytical results and composition of sintered samples.

Sintered samples W + 1% Ni				
	sintered W powder (prepared from APT by plasma activated hydrogen) with 1% Ni		sintered W powder (prepared from APT by mol. hydrogen) with 1% Ni	
Density g.cm^{-3} measured in He- densitometer	17.680	±0.003	17.601	±0.003
Density g.cm^{-3} measured in Hg- pycnometer	16.87	±0.07	15.86	±0.2
Open porosity (vol.%}	0.413		16.2	
Total pore area (m^2/g)	0.0002		0.049	
Total intrusion volume (ml/g)	0.0002		0.0390	
Volume contraction (%)	40.1	±1.6	30.2	±2.1
Linear contraction (%), in radial direction	23	±1.1	17	±2.5

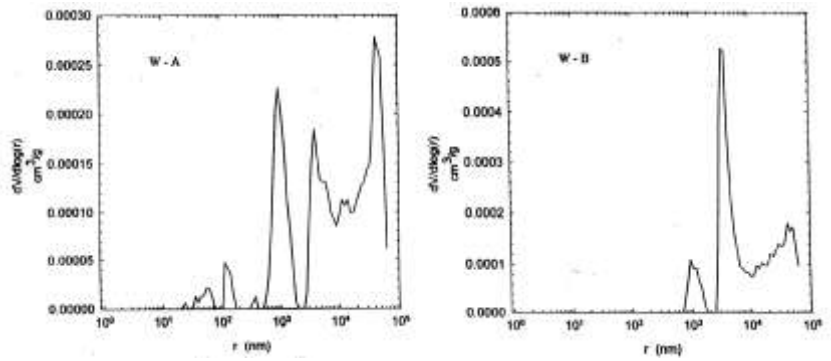

Fig. 5a and 5b. Results of Hg – pycnometer. a) APT reduced in molecular H_2 , b) APT reduced in inductively coupled hydrogen plasma.

From Table III it is evident that the He- pycnometer exhibits higher density values in the same samples, the difference between the plasma reduced samples not being significant. Their density with the mean deviation of measurements ± 0. 003 was ρ = 17.681 g/cm^3. This value corresponds quite to the results stated by Agte [3], where the effect of Ni-additive on the sinterability of tungsten is studied - see Table IV.

The mean density of the tungsten samples prepared by the reduction of APT with molecular hydrogen found in the same device was ρ = 17.601 g/cm^3.

From the results it is evident that there was a mild shift of the density increase in the samples containing tungsten prepared by the plasma reduction of APT. The actual conspicuous increase in the sintering activity from He- pycnometric measurements is, however, not confirmative, as on the contrary follows from the value of contraction and the measurements of Hg porosimetry, also expressed in Table III.

Tab. IV. Density of sintered samples in dependence on the sintering temperature. The starting density of the samples was 9.1 g.cm^{-3}.

Sintering temperature [^{o}C]	W+1% Ni Density [g.cm^{-3}]
1000	14.9
1100	17.6
1200	18.0
1300	17.8
1400	17.6
1470	17.4

From metallographic microsections a considerable difference is evident from the amount of pores, witnessing in favour of the plasma reduced precursor. The marked grain of the light phase in the picture corresponds to accidentally formed NiW_2, evidently from undissolved coarser shares of powder nickel. An important fact however remains that the tungsten powder obtained in the H_2 plasma exhibits good sinterability, which is evidently higher than in powders obtained by the usual methods of reduction.

4. CONCLUSIONS

Introductory experiments with applying the hydrogen plasma chemical activation for tungsten reduction from oxygen containing precursors indicate the possibility of further lowering the reduction temperature in comparison with conventional technologies.

Direct decomposition of precursors in the system, which allows hydrogen recyclation, appears economical for taking advantage of hydrogen reuse, which raises through ammonia thermal dissociation. This breakdown to hydrogen and nitrogen can be activated in a different manner. Preferentially it occurs on the solid phase surface. For metallic tungsten the zero-order reaction starts at about 850°C [7, 8]. This temperature complies with kinetics of reduction under industrial conditions. The lowest limit for atmospheric hydrogen pressure the temperature 600°C can be considered.

The plasma presence brings the temperature of ammonia decay from APT precursor down to 500°C and contributes according to stoichiometric proportions to the hydrogen enrichment in the system of about 25 %. The comparison of theoretical calculations with experimental results [9] is not reliable yet because of the low value of the statistical significance coefficient due to relatively high scatter of individual results. The experiments performed show that in the inductively coupled plasma reactor is the RF energy more effectively consumed in the reduction process.

As the next supporting argument for plasma chemical technology application is better sinterability of tungsten powder, which was demonstrated successively through evaluation of sintering tests.

ACKNOWLEDGEMENTS

This work was partly supported by the Ministry of Education Czech Rep. contract MSM 143100003 and COST project OC 527.20.

REFERENCES

[1] Haubner R., Schubert W.D., Lassner E., Schreiner M., Lux B., J. Refract. Met. Hard Mater. 2 108 (1983).
[2] Lassner E., Schubert W.D., Tungsten, Cluwer Academic/Plenum Publishers N.Y. 1999.
[3] Agte C., Vacek J., Tungsten and molybdenum, SNTL Praha 1954.
[4] Benešovský F., Pulvermetallurgie und Sinterwerkstoffe, Metallwerk Plansee 1980.
[5] Zvoníček V., PhD-Thesis, Masaryk University Brno 1997.
[6] Kudrle V., Janča J., Brožek V., Reduction of the iron oxides in MW and RF reactors. Proceedings 14th International Symposium on Plasma Chemistry, August 2-6, 1999 Prague, Vol.IV, p.1945-1950, ISBN 80-902724-4-4.
[7] Šarman L., Hák L., Janča J., Dufek V., Brožek V.,Proc. International. Conference on Tungsten, Hard Metals and Refractory Alloys, Sept. 25-27, 2000, Annapolis, Maryland, Sess.7/3. , pp. 151-158.
[8] Janča J., Eliáš M., Brožek V, Reduction of APT precursors in capacitive and inductive RF discharge plasma reactors, 15th Int. Symp. Plasma Chem., Proc. Vol. I., Orléans 2001, pp. 59 – 65.
[9] Tsvetkov Yu.V., Plasma Metallurgy - Current State, Problems and Prospects, Proc. 14th ISPC Prague 1999, Vol.I, p.11-13, ISBN 80-902724-1-X.

4th International Conference **ELMECO**
Nałęczów, Poland
September 2003

NATURAL-GAS PLASMA PROCESSING

Krzysztof SCHMIDT-SZAŁOWSKI, Teresa OPALIŃSKA, Jan SENTEK, Krzysztof KRAWCZYK, Joanna RUSZNIAK, K. RADOMYSKA

Faculty of Chemistry, Warsaw University of Technology,
ul. Noakowskiego 3, 00-664 Warszawa, e-mail: kss@ch.pw.edu.pl

Keywords: natural gas, dielectric-barrier discharges, gliding discharges.

1. BACKGROUND

Nowadays, natural gas (NG) plays an increasingly important role being not only an effective and desirable fuel but also one of the main row materials for chemical syntheses. Hydrogen produced from NG is a principal feedstock for ammonia and methanol syntheses, for benzene hydrogenation, for production of liquid fuels as well as of a number of chemicals. At least one half of hydrogen is produced from NG by steam reforming of methane (and other gaseous hydrocarbons) and by autothermic partial oxidation. It is taken into account that the role of hydrogen itself should increase in future, as it is the ultimate clean energy carrier, especially useful for feeding the fuel cells. Large amounts of NG are produced in the oil field areas at remote locations (Siberia, Alaska, Nigeria) where transport of gaseous products by pipelines is not economical. Methane, the main NG component, being one of the most effective greenhouse gases should not be released to the atmosphere. However, under the circumstances mentioned the real value of gaseous hydrocarbons accompanying crude oil is so small, as compared with the value of the oil itself, that they are just burned near the field (hence transformed into CO_2 which is also a greenhouse gas), or sometimes forced again into the oil deposit. One of the reasons of such an unfavourable situation is the underdevelopment of the gaseous hydrocarbons technology. Therefore it seems advisable to develop new, more efficient methods for NG conversion (preferably at the site of its release) into compounds that are more attractive and/or easier to transport. Nowadays, the following processes of methane conversion are of commercial significance: 1) production of syngas by high-temperature catalytic steam (or CO_2) reforming, 2) autothermic partial oxidation of methane with oxygen and steam mixtures, 3) synthesis of unsaturated hydrocarbons, mainly acetylene, by dehydrogenating oxidation of methane, 4) plasma synthesis of acetylene known as the Huels and DuPont processes, 5) manufacture of carbon blacks. There are many other methods for NG utilisation, e.g. the oxidising coupling of methane, which leads to synthesis of hydrocarbons of higher molecular weight, the oxidation of methane to methanol or to formaldehyde etc. Some of these methods are based

on plasma processing of gaseous hydrocarbons [1-7]. However, despite of many efforts, up till now none of them has been developed for commercialisation.

Two methods have been examined in this study: 1) methane conversion into unsaturated hydrocarbons in dielectric barrier discharges and in gliding discharges, 2) carbon black generation from methane in gliding discharges.

2. EQUILIBRIUM IN THE CH_4+H_2 SYSTEM

The equilibrium concentrations of the main products were studied in CH_4+H_2 system basing on thermodynamic data (for [C]/[H] = 1:4 and 1:32) within the temperature range 500-4000 K at pressures 1 and 10 bar (Figs. 1 and 2) [8]. It has been found that the presence of hydrogen influences strongly the equilibrium methane conversion to acetylene (Y_A) with the maximum value of 53.2% for [C]/[H] = 1:4 (at 3400 K) and 95.6% for [C]/[H]=1:32 (at 2900 K). Hence, in the mixtures of CH_4+H_2, the equilibrium methane conversion to acetylene Y_A can reach large values, but only in a narrow range of process parameters (temperature and [C]/[H] value). The solid carbon, being one of the main products of the methane conversion, occurs at a much wider range of parameters. However, it should be noted that the temperature range of solid carbon occurrence is evidently reduced by the increase of pressure. For example, at 10 bar and [C]/[H] = 1:32, carbon is stable within the temperature range 1300 - 2900 K, much smaller then that at a pressure of 1 bar. On the other hand, the pressure increase extends the range of temperatures at which considerable values of Y_A are attained (up to maximum 97% at 2900 K). At the pressure of 10 bar the equilibrium methane conversion to acetylene attains large values (>90%) in the temperature range of 3000 – 3500 K.

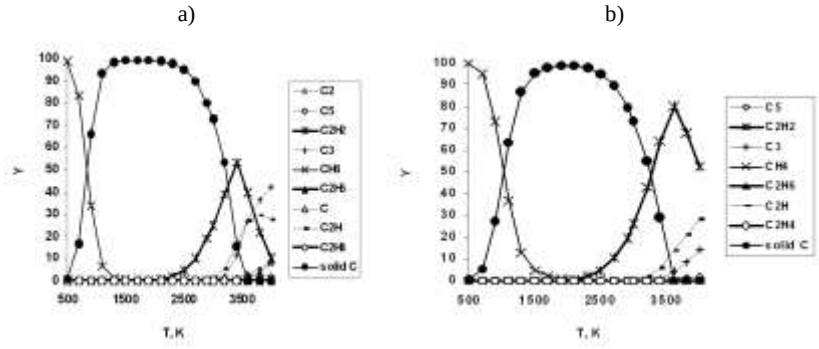

Fig. 1. Equilibrium state for the initial gas mixtures CH_4+H_2 with **[C]:[H]=1:4** at different pressures: **a – 1 bar, b – 10 bar. Y** – methane conversion to gaseous products and solid C (with contribution of remaining CH_4).

a) b)

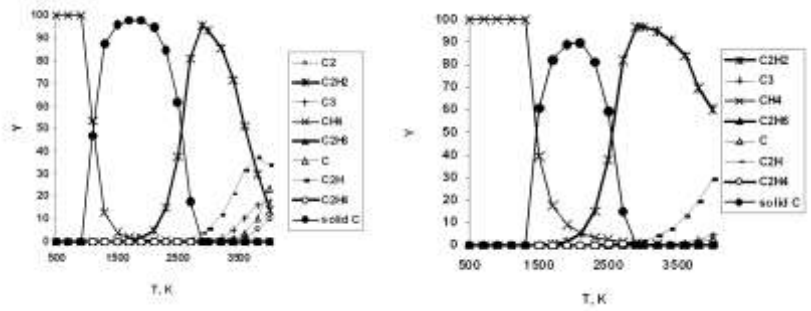

Fig. 2. Equilibrium state for the initial gas mixtures CH_4+H_2 with **[C]:[H]=1:32** at different pressures: **a – 1bar, b – 10 bar. Y** – methane conversion to gaseous products and solid C (with contribution of remaining CH_4).

3. EXPERIMENTS AND DISCUSSION

METHANE CONVERSION IN DIELECTRIC BARRIER DISCHARGES (DBD)

The methane conversion to higher hydrocarbons was examined under DBD conditions using a flow reactor operated at atmospheric pressure and the frequency of 50 Hz [9]. The reactor was made of a quartz-glass tube (serving as a dielectric barrier) with an inner metal (aluminium) high voltage electrode. The inter-electrode voltage was maintained constant at the level of 18 kV and the reactor temperature was about 45 ^{O}C. The methane conversion was examined in the presence of granular quartz-glass and silica gel grains (size of 1-2 mm), and with no packing. It has been found that those materials do not influence the current-voltage characteristics of the discharge. The results of experiments with CH_4+Ar mixture containing 7.5% methane, gas flow rate 2.7 - 16 Nl/h and discharge power 5 W, are presented (Fig. 3) in terms of the following quantities: the overall methane conversion X and the specific energy E_R per methane unit [J/mmol CH_4]. The growth of the overall methane conversion X, as well as the methane conversion rate and the energy efficiencies were observed using both packing materials: quartz-glass and silica gel (Table 1). Under the action of barrier discharges in CH_4+Ar mixtures, ethane and hydrogen were the main gas products with small addition of unsaturated hydrocarbons C_2 (C_2H_2 and C_2H_4). A part of methane was transformed into non-volatile products (not identified).

Table 1**.** Effect of the presence of packing on the overall methane conversion and conversion into C_2H_6 for CH_4+Ar mixture (7.5% CH_4) and flow rate 2.7 Nl/h.

Packing	Overall CH_4 conversion X [%]	CH_4 conversion to C_2H_6 [%]
None	33.8	8.4
Quartz-glass	43.5	9.2
Silica gel	38.9	9.2

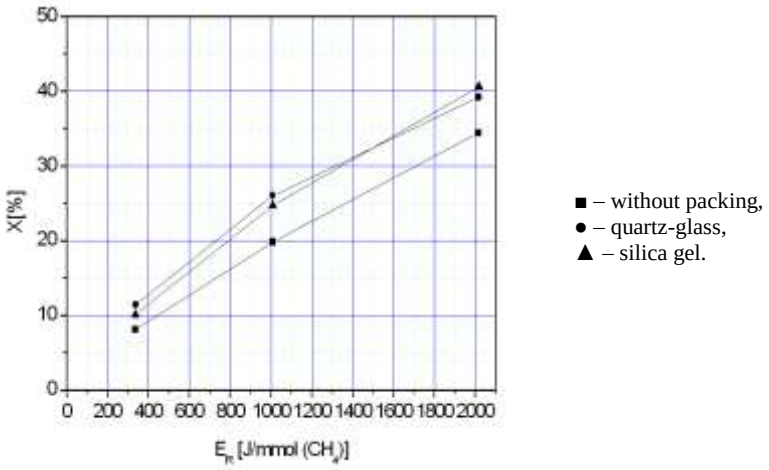

Fig. 3. Overall conversion **X** vs. specific energy $\mathbf{E_R}$ per unit CH_4 for CH_4+Ar mixture (7.5% CH_4); Gas flow rate: 2.7, 4.9, 15.6 Nl/h.

Taking into account the low conversion into unsaturated hydrocarbons it may be concluded that after the first steps of the chain reaction [10]

$$CH_4 \rightarrow C_2H_6 \rightarrow C_2H_4 \rightarrow C_2H_2 \rightarrow C \qquad (1)$$

in which methane was converted into ethane, the transformation path was terminated. It seems probable that the reaction of methane conversion starts in the short-lived filamentary microdischarge (during the period of several dozens of nanoseconds) and it is stopped shortly after the microdicharge disappears in the surroundings of cool gas. In addition, the solid surfaces of the packing grains may act as chain stoppers, being involved in the deactivation of high-energy particles (radicals, excited molecules). On the other hand, the surface feature of the microdischarges is a favourable circumstance for evolving the heterogeneous reactions of the active species on the grain surfaces. One can conclude that those processes take a part in the overall methane transformation under DBD conditions.

METHANE CONVERSION IN GLIDING DISCHARGES

A new type of gliding-discharge reactor was used for the experiment (Fig. 4). Starting gas mixture (CH_4+H_2) was introduced through a nozzle (diameter 0.75 mm) disposed between the electrodes at the axis of the reactor. The temperature was measured by means of a thermocouple located inside the tube being the grounded electrode. In two series of experiments with the constant flow rate (300 Nl/h) of CH_4+H_2 mixtures the reactor was supplied at the stable levels of overall power (A: 200 W and B: 300 W) measured at the mains. The overall methane conversion [x_c] and the conversion [x_a] into hydrocarbons C_2 (acetylene, ethylene, ethane) were examined (Fig. 5), x_c ranging from 25 to 28% in the series A and from 34 to 36% in B.

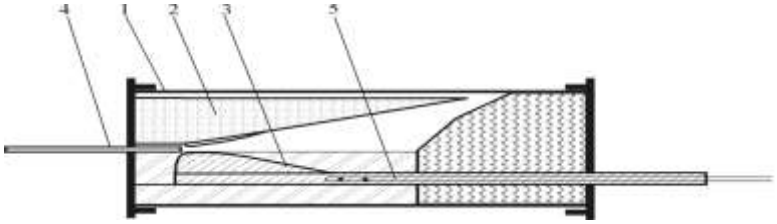

Fig. 4. Scheme of gliding discharge reactor. 1 - quartz tube, 2 - high voltage electrode, 3 - grounded electrode, 4 - nozzle, 5 – thermocouple.

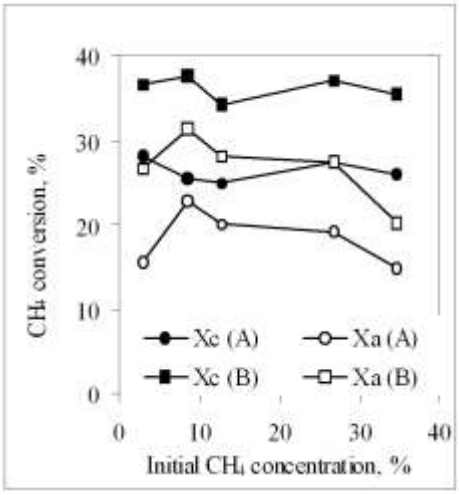

Fig. 5. Methane conversion vs. methane concentration in the initial mixture CH_4+H_2. Methane conversion: 1) overall X_c, 2) into acetylene X_a. Overall flow rate 300 Nl/h. Power: A - 200 W, B - 300 W.

In some of those experiments, the methane conversion into non-volatile products (soot and macromolecular substances) was high - up to 15% in series B. Nevertheless, in series A with the methane concentration of 12.8% in the starting mixture CH_4+H_2, the methane conversion into non-volatile products was 4.8% only with the conversion to C_2 at the level of 24.8%. An increase in the overall methane conversion as well as conversion into C_2 was observed when increasing the discharge power. It should be noticed that the series A and B were carried out under conditions where elemental carbon is not stable, thus it should not be produced. Account should be taken, however, of two points: 1) the gas temperature in the discharge zone might be much higher than the temperature measured at the grounded electrode, 2) the methane conversion was curried out in the non-equilibrium plasma where the reaction kinetics rather than the equilibrium state determined the reaction path. These might result in the elemental carbon formation as it was observed in the experiments.

CARBON BLACK GENERATION

Carbon blacks (CB), being an important group of industrial carbons, are used chiefly in the rubber tire, plastics, ink and paint industries. Some new concepts of CB manufacturing are based on processing of hydrocarbons in the arc plasmas and plasma-torch reactors. For studying the conversion of gaseous hydrocarbons into CB, a gliding-discharge reactor has been developed, operated at the frequency of 50 Hz [11-13]. It was made of a quartz-glass tube of 110 mm in diameter with three specially shaped main electrodes and the additional ignition electrode. Pure gases CH_4+Ar were the only components of the inlet gas mixture with the overall gas flow rate of 1500 Nl/h (Table 2 and Fig. 6).

Table 2. Carbon black generation from methane.

Methane concentration % vol.	Power kW	Conversion into:				
		Overall X	C X_C	C_2H_2	C_2H_4	C_2H_6
5	1.18	63.1	21.9	39.1	1.5	0.6
7.5	1.0	58.2	17.7	39	1.2	0.4
10	1.22	57.1	15.9	39.5	1.3	0.4
15	1.50	65.6	37.7	26.9	0.8	0.2
20	1.51	73.5	55.4	19.3	0.5	0.1

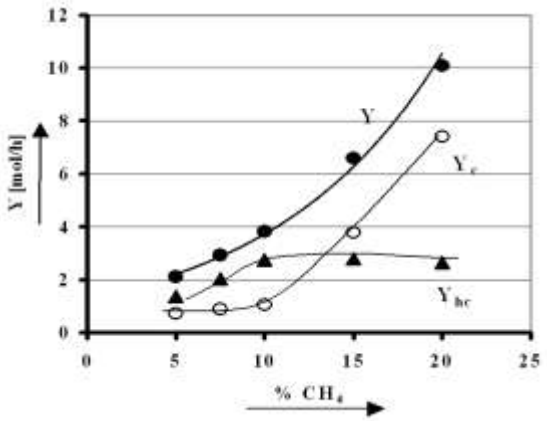

Fig. 6. Methane conversion rates: overall - **Y**, into CB - $\mathbf{Y_C}$, and into C_2H_n - $\mathbf{Y_{hc}}$ vs. methane concentration in the inlet mixture CH_4+Ar.

It should be pointed out that, under the fixed parameters of the supply system, the discharge power in the reactor changed depending on the composition of the inlet gas mixture (Table 2). Carbon black and acetylene were obtained as the main products with small amounts of ethylene and ethane. The overall methane conversion X was high (57 - 75%) in all the measurement series, whereas the methane conversion into CB X_C varied (within 16 - 55%) depending on the initial methane concentration. The methane concentration in CH_4+Ar mixtures influenced substantially the rate of CB formation. For

example, a 4-fold increase of initial methane concentration (from 5 to 20%) gave a 5-fold increase of the total rate of methane conversion Y but at the same time, a 10-fold increase of the rate of CB formation Y_C was observed. Thus, the ratio of Y_C/Y increased from 0.3 to 0.74. It is also interesting to note that the rate of acetylene and other C_2H_n formation (Y_{hc}) increased markedly with increasing initial methane concentration within 5-10%, whereas it remained nearly constant (2.7-2.8 mole/h) at higher methane concentrations. Therefore, if we assume that the CB is produced in the chain of reactions (1) [10] it can be concluded that the increase of the initial methane concentration within 5-10% results in a considerable increase in the rate of the initial stages where acetylene and other C_2H_n hydrocarbons are produced. At the same time the increase of the CB generation rate (the final stage) is much smaller. On the other hand, when higher methane concentrations were used (within 10 - 20%), the rate of all these stages increases almost equally. It may be concluded therefore, that the concentration of methane in CH_4+Ar mixtures determines the economy of CB production in the gliding discharges. High methane concentrations can give: 1) higher discharge energy, 2) higher rate of CB formation, 3) smaller unit energy consumption, and 4) lower consumption of argon being the auxiliary gas.

ACKNOWLEDGEMENTS

This work was supported by the State Committee for Scientific Research (KBN); grant No PBZ/KBN/018/T09/99

REFERENCES

[1] K. Thanyachotpaiboon, S. Chavadej, T.A. Caldwell, L.L. Lobban, R.G. Malinson, Reactors, Kinetics&Catalysis 44/10, 2252-2257 (1998).
[2] A. Czernichowski; Karbo-energochemia-ekologia N°11, 359-369 (1998).
[3] R. Azizov, M. Krotov, M. Deminskiy, B. Potapkin, V. Rusanov, Proc. 14 ISPC, 2279-2282, Praha 1999.
[4] A. Babaritski, M. Deminskiy, C. Etievant, V. Jivotov, B. Potapkin et al., Proc. 14 ISPC, 2289-2294, Praha 1999.
[5] C.-J. Liu, R. Mallinson, L. Lobban, Applied Catalysis A: General 178, 17-27 (1999).
[6] M. Okumoto, A. Mizuno, Catalysis Today 71, 211-217 (2001).
[7] X. Zhang, B. Dai, A. Zhu, W. Gong, Ch. Liu, Catalysis Today 72, 223-227 (2002).
[8] K. Krawczyk, J. Ruszniak, J. Sentek, K. Schmidt-Szałowski, Int. Symp. High Pressure Low Temp. Plasma Chem. HAKONE VIII, Contr. Papers, P3.2, 181-185, Puhajarve 2002.
[9] J. Sentek, K. Radomyska, K. Schmidt-Szałowski, Acta Agrophysica 80, 149-157 (2002).
[10] A. Holmen, O. Olsvik, and O.A. Rokstad, Fuel Processing Technology, 42, 249 (1995).
[11] T. Opalińska, T. Zieliński, K. Schmidt-Szałowski, Acta Agrophysica 80, 159-166 (2002).
[12] T. Opalińska, T. Zieliński, J. Polaczek, K. Schmidt-Szałowski, B. Ulejczyk, Pol. Patent Appl. P.355280.
[13] K. Schmidt-Szałowski, T. Opalińska, Pol. Patent Appl. P.361076.

ELECTROMAGNETIC PROCESSES AND DEVICES I

4th International Conference **ELMECO**
Nałęczów, Poland
September 2003

MATHEMATICAL MODEL OF GAS DIFFUSION ELECTRODE IN PROTON EXCHANGE MEMBRANE FUEL CELL

Eugeniusz KURGAN, Paweł SCHMIDT

AGH University of Science and Technology, Dept. of Electrical Engineering
al. Mickiewicza 30, 30-059 Krakow, Poland
e-mail: kurgan@agh.edu.pl, pschmidt@agh.edu.pl

Abstract

In this paper, a gas mixture model is developed to study hydrogen and water vapor flow in anode of the PEM fuel cell. First nonlinear partial differential equations with appropriate boundary conditions are formulated and then solved with the aid of finite element method. Because of anisotropy of the diffusivity of fibrous porous materials such as porous carbon fiber paper the dependence between anisotropy ratio and flux of the species is investigated. At the end some illustrative examples are given.

Keywords: fuel cell, anisotropy, mass transport, PEM, GDL.

1. INTRODUCTION

The electrode of the fuel cell, known as a gas diffusion layer (GDL), is a very thin layer of porous carbon fiber paper lying between platinum catalyst layer from one side and gas distribution layer from the other. The flow of gas mixture in the GDL is governed by the convection law, which governs the motion of the gas species through the porous medium caused by pressure gradients, and multicomponent diffusion of the reacting and nonreacting gas species caused by concentration gradients, relative to the convection velocity.

The carbon fiber paper building the GDL consists of single carbon fibers, which are crossed under right angle. This is a reason of anisotropy of GDL. We are assuming further, that direction of carbon fibers corresponds to domain coordinates system.

In the literature [5] the mathematical model of multicomponent gas transport in PEM of fuel cell is developed, but only the final system of equations is given. Authors used the finite volume method to solve the equations. In this paper we govern system of nonlinear partial differential equations as well as boundary conditions and solve the problem using finite element method.

2. MODEL OF THE DOMAIN

The cross section of the anode of the PEM fuel cell is shown in figure 1. The lower boundary, at $y = 0$, represents the interface between the GDL and graphite plates and open gas-filled flow channel. The upper boundary, at $y = H$, corresponds to platinum catalyst separating the GDL and PEM. The coupling of GDL to the rest of the fuel cell will be accounted for through the boundary conditions.

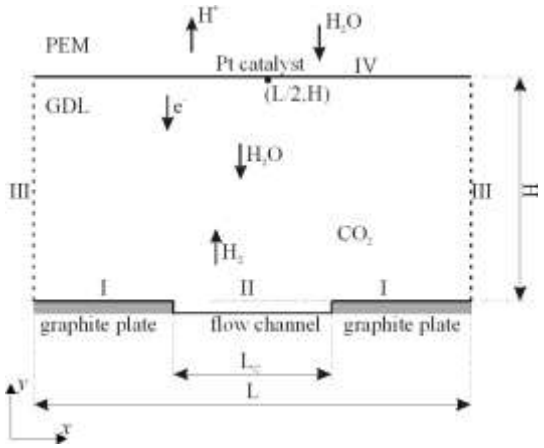

Fig. 1. Cross-section of the anode GDL.

The electric current in a fuel cell is derived from the two electrochemical reactions. The hydrogen ions generated at the anode catalyst layer migrate across the PEM, where they react with oxygen gas to produce water vapor. The anode electrochemical reaction is [6]:

$$2H_2 \rightarrow 4e^- + 4H^+ \tag{1}$$

The cathode reaction is given by:

$$O_2 + 4e^- + 4H^+ \rightarrow 2H_2O \tag{2}$$

We assume that the model is isothermal and does not include transport of charge and heat. We assume also, that all water vapour remains in the gas phase and all reactants are immediately consumed upon reaching the PEM.

3. MAIN EQUATIONS

The conservation law of mass for the convective flux of gas mixture is in steady state given by [1]:

$$\nabla(C\mathbf{U}) = 0 \tag{3}$$

where **U** is a total gas mixture velocity and C is a total gas concentration which is a sum of the concentrations of each species: $C = C_1 + C_2 + C_3$., where C_1 is concentration of

hydrogen, C_2 is concentration of water vapor and C_3 is concentration of carbon two-oxide. We assume further that CO_2 concentration is a fixed part of the total concentration C which is equal $(1 - \gamma_r)C$. Total flux of hydrogen is a sum of convection and diffusion fluxes [2]:

$$\mathbf{N}_1 = C_1\mathbf{U} + \mathbf{J}_1 \tag{4}$$

The diffusive flux of hydrogen $\mathbf{J}_1$ is given by Fick's law, which states that molar flux of this component is relative to the molar-averaged velocity is proportional to the gradient of the mole fraction x_1 according with relation [4]:

$$\mathbf{J}_1 = CD\nabla x_1 \tag{5}$$

Because the fibres making up the GDL are oriented the material is anisotropic and the diffuse coefficients are different across and along the GDL. We assume diffusivity as matrix:

$$\mathbf{D} = \begin{bmatrix} d_{11} & d_{12} \\ d_{21} & d_{22} \end{bmatrix} \tag{6}$$

In fact, the diffusivity matrix is diagonal. Alternatively it can be rewritten in form:

$$\mathbf{D} = D\begin{bmatrix} \chi_d & 0 \\ 0 & 1 \end{bmatrix} \tag{7}$$

Where χ_d is an anisotropy ratio. Thus, the equation (5) takes the form:

$$\begin{bmatrix} \mathbf{J}_x \\ \mathbf{J}_y \end{bmatrix} = CD\begin{bmatrix} \chi_d & 0 \\ 0 & 1 \end{bmatrix}\begin{bmatrix} \frac{\partial x_1}{\partial x} \\ \frac{\partial x_1}{\partial y} \end{bmatrix} \tag{8}$$

The fluid flow velocity in porous gas diffusion layer can be computed using Darcy's law. It gives the mixture velocity in terms of the fluid pressure as [2]:

$$\mathbf{U} = -\frac{K}{\varepsilon_0\mu}\nabla P \tag{9}$$

Where k_p is a permeability of the GDL and coefficient μ is the viscosity.

Ideal gas equation:

$$P = CRT \tag{10}$$

From (3), (9) and (10) we get:

$$\nabla(C\frac{KRT}{\varepsilon_0\mu}\nabla C) = 0 \tag{11}$$

Let

$$\Gamma = \frac{KRT}{\varepsilon_0 \mu} \tag{12}$$

So, finally the first equation is:

$$\nabla(C\Gamma\nabla C) = 0 \tag{13}$$

From (3), (4) and (5) we get mass conservation law for hydrogen:

$$\nabla(C_1 U - CD\nabla x_1) = 0 \tag{14}$$

And using (9), (10) and (12) we get:

$$\nabla(C_1\Gamma\nabla C - CD\nabla x_1) = 0 \tag{15}$$

Because:

$$x_1 = \frac{C_1}{C} \tag{16}$$

We get:

$$\nabla(x_1 C\Gamma\nabla C) - \nabla(CD\nabla x_1) = 0 \tag{17}$$

Finally, using (7), we get the second equation:

$$\Gamma\left(\frac{\partial}{\partial x}\left(Cx_1\frac{\partial C}{\partial x}\right)+\frac{\partial}{\partial y}\left(Cx_1\frac{\partial C}{\partial y}\right)\right)-D\left(\chi_d\frac{\partial}{\partial x}\left(C\frac{\partial C}{\partial x}\right)-\frac{\partial}{\partial y}\left(C\frac{\partial C}{\partial y}\right)\right)=0 \tag{18}$$

4. BOUNDARY CONDITIONS

SECTION I – GRAPHITE PLATE

Along this part of boundary graphite plate is in contact with carbon fibber material and throughout this section cannot be flux of any species, so Neumann's boundary condition for both of variables are equal zero.

SECTION II – FLOW CHANNEL

Because on this part of the boundary fibrous carbon material contacts with flow channel and on this part of the boundary reactant species enter the anode we get:

$$C = C_g \text{ and } x_1 = x_{1g} \tag{19}$$

SECTION III – LEFT AND RIGHT SIDES

We assume that solution is periodic with respect to the variables and thus boundary conditions are the same as for section I.

SECTION IV – PLATINUM CATALYST LAYER

Gas diffusion layer contacts platinum catalysis along this part of boundary. The electrochemical reaction takes place here. The hydrogen atoms in consequence of them lose their electrons, which flow through external circuitry and hydrogen ions flow further through proton membrane. We assume that electrochemical reaction efficiency is here equal 100% and no hydrogen atoms enter proton membrane. Thus [4]:

$$\mathbf{N}_1 \cdot \mathbf{n} = r_h C x_1 \tag{20}$$

The mass transfer coefficient r_H models electrochemical reaction, which takes place in catalyst layer. The total flux of hydrogen can be derived from Fick's and Dercy laws:

$$\mathbf{N}_1 = C x_1 \Gamma \nabla C - C D \nabla x_1 \tag{21}$$

Because of anisotropy we get:

$$\begin{aligned} \mathbf{N}_1 = C\left(\Gamma x_1 \frac{\partial C}{\partial x} + \Gamma x_1 \frac{\partial C}{\partial y} - d_{11} \frac{\partial x_1}{\partial x} - d_{12} \frac{\partial x_1}{\partial y} \right) \cdot \mathbf{e}_x + \\ + C\left(\Gamma x_1 \frac{\partial C}{\partial x} + \Gamma x_1 \frac{\partial C}{\partial y} - d_{12} \frac{\partial x_1}{\partial x} - d_{22} \frac{\partial x_1}{\partial y} \right) \cdot \mathbf{e}_y \end{aligned} \tag{22}$$

Normal part of the flux to the boundary is:

$$\Gamma x_1 \frac{\partial C}{\partial x} + \Gamma x_1 \frac{\partial C}{\partial y} - d_{12} \frac{\partial x_1}{\partial x} - d_{22} \frac{\partial x_1}{\partial y} \cdot = r_h x_1 \tag{23}$$

Flux of water vapor is strictly related to hydrogen flux flowing in opposite direction. This relation between hydrogen flux and water vapor flux is established by return coefficient *v*, which determine direction and magnitude water vapor flux $\mathbf{N}_2$:

$$\mathbf{N}_2 = (\nu - 1)\mathbf{N}_1 \tag{24}$$

where ν is a return coefficient. We assume that in steady state the majority of the water vapor remains of the cathode side. However, some of the water is transported through the PEM to the anode side. The total flux of water vapor is similar to total flux of hydrogen:

$$\begin{aligned} \mathbf{N}_2 = C\left(\Gamma x_2 \frac{\partial C}{\partial x} + \Gamma x_2 \frac{\partial C}{\partial y} - d_{11} \frac{\partial x_2}{\partial x} - d_{12} \frac{\partial x_2}{\partial y} \right) \cdot \mathbf{e}_x + \\ + C\left(\Gamma x_2 \frac{\partial C}{\partial x} + \Gamma x_2 \frac{\partial C}{\partial y} - d_{12} \frac{\partial x_2}{\partial x} - d_{22} \frac{\partial x_2}{\partial y} \right) \cdot \mathbf{e}_y \end{aligned} \tag{25}$$

Because

$$C_2 = \gamma_r C - C_1 \tag{26}$$

We get:

$$x_2 = \gamma_r - x_1 \tag{27}$$

So normal part to the boundary of the water vapor can be calculated as:

$$\Gamma(\gamma_r - x_1)\frac{\partial C}{\partial x} + \Gamma(\gamma_r - x_1)\frac{\partial C}{\partial y} - d_{12}\frac{\partial(\gamma_r - x_1)}{\partial x} - d_{22}\frac{\partial(\gamma_r - x_1)}{\partial y} = (\nu - 1)r_h x_1 \tag{28}$$

After simplification:

$$\Gamma(\gamma_r - x_1)\frac{\partial C}{\partial x} + \Gamma(\gamma_r - x_1)\frac{\partial C}{\partial y} + d_{12}\frac{\partial x_1}{\partial x} + d_{22}\frac{\partial x_1}{\partial y} = (\nu - 1)r_h x_1 \tag{29}$$

Because we assume:

$$\frac{\partial x_1}{\partial x} = 0 \text{ and } \frac{\partial C}{\partial x} = 0 \tag{30}$$

So finally, we get the system of the equations:

$$\begin{cases} \Gamma x_1 \dfrac{\partial C}{\partial y} - D\dfrac{\partial x_1}{\partial y} \cdot = r_h x_1 \\ \Gamma(\gamma_r - x_1)\dfrac{\partial C}{\partial y} + D\dfrac{\partial x_1}{\partial y} = (\nu - 1)r_h x_1 \end{cases} \tag{31}$$

Solving the system of the equations using $\frac{\partial C}{\partial y}$ and $\frac{\partial x_1}{\partial y}$ as variables, we get the Neumann's boundary conditions for C and x_1

$$\frac{\partial C}{\partial y} = \frac{\nu r_h x_1}{\gamma_r \Gamma} \tag{32}$$

and

$$\frac{\partial x_1}{\partial y} = \frac{r_h x_1(\nu x_1 - \gamma_r)}{D\gamma_r} \tag{33}$$

5. NUMERICAL RESULTS

The parameters values used for the GDL model are given below [4]:

	Parameter	Value
Geometry	H (GDL thickness, cm)	0.5
	L (domain width, cm)	1.0
	L_C (channel width, cm)	0.5
Gas properties	Γ (convection, $cm^5/s \cdot mol$	3.24×10^7
	C_g (concentration, mol/cm^3)	3.475×10^{-5}
	D (diffusivity, cm^2/s)	0.29
	r_0 (bottom transfer rate, cm/s)	0.005
	r_H (top transfer rate, cm/s)	0.0625
Nondimensional quantities	$\gamma = C_{1g}/C_g$	0.8
	$\gamma_r = (C_{1g}+C_{2g})/C_g$	0.9
	ν (return coefficient)	0.99

The dependencies between fluxes of species and anisotropy ratio were investigated during the calculations. In the figures 2 and 3 the dependence between flux of the diffusion of the hydrogen and anisotropy ratio is shown.

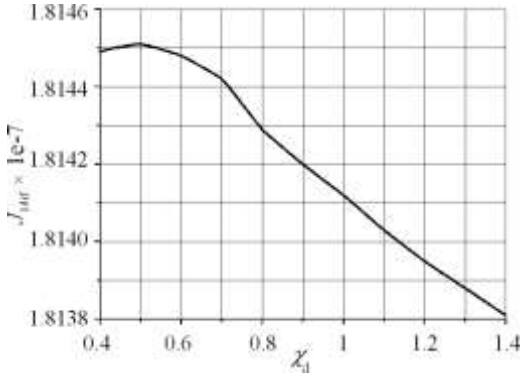

Fig. 2. Dependence between flux of diffusion of the hydrogen and anisotropy ratio at point (L/2,H).

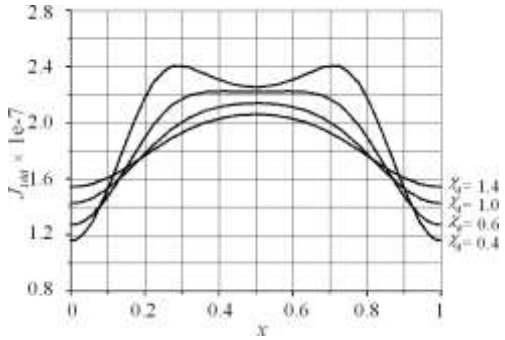

Fig. 3. Dependence between flux of diffusion of the hydrogen and anisotropy ratio GDL.

The calculations were carried out at point (L/2,H) in the middle of top domain boundary and across the GDL at *y*=H/2. We can see that, however, changes of anisotropy ratio have an influence on diffusion flux inside the GDL the changes of the flux near catalyst layer are minimal.

In the figures 4 and 5 we can see that there is almost no influence of anisotropy ratio for flux of the convection of the hydrogen. Also in the case of the diffusion flux, there are minimal changes of convection flux while changing anisotropy ratio at the top boundary at point (L/2,H).

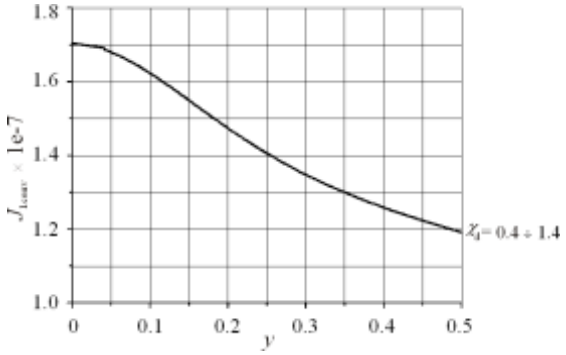

Fig. 4. Dependence between flux of convection of the hydrogen and anisotropy ratio along the GDL.

Because the total flux of the hydrogen is the sum of diffusion and convection flux, the influence of anisotropy ratio for total flux at the catalyst is also minimal (figure 6).

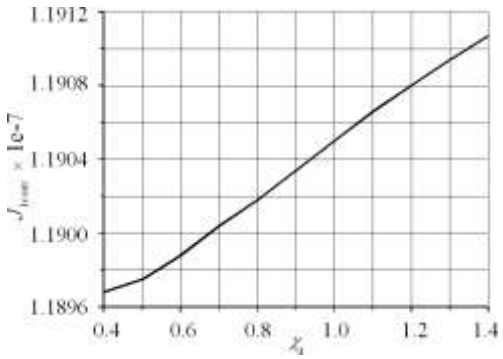

Fig. 5. Dependence between flux of convection of the hydrogen and anisotropy ratio at point (L/2,H).

The calculations are consistent with GDL model without the anisotropy. Comparing results for anisotropy ratio equal 1, which means the diffusion coefficients for both directions, are the same we can see no difference at results between developed model and model described in [4].

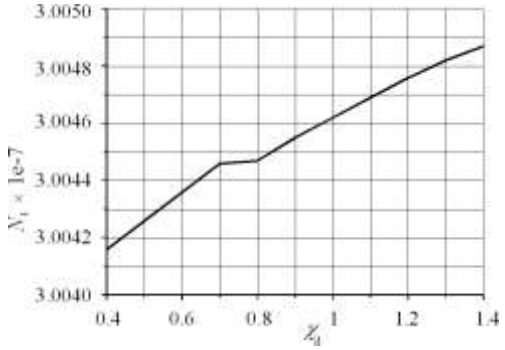

Fig. 6. Dependence between total flux of the hydrogen and anisotropy ratio at point (L/2,H).

6. CONCLUSIONS

The gas diffusion layer is an essential component of the proton exchange membrane fuel cell. However, most of the models of the fuel cell have focused on the complex mass, heat and change transfer simplified the process by assuming mass transport coefficients are constant and isotropic.

In this paper we present a model of multicomponent gas transport in the GDL which includes the anisotropy of porous fiber paper constructing the GDL. However, the anisotropy of diffusivity was respected the convection coefficients to be anisotropic as well. In the further work we will draw our attention to physics and material aspects of transport in GDL as much as possible.

ACKNOWLEDGEMENTS

This work was supported by AGH University of Science and Technology under grant 10.10.120.417.

REFERNCES

[1] R. B. Bird, W. E. Steward, E. N. Lightfood, Transport Phenomena, John Wiley & Sons, New York, 1960.
[2] R. Taylor, R. Krishna, Multicomponent mass transfer, John Wiley & Sons, New York, 1993.
[3] E. L. Cussler Multicomponent Diffusion, Elsevier Scientific Publishing Company, Amsterdam – Oxford – New York, 1976.
[4] K. Promislow, J. Stockie, Adiabatic relaxation of convective-diffusive gas transport in porous fuel cell electrode, SIAM J. Appl. Math, vol. 62, no 1, 2001, 180 – 205.
[5] K. Promislow, J. Stockie, B. Wetton, A finite volume method for multicomponent gas transport in a porous fuel cell electrode, Int. J. Numer. Math. Fluids 2003, 41: 577–599.
[6] E. Kurgan, Fuel cells – their essence and futures, Proc. of Seminar on Electrical Engineering BSE'2002, vol. 14, Istebna, 2002.

ELECTROMAGNETIC PROCESSES AND DEVICES FOR SUSTAINABLE DEVELOPMENT

4th International Conference **ELMECO**
Nałęczów, Poland
September 2003

TAKING ADVANTAGES RESULTING FROM MEASUREMENTS OF PARTICLE ELECTRIC PROPERTIES TO VERIFY GRAIN MILLING QUALITY

Marek HORYŃSKI

Lublin University of Technology,
20 - 618 Lublin, Nadbystrzycka 38A,
e-mail: mhor@elektron.pol.lublin.pl

Abstract

Grain electric properties such as: resistivity and electric permittivity are extremely important to dust removal efficiency by electrostatic filters. Test results suggest possibility to apply dust electric properties to evaluate grain milling quality and to detect impurities either in the material subjected to milling or in the product. The paper presents a laboratory stand, measurement procedures for electric permittivity and test results of frequency characteristics for grain fractions obtained from milling processes in a wheat mill.

Keywords: electric properties, grain milling, flour quality, frequency.

1. INTRODUCTION

Dielectrics consist of molecules that can be treated as electric systems consisting of positively charged nuclei surrounded by negative clouds of electrons. The external electric field acts on these charges and moves them. In symmetrically constructed molecules, the centres of gravity of positive and negative charges are in the same places and the molecule does not generate any external electric field. The introduction of such molecule in the external electric field causes some movement of the electron cloud in relation to the nucleus and then induced dipole moments occur resulting in a, so called, dielectric electron polarization.

Three dielectric properties: real and imaginary part of dielectric permittivity and dissipation factor can be presented vs. frequency in certain temperature T = const.

These graphs are called isotherms. They can be presented as the function of temperature when frequency f = const. They are called isochrones then. Grain fractions of different granulation occur in the result of industrial milling processes. These grain particles are dielectrics.

In the case of non-polar dielectrics [1] that have only electron polarization the dielectric loss coefficient is inversely proportional to the frequency:

$$tg\delta = \frac{1}{2\pi\ f\varepsilon\ \rho_S} \tag{1}$$

where: ρ_S - resistivity, f - frequency, ε - electric permittivity.

In the case of polar dielectrics, together with the frequency increase, the loss coefficient increases at the beginning because the loss of energy that goes to one turn of a dipole per time unit is greater. Then, at further frequency increases the loss becomes smaller because the turns cannot follow field changes any more. The dipole polarization component fades. The dependence of the loss coefficient on temperature can be different.

The parameter that is used to describe material electromagnetic properties is usually conductivity σ, electric permittivity or magnetic permeability. The conductivity is described by the following expression:

$$\sigma = 2\pi f \varepsilon_0 \varepsilon'', \tag{2}$$

where: σ - conductivity, f - frequency, ε_0 - vacuum electric permittivity, ε'' - imaginary component of complex electric permittivity.

Dielectrics consist of molecules that can be treated as electric systems consisting of positively charged nuclei surrounded by negative clouds of electrons. The external electric field acts on these charges and moves them. In symmetrically constructed molecules, the centers of gravity of positive and negative charges are in the same places and the molecule does not generate any external electric field. The introduction of such molecule in the external electric field causes some movement of the electron cloud in relation to the nucleus and then induced dipole moments occur resulting in a, so called, dielectric electron polarization.

The resistivity differs not only because of the type of material but also, in the case of biological materials, because of humidity and temperature. At higher temperatures collisions between electrons occur more frequently and thus shorten time intervals between collisions which results in higher resistivity. Because the resistivity is inversely proportional to the amount of free electrons in materials, these metals that have more free electrons per volume unit have much lower resistivity than the other ones.

The inverse of resistance R is conductance G. The inverse of resistivity is conductivity:

$$\sigma = \frac{1}{\rho} = \frac{L}{RS}, \tag{3}$$

where: ρ – resistivity, Ωm; L – conductor length, m; S – conductor cross-section area, m^2.

2. LABORATORY STAND

Dust electric properties are measured on the original test stand designed for the purpose of this research (Fig. 1). This stand enables to perform automatic process of investigations. Computer in this arrangement has three functions: the first one is registration of measured capacitance and resistance, the second aids calculations and the third visualization of measured and calculated dust electric properties.

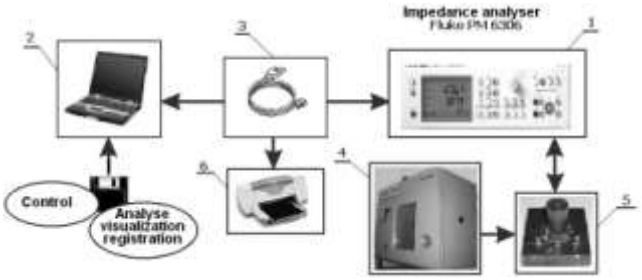

Fig. 1. Test stand: 1 - impedance analyzer, 2 – computer, 3 – connecting cable RS – 232, 4 - climatic chamber, 5 - measuring cylindrical capacitor filled by wheat fractions, 6 – printer.

3. MEASUREMENT PROCEDURES

The measurements methodology is the following: before measurements grain dust is specially prepared. The investigated object is a dielectric dust generated from milling processes of wheat grain. The dusts are divided into fractions and size classes [2].

The generation of particular dust fractions and size classes from the previously prepared raw material by means of a disc mill. The disk mill has the feature to control the milling gap width and mutually to sieve out the dust on specially designed sieves. The sieves are removable and have the following size of mesh: 500 μm, 230 μm and 150 μm.

The fractioned dust is placed in the climatic chamber before measurements.

After 72 hours a sample has been taken out and put in the measuring capacitor. Every time the measuring conditions and the way of introduction of dielectric samples to the capacitor must be maintained the same.

The capacitance is measured by means of the impedance analyzer PM3606 (Fig. 1).

The real component of complex electric permittivity for dielectric dust has been determined from the dependence:

$$\varepsilon' = \frac{C_r}{C_0} \tag{4}$$

where: C_r – capacity for the filled in capacitor, F; C_0 – capacity for the empty capacitor (air), F.

The imaginary component has been determined from the formula (5):

$$\varepsilon'' = \varepsilon' \tan\delta \tag{5}$$

where: δ - dielectric loss angle; $\tan\delta = 1/Q$ - dielectric loss angle tangent; Q - capacitor quality factor, obtained from impedance analyzer measurements.

4. RESULTS

The analysis of results helps to find out:

- Electric permittivity varies together with the voltage frequency. Electric permittivity of fractions differs in dependence on water content and voltage frequency (Fig. 2.).

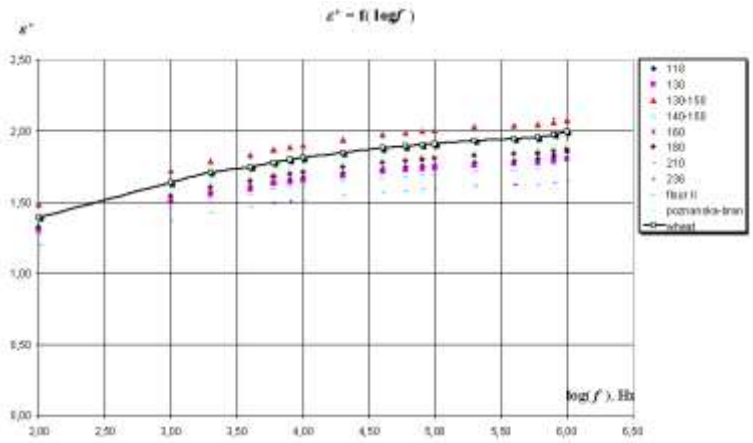

Fig. 2. The dependence of real component of complex electric permittivity for milled wheat fractions vs. voltage frequency: m.c. = 13%, T = 294 K.

- The real component of the dust electric permittivity rises together with the frequency increase. It is linearly decreasing.
- Test results suggest possibility to apply dust electric properties to evaluate grain milling quality and to detect impurities either in the material subjected to milling or in the product.

This research has been supported by Scientific Research Committee in 2002-2004 (grant No: 4 T10C 037 23).

REFERENCES

[1] Chełkowski A., Physics of dielectrics, Wydawnictwo Naukowe PWN, Warszawa 1993, pp. 11-18.

[2] Horyński M., W. Pietrzyk, A. Sumorek, M. Ścibisz, S. Walusiak, S. Grundas, Bifilar windings to dust control in agri-food industry, Acta Agrophysica PAN, Nr 43, Lublin 2001, monografia, ISBN 83-87385-61-3, pp. 58-60.

4th International Conference **ELMECO**
Nałęczów, Poland
September 2003

USING MAXWELL-STEFAN EQUATIONS IN ANALYSIS OF GAS DISTRIBUTION IN FUEL CELLS

Eugeniusz KURGAN, Paweł SCHMIDT

AGH University of Science and Technology, Dept. of Electrical Engineering
al. Mickiewicza 30, 30-059 Krakow, Poland
e-mail: kurgan@agh.edu.pl, pschmidt@agh.edu.pl

Abstract

The present article describes the method of computation of gas distribution in the cathode of the fuel cell. The diffusion coefficients are calculated using Maxwell-Stefan equations and then finite element method to solution of resulting partial differential equations is used. At the end some illustrative example is given.

Keywords: fuel cell, Maxwell-Stefan equation, mass transport, PEM, GDL.

1. INTRODUCTION

The present paper describes the method of computation of the polarization and secondary current density distribution in corroding pipe structure by means of finite element method. It is possible to determine minimum value of supply voltage sources to produce yet full protection against corrosion. At the end some illustrative example is given.

2. GOVERNING EQUATIONS

Let us consider diffusion layer in the cathode of the PEM fuel cell as in Fig. 1.

In the case when mixture consists of N species, the driving force of species i is balance by sum frictional drags of all other species, thus the Maxwell-Stefan equations for multicomponent in the case is given by [3,4]

$$-\nabla x_i = \sum_{\substack{j=1 \\ j\neq i}}^{N} \frac{x_j \mathbf{N}_i - x_i \mathbf{N}_j}{c_t Đ_{ij}} = \sum_{\substack{j=1 \\ j\neq i}}^{N} \frac{x_j \mathbf{J}_i - x_i \mathbf{J}_j}{c_t Đ_{ij}} \quad i = 1,2,...,N \tag{1}$$

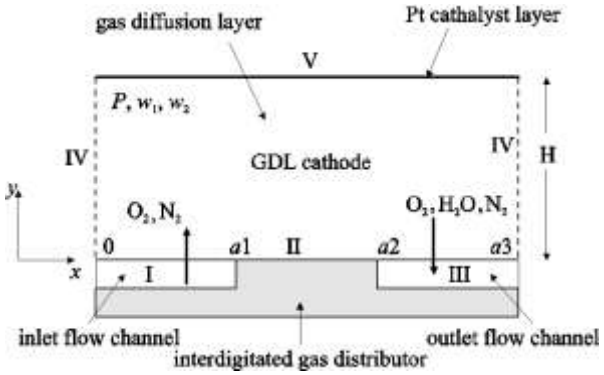

Fig. 1. Geometry and system variables in cathode of the PEM fuel cell.

The driving force in vector form can be written for all three coordinates as

$$\mathbf{f}_i = -\nabla \mu_i \tag{2}$$

If we introduce the following definition of quantity $\mathbf{d}_i$

$$\mathbf{d}_i = -\frac{x_i}{RT}\nabla \mu_i \tag{3}$$

what is equal to the left side of Maxwell-Stefan equation, then

$$\mathbf{d}_i = \frac{x_i}{RT}\mathbf{f}_i \tag{4}$$

and driving force acting on one mole of the species *i* will have the following form

$$\mathbf{f}_i = \frac{RT}{x_i}\mathbf{d}_i \tag{5}$$

Not all *N* Maxwell-Stefan equations are independent. Because of the Gibbs-Duhem restriction

$$\sum_{i=1}^{N} c_i \nabla_T \mu_i = \nabla p \tag{6}$$

only $N - 1$ equations are independent because.

$$\sum_{i=1}^{N} c_i \nabla_T \mu_i = \sum_{i=1}^{N} c_i \frac{RT}{x_i}\nabla x_i = cRT\nabla\left(\sum_{i=1}^{N} x_i\right) = cRT\nabla(1) = 0 \tag{7}$$

The N^{th} component is chosen arbitrary and artificially as solvent. This does not mean that this component occurs in the greatest quantity. Even just the opposite, its molar or mass contribution can be the smallest. Elimination $\mathbf{J}_N$ from relation:

$$\mathbf{J}_N = -\sum_{j=1}^{N-1} \mathbf{J}_j \tag{8}$$

and collecting coefficients by the same $\mathbf{J}_j$ we get

$$-c\nabla x_i = \sum_{\substack{j=1 \\ j\neq i}}^{N-1} B_{ij}\mathbf{J}_j \tag{9}$$

where

$$B_{ii} = \frac{x_i}{Đ_{iN}} + \sum_{\substack{k=1 \\ k\neq i}}^{N} \frac{x_k}{Đ_{ik}} \tag{10}$$

$$B_{ij(i\neq j)} = -x_i\left(\frac{1}{Đ_{ij}} - \frac{1}{Đ_{iN}}\right) \tag{11}$$

where $i, j = 1, 2, \ldots, N-1$ and species N is chosen as solvent. When we solve these $N-1$ equations in terms of $N-1$ diffusion fluxes $\mathbf{J}_j$ we get generalized form of the Fick's formulation of the multicomponent mixtures.

$$\mathbf{J}_i = -c\sum_{j=1}^{N-1} D_{ij}\nabla x_j \tag{12}$$

In matrix notation we have for $i, j = 1, 2, \ldots, N-1$ the following relation

$$\left[D_{ij}\right] = \left[B_{ij}\right]^{-1} \tag{13}$$

Generally for arbitrary value of N it is impossible to solve this equation symbolically, but for special case when $N = 3$ it is quite possible. In this case we will have two equations in two unknowns. For ternary system we have

$$\begin{bmatrix}\mathbf{J}_1 \\ \mathbf{J}_2\end{bmatrix} = c\begin{bmatrix}D_{11} & D_{12} \\ D_{21} & D_{22}\end{bmatrix}\begin{bmatrix}\nabla x_1 \\ \nabla x_2\end{bmatrix} \tag{14}$$

where D_{ij} are Fick's diffusion coefficients depending now on molar fractions of mixture components x_i and binary diffusion coefficients $Đ_{ij}$. For convenience all four coefficients are collected together:

$$D_{11} = \frac{Đ_{13}}{\Delta}\left[Đ_{23}x_1 + (1-x_1)Đ_{12}\right] \tag{15}$$

$$D_{12} = \frac{Đ_{23}}{\Delta}(Đ_{13} - Đ_{12})x_1 \tag{16}$$

$$D_{21} = \frac{Đ_{13}}{\Delta}\left(Đ_{23} - Đ_{12}\right)x_2 \tag{17}$$

$$D_{22} = \frac{Đ_{23}}{\Delta}\left(Đ_{12} + \left(Đ_{13} - Đ_{12}\right)x_2\right) \tag{18}$$

$$\Delta = x_1 Đ_{23} + x_2 Đ_{13} + x_3 Đ_{12} \tag{19}$$

Let us assume further that $D_{11} = D_{22} = D$ and other two diffusion coefficients are equal zero, then distribution of gases in diffusion layer can be described by the following three nonlinear partial differential equations:

$$\frac{\partial}{\partial t}\left(MP\right) - \frac{k_p}{\mu}\nabla\left(MP\nabla P\right) = 0 \tag{20}$$

and in terms mass fraction of oxygen w_1 and water vapor w_2 ($i = 1, 2$):

$$MP\frac{\partial w_i}{\partial t} - D_i\nabla\left(MP\nabla w_i\right) - \frac{k_p}{\mu}MP\nabla P\cdot\nabla w_i = 0 \tag{21}$$

3. AN ILLUSTRATIVE EXAMPLE

The example solved here is the same as in publication [5] but instead of given a priori Fick's diffusion coefficients are calculated by Maxwell-Stefan equations. Prior to time $t = 0$ sec values of all system variables in computational domain were assumed as inlet boundary values, that is as given in advance. At time $t = 0$ sec value of pressure P at outlet channel fall suddenly down from $P = 1{,}03$atm to $P^{out} = 1.0$atm [1]. This caused unsteady state of all variables. First system variables P, w_1 and w_2 as function of space and time were calculated and next current density distribution (Fig. 2 and 3) on the catalyst layer from the equation [2].

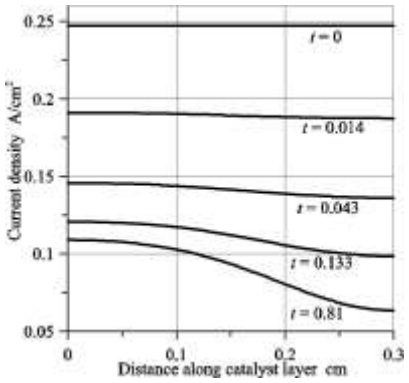

Fig. 2. Time evolution of the current density along catalyst layer.

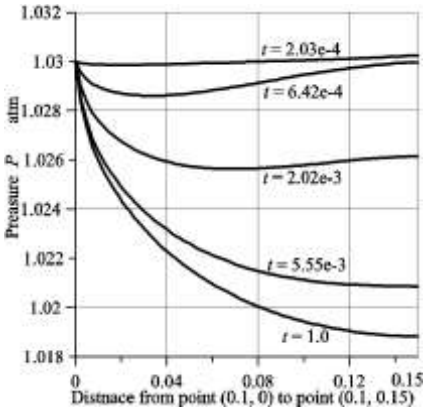

Fig. 3. Evolution pressure P along the path from point (0.1, 0.0) to point (0.1, 0.15).

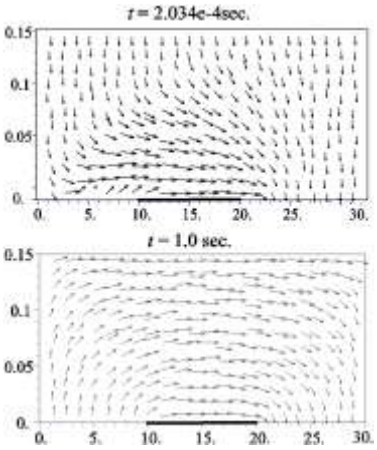

Fig. 4. Mixture velocity **u** at two different times: t = 2.034e-4 sec. and t = 1.0 sec.

4. CONCLUSIONS

It was shown that it is possible to apply finite element method to calculate distribution of reacting species in cathode of the fuel cell. Computation diffusion coefficients using Maxwell-Stefan equations is more accurate than applying these coefficients in Fick's form.

ACKNOWLEDGEMENTS

This work was supported by the University of Mining and Metallurgy, under grant 10.10.120.417.

REFERENCES

[1] I-Ming Hsing, P. Futerko, Two-dimensional simulation of water transport in polymer electrolyte fuel cells, Chemical Engineering Science, vol. 55, 2000, 4209 – 4218.

[2] J. S. Yi, T. V. Nguyen, Multicomponent transport in porous electrodes of proton exchange membrane fuel cells using the integrated gas distributors, Journal of the Electrochemical Society, vol. 146, no 1, 1999, 38 – 45.

[3] R. B. Bird, W. E. Steward, E. N. Lightfood, Transport Phenomena, John Wiley & Sons, New York, 1960.

[4] R. Taylor, R. Krishna, Multicomponent mass transfer, John Wiley & Sons, New York, 1993.

[5] E. Kurgan, Time domain model of gas distribution for the cathode PEM fuel cell, 11th International Symposium on Electromagnetic Fields in Electrical Engineering, Maribor, Slovenia, 2003.

[6] D. Singh, D.M. Lu, N. Djilali, A two-dimensional analysis of mass transport in proton exchange membrane fuel cells, J. Engrg. Sci. 37, 1999, 431–452.

4th International Conference **ELMECO**
Nałęczów, Poland
September 2003

TEMPERATURE FIELD ANALYSIS IN PASSIVE SOLAR WALLS

Dorota WÓJCICKA – MIGASIUK

Lublin University of Technology, Faculty of Civil and sanitary Engineering,
Dept. of Heating, Ventilation and Automation
ul. Nadbystrzycka 40, 20-618 Lublin
e-mail: dorota@akropolis.pol.lublin.pl

Abstract

The basis for this paper is formed on the reference [1,2] that present assumptions to provide self – heating of livestock buildings and the simulation analysis [3]. There has been found that the application of a composed structure, called Trombe wall, can distinctly improve thermal and air humidity conditions in these objects. This can be achieved with no additional energy supply. Some average calculation of thermal balance estimation is presented. Figures show FEM mesh on the analyzed object and transient results. Transient results show maps of isotherms indicating possible areas of condensation below the dew points that are vulnerable to mould growth.

Keywords: simulation analysis, temperature field, heat flux, solar passive.

1. INTRODUCTION

The purpose for simulation has been discussed a number of times and the author shares the undoubted opinion that this type of research cannot replace experiments, especially in relation to biological materials. Simulation analyzes can, however, simplify experimental research directions and prognoses. They can significantly reduce the need for experiments to some strictly necessary number to verify simulation results. They can correct and supplement each other.

Clarke J.A. [6] presents a wide range of possibilities to apply simulations in energy transfer presentations in building systems. HVAC systems are frequently the subject of traditional dimensioning, mostly in steady state conditions, when assumed inputs are based on ideal operation of particular incorporated systems, i.e.: heating, ventilation, air conditioning, cooling, even lighting and, if applicable, special environmental protection systems. One of the reasons for this is the large number of parameters, their options and need for multi-criterion optimization which leads to complex multinomial nonlinear systems of equations subjected to simulations. The other cause is that manufacturers and their constructors and designers would rather provide information on a system's operation

than precisely describe thermodynamic properties sufficient to perform a highly reliable simulation. That is why, simulations can still be used rather as a research tool than a designing one. Nevertheless, being aware of the continuous simultaneous influence among the building and its, often, hybrid plants one can take all advantages of simulation results to support the designing, particularly, of complex integrated systems to form indoor climate in the building in a sustainable way.

The basis for this paper is formed on the reference [1,2] that provide assumptions for self – heating of livestock buildings and on author's previous works on simulation analysis in solar design. There has been found that the application of a composed structure, called Trombe wall, can distinctly improve thermal and air humidity conditions in these objects. This can be achieved with no additional energy supply. Some average calculation of thermal balance estimation is presented related to climatic conditions in the central-eastern region of Poland. The analysis has been performed by Flux 2D.

2. HEAT TRANSFER THROUGH TROMBE WALLS

The demand for ventilation in livestock buildings results mostly from the need to remove moisture from these objects. Excess humidity leads to mould growth on the walls and makes the interior climate worse which has negative impact on animal production.

The conditions for self-heating and proper insulation have already been presented [1,2]. One of the aspects in proper insulation is worse humidity condition at the same time. Foamed polystyrene panels are frequently used because of reasonable price and easy construction but they make self-drying difficult for walls.

External walls of composed structure can be a passive solar system and thus improve thermal balance in the object. Trombe walls, patented in 19th century but used successfully for dwellings only in America, can significantly improve thermal balance in our climatic conditions too, especially in less restrictive buildings such as pigsty, cow house, etc. The construction of an uniform wall can consist of high thermal capacity elements such as massive walls, transparent insulation materials (TIM) or glass covers, antireflection surfaces, and layers of porous materials which are moisture transport zones. Glass panels let solar radiation in and also cover connective heat exchange channels.

The air circulation between a room and a Trombe wall is the following and the model is presented in Fig. 1.:

- external air lets in through the channel inlet below the glass cover,
- in the result of the heating from solar radiation and convection the air flows up to the inlet channel to the room,
- the air in the room is cooled and lows down and is removed through the bottom outlet channel,
- partial recirculation occurs and fresh air together with the recirculated volume is introduced to the cycle again under the glass cover,
- during night hours external outlets must be covered and insulated together with the glass panel – then the circulation is also possible because the massive part of the wall has accumulated heat.

Moreover, the other walls in the building must be properly insulated so the heat loss to the ambience is to be minimal.

The presented model has been analyzed by FEM in Flux 2D [5]. Fig. 1 presents the south oriented system during a day time phase with no insulation panels on the glass cover.

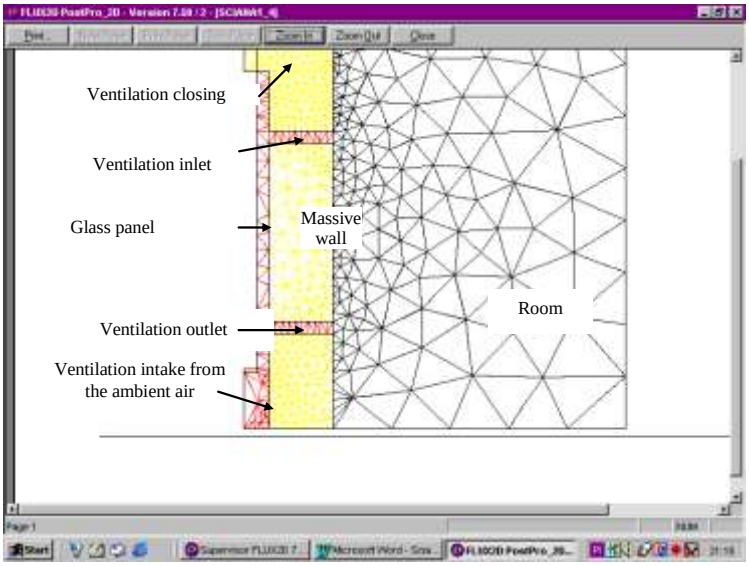

Fig. 1. Geometric model of Trombe wall with construction elements and finite element mesh for simulation analysis.

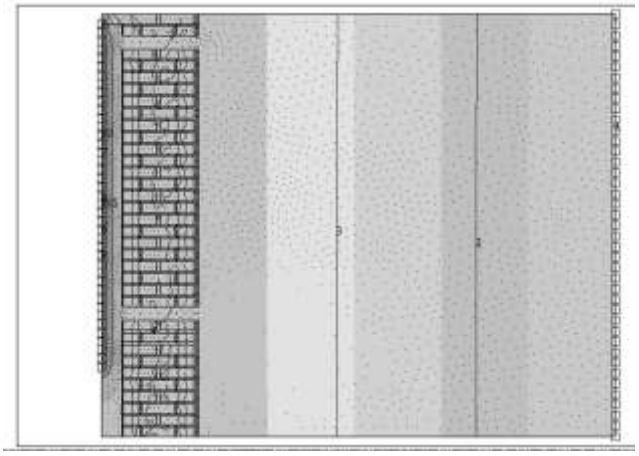

Fig. 2. The distribution of isotherms after 1 hour simulation at peak solar irradiance in spring season. Dots indicate mesh nodes, squares indicate Dirichlet's conditions on domene boundaries.

The analysis is the introductory part in the described problem. Figs. 2 and 3 present the resulting map of isotherms. The image indicates some areas of lower temperature than

surrounding areas (Fig. 2.). These indicate areas of mould hazard – humid air can enter the areas and reduce its temperature below the dew-point.

Some other results show that temperature at inner surfaces of walls does not drop below 15oC if ambient temperature is not lower than 5 ^{o}C. This suggests that no extra heating is required then. There are some isolines on an animal, which are to be neglected, as this software is not suitable to analyze living objects. These results give good reason to compare a building with a solar passive system to a traditional one. The procedure of the analysis is according to the reference instructions [5] and was described in detail in previous works [3].

3. THE COMPARISON

The comparison between the ventilation demand of a pigsty to the possibility of the ventilation through the Trombe wall enables us to estimate the improvement of thermal conditions in the analyzed object. The comparison is between the object described in [1] and the hypothetic one in which the southern wall is a Trombe wall. Table 1 presents some selected data for the object. The population of animals is established according to [2].

Selected specification for the compared pigsty		Pigsty mean population	
SW wall – area without doors and windows m^2	53,7	Mean mass of 1 animal, kg	75
SW windows – surface, m^2	6,5	Mean population, pcs.	266,6
Heat amount required to heat up the ventilated air for pigs W/h	37383	Emitted heat per kg, W/kg	0,534
Total thermal loss through SW wall, W/h	3034	Total heat emitted by the population, W/h	16850

The volume of the ventilation air should be within the range 0.12 – 0.7 m^3h^{-1} per kg of animal mass. At mean exemplary population of 266.6 pcs and mean animal mass of 75 kg, one can obtain the volume between 2399.4 m^3h^{-1} and 13996.5 m^3h^{-1}.

Channels in Trombe wall let the ambient air flow in heated of $\Delta T = 15K$ and humidity 40% lower at 0.8 m/s (as for natural ventilation) through holes of 0.0495 m^2 per m^2 of the wall. The humidity drop is determined from Molliere's h – x graph for the assumed heating-up in the result of flow through the channels.

Assuming from [1] the wall surface is 60.2 m^2 which gives the air flux up to 8582.1 m^3h^{-1}. This value is in the mean range of the demand. In winter, this flux can be reduced to minimum by the regulation of openings on ventilation holes. The expected result is that the determined negative thermal balance of -20533 W/h, between the emitted heat by animals and the heat loss caused by ventilation, can be removed. Some excess heat is even probable which can improve the total thermal balance that is deteriorated by the heat loss through the other walls, the ceiling and the floor.

The application of the collector wall causes that this wall does not need a foamed polystyrene insulation which can be used for night covers. The isotherm map in Fig. 3 proves that this wall temperature does not drop even at low ambient temperatures. Another gain is then obtained because there is no the assumed heat loss of 3034 W/h for this wall. Only in the case of piglet pens extra heating is needed.

As frequently mentioned [4], farmers are investors and manufacturers and thus all modernization works must take into account his technical capabilities. Solar walls, however unconventional, are simple to construct and available for most of farms.

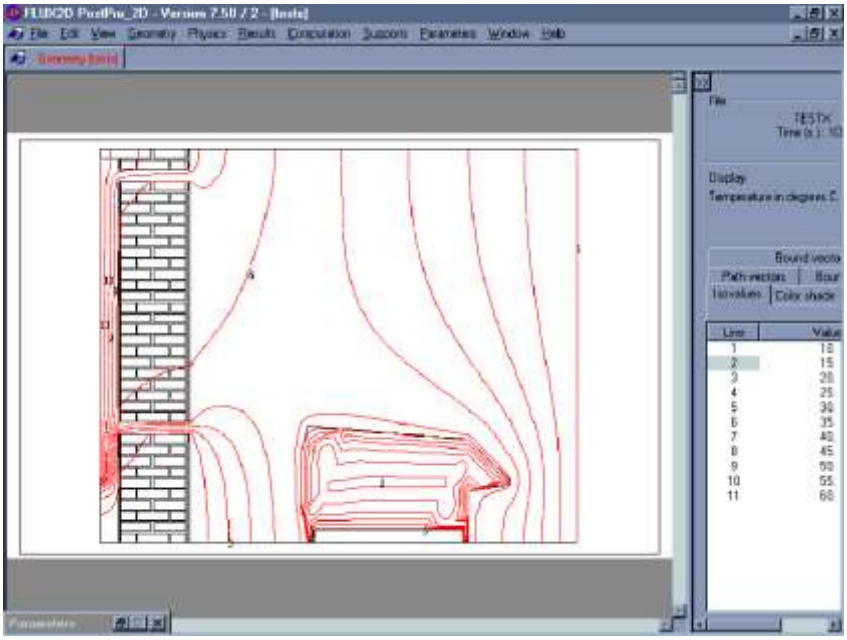

Fig. 3. Isotherm transient distribution in the analysed pigsty building.

4. CONCLUSIONS

The application of a solar wall can significantly improve thermal conditions in buildings. For the analysed object 22.3 kWh gain can be obtained. Moreover the humidity in the building can be reduced by the supply of the ventilated air of 40% lower humidity than in the ambient air. Even at -20^{o}C the self-heating for the building can be ensured if solar walls are applied as southern walls. The only restriction is when piglets are kept in the same building then additional conventional heating must be provided.

The research will be continued in the form of tests on physical models of Trombe wall in a climatic chamber to investigate the real heat transfer. Such tests could help to develop design procedures for solar walls in local climatic conditions.

REFERENCES

[1] Olkowska W.: Self heating of livestock buildings. (in Polish) Problemy Inżynierii Rolniczej 1, 1995, p. 109-119.

[2] Gedymin M.: Simplified method to calculate insulation thickness on self-heated livestock buildings.(in Polish), Problemy Inżynierii Rolniczej 1, 2000, p. 57 – 63.

[3] Wójcicka – Migasiuk D., The analysis of thermal states in external walls in passive solar systems. (in Polish) Techniczne, Ekologiczne i Ekonomiczne Aspekty Energii Odnawialnej, Wyd. SGGW Warszawa 2001, p. 104 – 111.
[4] Szeptycki A.: Problems of technical infrastructure in rural regions. (in Polish) Problemy Inżynierii Rolniczej 1, 2000, p. 65 – 70.
[5] Cedrat, Flux 2D v.7.50 Tutorials 2000.
[6] Clarke J.A. Energy simulation in buildings. Butterworth-Heinemann, Oxford, 2001.
[7] Wójcicka – Migasiuk D., The application of Trombe walls in livestock buildings (in Polish), Acta Agrophysica IA PAN Lublin, 2003, p. 205-210.

4th International Conference **ELMECO**
Nałęczów, Poland
September 2003

LABORATORY OF THE PHOTOVOLTAIC SYSTEMS

Krzysztof NALEWAJ

Institute of Electrical Engineering and Electrotechnologies,
Lublin University of Technology,
38A Nadbystrzycka St., 20-618 Lublin
e-mail: krzynal@eltecol.pol.lublin.pl

Abstract

This paper describes the possibilities of using solar energy in Poland, mainly in the Lublin Province. Initially, the laboratory of solar energy consisted of the test stand with six photovoltaic panels BPS 275 of maximal power 75W each. Photovoltaic panels have been placed on the roof construction on the four-storey building where the Faculty of Electrical Engineering of Lublin University of Technology is located. Results of the research carried out in the laboratory of solar energy at the Institute of Electrical Engineering and Electrotechnologies, the Faculty of Electrical Engineering, Lublin University of Technology have been presented.

Keywords: solar energy, photovoltaic panels.

1. INTRODUCTION

Poland is situated in the moderate climatic zone between 49^{o} and 54.5^{o} of the northern latitude. Daily interval (time from the sunrise to the sunset) covers over 51% of 8767 hours in the average year, and this period is longer of 24 hours in the northern parts compared with the southern ones. In winter, day is longer in southern regions of Poland of almost 1 hour compared with the northern regions whereas it is quite opposite in summer.

The scientific research that have already been carried out at the Institute of Electrical Engineering and Electrotechnologies for several years are aimed to evaluate the possibilities of solar systems' application in the region of the Lublin Province. The test stand described in the paper has been situated in so called helio-power part of the country – Podlasko-Lubelskie region, that has been regarded as the second region in respect of the demand for solar energy. Conducted research allow practically check the availability of solar energy in Lublin [1].

However, the research on the application of the heat pump for common usage, carried out in the laboratory of thermal energy at the Institute of IEEE resulted in designing heat pump model and the test stand of EDA SA. The construction of integrated heat system

comprising liquid solar collector, heat pump supplied from solar battery and system of heat removal is intended. Photovoltaic system that consists of six batteries of 450W and accumulator set is supposed to supply the heat pump in the period of high insolation. In the period of insufficient solar radiation intensity, the heat pump will be supplied from power network [2,3].

The research will contribute to the estimation of the usability of the described system, and its efficiency in the climatic conditions of the Lublin Province.

2. TEST STAND DESCRIPTION

The test stand has been located on the roof construction on the four-storey building in which, the Faculty of Electrical Engineering of Lublin University of Technology is located. Photovoltaic system units have been constructed with the financial support of Tempus Project.

The following elements constitute the system:

- photovoltaic panels BPS 275 BP Solar; total power 6x75W=450W,
- accumulator battery BP Solar 12V, capacity 640 Ah,
- control system BP Solar,
- Trace DR1512 inverter,
- PCL 818 HG Advantech measuring card,
- PC Pentium,
- single-phase induction meter,
- CM 3 pyranometer,
- voltage divider system with 12V measuring card,
- analogue meters with current and voltage shunts in meter circuit.

The operation of test stand has been presented below.

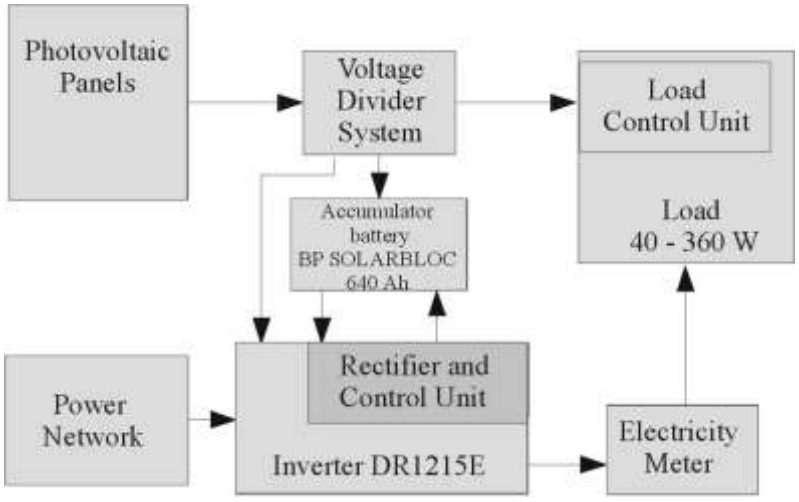

Fig. 1. Block diagram of test stand

Solar battery consists of six BP 275 modules. The parameters of each module are listed below:

- Maximum Power Point 75 W
- Peak Power Voltage, V_{mp} 17,0 V
- Peak Power Current, I_{mp} 4,45 A
- Short Circuit Current, I_{sc} 4,75 A
- Open Circuit Voltage, V_{oc} 21,4 V
- Reference Insolation 1000 W/m^2
- Temperature 25°C

Active array of tested battery:

$$A = \text{width x length x amount} = 0{,}5148 \cdot 1{,}1868 \cdot 6 = 3{,}67 m^2$$

The array has been located on the roof construction on the building of the Faculty of Electrical Engineering. The construction T6 enables to control the inclination angle.

Fig. 2. Photovoltaic Array BP 275

3. RESULTS OF THE RESEARCH ON SOLAR BATTERY

The measurements were taken in the system presented in Fig. 3. In this system, the bulbs (z), 60W each and sliding resistor were applied as receivers (R). The measurements were taken for several insolation values.

The researches were carried out with the application of the computer equipped with the measuring card. Professional software Genie was applied to develop suitable measuring method (Fig. 4). Essential parameters of the system such as solar battery voltage, current intensity, accumulator voltage, current flowing from and to the accumulator, current of the receiver, insolation have been measured with the application of PCL-818 PC measuring card. The card is provided with eight measuring input channels, two control output channels as well as output for pulses or signal release.

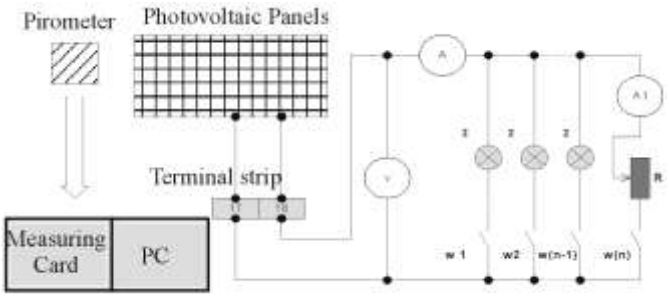

Fig. 3. Diagram of the Measuring System (Meter Circuit)

Data processing and the visualization has been performed with the application of GENIE 2.11 software adjusted to the card. Therefore, measurement results could be stored on a hard disc.

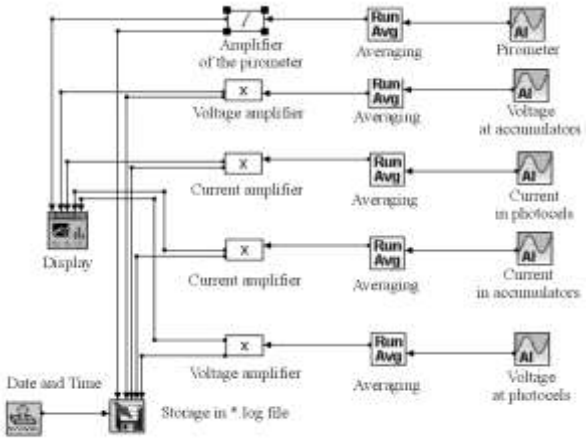

Fig. 4. Measurement with the application of Genie 2.11 software for separate channels

The devices could be graphically displayed and their indications could be easily analyzed. Selection of certain measuring channel assures required display of the devices, precise display and the presentation of diagrams of certain time intervals.

The results of measurements were recorded every second as text file *.log, then the data were transmitted to Microsoft Excel.

4. MEASUREMENTS OF ELECTRIC VALUES

The results of measurements have been presented in Table 1(at changeable insolation).

Tab.1. Measurements taken at various insolation.

No	Insolation I=300W/m^2 ±10%				Insolation I=450W/m^2 ±10%				Insolation I=900W/m^2 ±10%			
-	Active flank of the generator A= 3,67m^2											
-	I_g	U_g	P_{max}	η_g	I_g	U_g	P_{max}	η_g	I_g	U_g	P_{max}	η_g
-	A	V	W	%	A	V	W	%	A	V	W	%
1	0	19,5	0		0,0	19,5	0		0,0	20,5	0	
2	2,0	19,0	38,0		1,5	19,2	28,8		2	19,9	40	
3	3,5	18,5	64,7		3,5	18,6	65,1		3,5	19,6	67	
4	5,5	17,5	96,2		5,0	18,3	91,5		5	19,2	96	
5	7	16,6	116,2		7	17,5	122,5		7	18,7	131	
6	8	15,5	124,0		8,5	16,5	140,3		8,5	18,4	156	
7	8,5	12,5	106,2		9,5	15,6	148,2		11	17,6	194	
8	8,5	10,0	85,0		10,5	15,3	160,6		18	15,36	276	
9	8,5	8,0	68,0	11,3	11,4	13,5	153,9	9,7	22,5	13,73	309	
10	8,5	6,0	51,0		11,4	10,0	114,0		25	12,61	315	9,5
11	8,5	3,0	25,5		11,4	6,0	68,4		26	11,7	304	
12	-	-	-		-	-	-		27,5	9,7	267	
13	-	-	-		-	-	-		27,5	4	110	

where:
U_g – voltage of solar battery,
I_g – current intensity of solar battery,
P_{max} – maximal power of solar battery,
η_g – efficiency of solar battery.

The measurements taken enabled to present voltage-current characteristic (Fig. 5).

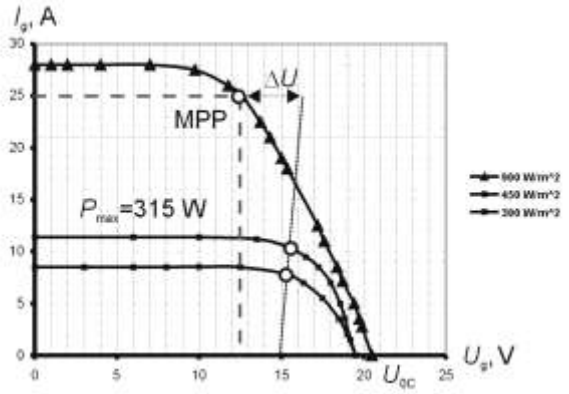

Fig. 5. Voltage-current characteristic at different insolation

The analysis of measurements revealed, that the efficiency of solar battery at the insolation of 300W/m^2 is around 11,3% and this value drops down to 9,5% along with higher insolation.

The essential factor that causes lower efficiency of the battery is significant voltage drop in the conductors connected with the measuring system. At the insolation of 450W/m^2 current flowing from the battery does not exceed 12A then, voltage drop is negligible. However, if the insolation reach 900 W/m^2 therefore maximal point will be shifted to the left and voltage drop amounts to ΔU=2,5 V.

5. CONCLUSIONS

The test stand, designed at the Institute of Electrical Engineering and Electrotechnologies enables to carry out the research on solar energy in the Lublin Province. The solar battery provided 2,5 kWh of electric energy each day, and solar battery has efficiently operated for 15 hours. The research experience will definitely contribute to the idea of further development of the system and described laboratory.

The TREACE inverter included in the system does not permit to transmit generated energy to power network. The development of the stand and the inclusion of the system cooperating with the network, as well as control system tracking the Sun would improve the efficiency of the system. However, the cost of the complete tracking system is significant, the amount of energy generated could rise only of 20% in the conditions of Poland [4]. The optimal solution that would reduce the cost would be the regulation in vertical axis, the regulation in horizontal axis could be done manually once a month.

REFERENCES

[1] Gogół W.: „Konwersja termiczna energii promieniowania słonecznego w warunkach krajowych – Ekspertyza", Oficyna Wydawnicza Politechniki Warszawskiej, Warszawa 1993.

[2] Nalewaj K., Bodziak K., Wójcicka-Migasiuk D. W. : Teaching Laboratory to Practice Use of Integrated Heating Systems. „EuroSun" 96 10. Internationales Sonnenforum 1996.

[3] Janowski T., Nalewaj K., Wójcicka-Migasiuk D., Złonkiewicz Z.: "Laboratory of Heating System Employing Solar Energy". Electromagnetic Devices and Processes in Environment Protection ELMECO, Nałęczów 12-15 czerwca 1997,

[4] Smolec W.: „Fototermiczna konwersja energii słonecznej", PWN, Warszawa 2000;

[5] Pluta Z.: „Podstawy teoretyczne fototermicznej konwersji energii słonecznej, WNT Warszawa 2000;

[6] Rodacki T., Kandyba A.: „Przetwarzanie energii w elektrowniach słonecznych", Wydawnictwo Politechniki Śląskiej, Gliwice 2000;

4th International Conference **ELMECO**
Nałęczów, Poland
September 2003

REDUCTION OF THE MAGNETIC FIELD DUE TO HIGH CURRENT LINE USING BOTH MAGNETIC AND ELECTROMAGNETIC OPEN SHIELDS

Ryszard GOLEMAN

Institute of Electrical Engineering and Electrotechnologies, Lublin University of Technology
20-618 Lublin, 38A Nadbystrzycka St., Poland
e-mail: ryszardg@eltecol.pol.lublin.pl

Abstract

The paper discusses the influence of the magnetic and electromagnetic shields in the form of individual discontinuous cover for each wire or one cover for the three phases on distribution of the magnetic field in the vicinity of the power line. The gape of the shields is oriented above the high current wires. The simplifying assumption is that the two-dimensional analysis is used, because the lines are very long compared with diameter. The consideration is based on the field equations coupled with the circuit equations of the line and shield. Finite element modelling is used to study the effect of various shield geometry and materials. The results enable to determine shielding effectiveness of the analysed shields depending on their shape, materials and the shield gape.

Keywords: electromagnetc field, magnetic shields, electromagnetic shields.

1. INTRODUCTION

Artificially generated electric and magnetic field influence living organisms and sensible electronic devices in different way. Magnetic field generated by the transformers and high-current lines is a weak field, that rarely exceeds the level of safety for human beings, however it may have noxious influence on a wide range of engineering devices somehow disturbing or even make their operation impossible. Therefore, shielding buses are often applied in industry, that reduces the influence of magnetic field generated by currents in buses on the surroundings. The paper describes the analysis of magnetic field around high current line and the influence of the shields on spatial distribution of the field [1, 2, 3, 4].

Open shields systems [5], individual for each bus (Fig. 1) and the systems with the shield common for all buses (Fig. 2), that are made of ferromagnetic or conductive materials. Open shields are characterised by the air gap (slot) above the conductor and current line. Conductive shields are made of sheet aluminium, earthed at both ends. Ferromagnetic shields are formed by ET-6 transformer sheets. The calculations were carried out for the shield of typical angles like 90^O, 120^O and 150^O and different thickness.

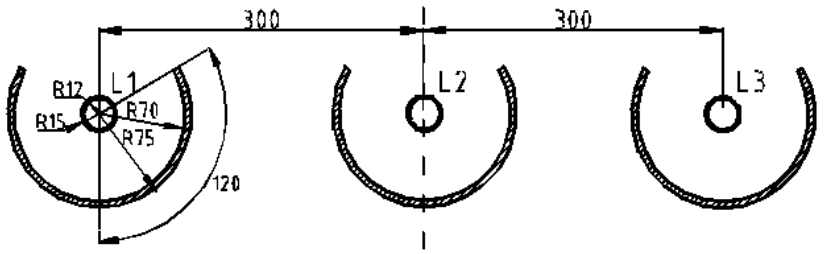

Fig. 1. Section of the examined bus – shield system, shielding of particular phases

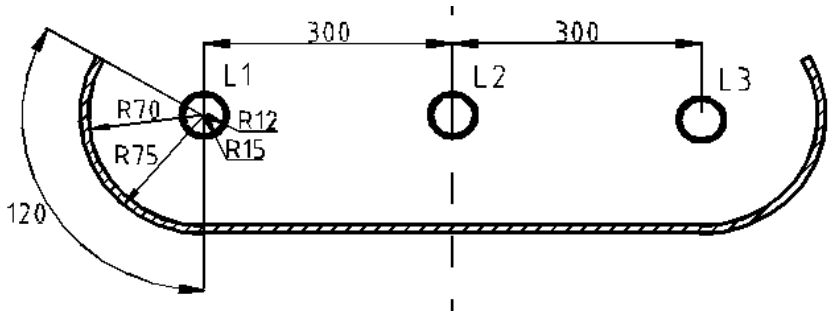

Fig. 2. Section of the examined bus – shield system, common bus shielding of all phases

Shielding efficiency can be determined by the shielding coefficient at considered point of a space. It has been defined as magnetic field induction B_e at given point in the system with the shield to induction value at the same point in the system without the shield B_0:

$$k = \frac{B_e}{B_0} \tag{1}$$

2. MODEL OF THE BUS SYSTEM WITH THE SHIELD

The system of conductor buses made of aluminium of circular section has been taken for the analysis. The assumption was made that current intensity in the bus is 3kA.

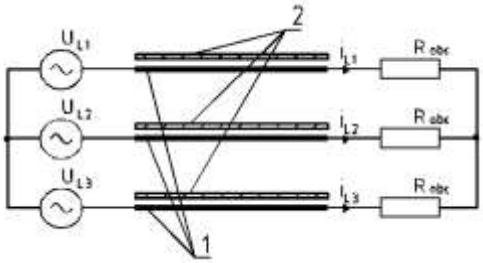

Fig. 3. Dedicated schema of analysed system with magnetic shield; 1–current buses, 2–shields

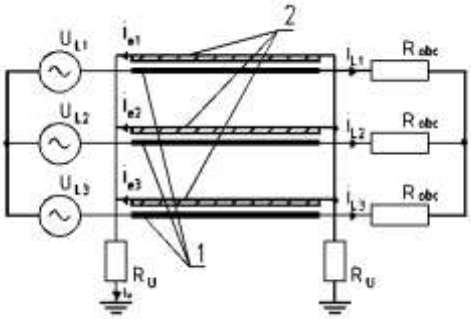

Fig. 4. Dedicated schema of analysed system with aluminium shield; 1–current buses, 2–shields

Vector potential in the system with the shield can be described by the following equations:

in current bus

$$\mathrm{rot}\left(\left(\frac{1}{\mu_0}\right)\mathrm{rot}\,\boldsymbol{A}\right)=\boldsymbol{J}_b \tag{2}$$

in air

$$\mathrm{rot}\left(\left(\frac{1}{\mu_0}\right)\mathrm{rot}\,\boldsymbol{A}\right)=0 \tag{3}$$

in magnetic shield

$$\mathrm{rot}\left(\left(\frac{1}{\mu_0\mu_r}\right)\mathrm{rot}\,\boldsymbol{A}\right)=0 \tag{4}$$

in aluminium shield

$$\mathrm{rot}\left(\left(\frac{1}{\mu_0}\right)\mathrm{rot}\,\boldsymbol{A}\right)=\boldsymbol{J}_s \tag{5}$$

where: $\boldsymbol{A}$ – vector potential, $\boldsymbol{J_b}$, $\boldsymbol{J_s}$ – current density vectors, μ_0, μ_r – magnetic permeability in vacuum and relative permeability of the shield, γ – conductivity, ω – pulsation

Current density in conductive medium, in two-dimensional field is expressed by the following relation:

$$\boldsymbol{J}=-\gamma\frac{\partial \boldsymbol{A}}{\partial t}-\gamma\,\mathrm{grad}\;V \tag{5}$$

Assuming, that scalar potential V is the constant value in cross-section of the conductor, taking the relation (5) into consideration and the following relation:

$$U=-\boldsymbol{l}\cdot\mathrm{grad}V \tag{6}$$

the voltage between the ends of the conductor is

$$U=Ri+R\gamma\int_s\frac{\partial \boldsymbol{A}}{\partial t}\mathrm{d}\boldsymbol{s} \tag{7}$$

where: R– conductor's resistance determined at direct current, $\boldsymbol{l}$ – conductor's length, $\boldsymbol{s}$ – conductor's section

According to II Kirchhoff's law for current circuits the following equations can be written:

$$\begin{aligned}U_{\mathrm{L1}}-U_{\mathrm{L3}}&=(R_{\mathrm{L}}+R_{\mathrm{obc}})(i_{\mathrm{L1}}-i_{\mathrm{L3}})+\\&+R_{\mathrm{L}}\gamma\left(\int_s\frac{\partial \boldsymbol{A}_{\mathrm{L1}}}{\partial t}\mathrm{d}\boldsymbol{s}-\int_s\frac{\partial \boldsymbol{A}_{\mathrm{L3}}}{\partial t}\mathrm{d}\boldsymbol{s}\right)\end{aligned} \tag{8}$$

$$\begin{aligned}U_{\mathrm{L2}}-U_{\mathrm{L3}}&=(R_{\mathrm{L}}+R_{\mathrm{obc}})(i_{\mathrm{L2}}-i_{\mathrm{L3}})+\\&+R_{\mathrm{L}}\gamma\left(\int_s\frac{\partial \boldsymbol{A}_{\mathrm{L2}}}{\partial t}\mathrm{d}\boldsymbol{s}-\int_s\frac{\partial \boldsymbol{A}_{\mathrm{L3}}}{\partial t}\mathrm{d}\boldsymbol{s}\right)\end{aligned} \tag{9}$$

Currents in buses fulfil the equation:

$$i_{\mathrm{L1}}+i_{\mathrm{L2}}+i_{\mathrm{L3}}=0 \tag{10}$$

AC magnetic field induces currents in conductive shields. Taking into account that the shields have been earthed, the circuits of individual shield can be described by the equations:

$$R_e i_{e1} + 2 i_u R_u + R_e \gamma_e \int \frac{\partial \boldsymbol{A}_{s1}}{\partial t} \mathrm{d}\boldsymbol{s} = 0 \tag{11}$$

$$R_e i_{e2} + 2 i_u R_u + R_e \gamma_e \int \frac{\partial \boldsymbol{A}_{s2}}{\partial t} \mathrm{d}\boldsymbol{s} = 0 \tag{12}$$

$$R_e i_{e3} + 2 i_u R_u + R_e \gamma_e \int \frac{\partial \boldsymbol{A}_{s3}}{\partial t} \mathrm{d}\boldsymbol{s} = 0 \tag{13}$$

$$i_{e1} + i_{e2} + i_{e3} = i_u \tag{14}$$

for the circuit with common shield we have:

$$(R_e + 2R_u) i_e + R_e \gamma_e \int_s \frac{\partial \boldsymbol{A}_s}{\partial t} d\boldsymbol{s} = 0 \tag{15}$$

At the assumption that current line and the shields are long enough, 2D analysis is sufficient. The equations (2-15) were numerically solved with the application of FLUX2D package. Cyclic boundary conditions were taken for the calculation of triple-phase models of shielded busses. They enable to calculate vector potential beyond the region limited by boundary curve, taking into account its decay into infinity. Computation results have been presented as maps of magnetic flux density and charts of maximum values of magnetic flux density and shielding coefficient. The charts of maximum values of magnetic field density

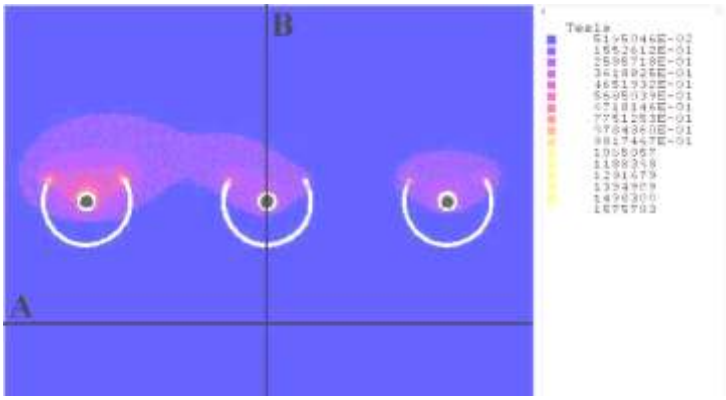

Fig. 5. Distribution of magnetic flux density around buses shielded with single magnetic shields (for ωt=0)

and shielding coefficient have been determined along straight line A (perpendicular to conductors' axes and distant from them of 500 mm) and straight line B (along symmetry axis of the system), which are presented in Fig. 5 and 6.

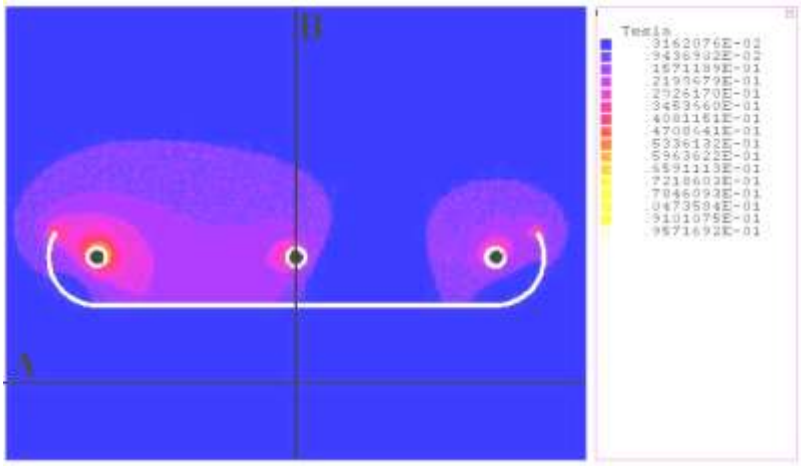

Fig. 6. Distribution of magnetic flux density around the shielded buses with common magnetic shield (for ωt=0)

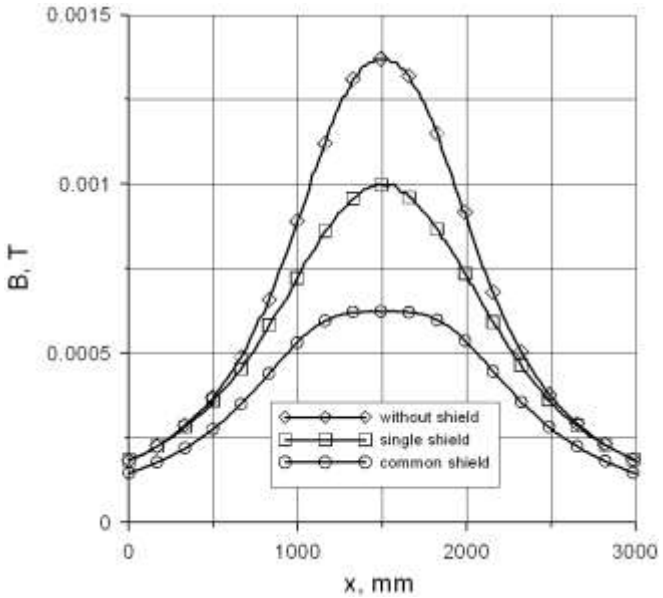

Fig. 7. Distribution of maximum value of magnetic flux density along straight line A for magnetic shields, ($\alpha=120^{o}$, thickness of the shield 5 mm)

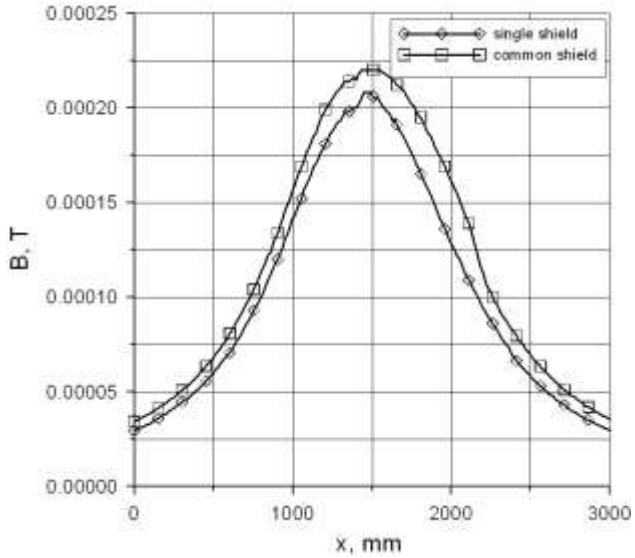

Fig. 8. Distribution of maximum value of magnetic flux density along straight line A for aluminium shields, (α=120^o, thickness of the shield 5 mm)

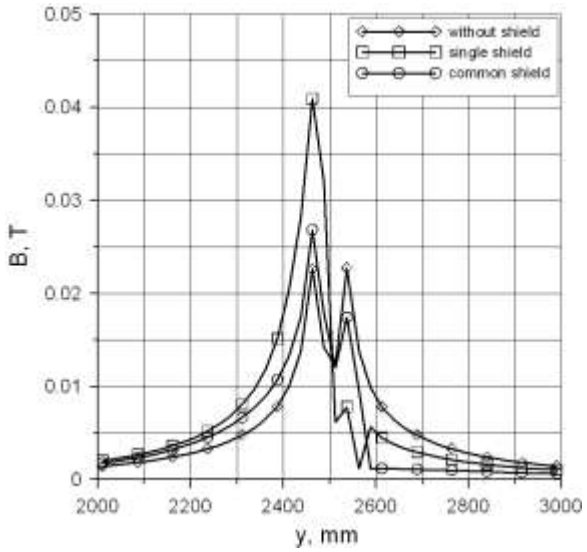

Fig. 9. Distribution of maximum values of magnetic flux density along straight line B for magnetic shields, (α=120^o, thickness of the shield 5 mm)

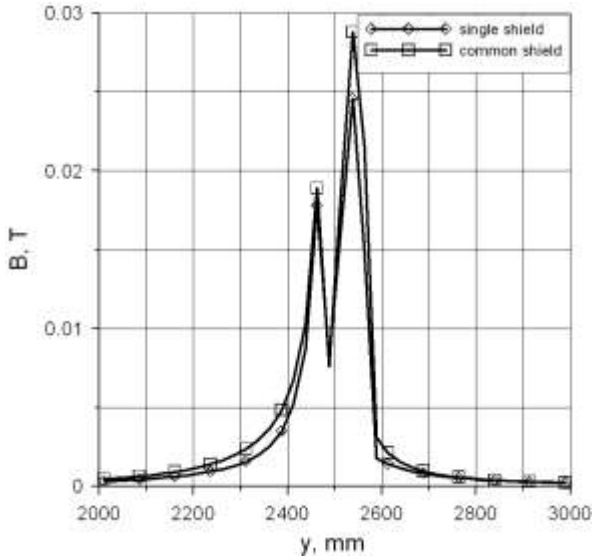

Fig. 10. Distribution of maximum values of magnetic flux density along axis B for aluminium shields, (α=120^o, thickness of the shield 5 mm)

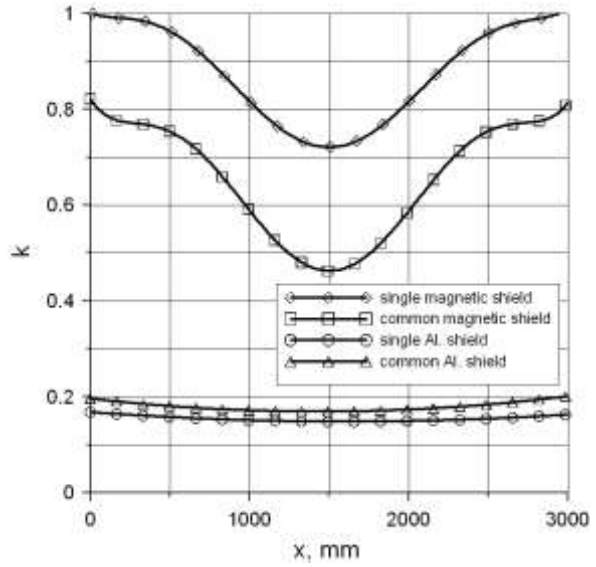

Fig. 11. Distribution of shielding coefficient along straight line A, (α=120^o, thickness of the shield 5 mm)

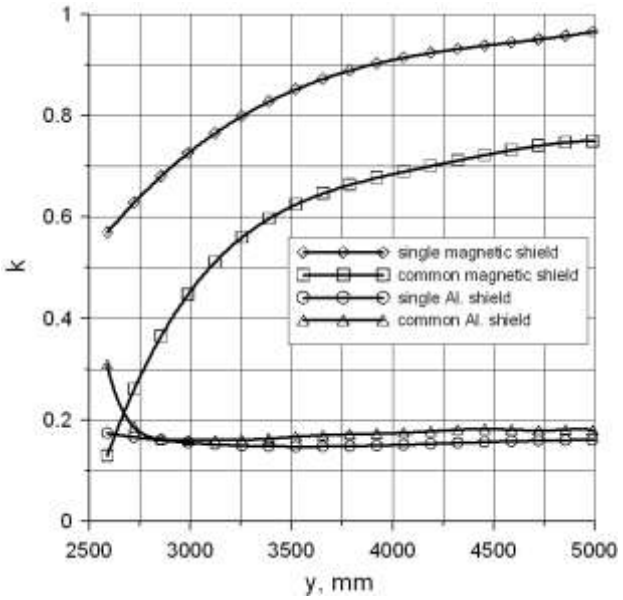

Fig. 12. Distribution of shielding coefficient along straight line B, (α=120^o, thickness of the shield 5 mm)

3. SUMMARY

The comparison of the systems with magnetic and electromagnetic shields and the evaluation of their influence on field distribution around high-current current buses have been presented in the paper.

Magnetic shields can be used to limit magnetic field only in the area directly in front of the shield. In such systems, the intensity of field above the shield increases and the highest values occur at shield edges. The system with common shield has better features i.e. maximal value of magnetic flux density is considerably lower than in case of individual shields. Change in the length of shield gap that responds the increase of shield's angle from 90^O to 150^O has small influence on shielding efficiency. Such influence is noticed in common shield. Change in magnetic shield's thickness in the range from 5 mm to10 mm does not influence on magnetic flux density and shielding efficiency.

Conductive shields have better shielding efficiency compared to magnetic ones. Currents induced in conductive shields and significant power losses are disadvantageous feature of conductive shields. Shielding coefficient is almost constant in the whole shielded space in the systems with conductive shields.

REFERENCES

[1] Bednarek K., Nawrowski R. Tomczewski A., Electromagnetic compatibility in the neighbourhood of high-current lines, X International Symposium on Electromagnetic Fields in Electrical Engineering, ISEF 2001, pp.423-428.

[2] Bottauscio O., Chiampi M., Chiarabaglio D., Zucca M., Use of grain-oriented materials in low-frequency magnetic shielding, Journal of Magnetism and Magnetic Materials, Vol. 215-216, 2000, pp.130-132.
[3] Goleman R.; Szponder J., Laminar screens applied to restrict magnetic fields of mains frequency, Electromagnetic Fields in Electrical Engineering, IOS Press, 2002, pp.411-414.
[4] Piątek Z., Baron B., Impedances of the non-coaxial system of two parallel tubular conductors, International Conference on Fundamentals of Electrotechnics and Circuit Theory, XII IC-SPETO, 1999, pp.101-108. (in Polish)
[5] K. Wassef, V.V. Varadan, V.K. Varadan, Magnetic field shielding concepts for power transmission lines, IEEE Transactions on Magnetics, Vol.34, No.3, 1998, pp.649-654.

4th International Conference **ELMECO**
Nałęczów, Poland
September 2003

SOFT MAGNETIC MATERIALS APPLIED TO LIMIT ELECTROMAGNETIC INTERFERENCES

Andrzej WAC-WŁODARCZYK, Paweł A. MAZUREK

Institute of Electrical Engineering and Electrotechnologies
Lublin University of Technology, Poland
andrzejw@eltecol.pol.lublin.pl
pawelm@eltecol.pol.lublin.pl

Abstract

The paper presents the parameters of the soft magnetic materials and their application possibilities in improvement of electromagnetic compatibility of electric devices.

Keywords: electromagnetic compatibility, electromagnetic interference, EMI filter.

1. INTRODUCTION

Various electrical, electromechanical, and electronic apparatus emit electromagnetic energy in the course of their normal operations. Such emissions may be widely divided into two categories: intentionally emitted signals, and unintentional electromagnetic emissions during the operation of the equipment.

One of the most efficient methods to limit the electromagnetic interference is the application of the reducing elements to an acceptable level. These elements are the filters and can operate both as a single element and create more complicated structures. The efficiency of EMI suppression depends on the properties of filtering elements, their type, qualities of galvanic connections and the volume input and load impedance of electric circuit.

2. ELECTROMAGNETIC COMPATIBILITY

EMC is defined as the ability of electrical equipment to function satisfactorily in its electromagnetic environment without affecting other equipment in this environment to an impermissible extent.

EMC problems occur when electromagnetic energy from one electrical or electronic device interferes with the operation or performance of other devices. Power system interference can affect system components as well as devices used in residential, commercial, and industrial settings and infrastructure such as railroad and

telecommunications systems resulting in increased liabilities and costs, power facility sitting problems, and sub optimal power system operation.

The concept of EMC includes both electromagnetic emission (EME) and electromagnetic immunity/susceptibility - EMS, (Fig. 1). An interference source may generate conducted or radiated electromagnetic energy, i.e. conducted emission (CE) or radiated emission (RE). This also applies to the propagation paths and to the electromagnetic susceptibility of disturbed equipment.

Power electronic equipment usually generates disturbances in two ranges: low frequency and high frequency. The low-frequency range disturbances are harmonic currents and the voltages generated by non-linear loads. The high-frequency disturbances are referred to as electromagnetic interference (EMI). EMI can be transmitted in two ways: radiating and conducting. The radiated form is propagated in free space as electromagnetic waves, while the conducted form is transmitted through power lines, especially at the distribution levels. Conducted EMI is usually higher in the range of magnitude than the radiated noise [1,2,10,12,13].

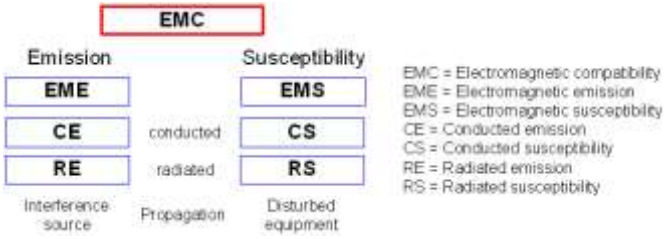

Fig. 1. EMC terms [1,10,13]

In order to be able to choose suitable EMC components, the way in which conducted interference is propagated needs to be known. Interference voltages and currents can be grouped into common-mode interference, differential-mode interference and unsymmetrical interference (Fig. 2). A floating interference source primarily emits differential-mode interference which is propagated along the connected lines. The interference current will flow towards the disturbed equipment on one line and away from it on the other line, just as the signal current does. Differential-mode interference occurs mainly at low frequencies (up to several hundred kHz). At frequencies beyond about 1 MHz, common-mode interferences are dominant [10,13].

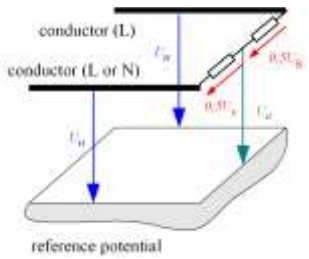

Common-mode interference (asymmetrical interference)
U_a – occurs between all lines in a cable and reference potential;
Differential-mode interference (symmetrical interference)
U_s – occurs between two lines (L-L, L-N);
Unsymmetrical interference U_n - this term is used to describe interference between one line and the reference potential.

Fig. 2. Propagation modes [1]

3. SOFT MAGNETIC MATERIALS

Since several decades, the basic soft magnetic materials used for cores of choking-coils are soft ferrites. Ferrites are oxides of their general formula: $MO \cdot Fe_2O_3$, where MO is a divalent metal ion such as Fe^{2+}, Mn^{2+}, Ni^{2+}, Zn^{2+}, Mg^{2+} [4]. The magnetic properties of ferrites are due to the magnetic moments of the metal ions. The characteristic features of ferrites are: high resistivity, higher than the resistivities of well-known magnetic alloys ($1 \div 10^6 \Omega mm^2/m$), low losses from rotary currents, and also large brittleness and hardness. Magnetic saturation of ferrites is considerably smaller than saturation of iron, at little inductions. Initial permeability μ_i of ferrites oscillates between 10÷10000 (Fig. 1a) [3,4,6,7].

Ferrites in the applications of low signals are characterized by low power losses and constant permeability, that does not depend on temperature. Application of ferrites in impulse systems requires the material that operates at high changes of magnetic flux value of low frequencies of work, and low power losses [8,9].

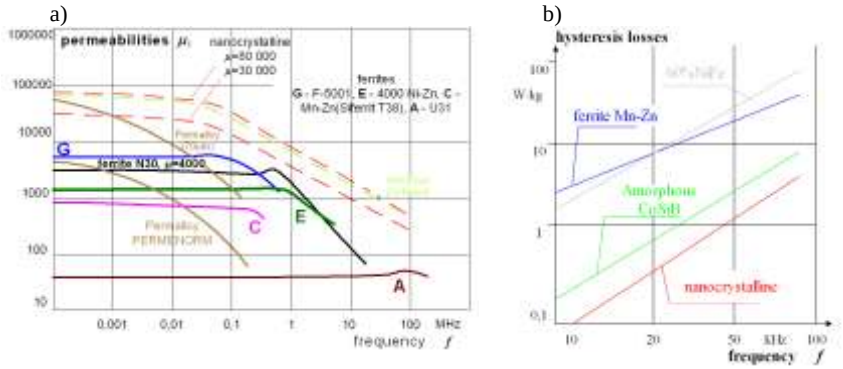

Fig. 3. Typical properties of nanocrystalline materials and ferrites: a) frequency dependence of relative permeability, b) hysteresis losses of various materials [9,11]

Nanocrystalline alloys are obtained by the controlled crystallization of the amorphous phase of the formula Fe-Si-B-CuNb. This process is conducted by the current flow through the material obtained in the process of magnetic liquid quench. In the crystallization in external magnetic field or under the influence of mechanical stress alloys micro-crystallographic anisotropy can be obtained. After crystallization the material is in the form of two phase structure in which a fine-crystalline grain of an average diameter of 10 to 20 nm is embedded in an amorphous residual phase. The resulting randomly oriented grains grow until the amorphous residual phase consists almost exclusively of iron, niobium boron and stabilizes [4,5,6].

According to the literature [3,4,5,6,9,11], the nanocrystalline material is used for cores due to the relatively high permeability 30000 ÷ 90000 (Fig. 3a), greater than in ferrites. Good dynamic properties of these materials are effective with lower total losses, and typical hysteresis losses for different materials are illustrated in Fig. 3b. The hysteresis loop (Fig. 4b.) of nanocrystalline alloys can be tailored to specific applications by means of induced anisotropies.

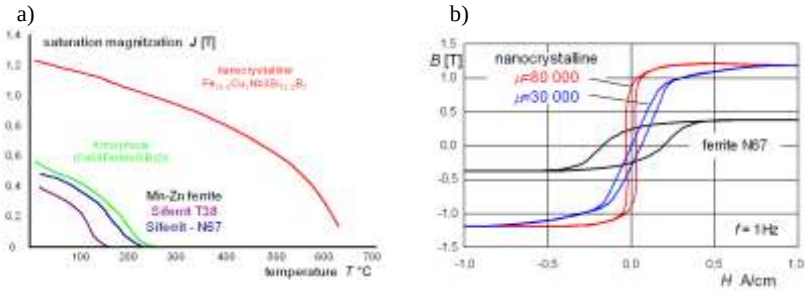

Fig. 4. a) Influence of temperature on saturation magnetization J (which is almost equal to saturation induction B_S in high permeable materials) of typical core materials, b) the magnetic hysteresis loop of soft magnetic materials [4,7,9]

For example [4], the commercial nanocrystalline material called FINEMET shows very good magnetic properties: magnetic permeability μ_i = 100000, saturation magnetization J = 1,2÷1,3T, low magnetostriction (λ = 10^{-6}) and high resistivity (ρ = 1,35Ωmm^2/m). In addition, material characterized by small strip thickness and relatively high electrical low eddy-current losses and excellent frequency behaviour and permeability.

4. UTILIZATION OF SOFT MAGNETIC MATERIALS IN CHOKING-COILS

The classical example is the core for electromagnetic interference suppression. The efficiency of such choking-coil depends considerably on the proper selection of magnetic material and the dimension and the shape of the core. The core for electromagnetic interference suppression is working as limiter of disturbances and is switching on in series of the circuit between the emission sources and receiver .

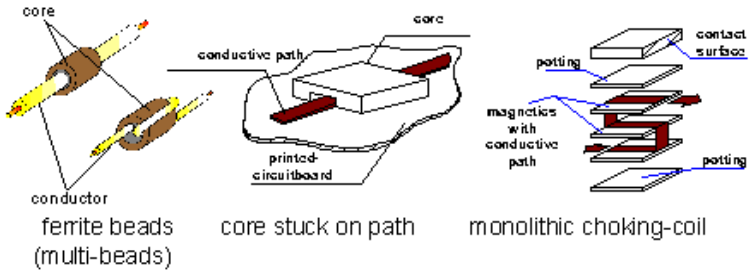

Fig. 5. Examples of construction of core for electromagnetic interference suppression: a) soft ferrite core, b) core stuck on path, c) monolithic choking-coil [1,8].

The simplest core (bead) for electromagnetic interference suppression is soft ferrite core installed on conductor (Fig. 5a), or ferrite core (nanocrystalline ribbons) stuck to conductive paths on printed circuit board (Fig. 5b). More composite is choking-coil of monolithic structure adapted to superficial switching (Fig. 5c).

In network filters the core choking-coils occure quite often with current neutralization. A schematic diagram of a common mode choke is illustrated in Fig. 6. Asymmetrical interference is superimposed on the operating currents, the magnetic fields of the interference signals no longer cancel each other. In this case the entire impedance of the choke acts against the interfering signal, causing the desired damping. Good damping characteristics call for the highest possible impedance, all the way up to the highest frequencies. However, in reality the damping behaviour is subdivided into different frequency intervals that are determined by the permeability behaviour of the core material, by the number of turns, and by the winding arrangement.

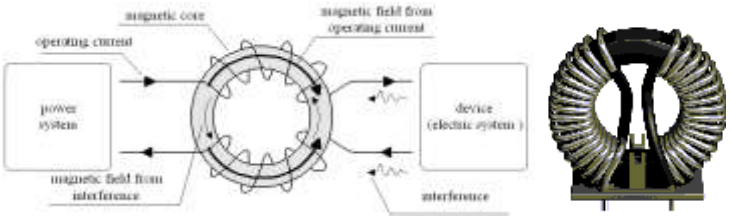

Fig. 6. Schematic diagram and picture of common mode choke [1,2,7,10,11]

1. Aluminium case for greatest structural strength ever attained.
2. Silicone glass or melamine insert, to break electrical path around core.
3. Inert cushioning, a high temperature silicone compound.
4. Magnetic materials, a selection of commercially available high permeability alloys

Fig. 7. Aluminium Core Box Construction

Noise generated by electrical equipment is primarily at the unit's fundamental frequency, plus higher harmonics. This means that the noise spectrum usually runs anywhere from 10kHz to 50MHz. To provide proper attenuation, the impedance of the inductor must be sufficiently high over this frequency range [4].

Total impedance of the common mode inductor is composed of two parts, the series inductive reactance (X_S) and series resistance (R_S). At low frequencies, the reactance is the primary contributor to impedance, but as the frequency increases, the real part of the permeability drops and losses within the core rise.

The insertion loss is a criterion for the efficiency of EMC components, as measured by using a standardized test setup. The EMI filter (or individual choke) for electromagnetic interference suppression is working as limiter of disturbances and is switching on in series of the circuit between the emission sources and receiver. The efficiency of choke (defined by characteristic parameter – insertion loss) presented equation 1 [1,13].

$$A = 20 \cdot \lg {U'_z}/{U''_z} \quad \text{dB} \tag{1}$$

where: U_Z' – disturbance without choking-coil , U_Z'' – disturbance with choking-coil

At high frequencies stand up capacities which bring to resonance. Frequency of resonance grows less with growing number of turns. Thus a small number of turns is advantageous. To achieve components with high impedance values and small volumes, the choke material must have the highest initial permeability with good frequency characteristics. Additionally, the core material must retain its high permeability even under the influence of interference signals with high amplitudes or in the presence of a high leakage flux [1,2,12].

Common - mode choke

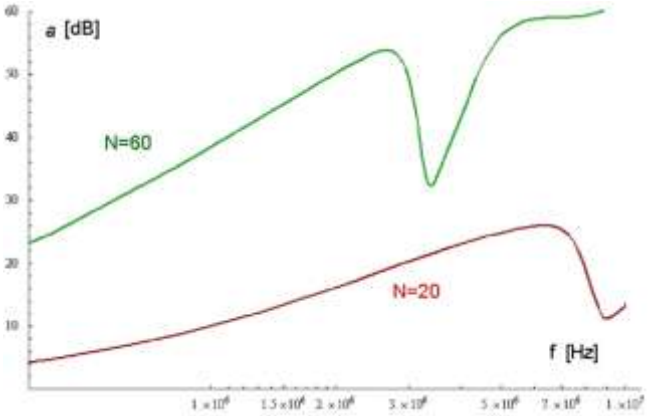

Fig. 8. Insertion loss μ_i =30000, overall dimensions 30×20×10 [12]

Differential - mode choke

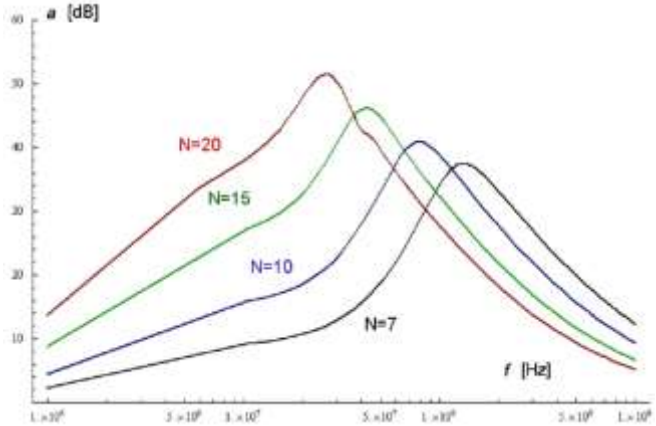

Fig. 9. Insertion loss μ_i =30000, overall dimensions 30×20×10 [12]

Common - mode choke

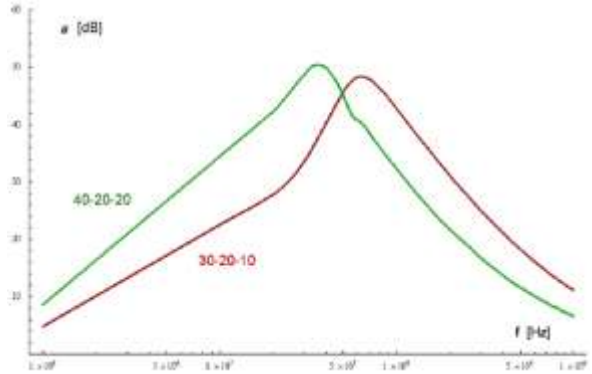

Fig. 10. Overall dimensions vs. insertion loss μ_i =15000, N=12 [12]

Differential - mode choke

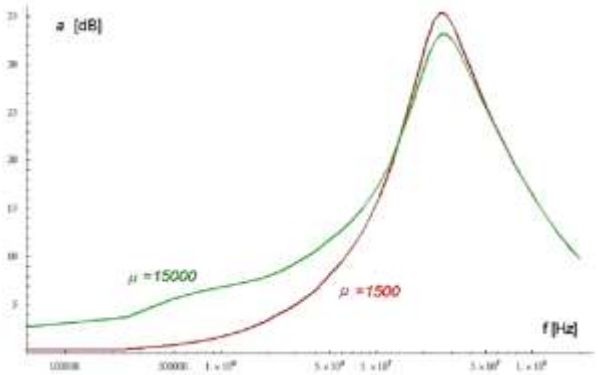

Fig. 11. Initial permeability vs. insertion loss, N = 7, overall dimensions 30×20×10 [12]

At EMC requirements relating to the obtainment of interference free signal in specific fragments of all frequency spectrum it appears, that the products existing on the market sporadically filter disturbances in satisfactory degree. Thus, it also in results the need for the filters designing of the parameters properly selected for applications. Efficient EMI suppression at utilization of choke forces to use correctly well chosen magnetic core. Examining dimensions of space special attention shell be paid to the dimensions of geometrical core, and self-inductance. The analyses of magnetic material are complicated. Enlarged volumes of core not always causes enlargement of module "suppression" impedance. Additionally, one should remember, that change of configuration of geometrical dimensions without the volume change of core causes changes L (Fig. 10).

The magnetic properties (initial permeability) of choking-coil depend on material, and are qualified by its impedance curve and insertion loss (Fig. 11), in all frequency spectrum of disturbances.

Environmental conditions, (temperature, magnetic and electric field intensity in which used choking-coil has to work) have influenced the work of choking coil by change of value of magnetic saturation of core. That effect can introduce high no linearity to circuit and become the following disturbance. Furthermore, the high thermal stability of soft magnetic material – their maximum application temperature (exceeds 100°C) makes it possible to use considerably thinner wires for the windings than in the case of ferrites or amorphous materials.

5. SUMMARY

There are various CISPR, IEC, VDE, FCC, and military standards that specify the maximum limit on the conducted EMI. These limits may vary for equipment used in commercial, industrial, and office or residential environments.

The core for electromagnetic interference suppression dampen electric signals on the all range of frequency spectrum. Realization of these criteria does not mean, that all problems of disturbances are dissolved. However, introduced information enables the correct choice of filter type with choke coils.

The paper verifies shortly the state of knowledge of materials technology, because that is modern technology and the lack of special-technical publications of undertaken theme of modern utilization of soft magnetic materials in applications improving electromagnetic compatibility of electric devices. Soft magnetic core materials for use in EMC noise suppression filters must have highest permeability up to the highest frequencies, highest induction swing values and excellent thermal properties.

The comparison of the impedances of common mode chokes made of new soft magnetic materials with similar core dimensions and identical winding shows a pronounced resonance increase and consequently significantly better damping properties of the nanocrystalline and amorphous choke. According to the presented information dealing with the obtaining and the properties of nowadays applied soft magnetic alloys – nanocrystallic alloy comes to the fore. It is a relatively cheap material that does not have expensive and strategic chemical elements. It is widely applied in the devices operating in the higher frequency. Due to their properties and rapid development of electromagnetic compatibility nanocrystalline alloys may be applied in power electronics. In this way the nanocrystalline materials satisfies the most important conditions for miniaturized chokes. It is thus the preferred material for the highest EMC requirements wherever volume is limited or integrated components are required.

REFERENCES

[1] A. Koszmider, Certyfikat CE w zakresie kompatybilności elektromagnetycznej, Alfa-Weka 2002

[2] A. Wac-Włodarczyk, P. A. Mazurek, J. Szponder, Electromagnetic compatibility problems included in the teaching curricula for "Electrical engineering" at Lublin University of Technology, 14th EAEEIE Conference, Gdansk, 2003, A53, ISBN 83-918622-0-8

[3] A. Wac-Włodarczyk, The development of the new nanocrystalline soft magnetic alloys in electro technology, II International Symposium NEET'2001 – Kazimierz Dolny, 14-17.II.2001, p.81-83

[4] J. Petzold, H.J. Poss, J. Richter, Nanocrystalline Materials-Soft Magnetic Alloys for High-Tech Devices, Reprint from Siemens Review, Specjal R&D, Fall 1997, Vacuumschmelze GMBH, VAC
[5] M. Leonowicz, Nanokrystaliczne materiały magnetyczne, WNT Warszawa, 1998
[6] M. Markuszewicz, A. Mierzyjewski, Materiały magnetyczne, WGH, Stalinogród, 1954
[7] M. Soinski, Wykorzystanie taśmy nanokrystalicznej w dławikach przeciwzakłóceniowych, Wiadomości Elektrotechniczne, nr10 1998 p.584-588
[8] P. Ruszel, Filtry przeciwzakłóceniowe, podstawowe właściwości i zasady wyboru, Elektronizacja, 9/1999, p.2-5
[9] P. Ruszel, Zastosowanie ferrytów do ograniczania sygnałów zakłóceń radioelektrycznych, Pomiary Automatyka Robotyka, 12/1999 p.9-13
[10] P.A. Chattterton, M.A. Houlden, EMC Electromagnetic Theory to Practical Design, John Wiley & Sons, 1991
[11] P.A. Mazurek, A. Wac-Włodarczyk, Zastosowania materiałów magnetycznie miękkich w ograniczaniu zakłóceń przewodowych, II Krajowe Sympozjum, Kompatybilność elektromagnetyczna w elektrotechnice i elektronice, EMC'01, Łódź 2001, s.241-250
[12] P.A. Mazurek, Grant badawczy dla młodych pracowników nauki nr 8T10A01521: Model ferrytowego ogranicznika zakłóceń elektromagnetycznych
[13] V. Prasad Kodali, Engineering Electromagnetic Compatibility, IEE PRESS, 2001.

4th International Conference **ELMECO**
Nałęczów, Poland
September 2003

THE SHIELDING EFFECTIVENESS OF THE ANECHOIC, SHIELDING CHAMBER AT THE INSTITUTE OF ELECTRICAL ENGINEERING AND ELECTROTECHNOLOGIES

Andrzej WAC-WŁODARCZYK, Paweł A. MAZUREK

Institute of Electrical Engineering and Electrotechnologies
Lublin University of Technology, Poland
andrzejw@eltecol.pol.lublin.pl
pawelm@eltecol.pol.lublin.pl

Abstract

The paper presents the shielding effectiveness of the existing acoustic, anechoic, shielding chamber at the Institute, with reference to investigations of the electromagnetic compatibility problems.

Keywords: electromagnetic compatibility, shielding chamber.

1. INTRODUCTION

The electromagnetic environment is self - characterized by the level of electromagnetic field intensity. That level depends on electromagnetic fields emitted by electrical device, systems and installations. Reliability and repeatability of the results should characterize the measurements of electromagnetic emission intensity in the surrounding. The conducted and radiated disturbances generated inside devices should be tested.

The investigations that define electromagnetic emissivity shall be done on special ground - open area test system (OATS). The influence of weather conditions, external electromagnetic fields and high maintenance costs have unfavourable influence on measurement results. In order to avoid such influence, special devices like electromagnetic shield and anechoic chambers are applied.

2. SHIELDING CHAMBER

The anechoic, shielding chamber was constructed at the Institute of Electrical Engineering and Electrotechnologies at Lublin University of Technology. The chamber is the part of the Laboratory of Acoustic and Electromagnetic Interferences at the Institute.

The chamber was designed for scientific and didactic purposes. Such device enables to investigate and measure acoustics, electroacoustics, acoustic disturbances and vibration of electrical equipment and electromagnetic compatibility.

The overall dimension of chamber was fit to the size of the laboratory room: length 2620 mm, width 2020 mm, height 2500 mm. The chamber and the location in laboratory room are shown in figure 1 [4].

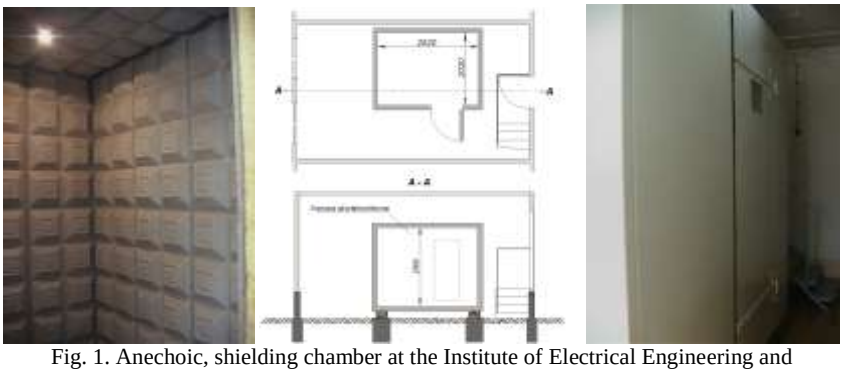

Fig. 1. Anechoic, shielding chamber at the Institute of Electrical Engineering and Electrotechnologies [4]

Support construction was made of 2 mm thick steel sheet. The floor was supported on channel sections and covered by the sheet steel. The stiffness of the construction was assured by suitable press forming of sheet metals. The additional strain hardening was done by the squares welded on the walls. The interior of the whole chamber was coated by the coset of silencing and damping vibration paste and double coset of soft rock wool. The soft panel board was installed on coset of rock wool. The sound absorbing panels "Porfles" were fastened to panel board [4].

The anechoic chamber has cubic shape. The absorbers of electromagnetic wave and metal shield make possible to obtain the space of well-known conditions of electromagnetic wave propagation. The chamber at the Institute hasn't got such absorbers. However, steel sheet metal creates shield which protects against electromagnetic release.

3. THE CALCULATIONS AND MEASUREMENTS

To verify the parameters of the chamber it is necessary to measure electromagnetic compatibility of the devices. The fundamental parameter is the shielding effectiveness.

At the beginning the theoretical considerations of shield suppression were done. The chamber construction was assumed as homogeneous shield in the analysis. The suppression of electromagnetic field can be done by basic physical phenomena – the reflection and the absorption of energy. Figure 2 and following examples show the influence of these phenomena.

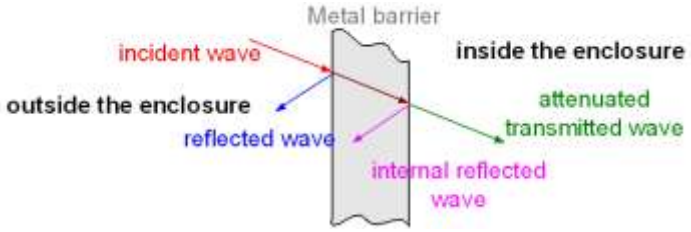

Fig. 2. Representation of shielding mechanisms for plane wave [1]

Total shielding effectiveness [1,2,3]

$$S_E = \alpha_R + \alpha_A + \alpha_{IR} \tag{1}$$

Where: the reflection loss - α_R, absorption loss α_A and internal reflection losses - α_{IR} in decibels.

Absorption [2]:

$$\alpha_A = 20\log e^{\alpha_m} = 3{,}34 \cdot t \cdot \sqrt{f \cdot \mu_r \cdot \sigma_r} \tag{2}$$

Reflection:

In the far field, $\left(r \geq \frac{\lambda}{2\pi} \right)$ for plane waves:

$$\alpha_{RP} = 168 - 10\log_{10}\left(\frac{f \cdot \mu_r}{\sigma_r} \right) \tag{3}$$

In the near field, for E fields [2]:

$$\alpha_{RE} = 332 - 10\log_{10} \cdot \left(\frac{\mu_r \cdot r^2 \cdot f^3}{\sigma_r} \right) \tag{4}$$

for H fields [2]:

$$\alpha_{RH} = 15 - 10\log_{10}\left(\frac{\mu_r}{\sigma_r \cdot r^2 \cdot f} \right) \tag{5}$$

Rereflection [3]:

$$\alpha_{IR} = 20\log\left(1 - e^{-2t\sqrt{\pi f \mu \sigma}} \cdot e^{-j2t\sqrt{\pi f \mu \sigma}}\right) \tag{6}$$

Where: μ_r - relative permeability with respect to air, σ_r relative conductivity, t - thickness of sheet in cm f - frequency in Hz, r - the distance from the source to the shielding barrier in meters.

The dates of real object were introduced to equations. The theoretical relation of shielding effectiveness of chamber are generated as graphic diagram in figure 3.

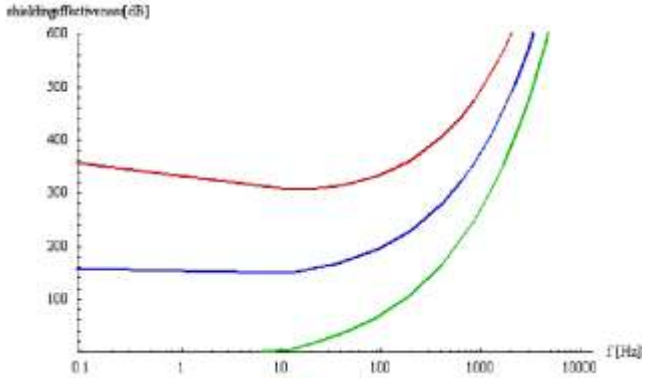

Fig. 3.Theoretical shielding effectiveness

The real measurements with theoretical analysis were performed simultaneously. Electromagnetic waves with frequency range 30MHz - 1GHz were investigated. The values measuring shielding effectiveness of construction (the chamber) ware qualified as relation of field intensity of incident wave to field intensity transmitted through screen. Shielding effectiveness for near field was defined separately for electric field and separately for magnetic field.

$$S_E = 20 \cdot \log \frac{E_i}{E_a} \quad [\text{dB}] \tag{7}$$

$$S_H = 20 \cdot \log \frac{H_i}{H_a} \quad [\text{dB}] \tag{8}$$

For far field the shielding effectiveness is defined as relation of power density incident and attenuated.

$$S_P = 10 \cdot \log \frac{P_i}{P_a} \quad [\text{dB}] \tag{9}$$

The measurements of the shielding effectiveness were done using the set measuring equipment: ULMZ-4/50 (25-300MHz) and DLMZ-4/50 (300-1000MHz). The received values of shielding effectiveness in graphic diagram are shown in figure 4.

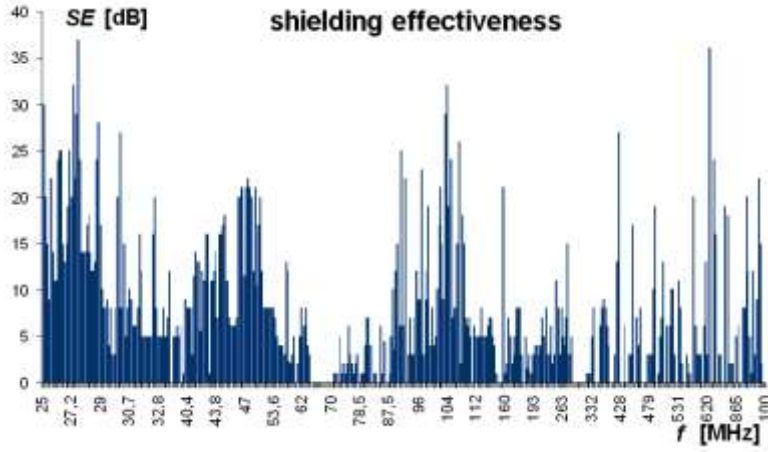

Fig. 4. Shielding of electromagnetic external field of the chamber

In order to estimate the disturbance level in the chamber, the measurements were taken inside the chamber as well. The results of measurements were verified with values of disorders admissible in this object type (EN 50147-3). Graphic interpretation of this verification was shown in Fig. 5.

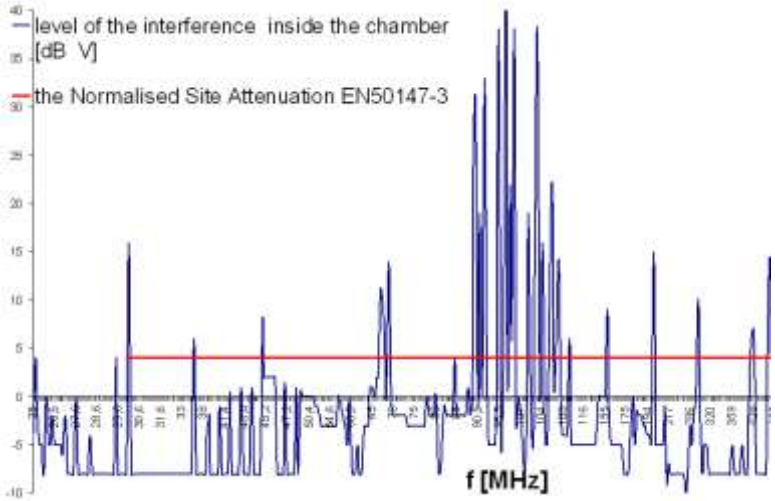

Fig. 5.The Level of the interference inside the chamber in dBμV

4. CONCLUSIONS

Theoretical analysis showed good parameters of chamber suppression. Unfortunately, it was only the theory. Steel construction of chamber was hermetic and closed shape. However, the practical solution is different. There are air holes, seal wire and doors with glass window in the chamber. These elements were the reason for leakage of electromagnetic wave to the chamber. Graphical diagram in figure 5 shows then serious problem. The values with radio frequency range considerably exceed admissible level. The level of electromagnetic disturbances inside the chamber can be improved by the application of radial packing.

In EMC testing of electric devices, the examined chamber could only be used for the me measurements of electromagnetic conducted interferences. Such measurements are only recommended but not obligatory.

REFERENCES

[1] P.A. Chattterton, M.A. Houlden, EMC Electromagnetic Theory to Practical Design, John Wiley & Sons, 1991.

[2] V. Prasad Kodali, Engineering Electromagnetic Compatibility, IEE PRESS, 2001.

[3] R.W. Evans, Design Guidelines for Shielding Effectiveness, Current Carrying Capability, and the Enhancement of Conductivity of Composite Materials, NASA Contractor Report 4784, August 1997.

[4] A. Nocoń, Komora bezechowa i ekranowa w Instytucie Podstaw Elektrotechniki i Elektrotechnologii, praca dyplomowa, promotor J. Szponder, Lublin 2000.

4th International Conference **ELMECO**
Nałęczów, Poland
September 2003

THE INFLUENCE OF ELECTROMAGNETIC INTERFERENCES ON ELECTRIC AND ELECTRONIC SYSTEM OF THE VEHICLE

Andrzej WAC – WŁODARCZYK, Sławomir BEDNARCZYK

Institute of Electrical Engineering and Electrotechnologies
andrzejw@eltecol.pol.lublin.pl

Department of Power Networks and Protection
stabed@elektron.pol.lublin.pl

Lublin University of Technology, 38A Nadbystrzycka St., 20 – 618 Lublin

Abstract

The paper presents the issues related to electromagnetic interferences that occur in electrical system of the vehicle. The attempt to classify these phenomena has been made through the investigation of their impact on vehicle's operation. Selected systems and elements of the vehicle have been presented that generate undesirable phenomena during their operation. Negative influence of electromagnetic surroundings of the vehicle has also been described. The paper shows destructive effects of the mentioned phenomena on vehicle's operation e.g. damage of the desk computer. Selected relations that allow to determine the type and the value of the occurred interference have also been presented.

Keywords: electromagnetic compatibility, electric and electronic system of the vehicle.

1. VEHICLE AS THE OBJECT OF INTERFERENCES

Electric elements operating in vehicles constitutes part of whole systems which are subject to different kinds of electromagnetic interferences. In digital and analogue measuring systems, which are placed in car, the driving transmission conductors lines are especially subject to interferences. In choosing appropriate protections of the circuit from interferences it is essential to have the knowledge concerning the sources of interferences, the awareness of how the interferences conjugate with the circuit, ways of penetration of interferences into electric circuits, models of electric circuits, models of circuits which are disturbed in connection in the capacitive and inductive and basic methods of protecting circuits from interferences [1].

Depending on very different mechanisms of connections, interferences can be radiated or connected with lines so-called conducted or transferred by capacitive and inductive.

In the case of single phenomena phases (connected with changes in time) the time of growing of an impulse and top values are very important. On the whole, an impulse of considerable amplitude consists of many harmonics of different – also high - frequencies.

Consequently, these harmonics may cause many resonances in the discussed cases. Cars are subject to interferences in frequencies which range from 50 Hz for power lines and other radio or television – transmitters, where frequencies reach hundreds of MHz, to mobile phones operating in GHz frequencies. In this range of frequencies the level of interferences is very different, mainly because the powers of sources of interferences are also different and range from several decimals to hundreds of kilowatts. Figure 1 illustrates the level of electric field which may exist on public roads. The measured frequencies can reach 1000 MHz.

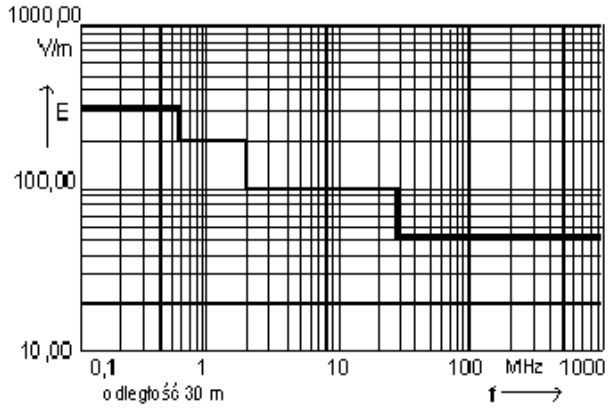

Fig. 1. Levels of electric fields' disturbances

Cars are particularly sensitive to emission in frequency range which can cause resonance in bunches of wiring. These frequencies are compatible in circumstances in which half of the wavelength is the some as the length of the wiring.

Dangerous range of frequencies is from 6 MHz if the length of the car does not exceed 18 meters. As a result of existing inductive connections among parallel lines quick changes of current intensity can disturb the work of electronic devices and even damage entrance-transistor. Relative mutual induction M for two non-ferromagnetic simultaneously arranged lines is [5]

$$M = \frac{\mu_0}{2\pi}\left(\ln\frac{2l}{a} - 1 + \frac{a}{l}\right) \tag{1}$$

where:

μ_0 – $1{,}257 \cdot 10^{-6}$ H/m,

l – length of parallel arranged lines,

a – distance between centres of lines.

In high-current circuit, voltage proportional to the speed of current change will appear

$$u_2 = \frac{-M \cdot l \cdot \frac{\mathrm{d}i_{1\max}}{\mathrm{d}t}}{1+\frac{Z_{in}}{Z_{out}}} \tag{2}$$

where:

u_2 – voltage in parallel circuit,
i_{1max} – current in circuit strong – current,
t – time,
Z_{in} – impedance of electronic input circuit,
Z_{out} - impedance weighting of electronic output circuit.

Another source of car interferences is static electricity which mainly results from tyres rolling on the roadway, friction against the air of the metal body, friction of V – belt ventilator and alternator, as well as dry winds carrying small particles of dust. Electric charges transferred by particles of dust settle on objects and cause potential on this object higher than the potential of earth. The voltage difference between the body and the earth may even reach several dozens of kV [2]. If the elements of the car, for example the doors, bonnet and boot cover are not connected together well, they will not shield and electric spark may appear. Electric charges may also accumulate on human body, brake – facings, clutch facings, driving shaft.

On the contrary to generally accepted opinions, the body of a car doesn't show properties of Faraday's cache. The body of modern car is constructed from metal sheet deeply embossed and it can cause loops of current to be created which results in radiation from the external part of the vehicle body [6]. We can experimentally report that electric discharge of passenger of car in comparison with the body may be 0,15 C[5]. This discharge may damage the deck computer due to the internal resistance of the human body Ri = 500 Ω.

Electrostatic interferences appear in the frequency spectrum up to 10 MHz. They are strongly felt especially in radio reception on long and medium frequencies as irregular cracks, very similar to the sound of distant discharges.

2. INTERFERENCES GENERATED BY CAR

In a vehicle there are a lot of devices which create electromagnetic interferences as a part of their normal functioning. The most important source of interferences in cars are spark ignition systems which at the absence of interference – limiting elements – make radio communication difficult within the radius of several dozens or even several hundreds of meters from the car. Other electric devices e.g. an alternator, a regulator of voltage, a sound signal, electric engines of windscreen wipers and also devices working by closing and opening joints (e.g. termobimetal sensors) create interferences of a considerable level, occurring especially inside the car.

3. INTERFERENCES GENERATED BY CAR'S ALTERNATOR

The operating alternator may be the source of many significant, even dangerous interferences for the car. There are two particularly dangerous cases which can appear during the work of the systems powered by an alternator:

- load current cut off,
- excitation current cut off.

A cut off load current appears when we disconnect the line between the exit connector (B+) and power during the work of alternator or as result of the disconnection in charging a battery.

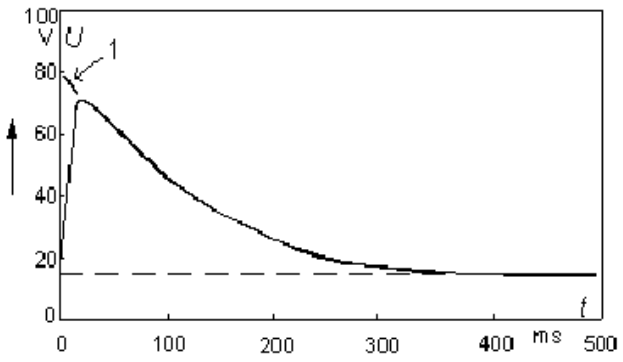

Fig. 2. Overvoltage generated at power drop of the alternator [5]
1 – sparking at circuit cut-off

The current in stator winding is reduced to zero that results in a surge expressed by the dependence:

$$u_L = L\frac{\mathrm{d}i}{\mathrm{d}t} \tag{3}$$

where:
u_L – voltage induced in stator winding,
L – inductance of stator's winding,
t – time.

Positive top value and steepness brow impulse voltage presented in Figure 2 is defined by electromotive force induce in stator winding alternator and decline when electric bow at the point break circuit appear (1, Figure 2).

A surge takes place after the electric arc appearing at the point of break goes out and the energy of the impulse is lower than energy loss in the electric bow. A break reduced by current generates negative impulses which can reach several dozens of volts when the diode connected to field winding is damaged.

The impulse of highest amplitude appears as the result of excitation current break cut off while switching off the ignition switch.

Figure 3 presents the shape of the impulse.

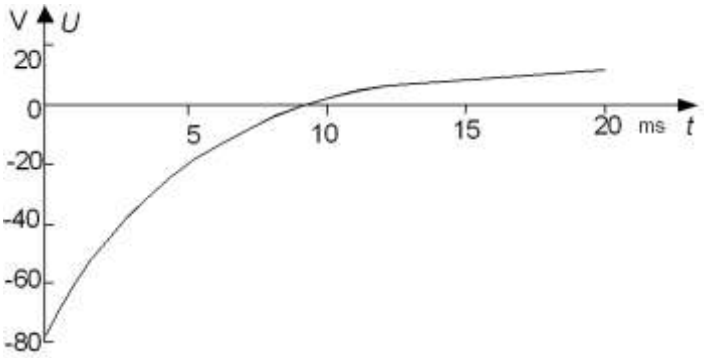

Fig. 3. Overvoltage generated at excitation current decay while the ignition switch is off [5]

Surge impulse coming from the excitation circuit reaches the voltage from –40 to –110 V depending on the type of alternator, the state of work of the system alternator – regulator and is characterized by significant steepness of the brow, the value of which is several milliseconds and long time of vanishing from 0,1 to 0,2 s.

4. HIGH FREQUENCY SURGES COMING FROM OTHER INDUCTION ELEMENTS

High frequency interferences impulses of a significant steepness can be induced in lines connecting a sensor with the electronic system. These surges are created by switching of the current in the circuit consisting of a battery, an inductance of winding and a joint (to which a capacitor is sometimes connected). The electric arc between the opening joints is characterized by negative resistance. As a result suppressed oscillations of high frequency are created in the resonance circuit consisting of a negative resistance of the electric arc, inductance, capacitive wiring. They last to the vanishing of the electric arc. Switching on the lights or the brake light of a car can cause oscillations of the frequency up to several MHz. Switching on the sound signal results in a strong hum signal with a frequency to ten MHz, of the top voltage of 50 V [5].

Impulses which are similar but have much smaller amplitude from 0,3 to 8 V are generated by direct current engines. The engine of windscreen wipers generates the greatest signals the amplitude of which reaches 8 V.

5. SURGE COMING FROM THE SYSTEM IGNITION

When the circuit of a battery is broken it may create a very unfavorable situation, especially if the battery was charged by strong current and if other devices are switched off. Then for a certain time the ignition system is powered by a higher voltage, which is created in the alternator inductance at the moment of jumped decrease of power.

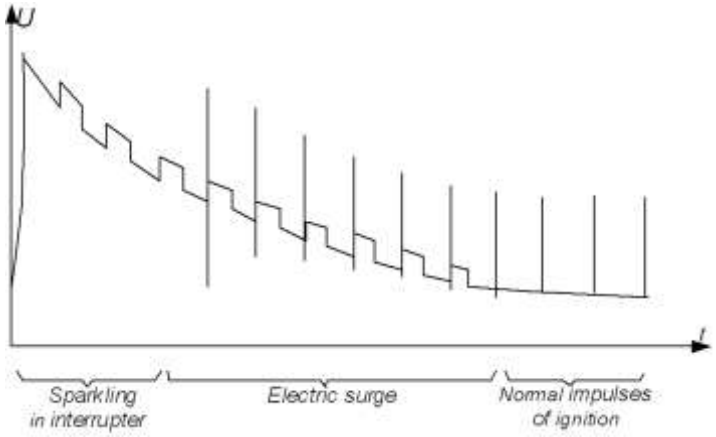

Fig. 4. The influence of the transition process initiated by drop powered for electric surge coming from ignition system [5]

Higher value of current flowing through the ignition coil results in the reduction of non-stationary state of the alternator however during such a short while significantly higher voltages are induced in the coil. The absence of the ignition impulses in the initial part of the diagram is caused by sparks in the interrupter. The oscillations which appear later (presented on the diagram by a vertical line because of the scale of time) many cause the voltage regulator to work with an unusually high frequency which may be the reason of a damage of out – transistor voltage regulator.

6. CONCLUSIONS

This article constitutes an introduction and a general review of electromagnetic compatibility problems in cars presented by given examples of elements included in electric installation systems. At present, electromagnetic compatibility becomes very important in vehicle's technology, however due to its diversity and complicated details, many issues require scientific analysis.

It is necessary to use sophisticated apparatus and prepare well educated staff for the operation. Thus, it's a great challenge for technical universities specialized in electrical engineering where special attention shall be paid to research on electromagnetic compatibility.

REFERENCES

[1] Bednarczyk S., Błażejczyk T., Wirtualny system pomiarowy z wykorzystaniem przetworników ADAM 4000 w środowisku LabView for Windows. Praca dyplomowa pod kierunkiem dr inż. Eligiusza Pawłowskiego, Politechnika Lubelska 2001.

[2] Charoy A., Zakłócenia w urządzeniach elektronicznych t.2, WNT Warszawa 2000.

[3] Koszmider., Certyfikat CE w zakresie kompatybilności elektromagnetycznej, Alfa-Weka 2000-2002.

[4] Kowalski B., Badania i diagnostyka samochodowych urządzeń elektrycznych, WKiŁ, Warszawa 1981.
[5] Konopiński M., Elektronika w technice motoryzacyjnej, WKiŁ, Warszawa 1987.
[6] Pietrzak B.: Zagadnienia kompatybilności elektromagnetycznej w samochodach. Praca dyplomowa pod kierunkiem dr hab. inż. Andrzeja Wac-Włodarczyka, Politechnika Lubelska 2000.
[7] Wac-Włodarczyk A., Szponder J., Mazurek P., Zajęcia z kompatybilności elektromagnetycznej na kierunku „Elektrotechnika" w Politechnice Lubelskiej. Sympozjum EMC – Łódź 2001, Zeszyty Naukowe Politechniki Łódzkiej Nr.96.

4th International Conference **ELMECO**
Nałęczów, Poland
September 2003

ARTIFICIAL NEURAL NETWORK APPLICATION FOR MATERIAL EVALUATION BY ELECTROMAGNETIC METHODS

Elżbieta RATAJEWICZ-MIKOLAJCZAK[1], Jan SIKORA[2], Ryszard SIKORA[3]

[1] *Lublin University of Technology, Institute of Electrical Engineering and Electrotechnologies, Nadbystrzycka 38a, 20-618 Lublin, Poland, elarm@eltecol.pol.lublin.pl*

[2] *Warsaw University of Technology, Institute of the Theory of Electrical Engineering and Electrical Measurements, Poland, sik@iem.pw.edu.pl*

[3] *Technical University of Szczecin, Theoretical Electrotechnics and Computer Science Department, Poland, rs@ketii.univ.szczecin.pl*

Abstract

The eddy current non-destructive testing of conductive materiale is well known problem. For some of eddy current transducer for flaw detection the mathematical modele were constructed and the Inverse Problem (IP) were formulated.

Two Artificial Neural Network reconstruction methods for Electrical Impedance Tomography (EIT) have been presented in this paper. The problem under study concerns the reconstruction of the conductivity distribution inside the investigated area using the information collected from the boundary. The first approach consists in ANN learning using electrical potential vectors, which were obtained from numerical solution of the forward problems. The second method using a standard feed forward multilayered neural networks applies the circuit representation for the finite element discretization.

Keywords: inverse problems, artificial neural network, non-destructive testing.

1. INTRODUCTION

A specific widy current transducer for flaw detection in conducting plates is described in this paper. The cross section of the transducer is presented in Fig. l.

The transducer operates above the conducting plate (6) with the crack or flaw (7). This crack needs to be detected. The transducer consists of a ferrite core (1) with two coils (2) exciting the magnetic flux in opposite directions.

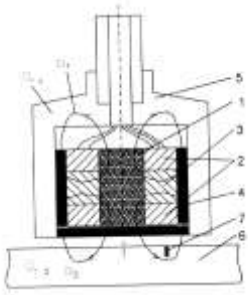

Fig. l. Model of transducer

Between them the signal coil (3) is placed. The coils are separated from the casing (5) by the insulating material (4). Usually the casing is made of the same material as the conducting plate (6).

2. MATHEMATICAL MODEL OF SINGLE CRACK IN THIN CONDUCTING PLATE

Let us consider the situation presented in Fig. 2. In order to build the mathematical model, the flaw was described by parameter vector $\{x\} = \{h,g,l\}^T$. This allows us to introduce a very simple mathematical model [2] and formulate the relation describing the absolute value of output voltage $U=f(\{x\})$ of the transducer. The problem is to estimate the parameter vector {x} on the basis of voltage measurements.

When the transducer is placed over the plate without a defect, both magnetic fluxes are equal and in opposite directions, so the voltage induced in the signal coil (3) is equal zero. But if conducting plate (6) contains a flaw then the fluxes are not the same and the voltage is induced in the signal coil. The induced voltage U depends on flaw's parameters (see Fig. 2).

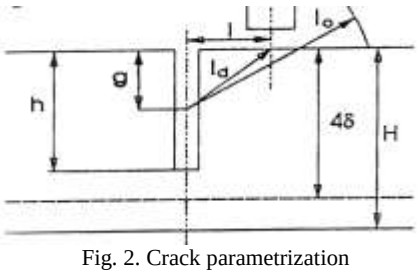

Fig. 2. Crack parametrization

where: h - depth of the flaw, l- the distance of the transducer from the flaw, H - thickness of the conducting plate, l_0 - working range of transducer, δ - skin depth.

After some test [2] it was observed that this particular transducer is not capable of recognising defects with depths greater than 4 δ. The skin depth b is defined by expression:

$$\delta = \sqrt{\frac{2}{\varpi \mu \gamma}} \tag{1}$$

where: ω – angular frequency, μ- permeability, γ – conductivity.

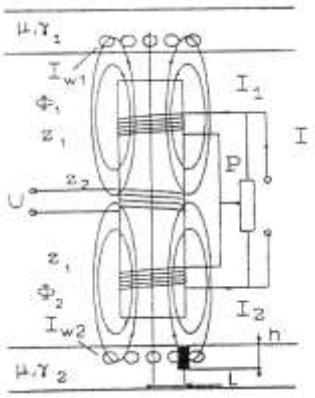

Fig. 3. Model of the transducer

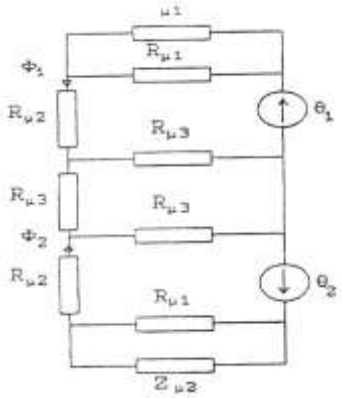

Fig. 4. Transducer's equivalent circuit

The simplified model of transducer is presented in Fig. 3 and its equivalent electric circuit is shown in Fig. 4. The equivalent circuit was synthesised using the simplifying assumption that the coils are fed from a current source and the nonlinearity of magnetic curve is not taken into account. Using the equivalent circuit we have:

$$\phi_1 = \frac{\theta_1}{R_\mu + R_{\mu 1} Z_{\mu 2} / (R_{\mu 1} + Z_{\mu 1})} \tag{2}$$

$$\phi_2 = \frac{\theta_2}{R_\mu + R_{\mu 1} Z_{\mu 2} / (R_{\mu 1} + Z_{\mu 2})} \tag{3}$$

where: $\theta_1 = I_1 z_1$, $\theta_2 = I_2 z_2$ – excitation, (magnetomotive forces), $R\mu = R\mu_2 + R\mu_3$ - reluctivity in the core and in the air, $R\mu_1$ - leackage reluctivity, $Z\,\mu_1$, $Z\,\mu_2$ - impedance for eddy current paths.

If we define the voltage signal as:

$$|U| = \varpi\, z_2 (\phi_1 - \phi_2) \tag{4}$$

then, after some mathematical mani-pulations we get [2]:

$$|U| = \frac{z_2 \theta \frac{h}{4\delta}\left[1-\left(\sqrt{\frac{h^2}{4}-l^2}\right)/l_0\right]^2}{4\sqrt{2}\cdot A\gamma\cdot\delta(k+1)^2\sqrt{1+\left\{1-\frac{h}{4\delta}\left[1-\left(\frac{h^2}{4}-l^2\right)\ l_0\ \right]^2\right\}^2}} \qquad (5)$$

where: $k = R\mu / R\mu_1$ (see Fig. 4), $A = z_w^2\ a/\ l_w$ - coefficient for representation of eddy current induced in the conducting plate, z_w - equivalent turns of eddy current path, l_w, a - equivalent length and width of eddy current path.

We evaluated the theoretical result through experimental tests conducted on aluminium plates (μ =1, y = 34 $\cdot 10^6$ S / m). Measurements and calculations was performed at a frequency equal to 300 Hz. At this frequency, the skin depth is equal to δ = 5 mm . The results of calculations (equation (5)) and measurements of the voltage signal are presented in Fig. 5.

There are mapy different methods for solving such problem. We will treat this problem as an Inverse Problem (**IP**) of Electromagnetic Field and we will apply the Artificial Neural Network in order to solve it [1,3].

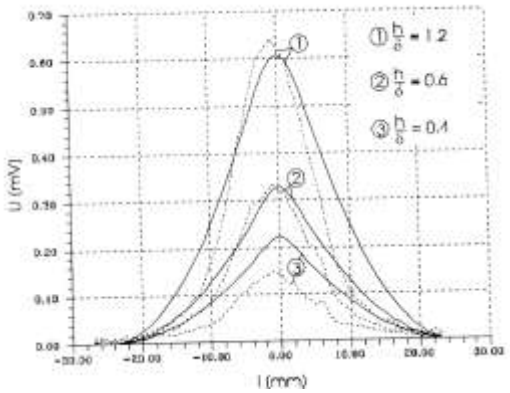

Fig. 5. Transducer's output voltage, solid line - mathematical model, doted line – nn measurements

3. NEURAL NETWORK APPLICATION

Equation (5) describing the relation between the voltage U with respect to depth of the flaw h and the distance 1 of transducer from the flaw is quite complicated. This equation can be written in the following form:

$$|U| = f(h,l) \qquad (6)$$

For Non DestructiveTesting (NDT) practice we have to find out the inverse relation, due to the fact that $|U|$ and l are known but the depth of the flaw remains unknown, so we are looking for relation:

$$h = f^{-1}(|U|, l) \tag{7}$$

The analytical approach to this problem using the mathematical model seems to be a tedious task. Instead the Artificial Neural Network approach was suggested. The structure of the net posses one input for voltage signal and one output for flaw parameter *h* which has to be identified. To solve such a problem a neural network with one hidden layer consisting of two sigmoidal neurons [1] was sufficient (see Fig. 6). The Neural Network was trained using data generated by the mathematical model.

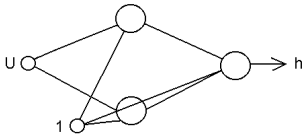

Fig. 6. Neural network structure

The graphical representation of the data base (column 2 of the Table 1) and the results of the training process (column3) are presented in Fig. 7 and Fig. 8 respectively.

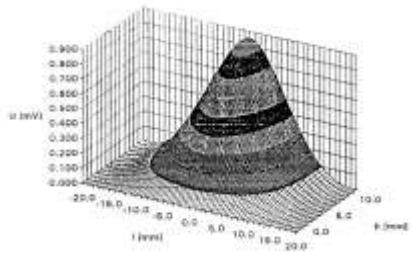

Fig. 7. Output voltage of transducer (calculated)

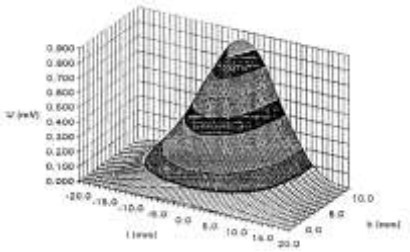

Fig. 8. Neural Network representation of output voltage

The absolute error values distribution (column 4) versus testing samples are shown in Fig. 9.

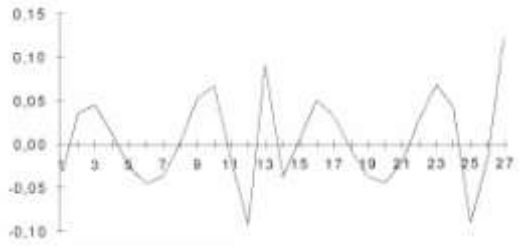

Fig. 9. Error distribution

The NETTEACH program needed 150 iterations only to train the neural network. So the teaching procedure is relatively easy in this case (see Fig. 10).

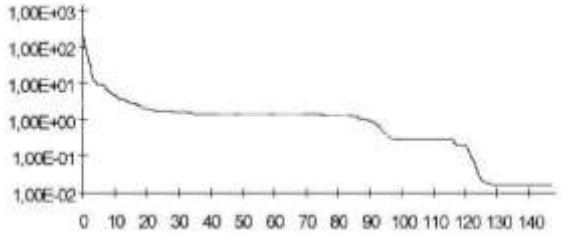

Fig. 10. The training process history

4. MATHEMATICAL MODEL

The main goal of this chapter is to present the new neural models for Electrical Impedance Tomography (EIT) [3,10], which could be regard as an noninvasive method for identification of internal structure of conducting regions. Using electric potential measurements on the boundary of a region, the conductivity distribution has been found. The simple model, shown in Fig.l1, was used for computer's simulation.

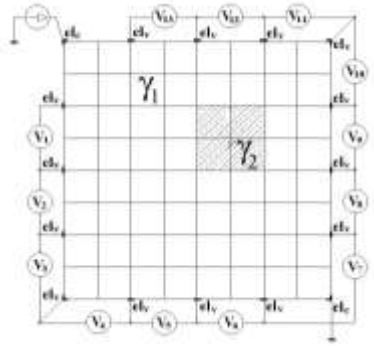

Fig. 11. The model of computer simulation

The region under consideration is a two-dimensional square area (square side d=4, any units of length) of specified electrical properties (conductivity $\gamma_1 = 1$ S/m). There is a sub-domain (object) inside, of other properties ($\gamma_2 = 3$ S/m). There is a system of 16 electrodes in order to collect the measurements along the boundary of the region (see Fig 11). The source of energy is connected to two electrodes (current electrodes) [3].

The other electrodes are used to measure potential differences along the boundary of the area. In order to get as much information as possible, eight independent arrangements of current electrodes, called projection angles, have been considered.

Fig. 11 shows configuration that corresponds to the first projection angle.

Than, 13·8=104 independent measurements for the same distribution of material coefficients can be obtained [3].

5. THE FIRST ANN METHOD

In the first method the ANN approach to inverse problem solution needs a huge database for neural network teaching [5,6]. In our case, the database consists of voltage difference measurements between the electrodes. At the beginning, the very simple case has been considered: only one inclusion (object), and shape and size is determined (square, side equal one unit only).

The idea of the first ANN approach is very simple. It is easy to collect measurements for all possible cases of object locations and using these data to train the neural network. In fact, it is not necessary and even not possible, to collect the data about all possible locations of the known object inside the region. The ANN behaves like an approximating system and is able to generalise the data. In order to prepare the database, the object of 1 unit size has Been moved by $\Delta l=0.5$ unit throughout the whole region. As the area side is $d=4$ units, there are 5 positions in the vertical direction and 5 in the horizontal direction. Totally, we have to consider $5 \cdot 5=25$ different object locations that means it is necessary to solve the forward problem $25 \cdot 8=200$ times (25 object locations and 8 projection angles).

The FAT (*Field Analysis Translator*) language has been used to solve the forward problems for every object's positions. The Finite Element model of the region, with two different Dirichlet boundary conditions is presented in Fig. 12.

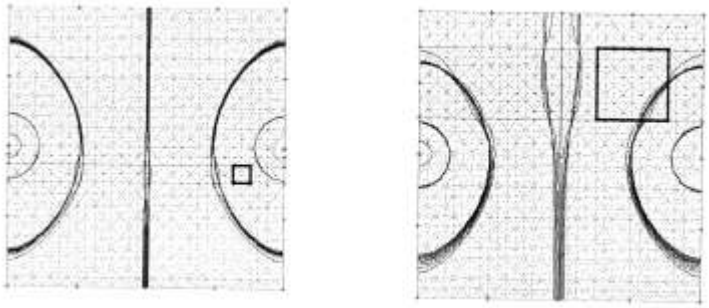

Fig. 12 The influence of small and big object positions on the potential distribution for two different projection angles

The database calculated by FAT language is collected in an ASCII file, and finally another ASCII file for ANN teaching has been created. The network trained with the aid of such a database, is able to construct the picture of the area interior, on the basis of the boundary voltage distribution, caused by the position of the object, which has never been seen by the neural network before.

Let the neural network evaluate the centre of the big -1 unit object (X,Y co-ordinates) on the basis of 104 linearly independent boundary voltage measurements. The ANN architecture should have 104 inputs and 2 outputs, providing only X and Y co-ordinates of the centre of the body.

Due to so urany inputs, it is very important to predict the proper number of hidden layers of neurones in the network structure, so that the training process would not be too long and the accuracy obtained could be satisfactory. The public domain program CASCOR (*Cascade Correlation Learning Algorithm*) has been used to design the structure

of the network. It can automatically optimise the ANN architecture by means of network expanding (adding new hidden layers when they are needed).

After training, the ANN is tested on the database consisted of 16 location cases, which have not been used for teaching. Some of the test results are presented in Fig. 13.

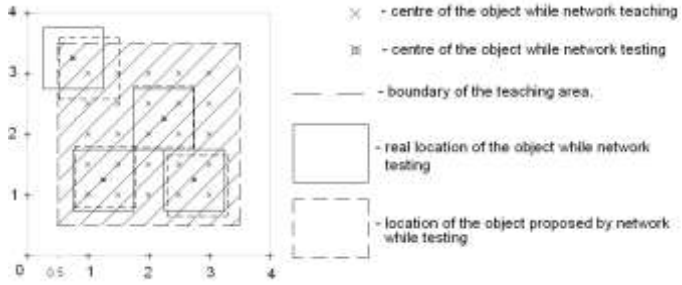

Fig. 13. Results of the object location test

The teaching area is the hatched sub-domain in this figure. There is a space (0.5 unit) between the boundary of the region and the teaching area in order to avoid the contact between the boundary and the inclusion. Such cases are particularly difficult for EIT. The maximal value of relative error, is less then 3% when the object is placed inside the teaching area, and about 8%, when the object is partially placed outside the teaching area (co-ordinates 0.75, 3.25 in Fig. 13). As a second stage of experiment different sizes of the objects was considered. The objects were divided for three classes: small (0.25 unit), medium (0.5 unit) and the big (1 unit) ones. That means that one additional output have to be considered. Results, for most difficult problem of small object identification is presented in Fig. 14.

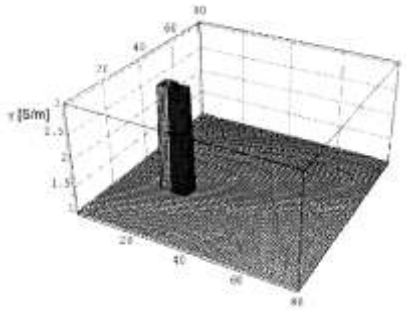

Fig. 14. Relief plot of object identification

6. THE SECOND METHOD - NEURAL NETWORK MODEL BASED ON FEM

From the very beginning the authors have applied the circuit representation for the Final Elements Method (FEM) and Kosugi et all [10] who applies neural networks to EIT.

In order to form the neural network model representing the FEM discretization of a certain region, one has to assign relevant neurons to each finite element and each node and connect them according to the geometry of the region. In other words our trik is to transform the expression minimising the energy functional, in order to use it as the mathematical model of a neural network [10].

After some mathematical manipulations we have achieved the following form [10]:

$$\frac{\partial F}{\partial V} = \sum_{i=1}^{m} \left\{ \frac{\partial V_i^e}{\partial V} K_i^e \left(\frac{\partial V_i^e}{\partial V} \right) \right\} V = 0 \tag{8}$$

where: F - functional equivalent of the partial differential equation and boundary conditions, V - state vector (in EIT - electric vector potential), V_i^e - nodal potentials for the i-th finite element, K_i^e - state matrix defined in the case of a square element.

The topology of neural network connections depends on the way of finite element discretization.

Mathematically, we can determine these connections calculating the first derivative of the nodal potential vector of a particular element with respect to nodal potential vector of the whole region (see eq.8).

Boundary conditions of the first kind (Dirichlet boundary conditions) are imposed as non-modifed input potentials (boundary nodes) and the relevant output signals equal zero in order not to modify the input potentials. The iterative solution to the system of equations (8) provides successive approximation of the solution. This is one possible approach. There is another one suggested in [10]. During the iterative process the input vector could be modified in such a way to minimise the error function, expressed by the following relation:

$$J = \left| Y - g(WX) \right|^2 \tag{9}$$

where: Y - output vector, X - input vector, W - weight matrix for each input connection with first hidden layer, g- activation function for connections between hidden layer and output layer.

The minimisation of the error function might be done changing the input vector when the weight matrix remains unchanged.

The difference between the two ways of iterative process depends on the calculation way of the vector improvement. For IP, the conductivity vector is an unknown value. To allow the conductivity change during the optimisation process the additional hidden layer has been introduced to the neural network architecture.

Now the error function for IP could be expressed as the sum of error functions J for all teaching vectors:

$$G = \sum_{k=1}^{T} J_k \tag{10}$$

where: T is a number of teaching vectors (projection angles), and J_k - back propagated error function defined by eq. (9).

So, we need to calculate the gradient of the error function with respect to unknown values: where the brackets and the subscript k mean that nodal potentials, are taken for the k-th teaching vector:

$$\frac{\partial G}{\partial \gamma_i^e} = \sum_{k=1}^{T} \left\{ \sum_j \left(\varepsilon_j \frac{\partial V}{\partial V_j} \right) \frac{\partial V_i^e}{\partial V} L_i^e \left(\frac{\partial V_i^e}{\partial V} \right)^t V \right\}_k \tag{11}$$

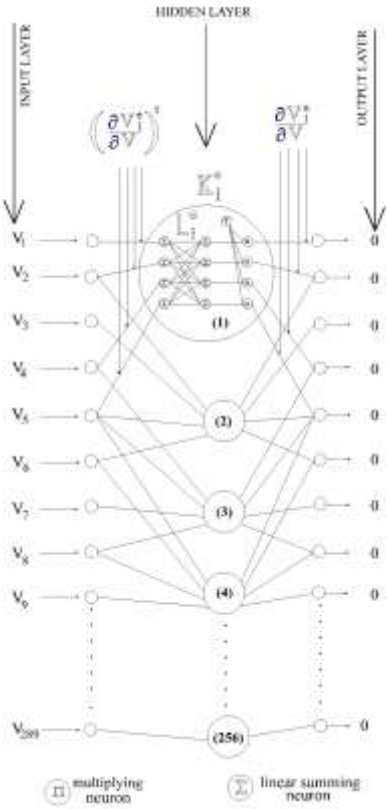

Fig. 15. Neural network representation of the region shown in Fig. 1

The conductivity vector is the same for all projection angles but potentials in the nodes are different (because.the boundary conditions are different), so they have to be modified during the optimisation process, espectively.

It means that for EIT, the optimisation process is more complicated than in the case, for example, of the forward problem (FP), so more effective optimisation methods are needed. We have adopted one of the simplest and most effective method, developed by Silva and Almeida [1].

In the Impedance Tomography applications the background conductivity has been almost exclusively selected as a starting point for optimisation process.

Let us consider the region shown in Fig. l1. Using the network structure presented in Fig. 6, the result of IP solution as a relief plot of conductivity distribution for all projection angles is presented in the following figure: as we can see the results are satisfactory. The surface of the background conductivity is flat and the object is placed correctly. Measurements have been simulated numerically and at this stage of numerical experiment the noise has not been introduced to the input signal.

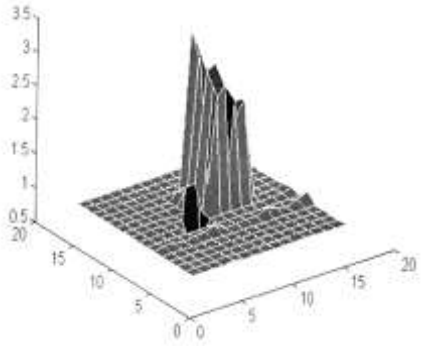

Fig. 16. Conductivity distribution for all 8 projection angles

7. CONCLUSIONS

A neural network has Been used to identify the parameters of the crack. The neural network serves to approximate relation (11). It is necessary to collect appropriate samples in order to train the neural network properly. In this case, the surface representing the inverse problem possesses is a very simple shape (see Fig. 16). Consequently the structure of neural network is not complicated (Fig. 15).

Traditional methods are difficult to implement due to the time consuming nature of the optimisation process. In contrast, the ANN approach is very fast, because the time consuming process is shifted from the optimization process to data preparation for ANN training. In the authors opinion this is the main advantage of this approach.

Using the ANN concept the two new approaches to EIT have been presented in this paper. The first approach, with the aid of Finite Element approximation, has created a training database to teach the net, which in consequence, leads to provide on-line images. The public domain software CASCOR was used to teach the net in this case. Unfortunately, until now, this method has only been valid for the narrow class of objects.

The second approach is more general than the first one. Only the numerical simulation is carried out now, and as such, it is not very efficient one. That is the main disadvantage of the second approach

REFERENCES

[1] Cichocki A., Unbehauen R.: Neural Networks for Optimisation and Signal Processing. John Wiley & Sons, 1993.

[2] Sikora R., Komorowski M., Chady T.: Defects Investigation in Conducting Sheets by Eddy Current Method. Internal Rapport (in Polish), 1994.

[3] E. Ratajewicz-Mikołajczak, G.H. Shirkoohi, J. Sikora: Two ANN reconstruction methods for electrical impedance tomography. IEEE Trans. on Mag. Vol. 34, No. 5, Sept. 1998, pp. 2964 - 2967.
[4] Enakizono M., Akinari Y.: Defect identification in magnetic materials by using genetic algorithm. The International Symposium on Advanced Computation and Design Techniques in Applied Electromagnetic Systems, S-y. Hahn (Ed.), 1995 Elsevier Science pp. 117-120.
[5] Morabito F.C., Albanese R., Coccorese E., Martone R., Rubinacei G.: Identification of Circular Holes in Thin Plates Using a Neural NetworkApproach, The Int. Symp. on Non-Linear Electromagnetic Systems ISEM'95, Cardiff, Wales, UK, Sept. 17-20, 1995.
[6] Takeo Ishikawa, Yusuke Tsukui, Michio Matsunami: Optimization of Electromagnetic Devices Using Artificial Neural Network with Quasi-Newton Algorithm; 10`" Conference on the Computation of Electromagnetic Fields COMPUMAG'95, Berlin, July 10-13, 1995, IEEE Trans. on MAG, Vol. 32, No 3, pp1226-1229.
[7] Kosugi Y., Takeuchi J.: Neural Network Representation of Finite Element Method. Contributed article Neural Networks Vo1.7 No.2, 1994.

4th International Conference **ELMECO**
Nałęczów, Poland
September 2003

HAZARDOUS EFFECTS OF ELECTROMAGNETIC FIELDS EMITTED BY COMPUTER DISPLAY UNITS (SELECTED EXAMPLES)

Zbigniew ZŁONKIEWICZ

Lublin University of Technology, Institute of Electrical Engineering and Electrotechnologies
20-618 Lublin, ul. Nadbystrzycka 38a, e-mail: zbigz@eltecol.pol.lublin.pl

Abstract

Display units are used to present the information in the form of graphics or text and to control visually input data during their operation. People are subject to the influence of electromagnetic fields generated by the display while working at the computer, or staying in the surrounding of operating computer. Working at the display unit has usually been performed while sitting in the distance of 0,3 to 0.5 m from the unit and watching the displayed data. It may last the whole working day with short breaks that result e.g. from labor regulation. The investigations were aimed to define the level of hazardous influence that may affect staff members and the students operating this sort of devices at the laboratory of the Institute of Electrical Engineering and Electrotechnologies. In the paper, the distributions of electromagnetic fields emitted by selected computer display units have been presented.

Keywords: electrical engineering, electromagnetic fields.

1. INTRODUCTION

Polish endeavours to become the member of the EU are deeply related to the necessity of adjusting legal aspects of industrial safety and health protection while operating the devices equipped with the display units (90/270/EWG). Display units are used to present the information in the form of graphics or text and to control visually input data during their operation. The most common display units are CRT-cathode ray tube (colour or monochromatic ones). However, rapid introduction of LCD-liquid crystal display units that operate both with portable and stationary computers has been observed lately.

CRT display units generate electromagnetic fields of wide frequency spectrum, from electrostatic fields to high frequency fields:

- electrostatic fields–of the display unit and high frequency feeder (30kV depending on the diagonal of the display unit),
- low-frequency fields of about 50-120Hz – of the supply system of the display unit (50Hz) and vertical deviation of triangular shape course or similar,
- medium-frequency fields of about 15-125 kHz – of the system of horizontal deviation of triangular shape course or similar,
- high-frequency fields – of the vision feeders.

People are subject to the influence of electromagnetic fields generated by the display while working at the computer, or staying in the surrounding of operating computer. Working at the display unit has usually been performed while sitting in the distance of 0,3 to 0,5m from the unit and watching the displayed data. It may last the whole working day with short breaks that result e.g. from labour regulations.

The investigations were aimed to define the level of hazardous influence that may affect staff members and the students operating this sort of devices at the laboratory of the Institute of Electrical Engineering and Electrotechnologies.

In the paper, the distributions of electromagnetic fields emitted by selected computer display units have been presented.

2. VARIOUS TYPES AND CONSTRUCTION OF DISPLAY UNITS

Computer display units can be divided into 5 types [16]:

- **Digital**, so-called marked or simply terminals (used before analogue ones in Fig.),
- **Analogue** with **perforated** mask,
- **Analogue** with **slotted convex** mask e.g. *Trinitron Sony*, *Diamondtron Mitsubishi* or developed *Croma Clear* of NEC,
- **Analogue** with **slotted concave** mask e.g. *FD Trinitron Sony* or *Diamondtron NF Mitsubishi*,
- **Flat Plasma Panels.**

Additionally, the following 2 sub-types of display units can be specified:

- **Monochromatic** e.g. white (white-black), green or ruby.
- **Colour**: digital (*LCD* and marked terminals) and analogue (*LCD* and *CRT*).

Such division seems to be suitable due to the differences in the construction of cathode ray tubes - *CRT* and electronics of *LCD*. *CRT* are almost identical with those applied in TV sets [1] e.g. *FD Trinitron* and *TV* of *WEGA Sony*. The tube is the most important element, which has been supported with electronic control systems.

PARAMETERS OF THE DISPLAY UNITS

Computer display units, depending on the applied technical solutions, materials quality and manufacture has different range of possibilities. The following parameters influence this range [16]:

- *Horizontal frequency* – describes how many lines of the display are able to serve electron stream per second.
- *Vertical frequency* – number of displayed pictures per second. The higher value of this parameter, the less thrashing occur; recommended value: higher of equal to *72 Hz.*

- Video bandwidth – no of picture points that can be displayed per second. For the display unit of 1024x768 and vertical frequency of 70 *Hz*.
- Temperature of the colour – value that describes the colours (compared to white) displayed by the unit;
- Size of the light spot – the lowest distance between two points of the picture of the same colour.

TENDENCY AND DEVELOPING PROSPECTS OF THE DISPLAY UNITS

Display units for many years have been the devices that consumed significant amount of electric energy. In recent years, this aspect has been highlighted and this has brought to the inclusion of managing power input function which commonly appears in nowadays display units. However, the activation of at least one level of energy savings is feasible only by the computer. The investigations among computer users revealed that *30-40%* of computer operation time is useless [16]. In order to decrease energy consumption, the devices of several activity levels are applied. In recent years, a lot of changes and improvements were introduced that significantly improved the quality of displayed picture. New materials like invar for masking frame construction show higher thermal stability and are more resistant on heat generated by electron beam. Technologies of display units manufacture like aperture grids, black matrix, *Trinitron Sony* and *Microfilter Toshiba* improve the contrast and colour brightness and the development in the manufacture of anti-reflection coatings improved the quality of vision.

This may lead to convergence interests of TV and computer monitors manufacturers because HDTV specification defines the resolution of 1920x1080, which is highly sufficient to display the data on computer monitors. *HDTV* offers wider spectrum to computer users i.e. on the display unit of 16:9 (compared to the units of 4:3). Finally, the prices of computer display units may be lower due to the application of the scale effect provided that the market of TV will adjust *HDTV technique*, and the same picture tubes could be used in both devices.

3. DEVICES AND METHODS USED FOR THE MEASUREMENTS OF ELECTROMAGNETIC FIELD

MEASURING DEVICES

Anechoic chambers are the devices that support the investigations on electromagnetic field. They should provide good acoustic insulation, and protect from the emission of electromagnetic field background. They allow precisely determine the emissivity of selected electric device. The dimensions of the chamber should depend on the dimensions of the investigated element. Their construction is more profitable than e.g. shielding the whole laboratory. During the emissivity measurements, measuring receiver is connected to the concentric cable that ends the spherical part of the anechoic chamber, thus it is possible to measure the signals proportional to electromagnetic radiation emitted by the device.

DESCRIPTION OF THE METERS

The Institute of Electrical Engineering and Electrotechnologies has been equipped with 4 meters for measuring electromagnetic interferences:

- ULMZ-4/50 interference meter – to measure impulse and sinusoidal voltage as well as the intensity of electromagnetic field in the range of *25 – 100 MHz*,
- DLMZ-4/50 interference meter – to measure impulse and sinusoidal voltage as well as the intensity of electromagnetic field in the range of 0.3 *– 1 GHz*,
- TRACER EF100 – meter of electric component of electromagnetic field in the range of
- *30* Hz to *400 kHz*,
- TRACER MR100 – meter of magnetic component of electromagnetic field in the range of *5 Hz* to *400 kHz*.

Due to the compatibility of the meter with the frequency of electromagnetic field emitted by the display unit, as well as the availability of technical specification and measurement accuracy - TRACER 100 meters have been selected.

Table 1. Technical specification of TRACER – 100.

Parameter	TRACER EF100	TRACER MR100
Measuring capacity (ELF)	1 - 15000 V/m	1 mGs – 15G
Frequency range (ELF)	30 Hz - 1 kHz	5 Hz – 2 kHz (-3 dB)
Measuring procedure (ELF)	rms value	rms value
Accuracy (ELF)	2%	1%
Measuring capacity (VLF)	1 – 1500 V/m	0.1 – 20 mG
Frequency range (VLF)	2 – 400 kHz	2 – 400 kHz (-3 dB)
Measuring procedure (VLF)	rms value	rms value
Accuracy	2%	1%

4. INVESTIGATION OF ELECTROMAGNETIC FIELD COMPONENTS AROUND SELECTED MONITORS

For the measurement of electric field the dipole sound sensor of its structure similar to the condenser has been applied. The measurement of current I (or charge) between two electrodes of the sensor allows for the measurement of field intensity according to the following equation:

$$I = k_E \cdot f \cdot E \tag{1}$$

where:
k_E – conversion ration determined through calibration,
f – frequency of measured field,
E – intensity of measured field.

The meter should be placed on the stand made of non-conducting material; the measurement shall be taken at a distance from human beings and conductive objects.

Low-capacity coil has been the common sensor typically applied in magnetic field meters. Voltage *U* induced at coil clamps depends on magnetic field intensity *H* measured in accordance with the analogue equation, where k_H is the adequate conversion ratio:

$$U = k_H \cdot f \cdot H \tag{2}$$

Magnetic field measurements do not require the application of the outrigger. Since magnetic field components are 3D, it is necessary to take 3 measurements at each point.

If these three measurements give three constituent results *X, Y, Z*, thus final result of magnetic field intensity *W* shall be calculated from the following equation:

$$W = \sqrt{X^2 + Y^2 + Z^2} \tag{3}$$

In both types of meters, output signal from the sensor (*I, U*) has been intensified and processed in the meter circuit. The result is the following: rms value of measured field in *V/m* or *kV/m* (electric component) and in *A/m*, *T* (tesla) or *G* (gauss) (magnetic component). Measurement result has been presented in digital form. In practice, the course of measured fields is often distorted and then the result obtained directly from the mean value may be burden with considerable error. Therefore, in modern meters, the methods for measuring the real rms value have been applied.

INVESTIGATION OF SELECTED MONITORS

Tested display units have been selected due to the following issues: diagonal of the display unit, date of manufacture, availability. Three 14-inches display units produced in the period of 1996-1998 enabled to analyse whether the date of manufacture has been the factor that disqualifies the manufacturer and the technology in respect of electromagnetic field emissivity. Two 15-inch display units have been included to the tests that allowed concluding whether the diagonal of the display unit influences the value of PEM components. The tests have been carried out at the same stand; the remaining elements of the computer system were placed identically in order to get uniform influence of each system components on taken measurements.

Taking both diagonal of the display unit and date of manufacture into consideration, 5 units have been tested.

Table 2. Specification of the examined display units.

Display unit	Date of manufacture	Diagonal of the display unit (inch)	symbol
LG	V-1998	14	
DAEWOO	VI-1996	14	CMC-1427X
GOLDSTAR	V-1996	14	
NOKIA	IX-1999	15	449ZA
SMILE	II-1999	15	KFC CA65 5DL

The measurements have been taken in the same room; the letters have been displayed at black background on the left side of the display unit. Other elements of computer set e.g. central unit have been located at the same place.

Table 3. Background level for particular range.

Measuring range	Frequency range	E	H		
		V/m	mGs	A/m	mT
ELF	2-1000 Hz	3,1	1,3	0,107	0,13
VLF	1-400 kHz	0,3	3,974	0,155	0,394

For each display unit, 4 measurements of display unit's components have been taken: electric and magnetic in ELF and VLF range.

The measurements were taken at 8 distance points from the display unit at each side, at 3 different height points.

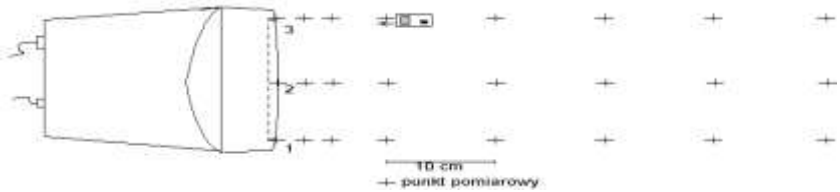

Fig. 1. Schema of the measuring stand - top view.

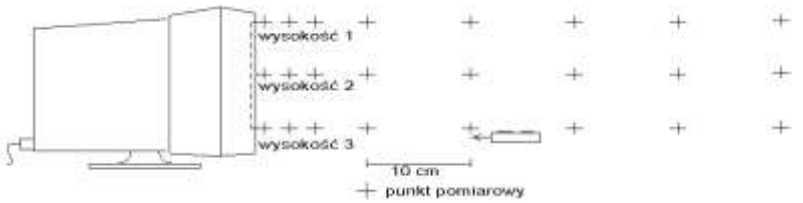

Fig. 2. Schema of the measuring stand – lateral view.

MEASUREMENT AND CALCULATIONS OF ELECTROMAGNETIC FIELD COMPONENTS (PEM)

After taking the measurements, the value of magnetic field component has been calculated from the equation (3).

Selected results of measurements and calculations are presented at the diagrams below. The colours at the diagrams are assigned to particular type of monitor.

Table 3. Electromagnetic field components at the distance of 0 cm.

ELF						
FRONT	E_1	E_2	E_3	H_1	H_2	H_3
	V/m	V/m	V/m	A/m	A/m	A/m
DAEWOO	92	210	190	1,54	0,82	1,56
NOKIA	26	30,5	26,4	0,72	0,44	0,60
GOLDSTAR	91	155	132	1,27	0,79	1,32
LG 15	64,1	100	99	1,87	0,90	1,85
SMILE	69	220	127	1,27	0,82	1,13
VLF						
DAEWOO	12	49,1	25,9	419,00	607,44	378,04
NOKIA	2,4	14,2	3,8	252,09	544,58	257,60
GOLDSTAR	21,3	25,8	27,6	896,50	663,81	427,03
LG 15	5,3	31,9	23,3	263,65	593,11	366,58
SMILE	21,2	34,7	27	1239,19	1894,12	1265,09

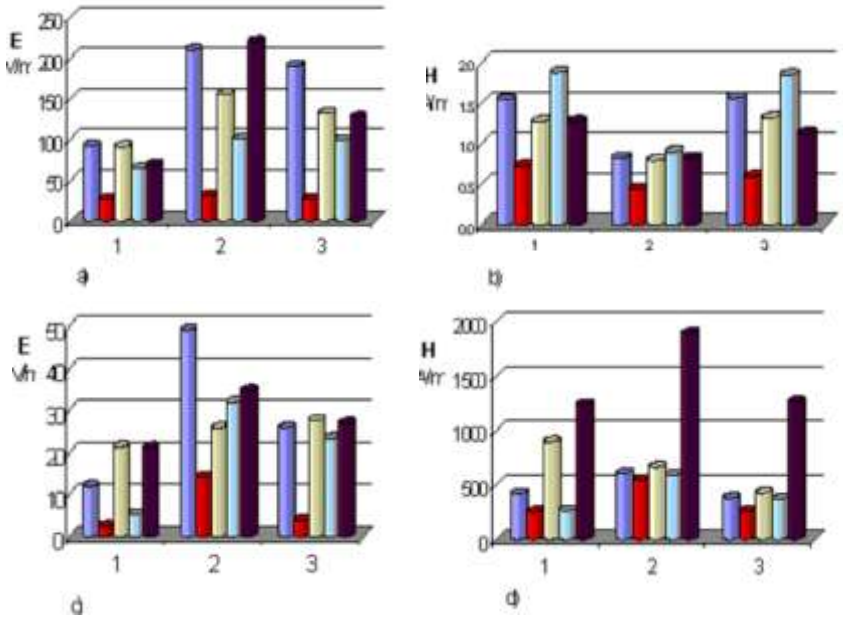

Fig. 3. Selected results of the measurements a) electric field components, ELF range, front side of the display unit, distance - 0 cm, b) magnetic field components, ELF range, front side of the display unit, distance - 0 cm, c) electromagnetic field components, VLF range, front side, distance - 0 cm, d) magnetic field components, VLF, front side of the display unit, distance - 0 cm, 1,2,3 – points on horizontal plane of the display unit (Fig. 2).

5. CONCLUSIONS

At the distance of 0cm (i.e. close to the display unit) electromagnetic field components reached the highest values. SMILE display unit received the most negative evaluation at which for magnetic component at VLF range (*2 – 400 kHz*) the value of field was as high as *1894 A/m* (Tab.3. Fig. d). High values of electric component have been noticed for GOLDSTAR I DAEWOO (*150 – 210 V/m*) also in the middle of the monitor. A lot of irregularities occur at the right and left side, however the highest value of magnetic field components has been measured at SMILE display unit at right and left side (*1949 A/m* and *2037 A/m*) for VLF component. At electric component the distinguished units were DAEWOO (*115 V/m* right side at ELF range (*5 – 2000 Hz*), and *270 V/m* at ELF at the left side). A very high value (171.9 V/m VLF range) has been measured in SMILE - at the left side – analogue measuring point on the right side, electric component = *16.8 V/m*. Maximal value taken at the back of the monitor was 843.6 A/m (monitor SMILE, VLF range), and 173 V/m (monitor GOLDSTAR, ELF range).

At longer distance (<30cm) from the examined display units the values of particular PEM components equalize – emissivity of magnetic component is at similar level, however, the attention shall be paid on SMILE display unit which similarly to the previous tests showed the tendency of increased medium emissivity level of the examined display units. The differences for DAEWOO or LG.

Among the examined ones, 15-inch NOKIA (449ZA) display unit received the highest rant; it showed the lowest electromagnetic field emissivity in all tests. Among 14-inch ones the display unit produced by LG shall be mentioned. Even though GOLDSTAR and DAEWOO display units were the oldest among tested ones they keep good results in respect of the emitted PEM.

REFERENCES

[1] Kameduła M., Kameduła T., Mikołajczyk H. Wymagania higieniczne na stanowiskach pracy przy monitorach ekranowych, Instytut Medycyny Pracy, Łódź 1996 r.

[2] Dr Lippmann C., Komputer a zdrowie - praca zbiorowa, CREDUS PUBLISHING HOUSE.

[3] Trzaska H., Pomiary pól elektromagnetycznych w polu bliskim, Wydawnictwo Naukowe PWN 1998 r.

[4] Presman A.S., Pola elektromagnetyczne a żywa przyroda, Warszawa PWN, 1968.

Decrees

[5] Decree of the Ministry of Labour and Social Policy, and Ministry of Health of 19.02.1977 on the safety at operating the devices that generate electromagnetic field in the range of 0.1 do 300 MHz. (Journal of Acts No 8, 1977, item. 33).

[6] Decree of the Council of Ministers of 25.05.1972 on the safety at operating the devices that generated electromagnetic field in microwave range (Journal of Acts No 21, 1972, item 153).

[7] Decree of the Council of Ministers of 05.11.1980 on detailed safety rules against electromagnetic non-ionised radiation dangerous for human beings and the environment (Journal of Acts No 25, 1980, item. 101).

[8] Decree of the Ministry of Labour and Social Policy of 02.01.2001 amending the decree on the highest permissible concentrations and intensity of dangerous factors in working environment. (Journal of Acts No 4, 2002, item. 36).
[9] Decree of the Ministry of Labour and Social Policy of 01.12.1998 on the safety and hygiene of work at the work place equipped with computer display units.
[10] Decree if the Ministry of Environment Protection, Natural Resources and Forestry of Aug. 11, 1998 r. on special safety rules against the radiation dangerous to human beings and environment, permissible levels of radiation, and obligatory instructions applied during measurements. (Journal of Acts No 98.107.676 of 20.08.1998).

Internet

[11] www.oko.info.pl, OKO CZŁOWIEKA – 2000.V.29
[12] www.strony.poland.com/pawelam/ – 2000.V.29
[13] www.elektronika.basnet.pl – 2000.V.29
[14] http://www.shinden.pl/newage/monitory.htm#index – 2000.V.28
[15] http://panda.tu.koszalin.pl/BK/monitory2/Bud_kine.html, Budowa monitora – 2000.VI.3
[16] http://panda.tu.koszalin.pl/BK/monitory2/B_mon_ki.html, Budowa i działanie monitora komputerowego – 2000.VI.3

Other

[17] Technical specification of TRACER 100.
[18] Technical specification of DLMZ-4/50.
[19] Technical specification of ULMZ-4/50.
[20] PN-EN 50081-1 – Requirements in respect of emissivity.
[21] Forowicz K., Nerwy i oczy przed monitorem, "Rzeczpospolita" of 22.07.99,No 169.
[22] Pole elektromagnetyczne „Twoja Komórka” No.6/99.
[23] Kalisz J. Mierniki do pomiaru szkodliwych pól elektromagnetycznych, „Bezpieczeństwo Pracy”, VIII-1997r.

4th International Conference **ELMECO**
Nałęczów, Poland
September 2003

NUMERICAL ANALYSIS OF MAGNETIC HYSTERESIS LOSSES IN HIGH TEMPERATURE SUPERCONDUCTORS

Dariusz CZERWIŃSKI, Tomasz GIŻEWSKI

Institute of Electrical Engineering and Electrotechnologies, Technical University of Lublin
ul. Nadbystrzycka 38A, 20-618 Lublin, Poland
e-mail: darekc@weber.pol.lublin.pl

Abstract

Power losses related with superconductor properties and magnetic field penetration are generated in AC superconducting devices based on HTS superconductors. The pinning of flux tubes is the main reason of hysteresis formation. Magnetic hysteresis additionally generates power losses in superconducting parts of AC devices.

Keywords: high temperature superconductors, magnetic hysteresis, flux pinning, AC power losses.

1. INTRODUCTION

Modern superconducting devices have many parts built of high temperature superconductors. HTS superconductors and the matrices are partially penetrated by magnetic flux. The tubes, through which the flux passes the superconductor, are 'pinned' to certain locations due to impurities in the crystal structure of the material. The transport current and external magnetic field are the determining factors of the tubes movement.

The critical state model is a well-known, macroscopic model is a good way to describe this partial flux penetration. Furthermore, the flux tubes can start to flow due to the Lorentz-force when a large transport current flows in the superconductor. This produces the additional resistive loss.

The concept of hysteresis in HTS superconductors is discussed and a few models describing this phenomenon are presented. An emphasis is put on the classical Preisach model of hysteresis.

2. TYPE I AND II SUPERCONDUCTORS

The superconductors, because of their behaviour, can be divided into type I and type II

Type I superconductors have a clear border between superconducting state and resistivity state. Supercondutors of type II have two values of critical magnetic flux density (Fig. 1. and Fig. 2.).

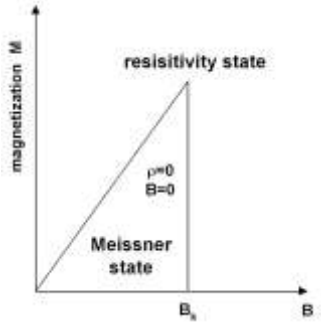

Fig. 1. Type I superconductor

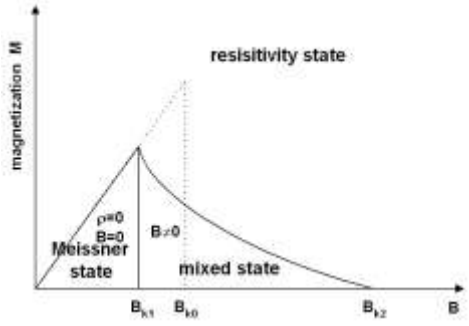

Fig. 2. Type II superconductor

3. MAGNETIC FIELD AND INTERNAL CURRENTS IN HIGH TEMPERATURE SUPERCONDUCTORS

In superconducting state the Lorentz force is less or equal to pinning force. In mixed state when the Lorentz force is greater than pinning force addition resistance appears.

Assuming that Lorentz force is greater than pinning force we obtain:

$$\boldsymbol{J} \cdot \boldsymbol{\Phi}_0 = \eta \cdot \boldsymbol{v} \tag{1}$$

– η - viscosity
– v - velocity of vortex drifting
– J - current density
– Φ_0 - vortex flux

The movement of vortices causes arising E which is parallel to J (Fig. 3. and Fig. 4.)

$$\boldsymbol{E} = \boldsymbol{B} \times \boldsymbol{v} \tag{2}$$

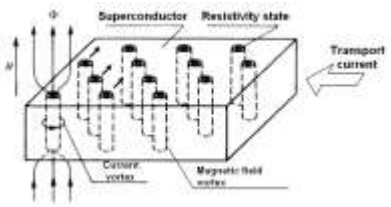

Fig. 3. Pinning forces are equal to Lorentz forces

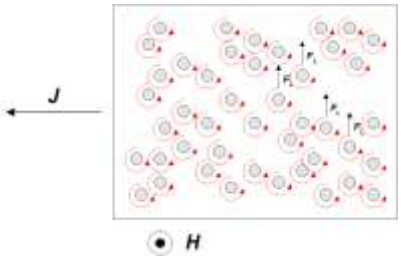

Fig. 4. Pinning forces are smaller then Lorentz forces

Resistivity connected with flux flowing in the superconducting part:

$$\rho_f = \frac{\boldsymbol{E}}{\boldsymbol{J}} = \boldsymbol{B}\frac{\boldsymbol{\Phi}_0}{\eta} \tag{3}$$

In rezistivity area

$$\rho_f = \rho_n \frac{H}{H_{c2}} \tag{4}$$

In modern supercodnucting devices their main elements are built of HTS tapes. The tape consists of HTS fibres and silver matrix (Fig. 5.). During regular work, when the device is supplied with AC current, the flux vortices are pinned to the pinning centers (Fig. 6.).

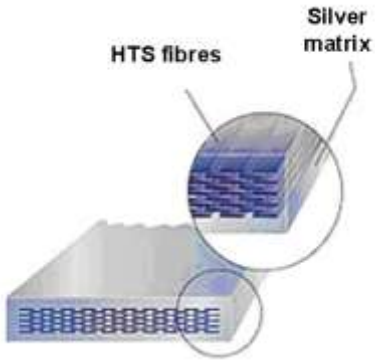

Fig. 5. HTS tape with silver matrix

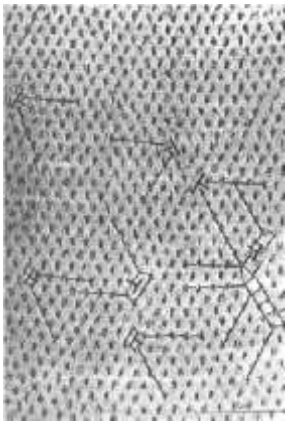

Fig. 6. Vortices net in mixed state HTS [2]

4. HYSTERESIS IN HTS

In superconducting state the Lorentz force is less or equal to pinning force. In mixed state when the Lorentz force is greater than pinning force addition resistance appears.

Forces acting on the flux vortices

Force affecting on single vortex

$$\boldsymbol{f} = \boldsymbol{J} \times \boldsymbol{\Phi}_o \tag{5}$$

Force affecting on volume unit of vortices network.

$$\boldsymbol{F}_L = \boldsymbol{J} \times n\boldsymbol{\Phi}_o = \boldsymbol{J} \times \boldsymbol{B} \tag{6}$$

– finally

$$\boldsymbol{F}_L = rot\boldsymbol{H} \times \boldsymbol{B} \tag{7}$$

For theoretical considerations let us assume that H vary only in X direction:

$$\boldsymbol{H} = H_x \tag{8}$$

– we receive

$$F = \frac{dH}{dx} B \tag{9}$$

Pinning force

$$F_p = J_c B = \frac{dH}{dx} B \tag{10}$$

5. MODELS DESCRIBING BEHAVIOUR OF MAGNETIC FIELD IN HTS

There are a few models, which try to describe the behaviour of magnetic field in high temperature superconductors. Following equation represents critical state model (Bean model):

$$\boldsymbol{J} = \begin{cases} 0, & \boldsymbol{E} < \boldsymbol{E}_c \\ \boldsymbol{J}_c, & \boldsymbol{E} \geq \boldsymbol{E}_c \end{cases} \tag{11}$$

The second one is principle of energy maintaining (E-J model):

$$\boldsymbol{E} = E_c \left(\frac{|\boldsymbol{J}|}{J_c(B)} \right)^{n(B)} \frac{\boldsymbol{J}}{|\boldsymbol{J}|} \tag{12}$$

where: n(B) and Jc(B) depends on value of internal flux density B.

Neither of the models describe the dependence of critical current density and external magnetic field. Additionally Kim and co-authors make dependent value of critical current density J_c on external magnetic field:

$$J_c(B,T) = J_{c0}(T) \left(1 + \frac{B_m}{B_0} \right)^{-1} \tag{13}$$

where: B_0 and $J_{c0}(T)$ are constant

AC losses generated in superconducting parts are given by equation (14)

$$P = \frac{1}{A} \oint dt \int_{Ss} E \cdot J dS \tag{14}$$

where: A - total area, Ss - cross-surface of the windings.

6. HYSTERESIS MODELLING IN HTS

Classical Preisach model and application

The most important references, on the modeling hysteresis, were described by the classical Preisach model. The equation (15) shows the basic definition of this method:

$$M(t) = \iint_P \mu(\alpha,\beta)\gamma_{\alpha,\beta}h(t)\mathrm{d}\alpha\mathrm{d}\beta \tag{15}$$

M(t) the function describing output signal (magnetization);
α, β - variations of Preisach space dependent on input signal;
$\gamma_{\alpha,\beta}$ - describes the state of a single domain,
μ(α,β), – variations of weighting function (Fig. 7.).

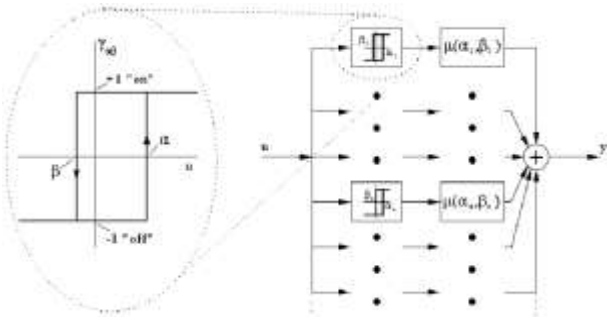

Fig. 7. Graphical representation of hysteresis relay operators and their influence on hysteresis loop

The area of Preisach surface was divided into two planes by signal input change. As it has been shown at equation (16), magnetization M was expressed as difference of double integrals of function μ(α,β) - negatively and positively oriented of plane P.

$$M(t) = \iint_{P-} \mu(\alpha,\beta)h(t)\mathrm{d}\alpha\mathrm{d}\beta - \iint_{P+} \mu(\alpha,\beta)h(t)\mathrm{d}\alpha\mathrm{d}\beta \tag{16}$$

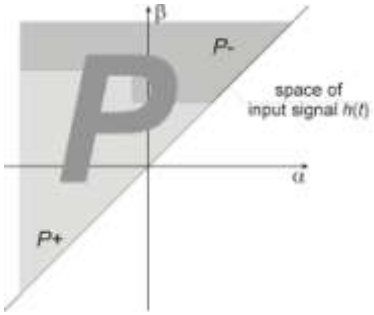

Fig. 8. Preisach plane

The area of plane P (Fig. 8.) has been swept across of input signal which changes monotonically. For positive increase, outlined area has been in relation to variable α (P+) and for negative area in relation to variable β has been separated (P-).

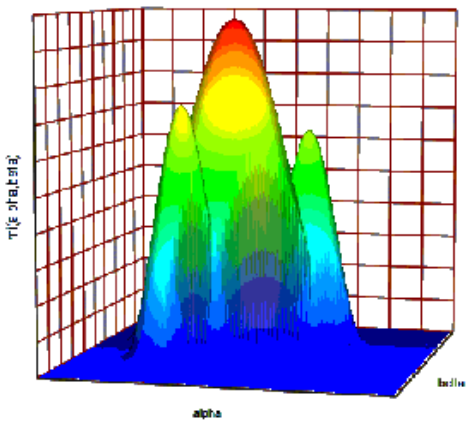

Fig. 9 Graphical representation of weighting function of Preisach model

The hysteresis loop was simulated by program, based on weighting function and Preisach model defined by equation (15). The result of calculation, algorithm and weighting function were shown in figure 10.

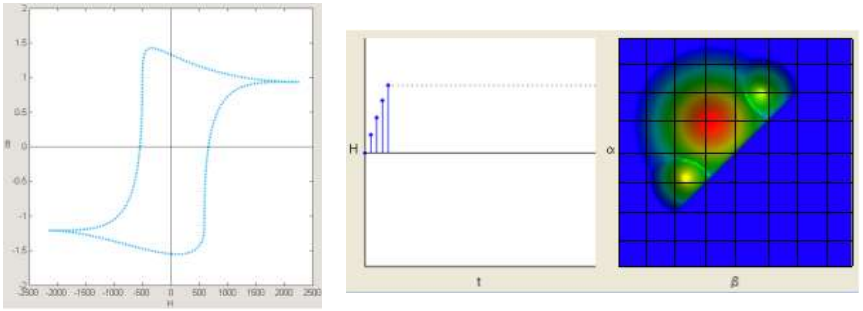

Fig. 10. Hysteresis loop simulated by program based on Preisach model in Matlab environment; algorithm and presentation of weighting function

Experimental process in determination of weighting function of Preisach systems

The elementary problem in Preisach system of hysteresis is the acquisition of data collection. To show the value of weighting function the experimental result has been employed to determinate it. The back propagation algorithm has been applied to approximate the weighting function.

The data collection assignments was coupled with application in the way, that could be executed in the track of measurement and could be realized by artificial neural network, classification or qualification of class of probability

Basing on equation (1) the alterations of the values of function B(H) are determined as follows:

$$b_{\alpha',\beta'} - b_{\alpha'} = -2 \iint_{T(\alpha',\beta')} \mu(\alpha,\beta)\mathrm{d}\alpha\mathrm{d}\beta \tag{17}$$

where: b – is a momentary value of function B(H), and curl value is determined in the triangle restricted wit values α, β (in boundaries <-1,1>) as also as Preisach plane (figure 11).

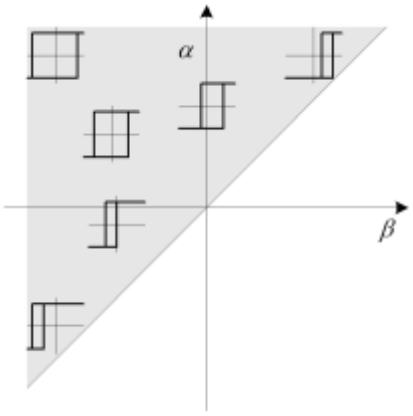

Fig. 11. Preisach plane and hysteresis relay operators

Assuming: $B(\alpha',\beta') = \frac{1}{2}(b_{\alpha'} - b_{\alpha',\beta'})$ and substituting into (4) we receive:

$$B(\alpha',\beta') = \iint_{T(\alpha',\beta')} \mu(\alpha,\beta)\mathrm{d}\alpha\mathrm{d}\beta \tag{18}$$

in this case the searched function is:

$$\mu(\alpha',\beta') = -\frac{\partial^2 B(\alpha',\beta')}{\mathrm{d}\alpha'\mathrm{d}\beta'} \tag{19}$$

CONCLUSIONS

There are flux flowing and arisen resistivity, if transport current “moves” magnetic vortices net.

Flux movement is a main reason of hysteresis phenomenon in HTS superconductors.

Hysteretic losses are the main part of AC losses in high temperature superconductors.

Artificial neural network could be used for optimization of data access. Neural networks could be used for generating of the indexes related to a matter of data stored on different levels.

The task of selection was implemented with Kohenen networks. These networks make possible in a simple way to implement the relationship between data (relationship in time domain, plane and space). Self-organisation is the advantage of the network.

REFERENCES

[1] Cyrot M. Pavuna D., Wstęp do nadprzewodnictwa, nadprzewodniki wysokotemperaturowe, Wydawnictwo Naukowe PWN, Warszawa 1996.

[2] Trauble and Essmann, The Direct Observation of Individual Flux Lines in Type II Superconductors, Phys. Lett. A24, 526 (1967)

[3] M. R. Koblischka, L. Pust, A. Galkin, P. Na´levka, M. Jirsa, T. H. Johansen, H. Bratsberg, B. Nilsson and T. Claeson, Flux penetration into an artificially granular high-Tc superconductor, PHYSICAL REVIEW B 1 MAY 1999-II VOLUME 59, NUMBER 18

[4] Mayergoyz I.D. Mathematical models of hysteresis, Springer-Verlag, New York 1991.

[5] Bertotti G., Hysteresis in magnetism, Academic Press, San Diego 1998.

[6] Wac-Włodarczyk A. Giżewski T., Analiza funkcji wagi □ (□ , □) modelu Preisach'a z wykorzystaniem algorytmu sztucznej sieci neuronowej, ZkwE, Poznań 2000.

[7] Handbook of neural network signal processing, CRC Press 2002.

4th International Conference **ELMECO**
Nałęczów, Poland
September 2003

NUMERICAL MODELS COMPARISON OF SUPERCONDUCTING FAULT CURRENT LIMITERS WITH CLOSED AND OPEN CORE

Janusz KOZAK, Tadeusz JANOWSKI

Electrotechnical Institute in Warsaw
ul. Nadbystrzycka 38A, 20-618 Lublin, Poland
e-mail: januszk@eltecol.pol.lublin.pl

Lublin University of Technology
ul. Nadbystrzycka 38A, 20-618 Lublin, Poland
e-mail: tadeuszj@eltecol.pol.lublin.pl

Abstract

This paper deals with the V-I characteristics of the numerical models of Superconducting Fault Current Limiters with closed and open core. The numerical models based on the finite element method were used to analyse the influence of structure of SFCL on voltage-current characteristics. The results show that the inductive type of SFCL can be built with comparable parameters with open core as well as with closed core.

Keywords: superconducting fault current limiters, magnetic field, superconducting tube, iron core.

1. INTRODUCTION

Superconducting fault current limiters use the natural ability of rapid shifting from the normal to the resistive state of superconductor due to their critical current value exciding. This special feature of superconducting materials enables designing of electrical devices with parameters that cannot be achieved by using conventional materials.

2. PRINCIPLE OF OPERATION

Fault currents result from power surges caused by lightning and short circuits, which send a surge of power through the grid. These surges can cause serious damage to grid equipment and cause circuit breakers to shut down the affected parts of the system. Serious faults can generate current surges of more than 100 times the normal operating current can

cause electricity to arc uncontrollably within the breaker, hindering its effectiveness and even destroying it and other utility or customer equipment [1].

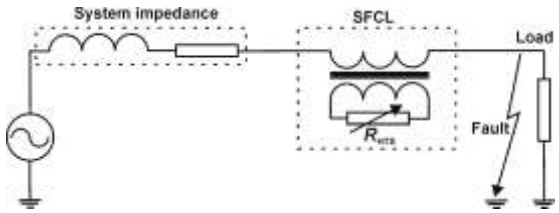

Fig. 1. Equivalent circuit of inductive SFCL and location in typical network.

A Fault Current Limiter is a device placed in electric network to limit the peak current in the event of fault. When the fault occur the increasing current exceed the critical value of the HTS element causing a rapid increase of impedance in the circuit, which limit the value of the fault current [2]. The limitation characteristic (Fig. 2) of the superconducting fault current limiter is expected to meet the principal specifications as follow:

- - Low or zero impedance during normal operation.
- - High impedance under fault condition.
- - Fast transition from normal to limiting state.
- - Fast recovery to normal operation after fault is interrupted.
- - Compact size.
- - Light weight.
- - Low cost and fail safe operation.
- - Activation current: $I_{activation} > 2.5\ I_{rated}$
- - Limitation of the peak current value: $I_{peak} < 10\ I_{rated.}$
- - Limitation value of the current in succeeding periods: $I_{limitation} < 3\ I_{rated.}$ [3].

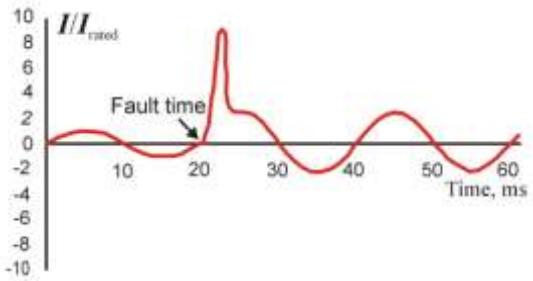

Fig. 2. Expected limitation curve of SFCL.

The inductive SFCL works like transformer with shorted superconducting secondary windings. Resistance of primary winding and the leakage inductance determines the impedance of this limiter during normal operation. In the event of fault the resistance of secondary winding is reflected into the circuit, and the magnetic flux penetrate the iron core increasing the impedance of limiter. The superconducting tubes (Fig. 3) are used to build the superconducting fault current limiters for power networks protection in a case of fault.

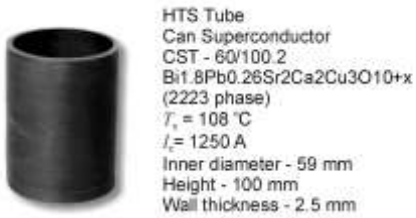

Fig. 3. Specification of the superconducting cylinder [4].

The numerical models presented in this article are based on the real parameters of the HTS tube. Two identical tubes shown in figure 3 were used.

3. DESIGN OF THE SFCL

The numerical models with open and closed core described in figure 3 were constructed to compare their limiting capabilities.

Primary and secondary windings of numerical models are identical. Primary windings consist of 500 turns of 2 mm copper wire, which was optimally calculated by the software written specially for this purpose to achieve the minimal impedance of the limiter in superconducting state.

Secondary winding consists of two identical HTS tubes to achieve double critical current I_C = 2500 A and reduce the leakage reactance which cause voltage drop on the limiter during the normal operation. The HTS tubes are used to be placed in cryostat assuring the thermal insulation and operation at cryogenics temperature 78 K. Therefore, the maximal diameter of the core is determined by the inner diameter of the cryostat.

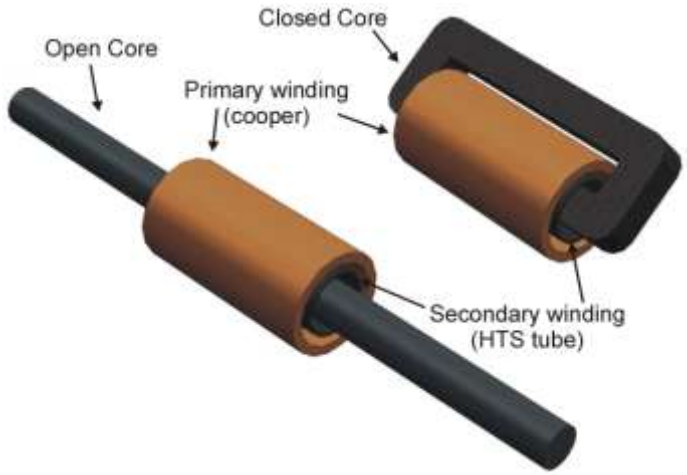

Fig. 4. SFCL's concept with an open and closed core.

Table 1. Parameters of SFCLs

	Open core	Closed core
Primary winding	500 turns of 2 mm copper wire Inner diameter = 82 mm External diameter = 102 mm Height = 200 mm	500 turns of 2 mm copper wire Inner diameter = 82 mm External diameter = 102 mm Height = 200 mm
Secondary winding	2 x HTS tube CST – 60/100.2	2 x HTS tube CST – 60/100.2
Core	Length = 700 mm Diameter = 40 mm Cross section = 1256 mm^2	Average length of magnetic flux path inside the core = 700 mm Cross section = 1256 mm^2

The cores of the limiters have the same cross section and the average way of the magnetic flux path in the closed core is similar to the open core length. The weight of the cores is almost the same. The most important advantages of construction of SFCL with an open core are the simplicity in structure and adjustability of *V-I* characteristic by core length extension. Disadvantage of such construction is closing the magnetic flux in unbounded surrounding area, which can cause other devices disturbances during the fault.

4. NUMERICAL ANALYSIS

In order to compute magnetic field distribution in the superconducting fault limiters the finite element method was used. Figure 5 and 6 show magnetic field distribution in resistive state inside the closed and open core respectively.

During the normal operation in superconducting state of the limiter the magnetic field does not penetrate the iron core due to the shielding by HTS tube. The maximal values of magnetic field density occur between the windings. Magnetic field density in superconducting state is tens times lower then in resistive state.

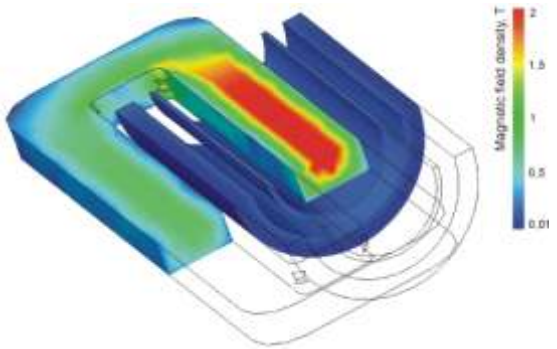

Fig. 5. Magnetic field distribution during the fault
(B shade of quarter of SFCL with closed core).

In resistive state magnetic field has the largest value in the core placed inside the windings. Limiter operates at core saturation state and magnetic permeability of the iron radically decreases to even several dozen. Magnetic flux is closing by surrounding air to a great extend, therefore the external limb of core is not as much saturated as the internal one.

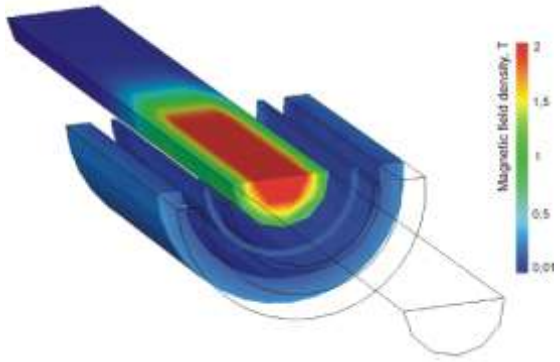

Fig. 6. Magnetic field distribution during the fault
(B shade of quarter of SFCL with open core).

Analysis results prove the proper choice of FEM method for solving this problem, because limiter operates at core saturation state. Therefore, calculations using analytical or empirical method where infinity magnetic permeability of the core is assumed can significantly differ from real value. It comes from the breakdown of the magnetic field line on border of environment

$$\mu_1 \, tg\alpha_1 = \mu_2 \, tg\alpha_2 \qquad (1)$$

where:

α_1, α_2 – angles between magnetic flux lines and the boundary surface

μ_1, μ_2 – magnetic permeability

In this case the numerical analysis was irrevocable because of complex dependence of magnetic permeability on magnetic flux density.

5. ANALYSIS RESULTS

Compared *V-I* characteristic of SFCL with open and closed core are shown in figure 7. The limiter with the closed core has the best performance. For the rated current I_{rated} = 2 A the activation current $I_{activation}$ = 5 A and the $I_{limitation}$ should not exceed 3 I_{rated}. The parameters of analysed limiters are similar to expected ones. The relation $I_{limitation} < 3\ I_{rated}$ can be achieved by using larger cross-section of the core and diameter of HTS tube, because the core cross section is determined by the inner diameter of the cryostat. Extension of open core radically increases the limitation capability of the limiter. The voltage on the limiter in superconducting state U_{sup}= 3.1 V, which is 1.35% U_N. However the *V-I* curve is steeper for the limiter with closed core due to the closed magnetic path the structure of open core limiter is simpler and the shape of the curve can be easily adjustable by changing the length of the core.

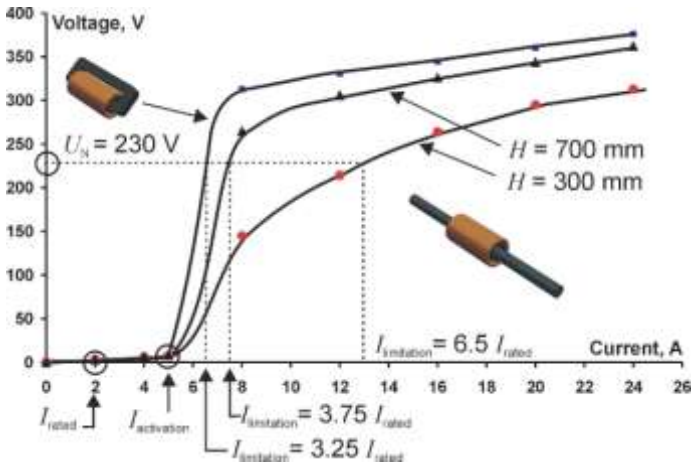

Fig. 7. *V-I* characteristics of SFCLs.

In superconducting state the limiter is expected not to insert the impedance into the system. The primary winding resistance and the leakage inductance caused the voltage drop during normal operation.

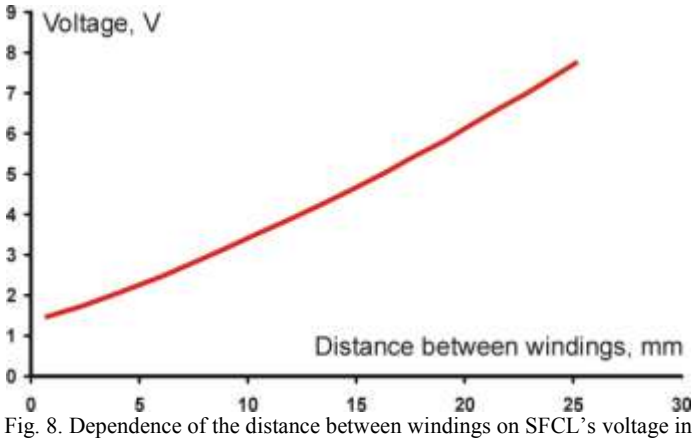

Fig. 8. Dependence of the distance between windings on SFCL's voltage in superconducting state at 200 mm windings height, I_{rated} = 2 A.

The leakage inductance strongly depends on the distance between the windings and the height of the windings.

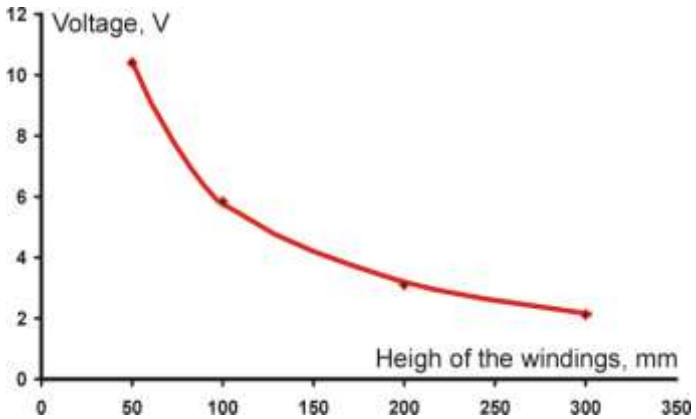

Fig. 9. Dependence of the height of the windings on SFCL's voltage in superconducting state at 9 mm distance between windings, I_{rated} = 2 A.

In this particular structure of the presented SFCLs consisting of the two HTS tubes CST-60/100.2 the influence of distance between primary and secondary windings is described by figure 8. Figure 10 shows the voltage on the SFCL in superconducting state at different height of windings. Two charts presented above prove that the slender construction and short distance between windings should be used in superconducting fault current limiters to assure the required limitation *V-I* characteristic and to obtain the lowest impedance during normal operation.

6. CONCLUSION

Numerical analysis of superconducting inductive fault current limiters with an open and closed core based on the FEM method has been described. The *V-I* characteristics of SFCLs obtained by numerical analysis fulfil the utility network expectations to a great extend. The numerical analysis of magnetic field is very helpful in designing of SFCL and obtaining the *V-I* characteristic of this device. Investigated numerical models prove that the inductive fault current limiters can be built with open core as well as with closed core with comparable parameters.

REFERENCES

[1] 15.5 KV Class HTS Fault Current Controller, web site: http://www.igc.com /superpower/products/hts_components/15kV.htm.

[2] Waynet J. A., Boeing H. J., Mielke C. H., Willis J. O., Burley B. L., Restoration and Testing of HTS Fault Current Controller, IEEE Transactions on Applied Superconductivity, vol. 13, No. 2, June 2003, pp. 1984-1987.

[3] Noe M., Oswald B. R., Technical and Economical Benefits of Superconducting Fault Current Limiters in Power Systems, Presented at ASC98, Palm Desert, USA.

[4] Web site: www.can.cz.

4th International Conference **ELMECO**
Nałęczów, Poland
September 2003

COMPUTER MODELING OF SUPERCONDUCTING SHIELD-CURRENT LIMITER

Michał ŁANCZONT, Tadeusz JANOWSKI

Lublin University of Technology
Institute of Electrical Engineering and Electrotechnologies
Nadbystrzycka 38A, 20-618 Lublin,
e-mail: michal@weber.pol.lublin.pl , tadeuszj@eltecol.pol.lublin.pl

Abstract

Superconducting shield current limiter is the most popular type of inductive current limiter. It's build base on single phase transformer's construction, as shown on Fig. 1. This feature gives possibility to make numerical analysis the operation of the limiter using modified numerical model of the transformer. Computer program was elaborated to simulate superconducting shield current limiter's work in network. This software gives possibility to calculate operation of limiter with different parameters of the limiter, network and current. Paper present principle of the numerical model of superconducting shield current limiter and results of the computer simulation made by authorship program written in Microsoft Visual Basic.

Keywords: superconducting fault current limiter, computer modeling, transformers.

1. INTRODUCTION

Critical currents occurred in energetic network may lead to irremovable failure of many devices, if protective equipment do not operate quickly enough. Fault current carry with it an energy even several times bigger then indicative current. So big current flow through an electrical equipment operated in network emit significant energy (kinetic and thermal) which could permanently damage those devices. Especially dangerous is a first peak of short-circuit current exceed amplitude of fixed critical current. Conventional protective devices are not able to cut so short pulse of current, and superconducting fault current limiters can be used as aid-tools.

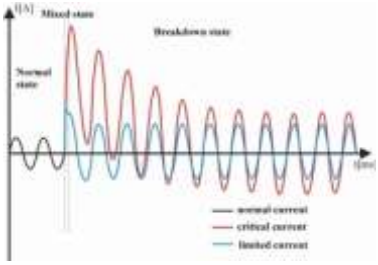

Fig. 1 Current run in the line with and without current limiter

Natural ability of superconducting material to limit flowing through the material current bigger then critical current gives possibility to build a device able to "cut" the first peak short-circuit current, as shown in Fig. 1. Many other type of superconducting fault current limiters (SFCL) were built up till now:

- Resistive
- Inductive
- Semiconductive
- Hybrid

Among listed SFCL's inductive shield-current limiters, shown in Fig. 2., can be distinguished by its simple construction, low cost of building and operation and high speed of function.

Paper presents proposed mathematical model of operation of the superconductive fault current limiter in power network. There was elaborated computer program, operating on numerical model of sheld-current limiter, presented run of current in the line with and without superconducting limiter.

2. INDUCTIVE „SHIELD-CURRENT" SUPERCONDUCTING FAULT CURRENT LIMITER

Superconducting inductive „shield-current" limiter is one of the first elaborated solutions of the superconducting current limiters. It was built on the basis on single phase transformer with coil coaxially placed, as shown in Fig 2. Primary winding of the limiter are made of copper and placed on carcass. Secondary winding was made of high temperature superconductor as a tube, put into liquid nitrogen batch in cryostat.

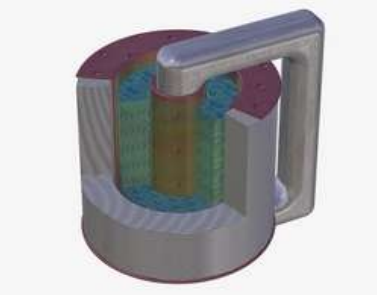

Fig. 2. Inductive superconducting fault current limiter

Used construction affor that employment of current leads is useless. This fact reduced cost of construction and operation, it simplifies the construction of cryostat and the whole device.

In nominal state of network operation secondary winding operate in superconducting state. The tube screes iron core against flux. This feature causes that limiter has been seen as a in series connected resistance and inductance. Its impedance is negligible.

The appearance of the short circuit current force secondary winding's tube to transition from superconducting state to resistive state. Impedance of the limiter increases and SFCL limits critical current to lower value (expect functioning of conventional protected devices), as shown in Fig. 3.

Flowing of high current through the limiter, at secondary winding in resistive state, cause increase of temperature and impedance of the superconducting tube.

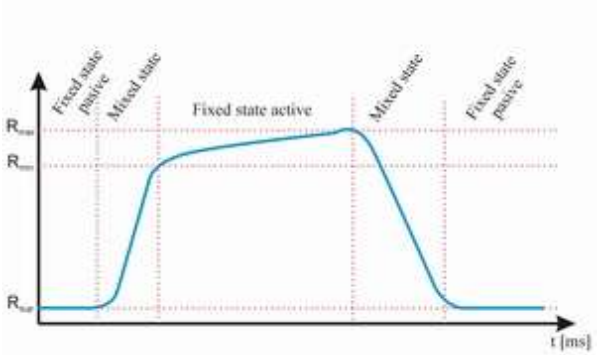

Fig. 3. Profile of changes of resistance limiter in duration of critical current

Critical current delay causes decreasing of induced current in secondary winding below critical current of the superconducting tube, allows for phase change from resistive to superconducting state.

3. MATHEMATICAL MODEL OF SFCL OPERATION

Great sibilantly of construction between shield-current limiter and single-phase transformer allow for using at calculations for limiter modified mathematical model of air-core transformer (Eq. 1.), as shown in Fig 4.

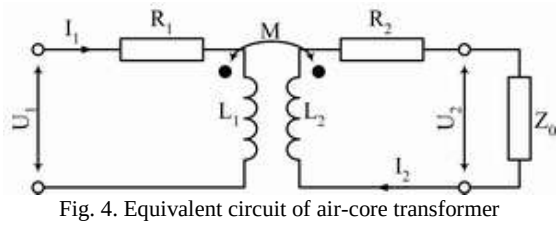

Fig. 4. Equivalent circuit of air-core transformer

$$\begin{cases} \underline{U} = R_1 \underline{I_1} + j\omega L_1 \underline{I_1} - j\omega M \underline{I_2} \\ 0 = R_2 \underline{I_2} + j\omega L_2 \underline{I_2} - j\omega M \underline{I_1} + \underline{Z_0} \underline{I_2} \end{cases} \quad (1)$$

Operation of limiter can be described by four states of work:

a) settled passive state

b) state transitory superconducting → resistive

c) settled active state

d) state transitory resistive → superconducting

Each of listed states of work is described by equations behavioral the current and tension of limiter arrangement. In the network limiter works as aid-tool safety helping classic device, alone it couldn't absorb whole energy carried by emergency current. Getting down to work classic preservative apparatus causes that current doesn't flow through the limiter. These devices are switching on after atrophy of critical current (the superconducting element of limiter is at superconducting state the process starts a new). It is possible to skip the last state in elaborate of mathematical model.

Writing the equations describing operation of limiter in network require few assumptions:

1) in settled passive we accept that from network limiter is seen as connection of coil and resistor (in superconducting state tube shielded core perfectly)
2) in transitory state and settled active the limiter works like the air-core transformer in short-circuit condition, we skip the influence of core
3) the resistances of secondary winding (the superconducting tube) is a function of the secondary current, described in equation Eq. 2.

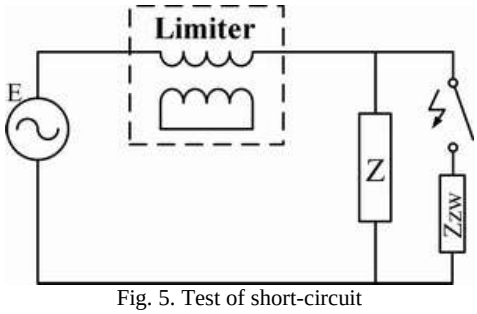

Fig. 5. Test of short-circuit

$$\begin{cases} R_2(I_2) = 0 \quad dla \;\; I_2 < I_c \\ R_2(I_2) = \dfrac{R_{sc}}{e^{\frac{I_c - |I_2|}{\Delta I_2}} + 1} \quad dla \; I_2 > I_c \end{cases} \quad (2)$$

On the basis of above assumptions we elaborated numerical model enabling to enumeration the course of current in the line with limiter, as shown in Fig. 5.

4. COMPUTER SIMULATION OF THE OPERATION OF SFCL IN THE NETWORK

Elaborated mathematical model of inductive suprconducting current limiter allow to write the computer program able to simulate course of current in line with limiter, as shown in Fig. 6. Computer program is based on set parameters, calculate the course of current in the line and show it in comparison with the course of current in the line without limiter, entrance parameters were enumerate in Tab. 1. Program was written in environment of Microsoft Visual Basic 6.

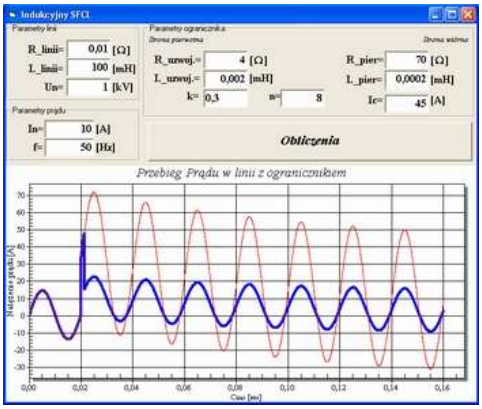

Fig. 5 The screenshot of simulation program

Tab. 1. Entrance parameters of program

Parameter	Description
R_linii	Fusion impedance of line
L_linii	
Un	Indicative tension of line
R_uzwoj	Impedance of primary winding
L_uzwoj	
k	Coefficient of coupling
R_pier	Impedance of secondary winding
L_pier	
Ic	Critical current of ring
n	Number of periods of signal showed on graph
In	Rated current of line
f	Frequency of current

5. CONCLUSIONS

The utilization among construction and principle of operation single-phase transformer and inductive current limiter allowed, with some simplification, to elaborate the numeric model of inductive superconducting fault current limiter. The proposed

mathematical model gives possibility to write the computer program drawing the course of current in line with limiter. The experience gained while studying on mathematical model and computer application will be very helpful elaboration of mathematical model of three-phase critical current limiter with two superconducting elements.

REFERENCES

[1] S. Bolkowski, Teoria obwodów elektrycznych, WNT, Warszawa 1995
[2] M. Jabłoński, Transformatory, Wydawnictwo Politechniki Łódzkiej, Łódź 1996
[3] Ch. P. Poole, Handbook of Superconductivity, Academic Press, 2000
[4] H. Hatta, Study on recovery current of transformer type superconducting fault current limiter, IEEE 2003, p. 2096-2099
[5] G. Zhang, The improved Magnetic shield type high Tc superconducting fault current limiter and the transient characteristic simulation, IEEE 2003, p. 2112-2115

4th International Conference **ELMECO**
Nałęczów, Poland
September 2003

ENVIRONMENT-FRIENDLY ENERGY STORAGE FOR POWER SYSTEMS

Paweł SURDACKI, Tadeusz JANOWSKI

Lublin University of Technology
Institute of Electrical Engineering and Electrotechnologies
Nadbystrzycka 38a, 20-618 Lublin,
e-mail: pawels@eltecol.pol.lublin.pl

Abstract

This paper presents different types of secondary energy storage systems and their overall structure including power transformation system, central store and charge–discharge control system. Energy storage is considered as a unit of a power system and the storage duties are grouped according to the required duration of their discharge times. Alternative energy storage techniques are described and their technical, economical and environmental features are compared.

Keywords: energy storage, energy conversion, power systems, environmental issues.

1. INTRODUCTION

Energy storage is an essential part of any physical process and a substantial enabling technology in the efficient management of energy. All the primary fuel- and energy-producing industries make significant use of their systems in both the initial extraction of primary fuel and the subsequent distribution to consumers.

Renewable energy sources have recently attracted considerable interest. However, they do not provide constant energy supply and, unlike fuels, cannot be directly stored. Electrical power systems are the most flexible and convenient carriers between energy producers and consumers, but their disadvantage is the impossibility of storing it in sufficient quantities. Possible way to overcome this disadvantage is to use secondary energy storage, which can partly or completely separate the processes of energy generation and consumption.

This paper describes secondary energy storage as an installation designed to accept energy generated by the power system, convert it into a form suitable for storage, keep it for a certain time and return as much of the energy as possible back to the power system, converting it into a form required by the consumer.

To compare different types of storage equipment, the following key parameters are discussed: energy density per mass and volume, cycle efficiency, permissible number of charge-discharge cycles, lifetime, reverse and response time level, optimum power output and stored energy. Basing on these parameters, the storage techniques, such as thermal energy storage, flywheel storage, pumped hydro-storage, compressed air energy storage, capacitor bank storage and superconducting magnetic energy storage, have been compared. The environmental aspects of different storage techniques have also been elucidated.

2. ENERGY CONVERSION AND STORAGE

Energy flow from the renewable sources, or natural energy storage media, such as sun light, water and wind, is not constant, but depends on season, time of day and wheather conditions. Energy demand is not constant either and it depends on the same circumstances. Secondary energy storages can be a mediator between the energy source and its consumer. They can partly or completely separate the process of energy generation and consumption.

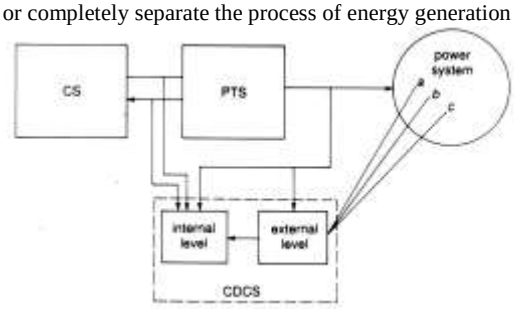

Fig. 1. Structure of energy storage: PTS – power transformation system, CS – central store, CDCS – charge–discharge control system [1]

The energy storage should consist of three parts (Fig. 1): power transformation system (PTS), central store (CS) and charge-discharge control system (CDCS). The power transformation system has to couple the power system and the central store. It also acts as power conditioning system and controls energy exchange between the central store and the power system. Essentially, there are three types of secondary energy storage systems: mechanical, chemical and electrical (Table 1).

The central store comprises two parts: storage medium and storage container. The following types of the cental store exist: thermal (using latent heat of the storage medium), mechanical (using gravitational, kinetic or elastic forms of energy), chemical (using chemically bound medium energy) and electrical (using electromagnetic or electrostatic energy of storage media). Energy can be extracted from the cenral store at any power rate within the PTS margin until it is discharged. The central store should be capable of charge (discharge) up to a predetermined power level throughout the entire charge (discharge) period. It means that a certain part of the stored energy must be kept in the CS to ensure the ability of the PTS to work at a required power level. No single type of CS allows the full discharge of stored energy without damage to the whole installation.

The charge-discharge control system controls charge and discharge power levels in accordance with the requirements of the power system's regime. It is an essential part of any storage device and usually comprises a number of sensors placed in certain nodes of the

power system, in the PTS and in the CS. The information from these sensors is used in a computer-based controller which produces commands for power flow management in the PTS.

Table 1. Types of secondary energy storage [1]

STORAGE TYPE	CENTRAL STORE		PTS SYSTEM	PTS CONTROL PARAMETERS
	medium	container		
MECHANICAL				
PUMPED HYDRO	water	upper and lower basins	motor-generator driven pump-turbine	water valves, motor-generator's excitation current
FLYWHEEL	rotating mass	rotating mass	motor-generator	excitation current of motor-generator
COMPRESSED AIR	air	artificial or natural pressurised air containers	motor-generator driven sompressor turbine	air valves, motor-generator's excitation current
SENSIBLE OR LATENT HEAT	water, gravel, rocks etc.	different types of artificial or natural containments	conventional thermal power plant	steam and water valves, generators
CHEMICAL				
SYNTHETIC FUELS	methanol, ethanol, hydrogen	fuel containers	any conventional thermal power plant	thermal plant conventional control means
SECONDARY BATTERIES	electrolyte system	battery casing	thyristor inverter/rectifier	inverter/rectifier's firing angles
FUEL CELLS	synthetic fuels (hydrogen)	fuel cell's casing	electrolyser plus inverter/rectifier	inverter/rectifier's firing angles
ELECTRICAL				
SMES	electromag-netic field	superconducting coil	thyristor inverter/rectifier	inverter/rectifier's firing angles
CAPACITOR	electrostatic field	capacitor	thyristor inverter/rectifier	inverter/rectifier's firing angles

Energy is stored at times when the available means of generation exceed demand and is returned when demand exceed generation. The installation of energy storage units on electricity utilities will permit them to store energy generated at night by coal or nuclear plants and release the stored energy to the grid during the day when demand is highest. This reduces the need for gas or oil turbines.

3. ENERGY STORAGE AS A UNIT OF A POWER SYSTEM

Energy storage in a power system can be defined [1] as any installation or method, usually subject to independent control, with the help of which it is possible to store energy, generated in the power system, keep it stored and use it in the power system when necessary. According to this definition, energy storage may be used in a power system in three different regimes: charge, store and discharge.

In each of these three regimes a balance between power and energy in the power system should be maintained so that the energy storage had the appropriate rated power and energy capacity. The duration of each regime, its switching time and storage efficiency are subject to power system requirements.

The reasons for energy storage development in power systems could be as follows: improvement of the system operation efficiency, reduction of primary fuel use leading to energy conservation, lack of available alternative energy source, security of energy supply.

All storage duties can be grouped according to the required duration of their discharge times. The discharge range of hours is connected with compensation of the load fluctuations in the following areas: utility load levelling (to improve load factors, reduce pollution in populated urban areas and to make better use of available plants and fuels), storage for combined heat and power systems, utilization of renewable energy to preserve the environment, storage for remoteusers and storage for electric vehicles. The minutes range is covered by storage for industrial mobile power units as part of uninterruptible power supply. The seconds range is represented by storage of necessary energy between pulses of a high-energy particle accelerator. Millisecond range energy storage units can be used for the improvement of stability, frequency regulation,voltage stabilization and and as a countermeasure against voltage flickering.

4. ENERGY STORAGE TECHNIQUES

Selecting the most appropriate storage technique is an essential problem for the power system engineer. It can be solved if the information on power system requirements for energy storage and storage equipment technical and economicat parameters are known. The following subsections describe the main features of different energy storage techniques [1,2,7].

Flywheel storage

A flywheel is a spinning disc with a hole in the middle to be used for rotation (Fig. 2 and 3). The design is aimed at increasing the mass to increase the rotary inertia and hence the stored kinetic energy. A flywheel can be designed to release either a large amount of energy in a very short period, or a small amount of energy over a longer period. When flywheels were first developed, the industry was more interested in long lasting energy storage. This however would cause a decrease in rotational speed. The voltage that is released gets decreased and this was not acceptable as component damage was possible. The total usable energy output was just 5% of the total energy of the spinning flywheel. To overcome this limitation, rectifiers were used to avoid the voltage decreasing and this actually made 75% of the stored energy of the flywheel usable in DC mode. The DC current could then be converted back to AC.

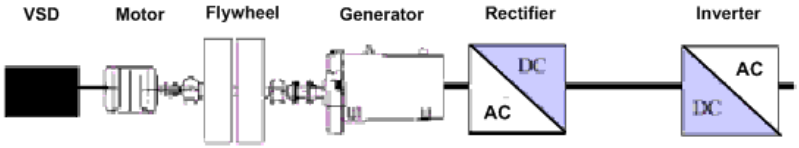

Fig. 2. A flywheel with a rectifier-inverter system [2]

The problem with this design modification was the increase in price. Moreover, these flywheels ran in air. This caused aerodynamic frictional energy losses and was also very noisy. However, traditional flywheels were safe. They were mostly made of steel, a low specific strength material compared to composite materials and could only be operated at low speeds. Steel flywheels can produce up to 1650 kW of power which is released for a few seconds.

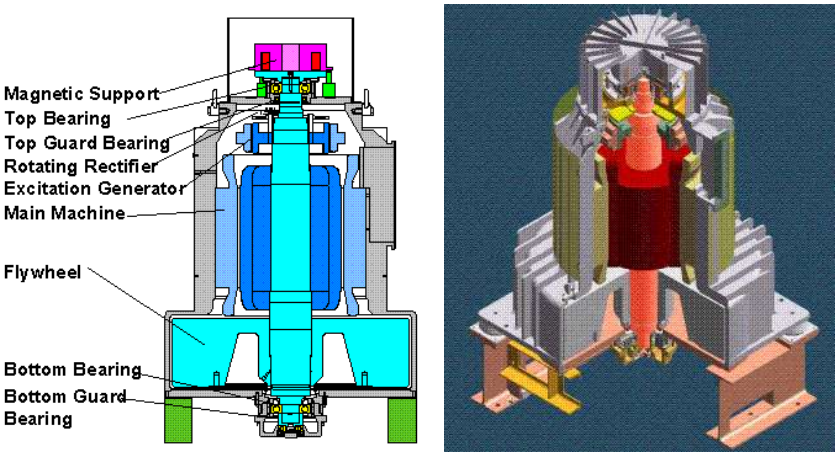

Fig. 3. UPS system with kinetic energy storage (flywheel) manufactured by Piller Premium Power Systems

Composite flywheels can also be made smaller in size and still store a usable amount of energy. Such flywheels are more suitable for storing large amounts of energy for a short time. Some prototype composite flywheels have been claimed to reach speeds in excess of 100,000 rpm but in commercial products, they spin at about 68,000 rpm. Large amounts of power, about 750 kW, can be released for about 20 seconds or even about 100 kW for up to one hour.

Recently passive magnetic bearings have been developed to control the flywheel's rotor, replacing active magnetic bearings. HTS are used for these bearings. HTS are materials of very low resistance that repel magnetic fields with no ohmic losses. The repulsion between the magnets in the rotor and other magnets distributed on a circle around the rotor keeps the flywheel centred [5]. In commercial applications, these flywheels spin at about 80,000 rpm and do not need a control system.

The main applications of flywheels are to supply components and machines with high output voltages when there is a power surge or a shutdown (Fig. 3). Although some flywheels are already available commercially, much work must be done to improve the design. One of the main features to consider is idling loss i.e. the energy lost when a spinning flywheel is on standby. These losses are due to external forces, like gravity and in commercial applications they are usually less than 2%. Some companies have made flywheels with almost zero idling losses, but they spin at low speeds. Flywheels are already a viable option for many applications, and will continue to attract new users as their technology improves.

Supercapacitors

Capacitors are some of the most essential building blocks of electronic circuits to hold DC voltages. Until some time ago, capacitors only managed to hold very little energy compared to a regular battery. The first supercapacitor, which could be used to store energy on a much larger scale than usual capacitor, was developed in 1997. This is basically a capacitor which is able to hold significantly more charge using thin film polymers for the

dielectric layer [4]. The electrodes are made of carbon nanotubes. The dielectric polyethylene terephthalate (PET) supercapacitors can store four times more energy compared to the normal capacitor. Carbon nanotubes and polymers are practical for supercapacitors. Carbon nanotubes have excellent nanoporosity properties allowing the polymer tiny spaces to sit in the tube and act as a dielectric.

Even though supercapacitors have a lower energy density compared to batteries, they avoid many of the battery's disadvantages: limited number of charge/discharge cycles due to chemical reactions that causes heating, limited lifetime and they are hazardous to the environment.

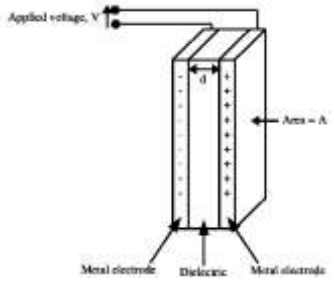

Fig. 4. Supercapacitor

Supercapacitors can be charged and discharged almost an unlimited number of times. They can discharge in matters of milliseconds and are capable of producing enormous currents. Hence they are very useful in load levelling applications and fields where a sudden boost of power is needed in a fraction of a second. They do not release any thermal heat during discharge. Supercapacitors have a very long lifetime, which reduces maintenence costs. They do not release any hazardous substances that can damage the environment. Their performance does not degrade with time. Supercapacitors are safe for storage as they are easily discharged.

Supercapacitors were initially used by the US military to start the engines of tanks and submarines. Most applications nowadays are in the field of hybrid vehicles and handheld electronic devices. A commercial supercapacitor can hold 2500 farads, release 300 A of peak current with a peak voltage handling of about 400 V.

Pumped hydro storage

Pumped hydroelectric energy storage is the oldest kind of large-scale energy storage technology. It is in active operation and it is an effective method for storing large amounts of energy. A pumped hydroelectic storage system consists of two large reservoirs located at different elevations [1,2]. During peak demand, water is released from the upper reservoir. It drops downward through high-pressure shafts where it passes through turbines and ultimately pools up in the lower reservoir. The turbines drive power generators that create electricity. Therefore, when releasing energy during peak demand, a pumped hydroelectric storage system works similarly to traditional hydroelectricity. When production exceeds demand, water is pumped up and stored in the upper reservoir, ready to be released as needed.

Pumped hydroelectric storage has the largest capacity and a very long period of storage of all large-scale energy storage methods. Due to the rapid response speed, pumped

hydroelectic storage systems are particularly useful as backup in case of sudden changes in demand. Partly due to the large scale and the relative simplicity of design, the operating cost per unit of energy is among the cheapest. Unlike hydroelectric dams, a pumped hydroelectic system has little effect on the landscape. It produces no pollution or waste.

However, the pumped hydroelectic storage system has the drawback: dependence on specific geological formations. Two large volume reservoirs along with sufficient altitude difference often force the location of the plants in remote places, like the mountains, where construction is difficult and the power grid is not present. Although the pumped hydroelectric storage has cheap operating cost, the capital cost of a pumped hydroelectric plant is massive, as it often involves building dams and enormous underground pipes. In terms of environmental issues, it disturbs the local habitat as the water level fluctuates daily.

Compressed air energy storage

In compressed air energy storage (CAES), off-peak power is taken from the grid and is used to pump air into a sealed underground cavern to a high pressure [1,2]. The pressurised air is then kept underground for peak use. When needed, this high pressure can drive turbines as the air in the cavern is slowly heated and released; the resulting power produced may be used at peak hours. More often, the compressed air is mixed with natural gas and they are burnt together, in the same fashion as in a conventional turbine plant. This method is actually more efficient as the compressed air will lose less energy.

The following geologic formations can be used for CAES systems: naturally occurring aquifers, solution-mined salt caverns and constructed rock caverns. In general, rock caverns are about 60% more expensive to mine than salt caverns for CAES purposes. This is because underground rock caverns are created by excavating solid rock formations, whereas salt caverns are created by solution mining of salt formations. Aquifer storage is by far the least expensive method and is therefore used in most of the current locations. The other approach is to store compressed air in vessels (high-pressure tanks).

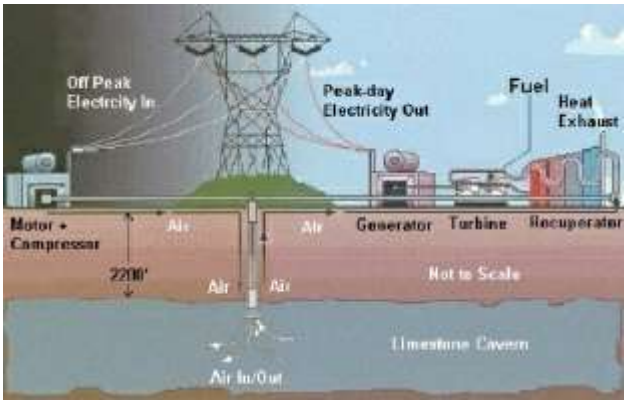

Fig. 5. Components of a CAES system [2]

A CAES operates by means of large electric motor driven compressors that store energy in the form of compressed air in the mine (Fig. 5). The compression is done outside

periods of peak demand. As part of the compression process, the air is cooled prior to injection to make the best possible use of the storage space available. The air is then pressurised to about 75 bar. To return electricity to the customers, air is extracted from the cavern. It is first preheated in the recuperator. The recuperator reuses the energy extracted by the compressor coolers. The heated air is then mixed with small quantities of oil or gas, which is burnt in the combustor. The hot gas from the combustor is expanded in the turbine to generate electricity.

CAES systems can be used on very large scales. Typical capacities for a CAES system are around 50-300 MW. The storage period is also the longest due to the fact that its losses are very small. A CAES system can be used to store energy for more than a year.

If a natural geological formation is used, CAES has the advantage that it doesn't involve huge, costly installations. Moreover, the emission of green house gases is substantially lower than in normal gas plants.

SMES

A superconducting magnetic energy storage (SMES) system is a device for storing and instantaneously discharging large quantities of power. It stores energy in the magnetic field created by the flow of DC in a coil of superconducting material that has been cryogenically cooled (Fig. 6). These systems have been used to improve industrial power quality and to provide a premium-quality service for individual customers vulnerable to voltage fluctuations. The SMES recharges within minutes and can repeat the charge/discharge sequence thousands of times without any degradation of the magnet. Recharge time can be accelerated to meet specific requirements, depending on system capacity.

A superconducting material enhances storage capacity. In low-temperature superconducting materials, electric currents encounter almost no resistance. The applications of superconductors have been limited by the conditions of low transition temperature, critical magnetic field and critical current density. Energy can be stored in a persistent mode virtually infinitely. Superconductors have zero resistance to DC electrical current at low temperatures so that ohmic heat dissipation is eliminated, hence the refrigerator is needed in the SMES to cool the coil. In AC applications, there are still electrical losses, but these can be minimised through appropriate wire and device design.

An SMES system (Fig. 6) includes a superconducting coil, a power conditioning system, a cryogenically cooled refrigerator and a cryostat/vacuum vessel. SMES are highly efficient at storing electricity (greater than 97% efficiency), and provide both real and reactive power. These facilities are used to provide grid stability in a distribution system and power quality at manufacturing plants requiring ultra-clean power, such as microchip fabrication facilities.

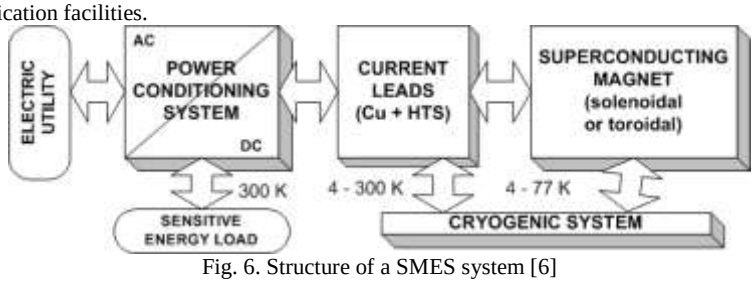

Fig. 6. Structure of a SMES system [6]

SMES systems are environmentally friendly because superconductivity does not produce a chemical reaction. In addition, there are no toxins produced in the process. SMES recharges within minutes and can repeat the charge and discharge sequence thousands of times without any degradation of the magnet.

Fuel cells

Fuel cells, like all electrochemical cells, convert stored chemical energy directly into electrical energy [1,2]. Often the source of the energy is a gaseous fuel, which reacted with oxygen in the atmosphere to produce energy. This is the equivalent of burning the fuel. However in a fuel cell the energy is directly converted to electricity resulting in an increase in its efficiency. Unlike fossil fuels, fuel cells do not produce any pollutants. Fuel cells are also more efficient mainly because the energy is directly converted to electricity resulting in less energy losses.

The most favoured and common fuel used in these cells is hydrogen. The combustion of hydrogen in oxygen produces only water, which is not a pollutant, and also hydrogen has a very high energy density when compared with other fuels.

A fuel cell consists of two electrodes, known as the anode and cathode that are separated by an electrolyte (Fig. 7). Oxygen is passed over the cathode and hydrogen over the anode. Hydrogen ions are formed together with electrons at the anode. The hydrogen ions migrate to the cathode through the electrolyte and the electrons produced at the anode flow through an external circuit to the cathode. At the anode they combine with oxygen to form water. The flow of electrons through the external circuit provides the current of the cell.

Due to the fact that fuel cells do no produce any pollutants and are very efficient, fuel cells are a viable alternative to petrol engines. Fuel cells may have efficiencies of up to 80%.

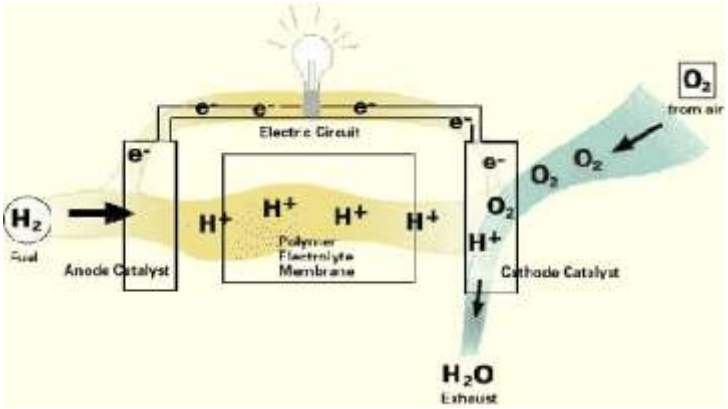

Fig. 7. Operation of fuell cell [2]

5. COMPARISON OF STORAGE TECHNIQUES

Pumped hydro is the only type of storage with a well-developed and highly reliable technology. The main problem with this type of storage is that it is not always easy to find

sites suitable for two reservoirs separated by at least 100 m, which are not remote from the power grid. CAES compared with pumped hydro method has apparent advantages: it provides a wider choice of geological formation and the density of the energy stored is much higher.

The storage techniques, such as flywheels, chemical batteries, capacitor banks and SMES, has the following common advantages: they are environmentally friendly (no requirements for cooling water, no air pollution, minimal noise, moderate siting requirements) and they have extremely small power reverse times (power can be transfered practically on demand). The main quantitative details of different storage equipment are given in Table 2.

Table 2. Storage equipment parameters [1]

Type	Efficiency	Energy capacity	Energy density	Life time	Reverse time	Siting suggestion
	%	J	J/m^3	years	s	
Flywheel	85	10^9	10^8	20	0.1	Close to consumer's load terminal
Pumped hydro	80	10^{13}	10^6	50	10	Geological considerations
CAES		10^{12}	10^5	25	360	Geological considerations
Batteries	80	Not constrained	10^8	10	0.01	Close to consumer's load terminal
Capacitor	80	Not constrained		10	0.01	Close to consumer's load terminal
SMES	90	10^{13}		30	0.01	Power systems's substations, generator's terminal

6. CONCLUSIONS

Such forms of storage as CAES and pumped hydro have a relatively large reverse time, and therefore their possible applications are limited compared with flywheels, chemical batteries and SMES, whose reverse time is very small. On the other hand, CAES and pumped hydro are suitable for large-scale applications in power systems while flywheels, owing to their limited size, or chemical batteries and capacitor banks, owing to their modular construction, are better for comparatively small-scale applications or as dispersed storage. Only SMES can be used anywhere in the power system but economic problems of this technically very attractive energy storage have to be still solved.

REFERENCES

[1] Ter-Gazarian A., Energy Storage for Power Systems, Peter Peregrinus, IEE, 1994.

[2] Cheung K., Cheung S., De Silva N., Juvonen M., Singh R., Woo J., Clarke T., Large-Scale Energy Storage Systems, Imperial College London, 2002/2003.

[3] Energy storage – key to renewables integration? REFOCUS The International Renewable Energy Magazine, May/June 2003, www.re-focus.net.

[4] Nowak M., Holdebrandt J., Barlik R., Supercondensators and their applications (in Polish), Przegląd Elektrotechniczny, 78 (2002) n. 8, 225-230.

[5] Vajda I., Kohari Z., Porjesz T., Benko L., Meerovich V., Sokolovsky V., Gawalek W., Operational characteristics of energy storage high temperature superconducting flywheels considering time dependent processes, Physica C 372 –376 (2002)1500 – 1505.
[6] Surdacki P., Superconducting magnetic energy storage – technology and application advances (in Polish), Przegląd Elektrotechniczny, LXXIX, Nr 9, 2003, pp. 605-611.
[7] Overview of energy storage technologies, http://www.eere.energy.gov/

4th International Conference **ELMECO**
Nałęczów, Poland
September 2003

IDENTIFICATION OF MAGNETIC MATERIAL WITH ARTIFICIAL NEURAL NETWORK

Tomasz GIŻEWSKI, Andrzej WAC-WŁODARCZYK,
Dariusz CZERWIŃSKI[1], Piotr WOLSZCZAK[2]

[1] *Lublin University of Technology, Institute of Fundamentals Electrical Engineering and Electrotechnologies, Nadbystrzycka 38a st., Lublin, Poland*

[2] *Lublin University of Technology, Department of Automation, Nadbystrzycka 36a st., Lublin, Poland*

Abstract

This article presents the construction of the magnetic material identification algorithm basing on the static hysteresis image. The Preisach model of hysteresis loop was the base of consideration. The essential element in dynamic hysteresis simulation is the weight function. The artificial neural network algorithm is applied to represent the weight function. On the base of detailed learning algorithm, the possibility of the direct integration of simulation environment with real measuring system was revealed. The authors present the possibility of using the Kohenen and other artificial neural network algorithm. The application of the algorithm as well as the grouping of records in similarity clusters will be done. In this article the sample process of magnetic material identification. Presented problems confirm in principle the application of artificial neural network algorithms in modelling of hysteresis loop with Preisach model.

Keywords: Preisach model, hysteresis, artificial neural network.

1. INTRODUCTION

Magnetic hysteresis describes non-linear relation between magnetization and outer magnetic fields. The interaction of elementary domain, introductory position and history of progress magnetic fields affect the shape of hysteresis.

The classical Preisach model describes explicitly the curves of magnetic hysteresis for optimal shape of signal input, on the base of weighting function. The above function presents the static hysteresis of the given material. The elementary problem in the analysis of systems with ferromagnetic elements (based on the Preisach method) is gathering and collecting data of static hysteresis.

The weight function values, formed on the experimental data, map to neurone weight values. Knowing the structure of the net, it is possible to construct the database containing the neurone weights. The database includes in each position single representation of the weight function. Each record is the unequivocal identifier of normalized magnetic material sample. The presented paper shows the problems connected with record grouping and data access optimization. The classical methods of database indexing are applied only with univocally defined master keys. In the case of weight function images this solution is misapplication. These resources show the big similarity to multimedia data.

The idea was to concentrae on the analysis of Preisach model, for which the approximation and data collection, was the algorithm of neural network.

2. CLASSICAL PREISACH MODEL AND APPLICATION

The most important references, about the modeling hysteresis, were described by the classical Preisach model. The equation (1) shows the basic definition of this method [1]:

$$M(t) = \iint_P \mu(\alpha,\beta)\gamma_{\alpha,\beta}h(t)\mathrm{d}\alpha\mathrm{d}\beta \tag{1}$$

where: $M(t)$ the function describing input signal (magnetization); α, β - variations of Preisach space dependent on input signal; $\gamma_{\alpha\beta}$ - describes the state of a single domain, $\mu(\alpha,\beta)$, – variations of weighting function (Fig. 1).

The area of Preisach surface was divided onto two planes by signal input change. How it became was shown in the equation (2), magnetization M were expressed as the difference of double integrals of function $\mu(\alpha,\beta)$ - negatively and positively oriented of plane P [2].

$$M(t) = \iint_{P-} \mu(\alpha,\beta)h(t)\mathrm{d}\alpha\mathrm{d}\beta - \iint_{P+} \mu(\alpha,\beta)h(t)\mathrm{d}\alpha\mathrm{d}\beta \tag{2}$$

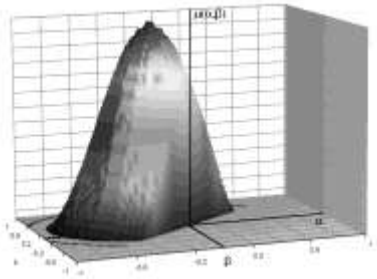

Fig. 1. Graphical representation of weighting function of Preisach model

The area of plane P (Fig. 2.) was swept across monotonically change of input signal. For positive increase, outlined area was in relation to variable α (P^+) and for negative area in relation to variable β was separated (P^-) [2].

In this article there was used the simulator of hysteresis based on Preisach model. This program was created by the author of this article during research on the magnetic hysteresis and approximate by neural network algorithm [3]. The hysteresis loop was simulated by the

program, based on weighting function and Preisach model defined by equitation (1). The result of the calculation was shown in Fig. 3.

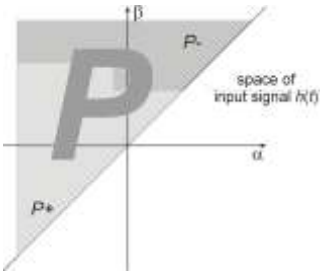

Fig. 2. Preisach plane

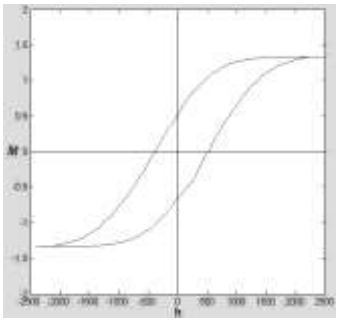

Fig. 3. Hysteresis loop simulated by program based on Preisach model in Matlab environment

The application created by our team has modelled the hysteresis based on collecting of weighting functions. The block diagram of applications was shown in figure 4. The system consists of two components, namely the: system measurement and the database of weighting function.

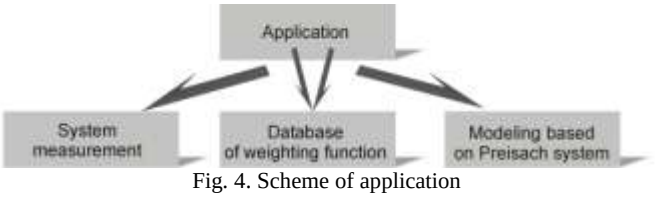

Fig. 4. Scheme of application

The creation of magnetic materials database requires detailed analysis of information stored in database resources. The above considerations point out, that besides identification data, the information about fundamental dynamic properties should be gathered. The collection of the static data is not very complicated. In the case of databases used for dynamic modelling it is necessary to collect additional information. The weight function of

Preisach model is one of these objects. Due to the complication of the structure it is difficult to collect the information about such object in relative database. Taking into consideration the searching and sorting systems the authors decided to use the techniques analogous to multimedia databases.

The elementary problem in Preisach system of hysteresis is the acquisition of data collection. To show the value of weighting function the experimental result has been employed in order to determine it. The back propagation algorithm has been applied to approximate the weighting function.

The data collection assignments were coupled with application in the way, that one could be executed in track of measurement and realized learnedly artificial neural network, classification or qualification of class of probability.

3. OPTIMIZATION OF ACCESS TO DATA

The database project consist of the representation of the weighting function required the construction based on algorithms similar to that used in multimedia databases.

Because of difficulty in foreseeing the data, which represent the function $\mu(\alpha,\beta)$, it was necessary to approximate the function with the algorithm of artificial neural network [1, 3]. Thinking over the specified above properties, the multi-layer unidirectional network was chosen from many existing algorithms. The network was learned according to method of back propagation. In that way, the collection of data representing the static image of hysteresis for each material sample was created.

The algorithm of back propagation derives from the existing theories of optimization of function minimization gradient methods. The task of algorithm is minimization of error defined as difference between the response of the network on input signal and real value of the function approximated for the set of input data.

Fig. 5. Scheme of artificial neural network in Kohonen algorithm

In the assignment of optimization of data (based on object as shape of $\mu(\alpha,\beta)$) the following algorithms of neuronal network of (classification of objects) were tested:

- Artificial neural network of Kohenen algorithm - classified as one of the oldest diagrams of the self-organizing network through the competition. Built-in mechanisms of the network initialization, assign space to neurons and determine the constant rules of neighbourhood and competition. In the moment of winner neuron calling, its weights are updated as well as the weights of neuron neighborhoods. The scheme of Kohonen network was shown in Fig. 5.

Collectivity is a very important property of the Kohenen network. Itis based on the dependence between the individual result of neuron activity and output of other neurons. This is done by the definition of the neighborhood in the network (for example two dimensional, see Fig. 5). The features of such a type of network are self-organization and transformation. The operation of networks is based on the transformation of the input signals set into output set determined only by input data. Grouping ability of input data in similarity classes is the final effect.

- Multilayer artificial neural network – was built by neurons arranged in some layers. In structure onsisted of partial input layer, output layer and minimum one hidden layer. At the Fig. 6 tested structure of multilayer artificial neural network was shown. This network was tested by three algorithms:
    - K-means algorithm - an algorithm to assign k centers to represent the clustering of n points that k<n. The points were adjusted so that each of the n points is assigned to one of the k clusters, and each of the k clusters was the centre of its assigned points. The K-means algorithm assigned radial centers to the first hidden layer in the network, if it consisted of radial units. The intention was to discover a set of cluster centers which represent in the best way the natural distribution of the training cases [5].

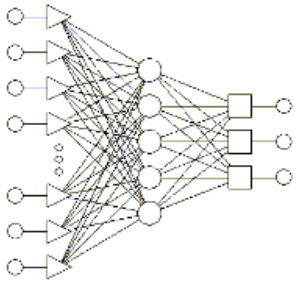

Fig. 6 Scheme of multilayer artificial neural network

- *K-nearest* neighbour deviation assignment algorithm assigned deviations to a radial units by using the Root Mean Squared distance from the *k* units closest to each unit as the standard deviation (Gaussian). Each of the units has own independently-calculated deviation, based upon the density of points close to itself [5].
- *Pseudo-Inverse algorithm* - this algorithm used the singular value decomposition technique to calculate the pseudo-inverse of the matrix. The algorithm needed to set the weights in a linear output layer, so as to find the least mean squared solution. It guarantees the finding of the optimal setting for the weights in a linear layer to minimize the Root Mean Squared training set error solution [5].

4. RESULT OF SIMULATION

The objects (numerical representation of weighting functions) were classified in three groups. All the groups were represented by a credible of number of input data. The size of the object was constructed as two dimensional array of 10 000 elements.

In the first experiment the artificial neural network in Kohenen algorithm was tested. An dimensional array has been constructed (10 000) as the input vector, were the output vector was a pointer of object. The result was not satisfy because the remaining time of learning network was about 24 hours. After resizing the array to a smaller one the identification process has detected an object in knowledge base in probability class (Fig. 7). The construction of network was build of 6×6 matrix. The process of choosing the parameters of learning function based on fail and success method assuming the 1% error criterion learning function select.

Fig. 7. Sample result of detecting image of weighting function of the Preisach model

The next step was to build the simulations based on multilayer network. The scheme of network from Fig. 6 was compiled at use as following criteria: input vector constrained all elements of matrix (10 000), network three layers, input canal - 4146, number of hidden neurons – 5, three elements of output vectors. Table 1 shows the parameters of the following network:

Table 1

Type	Training error	Verification error	Test Error	Training
RBF	0.003068	0.004495	0.01442	KM, KN, PI

Where training methods were:

KM - K-means algorithm
KN - K-nearest
PI - Pseudo-Inverse algorithm

Table 2

	P1	P2	P3	T. P1	T. P2	T. P3	Error
P1_1	1.000176	-0.0002622	8.659e-05	1	0	0	0.0007792
P1_2	0.9998238	0.0003699	-0.0001936	1	0	0	0.001079
P1_3	0.9971168	0.002809	7.375e-05	1	0	0	0.009589
P1_4	0.9963386	0.003624	3.713e-05	1	0	0	0.01227
P1_5	0.9999997	-0.0001173	0.0001176	1	0	0	0.0003957

Where: P1_1, P1_2,… - names of input vector fields; P1, P2, P3 – variables of output; T.P1÷3 standard output variables; Error – errors of network.

A result of testing network was compared in table 2. The errors were contained in column *Error*. It was clear that the network was the best classifier of the set of structure (the graphical representation of weight of neurons was shown in figure 8).

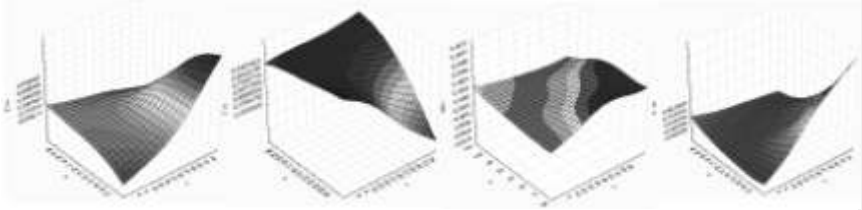

Fig. 8. Graphical representation of the weight of neurons in multilayer network (learned by Kohenen method)

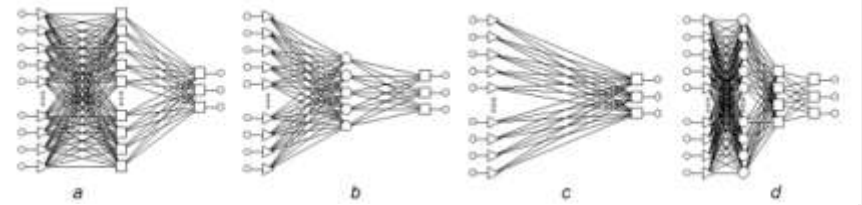

Fig. 9. Scheme of tested configuration network

In aim of verification of received results row of comparative simulation was executed. To prove this the following configuration of net was used:

- Multilayer Perceptrons model (Fig 9a),
- Radial Basis Function Networks (Fig 9b),
- Linear Networks (Fig 9c),
- Generalized Regression Neural Networks (Fig 9d).

The best results were reached on network drawing at structure of shown in Fig. 9d. The results of process of learnedly were presented on figure 10.

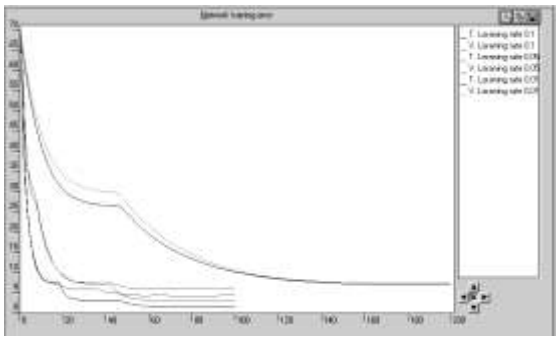

Fig. 10. Network training errors for structure Generalized Regression Neural Networks

5. SUMMARY

On base of quoted results of simulations it was affirmed, that artificial neural network could be used to optimize data access. Neural networks could be used to generate the indexes related to a matter of data stored on different levels. Following the example of multimedia data (text, static image and video).

The analysis of mentioned layers properties enable the generation of different kind indexes precisely related to the substance on particular level. The task of selection was implemented with Kohenen networks. These networks make it possible in a simple way to implement the relationship between data (relationship in time domain, plane and space). Self-organization is an advantage of the network.

The designed indexing system is used for precise record determination. In this system neural networks can be used for:

- filtering module,
- features detector,
- arbitrary unit.

Images obtained in that way can be used, thanks to simple navigation, for fast searching of desired information in specified context as well as the detection of data relations.

REFERENCES

[1] Mayergoyz I.D. Mathematical models of hysteresis, Springer-Verlag, New York 1991.

[2] Bertotti G., Hysteresis in magnetism, Academic Press, San Diego 1998.

[3] Wac-Włodarczyk A. Giżewski T. Analiza funkcji wagi μ(α, β) modelu Preisach'a z wykorzystaniem algorytmu sztucznej sieci neuronowej. ZkwE, Poznań 2000.

[4] Visintin A., Differential Models of Hysteresis, Springer-Vertlag, Berlin Heidelberg 1994.

[5] Krose B., Van der Smag P., An introduction to neural networks, The University of Amsterdam 1996.

[6] Freeman J. A., Skapura D. M., Neural Network Algorithms, Applications and Programming Technique, Addison-Wesley Publishing Company 1991.

[7] Handbook of neural network signal processing, CRC Press 2002.

4th International Conference **ELMECO**
Nałęczów, Poland
September 2003

DETERMINATION VALUES OF STATIC HYSTERESIS OF THE PREISACH MODEL BY EXPERIMENTAL RESULTS

Tomasz GIŻEWSKI, Andrzej WAC-WŁODARCZYK

Lublin University of Technology, Institute of Fundamentals Electrical Engineering and Electrotechnologies, Nadbystrzycka 38a st., Lublin, Poland

Abstract

The presented article describes the construction of static hysteresis of the magnetic material based on the algorithm of Preisach systems. The artificial neural network algorithm is applied to represent the of weight function. The weighting function values, formed on the experimental data, map to neuron weight values. This article shows the algorithm of preparing data from apparatus and transforming one to a Preisach plane. The next step of the authors was to present creating values of incoming vector of back propagation algorithm to use in learning procedure of artificial neural network algorithm. In this article the sample process of constructing the weighting function (static hysteresis of magnetic material) was depicted. The data, taken from real magnetic permeability characteristics, were processed with Preisach algorithm. Then we have proceeded to make the representation of the weight function in the shape of neurones weight making use of back propagation. Constructed image has been given as an input to algorithm of Preisach systems.

Keywords: Preisach model, hysteresis, artificial neural network.

1. INTRODUCTION

Magnetic hysteresis describes non-linear relation between magnetic induction and outer magnetic fields. The interaction of elementary domain, introductory position and history of progress magnetic fields affect the shape of hysteresis.

The classical Preisach model describes explicitly the curves of magnetic hysteresis for optimal shape of signal input, on the base of weighting function. The above function presents static hysteresis of given material. The obtainment of static hysteresis is the elementary problem in the analysis of systems with ferromagnetic elements (based on the Preisach method). The idea was to concentre on the analysis of Preisach model, for which the approximation and data collection, was the algorithm of neural network.

2. CLASSICAL PREISACH MODEL

The Preisach model has represented a ferromagnetic hysteresis as a collection of elementary hysteresis of domains. Switching loops were a construction of the model and were not to be confused with physically observable magnetic domains commonly in ferromagnetic materials.

Every domain was characterized by an elementary square hysteresis loop (Fig. 1) plane. The following equation (1) shows the basic definition of this method

$$M(t) = \iint_P m(a,b)\,g_{a,b}h(t)\,da\,db \tag{1}$$

M(t) - the function describing magnetization variable;
α, β - variations of Preisach space dependent on input signal;
$\gamma_{\alpha,\beta}$ - describes the state of a single domain,
$\mu(\alpha, \beta)$ -variations of weighting function (Fig. 1).

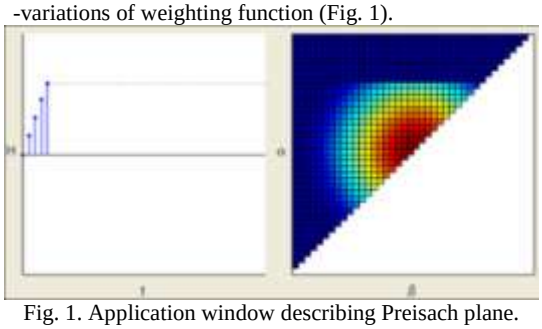

Fig. 1. Application window describing Preisach plane.

Area of Preisach plane has been limited by the following dependences (Fig. 2) [1, 2, 7, 9]:

$$\begin{cases} a < b \\ -H_{\max} < b < H_{\max} \\ -H_{\max} < a < H_{\max} \end{cases} \tag{2}$$

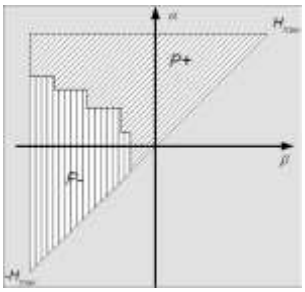

Fig. 2. The division of Preisach area on positively and negatively oriented areas.

Every domain has been characterized by elementary loop as well as the interaction between them. The area of the every switching loop was presented on the Preisach space (Fig. 3). The position on the space has an influence on the value of the weighting function. The calculation of the magnetisation values has depended on increment of value H. Magnetisation has been calculated on the basis on equation (3) and weighting function shown at Fig. 4 [9].

$$\begin{aligned} M(t) &= \iint_{P} m(a,b)\gamma_{ab}h(t)\,da\,db \\ &= \iint_{P_+(t)} m(a,b)\,da\,db - \iint_{P_-(t)} m(a,b)\,da\,db \\ &= 2\iint_{P_+(t)} m(a,b)\,da\,db - \iint_{P_r} m(a,b)\,da\,db. \end{aligned} \tag{3}$$

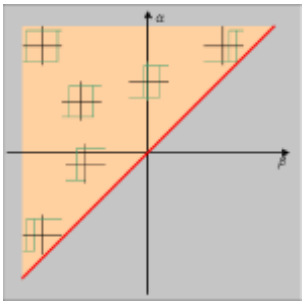

Fig. 3. Areas of occurrence of elementary switching loops

$$\begin{cases} a = h(t) & \text{for } \dfrac{dh(t)}{dt} \geq 0 \\ b = h(t) & \text{for } \dfrac{dh(t)}{dt} < 0 \end{cases} \tag{4}$$

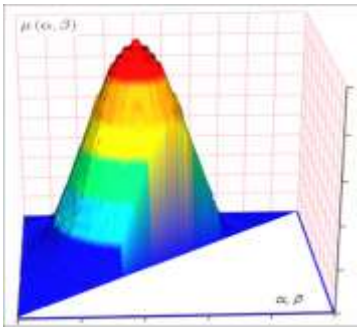

Fig. 4. Weighting function

3. PROPERTY OF WEIGHTING FUNCTION

The value of weighting function has been shown in the equation (5). The algorithm of Preisach model has determined the following properties of weighting function [1, 7]:

- should be permanent in whole plane,
- reached only one global maximum,
- beyond the area the function accepts value of weighting function equal 0,
- had an reciprocal function,
- had permanent derivatives I and II line,
- was symmetrical regard of unambiguously definite plane.

$$m(a,b) = -\frac{\partial^2 h(a,b)}{dadb} \tag{5}$$

4. EXPERIMENTAL MEASUREMENT

Example of measurement in the case of determination of the magnetic hysteresis loop was shown on the fig 5.

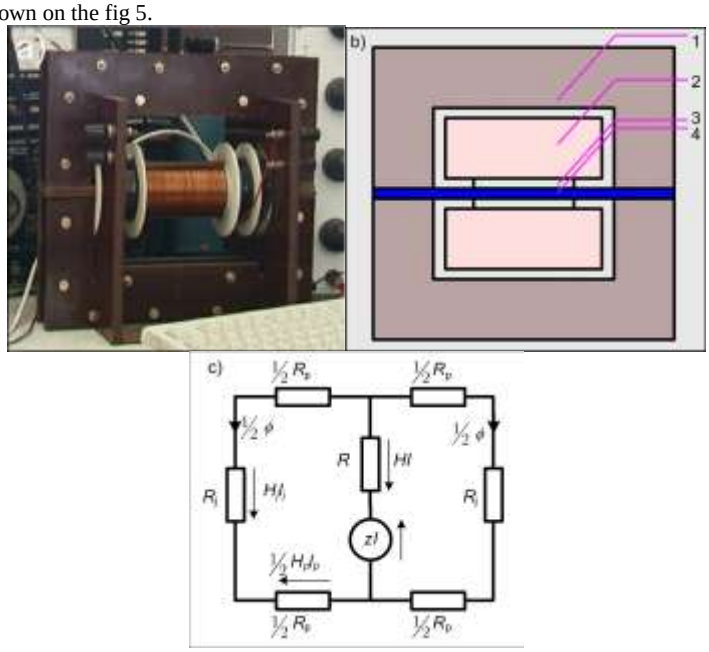

Fig. 5. Hopkinson permeameter: a) photograph, b) picture, c) electrical scheme

The technique was based on the methods of Mayergoyz and required the set of first order reversal curves (or first order transition curves) for a given system [7].

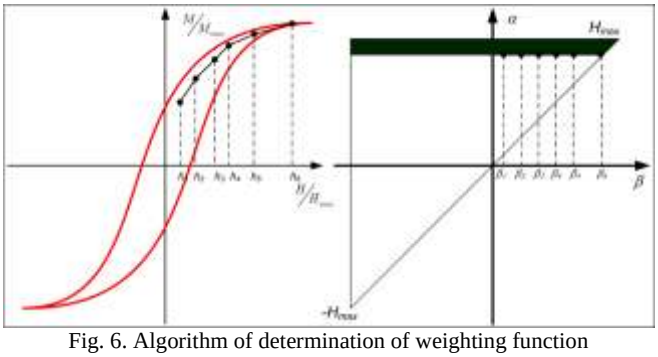

Fig. 6. Algorithm of determination of weighting function

The measured magnetisation was changed from the starting point to distinct locations on the example curve (Fig. 6).

The $\mu(\alpha, \beta)$ function has described the behaviour of hysteresis loop under the change of applied field (lesser or greater change) to the magnetisation of a system.

After being subtracted the total change in magnetisation for the reversal curve started at h_{k+1}, from that for the curve started at h_{k+2}, the contribution could be isolated to the change in magnetisation from those.

The difference between the points, located on first order reversal curves, was determined by the contribution to change in magnetisation.

5. APPROXIMATING WITH NEURAL NETWORK

The measured data has been collected in the shape of family of curves of the specific material. The graphical presentation of data was shown at the Fig. 7.

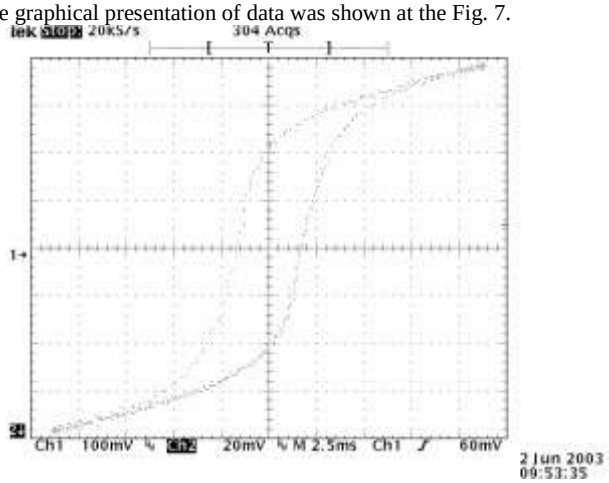

Fig. 7. Hysteresis loop

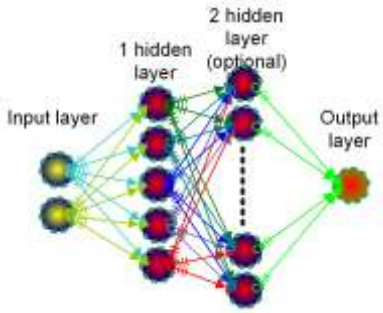

Fig. 8. Structure of back propagation algorithm of neural network used to approximate the weighting function

After the analytical calculation of weighting function the vector [α, β, μ] could be used as a variable on learning process of back propagation algorithm neural network (Fig. 8). The software simulator utilized the sigmoidal non-linear function in the hidden layer of proposed neural network. The process of choosing the number of neurons based on fail and success method assuming the 1% error criterion. The 3-5-7 structure of the neural network has been used as the basic one [4, 8, 11].

The difference between the points located on the first order reversal curves were determined the contribution to the change in magnetisation.

REFERENCES

[1] Berglund N., Adiabatic dynamical Systems and hysteresis, Institut de Physique Théorique Lausanne, Switzerland 1998.
[2] Bertotti G., Hysteresis in magnetism, Academic Press, San Diego 1998.
[3] Brzózka J, Dorobczyński L., Programowanie w MATLAB, Warszawa ZNI „Mikom" 1998.
[4] Giżewski T., Neuronowy aproksymator funkcji wagi klasycznej metody Preisach'a w modelowaniu pętli histerezy magnetycznej, Zaolzie 2000.
[5] Giżewski T., Współczesne metody modelowania pętli histerezy magnetycznej, I Seminarium doktorantów Wydziału Elektrycznego Politechniki Lubelskiej, Nałęczów 2001.
[7] Mayergoyz I. D., Mathematical models of hysteresis, Springer-Verlag, Berlin Heidelberg 1989.
[8] Tadeusiewicz R. Elementarne wprowadzenie do techniki sieci neuronowych z przykładowymi programami. Akademicka Oficyna Wydawnicza PLJ, Warszawa 1998.
[9] Visintin A., Differential Models of Hysteresis, Springer-Verlag, Berlin Heidelberg 1994.
[10] Wac-Włodarczyk A., Giżewski T., Analiza funkcji wagi □ (□ , □) modelu Preisach'a przy wykorzystaniu algorytmu sztucznej sieci neuronowej, V Konferencja naukowo-techniczna „Zastosowanie komputerów w elektrotechnice, Poznań 2000.
[11] Winston P.H., Artificial intelligence; Wesley Publishing Company, USA 1984.

4th International Conference **ELMECO**
Nałęczów, Poland
September 2003

COMPUTATIONAL SOLUTIONS OF STEADY AND TRANSIENT STATES IN TRANSFORMERS USING FEM

Dariusz CZERWIŃSKI, Ryszard GOLEMAN, Leszek JAROSZYŃSKI

Institute of Electrical Engineering and Electrotechnologies,
Lublin University of Technology, Nadbystrzycka 38A, 20-618 Lublin, Poland
e-mail: leszekj@weber.pol.lublin.pl

Abstract

Electromagnetic Field Theory is often perceived as one of the most difficult subjects of electrical engineering. Difficulties arise from a very complex mathematical background. Necessity of some simplifications and idealisations of analysed objects takes place. The investigation of real live electromagnetic systems, where phenomenological interpretation of obtained results is the most important, requires some modern numerical methods placed in user-friendly operational environment. The Finite Element Method (FEM) gives very versatile and powerful solution of that problem. However, despite its advantages, its usage is relatively expensive and difficult especially for slightly experienced users. Progress in the software development enabled a significant simplification of the user interface in packages and made FEM very attractive for every PC user.

Keywords: electromagnetic field, transformers.

1. INTRODUCTION

Electromagnetic Field Theory is often perceived as one of the most difficult subjects of electrical engineering. Difficulties arise from a very complex mathematical background. Necessity of some simplifications and idealisations of analysed objects takes place. The investigation of real live electromagnetic systems, where phenomenological interpretation of obtained results is the most important, requires some modern numerical methods placed in user-friendly operational environment. The Finite Element Method (FEM) gives very versatile and powerful solution of that problem. However, despite its advantages, its usage is relatively expensive and difficult especially for slightly experienced users [1, 2]. Progress in the software development enabled a significant simplification of the user interface in packages and made FEM very attractive for every PC user.

2. PROBLEM DESCRIPTION

Problems of the single phase transformer with ferromagnetic core, set of parallel current conducting strips and three phase transformer with five legs ferromagnetic core were solved as a samples of FEM computer aided solutions. Numerical models of these problems have been built. Firs and second one were solved using QuickField software [3] and the last one using FLUX2D package [4].

3. MAGNETOSTATIC FIELD ANALYSIS

The problem of a single-phase transformer has been the example of computer aided computations of magnetic field (Fig. 1). The transformer consists of low voltage and high voltage windings wounded on a ferromagnetic core. The core is made of a transformer plate (ET-6). Computations assume the plane geometry and a simplified mathematical model that assumes the isotropy of the core, the uniform distribution of current density in a cross-section of each winding. Moreover, power losses in the core and insulation are neglected.

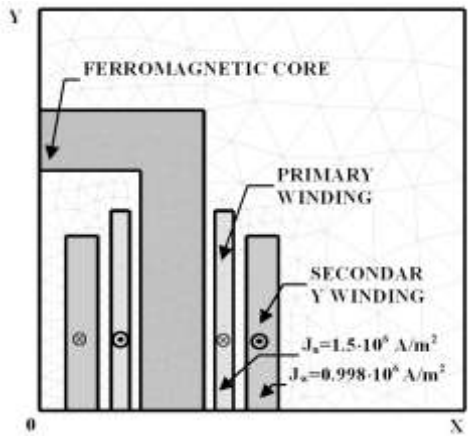

Fig. 1. Right upper corner of a single-phase transformer.

Current densities in the low voltage winding and in the high voltage winding are $J_n = 1.5 \cdot 10^6$ A/m^2 and $J_w = 0.998 \cdot 10^6$ A/m^2, respectively. The magnetic field generated in the transformer can be expressed by means of the non-linear Poisson's equation in a current area

$$\frac{\partial}{\partial x}\left(\frac{1}{\mu}\frac{\partial A_z}{\partial x}\right) + \frac{\partial}{\partial y}\left(\frac{1}{\mu}\frac{\partial A_z}{\partial y}\right) = -J_z \tag{1}$$

and the Laplace's equation in a non-current area

$$\frac{\partial}{\partial x}\left(\frac{1}{\mu}\frac{\partial A_z}{\partial x}\right) + \frac{\partial}{\partial y}\left(\frac{1}{\mu}\frac{\partial A_z}{\partial y}\right) = 0 \tag{2}$$

where: A_z - a vector magnetic potential component normal to the model cross-section, J_z - current density, μ - medium magnetic permeability.

The mathematical model assumes Neumann's boundary conditions along the axes OX and OY because of the symmetry

$$\frac{\partial A_z}{\partial n} = 0 \tag{3}$$

and the Dirichlet's condition $A_z = 0$ on the other edges where magnetic fields are neglectable.

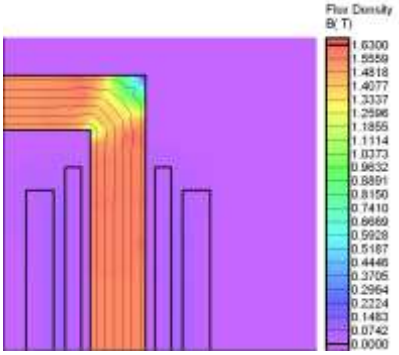

Fig. 2. Magnetic flux distribution and field lines in a single phase transformer.

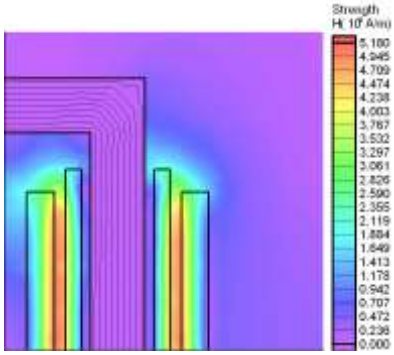

Fig. 3. Magnetic density distribution and field lines in a single phase transformer.

This vector magnetic potential distribution enables computations of magnetic field intensity (Fig. 2) and magnetic density (Fig. 3) in the whole area. Magnetic density values reach 1.63 T in straight line segments but in the corner is much smaller because of the bigger cross-section of a magnetic core.

The influence of a transformer tank on the field distribution in the transformer has been analyzed. The results indicate that if the transformer is placed in the ferromagnetic tank the outflow of the magnetic leakage is different. Some part of this flux is closed with the tank wall, which reflects in the comparison between the distributions of H_x component.

4. THREE PHASE TRANSFORMER WITH FIVE LIMB CORE

The numerical model of the power transformer of 250 MVA was assumed. This model is based on real transformer build for industrial purposes. Calculations were made for unsteady and steady states with fixed time step equal 0.001 s. Transient magnetic problem was coupled with circuit analysis. High and low voltage windings of the transformer are connected in star and stabilizing winding is connected in delta Fig. 4.

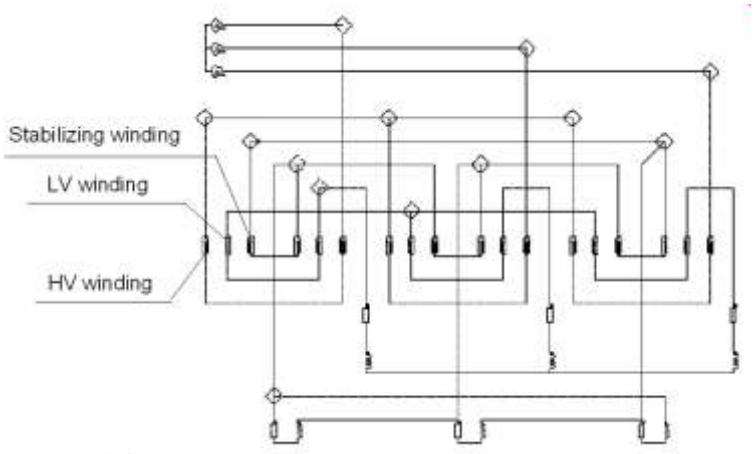

Fig. 4. Connection diagram of the windings of the transformer.

Vector potential in our model is given by equation (4)

$$\frac{\partial}{\partial x}\left(\frac{1}{\mu}\frac{\partial A_z}{\partial x}\right)+\frac{\partial}{\partial y}\left(\frac{1}{\mu}\frac{\partial A_z}{\partial y}\right)=-J_z+\gamma\frac{d}{dt}A_z \tag{4}$$

which is coupled with equations of an electrical transformer circuit.

$$\begin{aligned} e_A-e_C &= R_A\cdot i_A-R_C\cdot i_C+\frac{d\Psi_{AHV}}{dt}-\frac{d\Psi_{CHV}}{dt}\\ e_B-e_C &= R_B\cdot i_B-R_C\cdot i_C+\frac{d\Psi_{BHV}}{dt}-\frac{d\Psi_{CHV}}{dt}\\ i_A+i_B+i_C &= 0 \end{aligned} \tag{5}$$

$$\begin{aligned} \frac{d\Psi_{aLV}}{dt}-\frac{d\Psi_{cLV}}{dt} &= (R_{aLV}+R_{a1})\cdot i_a-(R_{cLV}+R_{c1})\cdot i_c+L_{a1}\frac{di_a}{dt}-L_{c1}\frac{di_c}{dt}\\ \frac{d\Psi_{bLV}}{dt}-\frac{d\Psi_{cLV}}{dt} &= (R_{bLV}+R_{b1})\cdot i_b-(R_{cLV}+R_{c1})\cdot i_c+L_{b1}\frac{di_b}{dt}-L_{c1}\frac{di_c}{dt}\\ i_a+i_b+i_c &= 0 \end{aligned} \tag{6}$$

$$\frac{d\Psi_{aCW}}{dt} - R_{aCW} \cdot i_{aCW} = R_{a2} \cdot i_{a2} + L_{a2} \frac{di_{a2}}{dt}$$
$$\frac{d\Psi_{bCW}}{dt} - R_{bCW} \cdot i_{bCW} = R_{b2} \cdot i_{b2} + L_{b2} \frac{di_{b2}}{dt}$$
$$\frac{d\Psi_{cCW}}{dt} - R_{cCW} \cdot i_{cCW} = R_{c2} \cdot i_{c2} + L_{c2} \frac{di_{c2}}{dt} \qquad (7)$$
$$\frac{d\Psi_{aCW}}{dt} + \frac{d\Psi_{bCW}}{dt} + \frac{d\Psi_{cCW}}{dt} = R_{aCW} \cdot i_{aCW} + R_{bCW} \cdot i_{bCW} + R_{cCW} \cdot i_{cCW}$$
$$R_{a2} \cdot i_{a2} + L_{a2} \frac{di_{a2}}{dt} + R_{b2} \cdot i_{b2} + L_{b2} \frac{di_{b2}}{dt} + R_{c2} \cdot i_{c2} + L_{c2} \frac{di_{c2}}{dt} = 0$$

where: Ψ - magnetic flux linkage with winding dependent on subscript, a, b, c - low and middle voltage phases, A, B, C - high voltage phases, LV - low voltage windings, HV - high voltage windings, CW - stabilizing windings, R - resistance of windings, L - inductance of windings, R_{a1}, R_{b1}, R_{c1}, R_{a2}, R_{b2}, R_{c2} - loads resistance of the LV windings and CW windings, L_{a1}, L_{b1}, L_{c1}, L_{a2}, L_{b2}, L_{c2} - loads inductance of the LV windings and CW windings.

Magnetic core of the transformer is made of ET6 laminations. Ratio of the yoke to main limb surfaces in our model is equal 0.58. Surfaces of the extreme yokes and limbs are reduced to 0.43 of the corresponding main limb.

Rated power of the transformer is 250 MVA and for stabilizing winding is 50 MVA. Delta voltage of the high and low voltage windings is equal 400 kV and respectively 123 kV. Phase to phase voltage of the stabilizing winding is equal 31.5 kV.

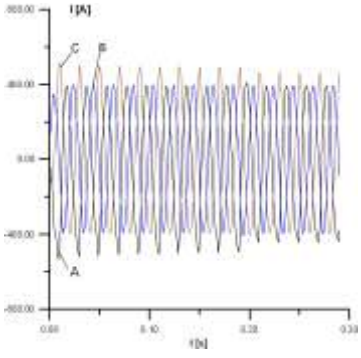

Fig. 5. Currents in the transformer primary windings.

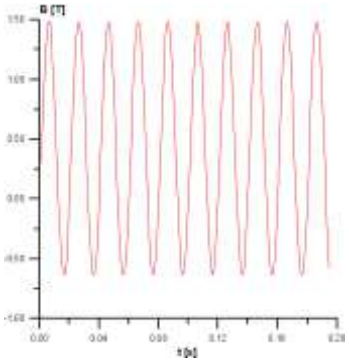

Fig. 6. Time characteristic of the flux density in the middle limb of the transformer.

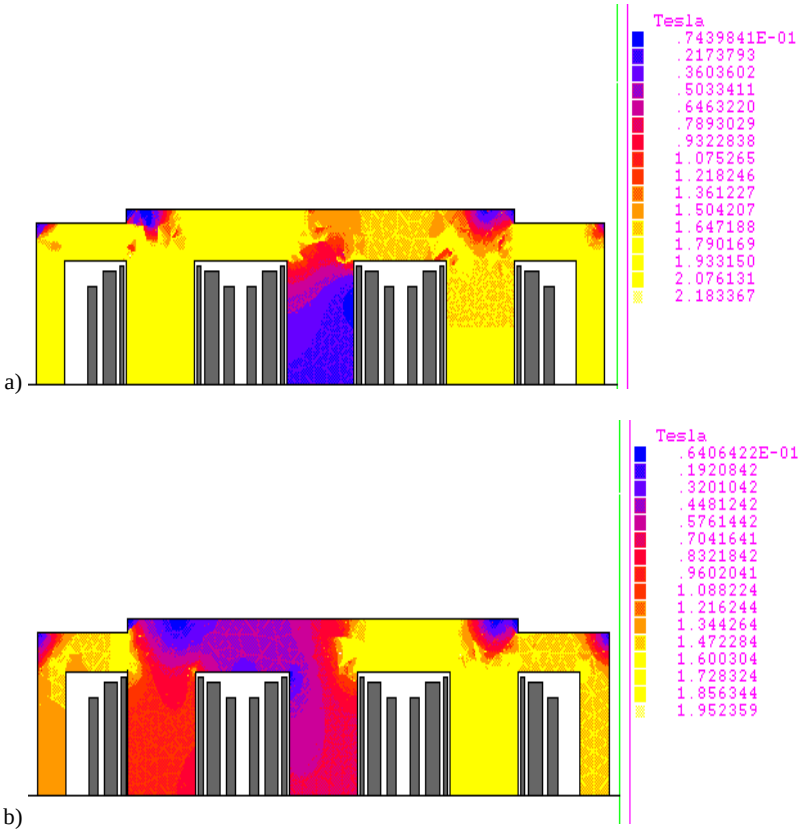

Fig. 7. Comparison of the flux density distribution in the core of the transformer at different time steps: a) t=0.1925s, b) t=0.1955s.

Obtained results enable us to tell, that unsteady state lasts until time is equal 0.3 s. Supplying voltage of the transformer is sinusoidal with constant amplitude. Currents in the primary windings of the transformer are also sinusoidal however after the switching in current waveforms appear the transient terms (Fig. 5). Waveforms and distribution of the magnetic flux density in the middle limb and transformer are shown at the Fig. 6 and Fig. 7. From Fig. 8 and Fig. 9, we can see that waveforms of the flux density in the external limbs and voltage on the inductance of the low voltage load are distorted and they consist the transient terms.

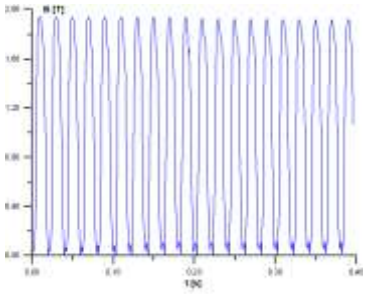

Fig. 8. Flux density in the external limb of the transformer.

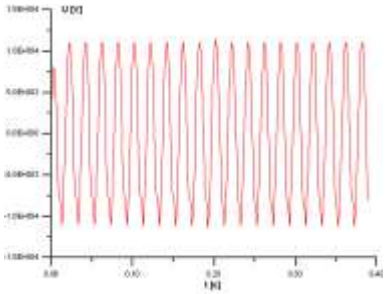

Fig. 9. Voltage on the inductance of the low voltage load.

5. CONCLUSION

The new generation of FEM software with an integrated, user-friendly programming environment greatly facilities Finite Element Analysis of electromagnetic systems for tutorial and professional applications. We have to care about the geometry and shapes of finite elements because of accuracy of the FEM.

Computational model of the transformer can be used in solution of additional winding losses.

Model of parallel strips with ferromagnetic plate enables to obtain distribution of the magnetic field and value of the eddy current losses.

The presented numerical model of the five limb transformer permits to determine multidimensional calculations at the both transient and steady state. It is possible to change the dimensions of our model e.g.: limbs, yokes and windings during calculations.

Required values of the flux density in the limbs and yokes can be obtained due to modification of the ratio of the limbs to yokes cross-sections.

Stabilizing winding connected in delta provides to the transformer odd harmonics of the order of 3n and permits pure waveform of the magnetic flux density in the main yokes.

Waveforms of the flux density in the external limbs and yokes are distorted.

REFERENCES

[1] S. Bolkowski, M. Stabrowski, J. Skoczylas, J. Sroka, J. Sikora, S. Wincenciak, Komputerowe metody analizy pola elektromagnetycznego, Warszawa, WNT,1993.

[2] D. S. Burnett, Finite Element Analysis, From Concepts to Applications, Addison-Wesley Publishing Company, 1988.

[3] Students' QuickField - Finite Element Analysis System, V. 3.4 - User's Guide, Tera Analysis, 1995.

[4] FLUX2D V. 7.20, User’s Guide, CEDRAT, August 1996.

4th International Conference **ELMECO**
Nałęczów, Poland
September 2003

THE APPLICATION OF HTSC ELEMENTS IN FAULT CURRENT LIMITERS

Beata KONDRATOWICZ-KUCEWICZ

Electrotechnical Institute
ul. Pożaryskiego 28 Warsaw
e-mail: beatakk@eltecol.pol.lublin.pl

Abstract

The paper describes the requirements that shall be fulfilled by the materials applied in fault current limiters. Depending on their fault limitation, superconducting limiters could be divided into resistive, inductive and hybrid ones. YBCO thin films are used in resistive type superconducting fault current limiters. Bi-2223, Bi-2212 as well as YBCO superconductors constructed in the form of rings and cylinders have been used in inductive type superconducting fault current limiters. Different constructions of high temperature superconducting fault current limiter are presented in the paper. The special feature of superconductors – resistance jumping growth of superconducting element beyond the critical current can be used to build the superconducting fault current limiter for power systems. Superconducting fault current limiters (SFCL) are one of the most promising devices for transmission and distribution of electrical energy due to low nominal losses, rapid reaction times to fault currents and an automatic response without external trigger mechanisms.

Keywords: high temperature superconductor, fault current, inductive SFCL.

1. INTRODUCTION

The special feature of superconductors – resistance jumping growth of superconducting element beyond the critical current can be used to build the superconducting fault current limiter for power systems.

Superconducting fault current limiters (SFCL) are one of the most promising devices for transmission and distribution of electrical energy due to low nominal losses, rapid reaction times to fault currents and an automatic response without external trigger mechanisms.

Depending on their fault limitation, superconducting limiters could be divided into resistive, inductive and hybrid ones.

2. THE OPERATION OF FAULT CURRENT LIMITER

The operation of superconducting element in fault current limiter consists of three phases:

I. **superconducting state**, $I < I_c$,
II. **transient state**, the growth of superconducting element resitance,
III. **resistive state**, $I > I_c$. [1]

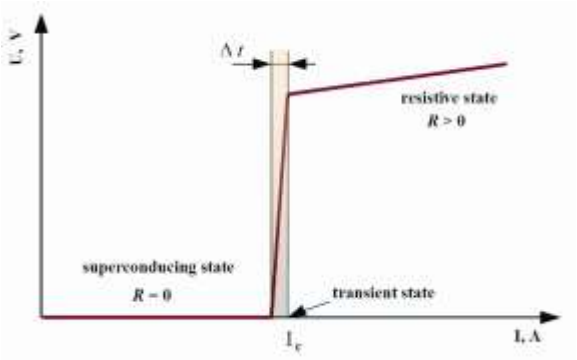

Fig. 1 V-A characteristic of superconducting element

The operation idea of superconducting fault current limiter is illustrated by current courses in Fig 2.

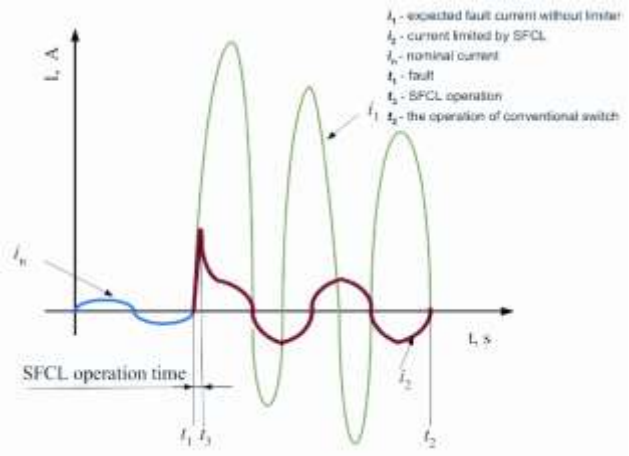

Fig. 2 Currents in SFCL

During a fault, the fault current pushes the superconductor into a resistive state and resistance, which limits the fault current, appears in the circuit.

3. HIGH TEMPERATURE MATERIALS FOR SFCL

Superconducting materials for fault current limiter shall fulfil 3 basic requirements:

- low AC losses
- high mechanical durability
- good thermal stability [2]

High temperature superconductors like YBCO thin films are used in resistive type superconducting fault current limiters. Superconductors Bi-2223, Bi-2212 as well as YBCO constructed in the form of rings and cylinders have been used in inductive type superconducting fault current limiters.

Fig. 3. Superconducting elements for fault current limiters
(Bi-2223 tubes made by Can Superconductors)

These superconducting materials have high critical temperature T_c>85 K, high critical current density - J_c from 0,1 to 0,5 GA/m^2 in 77 K, and resistivity ρ about 10 μΩm in 77 K.

4. THE CONSTRUCTION AND OPERATION OF SFCL

An inductive limiter works like transformer with shorted superconducting secondary winding. The impedance of this limiter under standard operation conditions is nearly zero, since the zero impedance of the secondary superconducting winding is reflected to the primary. In the event of a fault, the resistance in the secondary winding is reflected into the circuit and limits the fault current.

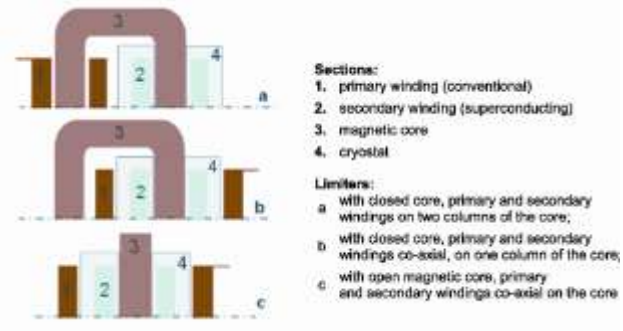

Fig. 4. Inductive current limiters (sections):

5. EXPERIMENTAL INVESTIGATION OF THE INDUCTIVE SFCL PHYSICAL MODELS

The physical models of the inductive-type screened iron core limiter has been performed and investigated in the Cryoelectromagnet Laboratory and University of Technology in Lublin. They consist of Bi-2223 superconducting tubes (I_c = 112 A, 625 A and 1210 A in temp. 77 K in self magnetic field) and some tape-wound and plated, closed and open cores.

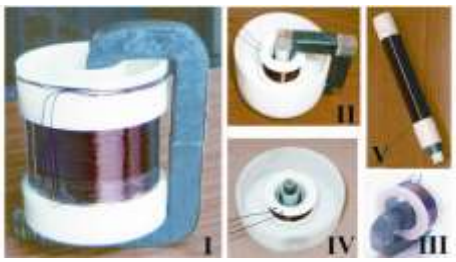

Fig. 5 The view of experimental physical models of superconducting fault current limiter

The limiting factor *wsp_ogr* have been introduced to estimate the current limitation caused by the investigated superconducting limiter. This factor has been defined as the relation of the voltage at the limiter to the voltage of the ideal shielding (voltage of the limiter without the core)[3].

$$wsp\_ogr = \frac{U - U_{br}}{U_{br}} \tag{1}$$

where: U – voltage of completed limiter, U_{br} – voltage of limiter without core

The charts presented below show the limiting factor of inductive SFCL models depending on superconducting elements and the type of magnetic core. The investigations were carried out in teperature 77 K

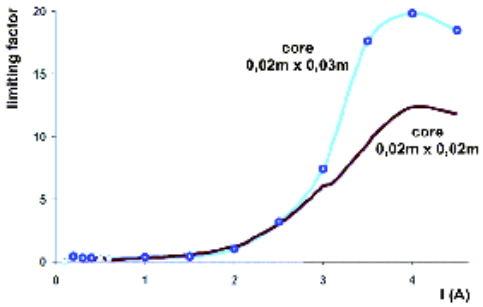

Fig. 6. The limiting factor for model I, I_c = 625 A (77 K) [3]

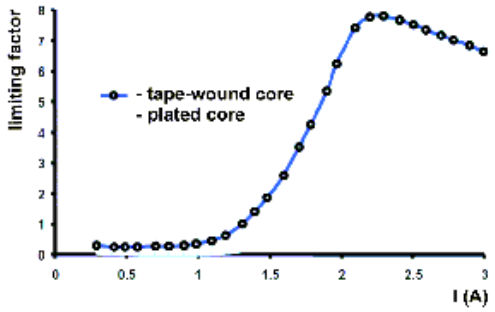

Fig. 7. The limiting factor for model II, I_c = 112 A (77 K) , 112 turns in primary winding [3]

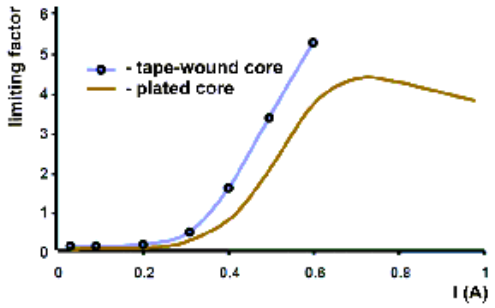

Fig. 8. The limiting factor for model III, I_c = 112 A (77 K) 448 turns in primary winding [3].

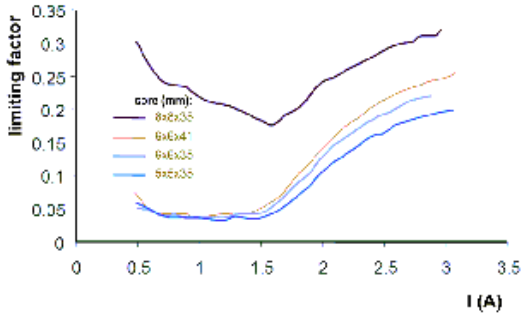

Fig. 9. The limiting factor for model IV, I_c = 112 A (77 K) 112 turns in primary winding [3]

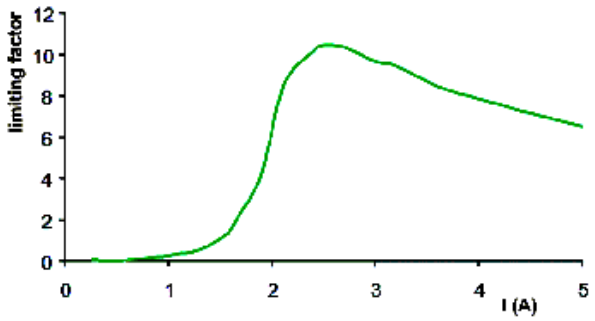

Fig. 10. The limiting factor for model V with open core, I_c = 1210 A (77 K) [3].

6. CONCLUSION

The idea of using superconducting element for building SFCL arose 20 years ago, however the conditions for it's realisation were created along with the development of high-temperature superconductors as well as modern cooling systems based on cryocoolers. Experimental research on physical models of SFCL in different configurations confirmed the efficiency of fault current limitation. Bi-2223 tubes with Ic =112 A (77 K), 625 A (77 K) and 1210 A (77 K) create the possibility of building inductive SFCL both with closed and open core of satisfying parameters. The application of magnetic core with bigger cross sections and better magnetic parameters increases limiting factor in inductive SFCLs. For SFCL with open magnetic core, superconducting tube should be possibly longer.

REFERENCES

[1] L. Salasoo, H. J. Boening, „Superconducting fault current limiter," Webster J. G. (ed.), Willey Encyclop. of Electr. and Electronics Eng., vol 20, John Willey & Sons, Inc., New Yorc 1999.

[2] M. P. Saravolac, P. Vertigen, „Development and testing of a novel design concept for high temperature superconducting fault current limiter," CIGRE'2000, 13-204.

[3] Janowski T., Stryczewska H.D., Kozak.S., Malinowski H., Wojtasiewicz G., Surdacki P., Kondratowicz-Kucewicz B., Kozak J.: Nadprzewodnikowe ograniczniki prądu, Liber, Lublin (2002)

4th International Conference **ELMECO**
Nałęczów, Poland
September 2003

DYNAMIC FORCES AND MAGNETIC FIELD ANALYSIS OF SUPERCONDUCTING TRANSFORMER

Grzegorz WOJTASIEWICZ

Electrotechnical Institute in Warsaw – Laboratory in Lublin
Nadbystrzycka 38a, 20-618 Lublin, Poland
e-mail: grzegorz@eltecol.pol.lublin.pl

Abstract

One of the most interesting applications of the superconducting technology is using high-temperature superconducting for windings of transformers. The superconducting transformers bring benefits such as low losses, smaller weight and volumes, as well as high efficiency and low cost of refrigeration. One of the problem, connected with designing and using superconducting transformers is the influence of the electromagnetic forces on the windings.

Keywords: superconducting transformer stresses and strains in superconducting windings, numerical model, magnetic field of superconducting windings.

1. INTRODUCTION

One of the most interesting applications of superconducting technologies is using high-temperature superconductors for windings of superconducting transformers. The usage of superconducting windings of the transformers, instead of conventional ones, brings more benefits such as low ac losses, smaller weight and volumes of magnetic core and windings as well as high efficiency and low cost of refrigeration.

One of the most important problems, connected with designing and using superconducting transformers is the influence of electromagnetic and dynamic forces, such as strains and stresses on the windings, due to brittle ceramic structure of HTS tape that was used to make the windings. The biggest value of the stresses and strains, acting on the windings, occurs during the short circuit.

In order to compute electromagnetic stresses and strains, occurring in the superconducting windings, the simple numerical model of superconducting transformer was made, using the OPERA 3D FEM software and the distribution of radial and tangential magnetic field components of the transformer were determined. On the basis of the obtained results of winding's magnetic field distribution electromagnetic forces can be calculated.

2. SUPERCONDUCTING TRANSFORMER CONFIGURATION

A superconducting transformer operates using the same principles and constituent parts as found in conventional transformer. Both employ an iron core and primary and secondary winding. However, the construction of the two types of transformers is quite different.

In conventional transformer primary and secondary windings are directly wound on the iron core and both iron core and coil assemblies are immersed in a tank filled with oil. On the other hand, in superconducting transformer, the iron core is usually maintained at room-temperature while the superconducting coils operate at cryogenic temperatures. The decision to maintain the iron core at room-temperature is dictated by the fact that the iron losses (hysteresis and eddy-current) go up when the iron core is operated at cryogenic-temperature.

On the other hand, the superconducting windings must be cooled to cryogenic temperature, therefore these winding must be enclosed in cryostats that could hold vacuum or cryogen or both.

The schematic diagram of simple physical model of 1-phase superconducting transformer, which has been made in Cryogenic Laboratory, is shown in Fig 1. Table 1 describes specification of the transformer.

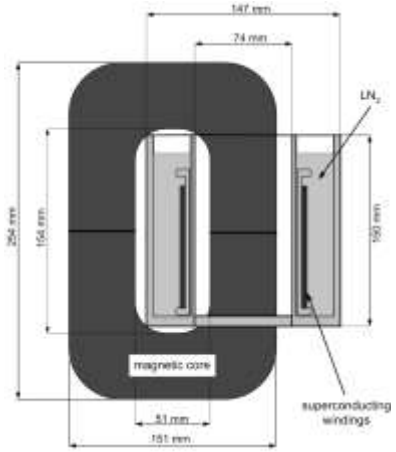

Fig. 1. Schematic diagram of superconducting transformer .

Table 1. Specification of superconducting transformer.

Parameters	Values
Capacity	900 VA
Primary / secondary voltage	90 V / 90 V
Primary / secondary current	10 A / 10 A
Frequency	50 Hz
Winding type	cylindrical
Layer numer	4 / 4
Operation Temperature	77 K
Magnetic induction in core	1.3 T
% impedance	0.5 %
Coolant	Liquid nitrogen
Strand	Bi-2223 multifilamentary tape
Matrix of strand	Ag
Core	Silikon sheet steel
Limb height	254 mm
Limb width	50 mm
Window width	51 mm

3. DYNAMIC STRESSES AND STRAINS IN SUPERCONDUCTING TRANSFORMER

In superconducting transformers electormagnetic forces acting on windings are much bigger than forces acting in conventional transformers, because the current density in superconducting windings is at least order of magnitude bigger than in copper ones.

Electromagnetic forces acting on the superconducting windings could be divided into two types:

- electromagnetic forces dependent on parallel component of magnetic flux density (radial forces),
- electromagnetic forces dependent on transversal component of magnetic flux density (axial forces).

The reason of axial forces acting is transversal component of magnetic flux density in perpendicular direction to the axis of windings, due to curvature of field lines. That forces cause the compression of winding, tend to change its height. The distribution of transversal component of magnetic flux density for primary and secondary cylindrical windings is shown in Fig 2.

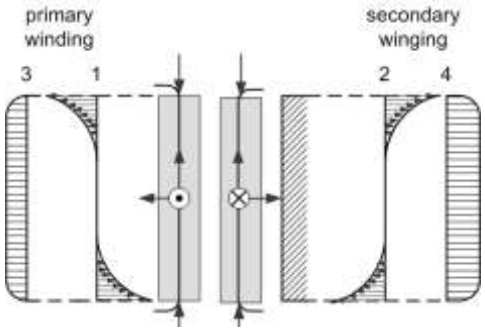

Fig. 2. Axial forces: 1,2 - transversal component of magnetic flux density, 3, 4 - distribution of the forces.

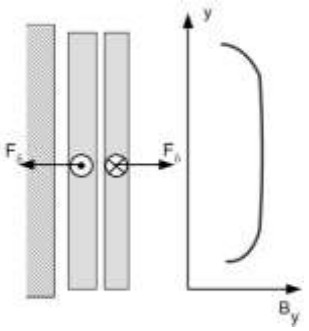

Fig. 3. Radial forces Fδ , and their summary distribution.

Radial forces occur as a result of parallel component of magnetic flux density acting in longitudinal direction to the axis of windings. Summary radial forces, F_δ, compress internal winding of the transformer and disrupt external one, tend to increase the inter-windings gap δ. Fig 3 shows distribution of summary radial forces.

The durability of brittle ceramic structure of superconducting tape used for construction of the superconducting winding is a decisive factor that influences the durability of those windings. The tape is effectively a composite in those superconducting fibres of high stiffness (tape core) are surrounded by a metal matrix with considerably higher ductility, Fig 4.

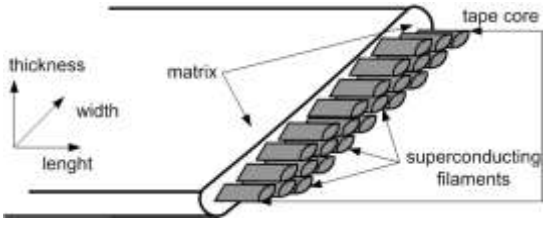

Fig. 4. Texture of high-temperature superconducting tape.

The superconducting material is not arranged in this way only to give the composite a mechanical advantage, it is more based on processing consideration and wanted electrical behavior. However, the material can be analysed mechanically like a composite.

Changing a material from a homogeneous structure into a composite with a distinct anisotropic structure will change the elastic properties. This means that stiffness and strength of superconducting tape will be different in different direction.

4. NUMERICAL MODEL OF THE SUPERCONDUCTING TRANSFORMER

Electromagnetic forces acting on the superconducting windings occur as a result of influence of alternating magnetic field and their components on the conductors carrying current. Because of large value of current density in superconducting windings, three-dimensional distribution of those forces may be different from the forces distribution of conventional transformer.

In order to compute the distribution of radial and tangential magnetic field components of the transformer the simple numerical model of superconducting transformer was made, using the OPERA 3D software. The numerical model of the transformer is shown in Fig 5.

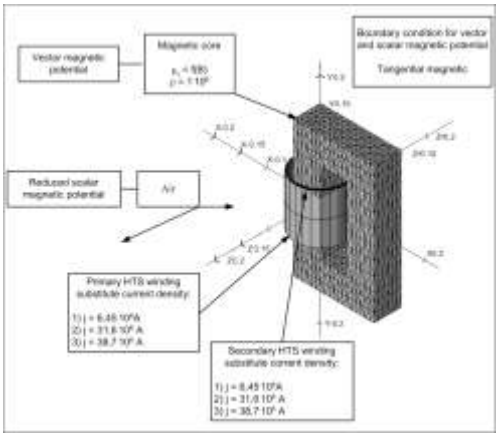

Fig. 5. Numerical model of the superconducting transformer.

As a result of numerical analysis the distribution of radial and tangential components of the transformer's winding stray field were determined. On the basis of the obtained results of winding's magnetic field distribution, electromagnetic forces can be calculated.

5. MAGNETIC FIELD DISTRIBUTION ANALYSIS IN WINDINGS OF SUPERCONDUCTING TRANSFORMER

The distributions of the transformer's winding stray field were determined for three characteristic values of current: 10 A – nominal current of transformer, 49 A – maximal

current of the transformer that induced maximal stresses in the tape, and 60 A critical current of HTS tape. Exceed of the current 60 A cause transition the superconducting winding from superconducting state to the resistive state.

The examples of the distribution of radial and tangential components of the winding stray field, for currents 10, 49 and 60 A, are shown below. The distributions were obtained in space between windings, on inner surface of primary winding and outer surface of secondary winding, where the influence of the magnetic field on the value of electromagnetic forces is the highest. Fig 6 shows the three-dimensional distribution of total magnetic flux density along the cross section of the transformer, Fig 7 and Fig 8 show the distribution of parallel and transversal components of magnetic flux density along the winding's height and Fig 9 shows the distribution of total magnetic flux density along the winding's height.

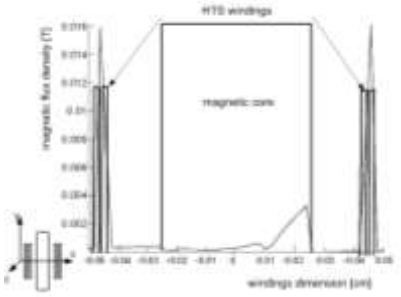

Fig. 6. Magnetic flux density along the cross section of the transformer.

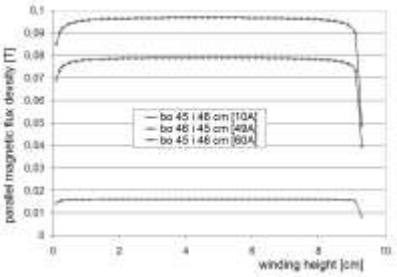

Fig. 7. Parallel component of magnetic flux density.

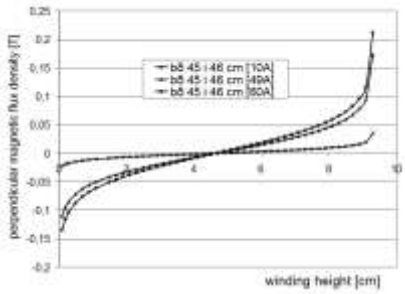

Fig. 8. Transversal component of magnetic flux density.

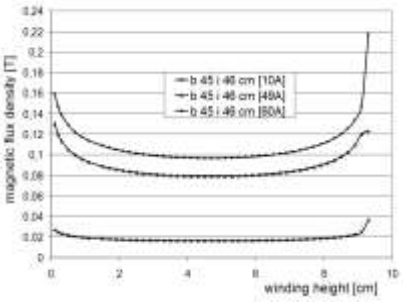

Fig. 9. Magnetic flux density.

6. CONCLUSION

Forces acting on the supeconducting windings could be divided into two types: electromagnetic forces acting as a result of influence of alternating magnetic field on the

conductors carrying current and dynamic forces induced in the winding due to mechanical properties of the conductors.

Dynamic forces, induced stresses and strains in superconducting windings, are able to dissipate energy in many different ways, producing a random disturbance spectrum with total destruction of the windings in the worst case. In superconducting windings like in conventional ones, dynamic forces can emit creaks, cracks and groans. The other type of dynamic forces induced in superconducting winding is frictional forces acting between neighboring turns of winding.

One of the methods for the analysis of electromagnetic forces, acting on superconducting windings of transformer, is their calculation according to the results of winding's magnetic field distribution.

As a result of numerical analysis the simple numerical model of superconducting transformer was made, using the OPERA 3D FEM software and the distribution of radial and tangential components of the transformer's winding stray field were determined. Obtained distribution of stray field components are not different from the stray field distribution of conventional (Cu) transformer.

On the basis of the obtained results of winding's magnetic field distribution, electromagnetic forces can be calculated.

REFERENCES

[1] Janowski T., Transformatory nadprzewodnikowe, Zeszyty Naukowe Elektryka, Politechnika Poznańska (2000).

[2] Wojtasiewicz G., Siły i naprężenia w uzwojeniach transformatorów nadprzewodnikowych, III Seminarium Zastosowania Nadprzewodników, Lublin-Nałęczów, 22-23.11 (2001), 133-142.

[3] Skov-Hansen P., Han Z., Bech J.I., Stresses nad Strains in Multi Filament HTS Tapes, http://www.nst.com/ASC98-PSH.PDF.

[4] Janowski T., Wojtasiewicz G., Analiza sił i naprężeń w modelu transformatora nadprzewodnikowego, XXVI IC-SPETO, Nidzica-Gliwice 28-31.05 (2003), 115-118.

4th International Conference **ELMECO**
Nałęczów, Poland
September 2003

TECHNOLOGY OF COOLING OF SUPERCONDUCTING DEVICES LIQUID CRYOGEN-FREE SYSTEM

Henryk MALINOWSKI

Electrotechnical Institue in Warsaw
Warszawa ul. Pożaryskiego 28
e-mail: henmal@eltecol.pol.lublin.pl

Abstract

Development of superconducting materials' technology, and new constructions of cryocoolers, has given ability of application superconducting devices in realms and places, where, until now, it was ungrounted, because of economic reasons. One of the examples can be superconducting energetic cables or superconducting fault current limiter.

To achieve high degree of superconducting devices' stability, it is crucial to supply proper cooling of their elements. New cryogenic cooling machines gradually substitute old ways of cooling and that is cooling in bath. Their usage with superconducting devices gives ability to automate their work, and makes the control easier. On the other hand it generates problems connected both with difference in conditions of environment in which particular parts work, and with efficiency of cryocoolers. Text presented below describes some of the problems that appear while their usage.

Keywords: superconductivity, cryocoolers.

1. INTRODUCTION

Technology of cooling plays significant role in the application of superconductivity. For every superconducting device there is the need for individual solution of cooling problems. It is required from the cooling system to be reliable and assure stable operation. Another absolutely important parameter of the device is price and exploitation costs. Reaching temperature lower than critical temperature is a condition to obtain the superconducting state.

Until recently common way of cooling, used to be cooling in cryogenic bath. Wider applications of superconductivity and the development of cosmic research shoved that such ways of cooling was no longer cheap and comfortable. Development of technology enables

to build cryocoolers that allow keeping temperature lower than temperature of liquid helium for long time.

Those devices are exploited in extreme conditions. They are used in space technology, and under surface of Earth in researches connected with physics. The application the latest material technology caused reliable operation in all conditions. Coolers situated in spaceships gave the opportunity to expand period of measuring apparatus. Energetic efficiency is so high, that they are used not only in cooling very small electronic parts, but also electromagnets of weight around few tons. It is worth saying that application of cryogenic temperatures is out of superconductivity's range. Nevertheless, they are used in different realms of science, such as: medicine, biotechnology and others.

2. TYPES OF COOLERS

Development in miniaturization of devices and in material technology has given the ability to use known ways of cooling gases. Many types of cooling devices have been constructed. Drawing on them, realms of coolers enabling choosing proper cooling system for given apparatus has emerged.

Reasons for such a huge technological development should be searched in demand, no longer demand of physicists in scientific aims, but also by companies which more and more widely use superconducting devices in commercial aims.

Large share in the progress has space technology that needs not only low temperatures for measurement sensors, but also miniaturization the cooling mechanism. Detectors used in space objects are thousands times more sensitive in cryogenic temperatures than in temperature around 20^0C.

3. CLASSIFICATION OF CRYOCOOLERS

Cooling methods depend on conditions, in which the cooled object operates and on functions that it is responsible for it. Because of specific operation of superconducting devices, it is necessary to supply them proper cooling power.

Ways of cooling evolve very quickly together with the development of superconducting technology. Great demand for helium in recent years caused trebling its price on world markets. The demand is still growing, and that trend is getting stronger. Therefore, great attention is paid on cooling systems, in which helium works in closed cycle. Cooling machines – cryocoolers, coolers, can be classified along different features. One of them is its operation. Coolers, as NASA does, can be classified in three groups:

- Passive cooling;
- Stored cryogens;
- Mechanical coolers.

Temperature Ranges

- Passive Cooler -- down to 30 Kelvin;
- Mechanical Cooler -- down to 6 Kelvin;
- Stored Cryogen Cooler -- down to 1.3 Kelvin.

Passive cryocoolers do not consist of any active cooling devices. Stored cryocoolers use the cumulated energy to cool. Mechanical cryocoolers contain at least one active cooling part.

In different types of cryocoolers many methods of cooling are applied. Those methods are determined mainly by demand for cooling power. The power reaches diverse values – from few microwatts to thousands miliwatts in temperature T = 4,2 K. For nitrogen

temperature reaching up few hundreds watts. Therefore coolers have been divided into big coolers and miniature coolers. Another classification shows more detailed division of coolers in view of their cooling powers:

- micro miniature (very small energetic efficiency for electronics applications),
- miniature (small energetic efficiency for electronics applications),
- small (for laboratory and commercial cryogenic systems),
- medium (refrigerators and non-large commercial systems),
- large (big refrigerator systems).

Other classification of coolers considers methods of achieving such low temperatures. Most commonly we can distinguish:

- coolers with J-T expansion valve,
- stored cryogen systems,
- cooler with expander.

In every of those types we can distinguish many variants that clearly differ between themselves. However, many devices combine various methods of cooling and it is hard to classify them in one of the determined groups. They are called "hybrid systems".

On market, most commonly we can find McMahon's coolers and tube-pulse. Scheme of their construction is presented in figure 1.

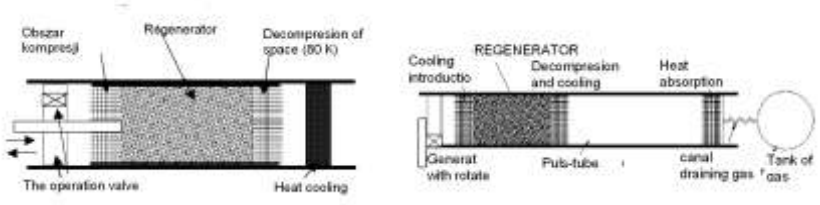

Fig. 1. Schemes of the MacMahon and Tube-pulse cryocoolers.

Requirements concerning all the coolers is striving for: minimizing their weight and size, limiting consumed energy, shortening cycle of loading and lengthen time of their exploitation, reliability in different exploitation conditions, and their autonomy. Evidence for progress in the field is the fact that until recently cooling apparatus of superconducting system has taken about 95% of the whole system's velocity. Nowadays, sizes of the apparatus are similar.

In conditions on the Earth's surface, obtainment of cryogenic temperature is extremely energy consuming. Factor of efficiency (in perfect Carnot's cycle) does not exceed 1.5%. In real, to achieve power 1W on the degree 4,2K, 600-800 W are needed. There are still helium liquefying devices which efficiency equal 0.002%.

In space, apparatus working on spaceships also requires cooling. Radiation of stars, Earth, Moon and work of deck instruments, are the cause of temperature of the object rising above 100 K, which is too hot for sensitive sensors' functioning. Ant radiation isolators are, in this case, parts, which enable proper cooling of the objects. Those devices do not work literally, but they give the effect of decrease of temperature. In this case we have static cooling.

For objects staying on the circumearth orbit: radiation screens prevent from warming of the object caused by Earth's or Moon's radiation. The application of such cooling system enables limitation object's temperature to the value around 60 K. For objects being far from Earth, ant radiation screen enables limitation of Sun's influence, providing temperature lower than 35 K.

Apart from preciously mentioned radiation screens, it is essential to radiators, which help in dispersion of heat that is secreted on spaceship's board, as a result of apparatus' activity.

Passive coolers use cryogenic liquid, which comes out of its container to the object's surface. While liquid's evaporation object's temperature decreases. Such cooling system was used in Hubble's telescope. One of space shuttle's missions has changed it, by using mechanical cooler.

Mechanical coolers are the most developed group of cooling devices. Electric energy is needed to enable functioning of compressors, or to move mobile parts (pistons, regenerators). Work of those devices is also possible in space, where energy is provided by solar batteries.

Big coolers are usually many degree-cooling devices. Power that supplies them reaches values over tens of watts, and their mass is bigger than 1 kg. Power achieved few hundreds miliwatts in temperature reaching few hundreds Kelvins.

Miniature coolers, are the ones, which consume up to 20 W. Their mass does not exceed 1 kg. They reach power of 0.3 watts in temperature 60K.

Non-helium vibration coolers should also be mentioned in the distinction. It is because of their unique functioning. Vibration coolers form special class of developing coolers, that are characterized by low vibration level – the parameter is absolutely crucial for proper work of measuring apparatus. Among all of mechanic coolers, that type distinguishes itself when size and efficiency per mass unit are considered. The cooler consist of three main parts: gas turbine rotating with speed over 1000 000 RPM; ant current flowing heat exchanger, and expander. The system is particularly efficient in range of temperatures 10K – 4K.

4. COOLING OF SUPERCONDUCTING MAGNETS.

Electromagnets with wiring made of low temperature superconductors, operate usually in temperature of liquid helium, and the ones with wiring made of high temperature superconductors – in temperature of liquid nitrogen. Parameters of superconducting electromagnets can be improved by descend of their work's temperature. Cooling with usage of liquid helium, provides work of NbTi wiring in state of superconductivity in temperature of 4.2 K (in normal pressure). The temperature may change along with change of pressure, and at the pressure of a few atmospheres it can exceed 5K.

Recently, more and more common mechanic system of cooling is used. It enables reaching temperature around 2K. In the area of cooling with temperature 4.2 K helium under pressure of few atmospheres is introduced. During it's decompressing to the atmospheric pressure, temperature can be decreased to 2K (1.67K has been reached by using that system).

The application demagnetisation process can obtain even lower temperature. Such devices have found practical use. Multisteps cooler of that type provides temperature of few hundreds Kelvin. Its scheme has been shown in figure 2.

Fig. 2. Multistep adiabatic demagnetisation cooling systems.

Good example of progress in miniaturization of coolers is helium minicooler sorption. It's not a new idea. In 1926 F. F. Simmon proposed the method of helium liquefying by sorption with use of active carbon, which follows helium decondensation in lower pressures. Decrease of temperature (from hydrogen temperature) has reached 39K in one cycle. It enabled to liquefy helium. But the process proceeded periodically, and the method did not find wider use then. Proposed, and implemented way of cooling occurred to be useful in cooling microelements. Figure 3 shows scheme of such apparatus.

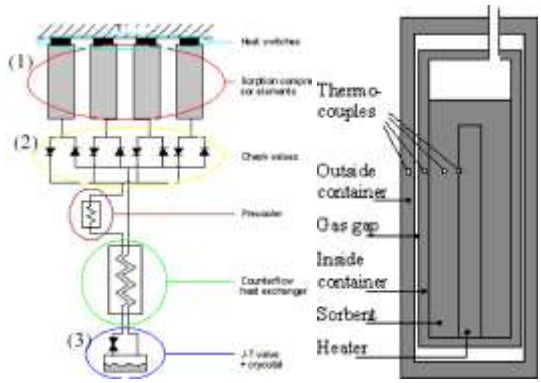

Fig. 3. Microcooler of sorption type and sorption element.

It's functioning base on Joule-Thompson (J-T) effect. In certain temperature, helium is being absorbed in sorption elements. After disengaging heater, sorption cell warms, and secrete helium. In sorption chamber pressure rises. Through valves (2), the only mowing part in the cooling system, helium passes through initial cooling system, and than it cools in heat exchanger, that is cooled by gas that evaporated in cryostat. Cooled and being kept under pressure helium flows to the J-T valve, and adiabatically cools, and simultaneously is partially liquefied. Total system size: < 250 cm^3. Heat rejection: < 10 W

5. EFFICIENCY OF COOLING

While cooling superconducting electromagnets, the efficiency has great value. Speed of cooling of parts directly connected with cooling element, relies on efficiency of cooler. Cooling of magnet's winding is realized by heat conductance of constructional parts of the electromagnet. Between winding and source of cold, i.e. cooling head or cryogenic liquid, few isolation layers are situated (external electromagnet's isolation, bandage made of stainless steel, interlayer isolation, wire's isolation). Similarly, internal parts of mass superconductor HTS are cooled worse than external parts, because of low heat conductivity of HTS conductor. Extremely relevant for property of cooling system used in objects, is the difference of temperatures between any two points of superconducting wiring in extremely adverse moments, and it is while cooling (in contact 'warm winding' with cryogenic liquid), or in quench. The greatest difference of temperatures occurs between middle part of winding, and external part of winding that is the closest to the cooling element. The difference can exceed 100 K.

In case of quench, due to speed if the process, there is no fast heat exchange between internal parts, and cooling object. For faster heat stabilization of winding, crucial role is played by heat velocity of the superconductor and isolation materials, and winding technology. Heat efficiency of the cooling system is not so important. It is worth saying, that those considerations refer to electromagnet with high level of stability that is supplied by constant current.

6. EXPERIMENT

To compare the influence of cooling system on quench course (especially maximum value of winding temperature), experiment has been performed, in which two electromagnets that were constructed in similar way, but using different technologies, has been subject to forced quench. The first electromagnet was made in classical way, with destination to cooling in cryogenic bath. The other one was constructed in new technology of winding, to work with cryocooler, in which heat conductivity factor (along the electromagnet's axis) has been extended. Picture 5 presents the section of the electromagnets.

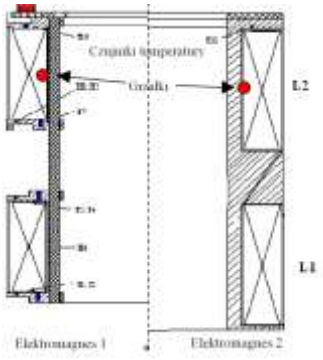

Fig. 4. The cross-section superconducting magnets at real proportion.

The first electromagnet has been totally dipped in helium bath. Supply current of it had a value of 175A. The other one was dip in the way, in which one base was touching cryogenic liquid. Cooling of the winding has been happening in contact way – through carcass material, isolation and construction material. Supply current had a value of 170A.

Heat impulse leading to loss of superconductivity, in both magnets was the same. Time of quench was a bit lower in the second electromagnet. Maximum temperature in windings of both electromagnets has differed. Temperature of winding placed outside the area of direct cooling with liquid helium, has reached 24K in the second electromagnet, and it was lower than in the first one (40K), despite the fact that wiring has been dip in liquid helium, and it has had lower (because of number of rolls) energy.

7. CONCLUSION

Superconducting magnets, that are constructed to work with mechanic coolers, are characterized by high level of application, supply currents, that are used in them, have values of 25%-40% of their critical current. In comparison with electromagnets cooled in bath, the current is 2 – 3 times lower. The experiment has proved the thesis, that maximum temperature of wiring in quench process, depends mainly on technology of it's realization, and that system of cooling does not determine the temperature in such big degree.

By choosing proper materials while constructing electromagnet (material of carcass, electric isolation with high level of heat conductivity), influence of cooler's efficiency and system of cooling on electromagnet's parameters can be minimized.

REFERENCES

[1] Wilson M.N., Superconducting Magnets, Clarendon Press, Oxford, 1983.

[2] Gordon Johnston, Instrument Cooler Technology Page, http://ranier.oact.hq.nasa.gov/Sensors_page/Cryo/CryoTemp.html#Goals.

[4] H.Malinowski, Sozdanie i issledowanie wysokoekonomiczeskich ustanowok s silnymi magnitnymi poliami dla jadernoj fiziki i ekologii Materiały kruglogo stola i Koordinacionnogo soweszczania 18-20 01 2001 pod redakcją W.G. Kadyszewskiego, A.N.Sisakiana. A.Hrynkiewicza; Dubna 2001 strona 89 – 91. ISBN 5-85165-668-9

[5] W.Okołotin, Swierhzadacza dla swierhprowodimosti, Wydawnictwo Znanie, Moskwa 1983

[6] NASA Goddard Space Flight Center, The Adiabatic Demagnetization Refrigerator (ADR), A Cyclic Magnetic Cooler: cryowwwebber.gsfc.nasa.gov/ADR

[7] A.Sato, S.Nimori, T.Numazawa, M.Maeda, F.Matsumoto, H.Nagai, National Institute for Materials Science; M.Takahashi, T.Kuriyama, Toshiba Corporation; T. Ito,T. Okamura,Tokyo Institute of Technology, Development of High Field Superconducting Magnet Cooled by 2 K Cryocooler (1) - Magnet and Cooling System CEC/ICMC 2001, Wisconsin, USA on July, 16, 2001.

[8] J.G.E. Gardeniers, A microcooler for low temperature electronics, http://www.el.utwente.nl/tt/projects/mucooler/

ELECTROMAGNETIC PROCESSES AND DEVICES II

4th International Conference **ELMECO**
Nałęczów, Poland
September 2003

ELECTRICALLY ASSISTED DEVICES FOR DUST CONTROL
Part 2. Wet electrostatic methods

Anatol JAWOREK, Marcin LACKOWSKI, Tadeusz CZECH, Andrzej KRUPA

Institute of Fluid Flow Machinery, Polish Academy of Sciences,
80-952 Gdańsk, ul. Fiszera 14, POLAND, e-mail: jaworek@imp.gda.pl

Abstract

Combining electrical processes with another mechanisms of particle removal is a new trend in improvement gas cleaning from submicrometer particles. Conventional electrostatic precipitators are equipped with spray nozzles wetting and washing collection electrodes instead of rapping them. This removes the problems with particle re-entrainment, and with back-corona discharge, which decrease the collection efficiency of dry precipitators. The wet-type electrostatic precipitator can also simultaneously absorb gaseous pollutants such as NO2, SO2, HCl, NH3, or malodorous gases. The second group of devices discussed in this part of the paper comprises wet-type electrostatic scrubbers. The method is based on electrical charging of dust particles and scrubbing droplets to the same or opposite polarities. The droplets collect the particles or repel them to the chamber walls were the dust is washed out.

Keywords: gas cleaning, wet electrostatic precipitators, electrostatic scrubbers.

1. INTRODUCTION

The second part of this paper considers combination of dry and wet methods with electrostatic assistance integrated in one device. Combining advantages of both hydrodynamic and electrical gas cleaning devices led to developing wet electrostatic methods. Two main classes of such devices can be distinguished: wet electrostatic precipitators and wet electrostatic scrubbers. In wet electrostatic precipitators the dust particles are charged by negative ions similarly to a conventional electrostatic precipitator but the collection electrodes are washed with water instead of to be rapped. This removes the problems with particle re-entrainment and with back-corona discharge, which both decrease the collection efficiency of dry precipitators. Other class of devices, which allow effective removal of fine dust particles from exhaust gases are the electrostatic scrubbers.

The method is based on employing the Coulomb forces by electrical charging of dust particles and scrubbing droplets to the same or opposite polarities. Devices based on this principle are designed for removal dust particles from exhaust gases in micrometer and submicrometer size range, and can be used as a last stage following a conventional electrostatic precipitator or bag filter. Water irrigated precipitators can be constructed from dielectric (PVC or composite) materials that eliminates the electrocorrosion problems.

2. WET-TYPE ELECTROSTATIC PRECIPITATORS

Wet electrostatic precipitators are usually of tubular configuration [1]. Tubular wet electrostatic precipitators consist of a cylindrical collection electrode and a discharge electrode located in the axis of the cylinder. Dust particles are charged by negative ions and migrate to the cylinder wall. The collected dust is removed from the tube by its washing with water spray from the upper part of the tube. Additionally, water-soluble gaseous compounds such as NO_x, SO_x and HCl can also be absorbed and removed from the gas. For example, the removal efficiency of dioxins by this system was of about of 99.7% [2]. The diameter of a tubular wet electrostatic precipitator varies typically from 0.15 to 0.3 m and its height from 1.5 to 5 m. Tubes of hexagonal cross-section are also used instead of cylindrical once for closer packing them. The dust removal efficiency is usually in the range of 85 - 99%.

In the wet electrostatic precipitator proposed by Pasic [3] a stiff collection electrodes were replaced by a soft woven material 0.5 to 1 mm thick, made of carbon and silica fibers. This type of the collection electrode can be also washed with water for remove the collected dust particles. Such device has improved dust collection efficiency, and solves many problems inherent to both dry and wet electrostatic precipitators, because the water can be more uniformly distributed throughout the membrane due to the capillary effect, minimizing the number of dry spots and lowering water consumption.

Water vapor or steam condensation on electrically charged fly ash particles for their easier precipitation was used by Dexuan et al. [4], and Bologa et al. [5] that allowed removal of extremely fine particles.

3. ELECTROSTATIC SCRUBBERS

The conventional inertial and turbulent scrubbers are inefficient in removal of small particles (<1 μm), and to solve this problem the electrostatic scrubbing method was proposed by Penny [6]. The method is based on electrical charging of dust particles and scrubbing droplets to opposite polarities. The falling charged droplets act as small spherical collectors collecting dust particles due to attractive Coulomb forces.

Five types of wet electrostatic scrubbers are met in literature, depending on the droplets and particles charge polarity:

Droplets are charged to either polarity and the particles to an opposite charge [6, 9-13]. In the submicrometer size range the electrostatic attraction forces are dominant causing the particles to be deposited on the droplets.

Droplets are charged to both polarities with an equal number of positively and negatively charged droplets [14]. The positively charged droplets capture the negatively charged particles due to attractive Coulomb forces, and finally they coagulate with negatively charged droplets.

Droplets and dust particles are charged to the same polarity [14-17]. The repulsive force of the space charge of the droplet cloud causes the particles to be precipitated on the

chamber walls rather than deposited on the drops. The particles are next washed out from the walls by this spray.

Droplets are charged to either polarity while the particles remain uncharged [7, 14, 18, 19]. The particles are deposited on the droplets due to image charge on the particle.

The particles are charged to either polarity and the droplets are uncharged [14]. The particles are deposited on the droplets because of image charge induced on the droplet.

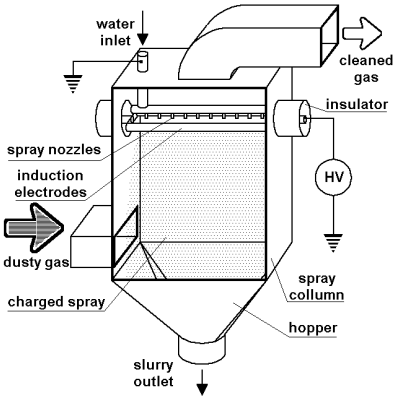

Fig. 1. Vertical type of electrostatic scrubber.

The schemes of vertical and horizontal type of electrostatic scrubber are shown in Fig. 1 and Fig. 2, respectively. Venturi scrubbers (Fig. 3) which can be positioned vertically or horizontally were also tested to be electrostatically assisted [7, 8]. In the Venturi scrubbers the charged spray is usually injected with high velocity close to the throat of the Venturi nozzle. Dust particles are usually repelled to the throat walls because the charges of the droplets and particles are of the same polarity. Wet methods are particularly suitable for removal dust particles from exhaust gases in micrometer and submicrometer size range and can be used as a last stage following a conventional electrostatic precipitator, bag filter, or cyclone.

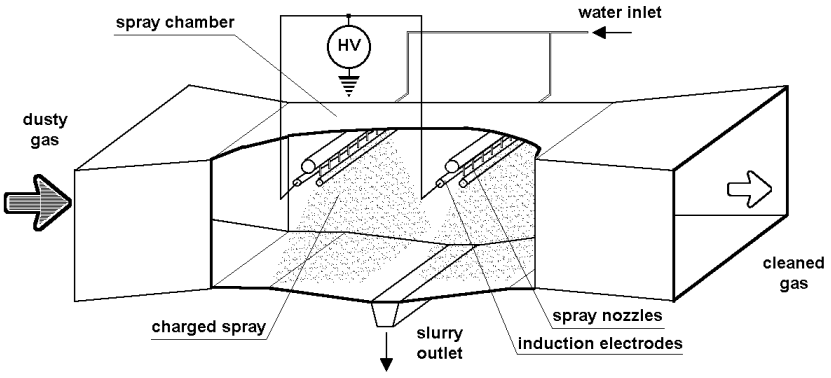

Fig. 2. Horizontal type of electrostatic scrubber.

The particles are usually charged in a corona discharge of different type and electrode configurations, or sometimes by the tribocharging during their pneumatic transportation through the channel. In order to increase the particle charge and optimisation the charging process two types of prechargers were proposed and tested in publications: the Masuda

boxer charger [20, 21], and Jaworek and Krupa alternating electric field charger [22-24]. Both of these chargers allow maximisation of the charge imparted to the particles with reduced precipitation on the charger electrodes.

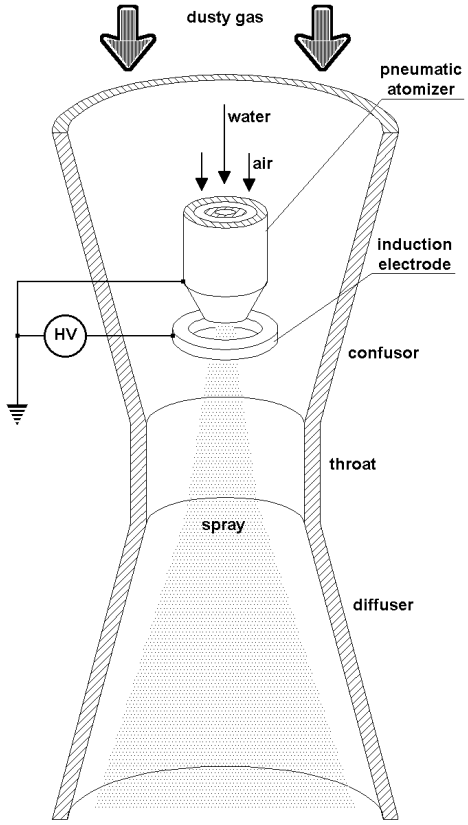

Fig. 3. Venturi type wet electrostatic scrubber.

The spray can remain uncharged [25, 26], or can be charged with one of the following methods:

- Corona charging [27, 28],
- Induction charging [6, 7, 15, 16, 18, 19, 29-32],
- Electrospraying [10, 17, 33-38].

In the process of electrostatic scrubbing the inertial deposition is dominant for large Stokes numbers >5, i.e., high relative velocities of dust particles and collecting droplets. This case take place also for large droplets (>300 μm) and dust particles (>5 μm). Particles smaller than <0.01 μm in diameter can be deposited on the collector due to the Brownian motion [33, 39], whereas the relative velocities are of minor importance in this type of

deposition. In intermediate particle size range, i.e., in the range from 0.1 to 1 μm the electrostatic forces can be effectively used [13, 40, 41]. The electrostatic deposition is the most effective for Stokes number lower than 5, independently of the Reynolds number based on the collector diameter.

The scrubbers utilising electrostatic deposition require lower water rate, and lower pressure drop through the equipment, operating at the same overall collection efficiency as an inertial scrubber. The equipment utilising electrostatic forces operates at lower relative velocities than that in which inertial collection is dominant. The advantages of the electrostatic scrubbers are low power consumption (similar to electrostatic precipitators), water consumption lower than in inertial scrubbers, pressure drop lower than in beg (a few cm H_2O), low sensitivity to physical and chemical properties of particles. The collection efficiency is higher in the submicrometer range.

The main trouble with practical use of the electrostatic scrubbers is the corrosion and electrocorrosion of metal elements, including electrodes [25]. Nowadays, the whole construction of the scrubber can be made of fiberglass reinforced plastic or from carbon fibers which are corrosion resistant. The conductivity of water film on a plastic wall is usually sufficient to serve as a ground electrode. The problem of reduction of energy and water consumption will certainly open new applications for electrostatic scrubbers. Wet scrubbers can be used to flow rates up to about $180*10^3$ Nm^3/h. For higher flow rates they are too expensive due to high power demands [42] and large water consumption.

4. CONCLUSIONS

It can be concluded that wet electrostatic devices combine the advantages of dry electrostatic precipitators and wet scrubbers. The dust control in submicrometer size range is more efficient, and the back-corona discharge inherent to dry electrostatic precipitators does not take place. Additionally they can also absorb various gaseous pollutants. The electrostatic scrubbers utilise electrostatic deposition of dust particles on electrically charged droplets. This type of devices require lower water rate, and lower pressure drop through the equipment than inertial scrubbers, while the overall collection efficiency can be higher. However, wet electrostatic methods cause problems with removal the slurry and electrocorrosion.

It was shown in the paper that current trends in air pollution control technology are aimed at development of new more efficient hybrid systems, i.e., those which utilize two or more physical mechanisms simultaneously for contaminants removal. The collection efficiency of such hybrid systems, to which also electrical forces are employed, can be higher than conventional cleaning devices. In many cases the electrically assisted systems can operate more economically than other devices, especially in removal of submicrometer particles, to which the regulations become more stringent each year.

REFERENCES

[1] Mycock J.C., McKenna J.D., Theodore L., Handbook of Air Pollution Control Engineering and Technology. Lewis Publishers (1995).

[2] Kim H.H., Yamamoto I., Takashima K., Katsura S., Mizuno A., Incinerator flue gas cleaning using wet-type electrostatic precipitator. J. Chem Eng. Japan, 33, No.4, (2000) 669-674.

[3] Pasic H., Membrane based electrostatic precipitation. Filtr.Separ. 38, No.9, (2001) 28-31.

[4] Dexuan X., Zhongyang L., Guojun W., Removal of the aerosol particles formed in PPCP and EBDS by a novel ESP. 7th Int. Conf. Electrostatic Precipitation. 20-25 Sept 1998, Kyongju, Korea, (1998) 224-229.
[5] Bologa A., Paur H.-R., Wäscher T., Electrostatic charging of aerosols as a mechanism of gas cleaning from submicron particles. Filtr. Separ. 38 (2001), No.10, 26-30.
[6] Penney G.W., Electrified liquid spray dust-precipitators. US Patent 2,357,354, Sept 5 (1944).
[7] Bologa A., Use of charged liquid aerosols for increasing of the efficiency of the process of dust precipitation. 6th Int. Conf. Electrostatic Precipitation. 18-21 June 1996, Budapest, (1996) 227-231.
[8] Yang H.T., Viswanathan S., Balachandran W., Ray M.B., Modeling an measurement of electrostatic spray behavior in a rectangular throat of Pease-Aanthony Venturi scrubber. Environ. Sci. Technol., 37, No.11, (2003) 2547-2555.
[9] Kraemer H.F., Johnstone H.F., Collection of Aerosol Particles in Presence of Electrostatic Fields. Ind. Eng. Chem. 47, No 12, (1955) 2426-2434.
[10] Jaworek A., Adamiak K., Krupa A., Particle Trajectories and Collection Efficiency of Submicron Particles on a Charged Spherical Collector. IEEE Ind. Appl. Soc. Annual Meeting, 5-10 Oct. 1996, San Diego, (1996) 2036-2043.
[11] Jaworek A., Krupa A., Adamiak K., Removal of Submicrometer Dust Particles by a Charged Spherical Collector. 6th Int. Conf. Electrostatic Precipitation. 18-21 June 1996, Budapest, 124-129.
[12] Jaworek A., Adamiak K., Krupa A., 3D Model for Trajectories of Airborne Particles near a Charged Spherical Collector. 3rd Int. Conf. Multiphase Flow, June 8-12, 1998, Lyon, Paper No. 438.
[13] Jaworek A., Krupa A., Adamiak K., Submicron Charged Dust Particle Interception by Charged Drops. IEEE Trans. Ind. Appl. 34, No.5, 1998 985-991.
[14] Melcher J.R. Sachar K.S., Warren E.P., Overview of electrostatic devices for control of submicrometer particles. Proc. IEEE 65, No.12, (1977) 1659-1669.
[15] Metzler P., Weib P., Büttner H., Ebert F., Krames J., Use of electrostatic forces to remove dust in a nozzle scrubber. 9th Int. Symp. High Voltage Engineering. Graz, Austria, 28 Aug.-1 Sept. 1995, (1995) 7860-1-4.
[16] Metzler P, Weib P., Büttner H., Ebert F., Electrostatic enhancement of the dust separation in a nozzle scrubber. J. Electrostatics 42, No.1-2, (1997) 123-141.
[17] Krupa A., Jaworek A., Czech T., Lackowski M., Luckner J., Dust particles removal by wet-type electrostatic scrubber. Electrostatics 2003, Inst. Phys. Conf. Series (in print)
[18] Balachandran W., Krupa A., Machowski W., Jaworek A., Smoke precipitation by charged water aerosols. J. Electrostatics 51-52, (2001) 193-199.
[19] Balachandran W., Jaworek A., Krupa A., Kulon J., Lackowski M., A., Efficiency of smoke removal by charged water droplets. J. Electrostatics (in print).
[20] Masuda S., State of art of precharging. 2nd Int. Conf. Electrostatic Precipitators, Kyoto, Nov.1984, (1984) 177-185.
[21] Masuda S., Washizu M., Mizuno A., Akutsu K., Boxer-Charger. A Novel Charging Device for High Resistivity Powders. Conf. Electrostatic Precipitation, Leura, Australia, 21-24 Aug. 1978.
[22] Jaworek A., Krupa A., Airborne Particle Charging by Unipolar Ions in AC Electric Field. J. Electrostatics 23, (1989) 361-370.
[23] Adamiak K., Krupa A., Jaworek A., Unipolar Particle Charging in Alternating Electric Field. Inst. Phys. Conf. Ser. No. 143, Bristol 1995, 275-278.

[24] Lackowski M., Unipolar charging of aerosol particles in alternating electric field. J. Electrostatics 51-52, (2001) 225-231.
[25] Ricci L.J., Electric spark of ionizers hikes scrubber efficiency. Chem. Eng., (1977) 52-58.
[26] Sheppard S.V., Ionizing wet scrubbers control plant emissions. Mech. Eng. 107, No.7, (1985) 72-75.
[27] Xu D., Liu Z., Wu G., Removal of the aerosol particles formed in PPCP and EBDS by a novel ESP. 7th Int. Conf. Electrostatic Precipitation. 20-25 Sept 1998, Kyongju, Korea, 224-229.
[28] Bologa A., Paur H.-R., Wäscher T., Electrostatic charging of aerosols as a mechanism of gas cleaning from submicron particles. Filtr. Separ. 38 (2001), No.10, 26-30.
[29] Pilat M.J., Jaasund S.A., Sparks L.E., Collection of aerosol particles by electrostatic droplet spray scrubbers. Envir. Sci. Techn. 8, No.4, (1974) 360-362.
[30] Pilat M.J., Collection of Aerosol Particles by Electrostatic Droplet Spray Scrubbers. J. Air Poll. Contr. Ass. 25, No.2, (1975) 176-178.
[31] Schmidt M., Löffler F., Investigations of Fine Particle Separation using an Electrostatic Nozzle Scrubber. J. Aerosol Sci. 23, Suppl.1, (1992) 773-777.
[32] Schmidt M., Löffler F., Experimentelle Untersuchungen zur Erzeugung eines elektrostatisch geladenen Sprays. Chem. Ing. Tech. 66, No.4, (1994) 543-546.
[33] Lear C.W., Krieve W.F, Cohen E., Charged Droplet Scrubbing for Fine Particle Control. J. Air Poll. Control Assoc. 25, No.2, (1975) 184-189.
[34] Hara M., Sumiyoshitani S., Akazaki M., Fundamental Processes of Fine Particle Collection by Charged Water Droplets. 2nd Int. Conf. Electrostatic Precipitation, Kyoto, Nov. 1984.
[35] Wang H.C., Stukel J.J., Leong K.H., Charged Particle Collection by an Oppositely-Charged Accelerating Droplet. Aerosol Sci. Techn. 5, No 4, (1985) 409-421.
[36] Wang H.C., Stukel J.J., Leong K.H., Particle Deposition on Spheres by Inertial and Electrostatic Forces. Aerosol Sci. Techn. 5, No 4, (1985) s.391-408.
[37] Jaworek A., Krupa A., Principles of Charged Droplets Scrubbing. Materials Sci. 16, No 1-3, (1990) 33-38.
[38] Jaworek A., Balachandran W., Lackowski M., Kulon J., Krupa A., Multinozzle electrospray system for gas cleaning processes. J. Electrostatics (submitted).
[39] Shahub A.M., Williams M.M.R., Brownian collision efficiency. J. Phys. D: Appl. Phys. 21, No 2, (1988) 231-236.
[40] Schmidt M., Löffler F., Calculation of Particle Deposition on Charged Droplets. 2nd European Symp. on Separation of Particles from Gases. 24-26 March 1992, Nürnberg, Germany.
[41] Adamiak K., Jaworek A., Krupa A., (2001) Deposition efficiency of dust particles on a single, falling and charged water droplet. IEEE Trans. Ind. Appl. 37, No.3, (2001) 734-750.
[42] Parker K.R., Effective capture of respirable-sized particulates using electrostatic precipitator technology. Eng. Sci. Educ. J. 9, No.1, (2000) 33-40.

4th International Conference **ELMECO**
Nałęczów, Poland
September 2003

THE APPLICATION OF SOLAR ENERGY IN THE CONDITIONS OF LUBLIN REGION

Tadeusz JANOWSKI, Krzysztof NALEWAJ,
Henryka D. STRYCZEWSKA, Zbigniew ZŁONKIEWICZ

Institute of Electrical Engineering and Electrotechnologies,
Lublin University of Technology,
38A Nadbystrzycka St., 20-618 Lublin

Abstract

In the paper, the possibilities of using solar energy in Poland mostly in the region of Lublin have been discussed. Results of the research carried out in the laboratory of solar energy at the Institute of Electrical Engineering and Electrotechnologies, Faculty of Electrical Engineering and Computer Science, Lublin University of Technology.

Keywords: solar energy, photovoltaic array.

1. INTRODUCTION

The Sun has been the source of energy for all physical chemical and biological processes on the Earth and in the atmosphere. The amount of solar energy that reach within 1 second the surface of 1 m², perpendicular to sun rays and located just behind the atmosphere in the average distance between the Earth and the Sun is called solar constant. It's value was determined as 1,4 kW/m². Solar constant depends on the distance between the Sun and the Earth, which changes within a year of ± 3,4%. At known value of solar constant it is possible to calculate the amount of energy that reach the surface of the Earth at different latitudes. In case of Poland, potential annual sums of solar energy differ between 8,4 and 9,25 GJ/m².

However, the amount of solar radiation used through the application of special systems for accumulation of energy is considerably lower. This is caused by the losses of the energy resulting from dispersion, absorption and losses in the converting system.

The scientific research that have already been carried out at the Institute of Electrical Engineering and Electrotechnologies for several years are aimed to evaluate the possibilities of solar systems' applications in the region of the Lublin Province. The test stand has been situated in so-called helio-power part of the country – Podlasko-Lubelskie region, that has been regarded as the second region in respect of the demand for solar

energy [4, 10]. Conducted research allow practically check the availability of solar energy in Lublin.

2. EVALUATION OF SOLAR RADIATION IN POLAND

Poland is situated in the moderate climatic zone between 49° and 54,5° of the northern latitude. In winter, day is longer in southern regions of Poland of almost 1 hour compared to the northern regions whereas it is quite opposite in summer. The insolation depends on the day length, cloud cover and atmosphere transparency. The longest continuous period of solar radiation during the day is 7,2 h in winter (about 30% of twenty-four hours) up to 15,5 h in summer (65% of twenty-four hours). In 1992 over 2000 hours of insolation was notified in Hel, Poland. The highest intensity of solar radiation was noticed on the mountain top Kasprowy Wierch (about 1200 W/m²) [4].

The most favourable solar conditions are at the seaside region, where since September, the highest sums of total radiation and the highest number of insolation hours have been observed. Podlasko-Lubelskie is also the region of great importance due to frequent flow of dry air from the Ukraine. The least favourable solar conditions are observed in the regions of Podgórze, Suwałki, Warsaw and Silesia.

3. SOLAR ENERGY SYSTEMS

Low amount of solar energy (>1%) is actively used (mostly in the process of photosynthesis and wind energy). The rest i.e. 99% of energy, has not been used because of the Sun incidence on the lands.

Solar energy can be used through thermal or photovoltaic conversion. Thermal conversion can be carried out in passive or active way. The application of passive ways for heating the building requires efficient designing of material components including windows and buffer space made of glass.

SOLAR COLLECTORS

Solar collector is the device that converts solar energy into heat in an active way. In the climatic conditions of Poland, plane collectors absorbing both direct and diffusive radiation have been applied. Such collectors can be divided into liquid ones in which liquid is the operating medium (usually water or non-freezing liquid) and dry collectors, in which the medium is gas, mostly air.

Solar collectors are mainly used to heat up warm water. Cost-effectiveness of the solar collectors applied for the above purpose depends on the demand for warm water and price of energy. In case of high demand for warm water, the installation costs of the solar collectors are refunded within a short period. Such investment is particularly profitable for the hotels, lodging-houses, recreation centres, swimming pools and sport centres used in summer.

It is also possible to use solar collectors to heat the houses. However, the usage of solar collectors for heating purposes is rather expensive investment. The usage of solar collectors enables to obtain 450 up to 600 kWh/m², in the conditions of Poland, that is enough to heat 4 to 6 m² of well-insulated building. Therefore, the application of solar energy for central heating needs significant surface of the collectors. The heating of 100 m² house would require the application of the collector of 50 m² surface.

Aerial solar collectors are mostly used in Poland to dry up agricultural crops. In drying processes relatively low increase of temperature is required: 5 – 15 K and high intensity of air flow: about 150-250 m^3/h for 1 m^2 of the collector's surface. In such conditions collectors gain high efficiency – about 50 % [5,7].

PV SYSTEMS

The devices, in which energy has been directly changed into electric energy are called solar cells. Photovoltaic panels are nowadays the devices of greatest importance. Photovoltaic system consists of the set of devices that convert solar energy into electric energy.

First simple installations emerged in the last decade of XIX century. Typical installation apart from the panels consists of the accumulators batteries for energy storage, voltage converters as well as the elements controlling accumulators' charge and the inclination angle of the panels. Such panels may have various dimensions and power, thus they are commonly applied in radio receivers, torches, small feeders, pumps and other devices.

A world-wide interest in photovoltaic systems has been noticed due to the fact that they convert sunrays directly into electric energy without producing impurities, noise and other factors harmful for the environment. Rapid development of photovoltaic technology was deeply connected with its application in space technologies as highly reliable source of energy. However, photovoltaic systems were too expensive for common usage. Increased price of energy resulting from the petroleum crisis in mid 1970s caused its profitability. Since that time, he cost of photovoltaic systems has been dropping down and more new installations have emerged.

The connection of solar collectors with photovoltaic ones into one system is the solution of great interest because most buildings require both heat and electric energy. In this case, the absorption surface of the collectors consists of solar panels that convert part of the radiation into electric energy, the remaining radiation - about 50%, has been converted into consumable heat. Although such connection results in lower efficiency of photovoltaic collectors however, this sort of installations allow for the usage of up to 60% of solar radiation and are more effective because joint surface for heat and photovoltaic collectors is used. The price of the solar panel converted into 1 W of the obtained power is the decisive factor, that respects the application of solar panels for electric energy generation. According to American investigations, the cost of photoelectric energy generation is 10 times higher than nuclear energy. However, it should be taken into consideration that solar panels become cheaper, the costs of energy generated in nuclear power plants increase.

4. LABORATORY TESTS OF SOLAR SYSTEMS

The scientific research that have already been carried out at the Institute of Electrical Engineering and Electrotechnologies, Lublin University of Technology for several years are aimed to evaluate the possibilities of using solar energy. In order to use solar energy, integrated heating system has been designed: solar collector – heat pump – photovoltaic panel [8]. Photovoltaic system that consists of 6 batteries of 450W and accumulator set is to supply the heat pump in the period of high insolation. In the period of insufficient intensity of solar radiation, the pump will be supplied from the power network.

Test stand comprising six photovoltaic panels BPS 275 of maximal power 75W each was the first element that emerged in the designed laboratory. The panels have been placed

on the roof construction on the four-storey building in which the Faculty of Electrical Engineering and Computer Science is located.

At the turn of 1999 from November to March solar battery has been tested, the measurements of insolation intensity and power generated were taken. During the whole examined period, power values obtained were significantly lower that the catalogue maximal power of single module that amounts 75W. Average power in the whole tested period was 28,75 W [9]. The measurements were also taken in spring and summer. Insolation measurements were taken between 1-3 June 2002. Solar battery was set up at the angle of 30º (the whole year). Average insolation results have been presented in the chart (Fig. 1).

The insolation in June reached its maximal value of 1100 W/m^2 at 1 p.m.

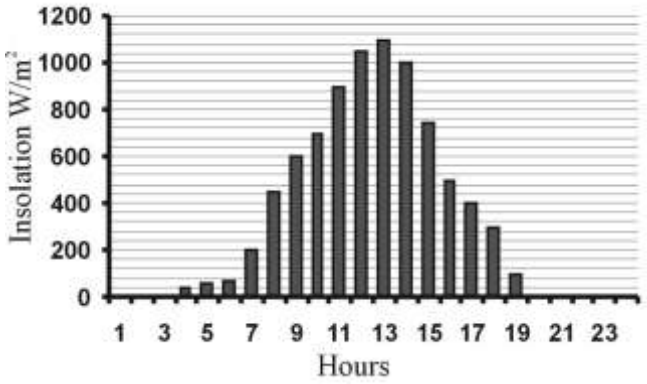

Fig. 1. The chart (day and night) insolation in Lublin between 1-3 June 2002

The results obtained are still insufficient to evaluate real available solar potential of the Lublin Province. Thus, additional measurements taken during longer period are still required.

5. CONCLUSION

In Poland the usage of solar energy has still been insufficient. Most often, the aerial collectors are applied to dry up agricultural crops. The usage of solar energy in the Lublin Province creates real possibilities of lower consumption of conventional fuel. However, the results of the investigations on the solar battery revealed, that the application of the photovoltaic system for heating purposes is possible only after prior energy storage or in the integrated system with other energy sources.

REFERENCES

[1] Jarzębski Z. : Energia słoneczna: konwersja fotowoltaiczna, PWN, Warszawa 1990.
[2] Smoliński S. : Fotowoltaiczne źródła energii i ich zastosowanie, SGGW, Warszawa 1998.

[3] Żdanowicz, Słaby M. : Tania Technologia wytwarzania krzemowych ogniw i modułów fotowoltaicznych – algorytm projektowania i możliwości instalacji systemów fotowoltaicznych w Polsce, Instytut Technologii Elektronowej Politechniki Wrocławskiej, Wrocław 1994.
[4] Gogół W. : Konwersja termiczna energii promieniowania słonecznego w warunkach krajowych- Ekspertyza - PAN Warszawa 1993.
[5] Pabis J., Chochowski A., Wiśsniewski G. : Opracowanie cząstkowe – Konwersja termiczna energii promieniowania słonecznego w produkcji rolniczej. SGGW IBMER, Warszawa 1993.
[6] Chwediuk D. : Opracowanie cząstkowe – Słoneczne aktywne systemy ogrzewania pomieszczeń. IPPT PAN, Warszawa 1993.
[7] Wnuk R. : Słoneczne instalacje do podgrzewania ciepłej wody użytkowej. IPPT PAN, Warszawa 1994.
[8] Bodziak K., Nalewaj K., D. Wójcicka-Migasiuk D. Stanowisko do badań zintegrowanych systemów grzewczych z wykorzystaniem energii promieniowania słonecznego. Rynek Energii, nr 3, 1996, s.14-17.
[9] Janowski T., Nalewaj K, Wójcicka-Migasiuk D., Złonkiewicz Z: Laboratory of Heating System Employing Solar Energy. Electromagnetic Devices and Processes in Environment Protection ELMECO, Nałęczów 12-15 czerwca 1997, s. 269-272
[10] Nalewaj K., D. Wójcicka-Migasiuk, Z. Złonkiewicz. Działanie stanowiska z baterią ogniw fotowoltaicznych w klimacie zimowym regionu Środkowowschodniego, Inżynieria Rolnicza nr 1 s. 2001, 219-225.
[11] Nalewaj K. Wójcicka-Migasiuk D., Złonkiewicz Z.: "Heat Pump System Supply in the Aspect of Application to Solar Laboratory" Electromagnetic Devices and Processes in Environment Protection ELMECO, Nałęczów, 04 - 06 czerwca 2000, pp. 138-143.
[12] Nalewaj K., Złonkiewicz Z.: “Wykorzystanie energii promieniowania słonecznego w warunkach województwa lubelskiego”. Rynek Energii nr 1 (38) 2002 s. 28-32.
[13] Internet: http://www.pv.pl
[14] Internet: http://www.netmark.waw.pl/Ofirmie/Badania/Konf990326/ konferencja990326RefPodegrocki.htm
[15] Internet: http://friko6.onet.pl/kn/bkelektr/enernatu.htm
[16] Internet: http://www.eren.doe.gov/millionroofs/whatispv. html

4th International Conference **ELMECO**
Nałęczów, Poland
September 2003

TECHNOLOGY OF SUPERCONDUCTING MAGNETIC SEPARATION IN ENVIRONMENTAL PROCESSING

Antoni CIEŚLA

AGH- University of Science and Technology, 30 –059 Kraków, al. Mickiewicza 30,
e-mail: aciesla@uci.agh.edu.pl

1. INTRODUCTION

The conventional magnetic separators used in the mineral industry are equipped with traditional magnetic circuits or with permanent magnets (rare earth). However, when processing minerals with low magnetic susceptibilities or minerals of very small particle size, these separators are inefficient. In addition, a conventional magnetic circuit consumes considerable amounts of electricity to generate a relatively low magnetic field (~2 Tesla). The equipment is also heavy and bulky. Only a separator having a superconducting solenoid can contribute in solving most of the problems, and only such a separator can produce high magnetic fields with low energy consumption.

It is clear that in large-scale high gradient magnetic separators, low-temperature superconducting (LTS) technology is displacing conventional water-cooled copper magnets. With the recent discovery of high-temperature superconductivity (HTS), it remains to be seen if these new ceramic-oxide superconductors will replace the traditional intermetallic low-temperature superconductors.

2. PRINCIPLES OF THE MAGNETIC SEPARATION

When fine particles are dispersed in air, water, sea water, oil, organic solvents, etc., their separation or filtration by using a magnetic force is called magnetic separation.

To understand the principles of magnetic separation for this, let us consider the magnetic forces [1]. By calculating the gradient of magneto-static energy difference between magnetized particles of volume, V_p and the dispersion medium of the same volume, ΔU_p , the magnetic force acting on a particle, $\vec{F}_m$, is:

$$\vec{F}_m = -\nabla\left(\Delta U_p\right) = -\nabla\left\{\frac{V_p\left(\mu_0 \vec{M}_p \cdot \vec{H}\right)}{2} - \frac{V_p\left(\mu_0 \vec{M}_f \cdot \vec{H}\right)}{2}\right\} \tag{1}$$

where:

$\vec{M}_p$ - particle magnetization, [A · m^{-1}]; $\vec{M}_f$ - magnetization of dispersion medium, [A · m^{-1}]; $\vec{H}$ - magnetic field. [A · m^{-1}].

By assuming a spherical particle with volume magnetic susceptibility, χ_p , and uniform magnetization $\vec{M}_p$, we obtain:

$$F_{m\xi} = V_p \cdot \mu_0 \cdot M^* \cdot \nabla_\xi H, \qquad \xi = x,y,z, \tag{2}$$

where:

$$M^* = H_0 \frac{9(\chi_p - \chi_f)}{(3+\chi_p)(3+\chi_f)} \tag{3}$$

χ_f - volume magnetic susceptibility of the dispersion medium, [-]; M^* - relative magnetization between the dispersoid and the dispersion medium, [A ·m^{-1}];

H_0 - applied magnetic field, [A ·m^{-1}].

Equation (2) indicates that the magnetic force on particles depends on three key parameters: V_p , M^*, and $\nabla_\xi H$. For $F_{m\xi} \neq 0$, V_p , M^*, and $\nabla_\xi H$ are all non-zero. Therefore, Eqs. (2) and (3) indicate that to generate a magnetic force ($F_{m\xi} \neq 0$), a dispersoid with susceptibility different from that of the dispersion medium (i.e., $\chi_p \neq \chi_f$) must be placed in nonhomogeneous magnetic field (i.e., $\nabla_\xi H \neq 0$).

When the dispersed particle is weakly magnetized, $M^* = (\chi_p - \chi_f)H_0$, and $F_{m\xi}$ is proportional to the susceptibility difference between the dispersoid and the dispersion medium; to H_0 ; and to $\nabla_\xi H$. When the dispersoid is a ferromagnetic particle, M_p becomes saturated at a relatively low magnetic field strength. The enhancement of $F_{m\xi}$ through the use of strong magnetic field is therefore limited. M_p also becomes saturated at relatively small susceptibilities of $\chi_p \sim 10$ because M_p is proportional to $\chi_p/(1+N\chi_p)$, where N is a demagnetizing factor [1].

Effective ways of enhancing the magnetic force include: (a) increasing M_p by "magnetic seeding" of the dispersoid, (b) increasing $\nabla_\xi H$, (c) using high intensity magnetic fields, and (d) selecting a dispersion medium with a large value of $(\chi_p - \chi_f)$.

Various devices have been used to generate strong magnetic forces, which are described in detail elsewhere [1]. Methods for increasing the magnetic field gradient include superconducting coils in a drum-type separator, multi-pole superconducting coil in separators or HGMS systems. In High Gradient Magnetic Separators, a field gradient $|(\nabla H)|$, as high as $1.6 \cdot 10^{10}$ A/m^2 ($|\nabla(\mu_0 H)|$ = 20,000 T/m) is reached, and the magnetic force is enhanced by a factor of 1000 – 10,000 [1].

Before the development of HGMS, magnetic separation was only performed on large diameter ferromagnetic particles, while using HGMS, weakly magnetized particles down to

tens of microns can be magnetically separated in practical systems. High-gradient magnetic fields are generated near a ferromagnetic wire with several hundred microns in diameter placed under an applied uniform magnetic field. If the magnetic field is strong enough, in principle, all the particles with either positive or negative magnetic susceptibility dispersed in the medium are captured onto the wire. Weakly magnetized particles and typical dispersion media have magnetic susceptibilities much smaller than 1. Substituting this condition into Eq. (3) yields $M^* = (\chi_p - \chi_f)H_0$ and $F_m \propto (\chi_p - \chi_f)H_0(\nabla H)$ (Eq. (2)). Thus, use of high intensity, high gradient magnetic fields is necessary to increase the magnetic force on magnetic particles. In conventional magnetic separators this force is less than 0.01 % of the magnetic force acting on ferromagnetic particles, and is usually disregarded. However, because the magnetic field gradient of HGMS systems is much higher than that used in conventional magnetic separators, separation of weakly magnetized particle is now possible.

3. SUPERCONDUCTING TECHNOLOGY FOR MAGNETIC SEPARATION

The early high-intensity magnetic separators (HIMS) used in the mineral industry were resistive electromagnets using either cooled copper coils or new ceramic permanent magnets (rare earth). About twenty years ago, superconducting magnets made their first entry into these applications, and, since that time, their number and popularity has steadily increased.

To have an industrial potential, a superconducting separator must meet the following requirements [2]:

- all cryogenic constraints on its operation (helium supplies, maintenance calling for specially trained technical staff, etc.) must be eliminated; and
- the operating costs must be low.

In other words, it is essential that a superconducting separator be a self-contained system, that it require minimum maintenance and that it be reliable.

Superconducting magnets have their own characteristic features that can be summarized as follows [2]:

- The superconducting coil needs to be cooled to temperatures below the superconducting transition for operation. In today's magnets, this is achieved with liquid helium refrigerant.
- Superconductors have essentially zero electrical resistance, which means that minimal electrical power is required for magnet energization. This also enables substantially lighter and smaller coil windings to be used compared with resistive magnets.
- Superconducting magnets can be operated in continuous mode. This useful feature takes advantage of the zero resistance of the coil, so that, after it has been energized, the coil ends can be shorted with a superconducting junction. The power supply can now be disconnected, leaving the magnet in a fully energized state.
- Superconducting magnets do not need to rely on massive iron frames for field concentration. This means that the whole magnet system can be made much lighter and smaller than resistive units.
- Substantially higher magnetic fields (compared to resistive systems) are possible with superconducting coils. This, in turn, results in higher magnetic forces being

generated within the matrix canister, which can be used to provide a higher brightness product or higher throughputs.

The preceding summary provides insight into the potential advantages offered by superconducting technology for magnetic separation. The extent to which these features are actually exploited depends very much on the overall design of the separator. In particular, it is important to note whether the cryogenic system is operated in a switched or in a continuous mode.

The technique of magnetic separation with superconducting magnets enables the extraction from a solid/water suspension of superfine (even colloidal) particles that are only weakly magnetic. It finds its application in the mineral industry for the purification of industrial minerals, in particular kaolin and tale. It is also of interest for other fields such as chemistry, biology and, especially, the environment. The application of this technique has enabled the extension of magnetic separation to ores that cannot be economically upgraded by any other means as well as to completely different fields of activity. It has, in particular, led to pushing back the frontiers of standard separation methods.

Today's fields of application of HGMS with superconducting or copper coil magnets cover or could cover [2]:

- the cleaning of products for the glass or ceramics industry, which require a high degree of purity in kaolin or glass sand;
- the cleaning of industrial and urban wastewater and cooling water from thermal or nuclear power plants;
- the extraction of contained particles for chemical-synthesis processes and from energy-transmission flu-ids or vapors used in electrical-power plants;
- the concentration of ultrafine minerals, such as Fe, Mo, W or rare earth minerals, or metallic residues for recycling;
- the processing of used catalysts; and
- the fields of biochemistry, biology and the food-processing industry.

The discussion presented above reveals that the HGMS separators have numerous applications. Thus, that type of the separators will be the subject of the following considerations.

There are 2 versions of matrix magnetic separators – based on the way of matrix cleaning. In the first one, proposed by ERIEZ Magnetics, accumulation ability renewal (cleaning) of the matrix takes place when the magnetic fields is turned off. Proper position of feed check valves allows to get considerable pressure of cleaning water that rinses out magnetic particles from the steel wool fibres. After the matrix cleaning, reset of the valves begins next cycle of the separation. Another type of the superconducting magnetic separator is a “ reciprocating” device constructed and patented by CARPCO SMS Ltd. This construction is preferred for technical and economical reasons. A construction of this types devices on industrial scale were presented in [3].

The use and operation of superconducting electromagnets as a source magnetic field in magnetic separators and filters is much more complicated than with conventional ones owing to the existence of strong magnetic fields, high energies accumulated in windings, low temperatures and a vacuum present. Superconductor electromagnets should be equipped with installations that comply with requirements and rules of cryogenic and vacuum technologies; also, they must respect characteristic conditions necessary for an electromagnet to operate, such as: cryostat and winding cooling, feeding of the winding, normal operation conditions, and emergency states during the operation.

The operation cycle of the superconducting separator consists of four following in succession phases: 1 - cooling of the cryostat, 2 - supplying with electrical power, 3 - stable work under rated current (separation cycle), 4 - switching off the supply and heating of the cryostat.

Some exemplary curves $T = f(t)$ and $B = f(t)$ for the operation cycle of the separator are presented in Fig. 1. The temperature change during cooling of the cryostat is presented (as magnified characteristic). The noticeable increase of temperature results from exchange of the vessel for liquid helium.

In the separation cycle (from Fig. 1), after the matrix is loaded with captured particles (after effective time t_e), a cleaning stage must follow (dead time t_d). In order to increase the effectiveness - the time t_e must be increased and t_d reduced. Cleaning of the matrix takes place in absence of magnetic field. The field on the matrix can be removed by three methods: by ramping the current in the magnet down, by using a continuously moving matrix, e.g. carousel, and by using a reciprocating canister. Principle diagram of separation cycles in matrix high gradient magnetic separator is presented in Fig. 2.

4. LABORATORY SUPERCONDUCTING SEPARATOR IN AGH – UST

A scheme of a laboratory superconductor magnetic separator at disposal of AGH - University of Science and Technology is presented in Fig. 3. Construction of superconductor magnet for the HGMS is presented in Fig. 4.

The technical data: $B_{max} = 6$ T (in the center of the separator canal), volume of the matrix: $1{,}5 \cdot 10^{-3}$ m^3, diameter of the magnet canal: $5.4 \cdot 10^{-2}$ m.

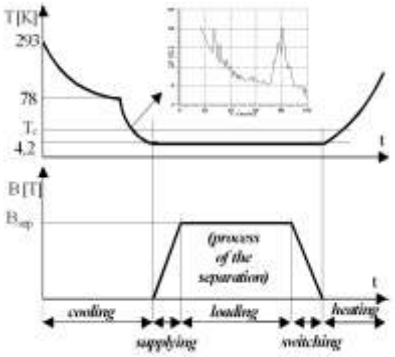

Fig. 1. Operation cycle of superconductor separator.

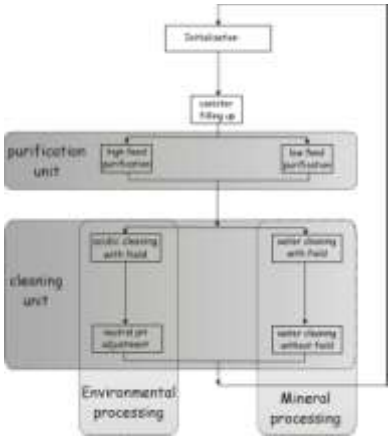

Fig. 2. Principle diagram of separation cycles.

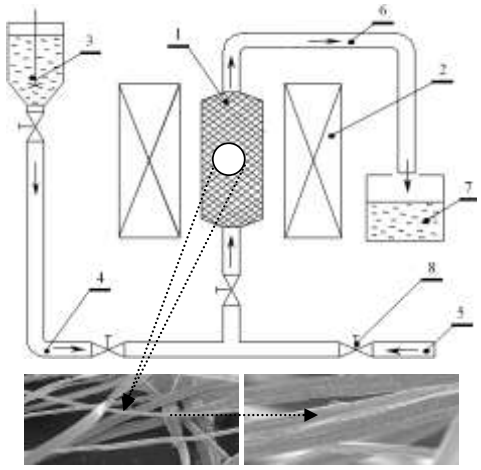

Fig. 3. Superconductor separator for HGMS and filling of the matrix with stainless steel magnetic wool (the wool seen with a magnifier):
1 – matrix of the separator, 2 – winding of the superconductor magnet, 3 - container for the feed to be separated, 4 – stream of the feed, 5 – stream of rinse water, 6 – stream of the separation product, 7 – container for the separation product, 8 – valve.

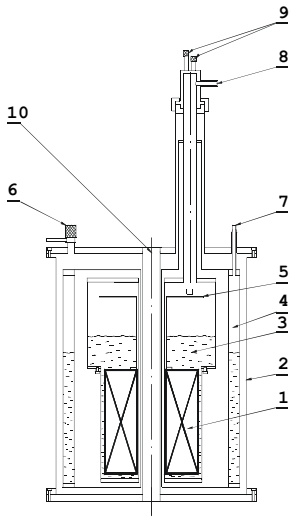

Fig. 4. Superconductor magnet for HGMS:
1 - winding of the superconductor magnet, 2 – cryostat, 3 – liquid helium, 4 – liquid nitrogen vessel, 5 – terminal plate, 6 – vacuum valve, 7- filler for liquid helium, 8 – outlet for gas helium, 9 – outlet ferrules for liquid helium, 10 – canal of the magnet.

Possibility of extraction of dispersed and trace components from two mineral wastes was examined in separator presented in Figure 3. Phoshogypsum obtained during production of phosphoric acid as well as cooper flotation tailing were subjects of investigations. Preliminary results of investigation on phoshogypsum show that magnetic separation in the applied conditions provide a concentrate with recoveries: about 15 % of REE, 99 % of V, 40 % Ta, 80 % Sn. Over 30 % of Cu, 26 % of Ag, 26 % of As, 20 % of Pb, and over 70 % of Au was separated from cooper flotation tailings [4].

5. APPLICATION OF HIGH-TEMPERATURE SUPERCONDUCTORS TO MAGNETIC SEPARATION

The discovery, in 1986, of high-temperature superconductivity by Bednorz and Müller in La-Ba-Cu-O stimulated an enormous amount of research throughout the world into these and related compounds. The discovery of the Y-Ba-Cu-O (YBC) compounds with superconducting transition temperatures as high as 92 K created in a very real possibility of practical devices operaring in liquid nitrogen at 77 K which implies that the capital and running costs associated with the production and maintenance of the necessary conditions to operate these devices is considerably reduced, perhaps by as much as a faktor 10 [5]. The further discoveries of the Bi(Pb)-Ca-Cu-O (BSCCO) materials and the Tl-Ba-

Ca-Cu-O (TBCCO) materials with values of T_c reaching 125 K made he possibility of the operation of large scale superconducting devices at liquid nitrogen temperatures even more attractive because of their lower values of reduced temperature T/T_c .

Designs for superconducting magnetic separators with high -T_c materials

a) A superconducting reciprocation canister separator with a superconducting wire-wound coil.

This method involves replacing the low- T_c coil shown in Figure 3 by a high- T_c coil. This approach has the advantage that the cryogenics are greatly simplified when the operating temperature is 77 K and the capital and running costs of the refrigeration system are greatly reduced. The system, when possible, runs in the persistent mode.

However, such an approach must wait for the development of long lengths of high- T_c superconducting wire with the current-carrying capacity approaching that of present-day low- T_c superconductors at high field before this approach is viable. It is unlikely that the capital cost of the separator magnet will be reduced much below that of the equivalent low-T_c separators. However, the advantage of this approach is that the design is based on a operational low - T_c system which has proved reliable in industrial applications [5]. Figure 5 shows the incorporation of a HTS magnet into a HGMS with a closed cycle cryocooler system [6].

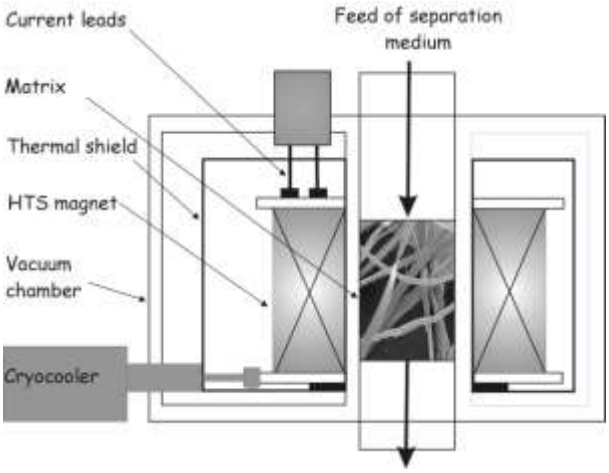

Fig. 5. HTS magnet operation scheme for HGMS [6].

b) The construction of a superconducting separator with an iron return circuit.

The magnet is an iron electromagnet with superconducting windings. Magnetic separators with iron return circuits have been employed in the minerals industry for many years. Because of diminishing resources and loss af grade in older mines, it is interesting to look at an application of superconductors where the coil provides extra ampere-turns which would be extremaly expensive for cooper coils if the magnetic circuit were close to

saturation. It might be interesting to remove the coils from older machines and replace them with superconducting coils and run them much more cheaply and much closer to saturation.

It is proposed that the high-T_c superconducting coil shold be mounted on the iron return-circuit as shown in Figure 6. Usually in this type of system there are two coils, but here it is proposed to use one coil as it is much more convenient to construct one liquid nitrogen container rather than two. The coil is placed further away from the gap yhan is normal because high-T_c superconductors are still quite magnetic field sensitive, and it is better to keep the coil away from the stray field from the gap. The canister containing the ferromagnetic stainless steel matrix is placed in the gap.

For the magnetic circuit we have that

$$\mu_0 N_c I_c = B_A A_A \left(d_A / \mu_A A_A + d_{RC} / \mu_{RC} A_A \right) \tag{4}$$

where:

$N_C I_C$ is the ampere turns provided by the superconducting coil, B_A is the flux density in the separation canister with area A_A and length d_A. μ_A is the relative permeability of the contents of the canister and d_{RC} is the length of the rest of the magnetic circuit with permeability μ_{RC}.

If a separation canister is filled with ferromagnetic spheres as a matrix with the same magnetic properties as the iron return circuit, then a randomly packed spheres occupy 66% of the space, and we can write: $\mu_A = 0.66 \mu_{RC}$.

For dimensions of the iron return circuit presented in [5], equation (4) we can write:

$$\mu_0 H_c = (0.5445) B_A / \mu_{RC} / L_C \tag{5}$$

In what follows it is assumed that the stainless steel wire has the same magnetic properties as the material magnetic circuit. Therefore, as the filling factor of the wire in canister is 5%, we have: $\mu_A = 0.05 \mu_{RC}$. In this case, for dimensions of the magnetic circuit as above, eq.(4) we can write as:

$$\mu_0 H_c = (1.1) B_A / \mu_{RC} / L_C \tag{6}$$

Now we can design magnetic separator in relation to the magnetic properties of the iron return circuit and the available high-T_c superconductors operating at 77 K for both considered types of the matrix (a ball matrix and wire matrix) as shown in [4].

The lay-out of the superconducting high-T_c coil, magnetic circuit and Dewar is shown in Figure 7.

6. CONCLUSIONS

The high force separation capabilities of superconducting magnets and their application for the most difficult separation problems of paramagnetic or low susceptibility materials are now recognised. The advances made in superconducting technology over the recent years have meant that this technology, at one time limited to the research, can now truly enter the industrial processing environment with confidence.

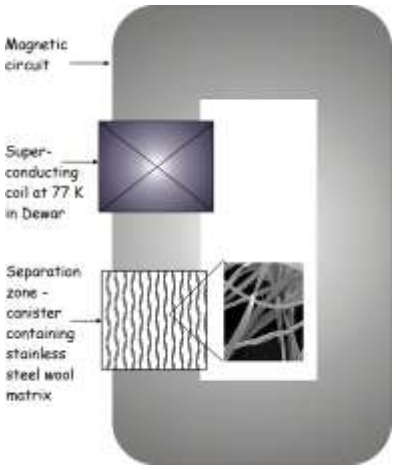

Fig. 6. Preferred orientation of the magnet for magneticc separation. The canister is positioned in the gap between the pole pieces

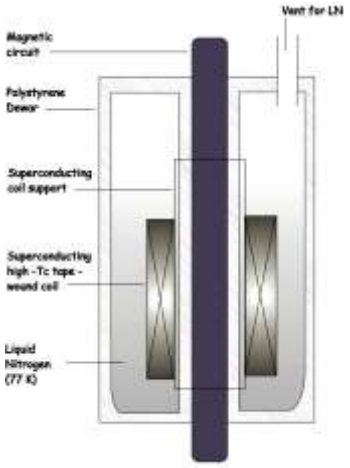

Fig. 7. Proposed design of the high-T_c magnet and Dewar

To promote new applications for superconductor magnetic separation, the fusion of science and technology from diverse areas is required. It can be executed through the interchange and co-operation of researches working in different fields: including superconductivity, electrical engineering, and mechanical engineering for equipment improvement, chemical engineering and applied chemistry for separation system and environmental, sanitation, and resource engineering for practical utilization of these systems. Organizations that promote the exchange of research information from different technical fields and collaboration are very desirable.

Two configurations for the separator were considered, a ball matrix separator and a wire matrix high gradient separator. Practical separations will be possible with such a system. It should be noted that this design is not ultimately the best for high-T_c magnetic separator but it is imposed by the inadequacies of present–day high-T_c materials. It is hoped that this situation will change in the near future.

REFERENCES

[1] Ohara T. et al.: Magnetic separation using superconducting magnets, Physica C 357 – 360 (2001), 1272 – 1280.

[2] Gillet G., Diot F.: Technology of superconducting magnetic separation in mineral and environmental processing, Minerals & Metallurgical Processing, Vol. 16, No 3, August 1999, pp. 1 – 7.

[3] Cieśla A.: Superconductor Magnetic Filter: Industrial Construction, Proc. Third Intetnational Conference Electromagnetic Devices and Processes in Environment Protection ELMECO2000, Nałęczów, 4 – 6 June 2000, pp.174 – 182.

[4] Cieśla A., Łuszczkiewicz A.: Preliminary extraction tests of dispersed and trace components from some mineral wastes using matrix superconducting magnetic separator, (in Polish), Inżynieria Mineralna, Nr S.3 (10), wrzesień 2003 (zeszyt specjalny), pp. 41 – 48.
[5] Watson J. H. P.: The design for a high T_c superconducting magnetic separator, Supercond. Sci. Technol. 5 (1992), pp. 694 – 702.
[6] Jin J. X., Liu H. K., Zeng R., Dou S. X.: Developing a HTS magnet for high gradient magnetic separation techniques, Physica C 341 – 348 (2000), 2611 – 2612.

ACKNOWLEDGEMENTS

The work presented in this paper was supported by the Polish State Committee for Scientific Research, Warsaw, in the frame of project Internal Research ("Badania własne"), Kraków, 2003.

4th International Conference **ELMECO**
Nałęczów, Poland
September 2003

Diagnostics of non - standard plasma sources burning at atmospheric pressure

Jan JANCA, Pavel SLAVICEK, Antonin BRABLEC, Vratislav KAPICKA, Vilma BURSIKOVA, Milos KLIMA

Dep. of Physical Electronics, Masaryk University
Kotlarska 2, 611 37 Brno, Czech Republic
e-mail: ps94@sci.muni.cz, jan92@sci.muni.cz

Abstract

It is well known that high frequency (HF) discharges can burn even at atmospheric pressure. Special properties of HF discharges offer many hopeful technological applications like plasma sources in spectroscopy, deposition of thin solid films, cleaning and treatment of surfaces, restoration of archaeological artefacts and many others [1]. It was also demonstrated that the discharges could burn under the liquid level. Next, they can interact with the material and then new chemical compounds can arise. Therefore, the detailed knowledge of their physical parameters has been required. Special modifications of these discharges have also been investigated at Masaryk University [2]. The parameters of the plasma discharge channel have been studied by different spectral and optical methods. Some typical properties of the discharge have been already reported before [3,4].

In this contribution we present the measurement of fundamental plasma parameters estimated from spectral lines emitted by two basic modifications of the HF discharges: the barrier torch discharge (HF BTD) and the torch discharge (HF TD) burning at atmospheric pressure.

INTRODUCTION

Different systems with nozzle and powered by HF generator have been investigated during several last years. Many systems working at reduced or atmospheric pressure, in subsonic or supersonic regime, were realized and studied (see [5,6]} and references herein).

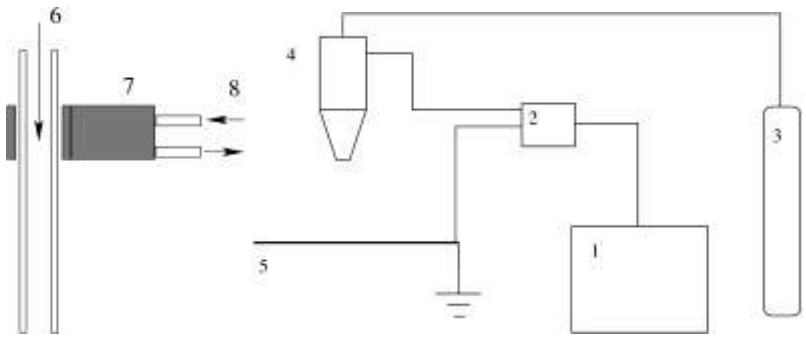

Fig. 1. The sketch of the simplest design of the nozzle for barrier torch discharge (BTD) with the nozzle coated by dielectrics is shown (left). The working gas (argon) enters into the nozzle. Schematic block is drawing of the torch discharge (TD) with the metal nozzle and experimental set-up (right). 1 - HF generator, 2 - matching unit, 3 - working gas reservoir, 4 - plasma nozzle, 5 - grounded electrode, 6 - inlet of working gas, 7 - powered electrode, 8 - cooling water.

It was concluded that the large variety of experimental conditions and possible modifications of arrangements allow driving both corona and torch arc discharge and the systems working in transition regimes. Of course, other dielectric barrier discharges burning in diverse configurations exist, e.g. described in [7].

The advantage of HF plasma discharges consists in the fact that the torch discharge remains stable up to the atmospheric pressure for surface coating, spectral analysis, treatment of archaeological glass artefacts, plasma polymerisation in liquids, etc. The device for hand employ investigated at Masaryk University has been also called plasma pencil.

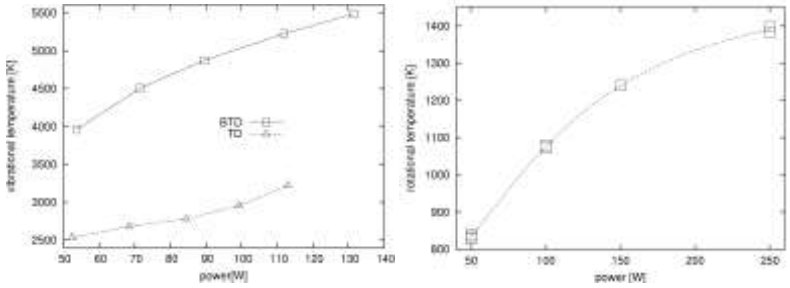

Fig. 2. Vibrational temperature estimated from nitrogen band as a function of input power for the BTD and the TD discharge (left) and rotational temperature estimated from OH lines as a function of power for the TD.

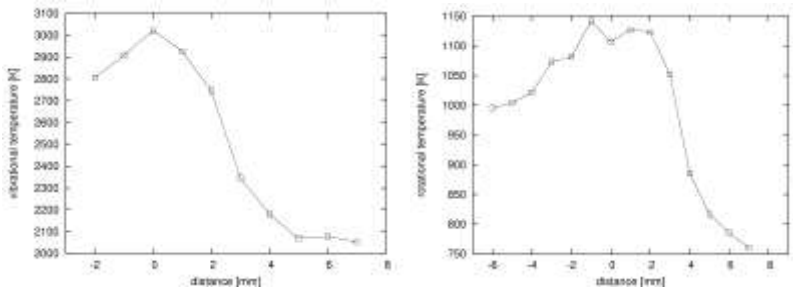

Fig. 3. Vibrational temperature estimated from the second positive system of nitrogen vs. the distance from the end of nozzle for the BTD (left). Rotational temperature calculated from OH lines vs. the distance from the end of nozzle for the BTD (right). The negative distance is taken in the nozzle. Power is 100 W, the electrode gap (between the mouth of the nozzle and ground electrode) is 8 mm.

In spite of various modifications, exist in fact two basic configurations driven at atmospheric pressure: the torch discharge (TD) and the barrier torch discharge (BTD) - see Fig. 1. In previous publications the individual systems and their versions were investigated separately. Simultaneously, based on obtained results individual systems were suggested for perspective industry applications.

At present, the TD and BTD applications are studied for the deposition of thin films and for the treatment of various surfaces, e.g. for the plasma activation of polymer fibres at atmospheric pressure.

EXPERIMENTAL SET-UP

The schematic block drawing of the experimental arrangement is shown in Fig. 1. The powered electrode (material: copper, iron, brass) was made from thin pipe with the inner diameter of 1 – 2 mm and with length of several cm. The discharge was driven at 13.56 MHz and at the power input between 40 - 500 W. The absorbed power has been adjusted in such a manner that at the electrode edge the torch discharge was created. The working gas, argon, which flows from the nozzle, stabilizes the torch discharge. In case of the BTD the dielectrics separates the powered electrode (see Fig. 1) and the own nozzle through which flows the working gas again. This is the fundamental difference from the TD. The experimental arrangement is the same as in case of the TD.

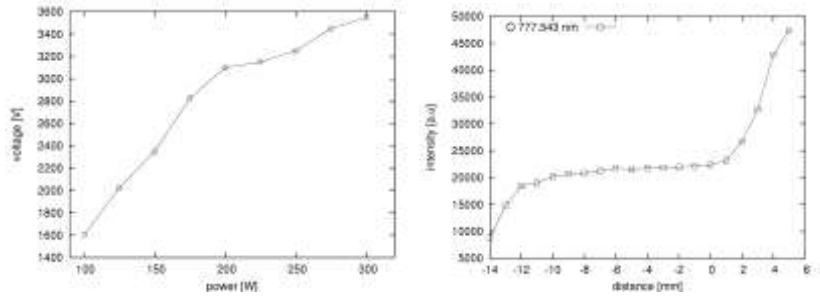

Fig. 4. The amplitude of hf voltage as a function of power. The electrode gap is 10 mm (left). The intensity of oxygen line 777.543 nm vs. the distance from end of the nozzle. The electrode gap is 6 mm (right).

The electrode is connected through the matching unit to the HF generator. Voltage and current measurements have been used as standard diagnostic tools.

The spectra emitted by the plasma channel were recorded by the Jobin - Yvon, TRIAX550 monochromator, with the CCD Spectrum One detector cooled by liquid nitrogen, for different parameters of the arrangements like HF power, working gas flow, etc.

RESULTS AND DISCUSSION

The rotational and vibrational temperatures were determined as a function of input power. Results are presented in Fig. 2, errors were always 10 % less. The rotational temperature approximated the temperature of neutral particles in the discharge. One can see that in general the barrier torch discharge is hotter than the torch discharge under the relative same design of the device and the same input power. This effect is important and could be used for more effective decomposition of chemical species.

The characteristic vibrational temperatures were determined as a function of distance from end of the nozzle. Results are presented in Fig. 3 (left). Negative distance is taken in nozzle, positive distance is out of nozzle. The rotational temperature as a function of distance from end of the nozzle is presented in Fig. 3 (right).

Measurements of amplitude of hf voltage as a function of power are presented in Fig. 4 (left), intensity of oxygen line 777.543 nm as a function of distance from end of the nozzle is shown in Fig. 4 (right), too.

Polymer films were deposited on the substrate such as Al sheet, Cu and brass substrate polished plates and Si wafers. The HF power absorbed in the torch discharge has been adjusted in the range from 50 W till 150 W. The length of the discharge was about 3~cm and the discharge has been not connected with the substrate. Typical deposition time was 10 minutes, input HF power was 125 W, and working gas was argon with an admixture of n-hexane.

This non-standard deposition source was used for deposition of thin films at atmospheric pressure and obtained films were tested by means of standard mechanical tools. The nanoindentation tests were made by means of Fischerscope H100 tester. This equipment enables to record the indentation depth dependence on the applied load during

both the loading and unloading part of the indentation test. In our case the so-called Vickers indenter (square based pyramid) was used for hardness measurement.

The universal hardness HU is defined [8] as the measure of the resistance against elastic and plastic deformation. Results of universal hardness for coated brass substrate are presented in Fig. 5. Deposition time was 10 minutes, input HF power was 125 W, working gas was argon with an admixture of n-hexane.

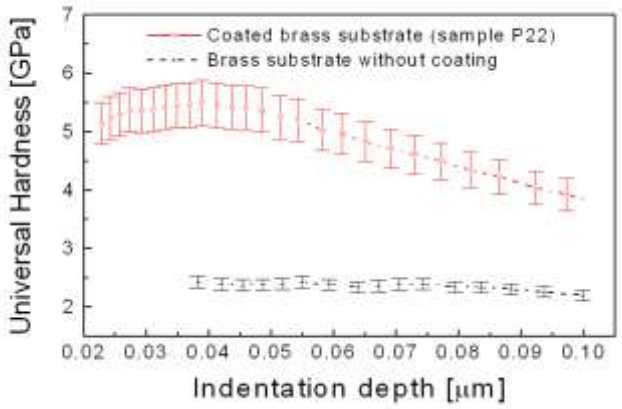

Fig. 5. Universal hardness vs. the indentation depth.

CONCLUSION

It was found, that in case of the BTD discharges maximum of rotational and vibrational temperatures are on the end of nozzle, while inside the nozzle these temperature decrease slowly than out of nozzle. Amplitude of hf voltage increases with increasing the input power.

The presented results show that HF discharges in atmospheric pressure could be suitable for plasmachemical and technological application. Namely, in this moment we conclude that the preparation of thin films is less expensive and easier at atmospheric pressure then at low one.

This work has been financially supported by grant 202/03/0708, 202/01/P017, 202/00/0843, 202/03/0011, 202/03/0708, 202/00/D057 of Grant Agency of the Czech Republic and research intent MSM 143100003, COST 527.20 funding by the Ministry of Education of the Czech Republic.

REFERENCES

[1] K. Wiesemann: in Book of Invited Lectures 20th SPIG, (Eds. by N. Konjevic, Z. L. Petrovic and G. Malovic), September 4 8, 2000, Zlatibor, Yugoslavia, p. 307.

[2] M. Klima, J. Janca, V. Kapicka, P. Slavicek, P. Saul: The Method of Making a Physically and Chemically Active Environment by Means of a Plasma Jet and the Related Plasma Jet, Czech patent No. 286310 (prior. 12.5.1998) or PCT/CZ99/00012.
[3] Brablec, P. Slavicek, M. Klima, V. Kapicka, J. F. Behnke, M. Sicha, Czech. J. Phys., Praha, Institute of Physics Academy of Sciences, 2002, 561-566.
[4] M. Stepan, M. Semerad, V. Kanicky, V. Otruba, Collect. Czech. Chem. Commun, 66, 2001, 1348-1358.
[5] M. Sicha, L. Bardos Tichy, L. Soukup, L. Jastrabik,H. Barankova, R. Soukup, J. Tous: Contrib. Plasma Phys. 34 (1994) 794.
[6] M. Novak, M. Sicha, V. Kapicka, L. Jastrabik, L. Soukup, Z. Hubicka, K. Wiesemann: in Book of Invited Lectures 20th SPIG, (Eds. By W.C. Oliver and G.M. Pharr), J. Mater. Res. 7 (1992), 1564.

4th International Conference **ELMECO**
Nałęczów, Poland
September 2003

INFLUENCE OF THE GEOMETRY ON DISTRIBUTION OF THE ELECTROMAGNETIC FIELD IN STRIPLINE STRUCTURE

Eugeniusz KURGAN, Marek SOŁEK

AGH University of Science and Technology, Dept. of Electrical Engineering
al. Mickiewicza 30, 30-059 Krakow, Poland
e-mail: kurgan@agh.edu.pl, somar@agh.edu.pl

Abstract

In this paper investigation of influence of the magnetic strip shield on the distribution of electric fields in stripline, ground plane, dielectric substrate and surrounding space is described.

Keywords: stripline structure, field computation, shielding, FEM.

1. INTRODUCTION

In [4] analysis of the ac resistance in a microstrip for any metallization thickness by deriving the current distribution over the strip cross-section was investigated. The authors calculated current density distribution both in stripline and the grounding plane using the method of separation variables and Green's function. They showed that for the ratio of the stripline width (w) to dielectric thickness (h) greater then 1, a current in the stripline was distributed mostly in the area closed to the dielectric and current density in ground plane was concentrated under the stripline. Recently, Yung-Kyi Kim considered the detailed current and electric field distribution both inside and outside the structure using FDTD method. He analysed distribution of the electromagnetic fields for different ratio w/h and his results generally agree with that given in [4]. The author, however, assumed simplifying assumption that stripline alone and ground plane are made from perfect electric metal with infinite conductivity.

The increasing importance in fabrication and development of planar integrated circuits has renewed interest in the use of the open microstrip geometry as transmission line in planar microwave integrated circuits. This form of transmitting structure is useful in both a monolithic integrated circuits on a semiconductor substrate and in hybrid microwave circuits on ceramic substrate. The thickness of the metallic strips in the first case is between 1 and 3 μm and in the second case between 5 and 20 μm.

In [3] it was shown that electric field extends substantially outside stripline structure in all directions. This may have serious consequences because such time varying field can induce in neighboring lines and other structures parasitic voltages and currents. Theoretically both shielding dielectric and magnetic layers to reduce field outside the structure can be used. Because of frequencies and geometrical dimensions typical for the considered problems displacement currents can be neglected [1, 2] only magnetic layer considered as shielding method.

In view of the above and recognizing the increasing importance of miniature planar microwave circuits, an investigation of the magnetic shield on the electric field in stripline, ground plane, dielectric substrate and surrounding space is investigated. To solve field equation in two-dimensions finite element method in complex frequency domain was chosen. The wave equation in complex frequency domain was split into two coupled real valued partial differential equations, which can be solved using FEM method in real domain.

2. DERIVATION OF THE MAIN EQUATIONS

Current density flowing in the stripline will be assumed as field excitation. This determines the mode as TM. The influence of magnetic shield placed above the strip and dielectric layer is also examined. Since the transfer components of the current density vector can be neglected compared with the longitudinal component for the case when $w > \lambda_0$, we assume that the current density vector in conductors has only a z component. Moreover we assume that electromagnetic field is independent of the z-coordinate and electric field has only longitudinal component. This allows as considering the problem as two-dimensional.

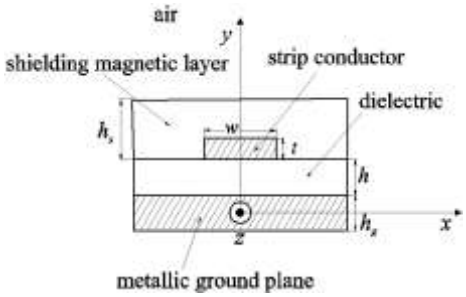

Fig. 1. Stripline with its cross section and dimensions.

Starting from Maxwell's equations we can easy derive the equation describing electric field in and around a strip line structure:

$$\frac{1}{\mu}\nabla\times\mathbf{E} = -\frac{\partial\mathbf{H}}{\partial t} \tag{1}$$

$$\nabla\times\mathbf{H} = \mathbf{J}_e + \mathbf{J}_c + \frac{\partial\mathbf{D}}{\partial t} = \mathbf{J}_e + \sigma\mathbf{E} + \varepsilon\frac{\partial\mathbf{E}}{\partial t} \tag{2}$$

After calculation of rotation of the first equation and substituting the second, we get:

$$\nabla \times \frac{1}{\mu}\left(\nabla \times \mathbf{E}\right) + \sigma \frac{\partial \mathbf{E}}{\partial t} + \varepsilon \frac{\partial^2 \mathbf{E}}{\partial t^2} = -\frac{\partial \mathbf{J}_e}{\partial t} \tag{3}$$

In two-dimensions electric filed **E** and impressed current density vector $\mathbf{J}_e$ have only the *z* components:

$$\mathbf{E} = \mathbf{E}(x, y, t) = E_z(x, y, t)\mathbf{e}_z \tag{4}$$

$$\mathbf{J}_e = \mathbf{J}_e(x, y, t) = J_{ez}(x, y, t)\mathbf{e}_z \tag{5}$$

Equation describing distribution of longitudinal component E_z both inside and outside the stripline structure can be derived from (3):

$$\nabla_t \left(\frac{1}{\mu} \nabla_t E_z \right) - \sigma \frac{\partial E_z}{\partial t} - \varepsilon \frac{\partial^2 E_z}{\partial t^2} = \frac{\partial J_{ez}}{\partial t} \tag{6}$$

In complex domain both vectors can be written as:

$$E_z = E_z(x, y, t) = E_{zm}(x, y)\cos(\omega t + \varphi_{Ez}) = \mathrm{Re}\left[\underline{E}_z(x, y) e^{i\omega t} \right] \tag{7}$$

$$J_{ez} = J_{ez}(x, y, t) = J_{ezm}(x, y)\cos(\omega t + \varphi_{Ez}) = \mathrm{Re}\left[\underline{J}_{ez}(x, y) e^{i\omega t} \right] \tag{8}$$

and thus equation (6) for the case, when $\varepsilon\omega << \sigma$, has the form:

$$\nabla_t \left(\frac{1}{\mu} \nabla_t \underline{E}_z(x, y) \right) - i\omega\sigma \underline{E}_z(x, y) = i\omega \underline{J}_{ez}(x, y) \tag{9}$$

where $\underline{E}_z(x, y)$ and $\underline{J}_{ez}(x, y)$ are complex amplitudes given by (7) and (8).
Equation (9) can be further separated into its real and imaginary parts to yield:

$$\begin{cases} \nabla_t \left(\frac{1}{\mu} \nabla_t E_{zr}(x, y) \right) + \omega\sigma E_{zi}(x, y) = -\omega J_{ezi}(x, y) \\ \nabla_t \left(\frac{1}{\mu} \nabla_t E_{zi}(x, y) \right) - \omega\sigma E_{zr}(x, y) = \omega J_{ezr}(x, y) \end{cases} \tag{10}$$

3. SHIELDING OF THE STRIPLINE BY THE MAGNETIC LAYER

Numerical results of simulation of the electric field in dependence on magnetic permeability of the shielding layer are discussed now.

Total conductor microstrip line analyzed in this section is composed of four layers with the following dimensions:

- metallic substrate thickness h_g = 15μm
- dielectric substrate thickness h= 20 μm.
- stripline line height t = 5 μm,
- magnetic layer thickness t = 12.5 μm,

- strip width $w = 40$ μm.

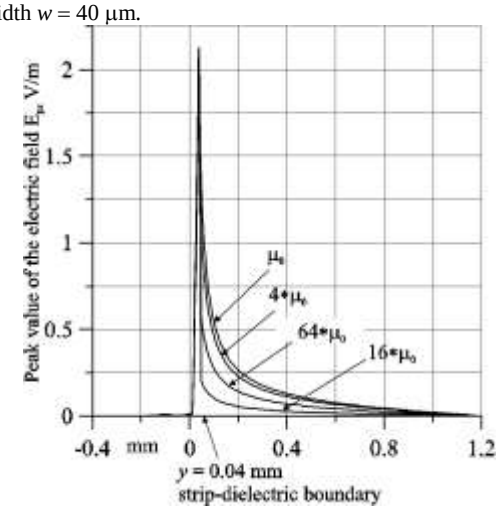

Fig. 2. Electric field distribution along *y* axis for different magnetic shield permeability values.

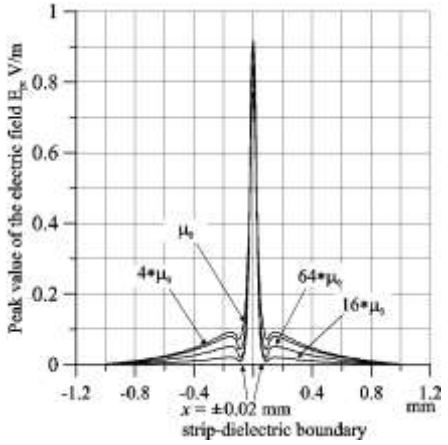

Fig. 3. Electric field distribution along *x* axis for different magnetic shield permeability values.

Figure 1 shows the PCB stripline structure with all geometrical dimensions. Contrary to some earlier publications [5], which as excitation assumed external to the strip structure electric field, in this investigation as excitation current flowing in the strip was chosen. Its value was $I_z = 1$ mA, what gives exiting current density $J_{ez} = 5.00\ 10^6$ A/m^2. Frequency for

this problem was chosen as f = 1 MHz. From fig 2 and 3 we can see that electric field in both coordinate directions is substantially attenuated.

CONCLUSIONS

Electric field distribution properties are evaluated by means of numerical solution of field equations dependent on **E** using finite element method and influence of magnetic shield on the field distribution is examined. The magnetic shield placed over the strip substantially attenuate a radiation of the electromagnetic field in direction perpendicular to the base plane. Another possible method of electromagnetic shielding could be applying shielding layer with anisotropy properties. In such case part of the radiating field could be directed not vertically but instead horizontally. This solution has also some drawback, namely this horizontal part of the field could induce in neighboring circuits parasitic voltages.

ACKNOWLEDGEMENTS

This work was supported by the University of Mining and Metallurgy, under grant 11.11.120.183.

REFERENCES

[1] H.A. Weeler, Transmission-line properties of a strip on a dielectric sheet on a plane, IEEE Trans. Microwave Theory and Techniques, vol.25, no 8, 1977, pp. 631–647.
[2] R.A. Purcel, D.J. Masse, C.P. Hartiwg, Losses in microstrip, IEEE Trans. Microwave Theory and Techniques, vol.33, no 10, 1985, pp. 1076-1082.
[3] E. Kurgan, Distribution of the Electromagnetic Field a Stripline, Electromagnetic Fields in Electrical Engineering, vol. 22, IOS Press, 2002, Amsterdam, 468 – 474.
[4] E. Kurgan, Magnetic analysis of inhomogeneous double-layer shields at low frequencies, Proc. of the 15th International Symposium on Electromagnetic Compatibility, Wrocław, 2000, 326 – 330.
[5] R.Faraji-Dana, Y.L. Chow, The current distribution and ac resistance of microstrip structure, IEEE Trans. Microwave Theory and Techniques, vol.38, no 9, 1990, pp. 1268 – 1277.
[6] K. J. Bathe, "The finite element procedures in engineering analysis", Prentice-Hall, Englewood Cliffs, N.J., 1982.
[7] A. Krawczyk, J.A. Tegopoulos, "Numerical Modelling of Eddy Currents", Oxford Science Publications, Oxford, 1993.

4th International Conference **ELMECO**
Nałęczów, Poland
September 2003

DISTRIBUTION OF THE CORROSION CURRENT DENSITY IN INHOMOGENEOUS SOIL

Eugeniusz KURGAN, Marek SOŁEK

AGH University of Science and Technology, Dept. of Electrical Engineering
al. Mickiewicza 30, 30-059 Krakow, Poland
e-mail: kurgan@agh.edu.pl, somar@agh.edu.pl

Abstract

The present article describes the method of computation of the secondary current density, potential and polarization distribution around pipes burred in soil which conductivity changes with a soil depth. Protection against corrosion of the pipe is attained by placing another metal pipe with given potential. The main goal of this publication is to calculate such protected potential that ensures full protection of the buried pipe against corrosion with minimal maintenance costs. The solution process is based on finite element method. At the end some illustrative example is given.

Keywords: corrosion processes, pipeline protection, finite element method.

1. INTRODUCTION

Accurate design of cathodic protection systems can result in significant savings for industry and environment. Misdesign of protection systems may result in accelerated destruction of both protected installation and environment. It is important, therefore, that accurate methods for calculation and prediction of corrosion activity and for design of protection systems are developed [1].

The economical importance of galvanic corrosion causes that large amounts of capital and engineering time invested in the design and construction of protection systems such as cathodic and anodic protection. The economic costs of corrosion are enormous. They can result from such factors as installation disconnection, loss of products, loss of efficiency, environment pollution and over design of working devices.

Corrosion is the result of the electrochemical reaction between a metal or composite materials usually having conducting current properties and its environment. In the cathodic protection problems the environment has to consist of an conducting electrolyte. Cathodic protection is one of the more frequently used method of corrosion prevention. It can be used to protect the corrosion of any metal, alloy or composites made of layers or regions of

corrosion prone materials. In principle, corrosion can be reduced by properly designed cathodic protection to zero, and such state can be maintained infinitely long [2].

One of the most important aspects of corrosion protection is protection buried in soil pipes by protecting electrodes supplied by voltage sources. In such types of protecting system it is easily possible to overprotect corroding structure by delivering to great total current. This results in unnecessary high maintenance costs because one has to provide additional electrical energy. To optimize such protecting structures one has to calculate exact distribution of currents and voltages in soil and on the corroding surfaces.

The present paper describes the method of computation of the polarization and secondary current density distribution in corroding pipe structure by means of finite element method. It is possible to determine minimum value of supply voltage sources to produce yet full protection against corrosion. At the end some illustrative example is given.

2. CORROSION PROCESS

Corrosion is the destruction of metals by interaction with environment. Material immersed in an electrolyte shell corrodes due to microscopic galvanic cells created on the material surface. In corrosion process there are two kinds of electrochemical reactions: the anodic and the cathodic reactions. Each has its own half-cell electrode potential and exchange current density. The most important cathodic reactions are:

- evolution of H_2 from acid, neutral or alkaline solution

$$2H^+ + 2e^- \rightarrow H_2 \qquad \text{ph}<7 \tag{1}$$

$$2H_2O+2e^- \rightarrow H_2 + 2OH^- \qquad \text{ph} \geq 7 \tag{2}$$

The most important anodic reaction is oxidation of metal or alloy M liberating into solution a metal ion M^{n+} and into the metal electrons ne^-:

$$M \rightarrow M^{n+} + ne^- \tag{3}$$

$$Fe+2H_2O \rightarrow Fe(OH)_2 + 2H^+ + 2e^- \tag{4}$$

Typical corroding reaction on metal surface is shown in Fig. 1.

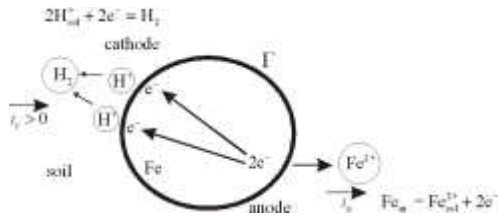

Fig. 1. The cathodic and anodic reactions on metal surface.

The tendency of a metal to liberate electrons, and to go as ions into solution in an electrolyte and thus to become corroded, is related to the potential of the metal measured with reference to some other elements of construction. The potentials developed by

electrode materials can be found tabulated in textbooks and handbooks [2]. The electrochemical potential difference between the anode and the cathode is the driving voltage source causing chemical reaction, and it is also the basis for cathodic protection.

The net applied cathodic current is described by well known Butler-Volmer equation [3]

$$i(\eta) = i_0 \left[\exp\left(\frac{\eta}{\beta_a} \right) - \exp\left(\frac{-\eta}{\beta_c} \right) \right] \tag{5}$$

where

$$\beta_a = \frac{RT}{\alpha nF} \qquad \beta_c = \frac{RT}{(1-\alpha)nF} \tag{6}$$

i_0 – exchange current density in A/m^2,
i – current density on the surface,
η – overpotential on the given electrode in V

$$\eta = \varphi_1 - E_o \tag{7}$$

where φ_1 is potential distribution on the corroding electrode and E_o is a potential of the electrode in equilibrium state, that is when anodic current is equal to the cathodic current and no net current i flows. Exact definitions of the above quantities together with adequate formulae can be found anywhere [2]. It is to point out, that above equations describe kinetics of the electrochemical reactions.

In the soil the current density is related to the electric filed strength by relation

$$\mathbf{J} = \sigma(x, y)\mathbf{E} \tag{8}$$

Electric strength vector is related to the potential φ by formula:

$$\mathbf{E} = -\operatorname{grad}\varphi \tag{9}$$

Current density field is divergence free vector thus

$$\operatorname{div}\mathbf{J} = 0 \tag{10}$$

From the above relation we get well known partial differential equation which has to fulfill potential in inhomogeneous soil:

$$\operatorname{div}\left(\sigma(x, y)\operatorname{grad}\varphi\right) = 0 \tag{11}$$

This equation has to be fulfilled together with Dirichlet's and Neumann's boundary condition:

$$\frac{\partial\varphi}{\partial n} = -\mathbf{E}\cdot\mathbf{n} = -\frac{1}{\sigma}\mathbf{J}\cdot\mathbf{n} = -\frac{1}{\sigma}J_{\mathrm{n}} \tag{12}$$

3. DISCRETIZATION OF THE FIELD EQUATION

Let us assume that we have independent function $\varphi(x, y, z)$ and functional defined as

$$I = \int_V F\left(x, y, z, \varphi, \varphi_x, \varphi_y, \varphi_z\right) \mathrm{d}V + \oiint_S G\left(x, y, z, \varphi\right) \mathrm{d}S \tag{13}$$

where

$$\varphi_x = \frac{\partial \varphi}{\partial x} \quad \varphi_y = \frac{\partial \varphi}{\partial y} \quad \varphi_z = \frac{\partial \varphi}{\partial z} \tag{14}$$

with boundary condition

$$\varphi\left(x, y, z\right) = g\left(x, y, z\right)\Big|_{(x,y,z)\in S} \tag{15}$$

It can be shown by means of variational calculus that function φ minimizing the functional I has to fulfill Euler's partial differential equation:

$$\frac{\partial F}{\partial \varphi} - \frac{\partial}{\partial x}\left(\frac{\partial F}{\partial \varphi_x}\right) - \frac{\partial}{\partial y}\left(\frac{\partial F}{\partial \varphi_y}\right) - \frac{\partial}{\partial z}\left(\frac{\partial F}{\partial \varphi_z}\right) = 0 \tag{16}$$

with following boundary conditions:

$$\left[\frac{\partial F}{\partial \varphi_x}\cos(n, x) + \frac{\partial F}{\partial \varphi_y}\cos(n, y) + \frac{\partial F}{\partial \varphi_z}\cos(n, z)\right]\delta\varphi\Big|_{(x,y,z)\in S} = 0 \tag{17}$$

In the equation (17) we can distinguish two cases. First when

$$\left[\frac{\partial F}{\partial \varphi_x}\cos(n, x) + \frac{\partial F}{\partial \varphi_y}\cos(n, y) + \frac{\partial F}{\partial \varphi_z}\cos(n, z)\right]\Big|_{(x,y,z)\in S} = 0 \tag{18}$$

and the second, when

$$\delta\varphi\big|_{(x,y,z)\in S} = 0 \tag{19}$$

Condition (18) is known as natural or free condition and corresponds to Neumann's boundary condition and (19) is known as geometrical, essential forced condition and corresponds to Dirichlet's boundary condition. It corresponds to the relation

$$\varphi\left(x, y, z\right) = g\left(x, y, z\right)\Big|_{(x,y,z)\in S} \tag{20}$$

In our case functional corresponding to the above equation has the following form:

$$I = \int_V \frac{1}{2}\left[\sigma\left(x, y\right)\left(\frac{\partial \varphi}{\partial x}\right)^2 + \sigma\left(x, y\right)\left(\frac{\partial \varphi}{\partial y}\right)^2\right]\mathrm{d}V + \oiint_S \left[J_a(x, y)\varphi\right]\mathrm{d}S \tag{21}$$

Extremum of this functional will be calculated using finite element method. Let us divide the whole domain on n_e elements. Thus the above integral can be represented as sum of the integrals over all elements.

$$I = \sum_{e=1}^{n_e} I_e \tag{22}$$

where

$$I_e = \int_{V_e} \frac{1}{2}\sigma(x,y)\left[\left(\frac{\partial \varphi_e}{\partial x}\right)^2 + \left(\frac{\partial \varphi_e}{\partial y}\right)^2\right] \mathrm{d}V + \iint_{S_e} \left[J_a(x,y)\varphi_e\right] \mathrm{d}S \tag{23}$$

In the *e*-th element potential function is approximated by following relation:

$$\varphi_e(x,y) = \sum_{i=1}^{n} N_i(x,y)\varphi_{ei} \tag{24}$$

In order to calculate extremum of the I_e in this element we have to calculate derivatives of this functional relatively to nodal value of the unknown variables:

$$\frac{\partial I_e}{\partial \varphi_{ej}} = \int_{V_e} \sigma(x,y)\left[\frac{\partial \varphi_e}{\partial x}\frac{\partial}{\partial \varphi_{ej}}\left(\frac{\partial \varphi_e}{\partial x}\right) + \frac{\partial \varphi_e}{\partial y}\frac{\partial}{\partial \varphi_{ej}}\left(\frac{\partial \varphi_e}{\partial y}\right)\right] \mathrm{d}V + \iint_{S_e}\left[J_a(x,y)\frac{\partial \varphi_e}{\partial \varphi_{ej}}\right] \mathrm{d}S \tag{25}$$

Utilizing relation (24) we can represent all derivations in terms of nodal values:

$$\frac{\partial \varphi_e}{\partial x} = \sum_{i=1}^{n} \frac{\partial N_i}{\partial x}\varphi_{ei} \tag{26}$$

$$\frac{\partial}{\partial \varphi_{ej}}\left(\frac{\partial \varphi_e}{\partial x}\right) = \frac{\partial N_j}{\partial x} \tag{27}$$

$$\frac{\partial \varphi_e}{\partial \varphi_{ej}} = N_j \tag{28}$$

Substituting the two above relation to the equation (25) we get

$$\frac{\partial I_e}{\partial \varphi_{ej}} = \sum_{i=1}^{n} \int_{V_e} \sigma(x,y)\left[\frac{\partial N_i}{\partial x}\frac{\partial N_j}{\partial x} + \frac{\partial N_i}{\partial y}\frac{\partial N_j}{\partial y}\right] \mathrm{d}V\varphi_{ei} + \iint_{S_e}\left[J_a(x,y)N_j\right] \mathrm{d}S = \tag{29}$$

Now we can introduce following element coefficients:

$$h_{eij} = \int_{V_e} \sigma(x,y)\left[\frac{\partial N_i}{\partial x}\frac{\partial N_j}{\partial x} + \frac{\partial N_i}{\partial y}\frac{\partial N_j}{\partial y}\right] \mathrm{d}V \tag{30}$$

and

$$g_{ej} = \iint_{S_e}\left[J_a(x,y)N_j\right] \mathrm{d}S \tag{31}$$

For the *e*-th element we have

$$\frac{\partial I_e}{\partial \boldsymbol{\varphi}} = \mathbf{H}_e \boldsymbol{\varphi}_e + \mathbf{g}_e = \mathbf{0} \tag{32}$$

Assembling the above equation for all elements and after introduction Dirichlet's boundary condition we finally get a set of linear equations with potential values in all nodes as unknowns. After calculation of potential we can easy calculate current density distribution and overpotential distribution on the corroding surface. We have Dirichlet's conditions on two different boundaries: first on the protecting pipe, which is assumed to be connected to external voltage source and can changed and second surface is assumed to have potential 0 and this part of boundary simulate infinite extend of the soil. The current density is flowing partially to the protected pipe and to the soil at infinity.

4. AN ILLUSTRATIVE EXAMPLE

As an example let us consider in two dimensions pipe protected against corrosion and buried in soil as in Fig. 2. In neighborhood of this pipe there is another pipe acting as protecting electrode. To this electrode, which acts as impressed current electrode, voltage source with prescribed value is applied. Soil conductivity changes with depth according to relation (Fig. 3):

$$\sigma(x, y) = \left(\frac{1}{20} - \frac{1}{60}\right)\frac{y}{40} + \frac{1}{60} \tag{33}$$

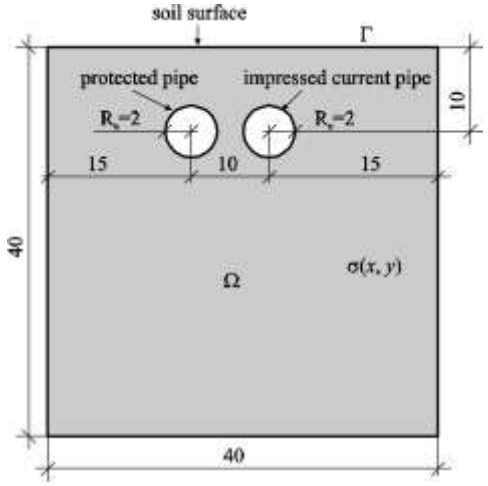

Fig. 2. Geometry of the studied problem.

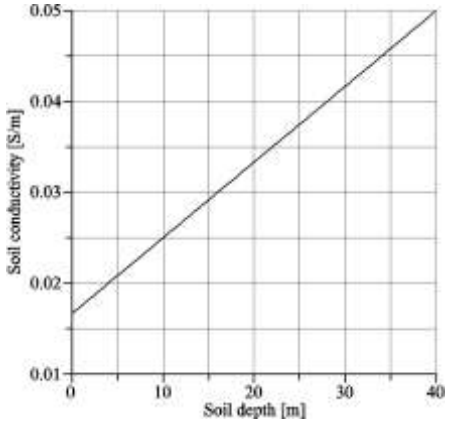

Fig. 3. Dependence of soil conductivity on depth.

The computational domain was divided into 3456 cubic triangular elements, 12503 nodes and together 12503 degrees of freedom. Fig. 4 shows distribution of current density for the case when potential on protecting electrode was $V = 1$V. In this picture we can see that left part of this pipe is not protected because the current is flowing outside the pipe. In Fig. 5 for protecting voltage $V = 5$V we attained full protection because at every point of the perimeter current is flowing into the protected object.

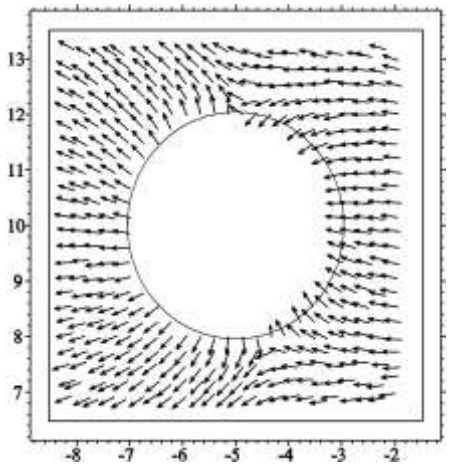

Fig. 4. Current density distribution around partially protected pipe.
All vectors are normalized to equal length.

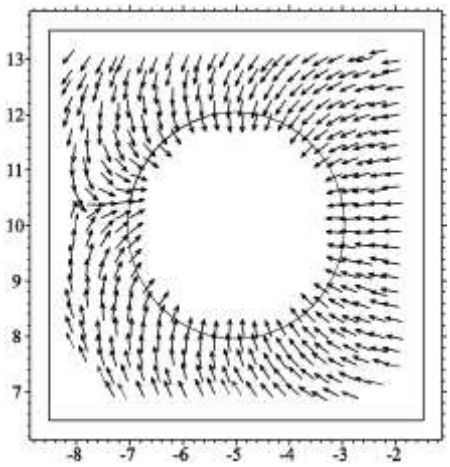

Fig. 5. Current density distribution around fully protected pipe.
All vectors are normalized to equal length.

In Fig. 6 we can see distribution of normal component of the current density around protected object with protecting electrode voltage as a parameter. We attain full protection when for all points on protected surface current is flowing into the structure. Such situation can be observed for protecting voltage V = 5V. From economical point of view it is important to have the possibility to minimize overall costs of protection. Such coasts are proportional to total energy used to protection. By fixed value of voltage applied to protecting electrode, these coasts are directly proportional to the total current flowing into protected object.

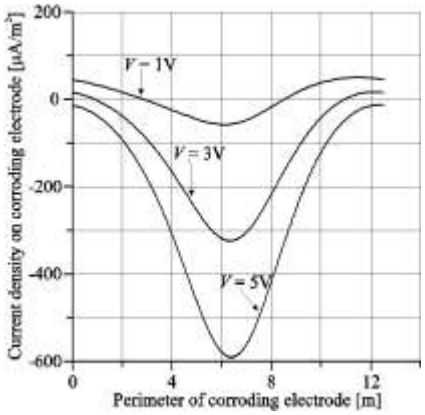

Fig. 6. Current density distribution around protected pipe for different potentials of impressed electrode.

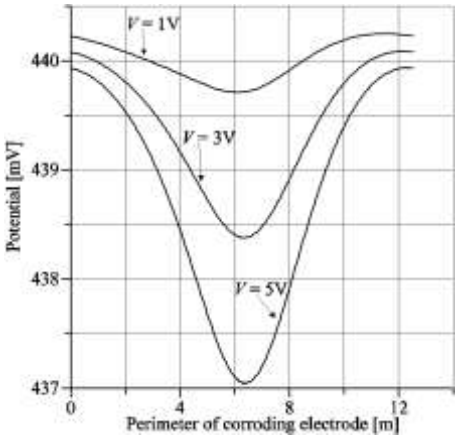

Fig. 1. Voltage distribution around protected pipe for different potentials of impressed electrode.

Full protection can be obtained on various ways. The most optimal protection from economical point of view is achieved when the lower value of the normal component of the current density flowing into the pipe approaches zero. This means that all parts of the structure are protected and total current flowing into the structure is minimal. Method presented in this publication allows computing such current for arbitrary geometry and arbitrary distribution of spatial dependence of soil conductivity. This is of great practical importance because soil humidity usually changes with the depth, weather conditions, the presence or the lack of water reservoirs and other factors which influence the soil humidity.

Examples of structures existing in inhomogeneous soil include underground storage tanks, offshore oil rigs, and reinforcing steel in chloride contaminated concrete [4]. The conductivity of the soil in which storage tanks are placed may vary with each soil layer and even within each layer. The conductivity of the sea water in which offshore oil structures are embedded may vary significantly with deep, and the difference in the electropotentials obtained from analysis performed with and without taking into account material inhomogenity is substantial [2]. The methods for analyzing structures with inhomogeneous electrolyte are available [1,2]. But most of authors assume that the resistivity of protected structure is homogeneous. This is by no means always the truth.

Mostly, for literature calculation of cathodic protection boundary element method is used. This method generally does not allow to calculate the distribution of current density in inhomogeneous medium. Therefore, finite element method here was chosen.

5. CONCLUSIONS

It was shown that it is possible to apply finite element method to calculate such distribution of current density and voltage distribution on protected object that total current needed for full protection has minimal value. This also means that protection costs are also minimal.

ACKNOWLEDGEMENTS

This work was supported by the University of Mining and Metallurgy, under grant 10.10.120.417.

REFERENCES

[1] R.S. Munn, "Microcomputer Corrosion Analysis for Structures in Inhomogeneous Electrolytes", in Heidersbach, J. Fu, and R. Erbar, editors, Corrosion/86 Symposium on Computers in Corrosion Control, pp. 240-255, NACE, Huston, TX, 1986.

[2] L.M. Applegate, Cathodic Protection, McGraw-Hill Book Company, Inc., New York, Toronto, 1960.

[3] E. Kurgan, "Boundary Element Method for the Analysis of the Galvanic Corrosion Problems", Proc. Internat. Conf. on Electromagnetic Devices and Processes in Environment Protection, Kazimierz Dolny, 251-256, 1994.

[4] D.J. Jones, "Principles and prevention of corrosion", Mcmillan Publishing Company, N.Y., 1992.

[5] E. Kurgan, Computation of Primary Current Density Distribution in a Corrosion Cell by Finite Element Method, Proc. Internat. Conf. on Electromagnetic Devices and Processes in Environment Protection, Nałęczów, 2000, 238 – 243.

[6] E. Kurgan, Simulation of Grounding Systems with Non-Linear Boundary Conditions, COMPUMAG – 13th Conference on the Computation of Electromagnetic Fields, Lyon-Evian, France, 2001, 208 – 209.

4th International Conference **ELMECO**
Nałęczów, Poland
September 2003

KARMAN FLOW PATTERN IN ELECTROSTATIC PRECIPITATOR

Jarosław DEKOWSKI[1], Jerzy MIZERACZYK[1], Janusz PODLIŃSKI[1], Marek KOCIK[1], Jen-Shih CHANG[2]

[1] *Centre for Plasma and Laser Engineering, Institute of Fluid Flow Machinery, Polish Academy of Sciences, Fiszera 14, 80-231 Gdańsk, Poland*
e-mail: jmiz@imp.gda.pl
[2] *Department of Engineering Physics, McMaster University, Hamilton, Ontario, L8S 4M1 Canada*

Abstract

In this paper results of the laser visualization of the particle flow in a wire-to-plate type ESP model with a single wire electrode are presented. In this investigation such flow patterns, as Karman vortex stream different voltage and polarity were found. The presented experiment is a part of a larger investigation which focuses on the mapping of flow patterns in different electrostatic precipitator geometries.

Keywords: corona discharge, EHD flow.

1. INTRODUCTION

In recent years a special environmental concern is directed towards controlling the emission of micron and submicron particles in electrostatic precipitators (ESPs), which operating with high overall efficiency, are not effective in the removal of fine particles (size range from 0.1 to 1 μm). Many of the fine particles contain toxic trace elements. Hence, there has long been interest in improving ESP collection of fine particles.

The motion and precipitation of particles in the duct of an ESP depend on the particle properties, electric field, space charge and gas flow field. It was shown (e.g. [1-3]) that a significant interaction between these factors exists. However, electrically generated secondary flow and turbulence in ESPs are still not well understood and their influence on the particle precipitation remains unclear. At different primary flow velocities, operating voltage and polarity, different flow patterns occur. These flow patterns have large influence on the particle precipitation due to the mixing of the gas by the turbulence. Some of the flow patterns in the wire-to-plate ESPs were presented by us in [4,5]. In this experiment we continue this work and present other flow patterns which occur in ESPs.

Due to the high operating voltage most of the classical intrusive techniques are unpractical for measuring the velocity field inside ESPs. The laser visualization was proved as very useful technique in investigations of flow patterns in ESPs [4,5].

In this paper results of the laser visualization of the particle flow in a wire-to-plate type ESP model with a single wire electrode are presented.

2. EXPERIMENTAL SET-UP

Experimental setup consisted of an ESP model, high voltage supply, Nd:YAG laser, telescope and CCD camera (Fig. 1).

The model of ESP was an acrylic box (100 mm x 200 mm x 1000 mm). A stainless steel wire (0.9 mm in diameter) was used as the discharge electrode. It was mounted in the middle of the ESP model, in the halfway between two grounded parallel plate electrodes (200 mm x 600 mm) used as the collecting electrodes, as shown in Fig. 1. The voltage was supplied to the wire electrode through a 10 MΩ resistor. The operating voltage, either negative or positive, was changed up to 35 kV. Air seeded with cigarette smoke (size of 0.5-1 μm), called a primary flow, was blown along the ESP duct with an average velocity ranged from 0.15 to 1 m/s (the flow velocity of about 0.8 m/s is typical of the flow in ESPs). Some measurements were carried out in stationary conditions, without any externally forced movement of the air in the duct.

For the flow visualization the twin second harmonic Nd:YAG laser system (λ = 532 nm, pulse energy 50 mJ, 7 ns pulse duration) was used. The so called "laser sheet" of a thickness of 1 mm was formed from the Nd:YAG laser beam by the telescope and set along the flow direction, perpendicular to the plate electrode in the middle of duct. The laser sheet light was scattered by the seed particles in the flow. Images of seed particles in the laser sheet plane were recorded by the Kodak Mega Plus ES 1.0 CCD camera. The CCD camera active element size was 1008×1018 pixels. In this experiment the observation area was 10 cm x10 cm.

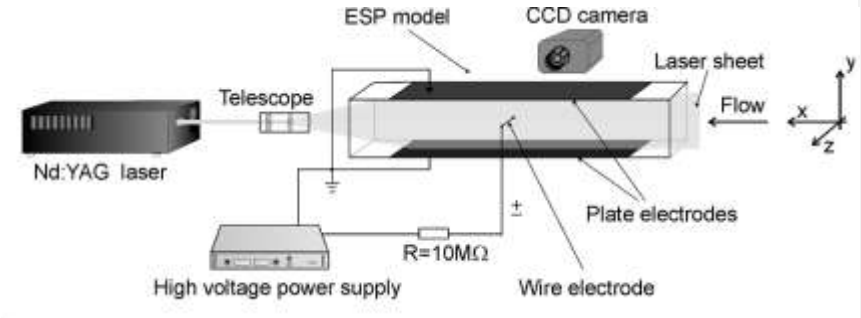

Fig. 1. Experimental set-up.

Without applied voltage, the seed particles, uniformly distributed in the flow, did not allow us visualise the flow patterns. When voltage was applied the seen seed particles were removed from some areas of the flow. These particle-free areas are seen as dark areas in the flow images.

a)

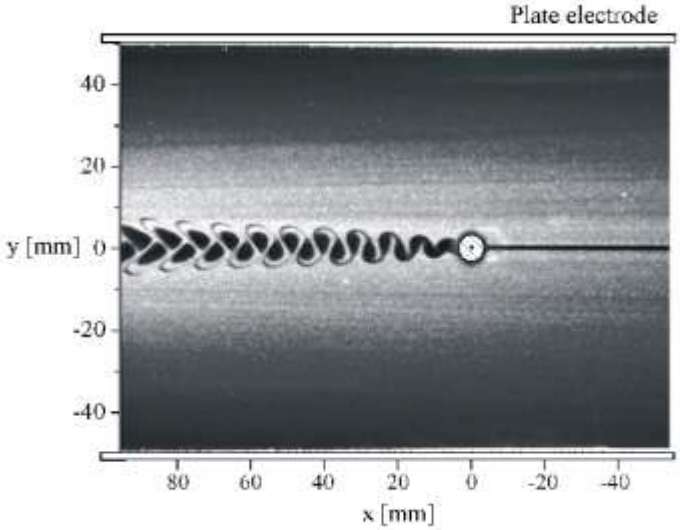

b)

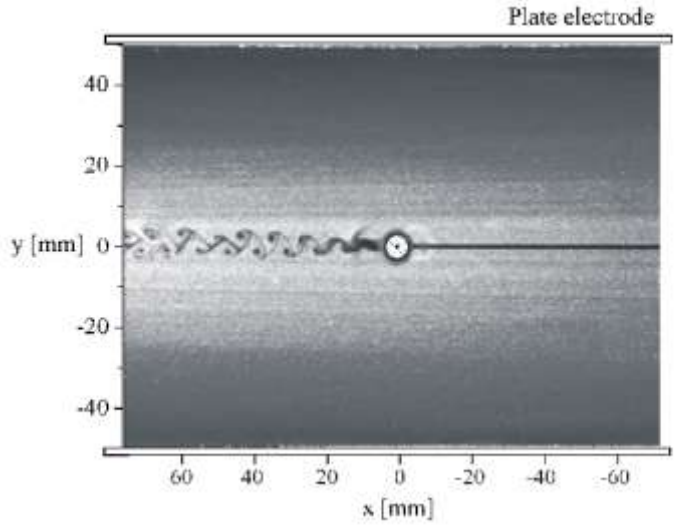

Fig. 2. Images of the flow pattern in the ESP model with single wire and two plate electrodes in the plane perpendicular to the plate electrodes (x-y plane) at a primary flow velocity of 0.65 m/s. Voltage 17 kV: a) positive polarity, b) negative polarity.

a)

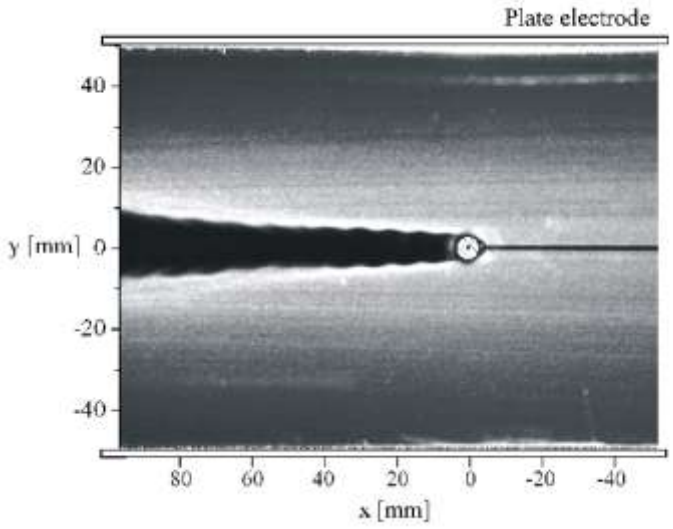

b)

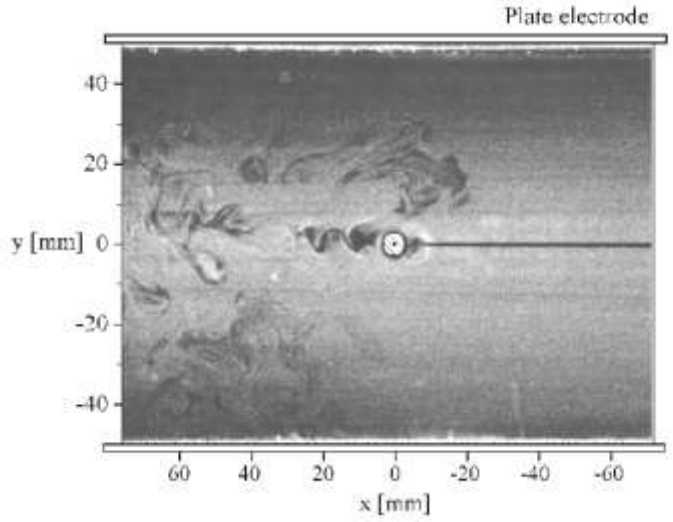

Fig. 3. Images of the flow pattern in the ESP model with single wire and two plate electrodes in the plane perpendicular to the plate electrodes (x-y plane) at a primary flow velocity of 0.65 m/s. Voltage 24 kV: a) positive polarity, b) negative polarity.

Because of technical problems we could not observe the vicinity of the wire electrode because of the mounting element of the wire. In the presented images it was shown as a white circle with a small black dot inside (which corresponds to the real electrode size). Another area where we could not observe was the shadow of the wire, which is seen in the images as a black line in the upstream area.

3. RESULTS

The flow pattern images around the wire electrode in the plane perpendicular to the plate electrodes for different positive or negative voltages (17 and 24 kV) are shown in Figs. 2 and 3. In all cases the primary flow velocity is 0.65 m/s.

Figs. 2 a and b show coherent vortex structures behind the wire electrode polarized positively or negatively with a voltage of 17 kV. The vortexes generated around the wire electrode are convected downstream alternately from the upper and bottom side of the wire electrode, similarly to the so-called Karman vortex stream [6]. The Reynolds number based on the discharge electrode diameter is Re = 40, which is enough to generate vortex street without applied voltage. However, the size of the vortexes near the wire electrode without voltage should be equal to about the wire diameter (0.9 mm). Here, with the voltage applied the vortexes electrically generated behind the electrode are larger (about 3-5 mm in diameter) than the vortexes formed when no voltage is applied. The shape of the area occupied by the flow cleaned from the seed particles is regular for the positive polarity. For the negative polarity particle-free areas are smaller and the shape of the particle-free area changes slightly from one vortex to another.

Figs. 3 a and b show the flow patterns in the ESP model at a voltage of 24 kV for the positive and negative polarity, respectively. For the positive polarity (Fig. 3a) there is a stable flow structure with regularly shaped area cleaned from the seed particles, which starting a few millimetres upstream from the wire electrode is widening downstream. The border of the particle-free area has small ripple-like curvatures, which most probably are result of Karman vortex stream behind the wire electrode. This Karman vortex stream could not be revealed by the laser beam due to the lack of the seed particles in the cleaned-up area. For the negative polarity (Fig. 3b) the flow is unstable and turbulent. There is Karman vortex stream but it is less regular than for the lower voltage(Fig. 2b).

4. CONCLUSIONS

The presented images of the flow pattern in the ESP model confirmed that the presence of the electric field and charge causes a significant change in the particle flow pattern. After applying the voltage, the secondary flow, significant flow turbulence and coherent vortex structures are formed in the ESP. There are different flow patterns for different primary flow velocities, applied voltage and polarity. These flow patterns have different influence on the particle movement and their precipitation (e.g. due to different turbulent diffusion of the particles). In ESP designing process not only the external parameters like the discharge current and flow velocity should be taken into consideration but also the possible flow patterns should be considered. Small changes of the external parameters can significantly change the flow pattern, for example, from laminar flow with Karman vortex stream to the fully developed turbulent flow which has different influence on the particle precipitation. Further works are needed to get the stability map of the flow structures in different ESP geometries.

ACKNOWLEDGEMENTS

This work was supported by the Foundation for Polish Science (FNP, subsidy 8/2001) and the State Committee for Scientific Research (grant KBN PB 1756/T10/01/21).

REFERENCES

[1] Ohkubo, T., Nomoto, Y., Adachi, T., and McLean, K.J, J. Electrostatics, 18, 289-303, 1986
[2] Atten, P., McCluskey, F.M.J., and Lahjomri, A. C., IEEE Trans. Ind. Appl., 23-4, 705-711, 1987
[3] Chang, C.L. and Bai, H., 2000, Aerosol Sci. Tech., 33-3, 228-238, 2000
[4] J. Mizeraczyk, M. Kocik, J. Dekowski, M. Dors, J. Podliński, T. Ohkubo, S. Kanazawa, T. Kawasaki, J. Electrostatics, 51-52, 272-277, 2001
[5] J. Mizeraczyk, J. Dekowski, J. Podliński, M. Kocik, T. Ohkubo, S. Kanazawa, Journal of Visualization, 6, 2, 125-133, 2003
[6] T. von Karman, Aerodynamics, Selected Topics in the Light of Their Historical Development, Cornell Univ. Press, 1957

4th International Conference **ELMECO**
Nałęczów, Poland
September 2003

FLUX2D FOR NUMERICAL MODELLING OF THERMAL PHENOMENA IN SUPERCONDUCTING DEVICES

Sławomir KOZAK

Electrotechnical Institute in Warsaw
Pożarskiego 28, 04-703 Warsaw
slawko@eltecol.pol.lublin.pl

Abstract

Cooling down to the operation temperature and keeping the temperature on adequately low level by good thermal insulation and good cooling conditions decide on superconducting state in the device. In low temperature below 200 K significant changes of electrical and thermal parameters vs. temperature are observed. The paper presents thermal numerical models (in FLUX2D) of force-cooled current leads and contact-cooled Nb-Ti magnet. The USER SUBROUTINES were used to define advanced temperature relations of physical properties of calculated regions and thermal flux to cryocooler. Experimental results were used to verify the parameters of numerical model. Nb-Ti magnet needs 5 h 43 min 20 s to superconducting transition, but only 1 h 40 min to reach 30 K.

Keywords: superconducting device, current lead, Nb-Ti magnet, numerical modelling, FLUX2D, user subroutines.

1. INTRODUCTION

Thermal phenomena are very important in all superconducting devices. Cooling down to the working temperature and keeping the temperature on adequate low level by good thermal insulation and good cooling conditions decide on superconducting state of device. The main difference between modelling thermal phenomena in superconducting devices at low temperature below 200 K and at room and higher temperatures results from very significant changes, vs. temperature, of thermal parameters values of materials used in devices. Additionally, the shapes of these changes are usually significantly different from these predicted in FEM CAD packages.

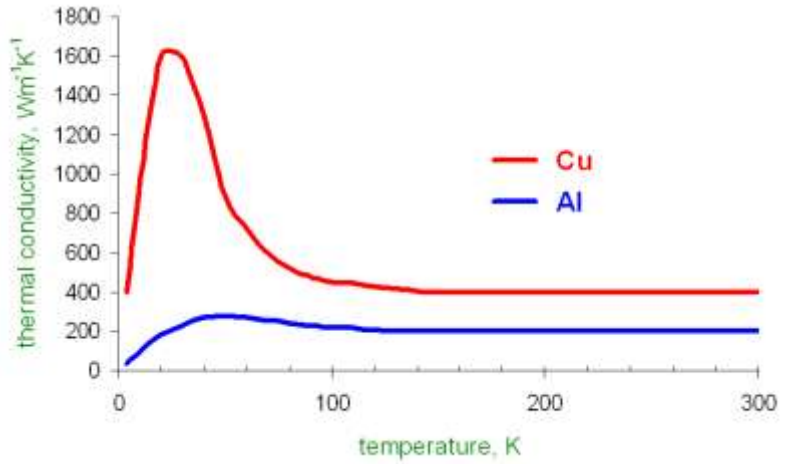

Fig. 1. Thermal conductivity vs. temperature for copper and aluminium [1, 2, 3]

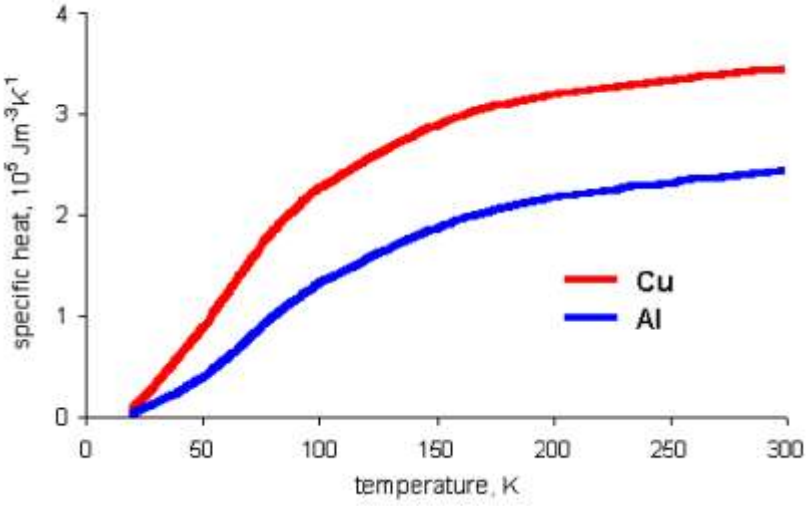

Fig. 2. Specific heat vs. temperature for copper and aluminium [1, 2, 3]

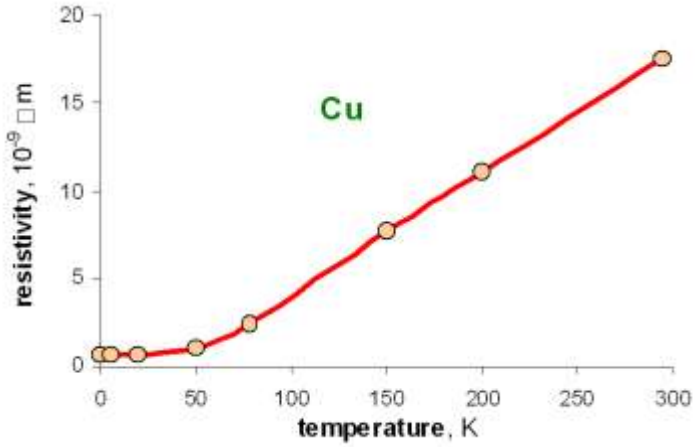

Fig. 3. Resistivity of copper vs. temperature [2, 3, 4, 5]

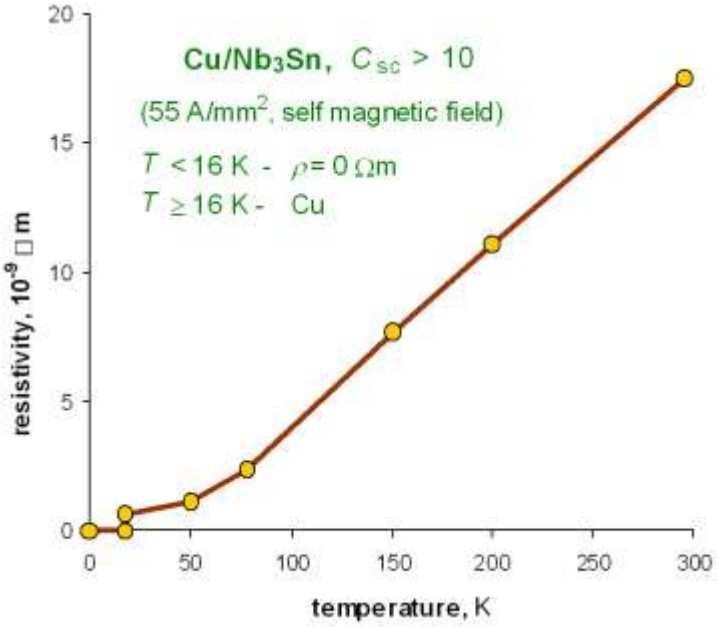

Fig. 4. Resistivity of Cu/Nb_3Sn vs. temperature [4, 5]

Fig. 1 and Fig. 2 present thermal conductivity k and specific heat c_v of copper and aluminum vs temperature T [1][2][3]. Presented shapes of those parameters are average for copper and aluminum because there are strong dependences of parameters values due to purity. According to Fig. 1, the maximal value of thermal conductivity of copper equals 1600 $Wm^{-1}K^{-1}$, however this value can vary from 800 $Wm^{-1}K^{-1}$ to 15000 $Wm^{-1}K^{-1}$ [1][3]. Fig. 3 and Fig. 4 present thermal resistivity ρ of copper and Cu/Nb_3Sn vs temperature [2][3][4][5]. Values of parameters k, ρ, c_v presented in figures from 1 to 4 are temperature dependent. Additionally, electric resistivity of Cu/Nb_3Sn depends not only on temperature but also on current density and magnetic field.

In the FLUX2D [6] the material properties are defined in CSLMAT module. The standard shapes of characteristics in CSLMAT anticipated for parameters in room and higher temperature are too simple and can not be adapted to more sophisticated shapes of functions: $k(T)$, $\rho(T)$ and $c_v(T)$ presented in figures from 1 to 4. The shapes of these functions can only be achieved by user subroutines [6]: USRKTH, USRRCP and USRSIG. User subroutines widen the range of applications of FLUX2D. Any of the physical properties can be handled as a user's subroutine: these include material properties, sources or boundary conditions. The interface with FLUX2D requires FORTRAN programming. The electric resistivity dependence on current density, and magnetic field and temperature has been taken into account, indirectly, in calculation by modification of subroutine USRSIG for every change of current in region.

2. FORCE-COOLED CURRENT LEAD

The current flows from energy source (power supply) to the superconducting device, placed in a cryostat, through current leads. A warm end of current lead, joined to the energy source, works in room temperature (293K). A cold end of the current lead, joined to the superconducting device, works usually in liquid helium temperature (4,2K). The simplified current lead is presented in Fig. 5. The current lead made of copper (or Cu/Nb_3Sn) rod is cooled by gas flowing along the wall of the lead. The temperature of gas flowing from z to $z+dz$ is increased by dT. The Joule heat generated in the element by the electric current in the lead is transferred to the helium.

Numerical model

An electro-thermal application of FLUX2D, which is the coupling of an electric conduction problem with a transient thermal problem [6], was used for force-cooled current lead calculations. The numerical model consists of 4 calculation objects (Fig. 6): the warm end represented by shell [6] on GORA, the cold end represented by shell region DOL, heat exchange between current lead and helium represented by shell region BOK and the current lead represented by surfacic [6] region PRZEWOD. It was assumed that PRZEWOD had thermal properties as presented in figures from 1 to 4 for copper or Cu/Nb_3Sn.

In electric part of solving problem the voltage U is the variable and the following equation is computed [6]:

$$\mathrm{div}(\sigma \cdot \mathrm{grad}\, U) = 0 \qquad (1)$$

where: σ - resistivity ($\Omega^{-1}m^{-1}$), U - voltage (V).

In thermal part of solving problem the temperature T is the variable and the following equation is computed [6]:

$$c_{\mathrm{v}} \cdot \frac{\partial T}{\partial t} + \mathrm{div}(-k \cdot \mathrm{grad}\, T) = Q_{\mathrm{H}} \qquad (2)$$

where: c_{v} – specific heat ($\mathrm{J \cdot m^{-3} K^{-1}}$), T – temperature of object (K), t - time (s), k – thermal conductivity ($\mathrm{W \cdot m^{-1} K^{-1}}$), Q_{H} – density of heat source ($\mathrm{W/m^3}$).

The shell regions are defined on the boundary domain [6]. The shell regions are very specific regions, which have a special function according to the applications. In electric conduction application the shell regions GORA and DOL are used to define a current going in and of the domain. The current flows from region GORA to region DOL through region PRZEWOD.

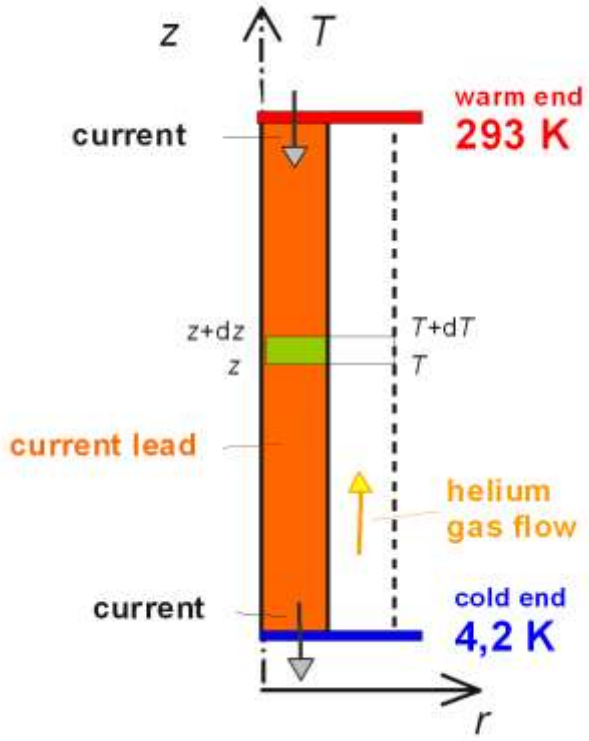

Fig. 5. Current lead cooled by helium gas flow (force-cooled)

In the thermal part the shell region is used to define a thermal flux transfer. The heat generated in the lead by current (PRZEWOD) is transferred to the cooling gas by shell region BOK. Neumann non-homogeneous boundary condition in case of convection, radiation coefficients or thermal flux transfer on shell region BOK is given by [6]:

$$k \cdot \frac{\mathrm{d}(T)}{\mathrm{d}n} = -\Phi_{\mathrm{H}} - h \cdot (T - T_{\mathrm{a}}) - \varepsilon \cdot (T^4 - T_{\mathrm{a}}{}^4) \tag{3}$$

where: k - thermal conductivity ($\mathrm{W \cdot m^{-1} K^{-1}}$), Φ_{H} - thermal flux from the outside ($\mathrm{W/m^2}$), h - convection exchange coefficient ($\mathrm{W \cdot m^{-2} K^{-1}}$), ε - radiation exchange coefficient, T – temperature of object (K), T_{a} - ambient temperature (K).

The heat flux exchange between the current lead and the flowing helium gas strongly depends on a velocity of helium. This velocity is not a parameter in FLUX2D. It can be taken into account indirectly by ambient temperature T_{a}. In FLUX2D T_{a} have a fixed value. In force-cooling problem the value of T_{a} is unknown and difficult to estimate, and it depends on cooling gas velocity. The subroutine USRAMB [6] was used to define the ambient temperature as a function of temperature and axial coordinate [5] of shell region BOK.

The regions GORA and DOL, used in electric part of problem, are ignored in thermal part. The region BOK, used in thermal part of problem, is ignored in electric part. The region PRZEWOD is used in both parts of the solving problem.

The thermal conductivity, the electrical resistivity and the specific heat are defined for region PRZEWOD. The convective exchange coefficient and the ambient temperature are defined for region BOK.

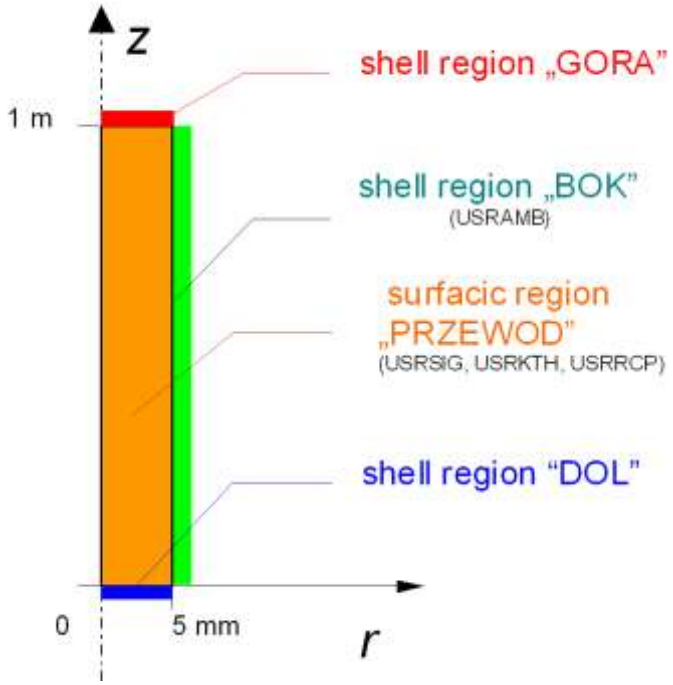

Fig. 6. Geometry of numerical model of current lead

Numerical results of computations of current lead temperature

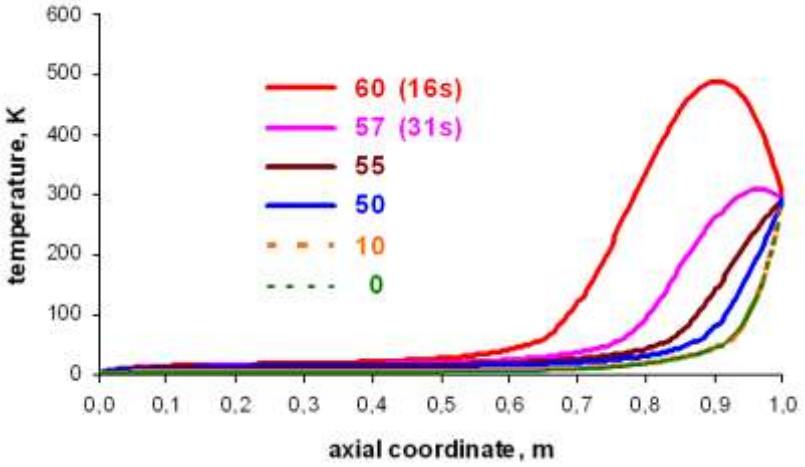

Fig. 7. Temperature distribution on shell region BOK for different current density (A/mm^2). Helium velocity = 2 m/s

Figure 7 presents the results of calculations of the temperature distribution in the current lead for different current densities. It can be seen that 55 A/mm^2 is the maximal current density for which this current lead works properly. The calculation for temperature was stopped after 31 seconds for 57 A/mm^2 and after 16 seconds for 60 A/mm^2, because the temperature increases in time. The temperature distributions in the current lead without current and for current density = 10 A/mm^2 are almost the same.

Figure 8 shows the temperature vs. time at the point (0,0025; 0,8) in the current lead for current density = 55 A/mm^2 and 57 A/mm^2 and for helium velocity = 2 m/s. For current density = 57 A/mm^2, heat generated in current lead is higher than heat transferred to the helium and the temperature does not approach the stable value. Under those conditions calculated current lead does not work properly. For current density = 55 A/mm^2, heat generated in it is not higher than the heat transferred to the cooling gas and the temperature approaches the stable value. Under those conditions the calculated current lead works properly.

Figure 9 presents the results of calculation of the temperature distribution in the current lead for different helium velocities and for fixed current density = 55 A/mm^2. For the velocity = 2 m/s the current density = 55 A/mm^2 is the maximal value of density for which that current lead works properly. For the cooling gas velocity lower than 2 m/s the temperature of current lead increases in time. The cooling gas velocity higher than 2 m/s decreases temperature in the current lead.

Figure 10 presents the results of calculation of the temperature distribution in the Cu and Cu/Nb_3Sn current leads for helium velocity = 2 m/s and current density = 55 A/mm^2. Superconducting current lead give much better temperature distribution than copper one.

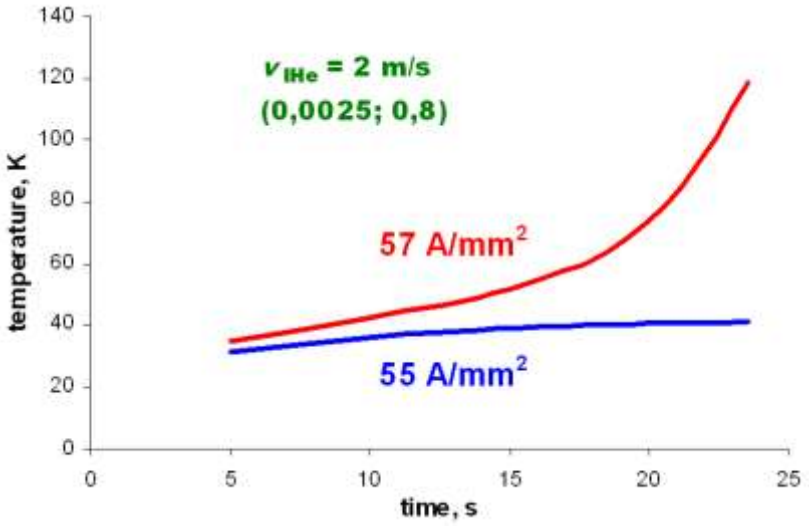

Fig. 8. Temperature vs. time at point (0,0025; 0,8) in the current lead

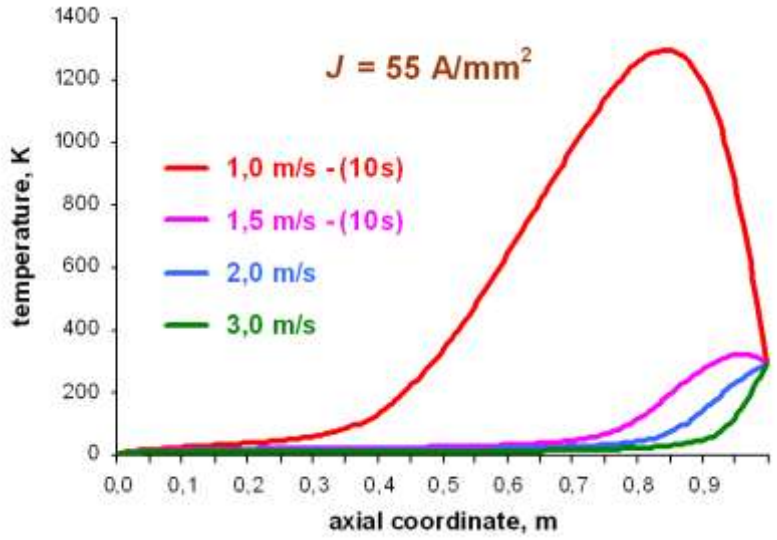

Fig. 9. Temperature distribution on shell region BOK for different helium flow

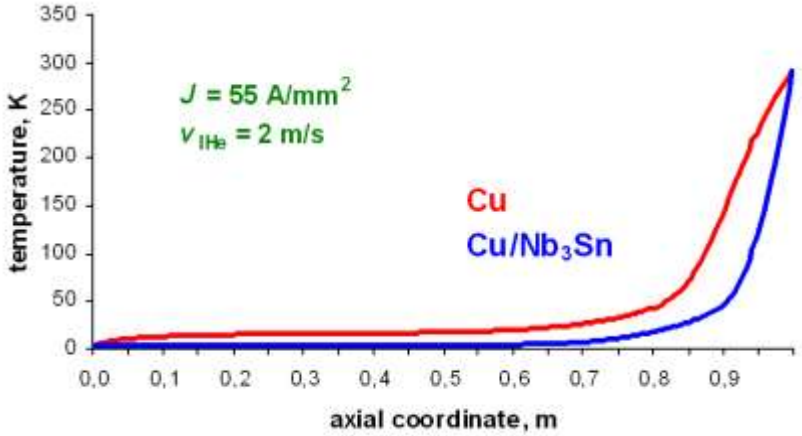

Fig. 10. Temperature distribution in Cu and Cu/Nb_3Sn current leads

3. CONTACT-COOLED NB-TI MAGNET

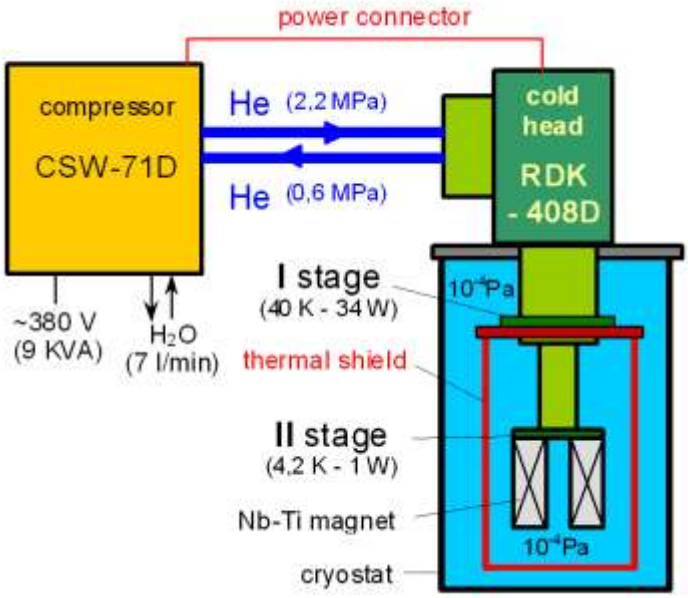

Fig. 11. SRDK-408 in cooling system of Nb-Ti magnet

Table 1. Parameters of Nb-Ti magnet of OGMS separator [7, 1]

Name	Value
Distance between coils	0,01 m
Inner radius of coils	0,0314 m
Outer radius of coils	0,0389 m
Length of coil	0,04 m
Operating current	±250 A
Maximal magnetic field	2,26 T
Winding package factor	0,32
Average current density	$\pm 4{,}17 \cdot 10^{8}$ A/m^2
Mass of magnet	1,46 kg
Resistance at 293 K	19,8 ohm

Nb-Ti magnet which parameters are presented in Tab. I, consists of two coaxial, adjacent coils [7]. Figure11 presents Nb-Ti magnet in cooling system with SRDK-408. Nb-Ti magnet is connected to II stage of cryocooler and thermal shield is connected to I stage (Fig. 12). Top part of thermal shield is equipped with supports for Bi-2223 current leads.

Fig. 12. Nb-Ti magnet connected to SRDK-408

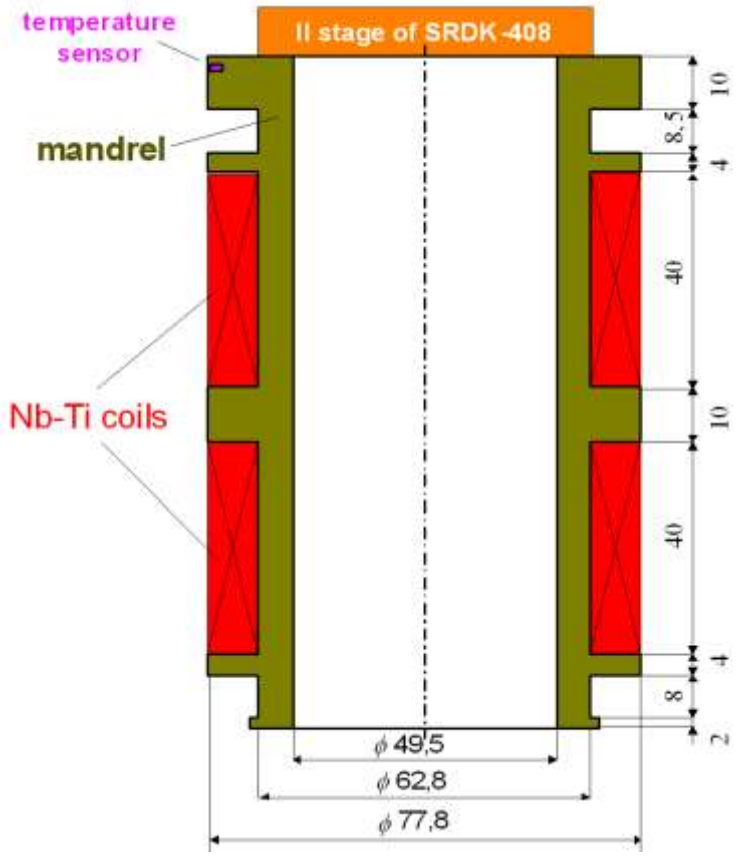

Fig. 13. AL-alloy mandrel of Nb-Ti magnet. Dimensions in mm

The one-piece Al-alloy mandrel of Nb-Ti magnet (Fig. 13) secures good thermal connection between superconducting coils and II stage of cryocooler [7][1].

Experimental Results

Figure 14 presents temperature measured in place shown in Fig. 13 and resistance of Nb-Ti magnet during cooling process. The registration of temperature by 218 Temperature Monitor and computer system [8][7][1] started at 1800 s after turn on the cryocooler. Figure 15 shows temperature and resistance of Nb-Ti magnet during superconducting transition.

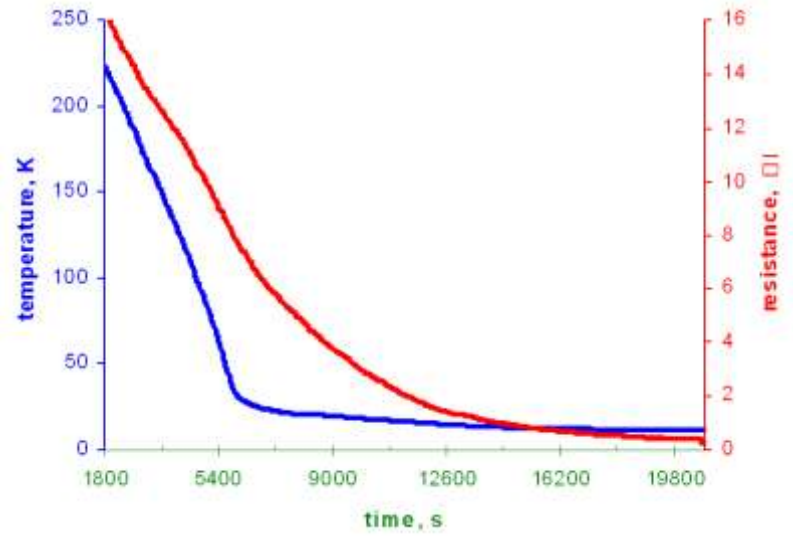

Fig. 14. Temperature and resistance during cooling down of Nb-Ti magnet

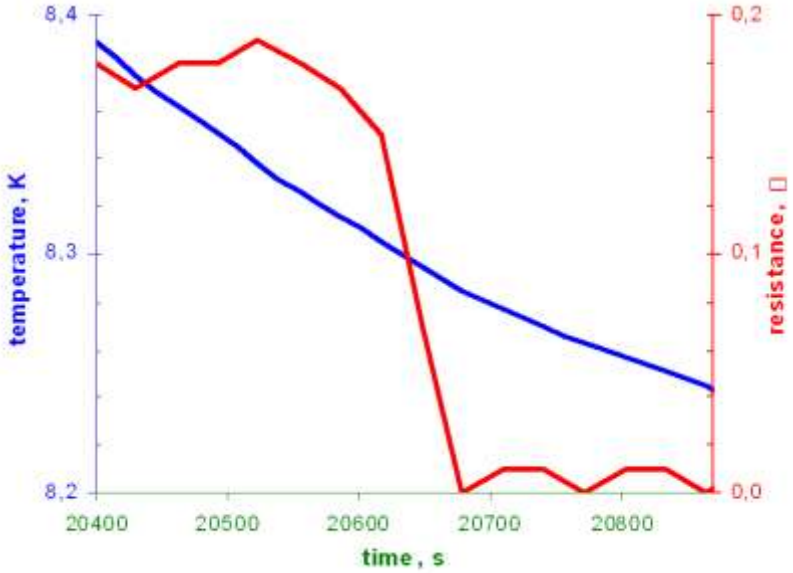

Fig. 15. Temperature and resistance during superconducting transition of Nb-Ti magnet

Numerical model

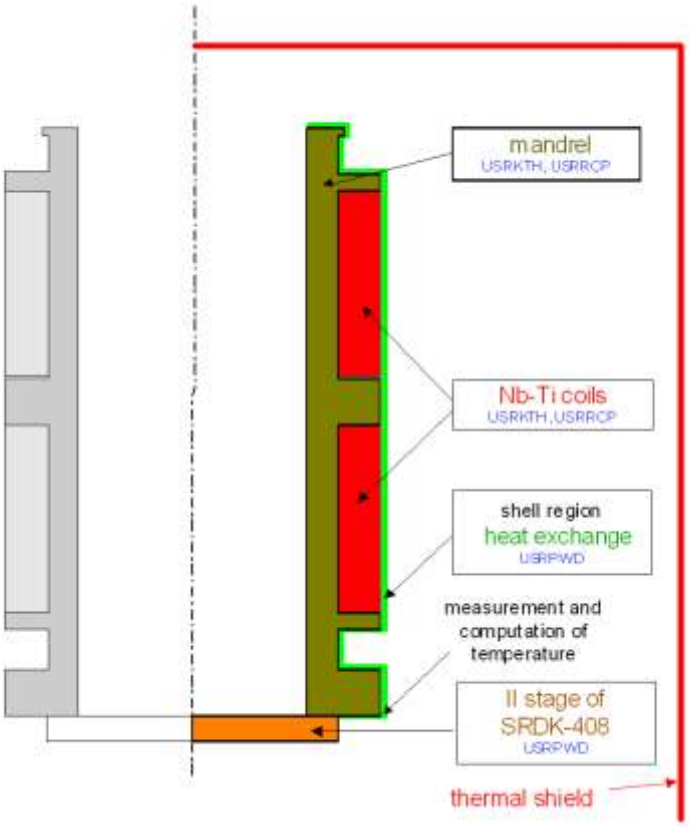

Fig. 16. Geometry of numerical model of contact-cooling process of Nb-Ti magnet

The numerical model consists of 4 calculation objects: II stage of SRDK-408, mandrel of magnet, Nb-Ti coils, Nb-Ti magnet - thermal shield heat exchange. It was assumed that mandrel had thermal properties as presented in Fig. 1 and Fig. 2 for aluminium. It was also assumed, that Nb-Ti coils had properties as presented in Fig. 1 and Fig. 2 for copper. The coils are not uniform and it has been assumed that winding package factor of this region is proportional to that shown in Tab. I [1]. The user subroutines [6][1] USRKTH and USRRCP were used to define thermal conductivity and specific heat of calculation regions in numerical model geometry presented in figure 16. The USRKTH and USRRCP have two parameters. The first defines the kind of material: Cu or Al. The second one defines value of winding package factor [7][1].

Numerical model of contact-cooling process of Nb-Ti magnet was made using transient thermal modules of FLUX2D [6] where the temperature T is the variable and the following equation is computed [6]:

$$c_v \cdot \frac{\partial T}{\partial t} + \mathrm{div}(-k \cdot \mathrm{grad}\, T) = Q_H \tag{4}$$

where: c_v – specific heat ($J \cdot m^{-3} K^{-1}$), T – temperature of object (K), t - time (s), k – thermal conductivity ($W \cdot m^{-1} K^{-1}$), Q_H – density of heat source (W/m^3).

Neumann non-homogeneous boundary condition in case of convection, radiation coefficients or thermal flux transfer on shell region is given by [6]:

$$k \cdot \frac{\mathrm{d}(T)}{\mathrm{d}n} = -\Phi_H - h \cdot (T - T_a) - \varepsilon \cdot (T^4 - T_a{}^4) \tag{5}$$

where: k - thermal conductivity ($W \cdot m^{-1} K^{-1}$), Φ_H - thermal flux from the outside (W/m^2), h - convection exchange coefficient ($W \cdot m^{-2} K^{-1}$), ε - radiation exchange coefficient, T – temperature of object (K), T_a - ambient temperature (K).

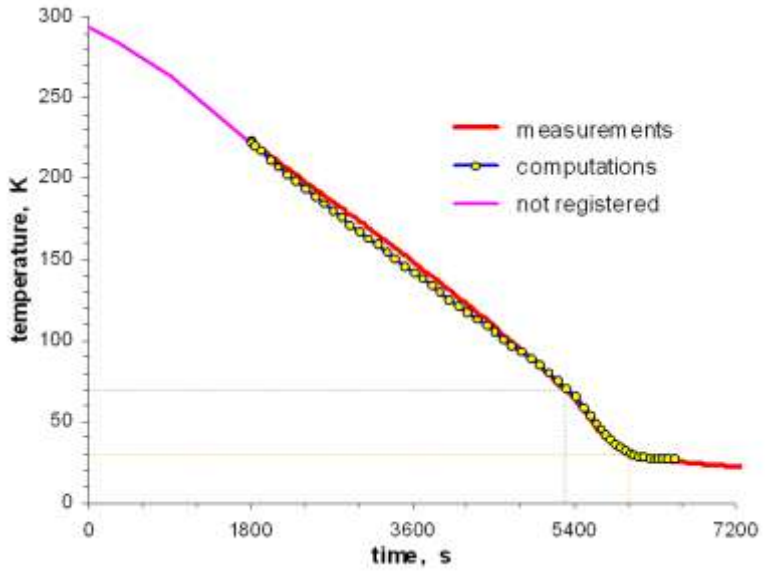

Fig. 17. Measured and computed temperature of Nb-Ti magnet

Heat flows from Nb-Ti coils to II stage of SRDK-408 through mandrel by conduction and radiates from shell region to thermal shield. The direction of heat radiation depends on gradient of temperature between shell region and thermal shield. Due to higher cooling power, the I stage and connected to it thermal shield are cooled down faster than II stage in the initial period of cooling process [8][1][7]. After about half an hour the II stage starts to

be colder than thermal shield and the heat radiates from it to magnet. Thermal source density of II stage and thermal flux from shell region are defined in USRPWD subroutine. USRPWD subroutine has 7 parameters [1] to define properly advanced temperature dependence of source density and thermal flux basing on scanty data of cooling power of SRDK-408 [9] and on experimental results [8][1][7].

Figure 17 presents temperature of Nb-Ti magnet, measured and computed in place shown in Fig. 13 and in Fig. 16. Experimental and computational results show good correlation of temperature during cooling process of Nb-Ti magnet. The increase of cooling speed between 70 K and 30 K (from 5300 s to 6000 s), in spite of decreasing cooling power, is caused by negative derivative of thermal conductivity (Fig. 1). When this negative derivative of thermal conductivity appears during computation, the solver of FLUX2D starts to increase the computation step uncontrollably and generate computation error. It is necessary to set proper computation parameters to solve this problem. After interruption, the computation was started with step = 1 s and limitation for step = 10 s.

4. SUMMARY

FLUX2D is a CAD program using the Finite Element Method for analysing electromagnetic and thermal phenomena. The paper shows how to calculate the temperature distribution in two superconducting devices with axisymmetrical geometry: force-cooled currant lead and contact-cooled Nb-Ti magnet. Lack or insufficient data are the main reason of difficulty in defining thermal properties and parameters of thermal sources of calculation regions. Due to very complicated temperature dependences of superconducting device parameters in very low temperatures, the adequate user subroutines and advance programming in FORTRAN were used for defining them. Numerical model of force-cooled current lead was made using electro-thermal module of FLUX2D which is the coupling of an electric conduction module with a transient thermal module. The force-cooling process has been modelled indirectly by multi-parametric subroutine USRAMB that defines ambient temperature versus temperature of object and axial coordinate. The electric resistivity dependence on current density and magnetic field has been taken into account in calculation, indirectly, by modification of USRSIG subroutine for every change of current in region.

Numerical model of contact-cooled Nb-Ti magnet was made using transient thermal module of FLUX2D. Physical properties were defined by 2-parametric subroutines USRKTH and USRRCP with winding package factor. Thermal source density and thermal flux to SRDK 408 were defined by multi-parametric USRPWD subroutine. Computation error due to negative derivative of thermal conductivity can be eliminated by proper computation parameters in FLUX2D solver. The computational results of numerical model of contact-cooling process of Nb-Ti magnet are convergent to experimental results.

The experimental results show that 4,2 K can be reached (using SRDK-408) after 5100 s when cooled object is very small [1][7][8]. Nb-Ti magnet (1,46 kg) needs about 20 600 s (5 h 43 min 20 s) to superconducting transition but only 5300 s to reach 70 K and next 700 s to reach 30 K. Below 30 K cooling process starts to be very slow. The fast reach of 30 K can be very useful in case of HTS magnets.

REFERENCES

[1] S. Kozak, “Numerical model of superconducting magnet of contact cooling process,” PRZEGLAD ELEKTROTECHNICZNY, no. 9, pp. 629-633, 2003.

[2] E. J. Kazowskij, Superconducting Magnet Systems, NAUKA, Leningrad, 1967.

[3] Russel B. Scott, Technika niskich temperatur, WNT, Warszaw, 1963.

[4] S. Kozak, „FLUX2D for current leads of superconducting device calculations”, ELMECO’97 Conference Proceedings, pp. 155-160, 1997.

[5] S. Kozak, "Current leads of superconducting device calculations", PROCEEDINGS OF 22nd IC-SPETO’99, pp.133-136, 1999.

[6] User’s Guide, CAD Package for electromagnetic and Thermal Analysis using Finite Elements, FLUX2D Version 7.20, CEDRAT, 1996.

[7] S. Kozak, "Superconducting magnets for OGMS type separators," PROCEEDINGS OF ELECTROTECHNICAL INSTITUTE, zeszyt 206, pp. 93-133, 2000.

[8] T. Janowski, B. Kondratowicz-Kucewicz, S. Kozak, H. Malinowski, G. Wojtasiewicz, “Measurement of critical parameters of superconducting devices", ELMECO 2000 Conference Proceedings, pp. 190-194, 2000.

[9] OPERATION MANUAL, SRDK-408, COLD HEAD: MODEL RDK-408, COMPRESSOR: MODEL CSW-71D, Sumitomo Heavy Industry, Ltd., 1998.

4th International Conference **ELMECO**
Nałęczów, Poland
September 2003

CCD CAMERA IMAGING OF PROPAGATION AND BRANCHING OF DC POSITIVE CORONA DISCHARGES

Jerzy MIZERACZYK[1], Seiji KANAZAWA[2], Toshikazu OHKUBO[2]

[1] *Centre for Plasma and Laser Engineering, Institute of Fluid Flow Machinery, Polish Academy of Sciences, Fiszera 14, 80-231 Gdańsk, Poland*
e-mail: jmiz@imp.gda.pl

[2] *Department for Electrical and Electronic Engineering, Faculty of Engineering, Oita University, 700 Dannoharu, Oita, Japan 870-1192*

Abstract ~~**dlaczego poniższy text jest węższy?**~~

Corona discharges in relatively short gaps regained their importance due to numerous new applications in plasma processing of gases, liquids and surfaces. Because of the complexity of the corona discharge plasma, the applications of the corona discharges are mainly based on empirical knowledge. This imposes a demand of new investigations for better understanding the fundamentals of the filamentary discharges. In this contribution, such properties as propagation and branching of the positive DC corona discharges in short gaps in air or NO/air mixtures are described, basing on the observation of corona discharges with an intensified CCD camera having high resolution in space and time. The discharge gap was either a needle-to-plate or nozzle-to-plate. The knowledge of the corona discharger propagation and branching is important for the application of the corona discharges to processing gases of large volumes.

~~*dlaczego keywords jest szerszy?*~~

Keywords: filamentary discharge, corona discharge, non-equilibrium plasma, plasma diagnostics, discharge visualization, CCD camera, plasma chemistry.

~~1.~~1. INTRODUCTION

Sformatowane: Punktory i numeracja

Recently the filamentary discharges, such as dielectric-barrier discharges (DBDs) and corona discharges once more became of high interest because of their new applications in industry. During the last 20 years the corona discharges became of interest because of their potential to be utilized in new technologies for the plasmo-chemical treatment of gases and liquids (for example, for the removal of SO_2 and NO_x from flue gases, destruction of other hazardous gaseous pollutants, and conversion of hydrocarbons) [1-9]. However, the progress in the implementation of corona discharges for environmental purposes is

slow. This is mainly caused by the poor understanding of corona discharges in spite of almost 100-year history of the investigation of the filamentary discharges, including the corona discharges (for example, see [10-14]). The poor understanding of corona discharges is due to the complexity of physical and chemical phenomena, which occur in the spatially and temporally complex plasma of corona discharges. These phenomena could not be studied with the required spatial and temporal resolution due to the lack of the appropriate equipment. Recent progress in the development of Charge Coupled Device (CCD) cameras, imaging spectrographs and fast digital image processing has made the investigation of the filamentary discharges possible with higher sensitivity and spatial and temporal resolution than ever. In this paper the recent results on the visualization of DC positive corona discharges with advanced CCD cameras are presented.

~~2.~~2. BASIC PROPERTIES OF CORONA DISCHARGES

Sformatowane: Punktory i numeracja

Corona discharges belong to a group of transient non-thermal plasma discharges. The existence of the transient discharge depends on the space charge movement in the electric field. If this movement stops for some reason then the space charge diffuses and recombines, the current goes to zero and eventually the discharge extinguishes. Therefore it is called a transient discharge.

Various aspects of the transient discharges, including coronas were described in standard books on gas discharges and plasma physics (e.g. [10-14]). The present view on the physics of the corona discharges is given in ([7], pages 5-21). Here only the basic properties of the corona discharges are briefly outlined.

The corona discharge designation refers to the polarity (positive or negative) of the voltage applied to the highly stressed electrode (also called the discharge electrode) in the electrode arrangement, and to the type of the applied voltage (DC, AC or pulsed). Also the corona discharges are distinguished referring to their length, which can be from micrometers to tens of meters. In this paper we deal with DC or pulsed corona discharges of positive or negative polarity in the electrode arrangement of size of several centimeters, which is of importance from the application point of view.

Several electrode arrangements are used to generate corona discharges. They are point-to-plane, nozzle-to-plane, sphere-to-plane, wire-to-cylinder, wire-to-plane, sharp edge-to-plane, etc. In the DC corona discharges the applied voltage is up to several tens of kV, and the current per corona discharge pulse is up to several tens of mA. In the case of pulsed corona discharges, the amplitude of applied voltage is several tens of kV, the amplitude of the discharge current pulse is several A. In both cases the discharge pulse duration is in the range of 20-500 ns. The values given above are approximate; in a particular case they may differ significantly from those given above. However, generally the current of the pulsed corona discharge is much higher that the DC case.

The corona discharges can have the form of avalanches, bursts, burst pulses, glows, streamers, and secondary streamers ([12], pages 319-383). The type of the corona discharge, which develops in the gap between the electrodes depends on the electrode geometry, applied voltage and working gas. Here we deal with streamer corona discharges.

A streamer is a well developed corona discharge, which consists of the space charge region formed by positive ions (in the number of 10^8-10^9), called the streamer head, propagating through the working gas towards the cathode, and of the quasi-neutral channel (called the streamer channel), which is formed on the track passed by the streamer head. The streamer head, difficult to be observed, is believed to be a disk of a diameter and

thickness of 200 μm and 20 μm, respectively [15-17]. The streamer head velocity is 10^5-10^6 m/s [17, 18].

Several conditions have to be fulfilled to develop a corona into a streamer. To incept a streamer the applied field strength has to be higher than the so-called inception (or critical) field strength, and a certain path on the way towards the anode, called the inception (or critical) distance, has to be available to develop the streamer. The inception field strength in air is about 30 kV cm^{-1} [12] and the inception distance is a fraction of a millimeter. Even if both of these conditions are met, the streamer may not start. This stochastic nature of the corona streamer is described by the inception probability. Even if the inception probability is one, the development of an corona avalanche into a streamer needs a time, called the inception time-lag, which is relatively long and has a stochastic uncertainty, called the inception time-lag jitter. The typical time-lag ranges from 0 to 400 ns, depending on the discharge conditions and power suppliers [17], see also 5.1.

Another important parameter of the streamer is the maximum field strength. The highest field strength, which can be built around the streamer head by the space charge is called the maximum field strength. Its value is limited by electrostatic repulsion of the positive ion charges in the streamer head, which hinders unlimited increase of the space charge in the streamer head. According to [17], the value of the maximum field strength in air can be estimated to be 520 ± 60 Td, which is equivalent to about 170 kV cm^{-1}. This corresponds to the average electron energy of the order of 5-10 eV, which was confirmed also experimentally [19, 20].

Once developed the streamer can propagate in an electric field, which strength is much lower than that necessary for its inception. The lowest applied field strength that permits the streamer propagation is called the stability field strength. It was shown theoretically that the electric field strength inside the streamer channel is equal to the stability field ([7], pages 21-48, [15]). The stability field strength in air is 5 kV/cm [21].

Another inherent property of the corona streamer is its branching. A sufficiently large streamer head may split in parts, propagating further as several almost independent streamers. The branching process may repeat several times on the pathway of the streamer corona discharge to the cathode. The branching depends on the electrode configuration, the gas composition and the power supplier in the case of the pulsed corona [17].

~~3.~~3. A BRIEF OVERVIEW OF THE DIAGNOSTICS OF CORONA DISCHARGES

Sformatowane: Punktory i numeracja

Comprehensive experimental investigations of corona discharges were carried out during the last century. They concerned such aspects~~in~~ of the corona discharge as current-voltage characteristics, neutral and charged particle interactions, dynamics of the neutral and charged particles, and branching and propagation of the streamers. Various diagnostics methods were used for these investigations. The reader is referred to the standard books [10-14]. In this section only the optical methods that were used for the corona discharge visualization are briefly surveyed.

Besides the useful but qualitative way of observing the corona discharge with eyes, photography was very early employed as a method of imaging these discharges. Very interesting images of corona discharges, known as Lichtenberg figures can be found in [10, 11]. The early imaging of corona discharges by photography were imprecise, due to long exposure time, to be useful in the studies of corona discharges that are inherently spatially and temporally transient. At that time more details on the development of the electron

avalanche into the corona discharge delivered a measurement in which a cloud chamber was used [22]. Using the cloud chamber made the imaging of the avalanche shape possible.

The methods to record the discharge images with nanosecond time resolution and relatively good spatial resolution are streak and Schlieren photography. The early investigations of the corona discharges using streak photography are presented in [23, 24]. Recent results on the visualization of the distribution of streamers in the pulsed corona using Schlieren photography are shown in [20].

The essential progress in the~~temporal resolution~~ time-resolved observation of the corona streamer properties was made when a photo-multiplier was employed as a light detector. In combination with a multi-channel analyzer it offered sub-nanosecond resolution, which was sufficient to determine streamer velocity and observe streamer propagation [25].

A new possibility in the high spatially and temporally ~~resolution~~resolved visualization of the corona discharges appeared when Charge Couple Device (CCD) cameras were introduced. The method of the corona discharge visualization using CCD cameras is described in the following chapters.

The advanced CCD cameras also contributed to the development of cross-correlation spectroscopy (CCS), which became a powerful tool to analyze the spatially and temporally resolved structure of the filamentary discharges [41].

~~4.~~4. CCD CAMERA VISUALIZATION OF CORONA DISCHARGES

Sformatowane: Punktory i numeracja

Recent technological progress in the development of intensified Charge Coupled Device (ICCD) cameras, imaging spectrographs and fast digital image processing has made visualization of complex gas discharges possible with higher sensitivity and space and time resolution than ever. In particular, it concerns the visualization of the transient filamentary discharges, like DBDs and corona discharges.

The modern ICCD cameras enable recording two-dimensional images of the transient discharges with high spatial and time resolution. The high spatial resolution is obtained owing to the high sensitive small pixel elements of the CCD. The nowadays ICCD cameras have several hundred x several hundred (horizontal x vertical) pixels with a pixel area of about 20 μm x 20 μm. Therefore the spatial resolution of the image is of that order [~~(~~the spatial resolution of the photographed object (e.g., of a discharge) depends on the magnification of the optics, which projects the object on the CCD element]. The high temporal resolution is a result of the image intensifier placed in the front of the CCD element, which operates as a fast shutter, yielding ~~an opening or~~(exposure) a time of the order of 1 nanosecond in more sophisticated ICCD cameras. Another advantage of the ICCD cameras is linearity of the dependence: output signal-input signal in a high dynamic range (more than 12 bits). This is very important in cases when the light emitted by the discharge changes considerably in time and space, as in the transient DBDs and corona discharges.

For the temporally resolved imaging of corona discharges the synchronisation of the discharge pulse and the opening of the ICCD camera (~~starting~~i.e. gate start and exposure time~~s~~) is a crucial point. The synchronization techniques have to be somewhat different for the DC corona discharges and pulsed corona discharges because of their different features. The DC corona discharge consists of more of less regular self-repetitive current pulses with a pulse duration up to several hundred nanoseconds and repetition frequency in the range of 1 to 100 kHz. When the DC voltage is high enough, the inception

probability of each DC corona current pulse is one. However, the inception time-lag of the DC corona current pulse has a jitter. The pulsed corona can ~~also~~ consists of current pulses, however each of them is triggered by an external pulsed power supply. When the triggering voltage pulse is high enough, the inception probability of the pulsed corona is one, but still the jittering of the inception time of the corona pulse exists. The repetition rate of the externally triggered corona pulses is controlled by the power supply. It reaches up to 1000 Hz. The pulse duration depends on the power supply and varies from several tens of nanoseconds to several hundred nanoseconds.

In order to perform a temporally resolved imaging of the transient discharge, a reference time must be assigned to the characteristic event related to the discharge, e.g. related to the inception of the current pulse. This reference time is required to establish the delay of the imaging (the moment of opening of the ICCD camera ~~gate~~) with respect to the characteristic event, and then to be able to trace the time evolution of the discharge ~~over~~ during the exposure time of the ICCD camera. Performing a temporally resolved imaging, the procedure consists in repeated image acquisition with the incremented delay between consecutive acquisitions. Such a procedure of scanning the time delay between the event and the image is known as Boxcar scanning. Using the Boxcar scanning, the time evolution of the discharge can be revealed.

The inception of the corona current pulse is commonly accepted as the most convenient characteristic event in both DC and pulsed coronas. However, as mentioned above, the inception of the DC corona current pulse is an uncontrolled stochastic process, while the inception of the pulsed corona is more or less (due to the inception time-lag jittering) controlled by the pulsed power supply. This makes the synchronization of Boxcar scanning easier in the case of the pulsed coronas.

In the pulsed coronas, a comprehensive spatial and temporal visualization of the corona current pulse using modern high sensitive and nanosecond-fast CCD cameras was carried out by the group of Eindhoven University of Technology. The reader is referred to the publications [7, 17, 20, 26-29].

Below the recent progress in the visualization of the DC corona current pulses is presented.

5. CCD CAMERA VISUALIZATION OF DC POSITIVE CORONA DISCHARGES

Laser triggering of the DC positive corona streamer

To control the inception time of the DC positive corona current pulse, a technique for the controlled inception of a DC corona pulse by an UV laser beam was developed [30-32]. As mentioned, the DC positive corona discharge is a train of more of less regular self-repetitive current pulses occurring between the electrode gap. However, when an UV laser beam pulse (of a pulse duration of about 20 ns) is shot between the electrode gap (Fig. 1), an additional corona current pulse is induced (Fig. 2). The laser induced corona pulse starts about 3~~5~~0-300 ns after the laser pulse, depending on the position of the laser beam in the gap, and it lasts over about 350 ns. At an appropriate position of the laser beam in the discharge gap the inception probability of the induced streamer is one and the inception time has a small jittering [33, 34]. Due to it, the image of the corona pulse can be recorded with high temporal resolution using an ICCD camera with an appropriate adjusted recording ~~gate~~ delay gate start and exposure time. The recording delay adjustment is related

to the UV laser beam pulse which plays a role of the characteristic event. Using the Boxcar scanning procedure, the time evolution of the discharge pulse can be revealed.

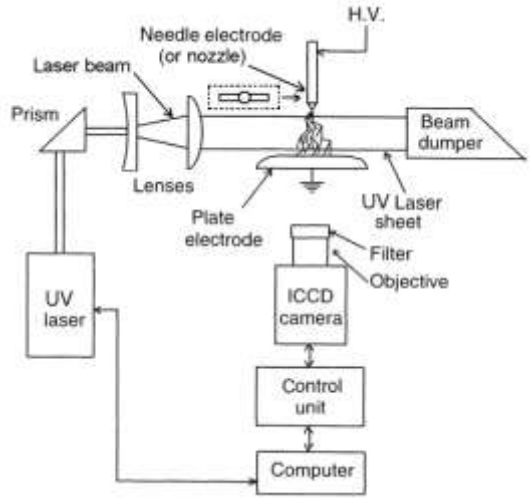

Fig. 1. Setup with an ICCD camera for generation and observation of the laser-induced DC positive corona streamers.

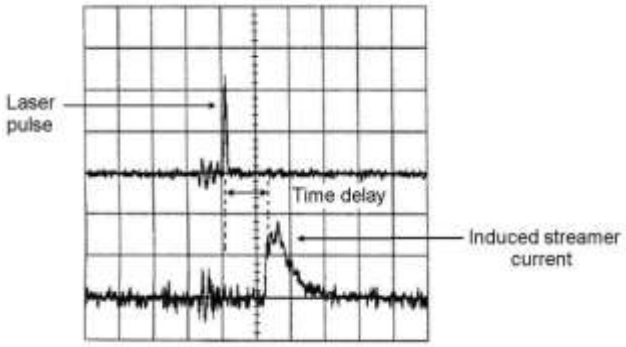

Fig. 2. Time relationship between the laser beam shot and the induced DC positive corona streamer in a needle-to-plate discharge gap in air. Laser beam wavelength λ=226 nm, laser beam pulse energy 13 mJ, gap 30 mm, DC positive voltage 25 kV, time scale 200 ns/div., current scale 20 mA/div., [34].

In the Boxcar scanning, it is important to deal with the repetitive corona current pulses of the same spatial and temporal characteristics. It was found out that the laser induced DC corona current pulses met this requirement with very high statistical probability [33, 34].

In contrast with positive coronas, no laser-induced streamer discharge was obtained for negative coronas [33, 34], probably due to difference in the behaviour of electrons in both discharges.

DC corona streamer propagation in a needle-to-plate electrode gap

Fig. 3 shows images of the streamers induced by a UV laser beam pulse of an energy of about 13 mJ~~in air~~ in a needle-to-plate electrode gap (30 mm) in air. The DC positive voltage applied to the needle electrode was 25 kV. Each subsequent photo shows an image of the streamer recorded ~~with the ICCD camera~~with an exposure time~~(gate time)~~ longer than the previous. In each case the ICCD camera was opened when the streamer started. Because of the good reproducibility of the laser-induced streamers, the images shown in Fig. 3 show time evolution of the positive corona streamer and its branching and propagation in the ~~gap~~gas.

The images showing the time evolution of the DC positive streamer in Fig. 3 may mislead the reader, who may get an impression that at a given time (e.g., at 180 ns after the streamer inception) the streamer looks as the Fig. 3e shows. First of all, the ICCD camera records the relatively intense light emitted by the streamer head, the high-energy front part of the streamer. On the other hand, usually the ICCD camera ~~usually does not~~ is not able to record the faint light emitted by the streamer channel that forms behind the streamer head. This means that the ICCD camera records the movements of the streamer head only, or in other words, the ICCD camera records the image of the streamer head pathway, which it "sees" over its exposure time. Therefore, the Fig. 3e is a record of the streamer head evolution from its inception to the moment when it reaches the plate electrode, bridging the gap, i.e. during 180 ns. We may call the images presented in Fig. 3 as "the time evolution of the streamer head integrated over the ICCD camera exposure time".

Fast ICCD cameras, however, give a possibility to record the image of the streamer head at a given time with a temporal resolution of about one nanosecond. Fig. 4 shows different stages of the DC positive corona development on his movement from the needle electrode to plate electrode in several consecutive time intervals. Because the light emitted by an individual streamer is very faint, each image is a result of accumulation of 30 images of the individual streamers, observed with the ICCD camera with fixed both the exposure time (20 ns) and delay between the streamer inception and the opening of the ICCD camera gate. Each next image in Fig. 4 was taken for the ~~consecutive~~subsequent time interval. Since the laser-induced streamers are alike in appearance, the accumulation of 30 their images reflects the actual steamer appearance. ~~the more the more the streamers are alike.~~

It is seen from Fig. 4 that the DC positive corona takes the form of a number of streamer heads, moving simultaneously through the gas. The number of heads increases during the propagation, which corresponds to the branching shown in Fig. 3. Since the exposure time was 20 ns, each image shows the pathway the streamer head passed during 20 ns. The shape of the streamer head could not be resolved in this experiment; for that a much shorter exposure time is needed.

The time evolution of the DC positive corona streamers shown in Figs. 3 and 4 makes the determination of the propagation velocity of the streamer head averaged over the exposure time (or corresponding streamer head pathway) possible. From Fig. 3 it can be found that the velocity of the streamer head propagation, averaged over the gap distance, is about $(2.5\text{-}3)\times10^5$ m/s. This is in a good agreement with the value measured with a photomultiplier in [18]. Using a shorter exposure time interval~~s~~ it is possible to scan

the velocity of the streamer along its trip from the needle to plate electrode (also in the lateral direction).

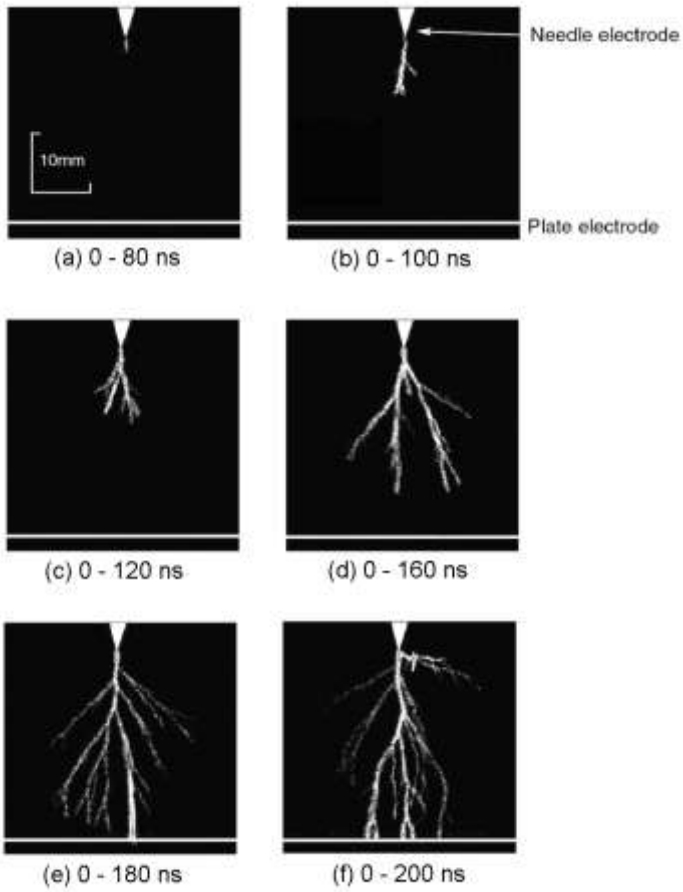

Fig. 3. Time evolution of a DC positive corona streamer in a needle-to-plate electrode gap in air ([33, 34], see also [31, 32, 35]). Laser beam wavelength λ = 226 nm, laser beam pulse energy 13 mJ, gap 30 mm, DC positive voltage 25 kV. Each image is a result of a single shot.

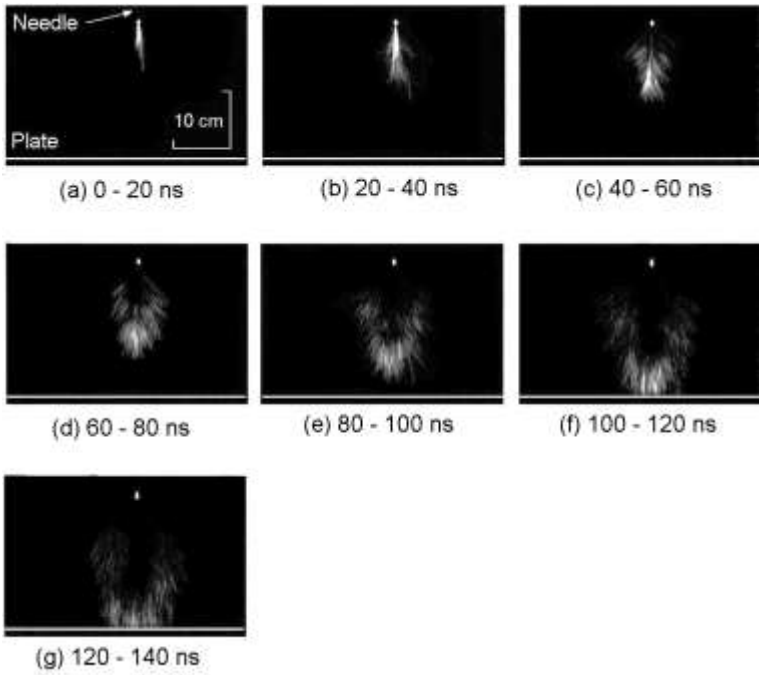

Fig. 4. DC positive corona streamer head development in consecutive time intervals (of 20 ns duration) in a needle-to-plate electrode gap in air [32, 35]. Laser beam wavelength λ = 226 nm, laser beam pulse energy 23 mJ, gap 30 mm, DC positive voltage 23 kV. Each image is an accumulation of 30 individual images.

Fig. 4 reveals an interesting feature of the DC positive corona streamer. The streamer heads emit light, whereby they are seen, or at least recorded by ICCD cameras. On the contrary, the streamer channels behind the streamer heads are dark, and thus invisible. However, a glow around the needle tip is seen over the life-time of the corona streamer, i.e. from its inception to the moment it bridges the gap. The nature of this glow is not clear.

The ICCD images make determination of the averaged streamer diameter possible. The average diameter of the streamers shown in Fig. 3 is about 150 μm. This is in agreement with other measurements [17, 27].

DC corona streamer propagation in a nozzle-to plate electrode gap

Recently, a corona radical shower discharge has been proved to be one of the most efficient non-thermal plasmas for NO_x removal., ~~which~~ Such a discharge is suitable for the retrofit of the existing electrostatic precipitators [9]. In the corona radical shower discharge reactor, the discharge electrode with one or several nozzles is used for injection of an

additional gas across the corona discharge zone into the flue gas [36-38]. The other electrodes (grounded) are plates. Therefore, the shape of the discharge in such a nozzle-to-plate electrode geometry is much complex than that of the conventional electrode arrangement, such as needle-to plate or wire-to-plate. The control of parameters of the streamer corona discharge in the nozzle-to-plate electrode arrangement is a key issue to obtain plasma suitable~~in the nozzle-to-plate electrode arrangement~~ for NO_x removal from the flue gas. Visualization of the corona discharges with an ICCD camera ~~became~~ is an important tool for studying the parameters of the streamer corona in that electrode arrangement.

Sformatowano

Sformatowano

Fig. 5 shows images (front and side view) of the DC positive corona streamers in a nozzle-to-plate electrode gap (50 mm) in NO (200 ppm)/air mixture taken with the ICCD camera with a long exposure time (0.6 ms). As seen, the streamers consist~~s~~ of several branches, propagating from the tip of the nozzle electrode to the plate electrodes. The plasma formed by the streamers looks like a flame when observed with the naked-eye or when photographed with a long exposure time, as in Fig. 5.

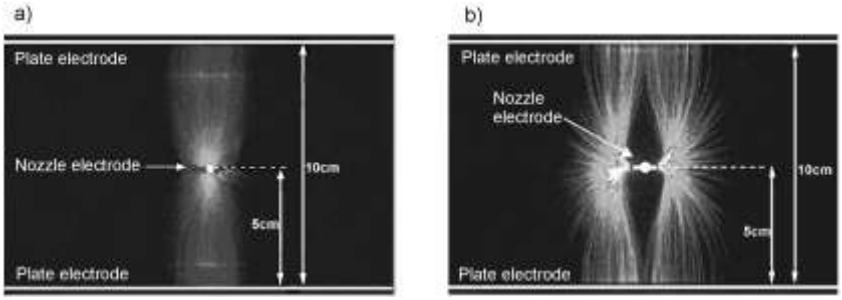

Fig. 5. Images of DC positive corona streamers in a nozzle-to-plate electrode gap in NO(200 ppm)/air mixture taken with a long exposure time (0.6 ms): (a) front view and (b) side view. Gap 50 mm, DC positive voltage 27 kV, time-averaged current 0.1 mA. Each image is an average of 100 images [39].

Fig. 6 shows images (side view) of the DC positive corona streamers ~~in NO(100 ppm)/air mixture~~ in the nozzle-to-plate electrode gap in NO(100 ppm)/air mixture taken with the ICCD camera with a long exposure time (0.6 ms) for various operating voltages. As it is seen, the area occupied by the streamers increases with increasing voltage (and corresponding increase of the discharge current). At low voltages (< 22 kV) relatively short streamers of similar length are formed around the nozzles. With increasing voltage the length of the streamers developed in the direction of the plate electrodes becomes longer than those directed parallel to the plates. The plate-directed streamers bridge the gap at voltages higher than 24 kV. A well developed streamer corona occurs at voltages higher than 30 kV.

Fig. 7 shows the time evolution of the DC positive streamer corona in ~~a~~the nozzle-to-plate electrode gap (50 mm) in NO(100 ppm)/air mixture. The positive voltage applied to the nozzle electrode was 30 kV, which was sufficient to get the bridged corona streamer (see Figs. 7e and 7f). In each subsequent image the exposure time of the ICCD camera is longer than in the previous. The ICCD camera was opened when the streamer started.

The images in Fig. 3 clearly show the evolution, branching and propagation of the positive corona streamer in the gap, "integrated over the ICCD camera exposure time".

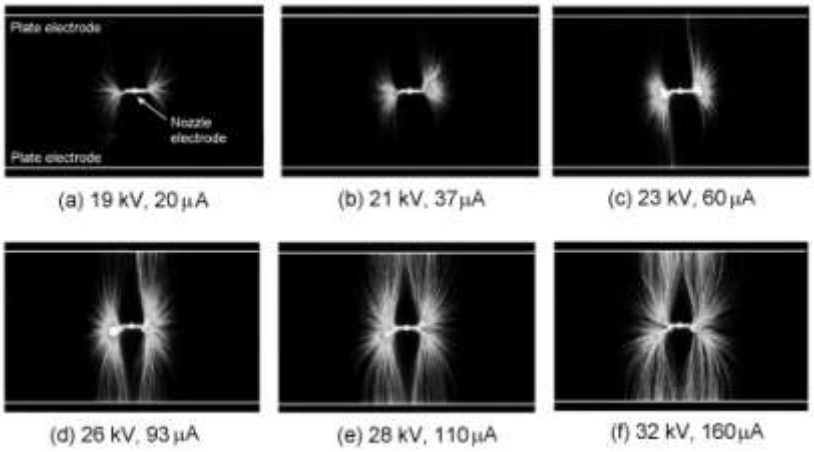

Fig. 6. Images (side view) of DC positive corona streamers ~~in NO(100 ppm)/air mixture~~ in a nozzle-to-plate electrode gap (50 mm) in NO(100ppm)/air mixture taken with a long exposure time (0.6 ms) for various operating voltages. Each image is an average of 100 images.

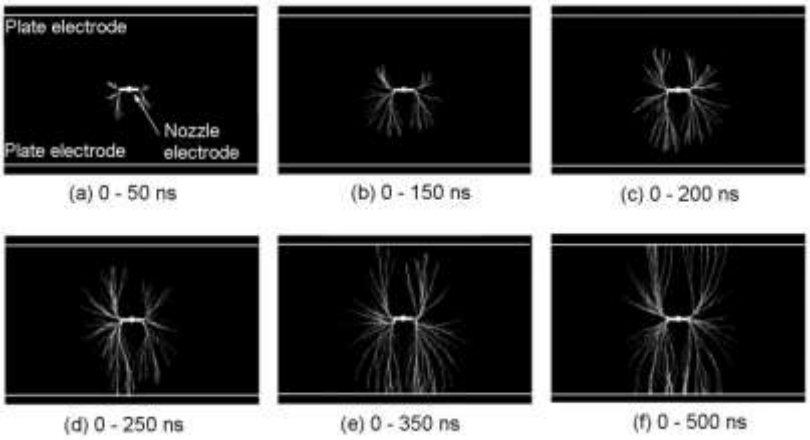

Fig. 7. Time evolution of DC positive corona streamer in a nozzle-to-plate electrode gap in NO(100 ppm)/air mixture [40]. Laser beam wavelength λ = 226 nm, laser beam pulse energy 13 mJ, gap~~nozzle-plate~~ 50 mm, DC positive voltage 30 kV, time-averaged current 134 μA. Each image is a result of a single shot [40].

Fig. 8 shows different stages of the DC positive corona streamer head development on ~~his~~ its movement from the nozzle to the plate electrode in NO(100 ppm)/air mixture in several consecutive time intervals (duration 50 ns). The operating voltage was 30 kV. Because the light emitted by the streamer head is very faint, each image is a result of accumulation of 100 images of the individual streamers, observed with the ICCD camera with an exposure time fixed at 50 ns. Since the laser-induced streamers are alike in appearance, the accumulation of 100 their images reflects the actual steamer appearance.

As in the needle-to-plate electrode geometry, the DC positive corona shown in Fig. 8 takes the form of a number of streamer heads, moving simultaneously through the gas. The number of heads increases during the propagation, which corresponds to the branching shown in Figs. 6 and 7. Since the exposure time was 50 ns, each image shows the pathways the streamer heads passed during 50 ns.

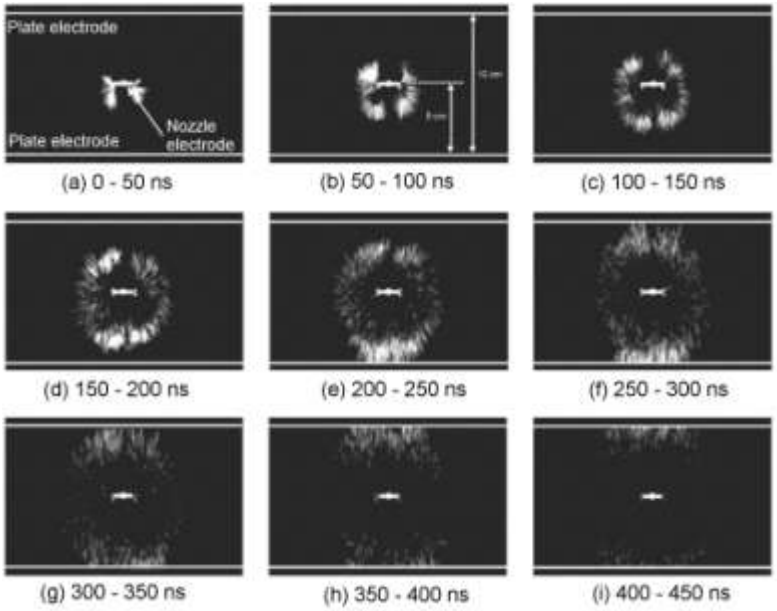

Fig. 8. DC positive corona streamer head development in consecutive time intervals (~~of~~ 50 ns duration) in a nozzle-to-plate electrode gap in NO(100 ppm)/air mixture. Laser beam wavelength λ = 226 nm, laser beam pulse energy 13 mJ, gap 50 mm, DC positive voltage 30 kV, time-averaged current 134 μA. Each image is an average of 100 images taken with the ICCD camera.

It can be found from Fig. 8 that the streamers directed towards the plate electrode (so-called vertical streamers) are faster than those moving parallel to the plates (lateral streamers). Besides, the velocity of both of the streamers is not constant along their pathways. At 30 kV, the velocity of the vertical streamers changes from about 3.5×10^5 m/s at the nozzle (the first 50 ns) to about $(1.3\text{-}1.5)\times10^5$ m/s in the middle of the gap (time period of 50-150 ns) and at the plate electrode (200-250 ns). The vertical streamer velocity

averaged over the distance from the nozzle to the plate electrode is 2.5×10^5 m/s, as that found for the streamer in the needle-to-plate gap. The velocity of the lateral streamers changes from about 1.7×10^5 m/s in the first 50 ns (at the nozzle), through about 1.3×10^5 m/s in the time period of 50-200 ns, to $(0.4\text{-}0.5)\times10^5$ m/s at 200 – 300 ns, i.e. when the corona extinguishes after bridging the gap.

Also Figs. 7 and 8 ~~s~~show the presence of the glows around the nozzle tip over the life-time of the corona streamer, i.e. from its inception to the moment it bridges the gap, similarly as in Fig. 4 for the needle-to plate geometry.

The average diameter of the streamers in the nozzle-to-plate electrode geometry found from Figs. 7 and 8 is about 150 μm. This is in agreement with that found for the streamers in the needle-to-plate electrode gap.

6. SUMMARY AND CONCLUSIONS

Recent progress in the development of ICCD cameras, imaging spectrographs and fast digital image processing has made visualization of complex gas discharges, like DBDs and corona discharges, possible with higher sensitivity and space and time resolution than ever.

In order to perform a temporally resolved imaging of the corona discharge, the corona inception time has been assigned as a reference time to establish the delay of the imaging to be able to trace the time evolution of the discharge over the opening time of the ICCD gate. To control the inception time of the DC positive corona current pulse, a technique for the controlled inception of a DC positive corona current pulse by an UV laser beam was developed. When an UV laser beam pulse (of a pulse duration of about 20 ns) is shot between the electrode gap, an additional corona pulse is induced with an inception probability of one. The inception time of the laser induced streamer has a small jittering. Due to it, the image of the corona pulse can be recorded with high temporal resolution using an ICCD camera with an appropriate adjusted recording delay and exposure time.

Using this visualization technique, the DC positive corona streamer propagation in the needle-to-plate and nozzle-to-plate electrode gaps in air or NO/air mixtures was investigated with high resolution in space and time. The obtained images showed the time evolution of the DC positive streamer and different stages of the streamer development on its pathway from the needle or nozzle electrode to the plate electrode in several consecutive time intervals. The ICCD camera images clearly showed the branching of the corona streamers.

The time evolution of the DC positive streamer~~s~~ made the determination of the propagation velocity of the streamer head averaged over the exposure time (or corresponding streamer head pathway) possible. The average velocity of the streamer head propagation is about (2.5-3) x 10^5 m/s. This is in agreement with other measurements.

In the case of the nozzle-to-plate geometry it was found that the streamers directed towards the plate electrode (~~so called~~ vertical streamers) are faster than those moving parallel to the plates (lateral streamers). In both cases the velocity of the streamers is not constant along their pathways.

The ICCD images revealed an interesting feature of the DC positive streamer corona, i.e. a glow around the needle (or nozzle) tip during the life-time of the corona streamer, i.e. from its inception to the moment it bridges the gap. The nature of this glow is not clear.

The ICCD images made determination of the averaged streamer diameter possible. The average diameter of the streamer is about 150 μm. This is in agreement with other measurements.

The presented results showed that the visualization with ICCD cameras of higher sensitivity and space and time resolution than ever offers unprecedented way of displaying the transient discharges. In particular, using sensitive ICCD cameras with a super fast optical shutter (the gate below 1 ns) would make the investigation of these discharges possible in detail. For example, the experimental study of the shape of the streamer head is of high interest. However, for that purpose a three-dimensional measurements are needed. The three-dimensional measurements are also required for a better understanding of the streamer propagation and branching.

ACKNOWLEDGEMENTS

This research was carried out under the joint Japanese-Polish Project sponsored by the Japan Society for the Promotion of Science and the Polish Academy of Sciences. The authors are indebted to Prof. Jen-Shih Chang of McMaster University, Hamilton, Ontario, Canada for fruitful discussion.

REFERENCES

[1] Chang J.S., Lawless P.A., Yamamoto T., IEEE Trans. Plasma Sci. 1991, 19, 1152-1165
[2] Non-thermal Plasma Techniques for Pollution Control, Eds.: Penetrante B.M., Schultheis S.E., NATO ASI Series G, vol. 34 A and B, Springer, Berlin, 1993
[3] Vercammen K.L.L., Berezin A.A., Lox F., Chang J.S., J. Adv. Oxid. Technol. 1997, 2, 312-329
[4] Plasma Science and the Environment, Eds.: Manheimer W., Sugiyama L.E., Stix Th.H., AIP Press, 1997
[5] Hammer T., Contrib. Plasma Phys. 1999, 39, 441-462
[6] Urashima K., Chang J.S., IEEE Trans. Dielectrics and Electrical Insulation 2000, 7, 602-614
[7] Electrical Discharges for Environmental Purposes: Fundamentals and Applications, Ed.:van Veldhuizen E.M., Nova Science Publishers, Inc., ISBN 1-56072-743-8, 2000
[8] Chang J.S., Science and Technology of Advanced Materials 2001, 2, 571-576
[9] Chang J.S., J. Electrostatics 2003, 57, 273-291
[10] Loeb L.B., Electrical Coronas, Univ. of California Press, 1965
[11] Nasser E., Fundamentals of Gaseous Ionization and Plasma Electronics, Wiley-Interscience, 1971
[12] Meek J.M., Electrical Breakdown of Gases, Wiley Interscience, 1978
[13] Raizer Y.P., Gas Discharges Physics, Springer, Berlin, 1991
[14] Bazelian E.M., Raizer Yu.P., Spark Discharge, MFTI, Moscow, 1997 (in Russian)
[15] Dyakonov M.I., Kachorovskii V.Yu., Sov. Phys. JETP 1988, 94, 321-332 (in Russian)
[16] Kulikovsky A.A., J. Phys. D: Appl. Phys. 1995, 28, 2483-2493 ~~(in Russian)~~
[17] van Veldhuizen E.M., Rutgers W.R., J. Phys. D: Appl. Phys. 2002, 35, 2169–2179
[18] Yan K., Yamamoto S., Kanazawa S., Ohkubo T., Nomoto Y., Chang J.S., J. Electrostatics 1999, 46, 207-219
[19] Spyrou N., Peyrous R., Gibert A., J. Phys. D: Appl. Phys. 1989, 22, 120-128
[20] Creyghton Y.L.M., Pulsed Positive Corona Discharges: Fundamental Study and Application to Flue Gas Treatment, PhD Thesis, Eindhoven University of Technology, 1994
[21] Allen N.L., Ghaffar A., J.Phys.D: Appl. Phys. 1995, 28, 338-343

[22] Reather H., The Development of Electron Avalanche in a Spark Chanell (from Observation in a Cloud Chamber), Zeitschrift für Physik, 112, 464, 1939. (Reproduced in: Electric Breakdown in Gases, Rees J.A., The Macmillan Press, London, 1973, pp. 18-26)
[23] Wagner K.H., Zetschrift für Physik 1966, 189, 465
[24] Wagner K.H., Zetschrift für Physik 1967, 204, 177
[25] Kondo K. Ikuta N., J. Phys. D: Appl. Phys. 1980, 13, L33-L38
[26] Blom P.P.M., High-power ~~p~~Pulsed ~~c~~Corona, PhD Thesis, Eindhoven University of Technology, ISBN 90-386-0250-2, 1997
[27] van Veldhuizen E.M., Baede A.H.F.M., Hayashi D., Rutgers W.R., Proceedings of APP Spring Meeting, ~~(~~Bad Honnef, Germany, ~~February~~2001~~)~~, pp 231–4, 2001
[28] Valette N., Internal Report EPG, Eindhoven University of Technology, 2001
[29] van Veldhuizen E.M., Kemps P.C.M., Rutgers W.R., IEEE Plasma Sci. 2002, 30, 162-163
[30] Mizeraczyk J., Ohkubo T., Kanazawa S., Nomoto Y., Proceedings of 1999 Annual Meeting of the Institute of Electrostatics Japan, Tsudanuma, Japan, 1999, pp. 231-234
[31] Mizeraczyk J., Ohkubo T., Kanazawa S., Nomoto Y., Kawasaki, T. Kocik M., in Laser Technology VI: Applications, Eds.: W.L. Woliński, Z. Jankiewicz, Proc. of SPIE Vol. 4238, pp. 242-245
[32] Ohkubo T., Akamine S., Kanazawa S., Nomoto Y., Mizeraczyk J., Proceedings of the First Polish-Japanese Hakone Group Symposium on Non-thermal Plasma Processing of Water and Air, Sopot, Eds.: J. Mizeraczyk and M. Dors, 2000, pp. 85-88
[33] Kanazawa S., Shuto Y., Ito T., Ohkubo T., Nomoto Y., Mizeraczyk J., Proceedings of the Second Asia-Pacific International Symp. on the Basis and Applications of Plasma Technology, Kaohshiung, Taiwan, 2001, pp.195-200; also in Papers of Technical Meeting on Plasma and Pulse Power, IEE Japan, 2001, pp.75-80
[34] Kanazawa S., Ito T., Shuto Y., Ohkubo T., Nomoto Y., Mizeraczyk J., J. Electrostatics 2002, 55, 343-350
[35] Ohkubo T., Ito T., Shuto Y., Akamine S., Kanazawa S., Nomoto Y., Mizeraczyk J., J. Adv. Oxid. Technol. 2002, 5, 2, 129-134
[36] Ohkubo T., Kanazawa S., Nomoto Y., Chang J. S., Adachi T., IEEE Trans. Ind. Appl. 1994, 30, 856-861
[37] Ohkubo T., Kanazawa S., Nomoto Y., Chang J. S., Adachi T., IEEE Trans. Ind. Appl. 1996, 32, 1058-1062
[38] Kanazawa S., Chang J. S., Round G. F., Sheng G., Ohkubo T., Nomoto Y., Adachi T., J. Electrostatics 1997, 40&41, 651-656
[39] Kanazawa S., Sumi T., Sato N., Ohkubo T., Nomoto Y., Kocik M., Mizeraczyk J., Chang J.S., Wide-range Two-dimensional Imaging of NO Density Profiles by LIF ~~t~~Technique in a Corona Radical Shower Reactor, IEEE Trans. Ind. Appl. 2003 (submitted)
[40] Kanazawa S., Sumi T., Simamoto S., Ohkubo T., Nomoto Y., Kocik M., Mizeraczyk J., Chang J.S., Diagnostics of NO_x Removal Process in a Non-thermal Plasma ~~r~~Reactor: Relationship between Streamer Corona discharge and NO LIF Profile, IEEE Trans. Plasma Sci. 2003 (submitted)
[41] Wagner H.-E., Brandenburg R., Kozlov K.V., Sonnenfeld A., Michel P., Behnke J.F., Vacuum 2003, 71, 417-436